Assessment of Tidal Power Opportunities in Indonesian Waters

Ahmad Mukhlis Firdaus
St Anne’s College
University of Oxford

A thesis submitted for the degree of
Doctor of Philosophy
Trinity 2021

To my parents, my partner and my precious little ones, Alaric and Kayra

Acknowledgements

I would like to thank Prof. Guy Houlsby and Prof. Thomas Adcock for their insight, supervision and encouragement over the course of the DPhil. In particular, Guy, who tirelessly guides and motivates me with the research in the assessment of Indonesian water, for which I am most grateful. I would also like thank to Tom, who kindly help me with all the technical insight on modelling that helps me through the DPhil course. Finally, I am thankful to my examiners, Prof. Jim Hall and Prof. Alistair Borthwick, for reviewing this thesis thoroughly and give valuable input to this thesis writing.

I am grateful for the generous financial support from the Indonesian Endowment Fund for Education (LPDP) for my scholarship and St Anne's College for the Covid hardship fund on my extended year due to the pandemic. I would like to thank Professor Barbara Rossi for giving me the opportunity to work as a graduate teaching assistant at New College in the last two years and ARC Oxford Supercomputing Centre to use their computing resources free of charge to run almost the entire simulations in this thesis.

This thesis would never be possible without help from; Tulio Moreira, Dr Aidan Wimshurst, Steven Ettema, Mohamad Bin Osman, Andrea Schnabl and Bowen Cao. Many thanks for being such helpful friends, especially for helping me with the software troubleshooting, for all the technical discussions we shared, and for invaluable feedback on my work that makes all analyses here are possible. I would also like to thank Toby Balaam and Iona Richard for willingly proofreading my transfer and confirmation reports.

I would also like to thank all colleagues in the Civil Engineering Research Group that were always providing such a warm and friendly working environment. In particular, Vance Tan, Dr Christopher Vogel, Jakub Kewcinsky, Federico Zilic de Arcos, Maria Garcia-Espinosa, Dr Christelle Abadie, Kuen Wei (Wayne), Bohan Chen, Sanjeev, Clive Baker and other colleagues. The lunchtime talks and discussions in Jenkin Room 11 was always joyful.

I would like to thank all Indonesian Societies in Oxford, either in PPI Oxford, OXONIS or the society in general, for all their supports. My appreciation to INNOVATOR 4.0 Indonesia and EuropeNET INOVATOR 4.0 for all discussions that make me have a getaway from exhausting research life, particularly Mas Budiman Sudjatmiko and Mas Teddy Tricahyono, for many opportunities and insight that broaden my knowledge.

I am grateful for the help that given by Raya Surverindo, particularly Pak Iman dan Pak Ratman that help me financially on my departure to Oxford. I would also express my thanks to Rajin Sihombing, Mauludin Dwiyoga and Adrian Firdaus for being such reliable friends, especially during my financial hardship in Oxford. I would also like to thank all of my friends, Kenindra, Paul, Weldy, Icak and all other friends in Sangkuriang Engineering Totalitas that I could not mention one by one, for all their supports.

I would also like to express my gratitude to all Ocean Engineering Program ITB colleagues for their support, particularly Dr Muslim Muin, Dr Krisnaldi Idris, and Dr Irsan Soemantri Brodjonegoro, for writing me the reference letters. I would also like to thank P3GL, particularly Dr Soesilohadi and Bu Ai Yuningsih, for the tidal observation and ADCP data.

I would like to express my gratitude to all my families; my siblings, Ahmad Fatah Muzafar and family, Ahmad Fazal Muqaddim and family, Nusrat Jihan Begum and family; my in-laws, Abah Ukun (Rahmat Syukur Maskawan), Ambu Lia (Alia Chasmira), Ami’s family, Sarah’s family, Azhar’s family, Zahra and Baim for all supports and prayers.

Most importantly, I would like to thank my parents, my late father, dr Sunirwan Ismail (alm), and my mother, Maryam Siddiqah, for their support and inspiration. I would never be able to dream this high without you.

This thesis would not have been possible without the love and support of my life partner, Reihan Hafizah Kautsar. Your love, advice, encouragement and support have made my time in Oxford wonderful. I would like to dedicate this thesis to my precious little ones, Alaric Mattara Firdaus and Azkayra Mirzakhani Kautsar. I understand that you would not be happy if I put this thesis as one of your bedtime reading lists. However, I hope you both will find this thesis could inspire you one day.

Body is purified by water, ego by tears. Intellect is purified by knowledge, and the soul is purified with love. ~Ali ibn Abi Talib~

Abstract

As the world's largest archipelagic country, Indonesia has enormous tidal resource potential. However, complexities that occur in this area complicate tidal resource assessment. The relative magnitude of different tidal components gives this area a variety of tidal types, from semidiurnal, as commonly found in the UK and Canada, to the diurnal type. There are not only daily and neap-spring cycle variations, but also in areas with significant diurnal components the power and thrust varies on an annual basis that follows the timing of the solstice-equinox cycle. These variations mean that an assessment in this region must be carefully planned in terms of the duration and the simulation start time. An assessment with a limited computational time should avoid the solstices and equinoxes in the simulation period.

The interaction between the diurnal and semidiurnal components also creates an asymmetric tidal flow. As the tidal stream moves bi-directionally, the asymmetry leads to uneven power production for flow in different directions. Therefore, turbine developers should consider this phenomenon in their turbine design, as the turbine might have more thrust in one direction. This asymmetry also tends to create a low Capacity Factor (*CF*).

Since the tidal stream varies daily, fortnightly and annually, it would not be practicable for a turbine developer to remove the maximum power from the flow. A capping strategy is necessary to address this issue. *CF* is a metric that is widely used to optimise turbine capacity. However, this thesis argues that *CF* might not be the only metric for decision making. The fraction of average power removed by the turbine and the thrust before and after the capping strategy is implemented are perhaps more important as decision-making tools in tidal energy exploitation.

The assessment of tidal energy resources in Indonesia shows that this country has a great opportunity for tidal energy exploitation. Five potential sites with different characteristics in terms of socio-economic background and environmental features are selected for assessment: Lombok Strait, Larantuka Strait, Sunda Strait, Lingga Regency and Sula Regency. A total of 5 GW average electricity production from just these five selected locations could be produced.

However, that number is based on analyses using a uniform blockage ratio. In reality, the deployment of turbines is limited by several factors, such as the use of straits for other purposes, the depth of the sites and environmental constraints. A study with more realistic turbines is essential for a proper assessment of tidal energy resources in an area. The assessments in this thesis also consider economic constraints. Based on realistic turbine deployment strategies, tidal energy exploitation in this area is economically viable. Apart from in Lingga Regency, the realistic assessments show that all other locations have a projected levelized cost of energy (LCOE) less than GBP 250/MW.

Nomenclature

Chapter 1

A	Turbine swept area
B	Blockage ratio
BPP	[In Bahasa Indonesia] *Biaya Pokok Pembangkitan listrik* (en- electricity generation cost)
BPS	[In Bahasa Indonesia] *Biro Pusat Statistik* (en- central bureau of statistics)
C_T	Thrust coefficient
C_P	Thrust coefficient
i_a - i_f	Doodson's numbers
ITF	Indonesian Throughflow
P	Power

$SAIDI$	System Average Interruption Duration Index
$SAIFI$	System Average Interruption Frequency Index
$SCSF$	South China Sea Flow
T	Thrust
u	Far upstream velocity
u_∞	Undisturbed kinetic flow
α_2	Turbine velocity coefficient
α_4	Wake coefficient
ρ	Fluid density
η_t	Turbine efficiency
η_{gen}	Generator efficiency

Chapter 2

a_{η_i}	The amplitude of water surface elevation
a_{ξ_i}	The amplitude of the head difference
a_{v_i}	The amplitude of tidal stream velocity
CF	Capacity factor
F_P	Power factor
$F_{P,\,max}$	Maximum power factor
F_T	Thrust factor
$F_{T,\,max}$	Maximum thrust factor
F_n	The naturally occurring friction
F_t	The resistance applied by turbines
f_η	*Formzahl* number (form factor) for tidal elevation
f_v	*Formzahl* number for tidal velocity
f_ξ	*Formzahl* number for head difference

$\hat{P}$	Power capping limit or maximum power after capping strategy
$\bar{P}_1$	Average power removed by turbines before the capping
Q	flow rate
TSR	Tips speed ratio
$\hat{T}$	Thrust capping limit or maximum thrust after capping strategy
$\bar{T}_1$	Average thrust before the capping
η	Water level
η_0	Mean water level
ξ	Head difference
ω_i	The angular speed of each constituent
ω_1- ω_6	Basic frequency
$\emptyset_i$	Phase lag
λ_0	Natural friction
λ_1	Additional friction by the turbine

Chapter 3

C_{P-all}	C_P based on the average velocity for the entire channel/flume's cross-section (U_{in-all})
C_{T-all}	C_T based on the average velocity for the entire channel/flume's cross-section (U_{in-all})
C_{P-disc}	C_P based on the average velocity for the streamwise velocity of the actuator disc area from the simulation without the turbine ($U_{in-disc}$)

C_{T-disc}	C_T based on the average velocity for the streamwise velocity of the actuator disc area from the simulation without the turbine ($U_{in-disc}$)
C_2	Pressure jump coefficient
D_T	Disc thickness
K	Momentum lost factor
U_d	Local streamwise velocity at the disc plane
U_{in}	Inlet (far-upstream) velocity

U_{in-all}	U_{in} for the entire channel/flume's cross-section
$U_{in-disc}$	U_{in} for the streamwise velocity of the actuator disc area from the simulation without the turbine

Chapter 4

CFL	Courant-Friedrichs-Levy
c_f	Empirical bed friction coefficient.
F_c	Coriolis force
g	Gravitational acceleration.
H	total depth of the water column ($H = \eta + h$)
u	Depth-averaged velocity components in x directions.
v	Depth-averaged velocity components in y directions.
WSE	Water surface elevation
η	Free surface elevation
P3GL	[In Bahasa Indonesia] *Pusat Penelitian dan Pengembangan Geologi Kelautan* (en-Marine Geology Research and Development Centre)

Chapter 5

Cp	Capalulu Strait
E_k	Kinetic power
La	Larantuka
LC	Lombok Cluster
Lf	Lifamatola Strait
LH	Lifamatola Headland
Mg	Mangole Strait
NPC	Nusa Penida Cluster
NLC	Nusa Lembongan Cluster
SSB	Sunda Strait Bridge
SS	SSB segment
TC	Toyopakeh Cluster

Chapter 6

AEP	Annual Energy Production
AMDAL	[in Bahasa Indonesia] *Analisa Mengenai Dampak social dan Lingkungan* (see EIA)
BCR	Benefit-Cost Ratio
BPP	[In Bahasa Indonesia] *Biaya Pokok Pembangkitan listrik* (en electricity generation cost)
B_{tp}	Interest rate
C_{tp}	The cost of the project
CAPEX	Capital Expenditure
D	Turbine diameter
DPBP	Discounted Payback Period
EIA	Environmental and social-economic Impact Assessment
IRR	Estimated Internal Rate of Return
i_r	benefit of the project
LCOE	Levelised Cost of Energy
MPA	Marine Protection Area
MEP	Monthly Energy Production
NPV	Net Present Value
n_s	number of maximum turbines per stack
OPEX	Operational Expenditure
PPA	Power Purchase Agreement
s	tip-to-tip spacing

Contents

Chapter 1. Introduction and Literature Review

Provision of renewable, clean energy is a challenge faced by all countries, including Indonesia. Renewable energy is expected to address the problem of energy deficit, and to improve environmental conditions in the future. Ocean energy, including tidal, wave, and thermal, is an attractive option for Indonesia, which is the world's largest archipelagic country.

Tidal current energy, as an alternative clean energy source from the ocean, has been receiving attention due to its unique characteristics. Unlike wind and wave energy, which are more uncertain due to their stochastic nature, tidal stream energy is more deterministic. Moreover, tidal energy extraction systems are relatively cheap compared to other ocean energy sources. For example, Ocean Thermal Energy Conversion (OTEC) requires a complex pipe system to carry the cold water from the deep-water to the surface.

1.1 Introduction

1.1.1 The Opportunity for Renewable Energy in Indonesia

As an emerging country economically, electricity demand in Indonesia is predicted to increase in the coming years. Within the next 20 years, Indonesia is predicted to need between 1,205 TWh/yr and 1,491 TWh/yr. As stated in Presidential Regulation (PR) No 79/2014, the total energy demand in Indonesia is expected to increase almost tenfold from 60.7 GW (175 Million Tonne of Oil Equivalent (MTOE)) to 430 GW in 2050 (see Figure 1-1). This PR also set a target to increase the renewable energy portion of Indonesia's energy mix to 23% by 2025. At the 21st Conference of the Parties (COP 21) in Paris, Indonesia pledged to cut greenhouse gas emission by 29% by 2030.

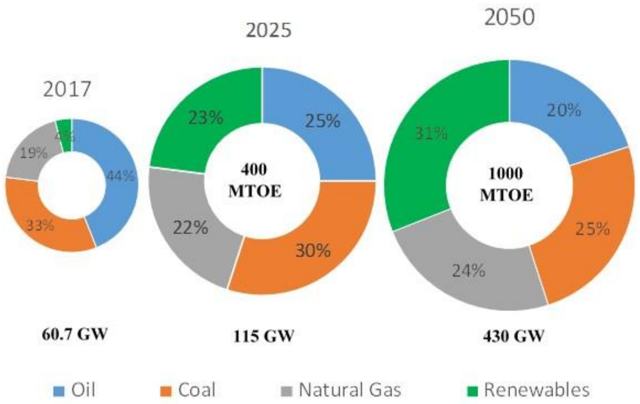

Figure 1-1: National Energy Mix Based on *Presidential Regulation 2014* (*PP No. 79 Tahun 2014*)

Indonesia would require 400 MTOE to provide 115 GW in 2025, with the implication of enormous greenhouse gases (GHG) emission (see Measey, 2010), as at present, Indonesia still relies on fossil fuels. The ADB report on Indonesia in 2015 (Tharakan, 2015) shows this country, with the fourth-largest population worldwide, relied on energy from fossil fuel (coal (44%), oil/diesel (23%) and gas power plants (21%)). Relying on fossil fuels threatens Indonesia with the consequences of climate change. Indonesia has already faced major problems believed to be the result of climate change, such as forest fires in dry seasons (Herawati & Santoso, 2011; Alisjahbana & Busch, 2017) and flooding in rainy seasons (Cahya 2020, Diela & Widianto, 2020).

The Electricity Supply Business Plan (*Rencana Umum Penyediaan Tenaga Listrik*-RUPTL) from PLN, a state company that provides electricity in Indonesia, shows that 48% of Indonesian electricity was still supplied by coal in 2018 (RUPTL 2018-2027). The RUPTL report indicates that GHG emission will increase by a factor of 1.7 times from 2018 to 2027. However, the operating margin emission factor (EF_{OM}) of 0.801 ton CO_2/MWh in 2018 could be decreased to 0.729 ton CO_2/MWh in 2027 by using 23% clean, renewable energy, as targeted in the national energy mix to fulfil the pledge to COP 21 (see RUPTL 2018-2027 for the detail).

In the last four years of his first term, President Joko Widodo’s administration focused on increasing the “electrification ratio”. A project to provide 35 GW electrical power was launched. Unfortunately though, this plan was still dominated by coal and gas-fired power plants.

1.1.2 Electrification Ratio and Inequality

Provision of energy for one of the world’s most populous countries, like Indonesia, is challenging. The approximately 255 million population, based on the 2015 census, is not distributed evenly (see BPS, 2019). About 60% of the population lives on the island of Java. Since the household sector dominates electricity consumption (BPPT, 2016), the population distribution plays a significant role in determining the future Indonesian demand for energy.

In 2014, the national electrification ratio was about 88.8%. This 88.8% of electrification ratio means that there were nearly 35 million people that did not have access to modern forms of energy (see Firdaus *et al.*, 2017). This electrification ratio is not distributed evenly across the country, and there were some regions where less than half the population had access to electricity. Figure 1-2 shows the 2014 electrification ratio and the population in each province in Indonesia. This figure indicates that the most populated regions, Java and Sumatra, had a relatively high electrification ratio. Meanwhile, the province with the lowest electrification ratio, Papua, also has the lowest population.

Access to electricity also indicates the state of development of a country. Chen & Nordhaus, 2011 found that satellite image of luminosity in a region, known as the Night Light Development Index (NLDI), is very useful in assessing economic activities of a region. Although NLDI analysis of Indonesia is not included in this thesis, the nightlight satellite image helps visualisation of the correlation between electricity access and the development distribution in Indonesia.

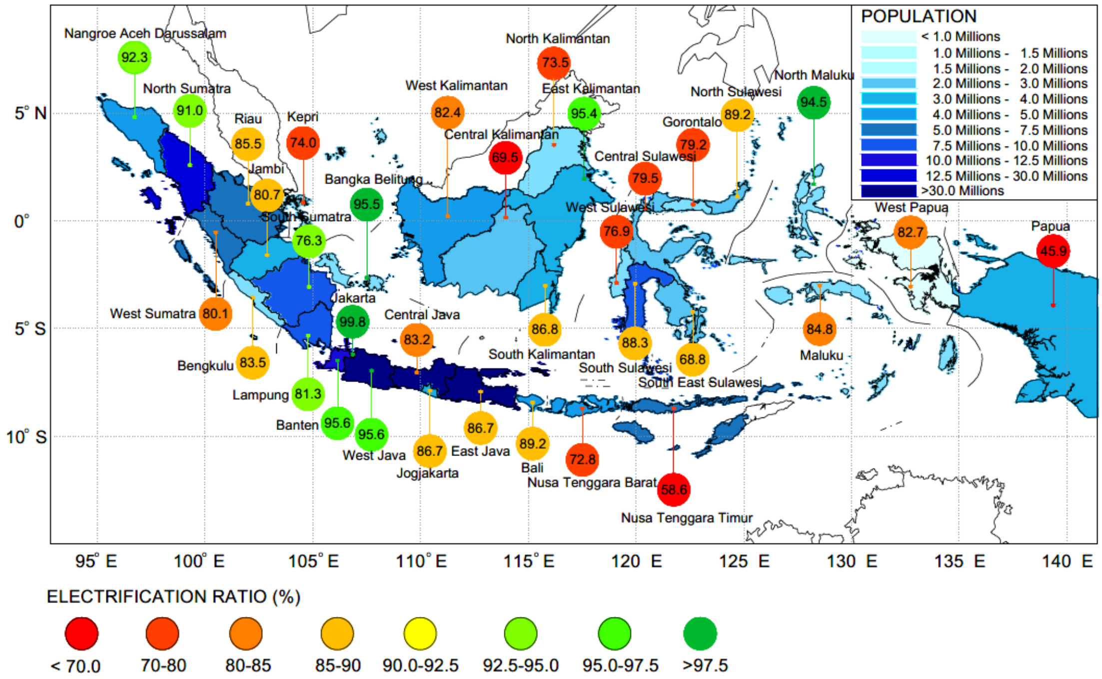

Figure 1-2: Map of Indonesian population (based on BPS, 2018) and Electrification Ratio based on RUPTL, 2015

Figure 1-3 shows the nightlight image for Indonesia based on NOAA data (NOAA/NGDC, 2015). This image, an annual exposure in 2015, is indicative of the development index and the population in each region. As the most populated area, Java was the most developed region in the country, while Papua and the other eastern provinces were the least developed regions in Indonesia.

As mentioned before, President Joko Widodo's administration focused on equalising the development of the entire country, including increasing the electrification ratio in many areas. As shown in Figure 1-4, the electrification ratio in 2018 shows a significant increase in the eastern area of Indonesia. In just four years, the electrification ratio in the most eastern provinces has risen from below 80% to higher than 90%. The national electrification ratio increased from 88% to 97% in the same period (see MoEMR, 2018; PLN, 2019).

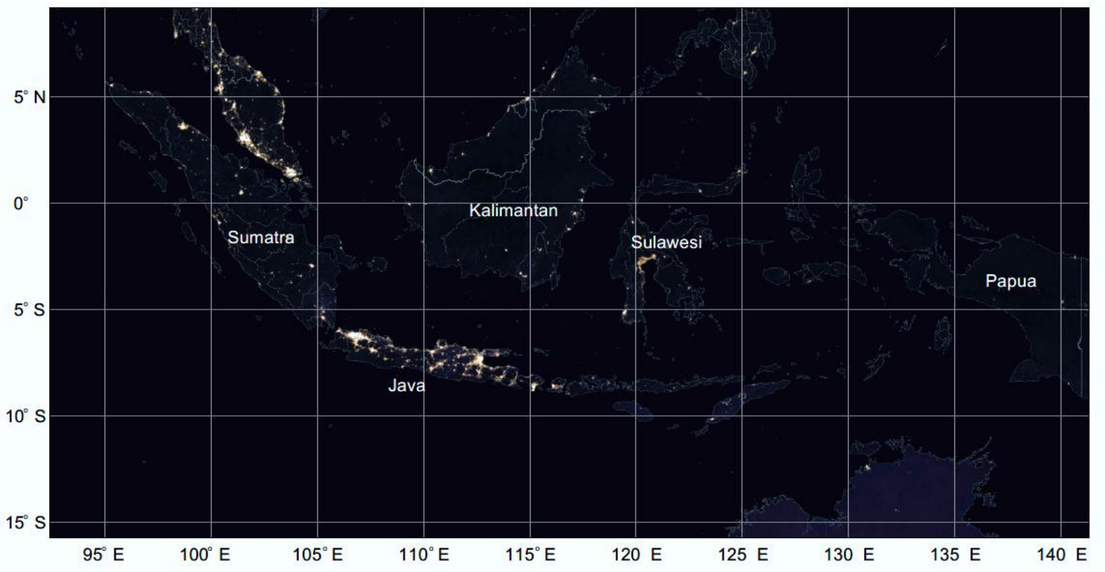

Source: NOAA/NGDC, 2015 (https://ngdc.noaa.gov)

Figure 1-3: Nightlight image of Indonesian territories extracted from NOAA/NGDC, 2015 showing the disparity of development in Indonesia

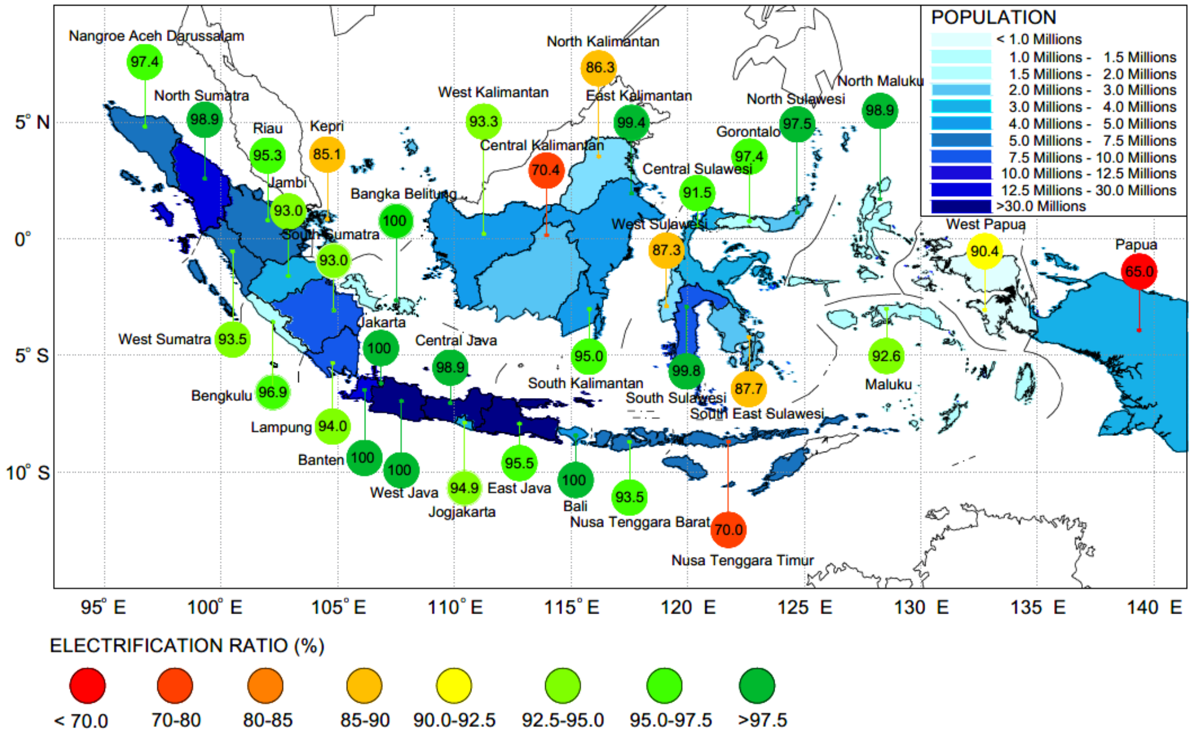

Figure 1-4: Indonesian Population (based on BPS, 2018) and Electrification Ratio in 2018 based on *RUPTL* 2018-2027

These facts explain the government's hesitant commitment to increasing the utilisation of clean, renewable energy. The development of coal-fired power plants has been taken to accelerate eradication of inequality. However, ocean energy, such as tidal, still has the opportunity to be developed in this country.

Furthermore, the rapid development of electricity in Indonesia has even caused a surplus of electricity supply in some areas, especially in Java and Bali. Therefore, investment in renewable energy, such as tidal turbines, requires careful planning both in resource assessment and economic feasibility. To deliver realistic results, assessing tidal resources also requires the consideration of population and electrification ratio.

Tidal power technology can be divided into two broad groups: megawatt and sub-megawatt installations. The demography and electrification ratio are important factors to be taken into account in selecting appropriate tidal technologies for particular locations in Indonesia. For instance, in some sites, sub-megawatt installations could play an important role in displacing reliance on diesel generation.

1.1.3 The Opportunity for Renewable Energy Investments

Despite the global economic slowdown due to falling commodity prices, Indonesia's GDP growth has been maintained. The World Bank shows Indonesia's GDP growth at 5.0 to 5.1% between 2014 and 2017, making Indonesia one of the fastest growing economies worldwide (see The World Bank, 2020). Infrastructure initiatives began to have an impact in 2017, and RUPTL 2019 shows electricity growth in Indonesia is at 6.9%. The planning and regulation of electricity supply in Indonesia is complex.

The RUPTL regulates a ten-year electricity development plan for the operational areas, or *Wilayah Usaha*, of PLN. The RUPTL contains demand forecasts, future expansion plans, and electricity production forecasts. The RUPTL also indicates which projects are planned to be developed by PLN and private investors. Thus, RUPTL is very important for the investment strategy in Indonesia. The RUPTL in turn is based on the National Electricity General Plan (*Rencana Umum Ketenagalistrikan Nasional* – RUKN) and Regional Electricity General Plan (*Rencana Umum Ketenagalistrikan Daerah* – RUKD).

The Ministry of Energy and Mineral Resources (MoEMR) is responsible for the RUKN and the regional governments (Provincials and Regencies) are responsible for preparing the RUKD based on RUKN. Energy investments are also governed by the 2009 Electricity Law, which has given PLN priority rights over the electricity supply business throughout Indonesia, with exceptions for certain *Wilayah Usaha* given to private enterprises, cooperatives and self-reliant community institutions involved in the electricity supply business. Although PLN has exclusive powers over the transmission, distribution and supply of electricity to the public, the private sector's participation is allowed through independent power producer (IPP) or Public-Private Partnership (PPP) initiatives.

The electricity purchasing tariff in Indonesia is determined by the electricity generation cost, known as *Biaya Pokok Pembangkitan* (BPP). The BPP is different in each region (see Figure 1-5) and is usually used as a benchmark to the purchasing price. The *MoEMR Regulation Number 50/2017 on the utilisation of renewable energy resources for electricity* set new tariffs for the renewable energy projects, including marine energy, subject to business-to-business (B2B) negotiation with PLN. This regulation is expected to give some leverage for the development of the renewable energy business. However, PWC, 2018 argues that this tariff regime remains untested. Turbine developers therefore need to relate costs to BPP tariffs when planning investment in the renewable energy business in Indonesia.

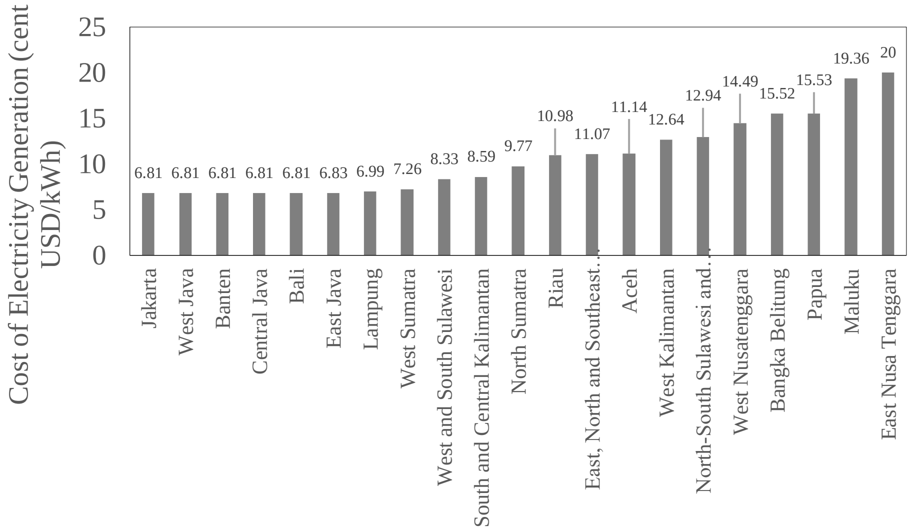

Figure 1-5: *Biaya Pokok Pembangkitan* (BPP) in different regions within Indonesia based on *MoEMR Decree Number 1772 K/20/MEM/2018*

1.2 General Tidal Power Review

Tidal resource assessment usually begins with a selection of potential sites. The potential sites are determined by several factors such as: average current speed, geographical position, to ensure accessibility; and existing site conditions, to ensure no environmental hazards.

1.2.1 Theory of Tides

An understanding of the theory of tides is essential before an assessment can be undertaken. Schureman, 1958; Pugh, 1987; and Parker, 2007; introduce the harmonic analysis approach. A brief explanation to summarise their works, especially on understanding the derivation of each component, might help to understand the complexities of tidal energy variation studied in this thesis.

Tides occur due to the dynamic response of the oceans to gravitational forces applied primarily by the Moon and Sun. The complex nature of the Moon's orbit around the Earth and the Earth's orbit around the Sun makes tides have many frequencies, and astronomers have precisely determined these frequencies. The tidal variation follows these astronomical frequencies and these frequencies, are the basis for the power and thrust variation analyses that are later demonstrated in this chapter.

The astronomical frequencies are used as basic frequencies in the tidal harmonics. The reference is the frequency of mean solar day (ω_0). A mean lunar day is approximately 1.0351 mean solar day, so the frequency of the mean lunar day (ω_1) is $\frac{1}{1.0351} = 0.96609 \frac{cycles}{mean\ solar\ day}$. By definition, the frequency of the mean solar day (ω_0) is 15°/mean solar hour. Therefore, ω_1 is 14.491°/mean solar hour. These calculations are extended to frequencies of the sidereal month (ω_2), tropical year (ω_3), moon perigee (ω_4), etc., as shown in Table 1-1. Later, all these basic frequencies are used to determine the frequencies of the tidal constituents, also known as Darwin's species.

Table 1-1: The six basic frequencies

	Period	Frequency		Angular speed	
	mean solar day	f (cycles/mean solar day)	σ (°/mean solar day)	symbol in radians	rate of change of
Mean lunar day	1.0351	0.96609023	14.49135349	ω_1	C_1
Sidereal month	27.3217	0.03660094	0.54901415	ω_2	s
Tropical year	365.2422	0.00273791	0.04106864	ω_3	h
Moon's parigee	3230.25 (8.85 Julian years)	0.00030957	0.00464360	ω_4	p
Regression of moon's nodes	6792.65 (18.61 Julian years)	0.00014722	0.00220827	ω_5	N
Perihelion	7,643,830 (20,492 Julian years)	0.00000013	0.00000196	ω_6	p'

1.2.2 Tidal Harmonics

The movements of the Moon and Sun, north and south of the equator and their varying distances and angular speeds can be represented by amplitude and angular frequency in tidal harmonics. For example, the harmonic of the tidal elevation (η) can be represented by a finite number N of harmonic terms of the form as described in eq (1.1).

$$\eta(t) = \eta_0 + \sum_{\mathrm{i}}^{\mathrm{n}} A_{\mathrm{i}} \cos(\omega_{\mathrm{i}} t - \emptyset_{\mathrm{i}}), \qquad (1.1)$$

where η_0 is the height of the mean water level above the datum used, A_i is an amplitude of each tidal constituent or also known as tidal species, ω_i is the angular speed of each constituent and $\emptyset_i$ is a phase lag. The datum for this phase lag is on the equilibrium tide at Greenwich (see Schureman, 1958; Pugh, 1987; Parker, 2007 in detail).

The angular frequency of each constituent or Darwin species is determined from six basic frequencies determined by an expansion the Equilibrium Tide, as discussed in section 1.2.1. There are a number of methods to calculate the frequencies of each species using the basic frequencies. The first method calculates the frequencies from the basic frequencies with the inclusion of solar frequency (ω_0) and the other method uses ω_0 just as a reference. The second method is found more convenient and is widely used. This method calculates the basic frequency of each constituent (ω_i) with the combination of $\omega_1$to ω_6 as shown in eq. (1.2)

$$\omega_i = i_a\omega_1 + i_b\omega_2 + i_c\omega_3 + i_d\omega_4 + i_e\omega_5 + i_f\omega_6, \qquad (1.2)$$

where the values of $\omega_1$to ω_6 are the angular speeds that represent respectively as the mean lunar day, sidereal month, tropical year, etc (see Table 1-1). The factors i_a i_b i_c i_d i_e and i_f are small integers that are called Doodson's numbers. The Doodson's numbers are also annotated as rates of change C_1, s, h, p, N, and p' respectively.

For example M_2 has Doodson numbers (i_a to i_f) of [+2 0 0 0 0 0], therefore the M_2 frequency is $\omega_{M_2} = 2\omega_1 = 2 * 14.4921 = 28.984^o/hour$. Since the frequency of the solar day is 15°/hour (ω_0=15°/hour), the period o M_2 is ${}^{15^o/hour}/_{28.984^o/hour} \times 24\text{ hour} = 12.4206\ hours$ (here and going forward figures are quoted to four decimal places). Whilst S_2 has Doodson number of [+2 +2 -2 0 0 0], therefore the S_2 frequency is $\omega_{S_2} = 2\omega_1 + 2\omega_2 - 2\omega_3 = 30.000^o/hour$ s. Therefore, the period of S_2 is 12.0000 *hours*. A similar exercise could be extended to other species.

The nomenclature used for most tidal harmonic constituents is to name each constituent with a capital letter followed by a subscript indicating the approximate number of cycles per day, for example, M_2, S_2, K_1, and O_1. However, there are also long-period tides which tend to have names with a capital letter and one or more lower case letters (e.g., Mm, Mf, Sa, Ssa, etc.).

There are 37 species/constituents which normally have the greatest effect on the tides and are used as the tidal harmonic constituents to predict tidal conditions for a location (Hicks, 2006). However, based on DISHIDROS, 2004 data, it is shown that there are only nine constituents that have a significant effect on the tidal harmonic process in Indonesian waters. The four principal constituents (M_2, S_2, K_1 and O_1), both semidiurnal lunar-elliptic components (N_2 and L_2), diurnal elliptic species (P_1) and two shallow-water constituents (M_4 and M_6) have the most significant effects in Indonesian waters. A later discussed, some long period constituents also matter. However, these may be hidden in the tidal harmonic process through use of a nodal factor. The nodal factor is discussed later alongside the long term constituents.

However, perhaps only the seven astronomical species (M_2, S_2, K_1, O_1, N_2, L_2 and P_1) and three long term constituents (Mm, Sa and Ssa) have a significant impact on the tidal power variation. Therefore, this chapter only analyses the impact of these seven species with the extension of three long-term constituents.

a) Semidiurnal and Diurnal Tidal Constituents

The largest semidiurnal harmonic is M_2, with a period of half a lunar day or 12.4206 hours. As the Earth also rotates exactly once every solar day, the main solar semidiurnal tidal constituent, S_2, has a period of half a solar day or 12.0000 hours. The M_2 component is usually larger than S_2, as the Moon is closer to the Earth in comparison to the Sun. The beating between these two astronomical forces produces the spring neap cycle. The sine curves of M_2 and S_2 are in synchronism after roughly seven days from neap to spring tide.

As the Moon's orbit is angled to the equatorial plane, the declination of the Moon in the tides is represented by two lunar diurnal tidal constituents, K_1 and O_1, with periods of 23.9345 and 25.8193 hours. There are many areas where hydrodynamics amplifies the diurnal and/or reduces the semidiurnal constituents. These cases are called diurnal tides, where there is only one main tidal cycle per day, while semidiurnal tides have two cycles per day. The differentiation of these cases is determined by a form factor that will be discussed later in section 1.2.3. The four constituents of semidiurnal (M_2 and S_2) and diurnal (K_1 and O_1) tides are also called the principal astronomical constituents.

However, there are other semidiurnal constituents that usually have a large effect on tidal harmonics due to the elliptical nature of the Moon's orbit. The larger lunar elliptic (N_2) and smaller lunar elliptic (L_2) constituents are the result of the variations from apogee to perigee over a 27.556-day period. Pugh, 1987 states that the relative amplitudes of N_2: M_2: L_2 are 0.196: 1.000: 0.027, respectively. As the Earth's orbit around the Sun is also elliptic, this movement also leads to another diurnal constituent which is represented by the very slow modulation of Solar Diurnal (P_1). Many other constituents represent tidal elevation as the result of modulation between the astronomical frequencies (see Parker, 2007 for detail).

b) Long-Term Constituents

The longest period that is perhaps worth considering in engineering infrastructure planning is the 18.61-year cycle of tide constituents associated with changes in the Moon's orbit around the Earth. This cycle is also known as a *Metonic* cycle. There are at least five different long period constituents in the tidal elevation. However, only three of these constituents are analysed in this chapter.

Firstly, the annual variation in mean sea level, also known as a solar annual (Sa), is usually the largest term of long period species. The Sa has an angular speed of ($\omega_3 - \omega_6$) However, this term is very small in the gravitational forcing. Secondly, the Solar semiannual (Ssa) is larger than the annual gravitational tide, and the observed tide also includes seasonal effects. Lastly the lunar monthly (Mm) tide which is equivalent for Sa and Ssa (as Sa and Ssa are the solar terms for the long period constituents).

These long-period species can also be represented differently in the tidal harmonic. In the pre-computer era, analysing 19 years of data was too labour intensive (Pugh, 1987). Therefore, for practicality, this term was considered as constant for some of the short periods. These constants are implemented as a multiplicative factor, usually called the nodal factor (f). These nodal factors are used with a phase difference (u) on each constituent. This nodal factor fluctuated around 1.0 for each constituent (see Table 1-2). For example, the nodal factor of M_2 fluctuates from 0.963 to 1.038 and back to 0.963 over the 18.61 years.

Some numerical models that are embedded within the global tidal model still use this nodal factor. For example, ADCIRC-DG and DG SWEM use the Le' Provost tidal model. These types of global tidal models do not resolve this modulation as independent constituents. The long-term modulations are represented by small adjustment factors f_n and u_n as shown in eq. (1.3).

$$\eta = A_{\mathrm{i}}(f_n)\cos\left(\omega_{\mathrm{i}}t - \emptyset_{\mathrm{i}} + (\varphi_i + u_n)\right). \tag{1.3}$$

Table 1-2: Basic nodal modulation terms for the constituents that are considered to have a significant effect on the power and thrust long term variation.

Constituent	f	u
Mm	1.000 - 0.130 cos (N)	0.0°
O_1	1.009 + 0.187 cos (N)	10.8°sin (N)
K_1	1.006 + 0.115 cos (N)	- 8.9°sin (N)
M_2	1.000 - 0.037 cos (N)	- 2.1°sin (N)

N is the longitude of lunar ascending node. N = 0 March 1969, November 1987, June 2006, etc. or at maximum amplitude of diurnal terms and M_2 at minimum (see Pugh, 1987)

c) Shallow-Water Constituents

Besides the semidiurnal, diurnal and long-term constituents, there are shallow-water constituents in the tidal dynamics. As the tidal wave propagates onto the continental shelf and into bay estuaries, the hydrodynamics of this process also become significant in the tidal pattern. The waves are reflected in full or partially when they propagate from the ocean basin into the shallow water. The basin lengths or shelf widths cause resonance for particular tidal frequencies. Continuity effects, frictional damping, and advective/inertial effects all affect the tide and tidal currents. These processes create “overtides” and compound tides, especially within the semidiurnal band.

These overtides and compound tides are called the shallow-water tidal constituents. In some regions these constituents are even larger than the astronomical constituents, especially in closed coastal basins. However, these constituents are not included in the analysis in this chapter. The DISHIDROS data shows that the M_4 and M_6 components are not significant in the potential locations that are assessed here. As later also demonstrated in this chapter, the shallow-water constituents have a small response in the 1-D channel that used in this chapter. Therefore, this chapter just focuses on the seven semidiurnal-diurnal and the three long-term constituents.

d) Summary

Table 1-3 shows the period and Doodson’s number of each constituent that is used in later analyses (see Doodson & Warburg, 1941; Pugh, 1987; Foreman & Henry, 1989). These numbers are used in the asymmetry analysis in this chapter.

Table 1-3: Summary of constituents' parameter used in this Chapter

Species	Darwin symbol	Period (hour)	Speed (°/hour)	Doodson Number					
				i_a	i_b	i_c	i_d	i_e	i_f
Semidiurnal									
Principal lunar semidiurnal	M_2	12.421	28.984	+2	0	0	0	0	0
Principal solar semidiurnal	S_2	12.000	30.000	+2	+2	-2	0	0	0
Larger lunar elliptic semidiurnal	N_2	12.658	28.440	+2	-1	0	+1	0	0
Smaller lunar elliptic semidiurnal	L_2	12.192	29.528	+2	+1	0	-1	0	0
Diurnal									
Principal Lunar diurnal	K_1	23.934	15.041	+1	+1	0	0	0	0
Principal Lunar diurnal	O_1	25.819	13.943	+1	-1	0	0	0	0
Solar diurnal	P_1	24.066	14.959	+1	+1	-2	0	0	0
Long period									
Lunar monthly	Mm	661.311 (2	0.544	0	+1	0	-1	0	0
Solar semiannual	Ssa	4383.076	0.082	0	0	+2	0	0	0
Solar annual	Sa	8766.153	0.041	0	0	+1	0	0	-1

1.2.3 Form Factor or *Formzahl* Number

As mentioned earlier, the diurnal (K_1 and O_1) and semidiurnal (S_2 and M_2) components create different patterns. The "form factor: of the sinusoidal signal formed by the four different astronomical constituents can be used to determine the pattern of each tidal type. It is important to note that the form factor is just an indicator of the type of tide. As the tidal harmonic is formed by multiple sinusoidal components, the form factor determines the number of cycles per day of each tidal pattern. This form factor is also widely known as *Formzahl* number (form number in German). The *Formzahl* number compares the amplitude of the principal diurnal and semidiurnal constituents (lunar and solar). It is expressed as:

$$f_\eta = \frac{AK_1 + AO_1}{AM_2 + AS_2}, \tag{1.4}$$

where AK_1 and AO_1 are the amplitudes of lunar diurnal tides and AM_2 and AS_2 are the amplitudes of principal lunar and solar semidiurnal tides.

Figure 1-6 shows the typical tidal pattern for different *Formzahl* number. A *Formzahl* number $f_\eta \leq 0.25$ indicates two tidal cycles per day or semidiurnal (Figure 1-6 a), and $f_\eta > 3$ indicates a single cycle per day (Figure 1-6 d). *Formzahl* number in between create mixed tides. For $0.25 < f_\eta \leq 1$ the mix is principally semidiurnal (Figure 1-6 b), partly diurnal, whilst for $1 < f_\eta \leq 3$ the mix is principally diurnal, partly semidiurnal (Figure 1-6 c). However, complex interactions between the components can also occur.

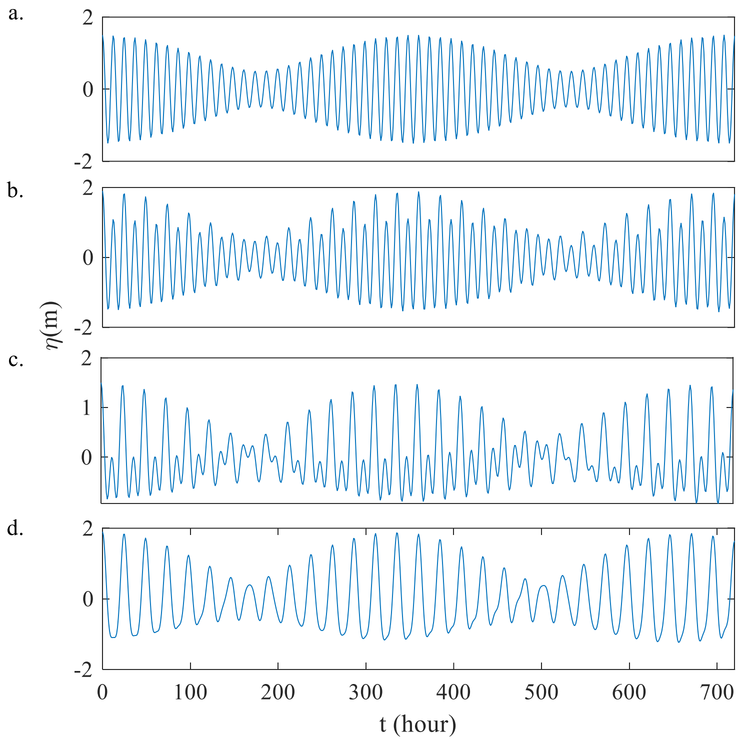

Figure 1-6: Typical tidal pattern for different *formzahl* number. a. f_n=0.1 (semidiurnal water), b. f_n =0.75 (mixed-diurnal with semidiurnal dominant), c. f_n =1.5 (mixed-diurnal with diurnal dominant), d. f_n =4 (diurnal).

1.2.4 Tidal Currents

Since astronomical forces mainly drive the ocean currents, the harmonic analysis approach is also applicable for the tidal current. The time variation of velocity can be written in the same manner as for water surface elevation (WSE), as shown in eq. (1.5)

$$\boldsymbol{v}(t) = \sum_{\mathrm{i}}^{\mathrm{n}} A_{\mathrm{i}} co\, s(\omega_{\mathrm{i}} t - \emptyset_{\mathrm{i}}), \tag{1.5}$$

where the amplitude (A_{i}) is the velocity magnitude for each tidal constituents and the angular speed (ω_{i}) for each constituent is the same as the angular speed of tidal elevation constituents, whilst the phase lag ($\emptyset_{\mathrm{i}}$) of velocity will differ from the phase lag of each constituent in the tidal elevation.

Tidal elevation uses mean sea level (MSL) as a reference, the elevations above MSL are positive and below MSL are negative. In a similar way, tidal velocity also could be distinguished by its direction. As the tidal flow moves bi-directionally, its directional changes could be considered similar to the rise and fall in tidal elevation. A typical channel has a tidal flow that moves back and forth in opposite directions, while headland types usually have more complicated patterns because the directions are affected by the geometry of the headland. Therefore, the direction of a channel could be represented as positive and negative in the Cartesian system.

However, currents are more complicated than water elevation in terms of analysis because currents are vector quantities with northing and easting components. There are many more difficulties with implementing harmonic analysis for the current, such as the influence on the current of non-tidal factors. For instance, Ekman transport (wind-induced current) may interact with the tidal current. The current measurements usually show a greater proportion of non-tidal energy compared to tidal elevation. However, since astronomical forces predominantly drive the ocean current, the analysis for the current still can be done.

Few authors have discussed the harmonic analysis of tidal currents. Godin, 1972 describes various analysis approaches for tidal currents and generally takes a very pessimistic view about how accurately they can be predicted. Parker, 2007 takes a much less pessimistic view, and argues that as long as the special aspects of tidal currents are kept in mind and accounted for in some fashion, there is no reason that the accurate tidal current predictions cannot be made for most situations.

However, as mentioned by Parker, 2007, several limitations should be noted when using harmonic analysis approach for tidal current. A harmonic pattern of the tidal current is only applicable for particular depths and locations. Such harmonic analysis may be usable at nearby locations (preferably at the same depth), but only if the bathymetry does not change dramatically. However, it is also very important to note that the bathymetry can slowly change over the years due to other processes related to sedimentation or erosion. Therefore the tidal current can also slowly change, while tidal elevation will not change over the long period in most cases.

As will be shown later, the variation of tidal elevation does not always reflect the variation of tidal velocity (in term of semidiurnal or diurnal type). However, the velocity variations still follow the same frequency of each tidal species that have been discussed previously. The variation of tidal flow, therefore, can also be distinguished by a form factor or *Formzahl* number. Since tidal stream power is predominantly driven by the flow, this thesis introduces the *Formzahl* number for the tidal current (f_v), as distinct from the conventional *Formzahl* number for tidal elevation.

1.2.5 Review of Actuator Disc Theory and Its Limitations

There are numerous designs of tidal stream turbines, and they have different working principles, (cross flow and axial flow, Savonius, and Darrieus, etc.). However, the leading order physics of the flow around the turbine can be analysed by a simple mathematical expression. An actuator disc is a convenient tool for such analysis in wind turbines. Although there are differences between wind turbines and tidal turbines, a similar principle can be applied for tidal stream turbines.

In actuator disc theory solution of the Bernoulli equation together with momentum balance leads to a solution for the thrust (T) and power (P). The thrust is governed by

$$T = \frac{1}{2}\rho u^2 A C_T, \tag{1.6}$$

and for the power extracted by the turbine is

$$P = \frac{1}{2}\rho u^3 A C_P, \tag{1.7}$$

where ρ is the fluid density, u is far upstream velocity, and A is the swept area of the turbine, or in this case is the frontal area of actuator disc. The non-dimensional thrust and power coefficient are denoted as C_T and C_P. Actuator disc theory is used to determine C_T and C_P.

Detailed reviews on the mathematical derivation and historical background is given by Garett & Cummins, 2007; Houlsby *et al.* 2008; Draper, 2011 and Vogel, 2014. However, a brief explanation of the implementation of actuator disc theory for tidal stream energy extraction is given here.

a) Tidal Power in Unbounded Flow

Linear momentum actuator disc theory was first used by Rankine, 1895 and extended by Froude, 1889 to analyse the flow field around a ship propeller. Later, Lanchester, 1915 and Betz, 1920 used actuator disc theory to assess the performance of an inverse propeller in an unconstrained flow, such as a wind turbine. They showed that it was not possible to extract all the undisturbed kinetic flux from a fluid stream.

The theory idealised the flow field around the turbine for an unbounded flow, as illustrated in Figure 1-7. A stream tube that bounds all the fluid which passes through the actuator disc is considered, and pressure and velocity evaluated at four stations, shown as dotted lines in the figure. The fraction of velocity at each station to the far upstream velocity the denoted as α, where $\alpha_1$is equal to 1.0 as the flow at this station is identical to the undisturbed flow far upstream.

The thrust coefficient (C_T) can be obtained from the following equation

$$C_T = (1 - {\alpha_4}^2), \tag{1.8}$$

where α_4 is the wake coefficient: the fraction of velocity far downstream, where the pressure is equalised. The power coefficient (C_P) is calculated by

$$C_P = \alpha_2 C_T, \tag{1.9}$$

where α_2 is the turbine velocity coefficient or the fraction of velocity at station 2. This α_2 is related to the wake coefficient (α_4) with the following equation

$$\alpha_2 = \frac{1+\alpha_4}{2}. \tag{1.10}$$

From this equation, there is an upper limit to the kinetic energy that can be converted to the usable power, treated as a function of α_4 (see Figure 1-8). The maximum C_P is 16/27 and C_T is 8/9 from α_4=1/3 and α_2=2/3. The maximum C_P =16/27 is known as the Lanchester-Betz limit. Note that van Kuik, 2007 called this limit as the Lanchester-Betz-Joukowsky limit to acknowledge the independent study by Joukowsky[1]

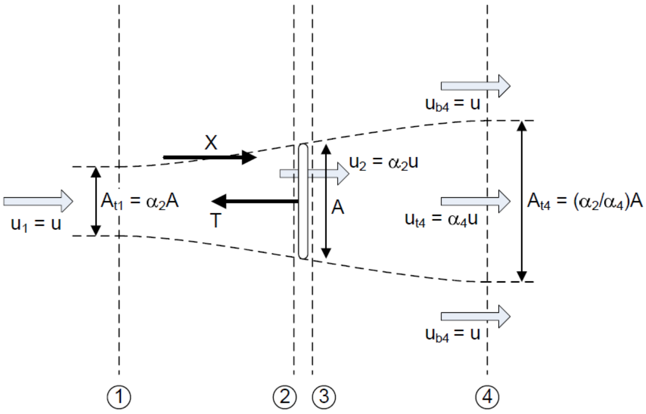

Figure 1-7: The classic actuator disc model for an unbounded flow (from Houlsby *et al.*, 2008)

In reality, it is almost impossible for turbines to reach the Lanchester-Betz limit, due to various mechanical and electrical energy losses. Therefore, early work on tidal energy (Black & Veatch 2005, Boud 2003 and Fraenkel 2007) suggested that the extracted power from a fluid stream, as shown in eq ((1.7), could be simplified as

$$P = \frac{1}{2}\rho u_\infty A\left(\eta_t \eta_{gen}\right), \tag{1.11}$$

where u_∞ is undisturbed kinetic flow, η_t is a turbine efficiency and η_{gen} is a generator efficiency, to accommodate further reduction from the available kinetic energy. Black & Veatch 2005 use the significant impact factor (*SIF*), which was applied to the natural kinetic flux through the turbine's frontal area, to account for the limiting effect of the flow diversion around the turbine and other

---

[1] As mentioned by van Kuik, 2007, Joukowsky's paper published in the *Transactions of the Office for Aerodynamic Calculations and Essays of the Superior Technical School of Moscow* 1918 (in Russian), and also published in Gauthier-Villars et Cie. (eds). *Théorie Tour billonnaire de l'Hélice Propulsive, Quatrième Mémoire*. 123–146: Paris, 1929 (in French)

regulatory constraints on the available power. This means that *SIF* is essentially equivalent to both efficiencies $(\eta_t \eta_{gen})$ in eq. (1.11).

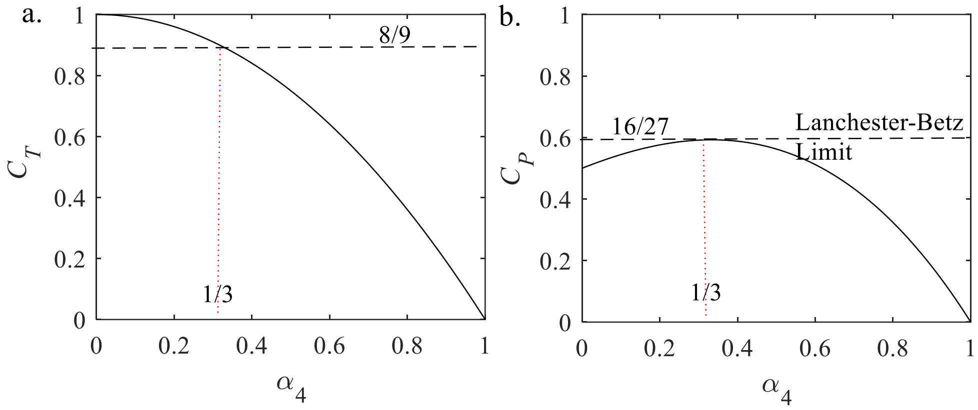

Figure 1-8: Power and thrust from the flow through an actuator disc in unbounded flow

Equation (1.11) has been widely used for tidal resource assessments in Indonesia (see Orhan *et al.*, 2015; Orhan *et al.*, 2017; Rachmayani *et al.*, 2006 and Coordinating Team of Research and Technology 2008). However, this approach has been criticised by MacKay, 2007; Garrett & Cummins 2004 and Garrett & Cummins 2005.

Although useful, Lanchester-Betz limit is based on an assumption of unbounded flow. This theory works well with the wind turbine, as the atmosphere boundary could be approximated as infinitely far from the turbine. However, it makes the Lanchester-Betz limit inapplicable to tidal energy extraction. An unbounded stream is unlikely to occur in a tidal current since there is a certain limit of feasible depth for deploying the turbines. Furthermore, the strongest currents are usually found in narrow straits or around coastal headlands (see Draper, 2011 and Bryden & Couch, 2007).

In a laterally bounded flow, the turbine array acts as an additional resistance to the flow in the channel. An increasing thrust applied to the flow by the turbines array results in flow retardation and diversion at the edges of the array. Almost a century after the original theory was developed, Garrett & Cummins 2004, 2005 further explain that the maximum average available power is dependent on the interaction of turbine array with the designated channel.

b) Extracting Power from a Channel

Garrett & Cummins 2004 (hereinafter GC04) and followed by Garrett & Cummins, 2005 (hereinafter GC05) demonstrate that there is no simple relationship between the average kinetic flux and the average maximum available power of a turbine. GC04 investigates the case of a tidal turbine in the closed basin while GC05 investigates an idealised channel that connects two large basins, where the different tidal elevations drive the flow. GC05 finds that the available power is not related to the kinetic flux in the channel in a simple way, and instead is determined by the tidal dynamics in the channel (see Garrett & Cummins, 2005).

The extracted power by a turbine spanning across a channel changes from 0.21 to 0.24, as the natural flow regime in the channel progresses from one with negligible background friction, or inertia dominated, to one that is friction dominated. This means, the power removed by the turbines is determined by the work done by the tide. Therefore, using a coefficient or the significant impact factor, as shown in the unbounded flow, could lead to an estimate with approximately 10% inaccuracy (see Garrett & Cummins, 2005).

This approach assumes the tidal fences are equivalent to a single turbine occupying the cross-section of the channel. Garrett & Cummins, 2007 (hereinafter GC07) considered a partially blocked channel. Their results indicate that the power available to the turbines is dependent on the mass flux and the downstream mixing that extends beyond the turbine(s) wake. They pointed out that tidal turbine efficiency is higher for the turbines that occupy a small fraction of the channel cross-section than one that occupies most of the section. Turbine efficiency is defined as the ratio of the power available to the turbines to the total power removed from the stream (including frictional and mixing losses).

The thrust coefficient (C_t) in GC07 is calculated by the following equation

$$C_T = {\beta_4}^2 - {\alpha_4}^2, \tag{1.12}$$

GC07 introduces β_4, the bypass coefficient that can be calculated from

$$\beta_4 = \frac{1 - B\alpha_2}{1 - B\frac{\alpha_2}{\alpha_4}}, \tag{1.13}$$

The turbine velocity coefficient (α_2) in GC07 is calculated from

$$\alpha_2 = \frac{1 + \alpha_4}{(1 + B)\sqrt{(1 - B)^2 + B\left(1 - \frac{1}{\alpha_4}\right)^2}}, \tag{1.14}$$

where B is the blockage ratio, the ratio of turbine swept area over the channel cross-section area. The GC07 model predicts the maximum power in the channel is proportional to the $(1 - B)^{-2}$. Therefore, the results could exceed the Lanchester-Betz limit, as shown in Figure 1-9. The figure also shows that if the blockage ratio (B) is set very low (B=0.01 and B=0.001), the predictions collapse to the unbounded flow calculation. GC07 solve the ambiguity at low $\alpha_4$or at $\alpha_4 = 0$, as demonstrated in eq. (1.10)). This approach returns a value of C_P at $\alpha_4 = 0$ that is equal to zero.

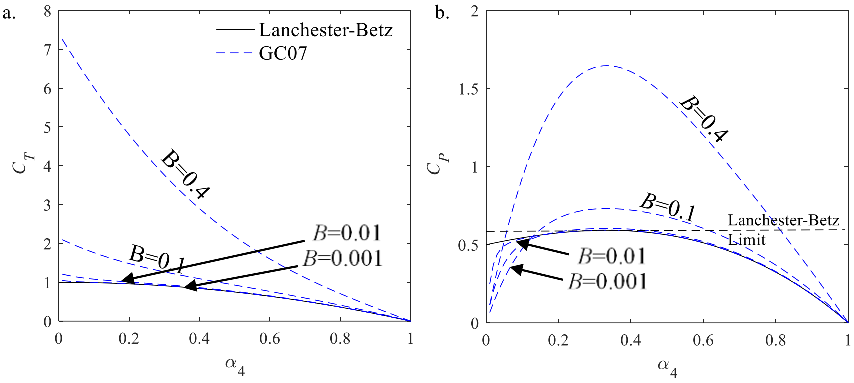

Figure 1-9: Power and thrust coefficient from GC07 and Lanchester-Betz

The maximum power based on GC07 can be calculated as

$$P_{max} = \frac{16}{27}(1-B)^{-2}\rho u^3 A. \tag{1.15}$$

Despite it being unrealistic for a turbine that occupies the entire cross-section, this theory suggests that at a very high blockage ratio (B~1) the maximum power (P_{max}) would be infinte. This anomaly is because theory also neglects the effect of the turbine resistance on the surface deformation. It is unrealistic to assume there is no deformation of the free surface at the high blockage.

c) *Surface Deformation Constraint*

Houlsby *et al.*, 2008 (later published in Houlsby & Vogel, 2017) and Whelan *et al.*, 2009 independently expanded GC07 model and include surface deformation and accounting for Froude number. Draper, 2011 named this model as W09 after Whelan *et al.*, 2009. However, this is called Houlsby-Whelan model here as the work has been done slightly earlier by Houlsby *et al.*, 2008. Furthermore, Whelan *et al.*, 2009 analysis did not include the downstream mixing.

The Houlsby-Whelan model extends the actuator disc model by considering the variation of the free surface. Figure 1-10 illustrates the actuator disc framework that takes into account the free surface as both an atmospheric pressure constant and a volume constraint to the flow field.

The turbine velocity coefficient (α_2) calculated as:

$$\alpha_2 = \frac{2(\beta_4 + \alpha_4) - \dfrac{(\beta_4 - 1)^3}{B\beta_4(\beta_4 - \alpha_4)}}{4 + \dfrac{({\beta_4}^2 - 1)}{\alpha_4\beta_4}}, \tag{1.16}$$

and β_4 is solved from:

$$\frac{F_r^{\,2}}{2}\beta_4^{\,4}+2\alpha_4 F_r^{\,2}\beta_4^{\,3}-(2-2B+F_r^{\,2})\beta_4^{\,2}-(4\alpha_4+2\alpha_4F_r^{\,2}-4)\beta_4+(\frac{F_r^{\,2}}{2}+4\alpha_4-2B\alpha_4^{\,2}-2)=0\,. \qquad (1.17)$$

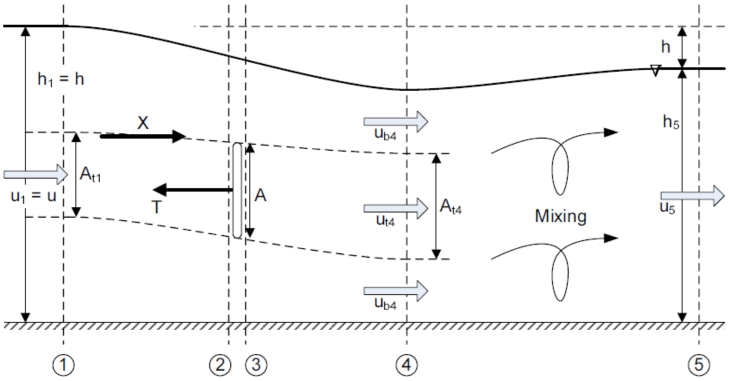

Figure 1-10. Illustration of surface deformation due to an actuator disc in the tidal stream with a free surface. Figure taken from Houlsby *et al.* 2008.

The available power and efficiency are enhanced as the Froude number increases, based on this model. Therefore, this model gives a higher $C_{P,\,max}$ if the Froude number is higher. In other words, a turbine produces more power (even when normalised by upstream kinetic energy) when the velocity increases. However, as discussed by Draper, 2011, has limits to its applicability in cases where there is no solution for β_4, the bypass coefficient, for certain Froude numbers.

1.2.6 The Highest Hypothetical Blockage Ratio

In tidal energy analysis, use of a uniform blockage ratio is convenient. Many authors use uniform blockage ratio to analyse certain phenomena related to tidal power extraction [Adcock *et al.*, 2013; Draper *et al.*, 2014; Coles *et al.*, 2017]. Furthermore, as shown in tidal energy extraction theory, a high blockage ratio give advantages, as the power that is removed from the stream could increase significantly. Therefore, in many analyses, high blockage ratios are considered, e.g. Vennel, 2011 shows the tuning of wake coefficient has a significant effect at blockage ratio higher than 0.5.

However, a very high blockage ratio ($B > 0.4$) might be only applicable to cross-flow turbines. As the swept area of cross-flow turbines is rectangular, they can fill the space in the cross-section of the channel. However, recent development of tidal turbines has focused on “propeller type” axial flow turbines.

The circular swept area makes the very high blockage ratio of B>0.4 hard to achieve. Furthermore, the turbines in an array need to have freeboard with the surface and seabed, while space between the turbines is also needed. This makes B > 0.4 harder to achieve because of the turbine geometry.

In this thesis we assume the achievable highest blockage ratio is *B*=0.4. Figure 1-11 shows an illustration of Blockage Ratio *B*=0.4 with a sensible freeboard and spacing between the turbines. Beyond simple geometric limits there are, of course, structural issues in making turbines very large.

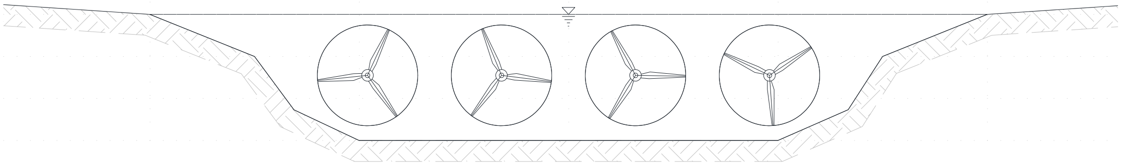

Figure 1-11. An example of blockage ratio (*B*) = 0.4, the diameter of the turbines is 24 m, and the channel cross-section is approximately 4,900 m^2

1.2.7 The Current Practice of Resource Assessment and Its Practicability

Some resource assessments have been done for the UK and Canada with only a single tidal constituent (M_2 only). This method of constituent reduction reduces the computational cost for the tidal resource assessments. Despite this simplification, the assessment with a single constituent (M_2 only) still gives satisfactory results. To date, most tidal resource assessments have been carried out for regions that are dominated by semidiurnal tides (M_2 and S_2). As discussed later, in Chapter 2, the sine curves of M_2 and S_2 are in phase every fourteen days. Therefore, by analysing seven days of power extraction in a semidiurnal regime will give satisfactory results. Table 1-4 shows some potential resources and the boundary forcing used for the assessments in the UK and Canada.

Table 1-4: Tidal resources assessments that have been done in the UK and Canada

Sites	Reference	Potential (GW)	Boundary Forcing
Minas Passage, Canada	Karsten *et al.*, 2008	2.5	M_2 only
Johnstone Strait, Canada	Sutherland *et al.*, 2007	1.3	M_2 only
Masset Sound, Canada	Blanchfield *et al.*, 2008	0.08	M_2 only
Pentland Firth, UK	Draper *et al.*, 2014	4.2	M_2 and S_2
	Adcock *et al.*, 2013	1.9	M_2 and S_2
Channel Islands, UK	Coles *et al.*, 2017	4.7-5.5	M_2 only
Alderney Race, UK	Coles *et al.*, 2020	3.26	M_2 and S_2
Anglesey Skeries, UK	Serhadlioğlu *et al.*, 2013	0.326	M_2 and S_2

The Pentland Firth, for example, a prime target site for tidal turbines in the UK, can be assessed in terms of M_2 and S_2. Adcock *et al.*, 2013 have carried out a resource assessment seeking an upper boundary for power availability using only S_2 and M_2 in the Pentland Firth. They compare the results with analyses using additional constituents (K_1, K_2, MU_2, N_2, NU_2 and O_1), and show that including these only increases the mean available power by about 7-9%. Other publications for this site also use just one or two principal semidiurnal constituents (M_2 only or both M_2 and S_2) for the forcing in the analysis [e.g., Draper *et al.*, 2014; O'Hara Murray & Gallego, 2017; Goward Brown *et al.*, 2017].

However, many Indonesian sites do not conform to this pattern, often being dominated by diurnal tides. The question then arises whether this simplification is also applicable to the areas where the diurnal constituents (K_1 and O_1) play an important role. Unfortunately, there appears to be little recent research addressing resource assessment in this type of environment.

1.3 Tidal Power Opportunity in Indonesia

Indonesia is the world's fourth most populous country, and Southeast Asia's largest economy. As well as other countries, the provision of energy is pivotal for Indonesia's future. However, provision of electricity across Indonesia needs proper study before deploying any investment in this region. Investment in the electricity sector is complex, and requires comprehensive information before committing to capital projects. Since tidal power is relatively new, an understanding of the engineering part is essential, but understanding the business issues is also vital. For instance, the available resource is not the only important information for turbine developers; the local demand is also important for the future development of the industry.

Understanding electricity regulation and demand in Indonesia provides the essential context for tidal resource assessment. As an archipelagic country with myriad and scattered islands, electricity provision in Indonesia is complicated by a variety of demands, both from very populous areas and from isolated communities. The scale of developments must be tailored to local demand to create a viable supply.

1.3.1 Previous Estimates of Indonesian Resources

There are limited publications on tidal resources for Indonesia. Rachmayani *et al.* 2006 studied tidal resources in Bali, Lombok and Makassar using the 3D Princeton Ocean Model (POM). They show the power density of the tide driven current during spring tides at each location, simulate the tidal currents and compare the results of a depth-averaged model and a 3D model. They found that the power density (for the total potential area) exceeded 596 kWh/m^2 (horizontal area) at peak velocity. However, they studied only the power density, not the extracted power, and they did not consider the effects of a turbine array on the flow.

Blunden *et al.*, 2013 studied tidal resources in the Alas Strait using POM and using a method that they called "per-generator tidal current energy". Flow retardation was taken into account in their analysis, and turbine rotor selection considered natural water depth limitations. They found that this site has "modest" resources of 640 GWh/annum due to moderate peak flow speeds of around 2 m/s. However, as mentioned in many government reports (see Coordinating team of Research and Technology, 2008 and Rachmat, 2013), this strait has less potential than other neighbouring sites.

Orhan *et al.*, 2015 investigated the potential tidal energy at Larantuka Straits using Delft3D developed by Deltares, and found that the power densities can exceed 6 kW/m^2 for a velocity exceeding 4 m/s. This research was continued by Orhan *et al.*, 2017 for seven straits between the inner Indonesian Sea and the Indian Ocean. Simulating the tidal current from the Sunda Strait located between Sumatra and Java Islands to Larantuka Strait in East Nusatenggara, they concluded that there are at least seven potential locations of tidal stream energy. However, neither of their studies consider the interaction between the turbine arrays and the flow, and the extracted power is computed from the kinetic energy flux multiplied by the rotor and generator efficiencies. Most of tidal energy resource assessments for Indonesia use undisturbed kinetic energy to estimate the resource. Adcock *et al.*, 2021 suggest that, whilst this is appropriate for making an initial estimate of the resource, more detailed methods are needed to refine the estimate.

The government of Indonesia has identified some candidate sites for tidal energy extraction based on field measurements (see Mukhtasor *et al.*, 2014). The early data from field measurement, in the "Ocean Energy Resources Map", identifies ten potential sites for tidal stream turbine extraction (Figure 1-12). There are possibilities of more locations besides these ten sites. Firdaus *et al.*, 2017 have briefly discussed these potential locations, and a summary is as shown in Table 1-5, including in which region the potential sites are located.

These ten sites can certainly be expanded since, after publishing this map, government agencies have further updated the potential sites in Indonesian waters. As a country of which two-thirds of the territory is the ocean, there are plenty of potential sites for tidal energy extraction.

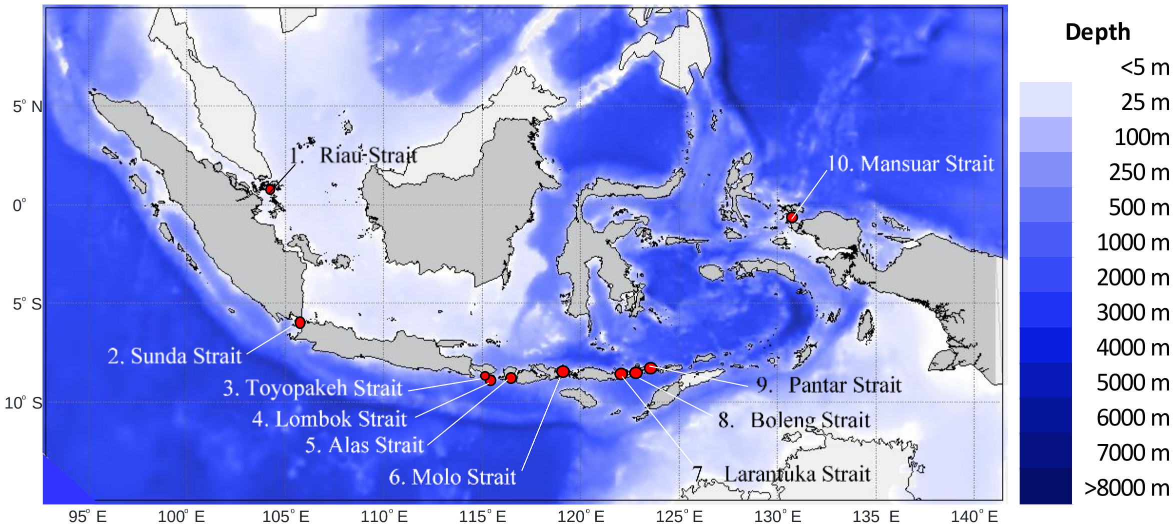

Figure 1-12: Ten potential sites for tidal energy generation from the Map of Potential Resources in Indonesia (see Firdaus *et al.*, 2017)

Table 1-5: Potential locations according to Map of Potential Resources in Indonesia (taken from Firdaus *et al.*, 2017)

Location	**Region**	**Max Vel. Mag. (m/s)**	**Depth**	**Electrification Ratio**	**Population**
1.Riau	Western	1.39 (a)	20-30	73.53% (Kepri)	<3 million
2.Sunda	Western	2.63 (a)		95.64 (Banten) and 84.71% (Lampung)	13-40 million
3.Toyopakeh	Central	3.2 (b)	80-100	89.19 (Bali)	3-6 million
4.Lombok	Central	2.44 (a)		89.19 (Bali) 72.77% (NTB)	
5.Alas	Central	2.4 (c), 2.9 (d)		72.77% (NTB)	3-6 million
6.Molo	Central	1.85 (e)	15-30	72.77% (NTB)	3-6 million
7.Larantuka	Central	3.4 (g)	20-35	56.64% (NTT)	3-6 million
8.Boleng	Central	1.5 (a)	125-150	56.64% (NTT)	3-6 million
9.Pantar	Central	2.91(d)		56.64% (NTT)	3-6 million
10.Mansuar	Eastern	1.79 (h)		82.7% (West Papua)	<3 million

(a)Mukhtasor *et al.*, 2014, (b)Yuningsih., (2008), (c)Blunden *et al.*, 2007, (d)Coordinating team of Research and Technology, 2008, (g) Orhan *et al.*, 2015 and Orhan *et al.*, 2017, (h) Rachmat, 2013, and (i) Yosi, 2013

1.3.2 The Complexity of Indonesian Waters

There are at least three features of the tides in Indonesian waters that differ from the majority of other candidate areas for tidal stream exploitation. Firstly, as the largest archipelagic country in the world, Indonesia has approximately 17,000 islands. This myriad of islands complicates the modelling for a tidal resource assessment in this country. Secondly, a global current caused by thermohaline circulation, also known as a “great ocean conveyor belt” passes through Indonesia (see Figure 1-13). Lastly, Indonesia has a complicated tidal regime. As mentioned in Chapter 1, the tides at many potential sites in the UK and Canada have a semidiurnal pattern. The tides in Indonesia exhibit a semidiurnal to diurnal tidal regime.

a) The Geographical Complexity of Indonesia

Indonesia is the only region that connects two major oceans (Pacific and Indian) and lies on the equator. Thus, this region is a pathway of inter-oceanic exchange between the Pacific and Indian oceans. This archipelago is very complex, with numerous narrow straits, atolls (submarine mountains) and semi-enclosed basins, with a sharp edge to the continental shelf down to 3,000-6,000 m depth in the area between the island chains of Bali-Nusatenggara and the Mollucas Seas - Sula Archipelago in North Maluku.

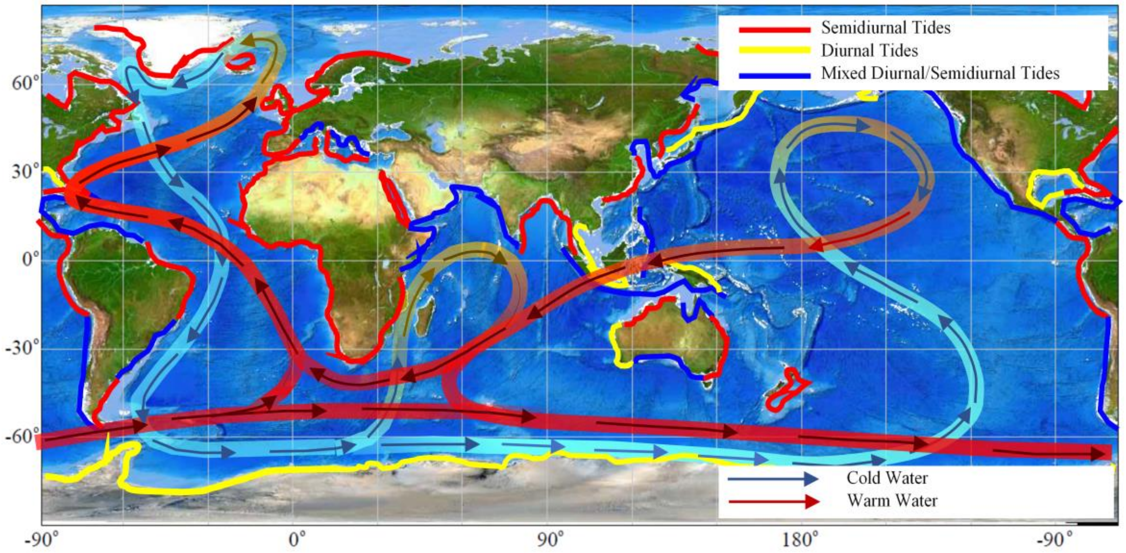

Figure 1-13: The World Tidal Types (based on NOAA, 2020. and Simplified Thermohaline Circulation (based on Encyclopaedia Britannica, 2020.)

Meanwhile, the Java Seas and Riau Archipelago are a shallow water region, with a depth of less than 50 m. These shallow water regions are connected to the deep Indian Ocean with a depth more than 6000 m via the Sunda Strait. A steep bottom gradient also can be found in the island chains of Bali-Nusatenggara, Lombok, Alas, Flores, Larantuka and Timor Straits. Moreover, the small islands in the interior seas complicate the bathymetry and the current features in this region.

To capture these complexities in an analysis, a larger model domain is required than commonly found in analysis of tidals around the UK. For comparison, most of the tidal resource assessment in the UK used a relatively small domain compared to that used in this thesis (Draper *et al.*, 2014;

Adcock *et al.*, 2013; Coles et al., 2017; O'Hara Murray & Gallego, 2017). However, this is problematic as it makes the tidal assessment in Indonesia more computationally demanding.

As later discussed in Chapter 5, the impact of turbine deployment on the flow field may also be essential for robust resource assessment. Therefore, it is necessary to understand the characteristics of tidal hydrodynamic features in the region. Thus, a regional scale model is needed for the assessment in Indonesian waters.

b) The Existence of a Global Current

Located between the Pacific and Indian Oceans, a global-current known as the "great ocean conveyor belt" flows through Indonesia. There is no single explanation for this current. However, there is a consensus that it occurs due to the joint effects of thermohaline forcing and turbulent mixing. The current is driven by gradients of temperature and salinity and the subsequent interior mixing of heat and salt (see Rahmstorf, 2002 and Wunsch, 2002).

Figure 1-13 illustrates the flow patterns of the worldwide thermohaline circulation. As seen in the figure, the circulation consists of warm currents and cold currents. The circulation that passes through Indonesia is warm water.

This thermohaline circulation then creates a complex pattern of sub-circulation in Indonesian waters that is known as the Indonesia Through Flow (ITF) (see Figure 1-14). This phenomenon has been extensively studied by the oceanographic community (Arief & Murray, 1996; Bray *et al.*, 1997; Fieux *et al.*, 1996; Godfrey, 1996; Gordon *et al.*, 1997; Gordon *et al.*, 2012; Kashino *et al.*, 1999; Lukas *et al.*, 1996; Meyers *et al.*, 1995; Murray & Arief, 1988; Susanto & Song, 2015; Vranes *et al.*, 2002; van Aken *et al.*, 2009 and Wijffels *et al.*, 2002). The motivation for investigating the ITF is varied, from understanding the nature of the thermohaline circulation to the prediction of the impact of this current on climate change and vice-versa. However, in this thesis we are only interested in understanding the flow characteristics.

The ITF passes through the islands from Sulawesi and Kalimantan to Bali and Nusatenggara with a velocity of 0.2-0.4 m/s (Gordon, 2005; Sprintall *et al.* 2009; Sprintall *et al.* 2014). The ITF goes through the Makassar Straits and divides through the Lombok Straits and Timor Passage. The velocity of the ITF varies from 0.1-0.2 m/s in Lombok and about 0.2 m/s - 0.3 m/s in the Flores area. Whilst relatively small compared to the tidal currents, this steady current could significantly influence the nature of the tidal resource in the region.

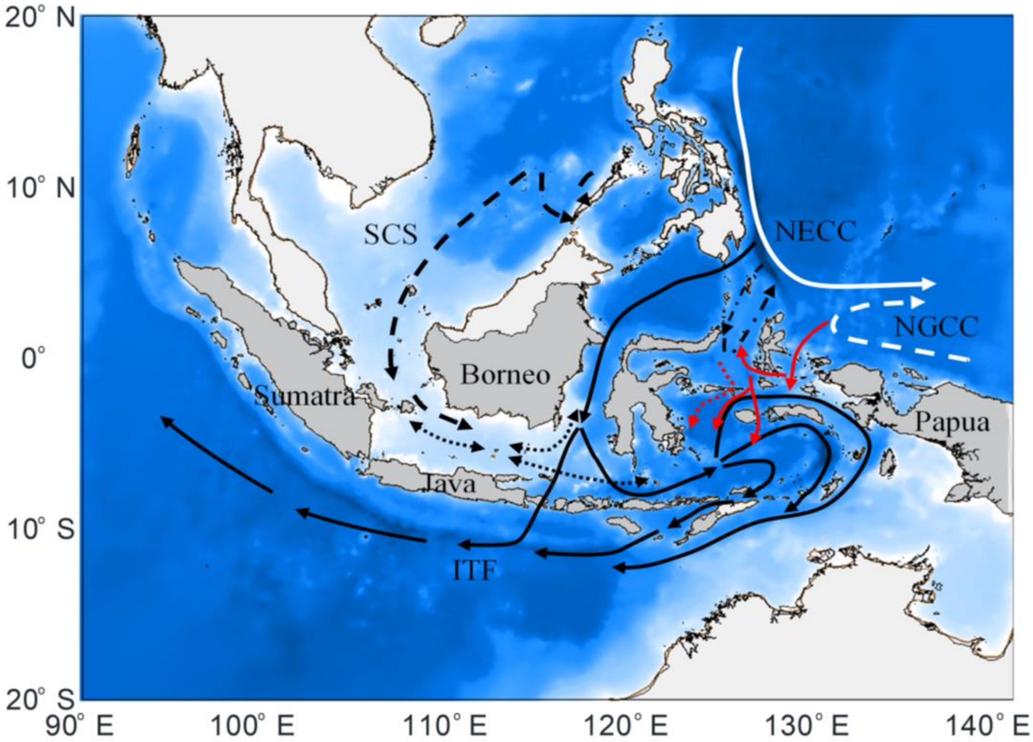

Figure 1-14: Indonesian Through Flow (solid black lines) (see Gordon, 2005; Sprintall *et al.* 2009; Sprintall *et al.* 2014) and South China Sea (SCS) Throughflow (black dashed line) (see Gordon *et al.* 2012). The North Equatorial Counter Current (NECC-solid white line), New Guinea Coastal Current (NGCC-white dashed line). Mindanao Retrospective Current (black dash-dot line)(see **(**Mayer *et al.*, 1995). Lifamatola passage (Red dotted line) (see van Aken *et al.*, 2009) and Halmahera Sub Current (solid red line) (see Morey *et al.*, 1999).

This non-tidal flow might have a significant impact on the tidal stream energy resource due to coupling effect between the flows. The modelling therefore requires incorporating this residual flow. The inclusion of this residual current is further discussed in Chapter 4.

This current also creates a highly stratified or sheared flow. In Indonesian waters, the sheared flow profile is generally much stronger in the upper layer of water column, as in Lombok Strait or stronger near the sea bed as in the Lifamatola Strait. However, the impact of this sheared flow on the turbine performance is negligible. The detail of analysis and discussion on this subject are presented in Chapter 3.

c) Complex Tidal Pattern

As briefly discussed in Chapter 1, most of studies of tidal resources have been undertaken for sites in the northern hemisphere.. Those sites are located in areas of semidiurnal tides (e.g. the UK and Canada). The tidal pattern in these sites is dominated by M_2, the principal lunar tidal constituent.

Therefore, tidal resource assessments could be conducted using a semidiurnal components only (M_2 only or M_2 and S_2) constituents.

This approach is not applicable in Indonesian waters. The NOAA, 2020's tidal type maps show that Indonesian tidal types vary from mixed diurnal to semidiurnal (see Figure 1-13). This means that K_1 and O_1 also play an important role in the tidal dynamics. A significant diurnal component (K_1 and O_1) results in different types of tidal cycles. Sites with dominant S_2 and M_2 tides show a simple pattern of two tidal cycles in a day, while areas dominated by diurnal components have one cycle a day; the intermediate types between semidiurnal and diurnal show more complicated patterns.

A more detailed map of tidal types in Indonesia is presented by Wyrtki, 1961. Although this data is slightly inaccurate when compared to the tidal station data provided by the Admiralty tidal chart (DISHIDROS, 2004) (see Figure 1-15), the Wyrtki, 1961 tidal map helps us to see the complexity of the tidal regime in Indonesian waters. The tidal type is semidiurnal in the Malacca Strait. This tidal type then changes to diurnal at Bangka-Belitung islands (station 24 and 31). The complexity is not just observed on the regional scale, but also at a local scale. For instance, the tidal type at Benoa (station 47) is mixed diurnal with predominantly semidiurnal, while at Lembar (station 48) it is mixed-diurnal with diurnal dominant. Both stations are in the Lombok Strait.

The strong K_1 and O_1 components in Indonesian waters make us unable to follow the method of using one or two principal lunar constituents (M_2 and S_2), commonly used for analysing tidal sites (Karsten *et al.*, 2008; Sutherland *et al.*, 2007; Blanchfield *et al*. 2008; Draper *et al.* 2014, Adcock *et al.* 2013, Coles *et al.* 2017, 2020 and Serhadlıoğlu *et al.*, 2013). Intuitively, we may think an assessment in the diurnal tidal regime, dominated by K_1 and O_1, could be done just using the two principal diurnal constituents. However, as later discussed in this chapter and in Chapter 5, this approach is inapplicable as well. The tidal velocity variation does not necessarily follow the tidal elevation pattern. The complexities of the tidal pattern, especially when other tidal constituents are introduced, and its implications for the resource assessment is further discussed later in this chapter.

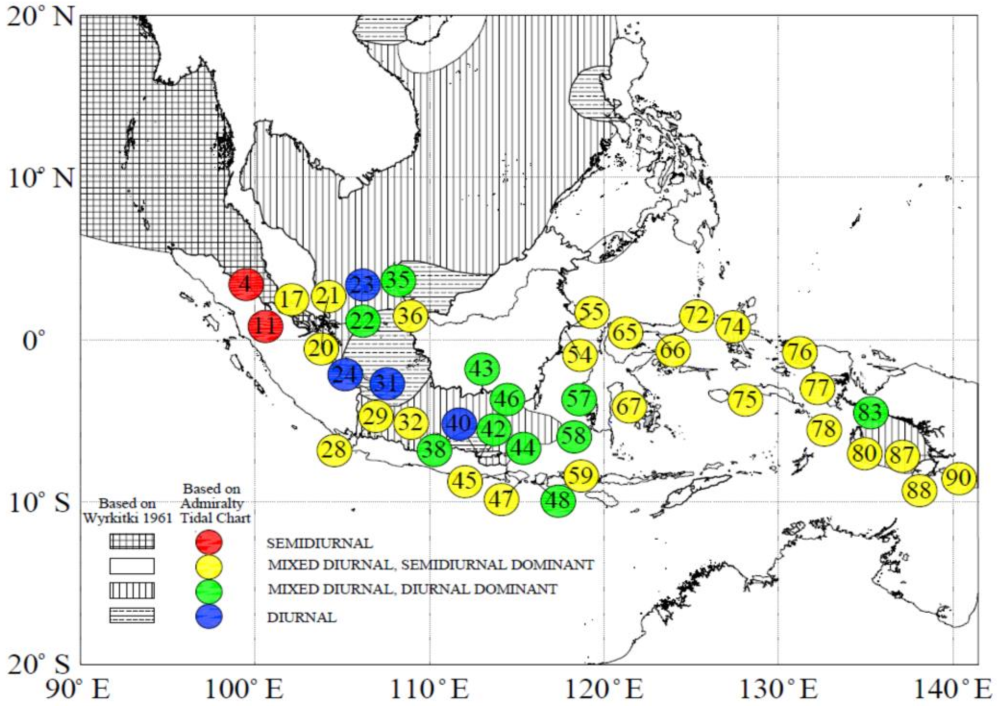

Figure 1-15: Tidal variation in Indonesian waters. The area shading is based on Wyrtki, 1961, and the circle with the number is based on the station's tidal components in admiralty tidal chart (DISHIDROS, 2004).

1.3.3 The Selected Sites for the Resource Assessment

This study selects five locations for assessment. Three of the potential sites are taken from the ten locations of the ocean energy resources map: the Lombok, Larantuka and Sunda Straits. Lombok and Larantuka are selected due to the imminent needs of upcoming projects on tidal energy extraction in Indonesia, whilst Sunda Strait is selected due to its proximity to the most populated region in Indonesia. Sunda Strait also has potential due to the long term plan for a bridge connecting Java and Sumatra.

The two other sites are from the outside the ten locations. Lingga Regency in Riau Archipelago Province and Small Straits Sula Regencies are selected to represent specific cases for a resource assessment. Small straits in the Lingga Regency represent tidal resource assessment in a diurnal tidal regime, while the sites in Taliabu and Sula Regencies represent unique deep-water characteristics and unusual site interactions.

a) Larantuka Strait; The Tidal Resources at Palmerah Bridge

The Larantuka Strait is planned as a site for a tidal project in Indonesia. Located in Nusa Tenggara Timur (NTT) Province, the Larantuka strait separates the Flores and Alor Island. Therefore, a tidal turbine is planned to be incorporated in the bridge connecting the Eastern tip of Flores to Adonara.

Larantuka strait has one of the strongest tidal currents in Indonesia. The tidal bridge is expected to provide electricity for approximately 80,000 people in East Flores. As shown in Figure 1-16, the population in the area is projected at around 200,000-300,000 in 2020. This means that the demand could be higher than the current approximate demand, which is for the 80,000 population. A new transmission line is planned which could provide additional demand in the future (see Figure 1-16).

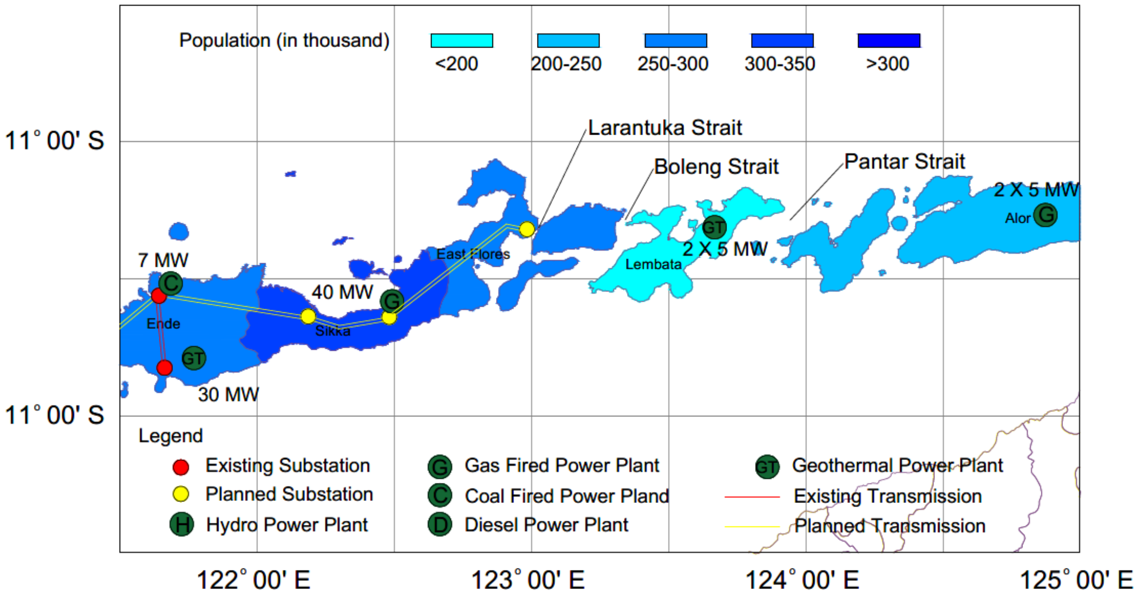

Figure 1-16: NTT's projected population in 2020 (www.ntt.bps.go.id) and the Electricity General Plan (RUPTL 2018-2027)

As shown in the RUPTL 2018-2027, the electricity system in NTT province is dominated by isolated grid systems with scattered small diesel power-plants for electricity generation. Although there are few potential geothermal resources available, the tidal resource is still appealing for this region. This site has one of the highest BPP rates in the country, with 20 cent USD/kWh based on MoEMR Regulation no. 1772 K/20/MEM/2018 (see Figure 1-5**).** Therefore, tidal power extraction might be viable economically for this area.

b) Lombok Strait; Potential Tidal Energy Sites in Tourism Locations

The Lombok Strait, a channel in between Bali Island and Lombok Island, has also been proposed for one of the tidal energy projects in Indonesia. The Islands of Nusa Penida, Nusa Lembongan and Nusa Ceningan divide the Lombok Strait into three different straits, Badung Strait, Toyopakeh and Lombok Strait itself (see Figure 1-17). This site has been awarded to a turbine developer for electricity extraction from tidal flows. These areas are attractive, not only because of the strong tidal current, but also because of their proximity to Bali and Lombok, which are important tourism locations in Indonesia.

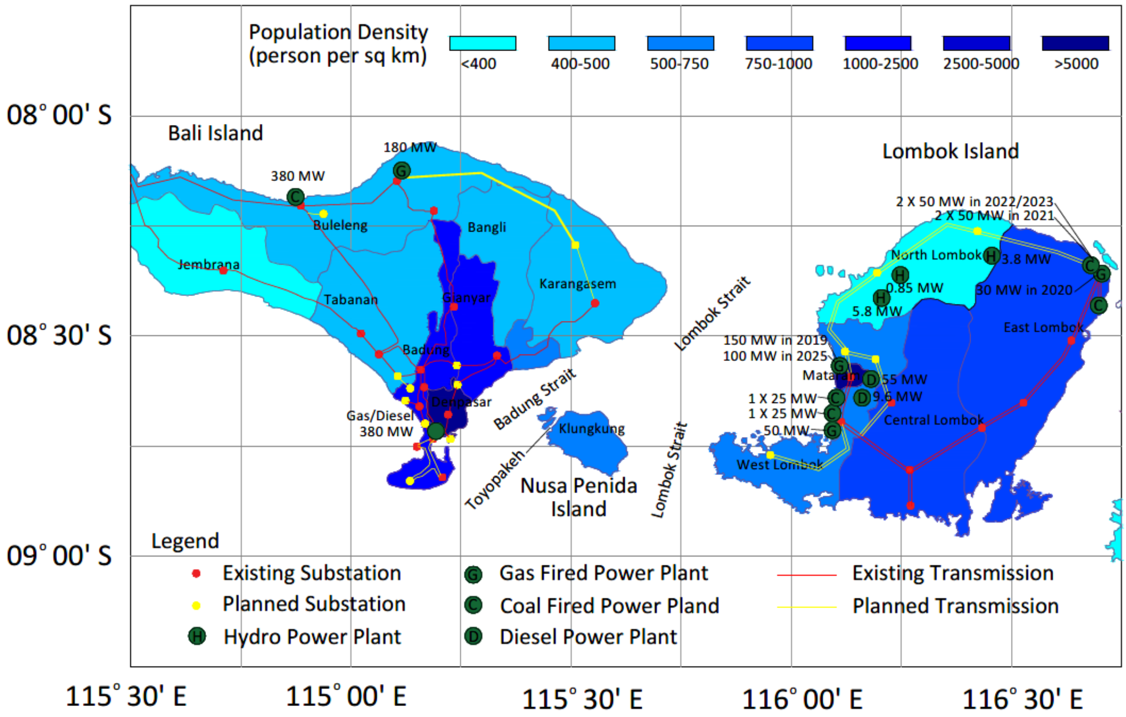

Figure 1-17: Bali and Lombok Projected Population Density in 2020 (www.bali.bps.go.id and www.ntb.bps.go.id) and the Electricity General Plan (RUPTL 2018)

Energy demand in both areas is high from the tourism industry and domestic demand. As shown in Figure 1-17, the densest population in Bali is in Denpasar, while in Lombok it is in Mataram. Both cities are located close to Lombok Strait. Although the West Lombok and Nusa Penida Island (part of Klungkung Regency) have a medium population density, these regions are also a prospective energy market.

Energy in Bali is provided energy from several sources. Since this system is part of the Bali-Java network, with undersea cables connected to the main Java grid, Bali is provided with 400 MW (27.7% of total capacity in Bali) by the Java-Bali grid. The electricity in Bali itself is generated by coal 426 MW (29.5%), by gas 208 MW (14.4%) and diesel power is 408 MW or about 28.3% of total capacity in 2018 (see RUPTL 2018-2027).

While Bali Island is part of the Java-Bali main grid, the islands of Nusa Penida, Nusa Ceningan and Nusa Lembongan have a separate transmission network. This area relies for its energy supply on local diesel power plants. As the islands become more popular with tourists, Nusa Penida Island certainly requires more electricity to match increasing demand. The Toyopakeh strait, in between Nusa Penida and Nusa Lembongan, is a potential candidate to fulfil this need.

Lombok island also has a separate network. As shown in Figure 1-17, a grid connects the power plants around the island. Lombok generates its electricity mainly from coal and diesel. RUPTL 2018 offers a plan for new 100 MW and 150 MW power plants in 2019 and 2025, and a new transmission grid to west Lombok (see Figure 1-17).

Lombok island is predicted to have a population of 3.5 million in 2020 (see bps.go.id), this number is in accordance with the electricity demand. Since the government also plans to develop the Mandalika special economic zone focusing on the tourism industry, the electricity demand for Lombok will certainly increase in the future. With infrastructure and demand ready, therefore, this site is able to absorb electricity from a megawatt scale tidal power plant.

c) Lingga Regency; the Tidal Resources in a Location with Diurnal Tides

Although this site is not included in the Ocean Resources Map, this site is selected to represent a diurnal tidal regime. The assessment in this site is focused on the best method for assessment in region with this tidal pattern. This site also represents a marginal region with a low electrification ratio.

Dasi strait is located in the Lingga Regency, Kepri Province. Inhabited by 89,330 people, this regency has one of the lowest populations in the province (see Figure 1-18). It is important to note that Kepri is also the province with the lowest electrification ratio in Sumatra. The Lingga Regency also has the lowest electrification ratio in Kepri Province, as shown by The Nightlight (Figure 1-19). As seen in the figure, the luminosity in Lingga is very low. This means the electricity services in this area, where there are any, are not reliable. Electricity outage rates in this area are relatively high.

Electricity reliability is often measured by the outage indices known as the System Average Interruption Frequency Index (SAIFI) or the System Average Interruption Duration Index (SAIDI). Kunaifi & Reinders, 2018 show the SAIFI and SAIDI in Riau and Kepri Provinces had SAIDI 11.1 and SAIFI 9.6 in 2015. This means that most of the population in Lingga Province only has electricity for about twelve hours a day. These indexes are lower than in Papua, which had the lowest electrification ratio in 2015. This data on reliability explains the low luminosity in the Lingga regency.

An investment in tidal turbine deployment might not be lucrative in Lingga. However, it could nevertheless be a solution for this region. Electricity is essential for poverty alleviation. Access to electricity is now considered as a basic need, and it is the government's responsibility to provide it. BPS 2018 estimates the average electricity consumption per capita in Indonesia is 117 watts/person. Therefore, based on its population number, Lingga regency approximately needs 10.45 MW of installed capacity.

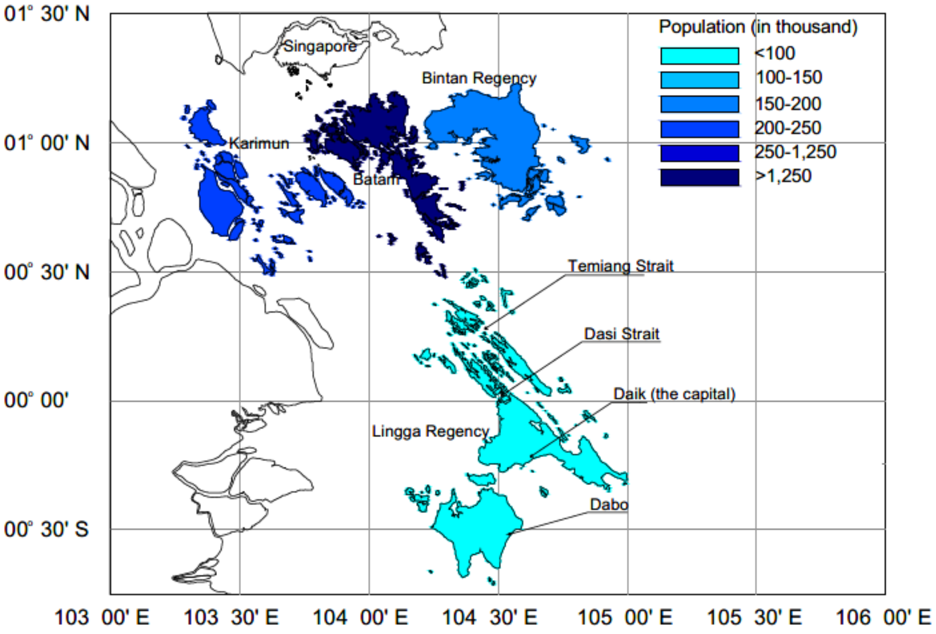

Figure 1-18: Population in Lingga Regency based on BPS 2019

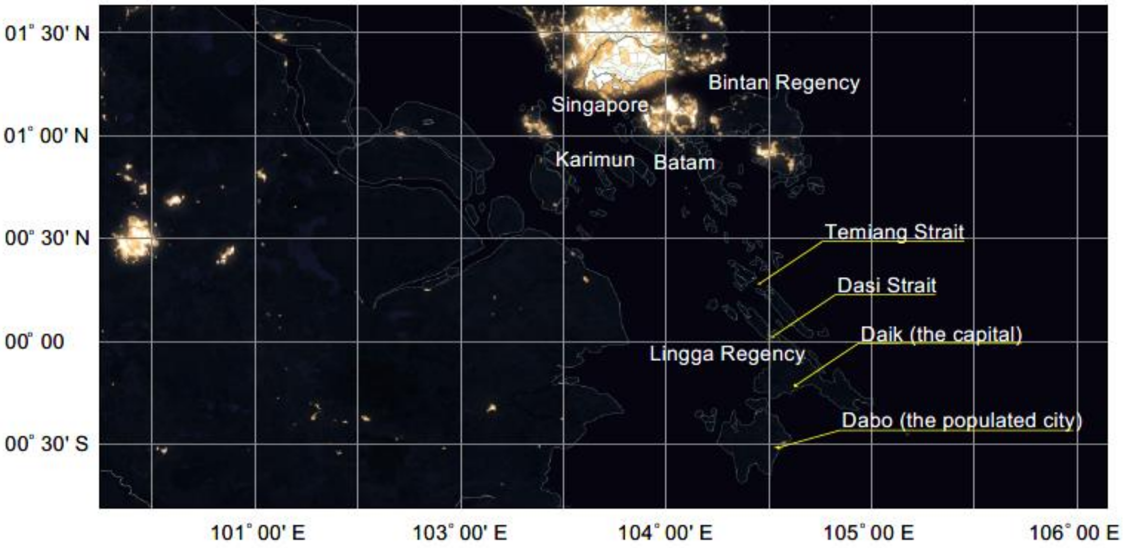

Source: https://ngdc.noaa.gov

Figure 1-19: Nightlight in Lingga Regency

d) *The Sunda Strait Bridge*

The proposal for a Sunda Strait Bridge (SSB) was first put forward in 1960 by Professor Sedyatmo from Institut Teknologi Bandung. The proposal is part of a broader plan, known as Tri Nusa Bimasakti, to link the three islands of Sumatra, Java and Bali. Indonesia's the first president, Soekarno, initially planned to build a tunnel to connect the islands. The idea later changed to connect the islands by the bridge. In 2014, this idea seemed about to be realised under President Yudhoyono's administration. Unfortunately, the 27-kilometre bridge required in an investment of 160 trillion IDR or around 80 billion GBP. Therefore, this plan was shelved when the administration changed to President Widodo in 2014 as this bridge is too costly whilst the economic impact of the bridge would be limited only to the two provinces.

As this bridge would be located near the most populated area in the country, there is an opportunity to develop a tidal bridge as well. A tidal power plant could make the bridge more viable economically. Therefore we examine the tidal resources in this area. The Sunda Strait is located in the territory of Lampung Province and Banten Province. Both locations have some of the most developed infrastructure in the country. Lampung Province has a total capacity of 1000 MW to provide the electricity needs for southern region of Sumatra island. On Java Island, there are power plants with approximately 7 GW total capacity interconnected by the Java main grid (see Figure 1-20). This also implies that the site has existing substations available to accept electricity resources. This means the cost of new electricity infrastructure would be relatively low.

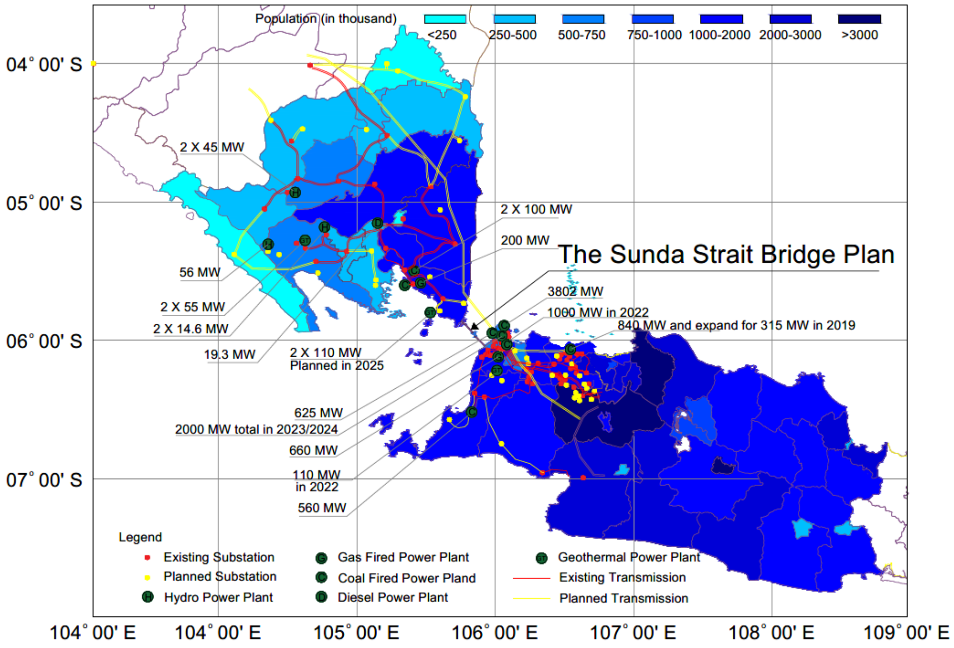

Figure 1-20: Projected population in 2020 for the area near Sunda Strait (www.bps.go.id) and the Electricity General Plan (RUPTL 2018-2027)

e) The Potential Resources in the Eastern Deepwater Sites, Sula Regencies

The Eastern Indonesian ocean is a deep-water system with a combination of a wide range of island sizes and rapidly changing bathymetry with atolls and underwater volcanoes reaching the water surface. The Sula and Taliabu Regencies in North Maluku Province have several straits with strong currents. The interaction between the tidal current and ITF in this area creates a sheared flow with a stronger current near the sea bed.

This area represents an area with a stronger deep-water current, although the Ocean Energy Potential Map (Figure 1-12) has not included this site yet. There are three straits and one headland that have the potential for tidal generation: Capalulu, Magola, Lifamatola Straits and Lifamatola headland (see Figure 1-21). These sites are assessed for tidal resources in this thesis.

The Taliabu Regency's population is projected to reach an estimated 53,411 in 2020, while the Sula Archipelago Regency population is estimated as 104,971 population in 2020. The demographics in this area are not distributed evenly. Sanana, the capital of Sula Regency, is the most populated area, with a population of 29,139 and a growth rate of 7.87% based on 2014-2015 data (see https://kepsulkab.bps.go.id). This district close to Lifamatola Strait and Lifamatola Headland, North East Mangole, has a population of less than 5000. Although Lifamatola Strait and Lifamatola Headland are interesting in terms of understanding the physical processes of tidal turbine implementation, there may not be a viable demand in this area.

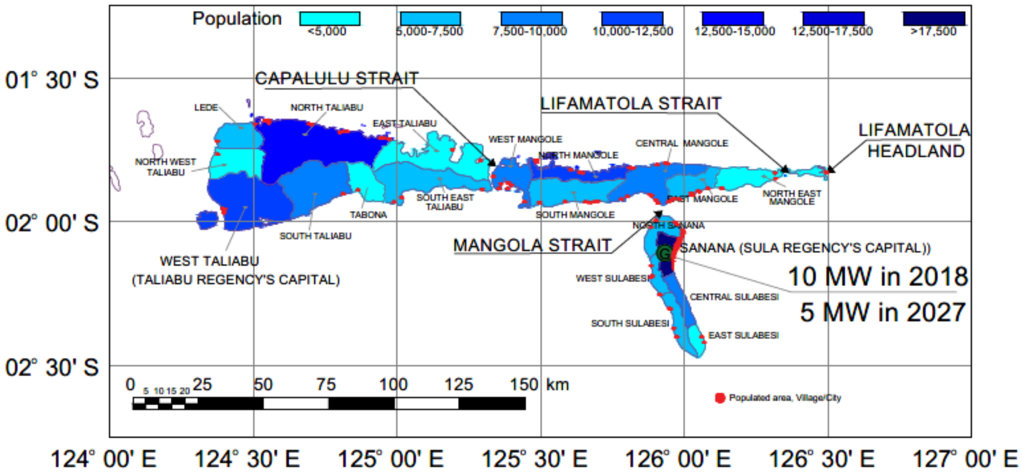

Figure 1-21: Projected population in 2020 for sub-districts in Taliabu and Sula Regencies (www.bps.go.id) and the Electricity General Plan (RUPTL 2018-2027)

1.4 Research Questions

The main research question of this thesis is to understand the opportunities to generate electricity from tidal turbines in Indonesian waters. A number of research questions arise in the quest of assessing the opportunities in this region.

1.4.1 Tidal Complexities

Unlike many developed areas for tidal resource assessment, such as the UK and Canada, where the tide in these regions is predominantly semidiurnal, the tidal variations in Indonesian waters show strong diurnal components. These dominant diurnal tidal constituents lead to important research questions, such as:

- How long a simulation is required in such conditions?
- What are the best constituent(s) to simplify the assessment?
- What is the best capping strategy for an area of non-semidiurnal tides?

1.4.2 Turbine Performance in a Sheared Flow

As a global flow of thermohaline circulation passes through Indonesian waters, the flow tends to stratify at particular locations. This flow stratification has some similarities to sheared flow in term of the physics. As has been addressed by Draper *et al.*, 2016, there are limitations of assessment methods in this case, especially related to highly stratified flow. Therefore, there are research questions that emerge from these phenomena:

- Is actuator disc theory (i.e. Houlsby-Whelan Model) still valid for an assessment in such locations?
- What is the fidelity of this model if the flow stratification is observable in the potential sites?

1.4.3 Robust Tidal Hydrodynamic Models

As discussed in section 1.3.2, the geographical complexity makes modelling using the shallow water equations (SWE) in Indonesia water complex. Therefore the research questions that arise from this are:

- Which model domains should be developed to solve the SWE in the area?
- How large a model domain should be built to capture the leading order of physics from deploying turbine fences in Indonesian water?

1.4.4 The Impact of Turbine Deployment on the Regional Flowfield

A deployment of turbine fences will partially obstruct the flow. Therefore it is important to understand the change made by the turbines to the flowfield. Therefore, it sensible to ask:

- How significant is the flowfield change in an area due to turbine deployment?
- What is the impact of turbine deployment on the thermohaline circulation in the area?

1.5 Aims and Objectives

Based on the research questions that arise in this thesis, the aims and objectives of this thesis could be broke down as follows:

- To understand the nature of power extraction in a complex tidal regime arising from the specific local effects of the diurnal components of the tidal regime.

- Investigate the effect of flow stratification/sheared flow that occurs due to the existence of the thermohaline circulation in the potential sites.
- To build robust SWE models to assess tidal energy potential in Indonesian waters.
- To assess tidal resources in Indonesia, addressing theoretical resources using a uniform blockage ratio, and realistic resources with implementation of turbine constraints such as turbine size and capping strategy.
- To understand the impact of turbine deployment on the regional flowfield.
- To consider the environmental constraints and the economic viability in the selected sites in Indonesia.

1.6 Synopsis

This thesis begins by investigating the nature of power extraction in a complex tidal regime. Tidal energy investment, as for investment in any sector, requires certainty. The limited knowledge of the tidal environment adds to the uncertainty for tidal energy investment in Indonesia waters. In order to understand the complexity arising from the specific local effects of the diurnal component on the tidal regime, a 1-D channel model is employed for the investigations (see Chapter 2).

Another important issue is the effect of sheared flow or flow stratification on the turbines' performance. Chapter 3 discusses flow stratification and sheared flow. Using ANSYS, a commercial three-dimensional CFD model, the impact of this phenomenon on the turbines' performance is investigated in this chapter.

This study assesses Indonesia's tidal resources using a shallow water equation model, and developing robust models are important for this assessment. An open-source shallow water equation (SWE) model, DG-ADCRIC, is modified to assess the tidal resources in the area. Three model domains to cover five different potential sites are developed in this study.

Careful validations were conducted for each domain, as shown in Chapter 4. However, relatively few studies of tidal hydrodynamics have been conducted for this region using a large scal domain. Reliable data for calibration of models are sparse in this region, with the available data in the open literature limited. Some measurement data at some sites from government agencies has, however, been obtained. The validations are conducted at key locations near the potential sites. The models are also validated against the admiralty tidal chart and a co-tidal chart from satellite altimetry. Many publicly available studies assess Indonesian waters using only a small model domain (e.g., Blunden *et al.*, 2013; Orhan *et al.*, 2015; Orhan *et al.*, 2017; Rachmayani *et al.*, 2006; and

Coordinating Team of Research and Technology, 2008). This approach leads to shortcomings; for instance, the interaction between sites or straits is not observable. Draper *et al.*, 2014 show the interdependency of the channels in Pentland Firth, UK. They conducted a study that showed that the power removed by the turbine in a channel is different when the channel is exploited in parallel with an adjacent channel. Coles *et al.*, 2017 carried out similar work in the Channel Islands, UK, finding a similar pattern also occurs at this site. Dependency and interdependency between the channels in the assessment are critical since they might lead to different strategies on the investment in tidal energy. This issue is explored in Chapter 5 as well as assessing tidal energy resources in the five selected locations

The thermohaline circulation is related to the ocean climate in the area such as La Nina and El Nino. A shutdown or slowdown of the thermohaline circulation is a possible effect of global warming on major ocean circulation (Vellinga & Wood, 2007; Rahmstorf *et al.*, 2015). This means that obstructing the circulation might have a significant impact on the regional environment. Therefore, understanding the impact of turbine deployment on the thermohaline circulation is important before tidal energy exploitation in this area. Since the circulation change could only be observable on a regional scale, an adequate model domain in an assessment for Indonesian water is necessary. The assessment in Chapter 5 also investigates the changes in the regional flowfield that might occur due to tidal turbine deployment.

The assessment is conducted in two stages. Firstly, the assessment in Chapter 5 uses a uniform blockage ratio. The assessment at this stage assumes the turbines could be installed in the entire section of the channel. In reality, the deployment of a turbine(s) is limited by several factors, such as the usage of straits for other purposes, the depth of the sites, and environmental constraints. Therefore, this study also assesses more realistic tidal resources in some potential areas in Chapter 6. The realistic scenarios use turbine array specifications such as turbine diameter and tip-to-tip spacing between the turbines. A capping strategy is also implemented in the realistic assessment in this Chapter. The economic viability in the selected sites is also assessed in addressing the opportunities for tidal energy exploitation.

Chapter 2. 1-D Analysis of Tidal Complexity Due to Pronounce Diurnal Component

This chapter discusses the special features of Indonesian waters regarding tidal energy exploitation. One of the unique features, the existence of strong diurnal tidal harmonic species (K_1 and O_1) is discussed in this chapter. The existence of these diurnal components creates complexity in the tidal hydrodynamics relative to a semidiurnal regime. The impact of the tidal complexity on tidal power extraction is also investigated in this chapter.

As briefly mentioned before, the presence of strong diurnal (K_1 and O_1) components in Indonesia creates a complex tidal pattern. The peaks of each cycle are varied significantly in a mixed diurnal regime. However, the diurnal components do not just create a daily variation. The interaction between diurnal and semidiurnal species also creates annual variations and tidal asymmetry. This section demonstrates the implications of the tidal pattern intricacy in the assessment. Furthermore, this section also aims to analyse the impact of the existence of other strong multiple-constituents in the resource assessment.

2.1 1-D channel Model

A robust model that can give a result which captures the leading order physics of real tidal sites within a sensible computational time is required for this analysis. A simple 1-D model is used here. Garrett and Cummins 2005 (GC05) introduced a simple 1-D model to demonstrate tidal power extraction in a channel connecting two large basins. This model has been used by researchers to explore various features of tidal stream energy (e.g. Vennell, 2011; Vennell, 2012; Adcock & Draper, 2014). The current speed $u(x, t)$ is a function of time (t), as well as the position x along the channel. The simple 1-D model governing the flow in a channel could be written as;

$$\frac{\partial u}{\partial t} + u\frac{\partial u}{\partial x} + g\frac{\partial \eta}{\partial x} = -F_n - F_t, \qquad (2.1)$$

where η is the free surface elevation, g is gravity acceleration, while u is velocity. The right-hand term represents the total force. The naturally occurring friction (F_n) represents the drag applied by seabed ($F_n = \frac{1}{2}C_d Q|Q|/{A_C}^2 h$), where h is water depth, A_C is a channel cross-sectional local area, C_d is the bed friction parameter and Q is the volumetric flow rate. Meanwhile, the resistance applied by turbines (F_t) is total thrust applied by turbines to the flow through the channel. As shown in Garrett and Cummins 2005 and Adcock & Draper, 2014, integrating eq. (2.1) along the channel will give:

$$c\frac{dQ}{dt} - g\xi = -\int_0^L F_t dx - (\delta_0)Q|Q|, \text{ with } \delta_0 = \int_0^L \frac{C_D}{2hA_C{}^2}dx + X, \qquad (2.2)$$

where $c = \int_0^L A_C{}^{-1}dx$ and $\xi$is the head difference between the ends of the channel. The X term in eq. (2.2) accounts for all losses at the exit, such as separation losses and any geometry abruption. The head difference follows the harmonic equation for the WSE and tidal current, as follows:

$$\xi(t) = \sum_{\mathrm{i=1}}^{\mathrm{n}} a_{\xi_i} \cos(\omega_{\mathrm{i}} t), \qquad (2.3)$$

Eq (2.2) is non-dimensionalised using $u_0 = \frac{u}{gT_0}$ and $\xi' = \frac{\xi}{a_0}$. The main purpose of this analysis is to explore the characteristics of power and thrust variation in a different tidal regime based on *Formzahl* number. Therefore the terms of frequency and time are non-dimensionalized with the period (T_0). Since $\omega_n = \frac{2\pi}{T_n}$, then ω_n is non dimensionalised by $\omega_n{}' = \frac{2\pi}{T_n}T_0$, while $t' = \frac{t}{T_0}$. Therefore, the eq. (2.2) can be written as:

$$\frac{dQ'}{dt'} = \xi'(t) - (\lambda_0 + \lambda_1)Q'|Q'|, \qquad (2.4)$$

where $\frac{dQ\prime}{dt\prime}$ is inertia and λ_0 is natural friction. The additional drag produced by the turbine (λ_1) is calculated based on the following equation

$$\lambda_1 = C_T B, \qquad (2.5)$$

where B is the blockage ratio, and C_T is the thrust coefficient. The C_T here is calculated using the Houlsby-Whelan model. The crossectional area (A_C) is assumed constant along the channel as the variation of tidal elevation is proportionately small. Therefore, the Q' follows the velocity variation.

This 1-D channel model is used in this chapter to explore power variation in the different tidal velocity regimes (characterised by different *Formzahl* number). The input for the 1-D channel model is $\xi'(t)$, but it is important to note that the head difference (ξ') variation does not always conform with the tidal velocity variation. A channel has a different response to the different frequencies of oscillatory head difference.

2.1.1 Channel Response

Simple $\xi'(t)$ of M_2 and K_1 signals, for instance, could be used to demonstrate the channel's response. The amplitude of the non-dimensional head difference (a_{ξ_i}) is set to 1.0 for both M_2 and

K_1. The 1-D model is run with two different λ_0 values (0.25 and 0.5), and no turbines are installed in the channel (λ_1=0).

The simulation results show that K_1 gives a higher volumetric flow rate (*Q'*) amplitude than M_2 (see Figure 2-1). The graph shows that for $a_{\xi'_i}$=1.0, K_1 gives an amplitude of volumetric flow rate ($a_{Q'_{K_1}}$) almost twice higher than M_2 ($a_{Q'_{M_2}}$>$a_{Q'_{K_1}}$). This volumetric flow rate comparison is in proportion to the comparison of frequencies (ω_i) or periods (T_i) between two constituents. The K_1 component has a period (T_{K_1}~23.934 hours) almost twice the M_2 (T_{M_2}~12.4206 hours). The complexity is observed in response to channel's friction (here we only account the natural friction-λ_0).

The simulation shows that the K_1 exhibits a significant difference when the λ_0 is increased. As seen in Figure 2-1, the amplitude of the volumetric flow rate from a channel solely driven by a head difference with K_1 frequency ($a_{Q'_{K_1}}$) is smaller when the λ_0 increases from 0.25 to 0.50. Meanwhile, the $a_{Q'_{M_2}}$ is relatively similar for the similar increase of λ_0. The M_2 exhibits a small shifting of the reference point when the λ_0 is increased from 0.25 to 0.3.

The example is then expanded with a wider range of frequency (ω_i). The ω_i is arbitrarily changed to match the tidal period, from the period of shallow water constituents (M_6, M_4, S_6, etc.) to the diurnal constituents (K_1 and O_1). The a_{ξ_i} is 1.0 for all frequencies, while the λ_0 is varied from 0.0000001 to 2.5 and the λ_1 is also set to zero in this exercise. This range is selected due to the range of admissible solutions given by the model. For this case, the ratio of the flow rate amplitude and head difference amplitude $\left(\frac{a_{Q'_i}}{a_{\xi'_i}}\right)$ is plotted against the periods (T_i).

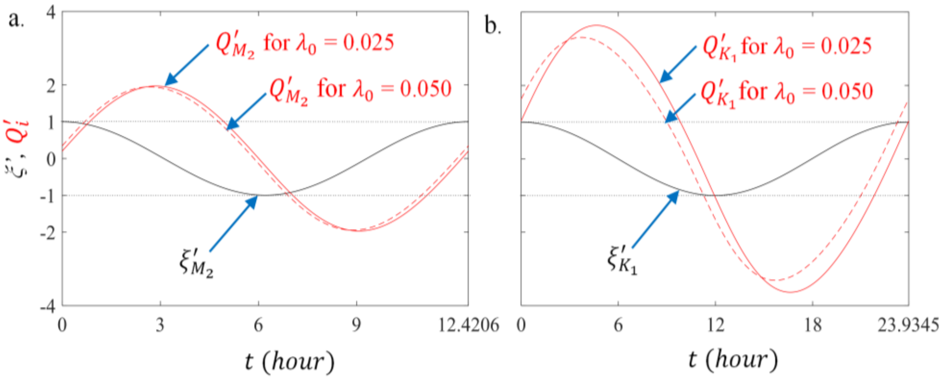

Figure 2-1: Comparison of the channel's response to a. M_2 and b. K_1 tidal components.

Figure 2-2 shows that the $\frac{a_{Q_i'}}{a_{\xi_i'}}$ increases with T_i at low λ_0. The longer the T_i , the higher the $\frac{a_{Q_i'}}{a_{\xi_i'}}$. However, at the same time, an oscillatory channel with a longer T_i is also more sensitive to the λ_0. The graph of $\frac{a_{Q_i'}}{a_{\xi_i'}}$ vs T_i at λ_0= 0.0000001 and λ_0= 0.0025 is almost linear, while at 0.0025 < λ_0< 2.0 the graphs are non-linear. At $\lambda_0 \geq 2.0$, the $\frac{a_{Q_i'}}{a_{\xi_i'}}$ is similar for all T_i.

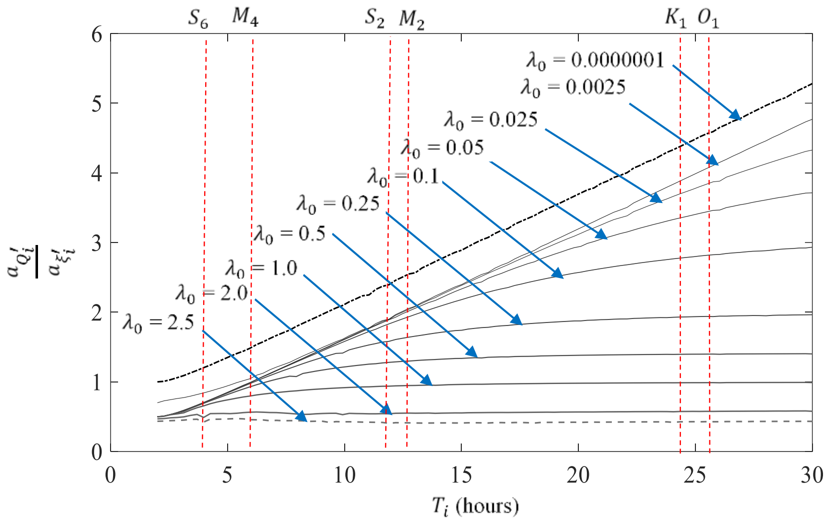

Figure 2-2: The channel response to the different sinusoidal periods

This implies that a channel carrying a flow predominantly driven by a head difference with a diurnal frequency is more susceptible to a change than one with a semidiurnal frequency. A channel that is driven by a $\xi'(t)$ with K_1 or O_1 frequency, for instance, exhibits significant differences of $a_{Q_i'}$ between λ_0 = 0.0025 and λ_0 = 0.05. Therefore, a channel could have a different *Formzahl* number in flow rate and head difference variations depending on the channel's friction, especially in the case of a mixed-diurnal variation.

2.1.2 Validation

Given that the main objective of this analysis is to investigate the implication of a strong diurnal component in potential locations for a tidal turbine, combinations of principal astronomical constituents (M_2, S_2, K_1 and O_1) are carefully selected to represent four categories of tidal regime based on *Formzahl* number. In these analyses, the velocity (v) is used rather than the flow rate (Q'). The velocity for each example is maintained at the same level. Therefore, the head difference is set in a particular combination to provide the desired results. This analysis set $\lambda_0$to 0.0025, while the $\lambda_1$is varied from 0.0025, 0.05 and 0.5. The analysis is run for 15 days of tidal cycles. The flow in a channel for each tidal type is generated by the different compositions of $A\xi(M_2)$, $A\xi(S_2)$ $A\xi(K_1)$ and $A\xi(O_1)$ as shown in Table 2-1.

Table 2-1: 1-D model input

Tidal Type	A_{M_2}	A_{S_2}	A_{K_1}	A_{O_1}	f_ξ
Semidiurnal	1.250	0.500	-	-	-
Mixed-diurnal, semidiurnal dominant	1.000	0.300	0.250	0.125	0.29
Mixed-diurnal, diurnal dominant	0.500	0.300	0.500	0.250	0.94
Diurnal	0.025	0.005	0.750	0.250	33.33

Figure 2-3.i shows the ξ (the red dashed line), and the velocity corresponding to the various λ_1. It is important to note, since the model uses the Houlsby-Whelan turbine model, the example is carefully selected to maintain similar Fr for all examples. Therefore, the joint amplitudes of the input are varied, from almost 2 m on the semidiurnal (Figure 2-3.i.a) down to 1 m in the diurnal type (Figure 2-3.i.d), to get the velocity in the range of 3.5~4.0 m/s. This result also shows that the longer period diurnal tide is more sensitive to $\lambda_1$than other tides.

As shown in the graph, the velocity magnitude at λ_1=0.005 is almost a half of that for λ_1=0.0025 for the diurnal tide, while for the semidiurnal tide the velocity for λ_1=0.005 is virtually the same as to the velocity of λ_1=0.0025. This result is consistent with the previous example with a single constituent. One of the observable features from this comparison is the change of phase lag. All tidal types exhibit a phase lag shift when the λ_1 is low (in this case the lowest $\lambda_1$is 0.0025). This shift tends to diminish at a higher friction (λ_1=0.5). The phase of velocity is synchronised with the phase of head difference at high λ_1.

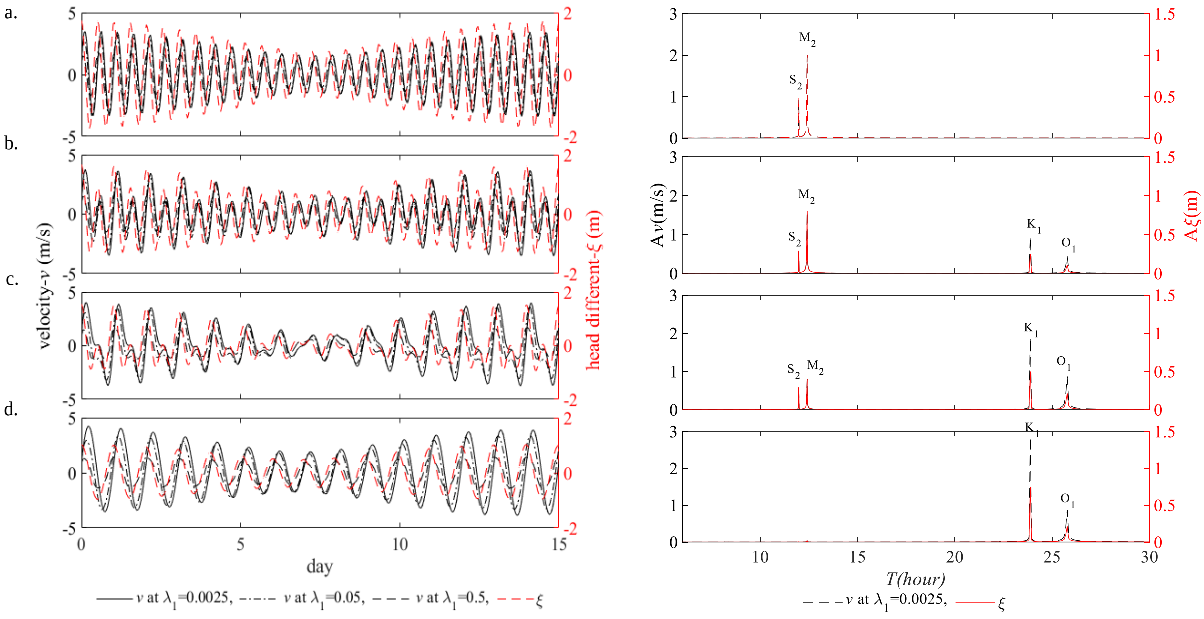

i. v_0 and ξ *profiles* in a channel with λ_0=0.0025, 0.05 and 0.5

ii. The example of Fast Fourier Transform (FFT) of head difference and the tidal velocity for λ_0=0.0025

Figure 2-3: Velocity ($\boldsymbol{v_0}$) and head different (ξ) in a channel with $\boldsymbol{\lambda_0}$=0.0025, 0.05 and 0.5

Fast Fourier Transform (FFT) analysis is employed here to ensure the examples still represent the desired *Formzahl* number representing each tidal regime. Figure 2-3.ii shows the example of FFT analysis of each case in Figure 2-3.i for λ_1 = 0.0025. The proportion of amplitude between diurnal and semidiurnal components tends to change. However, this result indicates that no new species emerge. Therefore, the phase lag is merely shifted in this case, and the frequency remains the same.

The detailed results of the FFT for each λ_1 are presented in Table 2-2. This table shows the input data for each tidal type and the velocity for different value of additional frictions (λ_1 =0.0025, 0.05 and 0.5). The FFT is also run for the input data to validate the error in this method. It is shown in the table that the FFT is relatively accurate to predict the amplitude of each specific component. Only in the semidiurnal case, where the amplitudes of K_1 and O_1 are set to zero (0), the FFT returns results with tiny values. Although f_ξ is affected, it remains within the semidiurnal range (f_ξ <0.25).

Table 2-2: The comparison of amplitudes on the different $\boldsymbol{\lambda_1}$

Constituents	ξ (input)	ξ (*FFT*)	v_0 (*FFT*) λ_1 = 0.0025	λ_1 = 0.05	λ_1 = 0.5
Semidiurnal					
M_2	1.25	1.25	2.497	2.429	1.477
S_2	0.5	0.5	0.966	0.93	0.49400
K_1	-	0.0000001	0.0001	0.0006	0.0004
O_1	-	0.0000006	0.0001	0.0005	0.0004
Formzahl	-	**0.0000004**	**0.00006**	**0.00033**	**0.00041**
Mixed-diurnal, semidiurnal dominant					
M_2	1.00	1.00	1.998	1.950	1.275
S_2	0.300	0.300	0.580	0.562	0.329
K_1	0.250	0.250	0.955	0.865	0.314
O_1	0.125	0.125	0.515	0.467	0.161
Formzahl	**0.29**	**0.29**	**0.57**	**0.53**	**0.30**
Mixed-diurnal, diurnal dominant					
M_2	0.500	0.500	0.999	0.952	0.634
S_2	0.300	0.300	0.580	0.559	0.362
K_1	0.500	0.500	1.909	1.766	0.823
O_1	0.250	0.250	1.030	0.931	0.412
Formzahl	**0.94**	**0.94**	**1.86**	**1.78**	**1.24**
Diurnal					
M_2	0.025	0.025	0.050	0.047	0.029
S_2	0.005	0.005	0.010	0.009	0.005
K_1	0.750	0.750	2.864	2.584	1.233
O_1	0.250	0.250	1.029	0.864	0.334
Formzahl	**33.33**	**33.33**	**64.88**	**61.57**	**46.09**

Except for the semidiurnal tidal type, the velocity tends to have smaller *Formzahl* numbers when the λ_1 is increased. The semidiurnal tides essentially have f_v =0.0, a small increase shown in the *Formzahl* number is due to small errors from the FFT process. The "decreasing" trend of *Formzahl* number for other types is consistent with the significant decrease of longer period constituents (T_i)

at higher friction, as shown in Figure 2-2. Therefore, these examples are arguably ideal for representing each tidal regime.

2.2 Power Variation Due To Multiple Constituents

This section explores the tidal power variation due to multiple tidal components. Long-term variability is also discussed here. The power extraction is calculated using Eqs (1.1), (1.2), (1.11) and (1.12). As mentioned previously, the GC05 model is employed for the channel model, while the C_T and C_P are calculated using the Houlsby-Whelan model (see Section 1.2.2 in Chapter 1 for detail).

The channel width is 1600 m, the average depth is 40 m, and the natural friction λ_0 is 0.0025. The simulations are based on optimum wake coefficients (α_4). The simulations are run with three different wake coefficients ($\alpha_4 = 0.33$, $\alpha_4 = 0.40$, $\alpha_4 = 0.56$). Figure 2-4 shows an example of normalised power against α_4 for each tidal type. Each example represents a tidal pattern from the previous example. The average power ($\overline{P_1}$) in this figure is the normalised by its maximum power ($max\ P_1$). As shown in this figure, the average for the semidiurnal tide gives slightly higher $\frac{\overline{P_1}}{max\ P_1}$ than other tidal types. Using the spline function in Matlab, the optimum power is obtained for each example.

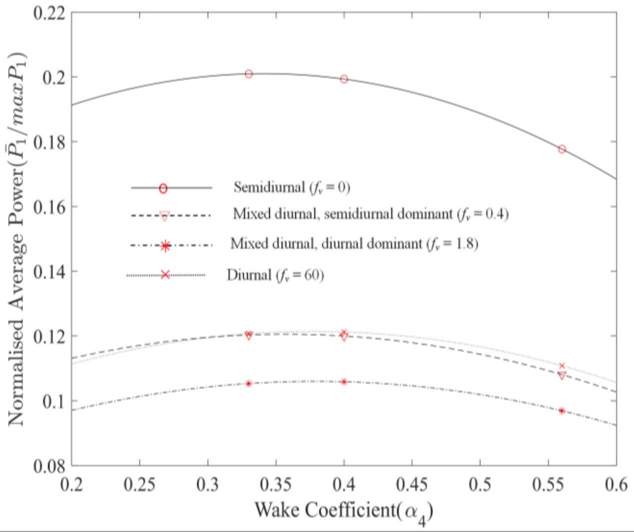

Figure 2-4: Example of optimum wake coefficient (α_4) at low blockage ratio for each tidal type.

2.2.1 The Variation Due To Diurnal Components (K_1 and O_1)

Tidal power variations are extracted from tidal velocities generated from the head difference derived from the combination of four principal diurnal and semi-diurnal constituents (M_2, S_2, K_1

and O_1). The diurnal components give variations in the daily cycle of tidal power production, as shown in Figure 2-5.i. The power and thrust variation in Figure 2-5.i.a is extracted from a semidiurnal tidal stream ($f_v = 0$), while Figure 2-5.i.b shows the power and thrust variation from mixed diurnal-semidiurnal dominant tides. Figure 2-5.i.c and Figure 2-5.i.d represent the variation of mixed diurnal-diurnal dominant and diurnal, respectively.

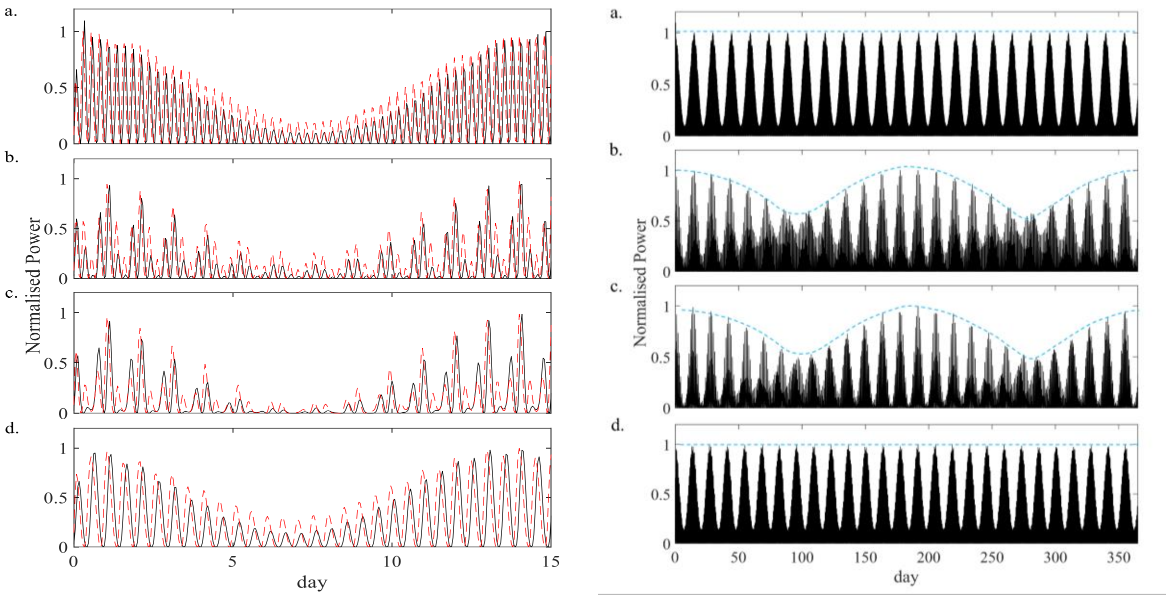

i. The first neap spring cycle continuous black lines represent low blockage ratio (*B*=0.1), and dashed red lines are for high blockage ratio (*B*=0.4)

ii. The annual variation of the low blockage (*B*=0.1)

Figure 2-5: Normalised power variation for each tidal type at optimum wake coefficient

The simulation is then extended to an annual variation. Figure 2-5.ii shows the variation in power production annually for the previous tidal types. The mixed diurnal type exhibits an interesting pattern in the annual cycle (Figure 2-5.ii). The variations are not just in the daily and monthly neap-spring cycles. Two peaks and valleys are observed in the annual cycle. This fact shows that the interaction of the diurnal components and semidiurnal constituents are modulated in the yearly cycle.

2.2.2 The Variation Due To the Elliptical Orbit Constituents (N_2 - L_2 and P_1)

As discussed previously in section 1.2.2a, there are other constituents that also usually have a significant amplitude. The constituents due to the elliptical shape of the Moon's orbit are the larger lunar elliptic (N_2) and smaller lunar elliptic (L_2). As discussed by Pugh 1987, these constituents usually pair symmetrically, and their amplitudes are usually smaller than M_2. Figure 2-6 shows the annual variation of the available power from four different tidal types normalised to the maximum available power from the examples presented in section 2.2 (as shown in Figure 2-5.ii).

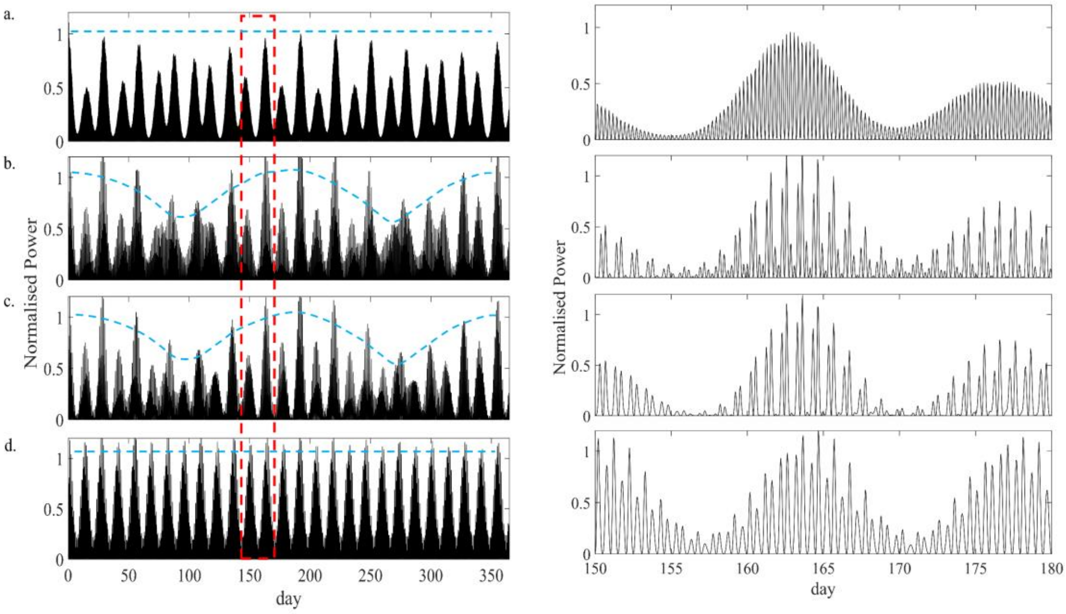

i. The annual (365 days) variation

ii. 60 days variation from red dashed box

Figure 2-6: The power variation due to the existence of N_2 and L_2 for low blockage ratio (*B*=0.1). The blue dashed lines are the peak lines from Figure 2-5.ii

The inclusion of N_2 and L_2 constituents in the head difference (ξ) creates uneven neap spring cycles, as shown in Figure 2-6.ii. Furthermore, these constituents also create an annual pattern in the semidiurnal tides (Figure 2-6.i.a). By contrast, N_2 and L_2 only have a small effect on the diurnal tides (see Figure 2-6.i.d and Figure 2-6.ii.d). This species creates a similar annual cycle as found in the interaction of four principal constituents.

The elliptical part of the Earth's orbit also affects the variation of the annual power production. Figure 2-7 demonstrates the influence of P_1 on power production in each tidal pattern. In contrast to the previous constituents (N_2 and L_2), this constituent shows a more observable annual pattern for the diurnal tidal type (Figure 2-7d). This pattern is expected as P_1 is a diurnal constituent.

2.2.3 The Variation Due To Long-Period Constituents

The long-period constituents influence the annual tidal power variations. This section analyses the impact of long-period species on the tidal variation in the annual pattern only. These species also affect the variation in the long term due to the 18.61-year *Metonic*-cycle. Three long-period constituents are considered in this example: Sa, Ssa and Mm. The Sa and Ssa constituents are the most important long-period species, especially for the variation in a *Metonic* cycle. The previous elliptical constituents (N_2, L_2 and P_1) are excluded in these examples. This thesis does not take into account the interaction of those elliptical constituents with the long period constituents. The elliptical constituents might, however, interact with the long-period species.

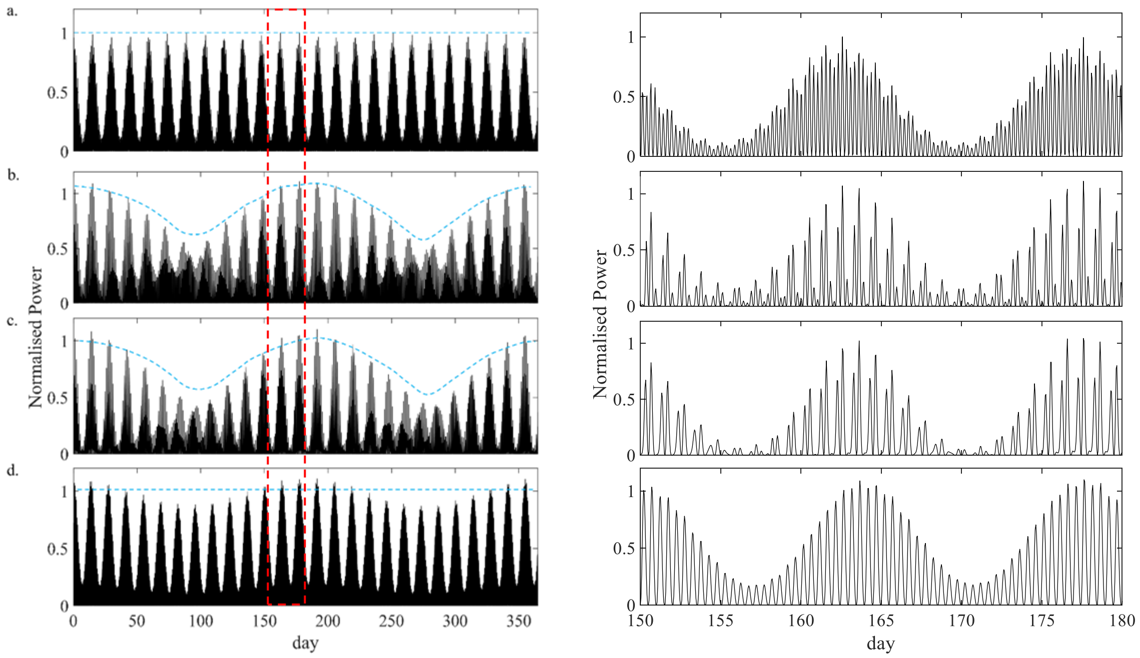

i. The annual (365 days) variation

ii. 60 days variation from red dashed box

Figure 2-7: The annual variation due to the P_1 constituent. The blue dashed lines are the peak lines from Figure 2-5.ii

Figure 2-8 shows an example of tidal velocity with nodal factor without Mm (see Table 1-2). The Mm influence on the power variation is presented separately later. Therefore these examples only have pronounced solar annual (Sa) and semi solar annual (Ssa) species in the tidal harmonic. In a similar way to the previous exercise, the power variations are normalised to the maximum power from simulation with S_2, M_2, K_1 and O_1 (as shown in Figure 2-5.ii). This example shows that the Sa and Ssa only have a small effect on the annual variation of the available power.

Meanwhile, the Mm constituent shows a more observable synchronising effect to the annual tidal variation (see Figure 2-8 ii). However, this component affects the annual variation only in the semidiurnal tidal type. As shown in Figure 2-8 ii.a, the annual variation, as observed in both mixed-diurnal, is exhibited in the semidiurnal. It shown by the grey dotted line in Figure 2-8 ii.a that gave annual variation as shown in Figure 2-8 ii.b and Figure 2-8 ii.c. Whilst this constituent only makes a small change to the diurnal variation. It is important to note that this example only set the Mm amplitude as relatively small (AMm=0.5). It is important to note that the amplitude of AMm here is nondimensionalised to the M_2.

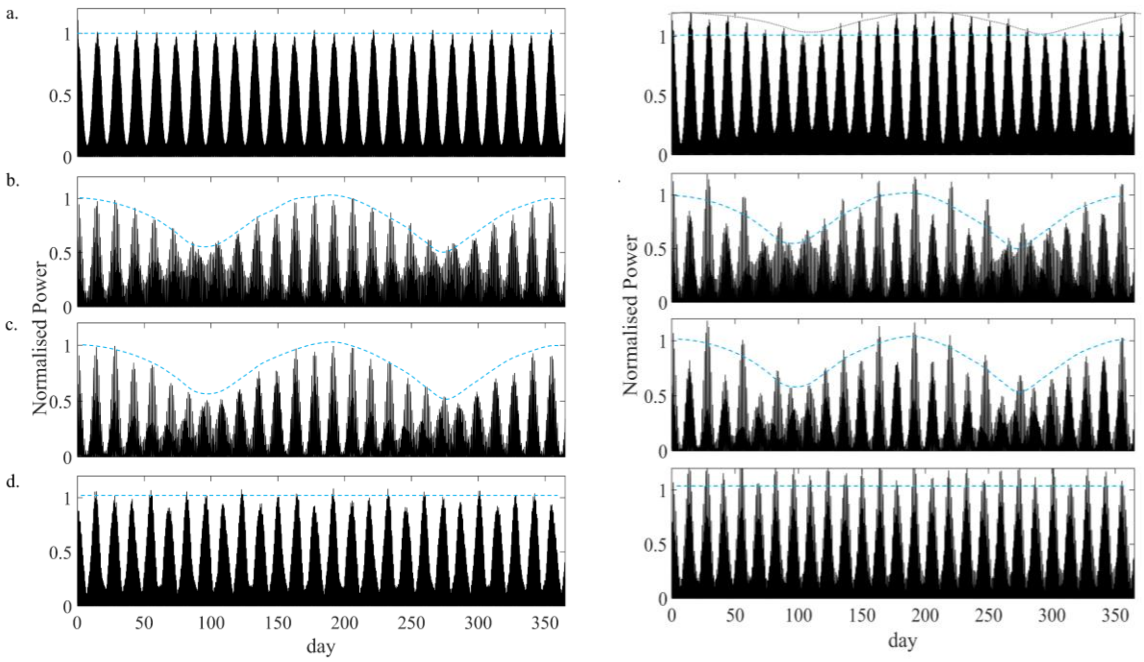

i. Only with nodal factor for M_2, S_2, K_1 and O_1.

ii. With nodal factor and AMm =0.05

Figure 2-8: An example of typical annual tidal power variation with the long term constituents included. The power variations are normalised to power variation without the nodal factor applied. The blue dashed lines are the peak lines from Figure 2-5.ii and the grey line in ii.a is the new peaks of neap-spring cycle

2.3 The Implication of Tidal Complexity for the Capping strategy

Tidal turbines have the advantage of energy production predictability. As shown in the previous examples, the power produced by the turbines fluctuates over the neap-spring cycles, with very high power-production on certain days but lower on other days. Due to this temporal variation, it may be economically advantageous to deliberately design a turbine array which does not maximise the peak of extracted power in the tidal cycle. Vogel 2014, Vogel *et al.* 2019 and Wang 2017 carry out preliminary analyses for the capping strategy. However, their work is limited to the semidiurnal case only, with the tidal forcing just from M_2 and S_2. This thesis extends their studies to the inclusion of the diurnal tidal components.

A tidal resource assessment needs to take into account this important feature. The power capping and thrust capping strategies will be specific to the tidal pattern at any given location. Furthermore, the strategy may also be affected by tidal asymmetry. This thesis addresses these issues from a theoretical basis below, deriving some results supporting the influence of tidal types and tidal asymmetry in the capping strategy. We can deduce some preliminary implications for Indonesian waters, although the details will require further research.

2.3.1 Power Capping and Thrust Capping

In axial-flow turbines, power capping can be achieved by feathering the turbine blade. Thus, the turbine is rotating at the same tip speed ratio (*TSR*) at the velocity limit. This power limit is also known as rated power, or power capping limit. Figure 2-9 illustrates the rated power and the thrust after implementation of the capping limit. From the wind turbine experience, we know that the turbine control system will start to feather the blades when the wind reaches the rated speed (u_a).

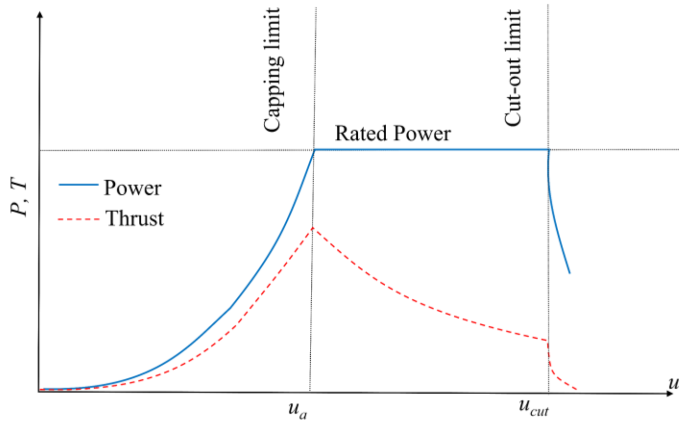

Figure 2-9: Illustration of rated power (P) and the thrust (T) due to rated power

As shown in Figure 2-9, by feathering the blade at the rated speed, the thrust is reduced. Therefore, a capping limit also can be introduced to the thrust as well. A turbine could be operated by applying both thrust and power capping simultaneously (Wang 2017, Wang & Adcock, 2019). However, this thesis only compares the application of Power Capping and Thrust Capping.

An example of power variation for power capping in a semidiurnal site is shown in Figure 2-10. The continuous red lines for normalised power and normalised thrust represent the power or thrust after the capping, while the dashed black lines are for the power/thrust before the capping is implemented. In this analysis, this capping strategy is implemented by increasing the wake coefficient (α_4). By increasing α_4, the peaks of available power are set to the capping limit (Figure 2-10a), and the thrust also reduces at the same time (Figure 2-10b). The 1-D channel model with the Houlsby-Whelan tidal model that is used in section 2.1 is modified to incorporate the wake coefficient tuning algorithm.

Another method is to limit the thrust applied by the turbine. The National Renewable Energy Laboratorium (NREL) shows the generator cost of a wind turbine is reducing (see Tyler & Beiter, 2020). Therefore, based on that development in wind energy, perhaps the fatigue life of the turbine blade is the primary constraint on tidal energy exploitation. The thrust loading affects the serviceability of the turbine blade and supporting structure. A similar trend is perhaps applicable to the tidal turbines as well.

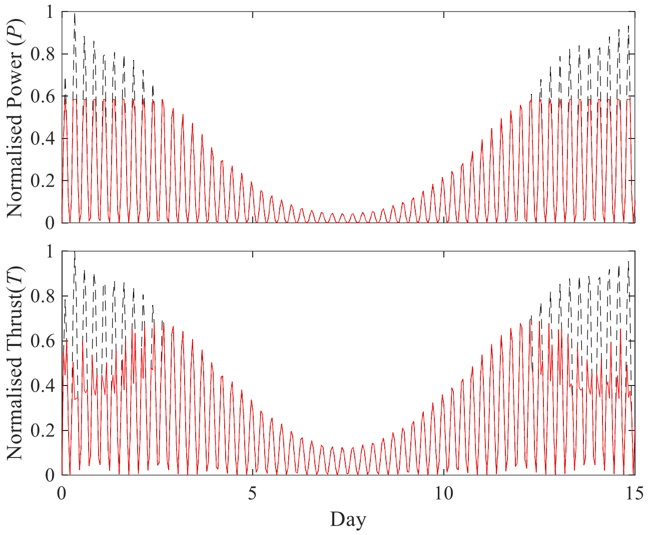

Figure 2-10: Power (above) and thrust (below) for power capping. The dashed black lines are the power/thrust before the capping while the continuous red lines are the power/thrust after capping.

Therefore, it would be sensible to limit the thrust rather than power production. In this analysis, capping is implemented by changing α_4, and so the thrust also reduces power availability. Figure 2-11 shows the power and thrust variation for thrust capping. The continuous red lines show the power/thrust variation after the capping limit is implemented while the black dashed lines represent the power/thrust without the capping.

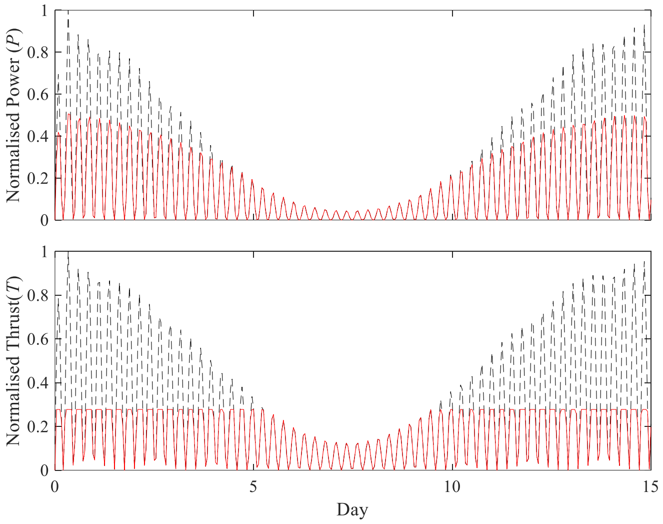

Figure 2-11: Power (above) and thrust (below) for thrust capping. The dashed black lines are the power/thrust before the capping while the continuous red lines are the power/thrust after capping.

2.3.2 Metric on Capping Limit

The net power production is widely expressed in terms of the capacity factor (*CF*), which is the ratio of the average power production to the installed power capacity. In energy generation, this *CF* metric describes the utility of the technology. A higher *CF* means power conversion at a higher percentage of its capacity.

However, for most renewable energy sources, electricity is intermittent, and a high *CF* is very unlikely to be achieved. In a wind turbine, for example, the desired *CF* is in typically range 0.2~0.4, which is economically viable for a wind turbine. Therefore, a similar range of *CF* could be used as a target for a tidal turbine.

Figure 2-12 shows the correlation of the rated power and average power after the capping for the previous example. The continuous black line represents power capping (from the example shown in Figure 2-10) while the red dashed line represents thrust capping (as presented in Figure 2-11). If the cut-out velocity is set to a maximum (normalised $\hat{P}$=1), this means the average power is the same with the average of power without cut-out.

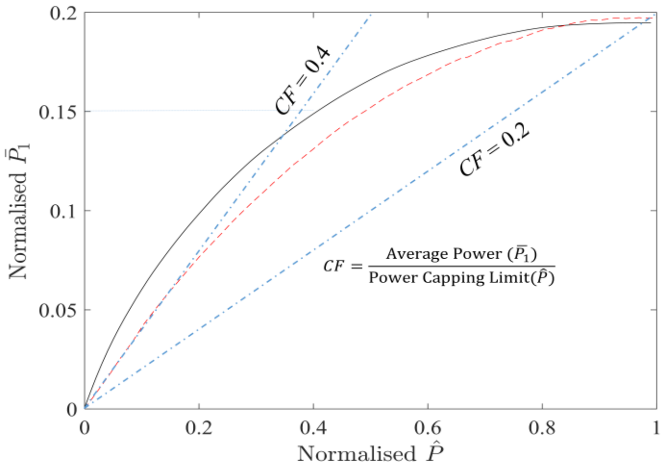

Figure 2-12: The capacity factor for power capping (continuous black line) and thrust capping dashed red line)

The choice of cut-out becomes a trade-off for the turbine developer. A high cut-out will give high available power, but the capacity factor will be low. The maximum cut-out for exploiting the tidal resources without capping gives *CF* less than 0.2. That would mean that the turbine is over-designed for this particular site. A turbine has to be optimised for the capacity factor and average power that is produced by the turbine. The desired *CF* is in range of 0.25~0.4 to give the optimum turbines for a particular site.

However, Vogel, 2014 argued that the *CF* does not directly reflect the power available in a time-varying flow. Therefore, Vogel, 2014 introduced a Power Factor (F_P), which is the ratio between the maximum available power after capping and before capping. Vogel, 2014 shows that F_P in M_2 only driven channel is significantly higher than the power factor of a channel that is driven by M_2 and S_2. This conclusion is obvious, since the combination of M_2 and S_2 will create a neap-spring cycle, in which the power production is lower at neap tide. Wang, 2017 introduces the thrust factor (F_T), that is defined as the ratio of rated thrust to the maximum power-capped thrust (rather than the maximum uncapped thrust). Essentially, F_T is similar to the capacity factor (*CF*), but in term of thrust.

Therefore, this thesis uses a redefined Power Factor (F_P) and thrust factor (F_T). Since average power is used to assess a potential site, the F_P here uses average power removed by the turbine rather than the maximum power as used in Vogel, 2014. Defining F_P as a fraction of the average power after the capping over the average power without the capping helps describe the percentage of power reduction after capping. Thus, turbine developers could decide what maximum power reduction is acceptable for the site.

The F_T is also redefined as the ratio of the average thrust after capping to that before. Therefore, F_T here describes the reduction in average thrust after capping. The ratio of maximum thrust is also necessary for the analysis. Thus, the ratio of maximum thrust after the capping strategy over the maximum thrust before the capping strategy is defined as $F_{T,\,max}$.

The easiest way to do the analysis is to compare the rated power, or power capping limit ($\hat{P}$), and the average available existing power before the capping ($\overline{P_1}$). Turbine developers could determine the best generator capacity at any given site by comparing their turbine capacity with the available power that could be removed by the turbine $\left(\frac{\hat{P}}{\overline{P_1}}\right)$. Using the average value for the $\frac{\hat{P}}{\overline{P_1}}$ perhaps is more useful than the maximum. As the power and thrust vary over the neap/spring cycle (and the solstice-equinox cycles), the maximum value varies significantly in those cycles.

A similar approach could be used for thrust capping. However, instead of using $\frac{\hat{P}}{\overline{P_1}}$, this thesis uses the comparison of thrust capping limit ($\hat{T}$) and the average thrust before the capping applied ($\overline{T_1}$). The $\frac{\hat{T}}{\overline{T_1}}$ metric is simpler than using $\frac{\hat{P}}{\overline{P_1}}$ in thrust capping. Furthermore, the average available power after the capping is applied might be higher than in the scenario without capping, as demonstrated later in this chapter. Figure 2-13 shows the example of implementation, plotting *CF* against $\frac{\hat{P}}{\bar{P}_1}$ for power capping and against $\frac{\hat{T}}{\bar{T}_1}$ for thrust capping. This implementation is also demonstrated later in this chapter for different tidal types.

Although the thrust capping strategy aims to reduce the thrust applied to the turbine, the maximum power produced by the turbine is still required to determine generator capacity. The maximum power from the turbine using a thrust capping strategy ($max\ \hat{P}$) is used to determine generator capacity.

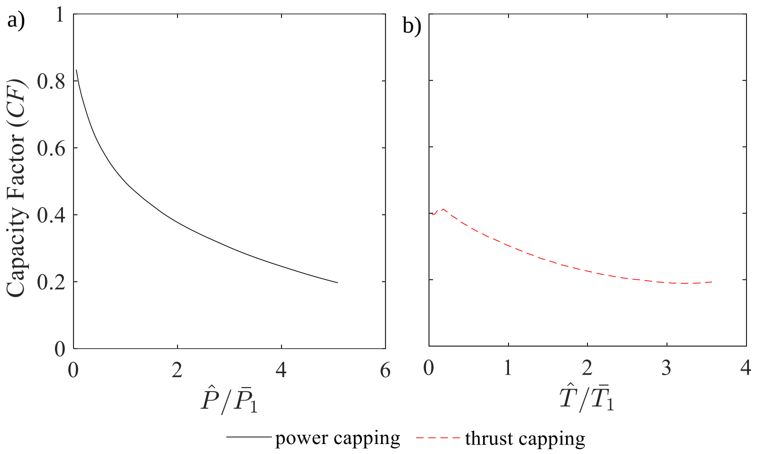

Figure 2-13: Variation of the capacity factor (a) with the capacity factor against $\frac{\hat{P}}{\bar{P}_1}$ for power capping (figure (a) - continuous black line), and b) with capacity factor against $\frac{\hat{T}}{\bar{T}_1}$ for thrust capping (figure (b) - dashed red lines), from the previous example.

2.3.3 Capping strategy in Varied *Formzahl* Number

The four example cases that represent the four tidal types, as discussed in section 2.2, are used here to demonstrate the utility of the F_P, F_T, $F_{T,max}$, $\frac{\hat{T}}{\bar{T}_1}$ and $\frac{\hat{P}}{\bar{P}_1}$ metrics for power and thrust capping. The GC05 1-D Channel model incorporating the Houlsby-Whelan model for turbine representation is again used. The power and thrust capping simulations are undertaken by altering the wake coefficient (α_4). It is important to note that the simulation here is run with optimum α_4 before implementing power or thrust capping. Thus, the model algorithm starts tuning when the power exceeds the capping limit. The truncated power at the capping limit is obtained by increasing α_4 until it reaches the rated power. The scheme is also similar for thrust capping, the algorithm sets the thrust limit and increases α_4 until it reaches the limit.

The desired *CF* is in the range of 0.25-0.45. To obtain the same value of *CF*, both groups (semidiurnal-diurnal and mixed diurnal) require different capping limits. To explore the capping strategy features for each tidal type, a *CF* of 0.3 (pointed by red dashed lines in Figure 2-14 a) is used here as an example. Figure 2-14 shows the capacity factor *CF* for four different tidal types. *CF* is plotted against $\frac{\hat{P}}{\overline{P_1}}$ for power capping and against $\frac{\hat{T}}{\overline{T_1}}$ for thrust capping. These examples show the difference between tidal types. In general for the same $\frac{\hat{P}}{\overline{P_1}}$ or $\frac{\hat{T}}{\overline{T_1}}$, the mixed diurnal tides tend to have lower *CF* than the semidiurnal and diurnal.

A value of *CF*=0.3 in the semidiurnal and diurnal cases can be obtained by limiting the power at 2.75 of the average power before the capping ($\overline{P_1}$) for the power capping scenario (the continuous line and dotted line in Figure 2-14a). Both examples of the mixed diurnal type (f_v = 0.57 and f_v =1.87), however, must truncate their power production at 3.5 $\overline{P_1}$.

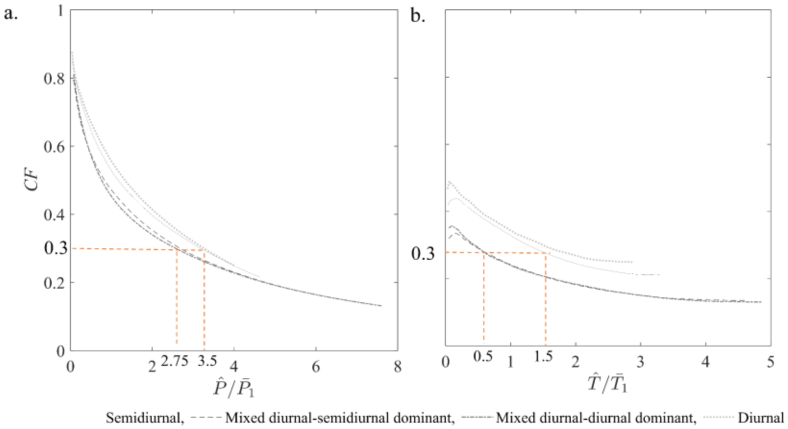

Figure 2-14: Capacity factor (*CF*) for four different tidal types, left (a) is for power capping and the right (b) is for thrust capping.

In a mixed diurnal tide the thrust needs to be capped at half of the average thrust (0.5 $\overline{T_1}$) to obtain *CF* = 0.3, whereas in semidiurnal and diurnal tides thrust should be capped at 1.5 $\overline{T_1}$ to obtain the same *CF* (see Figure 2-14b). In general, the thrust capping scenario shows a tendency towards having lower *CF* than the power capping strategy. The limit of *CF* for thrust capping is because the thrust capping scenario still gives fluctuations in power output, whereas for power capping the peak available power is truncated at the capping limit ($\hat{P}$). However, it seems sensible to set the thrust capping limit at 0.5~1 of the average thrust before the capping ($\overline{T_1}$), as this it will give *CF* in the range of 0.2~0.25.

To see the impact of this capping strategy on the power production, F_P is plotted against $\frac{\hat{P}}{P_1}$ for power capping and against $\frac{\hat{T}}{T_1}$ for thrust capping (see Figure 2-15). The *CF* of 0.3, as shown in Figure 2-14, is shown by the dashed red lines. The figure shows that both mixed-diurnal cases give lower F_P than the semidiurnal and diurnal cases for both capping strategies. Both mixed diurnal cases indicate $F_P = 0.8$ is required to obtain $CF = 0.3$. The F_P of 0.8 means the turbine in a channel has a 20% reduction of average power when the capping strategy is introduced.

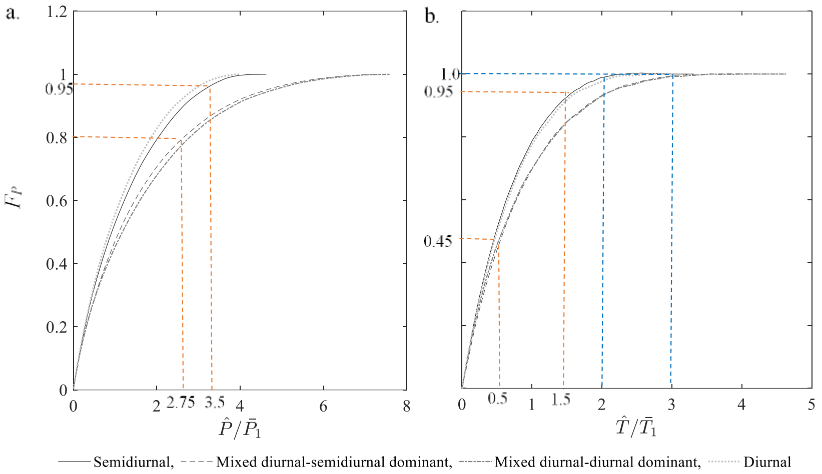

Figure 2-15: F_P from four different tidal types, right is for power capping, and the left is for thrust capping.

The semidiurnal case achieves only an approximate 5% reduction ($F_P = 0.95$) when the power capping strategy that aims to achieve *CF*=0.3 is implemented, while mixed diurnal shows a slightly higher F_P. At the same time, both mixed diurnal cases lose almost half ($F_P = 0.55$) of their potential power when using thrust capping (Figure 2-15b) to get $CF = 0.3$, while for the semidiurnal case, the loss is approximately 5% to obtain the same *CF*.

It is interesting to look in more detail for the thrust capping implementation. These examples show it is possible to have no power reduction (or almost none) for this capping strategy. If the thrust limit is set at 2.0 (for diurnal and semi diurnal) and 3.0 (for both mixed diurnals — see the blue dashed line in Figure 2-15b), it will give the F_P of 1.0. Importantly, this strategy still gives a reduction on the thrust, as shown in the next analysis of F_T and $F_{T,max}$.

If in the F_P we expect to have a high F_P, in the F_T and $F_{T,max}$ should be as low as possible. Both mixed-diurnal tidal types have a similar thrust factor ($F_T = 0.75$) to get $CF = 0.3$ in the power capping strategy (see Figure 2-16a). While semidiurnal and diurnal have $F_T = 0.95$, which means the turbine only has a 5% reduction for the same $CF = 0.3$ in the power capping strategy, the mixed-diurnals show lower F_T than both the semidiurnal and diurnal cases (see Figure 2-16b).

To obtain $CF = 0.3$, the mixed-diurnal cases will have $F_T = 0.35$. This means a turbine developer could cut 65% of the average thrust in the thrust capping strategy. In the semidiurnal and diurnal cases, the turbine developers only get F_T =0.80, or only 20% thrust reduction. Meanwhile, the thrust capping limit that is set to give $F_P = 1.0$ will give F_T =0.9 for semidiurnal and diurnal tidal flows, which means the average thrusts are reduced by 10% when the capping is limited. The thrust capping strategy in the mixed diurnals gives slightly higher than 0.9 by one or two percents. However, this capping strategy will give lower $F_{T,max}$.

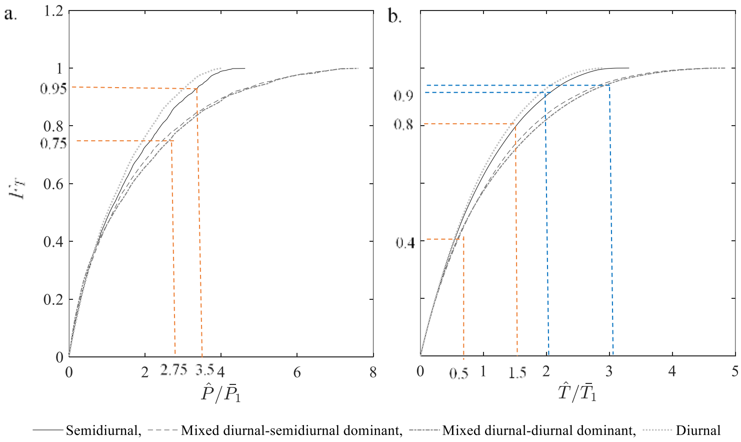

Figure 2-16: Thrust Factor (F_T) from four different tidal types, left (a) is for power capping, and the right (b) is for thrust capping.

Following the previous analysis, $F_{T,max}$ is also analysed in terms of achieving a target of CF=0.3. The $F_{T,\ max}$ for the semidiurnal case is 0.775 for power capping and 0.4 for thrust capping (see Figure 226). This means the maximum thrust reduction by approximately 22.5% in the semidiurnal case for power capping. At the same time, the mixed-diurnal tides have $F_{T,max}$=0.5 for power capping strategies to get $CF = 0.3$.

In thrust capping, the semidiurnal case has a 60% reduction of maximum thrust. The diurnal case shows a slightly higher $F_{T,max}$ than semidiurnal. To get CF=0.3 in power capping, the turbine in a diurnal tidal regime could reduce the maximum thrust by only 10%, while thrust capping could reduce by 52.5%. The $F_{T,\ max}$ for both mixed-diurnal tides are significantly lower than the semidiurnal and diurnal cases in thrust capping strategies. The thrust capping strategy gives $F_{T,max}$ = 0.1, and CF=0.3, a very significant reduction in thrust (see Figure 2-17b). The thrust capping strategies in the semidiurnal and both mixed diurnals give $F_{T,\ max} = 0.7$ to get $F_P = 1.0$, whereas for the diurnal the $F_{T,\,max}$ = 0.75. This means the thrust capping strategy could be implemented without lowering the average power removed by the turbines, but the maximum thrust is still reduced.

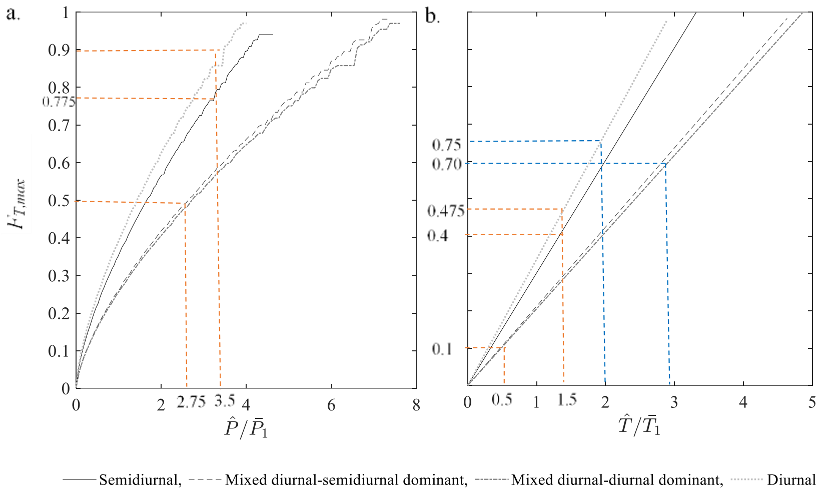

Figure 2-17: Maximum Thrust Factor ($F_{T,\,max}$) for four different tidal types, left (a) is for power capping, and the right (b) is for thrust capping.

The thrust capping strategy could also optimise α_4. If the simulation is set at α_4= 0.33, thrust capping gives F_P > 1.0. The higher the blockage ratio, the higher the increase. Figure 2-18 shows the example of F_P > 1.0 for the blockage ratio (B=0.4). This increase is only observed for the thrust capping, but not on the power capping strategy. The F_P in this strategy for the high blockage ratio could increase to more than two times the average power without the capping strategy.

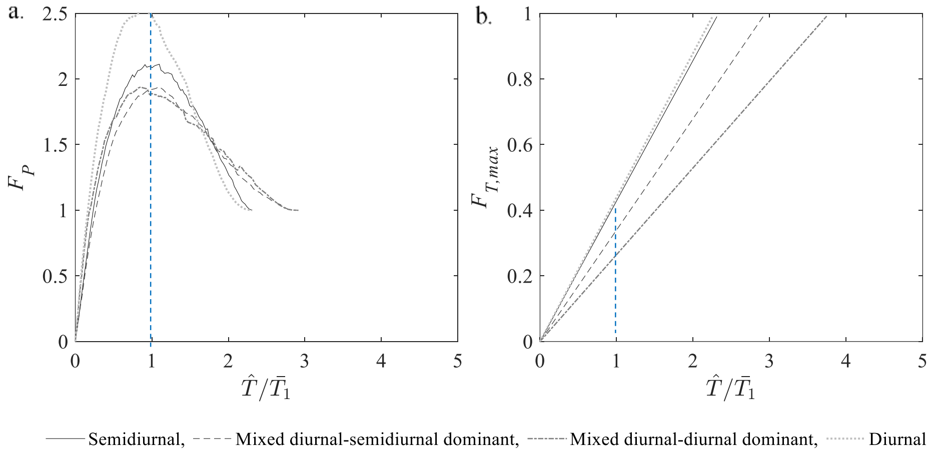

Figure 2-18: F_P and $F_{T,\,max}$ for four different tidal types, with initial $\boldsymbol{\alpha_4}$= 0.33 and B =0.4.

The power and thrust variations in the diurnal tidal regime shows that the peak power increases significantly when thrust capping is set at $\frac{\hat{T}}{\bar{T}_1}$ =1.0 (see Figure 2-18a). The power variation after the capping (dashed red lines) is increased at its peaks. The increase is 2.5 times the power without the capping or existing condition (the solid black lines — see Figure 2-19 a). At the same time, the thrust is capped at the average thrust without the capping (see Figure 2-19 b). Therefore, the result shown in Figure 2-18 is sensible.

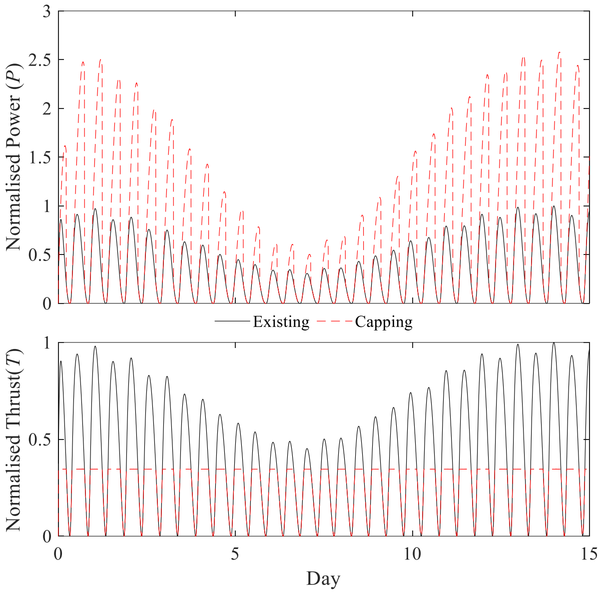

Figure 2-19: Power and thrust variation before and after the capping for high blockage ratio (B=0.4) in diurnal tides and α_4 =0.33

2.4 Tidal Asymmetry

The existence of a strong diurnal component creates additional complexity. A simple tidal flow, such as the ones considered so far, has no asymmetry in the current. Thus, the power production and the thrust that is applied to the turbines are also expected to be symmetric. However, there can be differences between the currents in each direction in real scenarios, and hence the power.

This asymmetry phenomenon is usually an important matter for sediment transport problems. Sediment accumulation occurs due to an uneven stream of tidal currents. Meanwhile, in tidal resource assessment, this phenomenon is often ignored. Neill *et al.*, 2014, examined the characteristics of tidal energy resources in Orkney due to asymmetry. However, it is unclear what the direct impact of this phenomenon is on tidal resources.

2.4.1 Asymmetric Power and Thrust

The complexity of tidal power due to the existence of asymmetry due to diurnal constituents is further explored in this thesis. The investigation is undertaken using similar combinations of tidal components as in the previous example. Eq. (1.7) is modified to capture the bi-directional nature. The thrust then is rewritten as:

$$T = \frac{1}{2}\rho u|u|AC_T. \qquad (2.6)$$

Figure 2-20 shows similar graphs to those in Figure 2-5. However, the power and thrust are distinguished by their direction. Figure 2-20 shows the powers and thrusts for mixed tidal systems (Figure 2-20b and Figure 2-20c) are uneven in both directions. For example, Figure 2-20b shows the power in the negative direction peaks at a quarter of the positive direction value. Similarly, the thrust in the negative direction is on average half of the thrust in the positive direction.

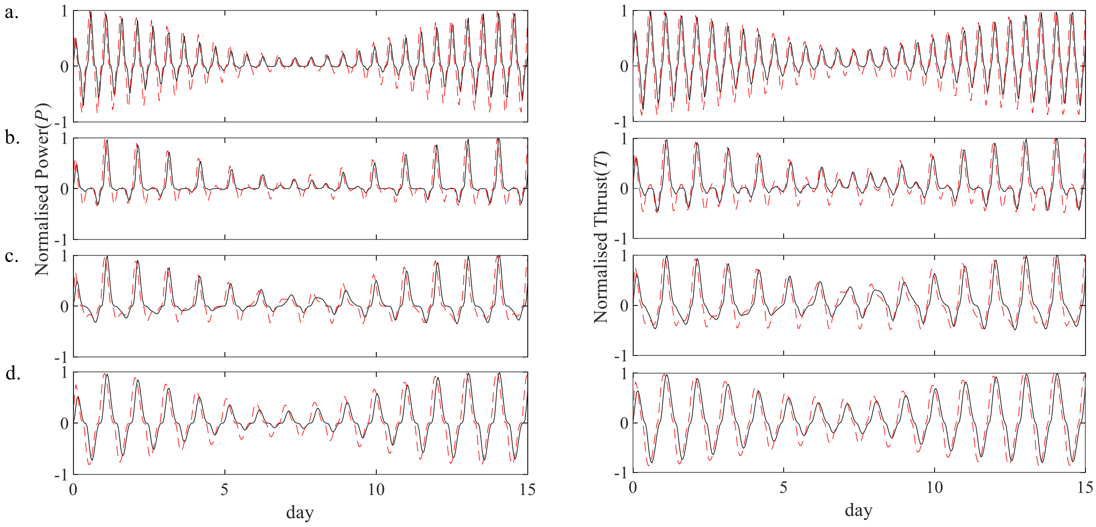

Figure 2-20: Normalised power and thrust with direction for each tidal type

Although the power and thrust in semidiurnal and diurnal cases (Figure 2-20a and Figure 2-20d) show a slightly uneven magnitude between positive and negative directions, in a longer duration simulation, these patterns become symmetric as no components are orthogonal to one another. The asymmetric patterns of power and thrust variation for all tidal types are shown in Figure 2-21, extending the previous simulation to a tropical year. Since both blockage ratios exhibit a similar pattern, the extensions of the previous examples are only shown for the low blockage ratio (B=0.1). Regarding the asymmetric pattern in both the semidiurnal and diurnal tidal regimes, Figure 2-21a and Figure 2-21d show that the variations are symmetric over a longer duration. Therefore, the asymmetry only appears in the mixed diurnal tidal type (see Figure 2-21b and Figure 2-21c).

Therefore, based on these examples, the interaction of M_2, S_2, K_1, and O_1 also creates the phenomenon known as tidal asymmetry. Asymmetry in tidal elevation (WSE) is defined in terms of different patterns of elevation during the ebb and flood phases of a tidal cycle. Tidal asymmetry in terms of the tidal flow is defined as uneven peak velocity magnitudes between each direction. This uneven magnitude may be observable in the ebb-flood, neap-spring or even the longer cycles. When the ebbs and floods have unequal periods, the asymmetry will be pronounced. If the periods of water level rise are shorter than periods of water level fall, this is called flood dominant and the opposite case is ebb dominant. However, given that variations of the power and thrust pattern follow the flow variation, the asymmetry could be analysed based on the flow variation.

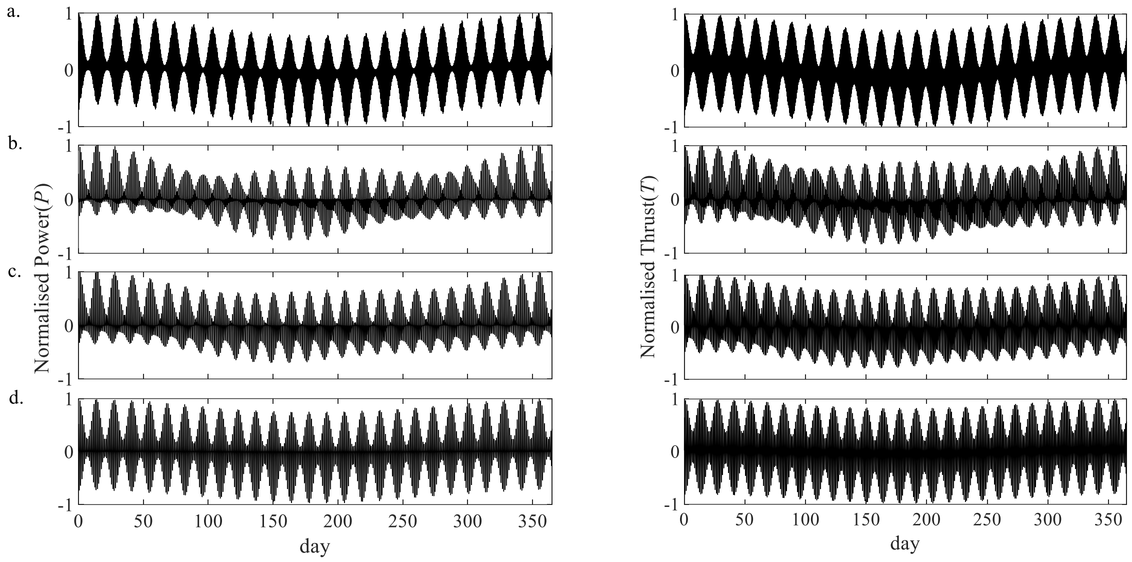

Figure 2-21: Extended normalised power and thrust with direction for each tidal type at low blockage ratio.

It is also important to note that the mixed-diurnal tidal type does not always have uneven thrust and power. For example, the mixed diurnal tidal regime with $f_v = 1$ could create both even and uneven power and thrust. Figure 2-22 shows the normalised power and thrust for the flow direction with $f_v = 1$. In this example, the variations are represented by the combination of tidal flow as shown in Table 2-3. This example shows that the flow can be either even or uneven between positive and negative direction for the same *Formzahl* number.

Table 2-3: Velocity combination for tidal asymmetry analysis

Case	A_{vM_2}	A_{vS_2}	A_{vK_1}	A_{vO_1}	f_v
a.	1.0	0.0	1.0	0.0	1.0
b.	0.5	0.5	1.0	0.0	1.0
c.	1.0	0.0	0.5	0.5	1.0
d.	0.5	0.5	0.5	0.5	1.0

Figure 2-22, representing a combination with $f_v = 1$, which is a mixed diurnal type, shows a symmetric variation. This case, as shown in Figure 2-23, still exhibits a symmetric pattern if extended in a longer duration, while (c) and (d) are still asymmetric. However, example (b) shows a symmetric variation in an annual cycle. Therefore, the symmetry or asymmetry is not just related to the mixed diurnal type. Further investigation is required in order to understand its nature fully.

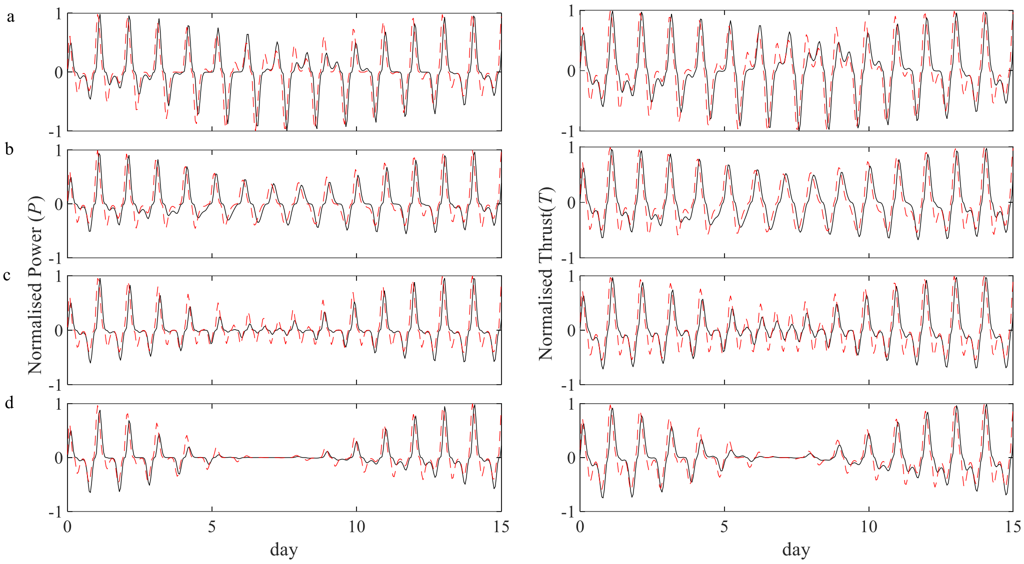

Figure 2-22: Normalised power and thrust with direction for each composition for f_v=1

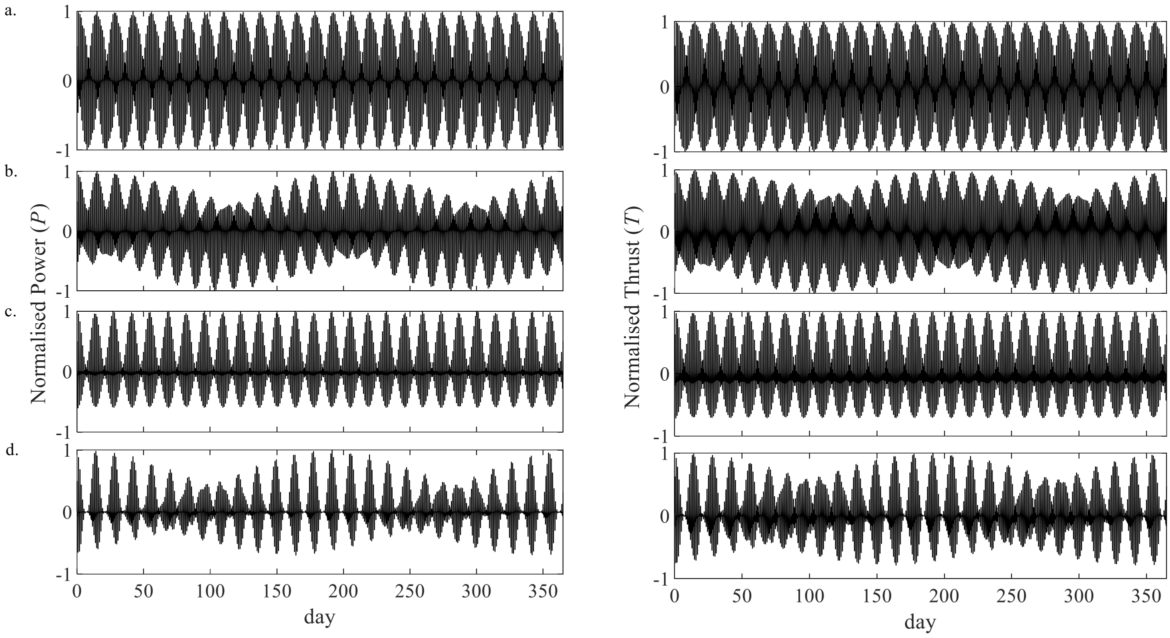

Figure 2-23: Extended normalised power and thrust in Figure 2-22

2.4.2 Determining the Tidal Asymmetry

It is widely known that tidal asymmetry is generated by the interaction of the semidiurnal components and the shallow water components (M_4 and M_6) [Dronkers, 1986; Blanton *et al.*, 2002; Mazda *et al.*, 1995; Chernetsky *et al.*, 2010; Scully & Friedrichs, 2007]. However, tidal asymmetry also appears in the interaction of astronomical components. Hoitink *et al.*, 2003 and Nidzieko, 2010 have demonstrated how tidal asymmetry appears in the form of mixed diurnal tides. However, they investigate this asymmetry in the tidal elevation and head difference, which might not represent the tidal regime in the case considered here.

Here, the asymmetry is investigated in terms of the velocity pattern. The triad of interactions between a principal lunar semidiurnal (M_2) and principal diurnal constituents (O_1 and K_1) can also be derived for the tidal velocity. Using tidal equilibrium concepts, a tidal velocity that consists of three principal astronomical constituents can be written as follows;

$$v(t) = A_{vK_1}\cos\left((\omega_1+\omega_2)t-\emptyset_{K_1}\right)+A_{vO_1}\cos\left((\omega_1-\omega_2)t-\emptyset_{O_1}\right)+A_{vM_2}\cos.\left((2\omega_1)t-\emptyset_{M_2}\right) \qquad (2.7)$$

where ω_1 and ω_2 are the basic frequencies that have been discussed in section 1.2.2. Following Hoitink *et al.*, 2003 and Nidzieko, 2010, the asymmetric signal is given by comparing the joint amplitude of K_1-O_1 and the amplitude of M_2. The joint amplitude of K_1-O_1 is derived from the joint harmonic equation, which in Eq. (1.5) can be written in a slightly different form, as shown in the following equation;

$$a_1(t)e^{i\varphi_1(t)} = A_{K_1}e^{i((\omega_1+\omega_2)t-\emptyset_{K_1})} + A_{O_1}e^{i((\omega_1-\omega_2)t-\emptyset_{O_1})}. \qquad (2.8)$$

Then, the joint amplitude of K_1-O_1 is described as;

$$a_1(t) = \sqrt{{A_{K_1}}^2 + {A_{O_1}}^2 + 2\,A_{K_1}\,A_{O_1}\,cos\left(2\omega_2 t+\emptyset_{O_1}-\emptyset_{K_1}\right)}, \qquad (2.9)$$

and the joint phase of K_1-O_1 as

$$\varphi_1(t) = (\omega_1 t-\psi_1), \qquad (2.10)$$

where,

$$\psi_1 = \frac{A_{K_1}\,sin\left(\phi_{K_1}-\omega_2 t\right)+A_{O_1}\,sin\left(\phi_{O_1}+\omega_2 t\right)}{A_{K_1}\,cos\left(\phi_{K_1}-\omega_2 t\right)+A_{O_1}\,cos\left(\phi_{O_1}+\omega_2 t\right)}. \qquad (2.11)$$

While the amplitude of M_2 can be written:

$$a_2(t)e^{i\varphi_2(t)} = A_{M_2}e^{i((2\omega_1)t-\emptyset_{M_2})}. \qquad (2.12)$$

The a_1/a_2 ratio can capture the asymmetric signal. Figure 2-24 shows the variation of velocity and a_1/a_2 ratio for the power and thrust variation that is shown in the previous example (Figure 2-22 and Figure 2-23). It is shown that those combinations form different tidal symmetric/asymmetric signals based on the a_1/a_2 ratio.

As mentioned previously, the example in Figure 2-24a and Figure 2-24b are symmetric, while Figure 2-24c and Figure 2-24d are asymmetric. Figure 2-24a and Figure 2-24b show the ratio of a_1/a_2 is constant at 1 and 2, respectively. Meanwhile, the ratio of a_1/a_2 in Figure 2-24c and Figure

2-24d show a fluctuation. It appears from this example that the asymmetric signal could be detected if the a_1/a_2 ratio fluctuates from zero to the *Formzahl* number.

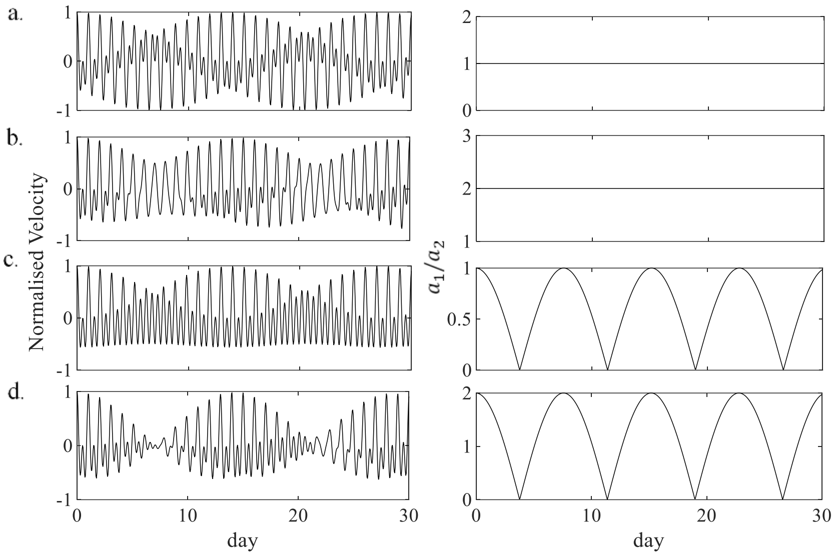

Figure 2-24: Asymmetry analysis of tidal velocity for the same *Formzahl* number (*Fv*=1) but for different S_2, M_2, K_1 and O_1 compositions.

2.4.3 Capping Strategy and Tidal Asymmetry

The previous analyses in section 2.3 show that the turbine in both mixed-diurnal tides tends to have lower *CF*, F_P, F_T and even $F_{T,\ max}$ than in the semidiurnal and diurnal tides. The discrepancy between both mixed diurnals and the semidiurnal and diurnal cases shows that perhaps the main issue is not the *Formzahl* number. These results indicate that asymmetry might play an essential role in the discrepancy. Therefore, it worth exploring the capping strategy metrics in the case of tidal asymmetry.

The examples of asymmetric tidal patterns for this analysis are taken from the examples in section 2.4.2. As discussed previously, Figure 2-22a, b represent a symmetric signal while an asymmetric signal is described by Figure 2-22c-d. In this section, the example in Figure 2-22a is annotated as Symmetry 1, while Figure 2-22b is Symmetry 2. Figure 2-22c and Figure 2-22d are Asymmetry 1 and Asymmetry 2, respectively.

The results show that the asymmetry tends to have lower Capacity Factor (*CF*), Power Factor (F_P) and maximum thrust Factor ($F_{T,\ max}$), as shown in Figure 2-25, Figure 2-26, and Figure 2-27 respectively. This result explains the discrepancy exhibited in the previous examples.

2.5 Discussion

This chapter discusses the implication of having a complex tidal regime when strong diurnal components existed in the tidal velocity variation. It can be concluded that reducing the analysis to only the semi-diurnal constituents is not appropriate for such an area like Indonesia. The diurnal components have a different response to the channel friction in comparison to the semidiurnal components.

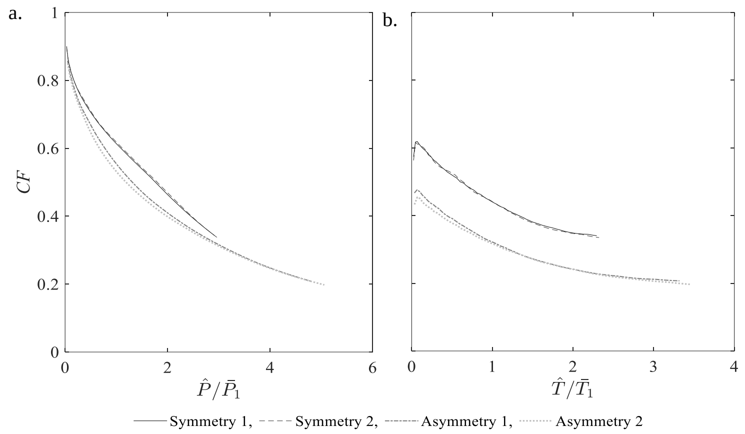

Figure 2-25: *CF* for the different asymmetry signals

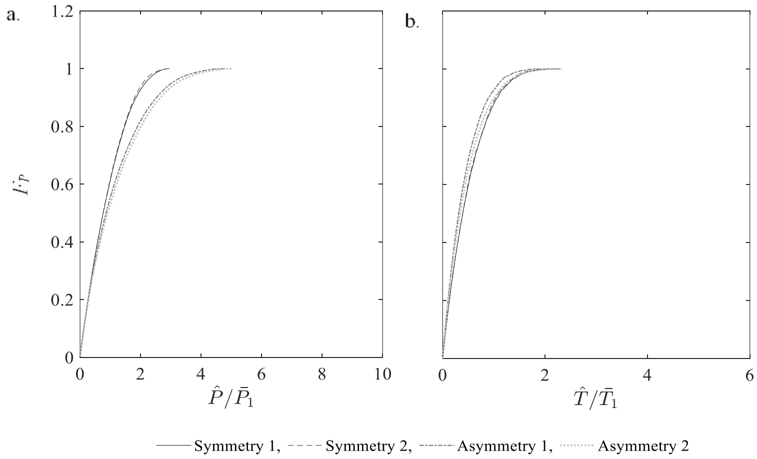

Figure 2-26: Power Factor *(F_P)* for different asymmetry signals

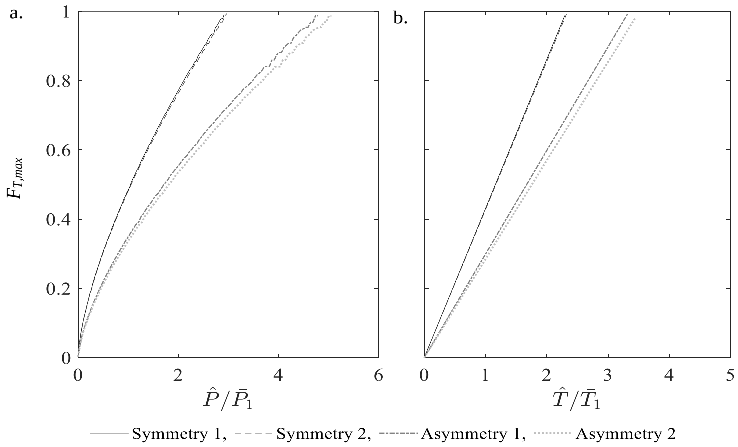

Figure 2-27: Maximum Thrust Factor *($F_{T,\,max}$)* for different asymmetry signals

Examples in section 2.2 show that the power variations due to the interaction of semidiurnal (M_2 and S_2) and diurnal components (K_1 and O_1) are not just on the daily tidal cycle and monthly neap-spring cycle. The modulation of both semidiurnal and semidiurnal components creates an annual pattern. These patterns are similar to the Equinox-Solstice cycle. This means there are certain months when the turbine produces less power than other months. Therefore, the assessment in an area of diurnal components should consider this annual variation.

However, an assessment with a simulation that covers annual variation might be unaffordable. Therefore, avoidance of months where the simulation would give an over- or under-estimate is recommended to reduce computational cost. Two equinoxes occur in a year, vernal equinox around March 21st and autumnal around September 21st. Meanwhile, two solstices also happen in a year, summer solstice that occurs on June 21st and winter solstice on December 21st. Therefore, in undertaking the assessment a simulation of limited duration is conducted that avoids these dates.

New metrics, F_P, F_T, $F_{T,\,max}$, $\frac{\hat{T}}{T_1}$ and $\frac{\hat{P}}{P_1}$, are introduced in the application of power and thrust capping. These metrics could be used alongside *CF* for a capping strategy decision. As shown in the examples, a capping strategy could maintain the $F_P > 0.8$. This means that the average power removed by the turbine could be held at the same level as the average power without capping. Simultaneously, this strategy could still reduce the average thrust and the maximum thrust.

The exercises in this chapter show that a turbine in mixed-diurnal tides tends to have lower *CF* than in the semidiurnal and diurnal tides for both capping strategies. This low *CF* is due to tidal asymmetry. Therefore, the expected *CF* in the range 0.35 – 0.45, as seen in the wind turbine industries, might be inapplicable in the mixed diurnal case. Furthermore, for all tidal types, a tidal turbine farm could be operated below the desired *CF* range and still *economically* viable. Reduction of thrust (maximum and average) could reduce the cost of technology. Later, in Chapter 6, the implementation of these capping metrics is demonstrated for real sites.

The interaction of diurnal constituents and semidiurnal constituents also creates an asymmetry phenomenon. The low values of *CF* are due to this asymmetry. Furthermore, tidal asymmetry certainly affects support structure design for turbines, and to some extent affects the operation of the turbines. For instance, tidal stream turbines are mostly designed for bi-directional symmetric flow. It means that most developers expect that the amplitude of the tidal stream velocity in the channel is the same for both directions, whereas this would not be true in an asymmetric flow.

Chapter 3. The Importance of Flow Stratification in Resource Assessment

Sheared or vertically stratified flow might be an important issue in Indonesian waters. As mentioned in Chapter 2, many potential locations for tidal turbines are located in deep water (>100 m) with the vertically stratified flow. This chapter explores whether the blockage ratio used in the rest of this thesis needs to be modified to account for the non-uniform flow.

Implementing tidal turbines in a flow known to be sheared in a large-scale model of shallow water is challenging, especially in terms of computational cost. It is not feasible to resolve directly the three-dimensional physics in a large scale model, such as that used in this thesis. Moreover, there is currently no well-established, simplified turbine representation for use in a 3D flow field available.

Therefore, to understand the performance of a turbine in the sheared flow profile, a commercial three-dimensional (3D) CFD model, ANSYS Fluent, has been employed to evaluate turbine performance in this chapter (ANSYS Inc., 2018). The devices are represented by using an actuator disc to investigate the effect of sheared flow on turbine performance.

Furthermore, there is the possibility of extreme flows occurring in Indonesian waters. The region hosts the Indonesian Through Flow (ITF), and oceanographers believe this current creates a sheared flow profile. However, since the ITF is a deep current, it is uncertain whether this extreme flow profile also occurs at the potential tidal sites, which are usually located in much shallower water.

3.1 Sheared Flow

In most cases, sheared flow is due to the presence of significant bed friction. However, in Indonesia waters, sheared flow occurs due to the so-called Indonesian Through Flow (ITF). It is important to note that there different terms are used in the oceanographic and tidal turbine fields. The oceanographers use term stratification to describe the different flow profiles in a water column, while sheared flow is more commonly used in the tidal turbine field.

3.1.1 Stratified Flow in Indonesian Waters

As mentioned in Chapter 2, a global-current known as the ocean conveyor belt passes through Indonesian waters. This circulation drives a large volume of water from the Pacific to Indian ocean [Van Aken *et al.* 2009; Potemra *et al.* 2003; Sprintall *et al.* 2009; Tillinger and Gordon 2009;

Gordon *et al.* 2017; Susanto & Song 2015; Feng *et al.* 2018]. As this global current occurs in a particular layer of the water column, depending on whether the flow is part of a warm current or cold current, this flow creates a stratification of the flow in a vertical direction. The density gradient due to temperature and salinity in the water column maintain this global current at a particular depth. The flow that passes Indonesia is mainly part of a warm current.

Due to its proximity to the equator, the ocean near Indonesia contains a pronounced thermocline layer. As sunlight warms the upper layer, the sea temperature rises to 33^{o}C and then drops to 4^{o}C below a mixed layer (around 50-100 m from the surface). The high precipitation rate significantly lowers the salinity at the surface. This leads to a rapid change of salinity within the water column, known as a halocline. The combination of the thermocline and halocline creates a density gradient that is known as a pycnocline.

For instance, Figure 3-1 shows the example of temperature and salinity at several locations in Indonesian waters. The water temperature at the upper layer is higher than in the layer below. By contrast, the salinity slightly increases from the surface layer to a depth of 100 m. The colour profiles denote specific stations within the Indonesian seas (the positions are shown on the map insert), while the grey tone profiles represent the North Pacific and South Pacific. These gradients maintain the flow stratification at a certain depth.

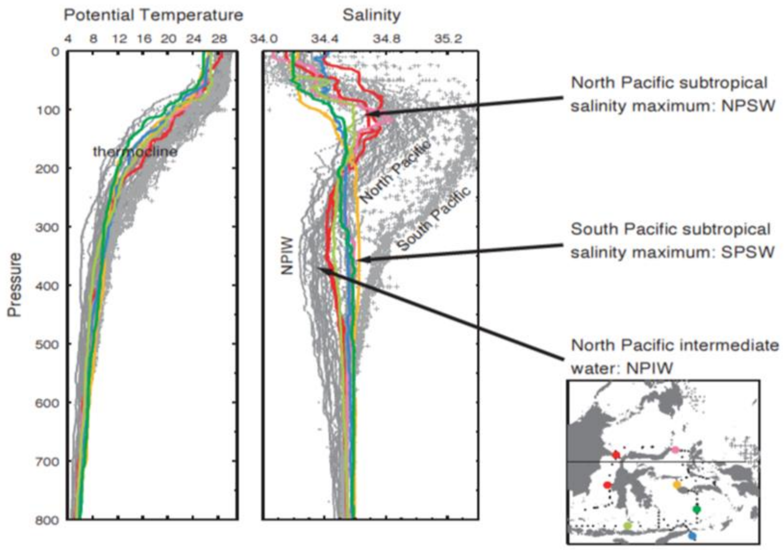

Figure 3-1: Thermocline and halocline in Indonesian waters, taken from Gordon, 2005.

A complex interaction between the barotropic current, tidal mixing and the thermohaline circulation, creates a zone of high velocity, sometimes concentrated in the upper layer of the water column. Hence, the velocity profile is stratified in a similar way to the density gradient. This density gradient creates additional complexity when modelling. Furthermore, the effect of a vertical density gradient on turbine performance has not yet been examined in the literature. However, this thesis does not explore these effects, since it is considered that there are other areas of study that have more impact on energy extraction in Indonesian waters.

3.1.2 Sheared Flow at Potential Sites for Tidal Power

The ITF passes through two of the five potential locations, Lombok Strait and Lifamatola. As discussed previously, the global flow that passes through Indonesia is a warm part of the ocean conveyor belt. This means the flow is strong in the upper layer of the water column, and a strongly sheared or stratified profile is observed in this area. Sprintall *et al.* 2009 conducted long term observations in some locations, including Lombok strait, from 2004-2006. Using ADCP mooring data, Sprintall *et al.* carried out direct estimation of the global current that crosses the island chain from the Pacific to the Indian Ocean. Figure 3-2 shows the mean velocity along the cross-section of the Lombok Strait. The higher velocity of the ITF is concentrated in the upper layer.

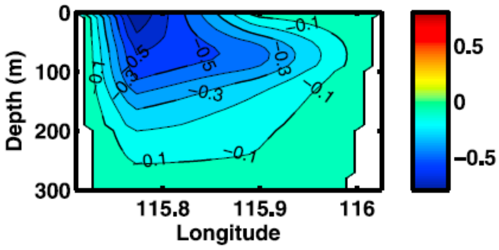

Figure 3-2: Mean ITF velocity along-strait in Lombok Strait based on ADCP measurement taken from Sprintall *et al.* 2009. Colour bar shows mean velocity in m/s.

Hautala *et al.* 2001 also show the velocity structure in some sites in Indonesia is stratified due to the pressure gradient. Figure 3-3 shows the vertical profile of ITF velocity in the Lombok strait area. This figure shoes the mean velocity of a residual flow, which is obtained after excluding the periodic current (i.e tidal flow).

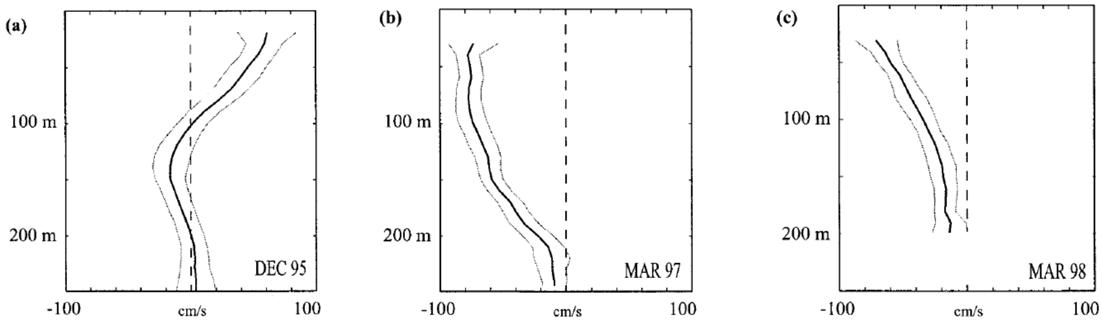

Figure 3-3: Laterally averaged along-strait velocity profiles, with error bars shown by grey lines, for (a) December 1985, (b) March 1997, and (c) March 1998, taken from Hautala *et al.* 2001.

However, it is important to note that this ITF is a deep current. As mentioned previously, the stratification profile is maintained by the thermocline and halocline layers. This layer is 250 m deep on average, which means that at a depth of less than 200 m, or in the mixing layer, an extreme sheared flow is very unlikely to occur. The deployable depth for the turbines, with a financial viability constraint, is usually in the range of 30-50 m, although this depth might be extended to 100 m if the turbine was installed from a floating platform.

Clear evidence of sheared flow in Indonesian waters is from field data obtained by P3GL, an Indonesian government agency that mapped the potential locations for tidal stream energy. P3GL used a mobile ADCP mounted from a boat to measure the spatial profile of flow in the strait's cross-section. Figure 3-4 shows the mobile ADCP data from Larantuka strait, one of the potential sites. This figure shows that the higher velocity is concentrated in the upper layer of the water column.

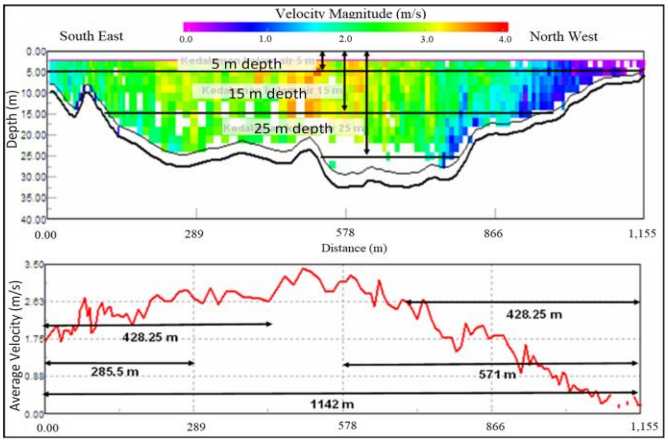

Figure 3-4: Mobile ADCP survey results at two of the potential sites with highly stratified current taken from Rachmat, 2013

However, examining the stationary ADCP data in the Larantuka, the sheared profile was not as extreme as expected. Furthermore, the data also showed the possibility of measurement error. A layer with lower velocity always appears at a depth of about 6 m. This vertical variation is thought to be due to instrument error (see Figure 3-5).

The potential sites for turbine deployment examined in this thesis are limited to depths below 90 m, which is within the mixing layer in the thermocline profile. Therefore, the extreme sheared or stratification profile is unlikely to occur in the potential sites in Indonesia. However, all sites will have some shear, and understanding the impact of this on the resource assessment is important.

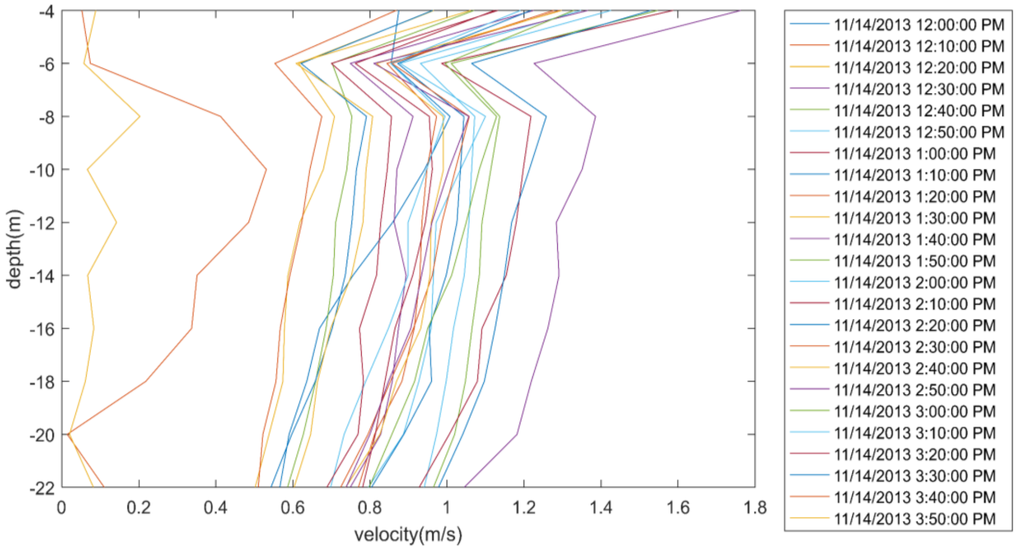

Figure 3-5: Raw data velocity from ADCP measurement in Larantuka

3.2 Literature Review on Turbine Performance in Sheared Flow

Most tidal energy extraction theories are developed using an assumption that the turbine is operated a uniform flow. The well-known actuator disc model for unbounded flow proposed by Lanchester, Betz and Joukowsky [van Kuik, 2007], the GC07 model introduced for laterally bounded flow [Garrett & Cummins, 2007], and the model that considered surface deformation [Houlsby *et al.*, 2008, Whelan *et al.*, 2009, Houlsby & Vogel, 2017], are based on the assumption that the flow could be simplified as a steady and spatially uniform flow.

In reality, turbines do not operate in uniform flows. Mostly, the turbine operates in a turbulent flow that is vertically and horizontally sheared. Therefore, turbine performance in sheared flow might be a significant issue in a resource assessment. Neglecting this sheared flow might lead to overestimate or underestimate the resources. Thus, this case potentially becomes a concern for turbine developers that would like to deploy their turbines in various locations.

A few studies have investigated this sheared flow issue. These include laboratory experiments, three-dimensional CFD modelling and analysis. However, hardly any data from an actual turbine operating in a sheared flow environment are available in the public domain. Only a few publications focus on turbine performance in sheared flow. For example, Vermeer *et al.*, 2003 and Gaurier *et al.*, 2020 conducted laboratory experiments for a turbine operated in turbulence and a sheared flow condition. Their study, however, is focused on the effect of sheared flow on the blade load. At the same time, the discussion on turbine performance in a sheared flow environment is very limited.

Three-dimensional CFD analyses has also been used to investigate this problem. However, there are discrepancies between their conclusions. For instance, McNaughton, 2013 investigated using EDF's open-source CFD solver *Code_Saturne*. He suggests that the power coefficient in the sheared profiles increases by 1-3%, although the thrust coefficient stays the same as the thrust coefficient in uniform flow.

Fleming, 2014 undertook CFD modelling using ANSYS Fluent for turbine performance in sheared flow. He used term efficiency as a metric to evaluate the turbine performance in the sheared flow. The efficiency is defined by the fraction of what he called P_{mech} over P_{lost}. P_{mech} is simply calculated from the product of torque produced by the turbine and the turbine's angular velocity while P_{lost} is calculated by the integral product of thrust on device and upstream velocity (see Fleming, 2014 for detail). His investigation showed efficiency increases in sheared flow of 4.7%-6.6%. However, he also mentioned that this efficiency is related to the presence of the turbine tower in his model. Meanwhile, a study by Ke *et al.*, 2020 argued that there is no effect of shear flow on turbine performance. Their ANSYS Fluent simulation results suggest that a difference between the uniform-flow and the shear-flow is "not apparent".

A theoretical approach proposed by Draper *et al*., 2016 extended the classical actuator disc to the case of a bounded inviscid shear flow. Draper *et al*., 2016 suggest that the turbine performance (determined by the obtainable maximum power coefficient($C_{P,max}$) should collapse to classical actuator disc theory in the uniform flow for laterally unbounded flow, while for laterally bounded flow, the turbine tends to have a lower $C_{P,max}$ than in uniform flow.

They suggest adjusting the blockage of a classical actuator disc in uniform flow to give equivalent results for a sheared flow. This gives an effective blockage (B_{eff}) to normalise the discrepancies that appear due to the sheared flow. They conclude that the power could be overestimated by 13% for a global blockage of 0.3, for instance, if B_{eff} is ignored. Note that the upstream velocity has been corrected in the normalisation. Therefore, Draper *et al*., 2016 suggested that the power and thrust in a sheared flow can be obtained from analysis of uniform flow by applying a B_{eff}, which is a function of the actual blockage ratio and the shear profile.

However, it is important to note that Draper *et al.*'s 2016 theoretical model neglects the influence of gravity and therefore does not distinguish between shearing of the flow in the horizontal or vertical planes. Lin *et al.*, 2020 conducted a thorough study exploring the gravitational effect on the turbine performance in a sheared flow.

Lin *et al.*, 2020 found that by creating a water level drop between the upstream and downstream ends of the strip, the gravity effect improves the performance of actuator discs for free surface flows, which in turn provides an extra source of energy. They also found that the shear effect can either improve or diminish disc performance by inducing upstream and bypass flow velocities that are different to each other. Based on Lin *et al.*, 2020, actuator discs located at high-velocity regions have lower power coefficients, whereas turbines located at low-velocity regions have higher power coefficients.

3.3 Turbine Performance in Sheared Flow

As there is no consensus on the performance of a turbine in a sheared flow, this chapter investigates this issue further. A commercial Reynolds Averaged Navier-Stokes (RANS) flow solver ANSYS Fluent (ANSYS Inc., 2018) is used to investigate turbine performance in a sheared flow.

3.3.1 Turbine Representation

Following Wimhurst, 2018 and Nishino & Wilden, 2012a, the actuator disc is modelled as a stationary permeable disc. The turbine is represented as a porous jump in the ANSYS Fluent model, placed perpendicular to the inflow from the inlet boundary. The change in the momentum flux, representing the momentum loss from viscous drag and wake rotation, is calculated using eq. (3.1).

$$M_x = K\left(\frac{1}{2}\rho {U_d}^2\right), \tag{3.1}$$

where ρ is the fluid density, U_d is the local streamwise velocity at the disc plane, and K is a momentum loss factor. The momentum loss factor determines the load or thrust acting on the disc. The total thrust acting on the disc is calculated by integration over the disc area as follow:

$$Thrust = \int M_x dA = K\left(\frac{1}{2}\rho \int {U_d}^2\, dA\right), \tag{3.2}$$

where A is disc area, and the thrust coefficient is a fraction of the thrust acting from the turbine over the thrust that is available from the stream. Therefore the thrust coefficient can be calculated by the comparison of flow speed squared through the actuator disc over the flow speed squared over the streamwise flow upstream of the turbine or actuator disc.

$$C_T = \frac{Thrust}{\left(\frac{1}{2}\rho {U_{in}}^2\right)} = K\frac{\langle {U_d}^2\rangle}{{U_{in}}^2}, \tag{3.3}$$

where U_{in} is discussed below. Similarly, the power removed from the mean flow at the disc plane is calculated by :

$$Power = \int M_x U_d dA = K\left(\frac{1}{2}\rho \int {U_d}^3\, dA\right), \tag{3.4}$$

and the power coefficient defined as :

$$C_P = \frac{Power}{\left(\frac{1}{2}\rho {U_{in}}^3\right)} = K\frac{\langle {U_d}^3\rangle}{{U_{in}}^3}. \tag{3.5}$$

The bracket $\langle\ \rangle$ in U_d, the streamwise flow through the actuator disc, indicates the spatial average of a variable/over the disc. As ANSYS fluent gives the flux of a particular area from its results, the spatial average of U_d is obtained by dividing the flux through the actuator disc by the area of the actuator disc. U_{in} is essentially the inlet (far-upstream) velocity. In this case, there are two possibilities for calculating U_{in}.

As the SWE model that is used to assess the tidal energy resources in this study is a depth averaged model, therefore there are two possible methods to determine the C_T and C_P (as shown in eq.(3.3 and eq. (3.5). Since the velocity in the depth average model is based on the average of the velocity of the water column, the first method of calculating U_{in} is by averaging the flux upstream across the entire cross-section. Hereafter, U_{in} for the entire channel/flume's cross-section is defined as U_{in-all}.

The second possible method is by normalising to the average U_{in} only over the projection of the actuator disc. In other words, the U_{in} is calculated from the streamwise velocity of the actuator disc area from the simulation without the turbine (hereafter is denoted as $U_{in-disc}$). In this method, $U_{in-disc}$ is calculated from the streamwise flux of the actuator disc area with no actuator disc installed in the flume (the disc is set as the interior in ANSYS fluent, which means there is no resistance applied at mesh in the disc area). This method is widely used by researchers, including (Nishino & Willden, 2012a; Fleming, 2014; Wimshurst, 2018; and Draper *et al.*, 2016). It is important to note that Draper *et al.*, 2016 used the length of the strip as they used a 2D approach in their analysis.

As in ANSYS fluent, the setup parameter is a pressure jump coefficient (C_2). Therefore, in this case, the momentum lost factor (K) is calculated from the comparison of C_2 over the actuator disc thickness (D_T) as follows:

$$K = \frac{C_2}{D_T}. \tag{3.6}$$

3.3.2 Turbulence Model

The turbulence model is essential to the modelling of flow separation in the boundary layer. Researchers in tidal turbine field have used a variety of different turbulence models in their CFD analysis. Nishino & Willden, 2012a, for example, use a standard $k - \varepsilon$ model to analyse an actuator disc in a 3D environment while Fleming, 2014; Wimshurst, 2018 and Ke *et al.*, 2020 use the $k - \omega$ SST to analyse an actuator disc performance in bed slope conditions.

The temporal and spatial derivative of the standard RANS equation could be written as follows:

$$\frac{\partial(\rho U)}{\partial t} + \nabla.(\rho U) = \nabla.(\rho UU) + \nabla.\left[(\mu + \mu_t)\left((\nabla U) + (\nabla U)^T\right) - \frac{2}{3}\mu(\nabla.U)I\right] + \rho g \tag{3.7}$$

where U is the velocity vector, g is acceleration due to gravity, ∇ is the vector of spatial derivatives, μ is the dynamic fluid viscosity, μ_t is the turbulent viscosity and I is turbulence intensity. The difference in the turbulence model is from μ_t, the turbulent/eddy viscosity. μ_t is computed from a turbulence model to solve the transport model. There are many turbulence models available to be used in CFD modelling. However, this section only discusses the three turbulence models that are widely used in the CFD turbine modelling, standard $k - \epsilon$, standard $k - \omega$ and $k - \omega$ SST.

The $k - \epsilon$ model was initially proposed in 1974 by Launder and Spalding (Launder & Spalding 1974). The kinematic/eddy viscosity μ_t is computed from k and ϵ.

$$\mu_t = C_\mu \frac{\rho k^2}{\epsilon}, \tag{3.8}$$

where is C_μ=0.09, k is the turbulent kinetic energy, ϵ is turbulence dissipation rate (unit m^2/s^3) that is acting as a sink in the RANS equation. In tensor notation, ϵ could be written as the product of kinematic viscosity and the velocity gradient of the turbulence variation.

$$\epsilon = v\overline{\frac{\partial U_i'}{\partial x_j}\frac{\partial U_i'}{\partial x_j}}. \tag{3.9}$$

However, ϵ cannot be solved directly in a RANS model as U_i' is unknown. Therefore, two additional transport equations are solved for the turbulent kinetic energy (k) as seen in eq. (3.10) and for the rate of dissipation (ϵ) as presented in eq. (3.11).

$$\frac{\partial(\rho k)}{\partial t} + \nabla.(\rho k U) = \nabla.\left(\left(\mu + \frac{\mu_t}{\sigma_k}\right)\nabla k + P_\epsilon - \rho\epsilon\right), \tag{3.10}$$

$$\frac{\partial(\rho\epsilon)}{\partial t} + \nabla.(\rho U\epsilon) = \nabla.\left(\left(\mu + \frac{\mu_t}{\sigma_k}\right)\nabla\epsilon\right) + C_{1\epsilon}P_k\frac{\epsilon}{k} - C_{2\epsilon}\rho\frac{\epsilon^2}{k}, \tag{3.11}$$

where P_k is the production due to mean velocity shear, while C_1 and C_2 are the model coefficients. The dissipation rate (ϵ) is expected to be high near to walls and in shear layers.

The $k-\epsilon$ is model inaccurate at predicting the boundary layer with an adverse pressure gradient. This issue becomes problematic in the particular area of modelling wind or tidal turbines that involve the turbulence effects and flow separation problems—for example, the flow separation behind the aerofoil at a high angle of attack. As the sheared profile might be sensitive to the flow separation at near the sea bed, this model might give inaccurate results.

The $k-\omega$ model is essentially similar to the $k-\epsilon$. The ω is the specific turbulence dissipation rate, calculated by dividing ϵ with $C_\mu k$ as follows:

$$\omega = \frac{\epsilon}{C_\mu k}. \tag{3.12}$$

Therefore the transport equation for k is the same as in the $k-\epsilon$ model (see eq (3.10). The $k-\omega$ model only needs to solve the additional transport equation for ω.

$$\frac{\partial(\rho\omega)}{\partial t} + \nabla.(\rho U\omega) = \nabla.\left(\left(\mu + \frac{\mu_t}{\sigma_k}\right)\nabla\omega\right) + \frac{\gamma}{v_t}P_k - \beta\rho\omega^2. \tag{3.13}$$

Similarly to the $k-\epsilon$ model, this $k-\omega$ model also has empirical coefficients (α, β, β^*, σ_k, σ_ω). However, this $k-\omega$ model also has weaknesses. Menter, 1992 shows that it is dependent on the freestream turbulence conditions. Therefore, $k-\omega$ is not as good as $k-\epsilon$ to solve the turbulence in the far-field.

Thus there is a dilemma for CFD modellers, using $k-\epsilon$ we have to give up detail near to the wall or the boundary layer, while using $k-\omega$ we have a sensitive dependency on the inlet freestream turbulence condition. This situation is not ideal, especially for modelling wind or tidal turbines.

Menter 1994 proposed the $k-\omega$ SST turbulence model. Essentially, the $k-\omega$ SST model is developed to incorporate both $k-\varepsilon$ and $k-\omega$. By substituting the correlation of ω and ϵ as shown in eq. (3.12), the dissipation equation in $k-\varepsilon$ (eq. (3.11) could be written for the $k-\omega$ with an additional term.

$$\frac{\partial(\rho\omega)}{\partial t}+\nabla.(\rho U\omega)=\nabla.\left(\left(\mu+\frac{\mu_t}{\sigma_k}\right)\nabla\omega\right)+\frac{\gamma}{v_t}P_k-\beta\rho\omega^2+2\frac{\rho\sigma\omega^2}{\omega}\nabla k:\nabla\omega. \qquad (3.14)$$

The additional term of $2\frac{\rho\sigma\omega 2}{\omega}\nabla k:\nabla\omega$ in eq. (3.14 is then multiplied by a factor of $(1-F_1)$, where if $F_1=0$, the model is $k-\varepsilon$ and if $F_1=1$ the model becomes the $k-\omega$ model. This allows control of the model for every cell in the mesh, so that near to the wall boundary the model solves $k-\omega$ while far away from the wall it solves $k-\varepsilon$. This function allows the model to blend $k-\varepsilon$ and $k-\omega$ smoothly. The value of F_1 could be set in between 0 and 1 $(0<F_1<1)$ for the intermediate cells. Thus the $k-\omega$ SST model is one of the most popular turbulence models used in tidal turbine CFD modelling.

3.3.3 Model Domain

Following Draper *et al.*, 2016, this thesis investigates the performance of the turbine for laterally bounded and unbounded sheared flow. Two different domain widths are adopted in this investigation for both scenarios. The turbine is represented by an actuator disc. In reality, turbines could be seated on the seabed, installed on a tower platform or mounted a floating body, as illustrated in Figure 3-6. Therefore, the effect of turbine position in the sheared flow profile is also considered in this investigation.

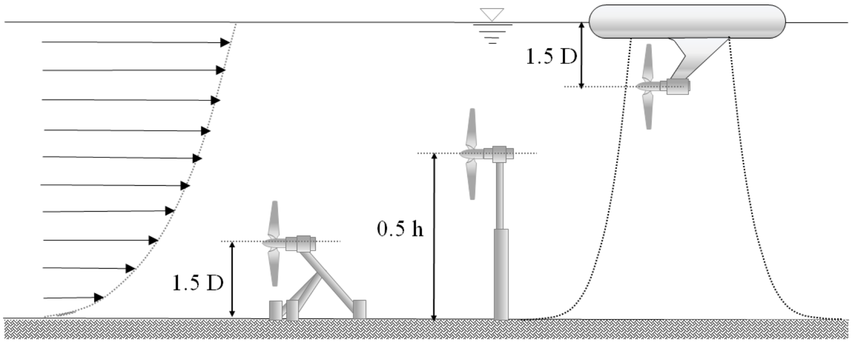

Figure 3-6: The illustration of turbine installations that represents the elevation of the turbine in a sheared flow.

The investigation is conducted using a 24 m diameter actuator disc. The actuator disc is installed at three different positions. Firstly, an actuator disc is installed near to sea bed. The centreline of the actuator disc is 1.5 D from the bottom. This case is named “Bottom (Bot) case”. Secondly, the actuator disc is in the middle of the cross-section, or 0.5*h*, where *h* is the depth. This case is called "Middle (Mid) case". Lastly, the actuator disc is installed at the top layer of the water column or 1.5 D from the surface. This case is named "Top case" (see Figure 3-6).

Two different sizes of virtual flumes were employed in the simulation to represent two different blockage ratios. A flume with the cross-section of 48x100 m, giving 0.0942 blockage ratio, is set up for the laterally bounded scenario. Then, a larger flume (cross-section of 248×100m) to give a blockage ratio of 0.0018 is set for the laterally unbounded scenario. The three different positions are applied to represent turbine position as discussed previously. Therefore, there are six separate model domains created for the turbine.

Figure 3-7 shows the schematic of the model domain investigated using ANSYS fluent. The left and right walls of the flow tank in the laterally unbounded scenario (Figure 3-7a.) are set as symmetry boundaries. While on the laterally bounded scenario (Figure 3-7b.), the right and left sides are set as wall boundaries.

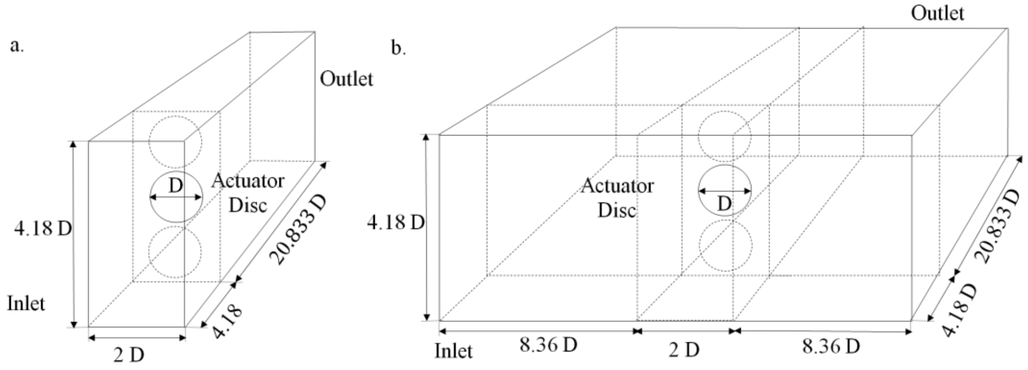

Figure 3-7: Schematic model domain

Figure 3-8 presents the schematic of the flume in a streamwise manner and the positions of observation points in the analyses. Eight observation stations are set up to evaluate the flow profile in the flume. The observation at "1D" means the station is one diameter downstream from the turbine. The negative sign (-) means the position is at the upstream of the turbine, while the positive (+) sign indicates the station is at the downstream of the disc position.

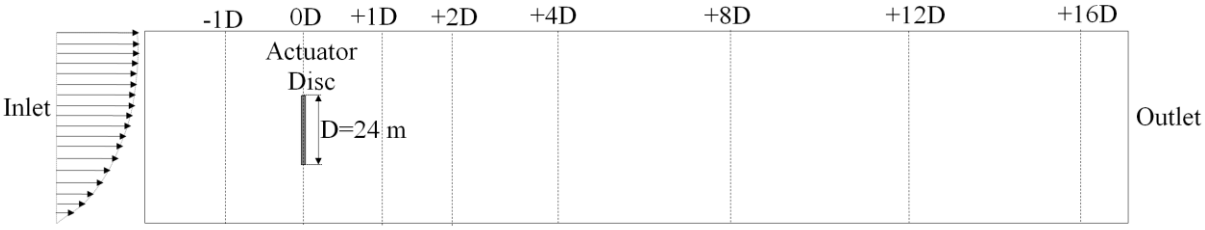

Figure 3-8: Schematic of observation points

The investigation of the performance in the sheared flow is carried out with a sheared flow profile used by Draper *et al.*, 2016. This chapter focuses on the asymmetric flow type as the flow stratification in some areas of Indonesia is asymmetrical. The sheared flow profile is defined by the following equation:

$$u_1(y) = U_0\left(y\frac{B}{D}\right)^n, \tag{3.15}$$

where n is the shape parameter, B is the blockage ratio, and D is turbine diameter. U_0 is the uniform inlet velocity, which is determined to get the same maximum velocity for all profiles.

3.3.4 Model Checks

Before conducting the analysis of turbine performance in sheared flow, it is necessary to conduct some checks on the fidelity of the model. Four different aspects are checked, the first being for mesh independence. Meshing is considered critical in CFD modelling. The cell size or the mesh density must be sufficient for the model to resolve the flow, so that the results capture the flow characteristic correctly. The cell size near the wall needs special attention. The mesh convergence study is therefore conducted before further investigations of turbine performance in sheared flow are carried out.

Since the turbine performance is expected to be sensitive to the position in the sheared flow, a second check is on the actuator disc performance at different positions in a uniform flow. The third check is the effect of the velocity on turbine performance. The sheared flow involves a variation of velocity in the water column, therefore it is necessary to check whether the velocity profile affects the turbine performance. The ANSYS Fluent model in this chapter neglects surface deformation. Therefore, performance is expected to be satisfactorily modelled by the theoretical model of Garrett & Cummins, 2007. The C_P and C_T coefficients are expected to be independent of velocity.

The literature study above suggests that the $k-\omega$ SST model will give the best results. However, for completeness, this study also considers other turbulence models. Two turbulence models, the standard $k-\epsilon$ and standard $-\omega$, are compared with the $k-\omega$ SST in this check.

a) Mesh Independence

The meshing structure for these investigations is hexahedral for all computational domains. An O-grid blocking was employed in the disc region. The grids are finer at the edge of the disc area than at other locations. The grids become gradually coarser in the far-field area. The simulations for the mesh convergence study are done for each case and scenario. Three different disc positions are analysed in this study. The analyses are also conducted for both laterally bounded and unbounded scenarios. The simulations for this check are run for a uniform flow.

1) Laterally Unbounded Scenario

Three different meshes are constructed for the mesh convergence study for the laterally unbounded scenario. For instance, the case of the turbine placed at the centre of the flume, as shown in Figure 3-9 used three different mesh densities. Hereafter, the three meshes densities are referred to as Coarse (Figure 3-9a), Moderate (Figure 3-9b) and Fine (Figure 3-9c).

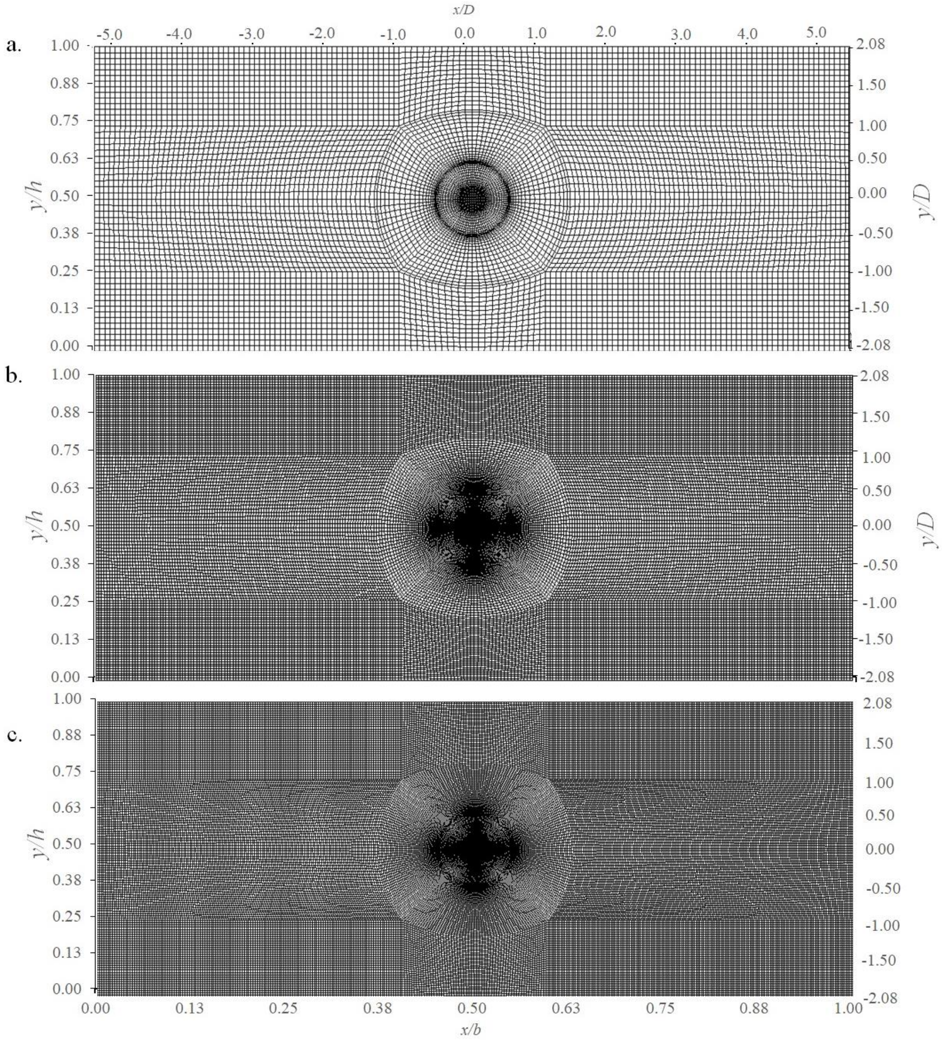

Figure 3-9: Three different meshings for the laterally unbounded scenario

The simulation results for each mesh are presented in Table 3-1. The C_P and C_T for Moderate (Mod) and Fine meshes are almost the same. Furthermore, the C_P and C_T are plotted against momentum loss factor (K) as shown in Figure 3-10. Three mesh densities show agreement for the optimum C_P at K=2.0 ~ 2.5. However, the coarse mesh tends to have higher a C_P and C_T at higher K.

Table 3-1: The trust and power coefficient obtained using three different meshes for laterally unbounded scenario

K	α_2			C_T			C_P		
	Coarse	Mod	Fine	Coarse	Mod	Fine	Coarse	Mod	Fine
1	0.803	0.802	0.802	0.644	0.644	0.644	0.517	0.516	0.516
1.5	0.732	0.732	0.732	0.805	0.803	0.803	0.589	0.588	0.588
2	0.674	0.673	0.673	0.910	0.907	0.907	**0.614**	**0.611**	**0.611**
2.5	0.626	0.625	0.625	0.980	0.977	0.976	**0.614**	0.610	0.610
3	0.585	0.584	0.584	1.027	1.022	1.022	0.601	0.597	0.596
4	0.520	0.517	0.517	1.081	1.068	1.070	0.562	0.552	0.553
5	0.472	0.470	0.469	1.114	1.104	1.102	0.526	0.519	0.517

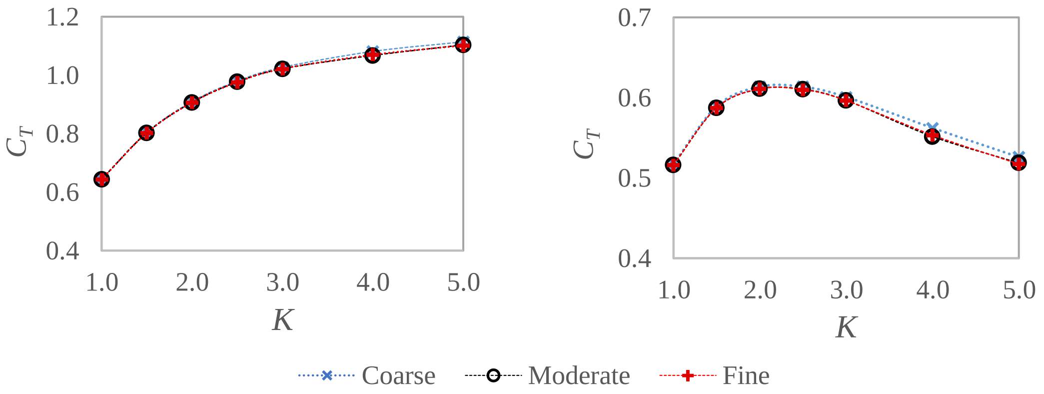

a. Thrust b. Power

Figure 3-10: Thrust and Power Coefficient against momentum loss factor (K) obtained using the three different mesh density for the laterally unbounded case for turbines in the

The simulations in ANSYS Fluent are set up with no surface deformation. This condition is similar to the assumption used in GC07. These results are also compared with theoretical C_P and C_T from GC07. As this case represents of the laterally unbounded case, it is sensible also to compare with Lanchester-Betz results (essentially GC07 as blockage tends to zero) (see Figure 3-11).

As shown in Figure 3-11, the results from the three different meshes all agreed with the GC07, whereas Lanchester-Betz gives lower C_P and C_T than all meshes. The mismatch with Lanchester-Betz is expected, since the laterally unbounded case uses a blockage ratio of 0.018, this blockage ratio is not sufficiently small to make this simulation have good agreement with Lanchester-Betz.

Since the analyses are conducted to examine the turbine performance at different positions in a water column, the mesh independence study is also performed for each turbine position. Three different positions are employed for this analysis. Table 3-2 shows a summary of mesh independence for each case. The total element for each mesh density is in the range of 800 thousand to approximately 1.2 million elements for coarse mesh, six million to seven million elements for moderate mesh and up to 12.5 million for the fine mesh.

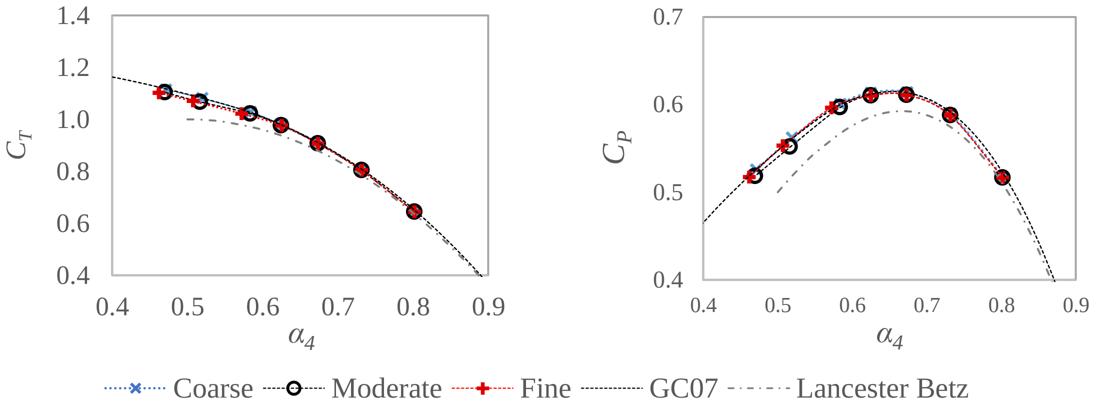

a. Thrust b. Power

Figure 3-11: Comparison of Thrust and Power Coefficient with theoretical C_T and C_P from Lanchester-Betz and GC07 from different mesh for the laterally unbounded case for turbines in the centre of the flume.

The fluxes from the simulations without the actuator disc show agreement for each mesh density. The comparison for the C_P and C_T is only shown for K= 2.5, as this is the optimum K for C_P. These results show that almost every mesh density gives the same C_P. Therefore it is safe to conclude that the moderate mesh is adequate for use in this analysis.

Table 3-2: Summary of mesh independence study for laterally unbounded flow

		Bottom			Middle			Top	
	Coarse	Moderate	Fine	Coarse	Moderate	Fine	Coarse	Moderate	Fine
Elements Part									
- Total elements	882,388	6,079,248	10,337,073	931,332	7,156,272	12,499,697	1,127,108	6,079,248	10,573,073
- Disc	1,920	7,040	10,325	1,920	7,040	7,965	1,920	7,040	10,325
- Inlet	10,080	35,200	50,995	10,648	41,488	61,713	12,824	35,024	51,939
n Nodes	854,700	5,978,375	10,188,800	902,748	7,045,103	12,332,428	1,094,940	5,978,375	10,423,620
Simulation with no turbine									
- flux-inlet (m^3/s)	24,799.90	24,799.92	24,800.83	24,799.74	24,800.69	24,799.89	24,799.70	24,800.49	24,800.83
- flux-disc (m^3/s)	452.15	452.78	452.50	452.59	452.55	452.01	452.50	452.45	452.50
- u-inlet (m/s)	1.00	1.00	1.00	1.00	1.00	1.00	1.00	1.00	1.00
- u-disc (m/s)	1.00	1.00	1.00	1.00	1.00	1.00	1.00	1.00	1.00
Simulation with turbine (K= 2.5)									
- flux-disc (m3/s)	283.11	283.38	283.32	283.00	282.86	282.83	283.42	283.27	283.32
- C_T	0.980	0.981	0.980	0.980	0.977	0.977	0.981	0.980	0.980
- C_P	0.614	0.614	0.614	0.614	0.611	0.611	0.614	0.614	0.614
- α_2	0.626	0.626	0.626	0.626	0.625	0.625	0.626	0.626	0.626

2) *Laterally Bounded Scenario*

As discussed previously, the laterally bounded scenario used a blockage ratio ~0.09. Figure 3-12 shows the meshes used in the mesh independence study for the turbine at the centre of the flume cross-section. In a similar way to the previous case, Figure 3-12 shows the comparison of grid resolution at three different stages of mesh density, coarse (Figure 3-12 a.), moderate (Figure 3-12 b.) and fine (Figure 3-12 c.).

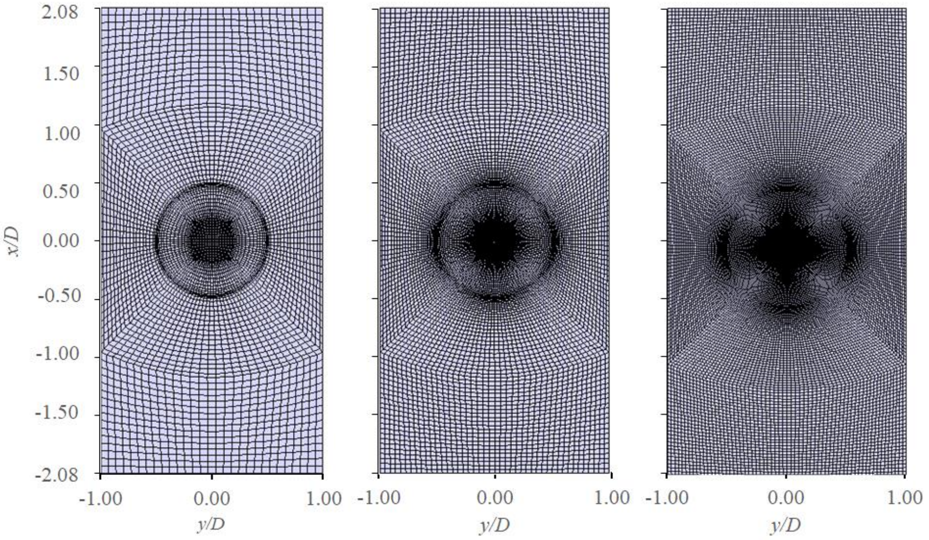

a. Coarse b. Moderate c. Fine

Figure 3-12: Three different meshes for the laterally bounded scenario

The simulation results for each *K* are presented in Table 3-3. Similar to the laterally unbounded scenario, C_T and C_P from the simulations are also plotted against *K* (see Figure 3-13). The maximum C_P is obtained at $K = 2.5{\sim}3.0$. The three mesh densities show that all meshes of this scenario also have a good agreement with each other.

Table 3-3: The trust and power coefficient from three different meshes for the laterally bounded scenario

K	α_2			C_T			C_P		
	Coarse	Mod	Fine	Coarse	Mod	Fine	Coarse	Mod	Fine
1	0.821	0.821	0.821	0.673	0.674	0.674	0.553	0.553	0.553
1.5	0.755	0.755	0.755	0.856	0.856	0.856	0.646	0.647	0.647
2	0.702	0.702	0.702	0.985	0.985	0.985	0.691	0.691	0.691
2.5	0.657	0.657	0.657	1.079	1.080	1.080	0.709	0.710	0.710
3	0.619	0.619	0.619	1.150	1.151	1.151	**0.712**	**0.713**	**0.713**
4	0.559	0.559	0.559	1.249	1.249	1.249	0.698	0.698	0.698
5	0.512	0.513	0.513	1.313	1.314	1.314	0.673	0.674	0.674

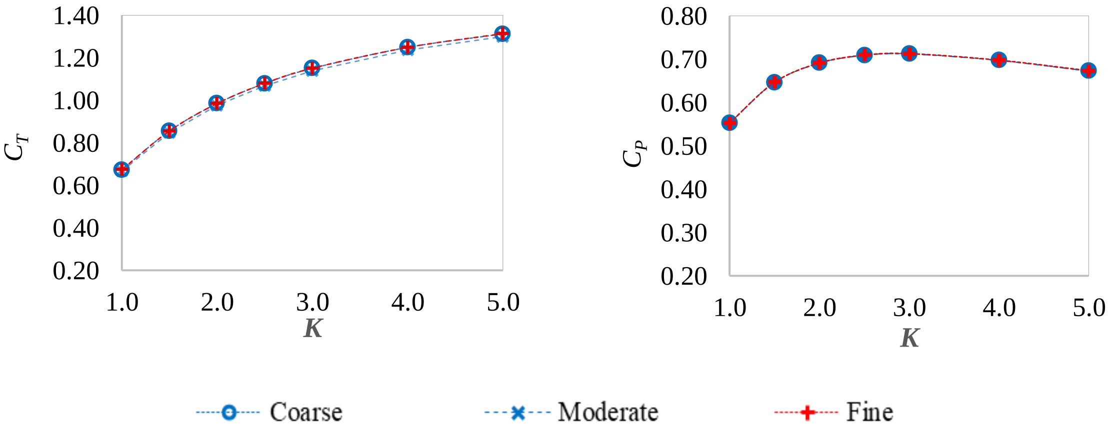

a. Thrust b. Power

Figure 3-13: Thrust and power coefficient against momentum lost factor (*K*) from different mesh for the laterally bounded case and the turbines in the centre of the flume

The comparison of C_T and C_P against GC07 is presented in Figure 3-14. The curves are plotted against turbine velocity coefficient (α_2). Both figures show that the meshes give almost the same results for C_T and C_P. Similar to the previous simulation on the laterally unbounded case, the mesh independence study for the laterally bounded case also shows good agreement with the theoretical C_T and C_P from GC07.

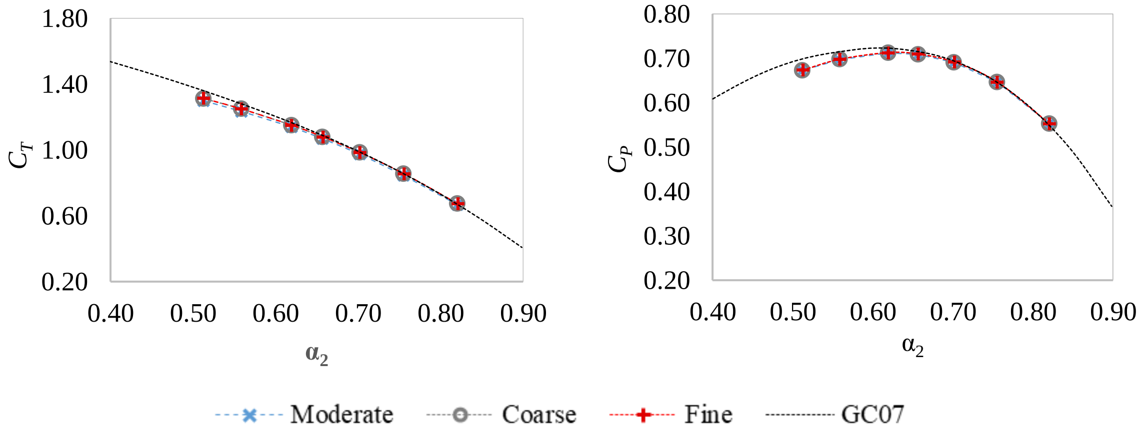

a. Thrust b. Power

Figure 3-14: The comparison of thrust and power coefficient with theoretical C_T and C_P from GC07 from different meshes for the laterally bounded case and the turbines in the centre of the flume.

In a similar way to the laterally unbounded scenario, the mesh independence study is also conducted for every disc position case. Table 3-4 shows the summary of the mesh independence study for each mesh density in all cases. The fine meshes for this scenario are widely varied. For instance, the fine mesh for the actuator disc in the middle has 4.9 million elements while the other cases have more than 15 million elements. The larger number of elements in the bottom and top cases is because of the proximity of the turbine to the mesh boundary.

The simulations show that the discrepancy of thrust and power from coarse mesh to fine mesh is small. For instance, the moderate mesh for the bottom case with ~2 million elements gives C_P = 0.705 and for the fine mesh with 16.4 million elements gives C_P = 0.701. Therefore, the moderate mesh is adequate to be used in the analyses for this scenario as well.

b) The Turbine in Different Positions

The turbine performance in the sheared flow is investigated for the turbine in different positions. The actuator disc position sensitivity in a uniform flow is first examined here. The water surface is set as a symmetry boundary while the flume bottom is set as a wall. This set up means that the actuator disc installed near to the surface is near to a boundary with no friction. In contrast, the actuator disc installed near the bottom is close to a boundary with bottom friction imposed as a no-slip condition. This analysis is performed to check whether the friction affects the performance of the turbine.

Table 3-4: Summary of mesh independence study for every case of the laterally bounded scenario

	Bottom			Middle			Top		
	Coarse	Moderate	Fine	Coarse	Moderate	Fine	Coarse	Moderate	Fine
Elements Part									
- Total elements	316,800	2,018,720	16,426,285	984,543	2,775,984	4,691,264	316,800	2,018,720	15,116,065
- Disc	1,440	5,280	21,805	2,465	7,040	11,520	1,440	5,280	21,805
- Inlet	3,456	12,496	51,086	5,713	16,192	27,392	3,456	12,496	47,081
n Nodes	305,537	1,980,027	16,268,362	961,272	2,729,857	4,619,277	305,537	1,980,027	14,976,412
Simulation with no turbine									
- flux-inlet (m^3/s)	4,800.00	4,800.00	4,799.99	4,800.01	4,800.00	4,799.99	4,800.00	4,800.01	4,800.03
- flux-disc (m^3/s)	454.66	454.92	452.90	454.64	452.54	454.74	454.66	454.56	452.52
- u-inlet (m/s)	1.00	1.00	1.00	1.00	1.00	1.00	1.00	1.00	1.00
- u-disc (m/s)	1.01	1.01	1.00	1.00	1.00	1.01	1.01	1.00	1.00
Simulation with turbine (K= 2.5)									
- flux-disc (m3/s)	295.92	296.60	296.48	297.23	297.25	297.31	295.92	296.39	296.22
- C_T	1.059	1.075	1.071	1.079	1.079	1.080	1.059	1.073	1.071
- C_P	0.689	0.705	0.701	0.709	0.709	0.710	0.689	0.703	0.701
- α_2	0.651	0.656	0.655	0.657	0.657	0.657	0.651	0.655	0.655

1) *Laterally Unbounded Scenario*

Three sets of meshes are developed to analyse the turbine performance in three different positions, as shown in Figure 3-14. The first position is near to the surface, hereafter named as “top case” (see Figure 3-14a). Secondly, the actuator disc is installed in the middle of the flume, hereafter referred to as mid-case (Figure 3-14b). Lastly, the actuator is installed near the bottom of the flume, the bottom case (Figure 3-14c).

The comparison of C_T and C_P for the actuator disc at the three different positions shows that the effect of bottom friction on the turbine performance is relatively small. Table 3-5 and Figure 3-15 shows that the actuator disc installed in the middle of the flume (the mid-case) gives a very slightly lower optimum C_P than other cases (top and bot). The detail of C_T and C_P at the optimum C_P is shown in the small boxes inside the graph in Figure 3-16. However, the discrepancy of C_P is approximately 0.5% only. This is in the range of simulation error.

The comparison of the flow fields for each case is shown in Figure 3-16 and Figure 3-17. Figure 3-16 is the flow field in the vertical plane while in Figure 3-17 is in the horizontal plane. The flow fields in both figures are normalised by the uniform velocity at the inlet (U_0= 1 m/s). The vertical flow field contours are taken along the mid-plane of the channel for all cases, while the horizontal flow field for each case is taken across the elevation of the centre point of the disc. Therefore, the slice elevation for each case is different. For instance, the horizontal flow field for the Top case (Figure 3-17a) is taken at y=0.76h or 1D from the surface while for the Bottom case (Figure 3-17c) is taken at y=0.24h or 1D from the bottom of the flume.

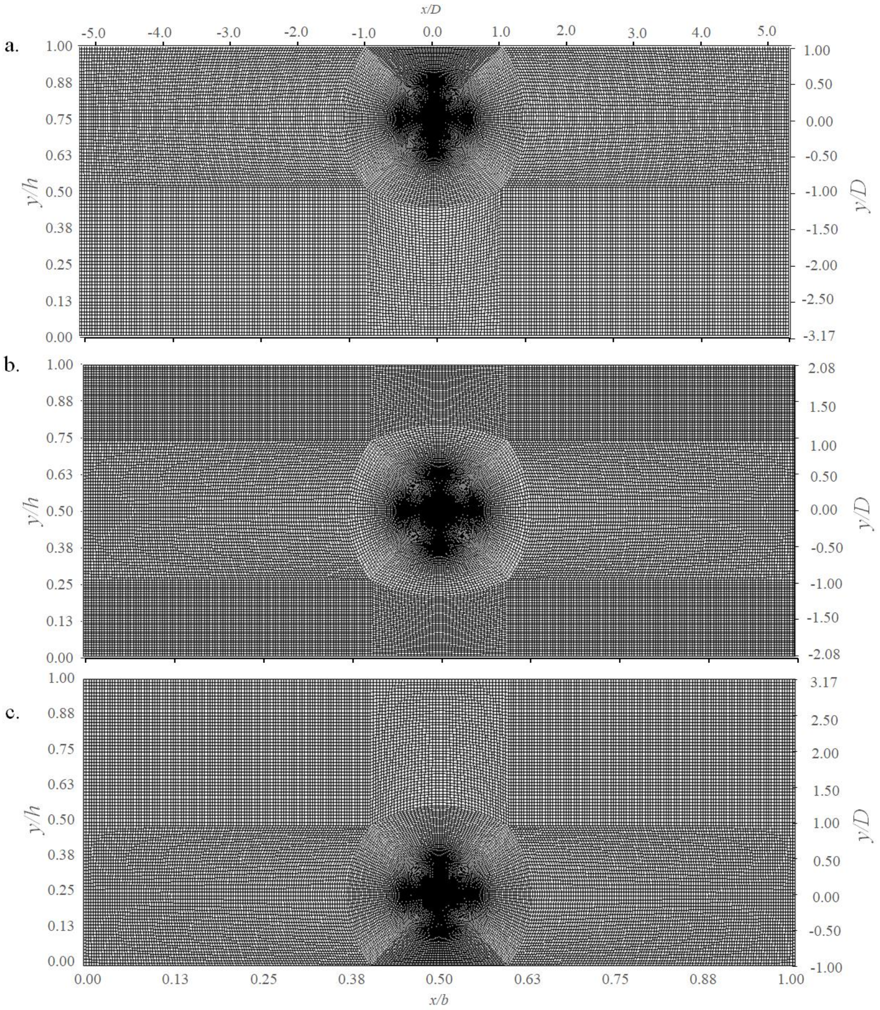

Figure 3-14: The meshes of the simulation for the turbine located at three different positions. a is the meshes for the top case, b is the mid case, and c is the bottom case.

Table 3-5: C_T and C_P for three different turbine positions for the laterally unbounded scenario

K	α_2			C_T			C_P		
	Top	Mid	Bot	Top	Mid	Bot	Top	Mid	Bot
1	0.803	0.802	0.803	0.645	0.644	0.644	0.518	0.516	0.517
1.5	0.732	0.732	0.732	0.805	0.803	0.804	0.590	0.588	0.589
2	0.674	0.673	0.674	0.910	0.907	0.909	**0.614**	**0.611**	**0.613**
2.5	0.626	0.625	0.626	0.980	0.977	0.979	**0.614**	0.610	**0.613**
3	0.585	0.584	0.585	1.028	1.022	1.027	0.602	0.597	0.601
4	0.521	0.517	0.520	1.084	1.068	1.083	0.565	0.552	0.563
5	0.472	0.470	0.471	1.112	1.104	1.110	0.525	0.519	0.523

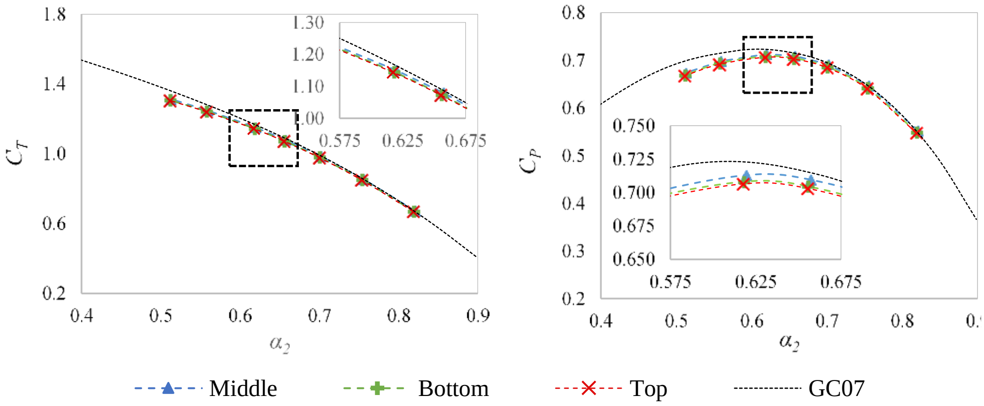

a. Thrust b. Power

Figure 3-15: Power and thrust coefficient for the turbine located at three different positions for uniform flow and the laterally unbounded scenarios

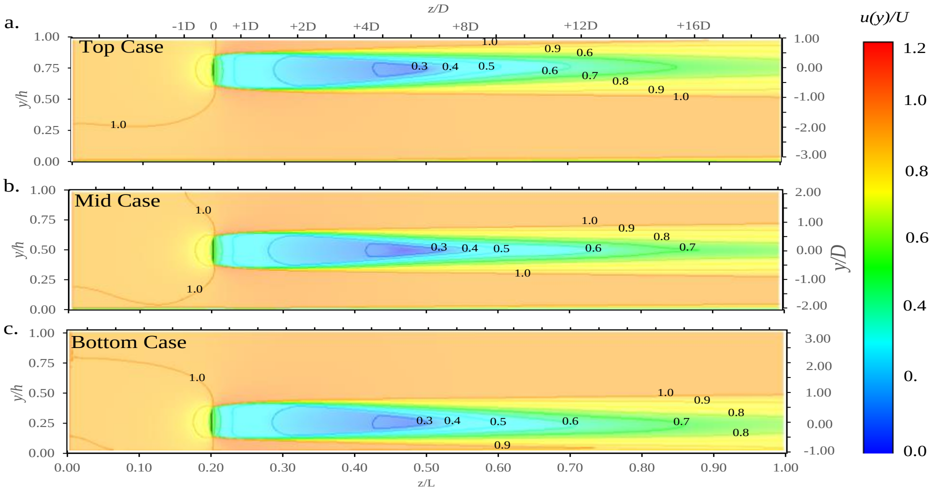

Figure 3-16: Normalised flow field in the vertical plane for the turbine in uniform flow and the laterally unbounded scenario

The vertical flow field shows a similar pattern for the top case and the bottom case. Both cases (Bot and Top) have a mirror shape of the flow field relative to each other. Despite this, the bottom boundary is set as a no-slip wall while the top boundary is set as symmetry boundary. This flow field indicates that the bottom friction has a negligible effect on the disc performance. This result is also consistent in the horizontal flow field. The length of flow recovery for all cases are similar, as well as the flow field pattern.

2) *Laterally Bounded Scenario*

A similar check is also conducted for the laterally bounded scenario. Three different positions of the actuator disc are employed as in the previous scenario. An actuator disc is installed at one diameter of the actuator disc (1D) from the surface for the top case, at half of the flume height (0.5h) for the middle case and 1D from the bottom of the flume for the bottom case (see Figure 3-18).

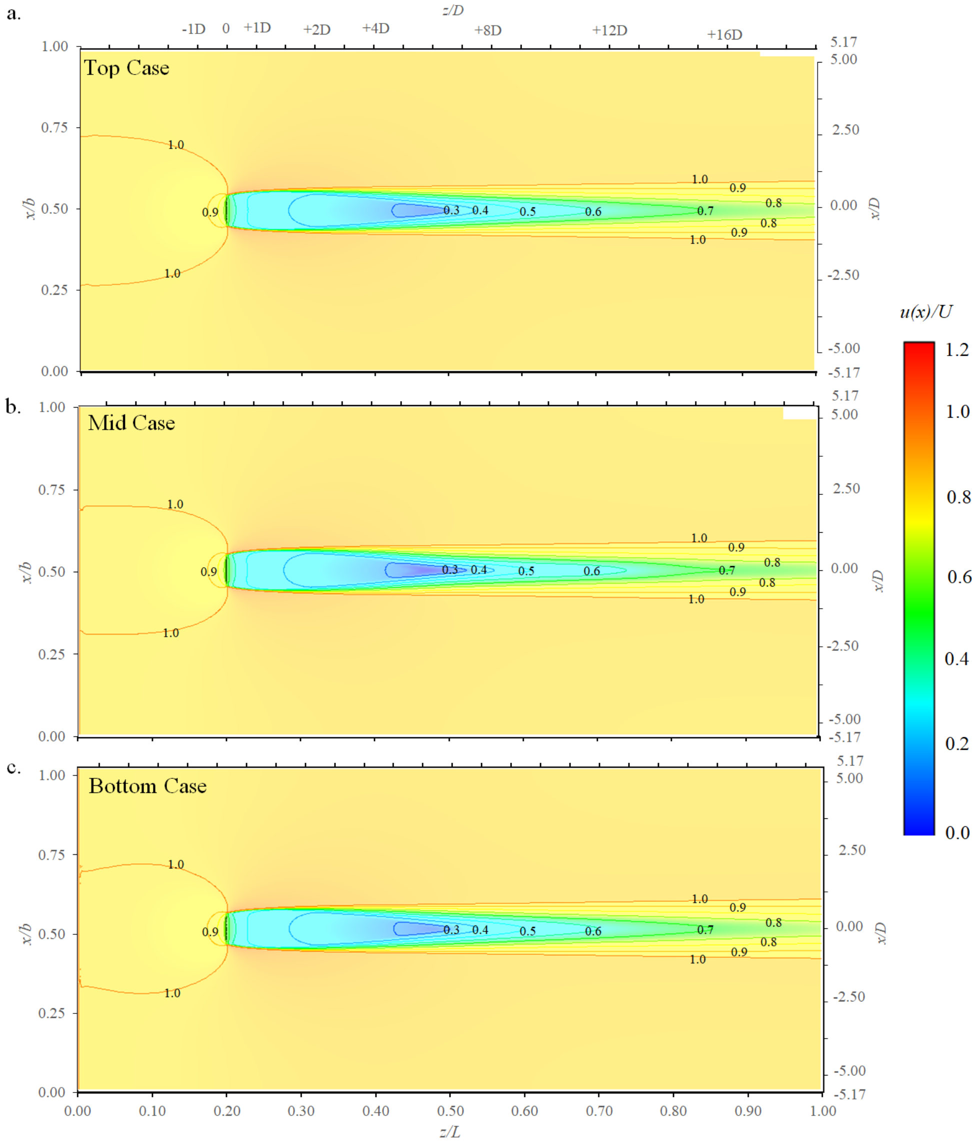

Figure 3-17: Normalised flow field in the horizontal plane for the turbine in a uniform flow and the laterally unbounded scenario

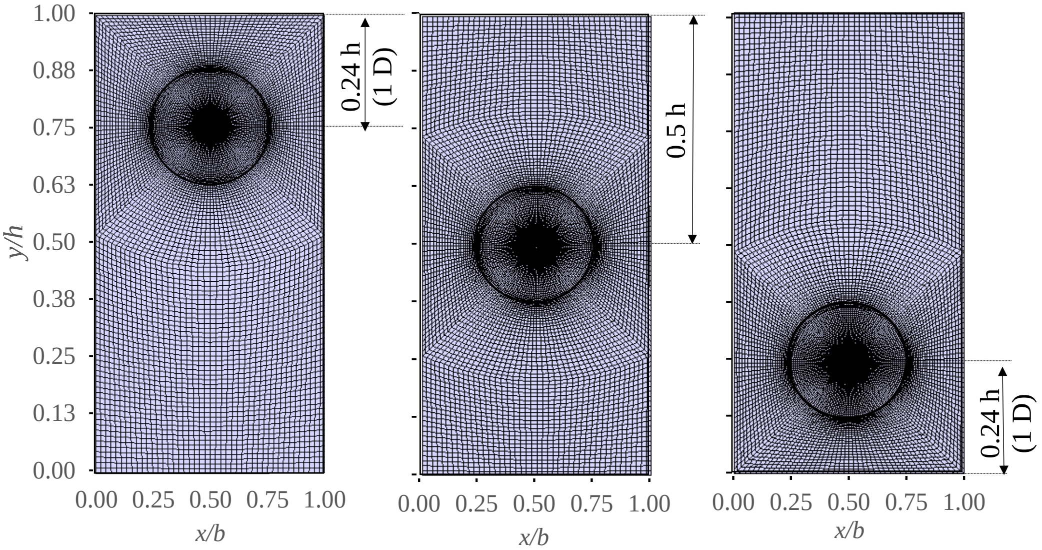

a. Top b. Middle c. Bottom

Figure 3-18: Three different turbine positions for the laterally bounded scenario

As shown in Table 3-6 and Figure 3-19, the C_T and C_P are the same for each turbine position. Similarly to the laterally unbounded scenario, these results tell us that the turbine position has negligible impact on the power and thrust. The turbine performance remains the same at every depth of the flume. These C_T and C_P results also show an agreement with the classical theory of GC07.

Table 3-6: Thrust and power coefficient from different position for the laterally bounded case.

K	α_2			C_T			C_P		
	Top	Mid	Bot	Top	Mid	Bot	Top	Mid	Bot
1	0.818	0.821	0.819	0.670	0.674	0.671	0.548	0.545	0.549
1.5	0.753	0.755	0.754	0.851	0.856	0.852	0.641	0.637	0.642
2	0.700	0.702	0.700	0.979	0.985	0.981	0.685	0.681	0.687
2.5	0.655	0.657	0.656	1.073	1.080	1.075	0.703	0.699	0.705
3	0.618	0.619	0.618	1.144	1.151	1.146	**0.706**	**0.702**	**0.708**
4	0.557	0.559	0.558	1.241	1.249	1.244	0.692	0.687	0.694
5	0.511	0.513	0.511	1.306	1.314	1.308	0.668	0.663	0.669

In a similar way to the previous scenario, the normalised flow fields for each turbine position are shown in Figure 3-20 for the vertical plane view and Figure 3-21 for the horizontal plane view. Although the C_T and C_P show that the bottom friction almost has no impact on the turbine performance, the flow fields show a more noticeable discrepancy between mid-case and other cases (Bottom and Top cases).

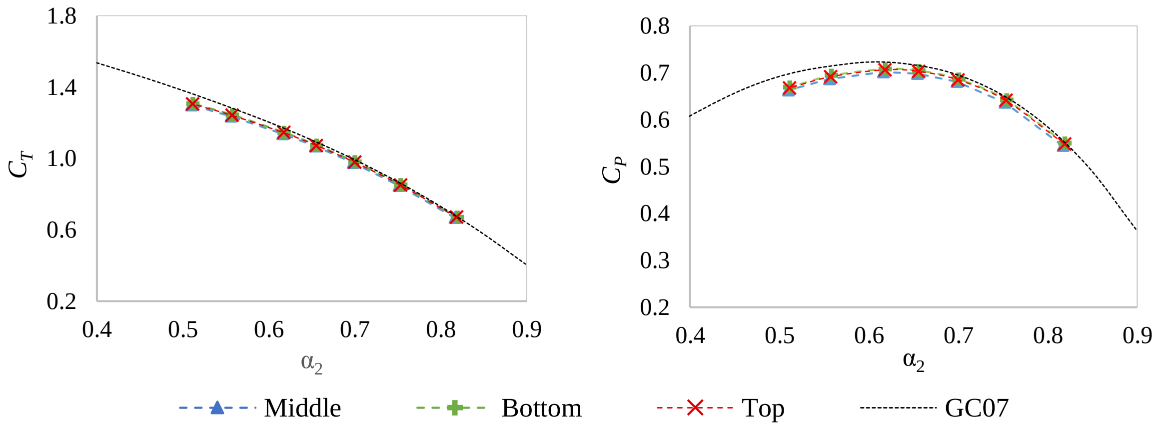

a. Thrust

b. Power

Figure 3-19: Power and thrust coefficients for the turbine at different positions for uniform flow and the laterally bounded scenario

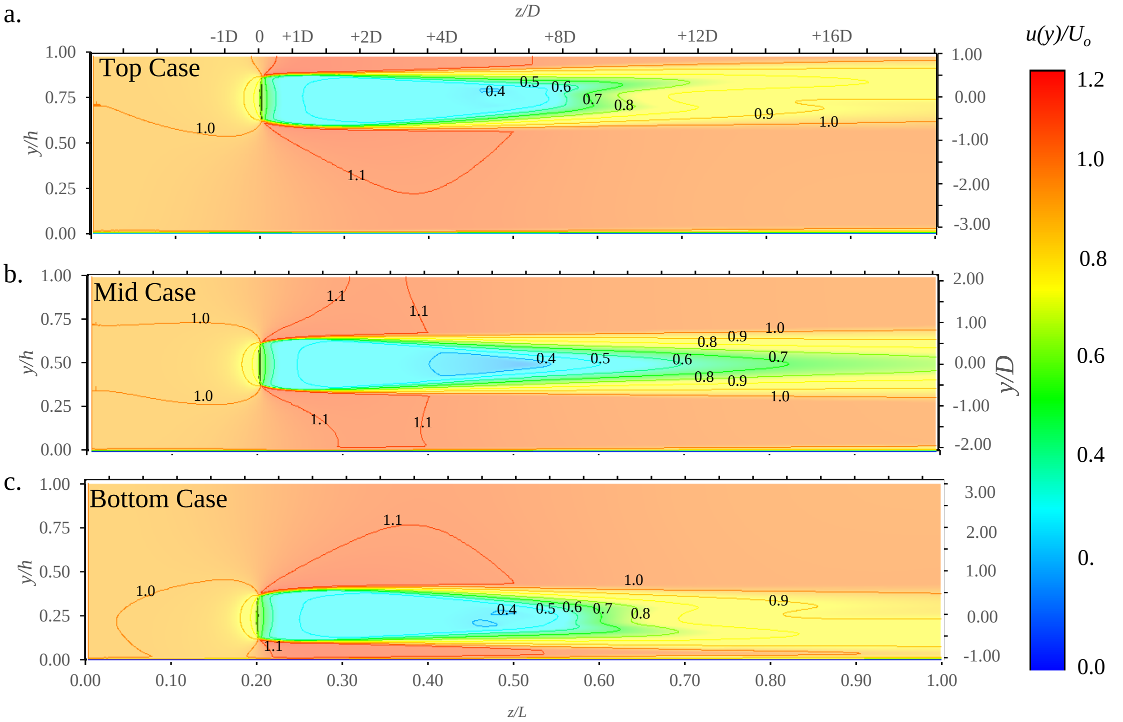

Figure 3-20: Normalised flow field for the turbine in uniform flow and laterally bounded scenario on the vertical plane.

c) *Different Velocities*

As the sheared flow involves a variation of velocity, it is important to check whether the turbine performance is dependent on the velocity magnitude. This check is also carried out to examine the consistency with GC07. As the simulations are run without surface deformation, the C_T and C_P should be the same for different velocities or Froude numbers, following the theoretical C_T and C_P from GC07. The simulations for this check are run using the moderate mesh and middle case for simplicity.

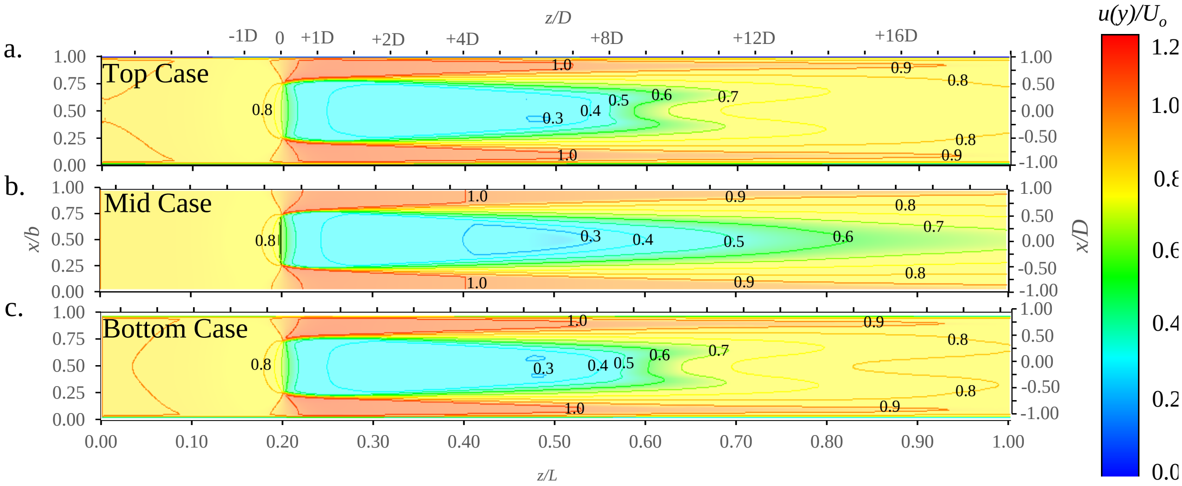

Figure 3-21: Normalised flow field for the turbine in uniform flow and laterally bounded scenario on the horizontal plane view.

The detail of the simulation results is presented in Table 3-7 for the laterally unbounded scenario and Table 3-8 for the laterally bounded scenario. These results are also compared with the theoretical GC07. Figure 3-23 shows the comparison for the laterally unbounded scenario and Figure 3-23 for the bounded scenario. For both laterally scenarios, the velocity does not affect C_T and C_P. The results also show the agreement with the theoretical GC07.

Table 3-7: Thrust and Power Coefficient from different velocities for the laterally unbounded case.

K	α_2				C_T				C_P			
	1 m/s	2 m/s	3 m/s	4 m/s	1 m/s	2 m/s	3 m/s	4 m/s	1 m/s	2 m/s	3 m/s	4 m/s
1	0.802	0.802	0.802	0.802	0.644	0.643	0.644	0.644	0.516	0.516	0.516	0.516
1.5	0.732	0.732	0.732	0.731	0.803	0.802	0.803	0.803	0.588	0.587	0.587	0.587
2	0.673	0.673	0.673	0.673	0.907	0.906	0.906	0.906	**0.611**	**0.610**	**0.610**	**0.610**
2.5	0.625	0.625	0.624	0.624	0.977	0.974	0.974	0.973	0.610	0.608	0.608	0.607
3	0.584	0.583	0.583	0.582	1.022	1.019	1.018	1.017	0.597	0.594	0.593	0.592
4	0.517	0.514	0.515	0.514	1.068	1.056	1.063	1.057	0.552	0.543	0.548	0.544
5	0.470	0.467	0.464	0.464	1.104	1.088	1.077	1.077	0.519	0.508	0.500	0.500

Table 3-8: Thrust and Power Coefficient from different velocities for the laterally bounded case.

K	α_2				C_T				C_P			
	1 m/s	2 m/s	3 m/s	4 m/s	1 m/s	2 m/s	3 m/s	4 m/s	1 m/s	2 m/s	3 m/s	4 m/s
1	0.817	0.817	0.817	0.817	0.668	0.667	0.667	0.667	0.545	0.544	0.544	0.544
1.5	0.752	0.752	0.752	0.752	0.848	0.847	0.847	0.847	0.638	0.637	0.637	0.637
2	0.699	0.698	0.698	0.698	0.976	0.975	0.975	0.975	0.682	0.681	0.681	0.681
2.5	0.654	0.654	0.654	0.654	1.070	1.068	1.068	1.068	0.700	0.698	0.698	0.698
3	0.617	0.616	0.616	0.616	1.141	1.139	1.138	1.138	**0.703**	**0.702**	**0.701**	**0.701**
4	0.556	0.556	0.556	0.556	1.238	1.236	1.235	1.235	0.688	0.687	0.687	0.686
5	0.510	0.510	0.510	0.509	1.302	1.298	1.298	1.298	0.665	0.661	0.661	0.661

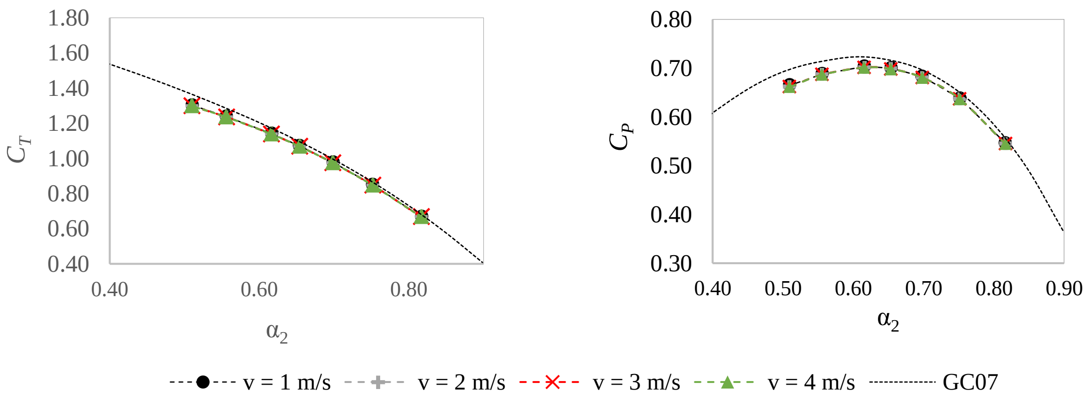

a. Thrust

b. Power

Figure 3-22: Thrust and power coefficient from different velocities for the laterally unbounded case and the turbines in the centre of the flume.

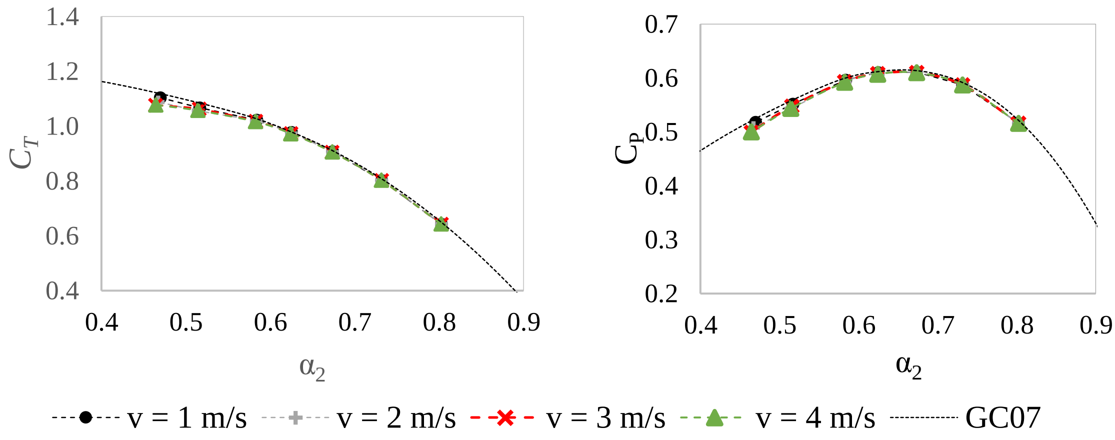

a. Thrust b. Power

Figure 3-23: Thrust and power coefficient from different velocities for the laterally unbounded case and the turbines in the centre of the flume.

d) Turbulence Model Check

This check examines the sensitivity to the different turbulence models. This check is conducted for the laterally bounded scenario only and just uses the moderate mesh density to save computational time. The simulations are run for the actuator disc installed at the middle of the flume (mid-case). Three different turbulence models ($k-\varepsilon$, $k-\omega$ and $k-\omega$ SST**),** are employed to ensure that the simulation is independent to the different turbulence model. Figure 3-24 and Table 3-9 shows the comparison of C_P and C_T from the different turbulence models in the uniform flow. The results show that the models give a similar performance for the different turbulence models.

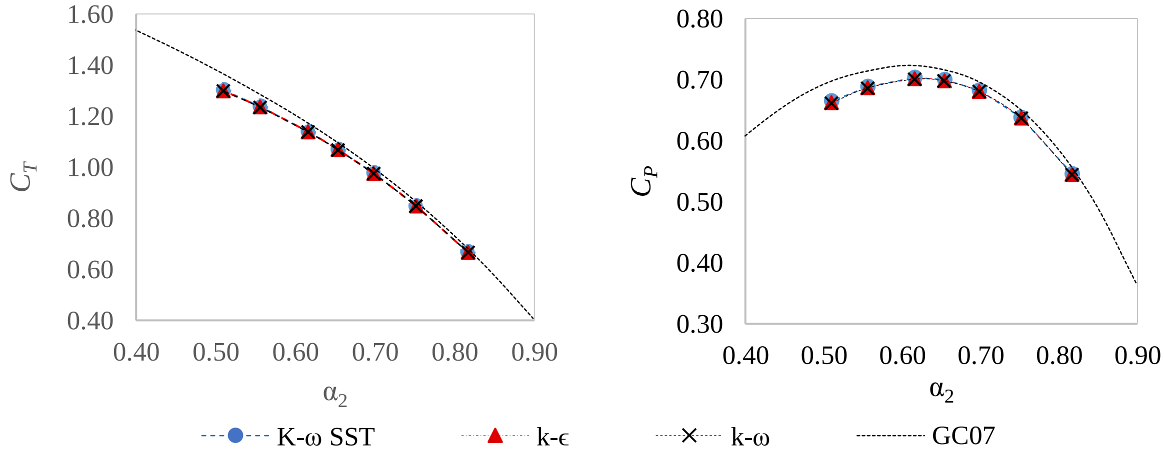

a. Thrust b. Power

Figure 3-24: Thrust and power coefficient from different turbulence models for the laterally bounded case and the turbines are in the centre of the flume.

Table 3-9: Thrust and power coefficient from different turbulence models for the laterally bounded case in the uniform flow.

K	α_2			C_T			C_P		
	k-ω SST	*k-ω*	*k-ϵ*	*k-ω SST*	*k-ω*	*k-ϵ*	*k-ω SST*	*k-ω*	*k-ϵ*
1	0.817	0.817	0.817	0.668	0.667	0.667	0.545	0.545	0.545
1.5	0.752	0.752	0.752	0.848	0.847	0.847	0.638	0.637	0.637
2	0.699	0.698	0.698	0.976	0.975	0.975	0.682	0.680	0.681
2.5	0.654	0.653	0.654	1.070	1.068	1.068	0.700	0.698	0.698
3	0.617	0.616	0.616	1.141	1.138	1.138	**0.703**	**0.701**	**0.701**
4	0.556	0.556	0.556	1.238	1.235	1.236	0.688	0.686	0.687
5	0.510	0.510	0.510	1.302	1.298	1.299	0.665	0.661	0.662

The simulations are also run for the sheared flow employing the n=1/5 sheared profile (as described in eq. 3.16). The first check is on the undisturbed profile from the simulations run without an actuator disc installed at the flume. The velocity profiles are expected to be the same for each observation point. Figure 3-25 shows that the profiles at each observation station for the sheared flow profile are the same for all turbulence models, despite the fact that near the bottom of the flume there are minor discrepancies between each of the turbulent models.

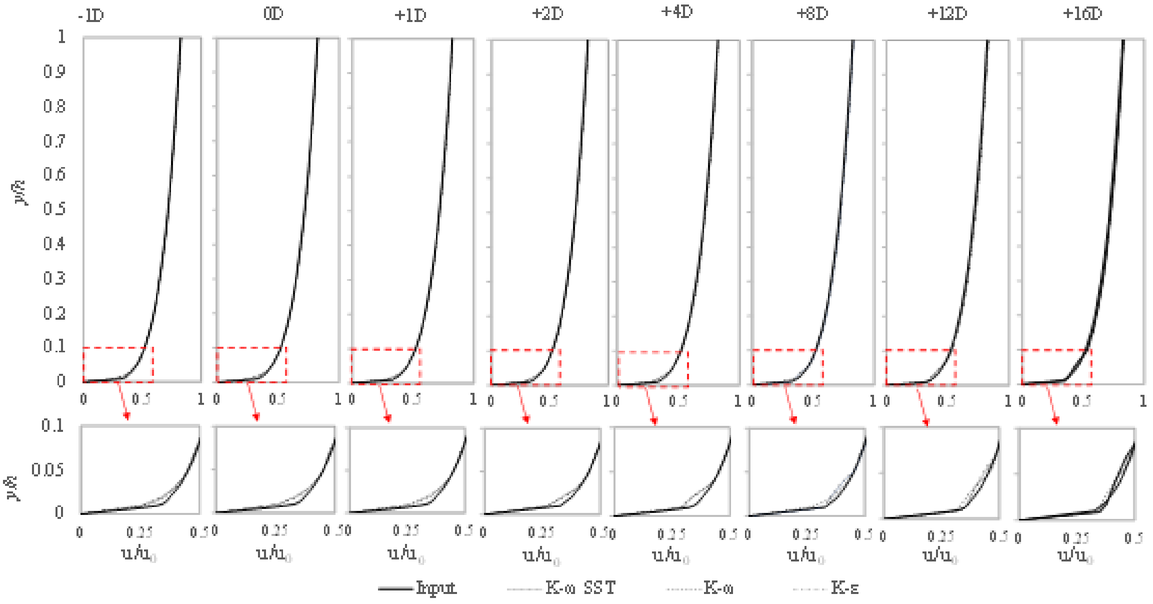

Figure 3-25: Fully developed axial velocity profiles at observation points for a simulation before an actuator disc is introduced and a sheared profile with n= 1/5, with three different turbulence models ($k-\varepsilon$, $k-\omega$ and $k-\omega$ SST).

This check also compares the results of the different turbulence models in the sheared flow. Table 3-10 and Figure 3-26 shows the comparison of C_P and C_T from the different turbulence models in the sheared flow, showing that C_P and C_T from each turbulence model are the same. Figure 3-26 also shows that C_P and C_T for sheared flow are slightly lower than the theoretical GC07 and the uniform flow. This discrepancy is discussed in the following section of this chapter. Thus we conclude that there are minimal differences between the different turbulence models. In this study, $k-\omega$ SST model has been selected, based on the argument presented in section 3.3.2.

Table 3-10: Thrust and power coefficient from different turbulence models for the laterally bounded case in the sheared flow.

K	α_2			C_T			C_P		
	k-ω SST	*k-ω*	*k-ϵ*	*k-ω SST*	*k-ω*	*k-ϵ*	*k-ω SST*	*k-ω*	*k-ϵ*
1	0.821	0.814	0.814	0.673	0.667	0.667	0.539	0.540	0.545
1.5	0.755	0.748	0.748	0.856	0.847	0.847	0.628	0.628	0.637
2	0.702	0.694	0.694	0.985	0.975	0.975	0.670	0.669	0.681
2.5	0.657	0.649	0.649	1.079	1.068	1.068	0.685	0.683	0.698
3	0.619	0.611	0.611	1.150	1.138	1.138	**0.686**	**0.684**	**0.701**
4	0.559	0.550	0.550	1.248	1.235	1.236	0.669	0.667	0.687
5	0.513	0.504	0.504	1.312	1.298	1.299	0.642	0.640	0.662

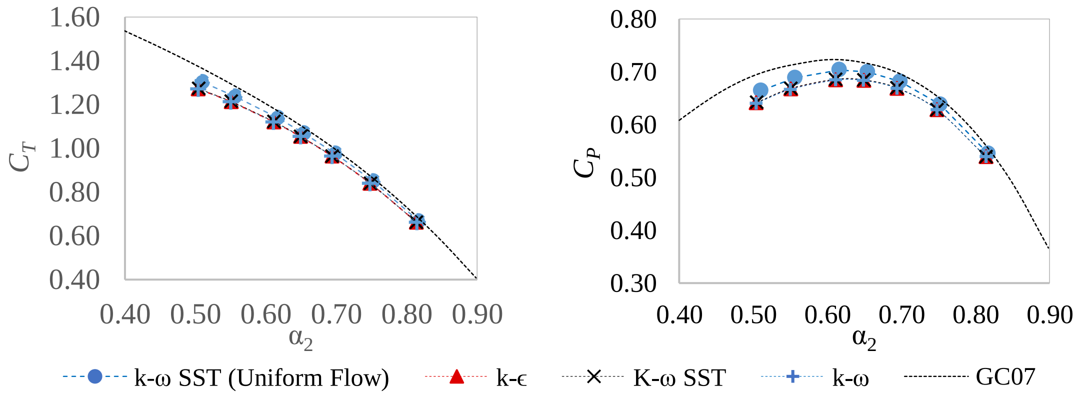

a. Thrust b. Power

Figure 3-26: Thrust and power coefficient from different turbulence models in the sheared flow for the laterally bounded case and the disc in the centre of the flume.

3.3.5 Modelling Turbine Performance in the Sheared Flow

The simulations for turbine performance analysis are run with the moderate mesh for all cases and scenarios. As discussed previously, there are three cases for each scenario based on turbine position. These analyses are separated into two parts. The first involves simulations to explore the turbine performance in sheared flow for the turbine in different positions. The second is focused on the effect of different types of sheared flow profile.

As mentioned in section 3.3.1, there are two possible methods to calculate C_T and C_P in turbine performance. Firstly, the velocity at the far upstream inlet (U_{in}) is calculated based on the average velocity of the entire channel cross-section (U_{in-all}) while the other method is to normalise by the velocity over the projection area of the turbine only ($U_{in-disc}$). Hereinafter, the C_T and C_P that calculated using U_{in-all} are denoted as $C_{T\text{-}all}$ and $C_{P\text{-}all}$, while the $C_{T\text{-}disc}$ and $C_{P\text{-}disc}$ are for the calculation based on $U_{in-disc}$.

a) Actuator disc in the different positions

The analysis of turbine performance in this section uses the sheared flow profile with n=1/5 Eq. (3.15). As with the previous simulation, the analysis is differentiated into two categories, laterally unbounded and laterally bounded.

1) Laterally unbounded sheared flow scenario

Table 3-11 and Figure 3-27 show C_T and C_P from the actuator disc installed at three different positions (Top, Middle (Mid) and Bottom (Bot)) with U_{in} defined as the average velocity of the entire inlet cross-section (U_{in-all}). The $C_{T\text{-}all}$ and $C_{P\text{-}all}$ from the simulation in uniform flow (n=0) and the theoretical GC07 are also included in this graph as a benchmark. The graph shows the simulations give the highest $C_{T\text{-}all}$ and $C_{P\text{-}all}$ for the turbine installed at the top, and the lowest when it is installed at the bottom. The optimum power coefficients for mid and top cases are higher by about ~14 % and ~46% respectively than that of the optimum power coefficients from GC07 and the uniform flow. Meanwhile, for the Bottom case, the optimum $C_{P\text{-}all}$ is lower by ~25% than the optimum C_P from GC07 and uniform flow.

Table 3-11: The trust and power coefficient in *n*=1/5 sheared flow for the laterally unbounded scenario with $\boldsymbol{U_{in}}$ defined as the average velocity of the entire cross-section ($\boldsymbol{U_{in-all}}$)

K	α_2			$C_{T\text{-}all}$			$C_{P\text{-}all}$		
	Top	Mid	Bot	Top	Mid	Bot	Top	Mid	Bot
1	0.911	0.838	0.728	0.830	0.703	0.530	0.757	0.589	0.385
1.5	0.831	0.764	0.664	1.036	0.876	0.661	0.861	0.670	0.439
2	0.765	0.703	0.612	1.169	0.989	0.748	**0.894**	**0.696**	**0.457**
2.5	0.709	0.652	0.568	1.258	1.063	0.806	0.892	0.693	**0.457**
3	0.662	0.609	0.531	1.316	1.111	0.845	0.872	0.677	0.448
4	0.587	0.538	0.471	1.379	1.160	0.889	0.810	0.625	0.419
5	0.530	0.487	0.426	1.406	1.187	0.908	0.746	0.579	0.387

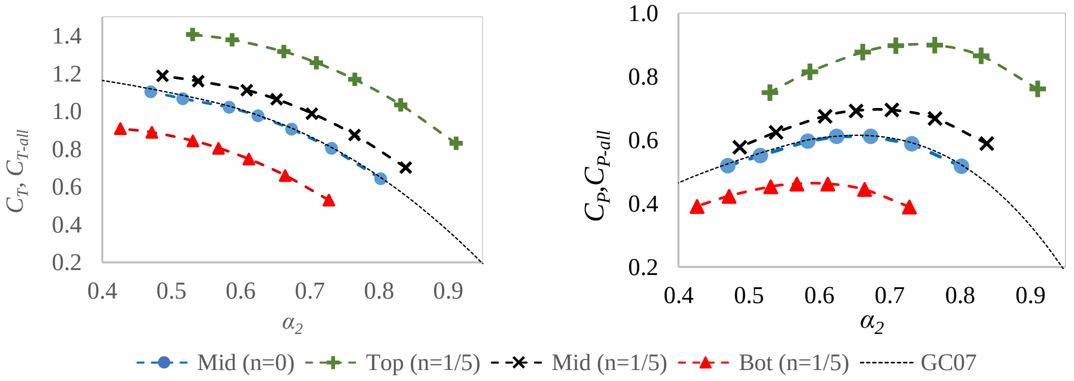

a. Thrust b. Power

Figure 3-27: Thrust and power coefficient normalised to the velocity from the flux of the inlet cross-section for laterally unbounded scenario ($\boldsymbol{U_{in-all}}$).

Based on the Draper *et al*., 2016 theoretical model, the C_T and C_P for the laterally unbounded case should collapse to the classical GC07 actuator disc model. However, as mentioned earlier in this section, Draper *et al*., 2016, as well as other publications, used U_{in} defined as the upstream average velocity only at the turbine stripe depth. In other words, they use $U_{in-disc}$ instead of U_{in-all}. The calculations based on $U_{in-disc}$ are presented in Table 3-12 and Figure 3-28).

Table 3-12: The trust and power coefficient in n=1/5 sheared flow for the laterally unbounded scenario with $\boldsymbol{U_{in}}$ defined as the average velocity of the disc area ($\boldsymbol{U_{in-disc}}$)

K	α_2			$C_{T\text{-}disc}$			$C_{P\text{-}disc}$		
	Top	Mid	Bot	Top	Mid	Bot	Top	Mid	Bot
1	0.802	0.802	0.804	0.644	0.643	0.646	0.517	0.516	0.519
1.5	0.732	0.731	0.734	0.803	0.802	0.807	0.587	0.586	0.592
2	0.673	0.673	0.676	0.907	0.905	0.913	**0.610**	**0.609**	**0.617**
2.5	0.625	0.624	0.627	0.975	0.973	0.983	0.609	0.607	**0.617**
3	0.583	0.582	0.586	1.020	1.017	1.031	0.595	0.592	0.604
4	0.517	0.515	0.521	1.069	1.062	1.085	0.553	0.547	0.565
5	0.467	0.466	0.471	1.090	1.087	1.108	0.509	0.507	0.521

The results show the $C_{T\text{-}disc}$ and $C_{P\text{-}disc}$ are collapsed to the classical GC07 actuator disc theory with the discrepancy of <1%. These discrepancies are in within of the error bounds of the simulations. However, it is important to note that the $C_{T\text{-}disc}$ and $C_{P\text{-}disc}$ of the Bottom case are slightly (~1%) higher than the C_T and C_P from GC07 and the uniform flow. The calculations $C_{T\text{-}all}$ and $C_{P\text{-}all}$ are in alignment with the fraction of U_{in-all} and $U_{in-disc}$. If the actuator is installed where U_{in-all} exceeds $U_{in-disc}$, then the $C_{T\text{-}all}$ and $C_{P\text{-}all}$ exceed C_T and C_P from classical GC07 and the uniform cases, and *vice versa*.

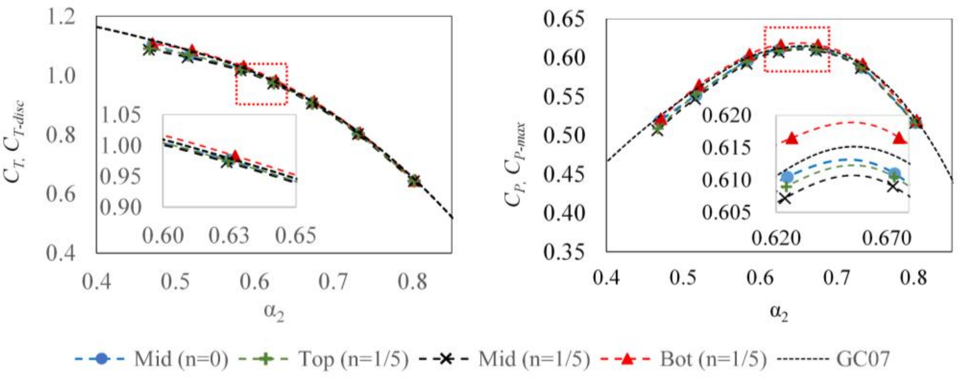

a. Thrust b. Power

Figure 3-28: Thrust and power based on the average flow at the actuator disc only for the laterally unbounded scenario ($\boldsymbol{U_{in-disc}}$)

Table 3-13 shows that the average velocities of the flow at the disc area are higher than the average velocity of the entire inlet cross-section for top and middle cases by ~14% and ~5% respectively. In contrast, for the Bottom case, it is lower by 9%. As the C_P is normalised by the cube of velocity, therefore the optimum C_P follows a similar trend of the velocity fraction. A similar correspondence also is applied to C_T.

Table 3-13: The flux and the U_{in} and U_d from the simulation with and without actuator disc for the laterally unbounded scenario in sheared flow profile n=1/5.

	Flux (m^3/s)				U_{in} (m/s)		
	Top	Mid	Bot		Top	Mid	Bot
Simulation without the turbine							
Inlet	33,883.47	33,911.56	33,938.24	U_{in-all}	1.37	1.37	1.37
Disc	701.97	646.61	560.46	$U_{in-disc}$	1.55	1.43	1.24
Simulation with the turbine							
K	Flux (m^3/s)				U_d (m/s)		
1	563.23	518.62	450.52		1.245	1.146	0.996
1.5	513.60	472.82	411.12		1.135	1.045	0.909
2	472.64	435.02	378.61		1.045	0.962	0.837
2.5	438.40	403.43	351.46		0.969	0.892	0.777
3	409.39	376.53	328.51		0.905	0.832	0.726
4	362.96	333.11	291.87		0.802	0.736	0.645
5	327.79	301.45	263.80		0.725	0.666	0.583

The flow field for the sheared flow cases is also shown for this analysis. Figure 3-29 represents the normalised flow field in the vertical plane, whilst Figure 3-30 illustrates the flow field in the horizontal plane. The U_0 for the normalisation is taken from eq. 3.16. For the n=1/5 profile, U_0 is 2.0 m/s. The flow fields indicate that the bottom case has a slightly longer flow recovery than in other cases. Both vertical and horizontal flow fields also show that the bypass flow of the top case is more significant than in other cases (mid and bottom).

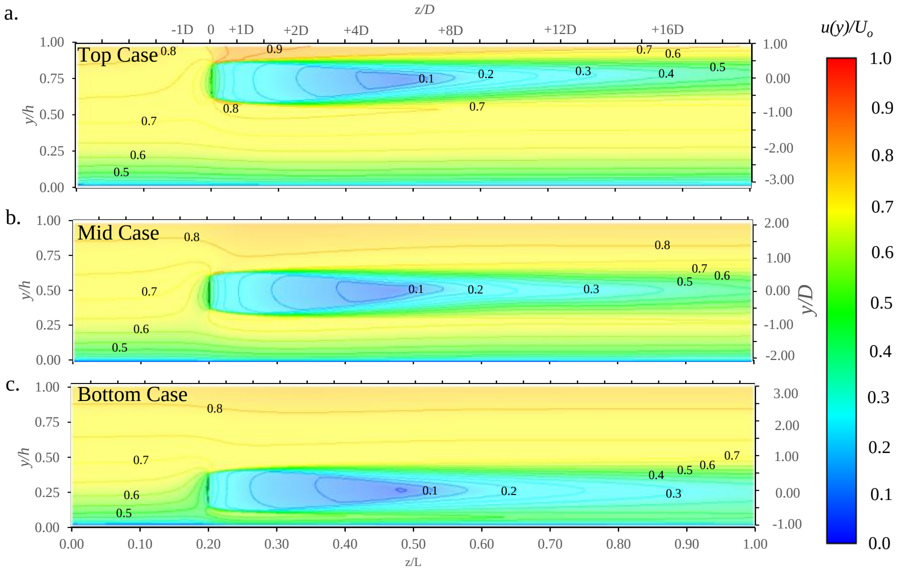

Figure 3-29: Normalised flow field for the turbine in the sheared flow and laterally bounded scenario on the vertical plane.

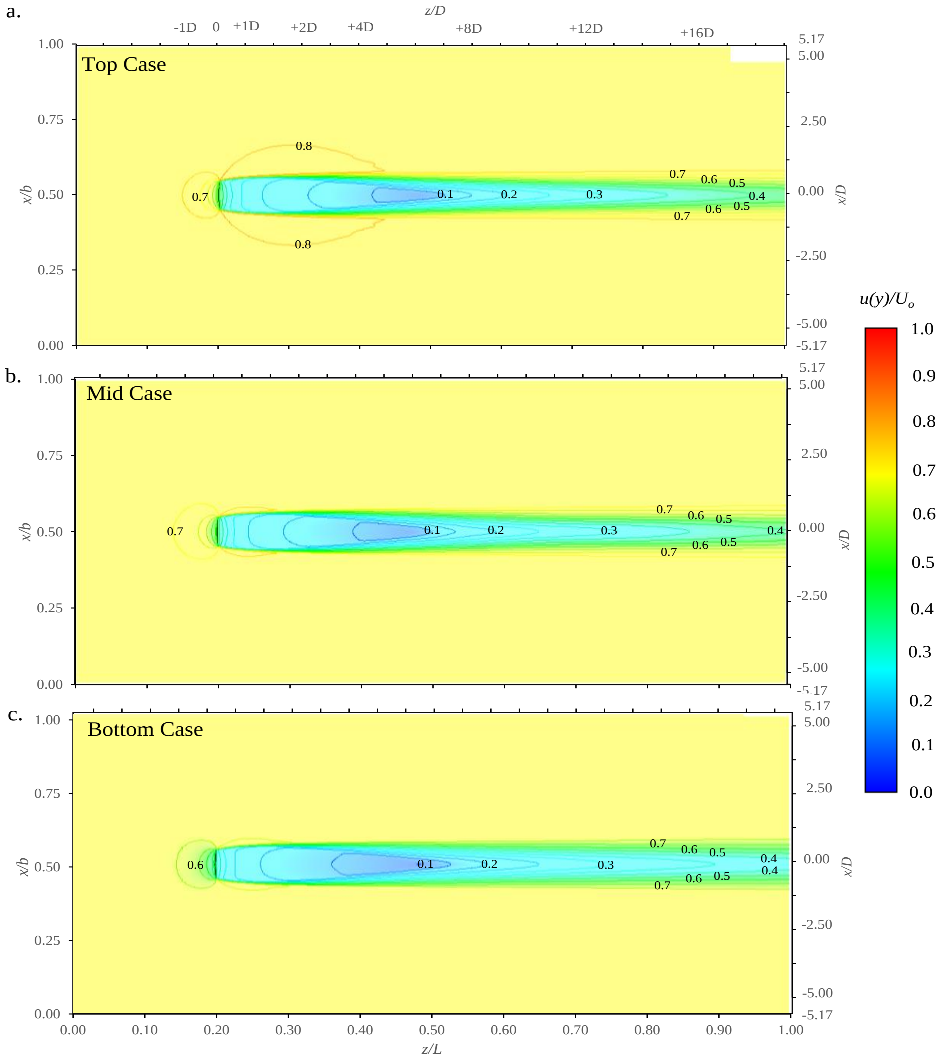

Figure 3-30: Normalised flow field for the turbine in sheared flow and laterally bounded scenario on the horizontal plane.

2) Laterally bounded sheared flow scenario

Similar to the previous scenario, two U_{in} definitions are also used in the laterally bounded scenario. The calculations based on U_{in-all} are presented in Figure 3-31 and Table 3-14. The actuator disc that is placed at the bottom of the flume also gives lower C_T and C_P than the other cases (top and middle). These results are consistent with the previous scenario for the laterally unbounded case. The comparison of U_{in-all} and $U_{in-disc}$ show similar trends to the previous scenario.

The C_T and C_P calculations based on the velocity of the disc area show that all cases (the top, middle and bottom cases) have lower C_T and C_P than the uniform flow and GC07 (see Figure 3-32 and Table 3-15). However, the discrepancies are relatively low for this scenario. For instance, the Top case has a lower optimum C_P by almost 5% than the uniform flow and GC07. In contrast, for the Mid case, the optimum C_P is lower by ~3% than the theoretical GC07. The optimum C_P of Bot case is only ~1% lower than the optimum C_P of the uniform flow and the GC07. The actuator disc that is installed at the bottom has a slightly better performance than the actuator disc installed near to the surface in terms of the dimensionless C_P, but of course delivers more power because the local velocity is higher.

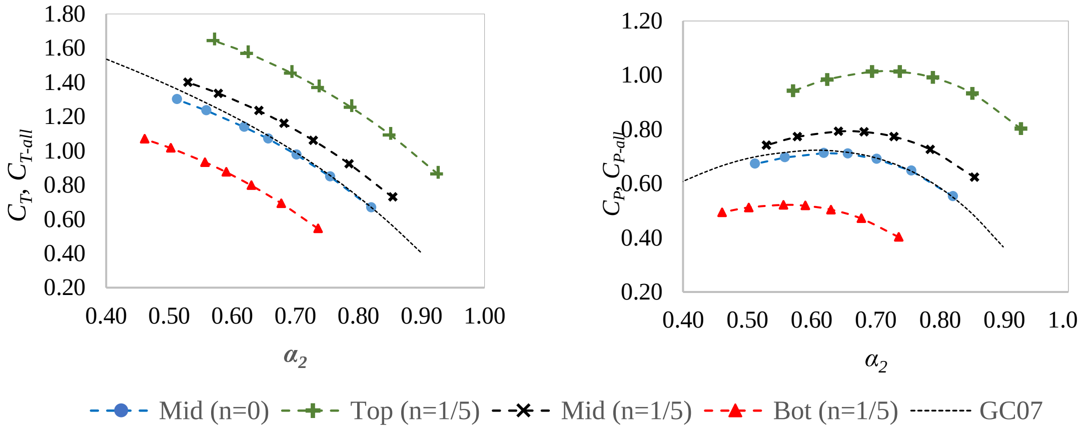

a. Thrust b. Power

Figure 3-31: The C_T and C_P based on $\boldsymbol{U_{in-all}}$ of the actuator disc at different positions in the n=1/5 sheared flow profile for the laterally bounded scenario

Table 3-14: The C_T and C_P based $\boldsymbol{U_{in-all}}$ of the actuator disc at a different positions in the n=1/5 sheared flow profile for the laterally bounded scenario

K	α_2			$C_{T\text{-}all}$			$C_{P\text{-}all}$		
	Top	Mid	Bot	Top	Mid	Bot	Top	Mid	Bot
1	0.923	0.854	0.736	0.851	0.729	0.541	0.786	0.623	0.398
1.5	0.847	0.785	0.677	1.077	0.924	0.688	0.913	0.726	0.466
2	0.786	0.728	0.630	1.235	1.061	0.793	0.971	0.773	0.499
2.5	0.735	0.681	0.590	1.349	1.160	0.869	**0.991**	0.791	0.513
3	0.691	0.641	0.556	1.434	1.235	0.928	**0.991**	**0.792**	**0.516**
4	0.622	0.578	0.502	1.549	1.336	1.009	0.964	0.772	0.506
5	0.569	0.529	0.461	1.620	1.400	1.061	0.922	0.741	0.489

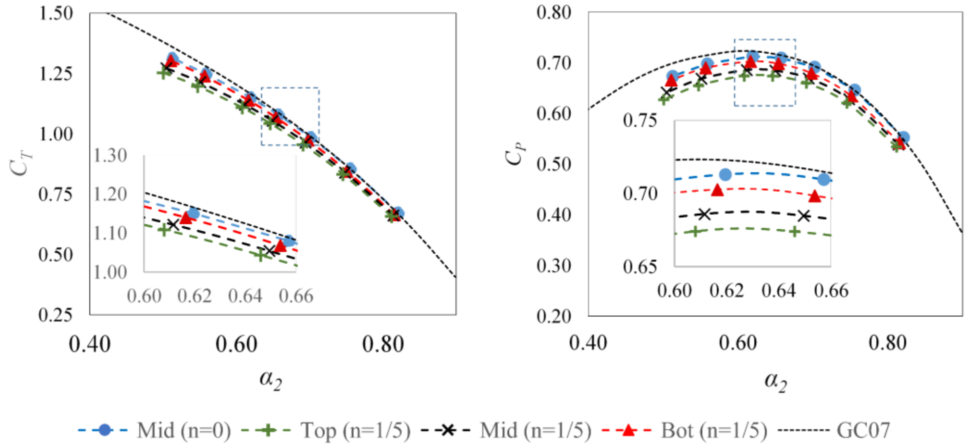

a. Thrust b. Power

Figure 3-32: Thrust and Power based on the average flow at the actuator disc only for blocked scenario

Table 3-15: The trust and power coefficient in *n*=1/5 sheared flow for the laterally bounded scenario based in $\boldsymbol{U_{in-disc}}$

K	α_2			$C_{T\text{-}disc}$			$C_{P\text{-}disc}$		
	Top	Mid	Bot	Top	Mid	Bot	Top	Mid	Bot
1	0.811	0.814	0.816	0.658	0.663	0.665	0.534	0.539	0.542
1.5	0.745	0.748	0.751	0.833	0.840	0.846	0.621	0.628	0.635
2	0.691	0.694	0.698	0.955	0.964	0.974	0.660	0.670	0.680
2.5	0.646	0.649	0.654	1.043	1.054	1.068	**0.674**	0.685	0.698
3	0.608	0.612	0.616	1.109	1.122	1.140	**0.674**	**0.686**	**0.703**
4	0.547	0.551	0.557	1.198	1.214	1.239	0.655	0.669	0.690
5	0.501	0.504	0.511	1.253	1.273	1.304	0.627	0.642	0.666

The theoretical model of Draper *et al.*, 2016 suggests that the optimum C_P from the sheared flow profile should be lower than the optimum C_P obtained from the classical GC07. This result is in agreement with Draper *et al.*, 2016's findings. However, the discrepancies are not as significant as their prediction. Furthermore, Draper *et al.*, 2016 indicate the optimum C_P ($C_{P,\,max}$) should be lower if the turbine is installed at the seabed or when it is further away from the strongest current within the vertically asymmetric flow (see section 3.2 for detail). By contrast, the results from this section show the C_P of the Bottom case slightly higher than the Top case, where the turbine is installed at the strongest velocity in the profile (see Figure 3-32 and Table 3-15).

Table 3-16 shows $U_{in-disc}$ is higher than U_{in-all} for the top and middle cases. The discrepancy in these results is on average 13.7% and 4.9% higher than the average velocity of the inlet for top and mid cases, respectively. Meanwhile, for the bottom case, U_{in-all} is higher than $U_{in-disc}$by 9.79 %. In consequence, the C_T and C_P of the mid-case are 39%~43% higher than the C_T and C_P from GC07 and the uniform flow cases, while for the bottom case, the C_T and C_P are lower by 26% than GC07 and the uniform flow cases. Therefore, the C_T and C_P are also dependent on whether $U_{in-disc}$ is higher than the U_{in-all} as in the laterally unbounded scenario.

In a similar way to the laterally unbounded scenario, the flow fields are presented for this scenario as well. Figure 3-33 illustrates the normalised flow field in the vertical plane, while Figure 3-34 shows the flow field in the horizontal plane. These flow fields exhibit a similar pattern to the flow field in the previous scenario, where the Bottom case shows a tendency to have a longer flow recovery than other cases.

Table 3-16: The flux and the $\boldsymbol{U_{in}}$ and $\boldsymbol{U_d}$ from the simulation with and without actuator disc in sheared flow profile n=1/5 for the laterally bounded scenario.

	Flux (m^3/s)			U_{in} (m/s)		
	Top	Mid	Bot	Top	Mid	Bot
Simulation without the turbine						
Inlet	6,590.77	6,565.77	6,567.97	1.37	1.37	1.37
Disc	706.36	649.15	558.40	1.56	1.43	1.23
Simulation with the turbine						
K	Flux (m^3/s)			U_d (m/s)		
1	573.17	528.43	455.39	1.267	1.168	1.007
1.5	526.43	485.74	419.26	1.164	1.074	0.927
2	488.17	450.74	389.69	1.079	0.996	0.861
2.5	456.33	421.59	365.05	1.009	0.932	0.807
3	429.46	396.96	344.21	0.949	0.877	0.761
4	386.50	357.62	310.84	0.854	0.791	0.687
5	353.60	327.49	285.17	0.782	0.724	0.630

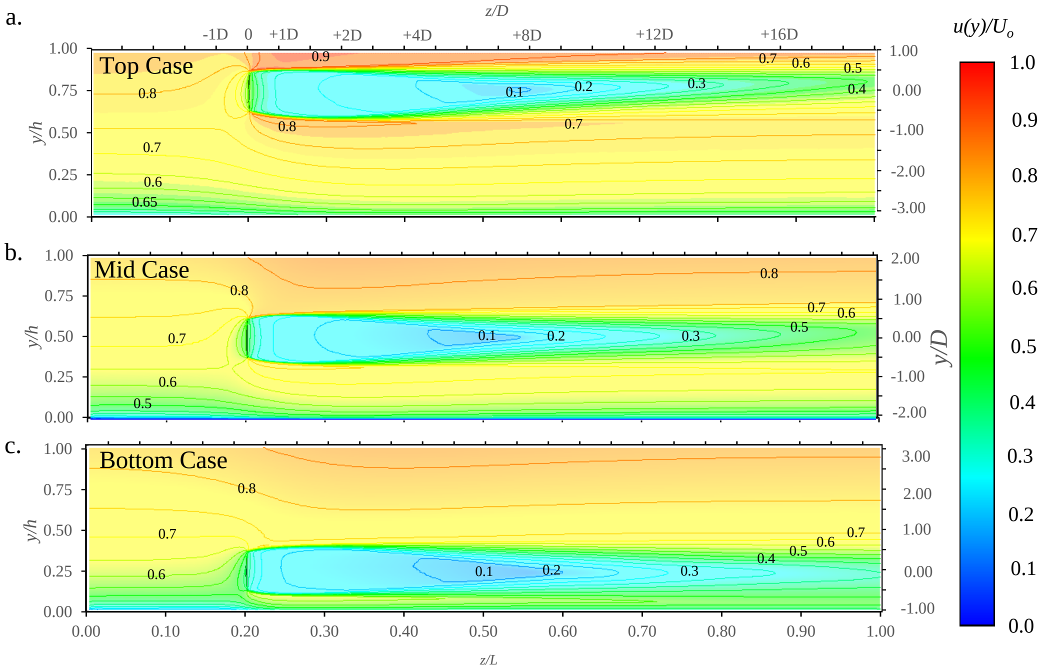

Figure 3-33: Normalised flow field for the turbine in sheared flow (*n*=1/5) and laterally bounded scenario on the vertical plane.

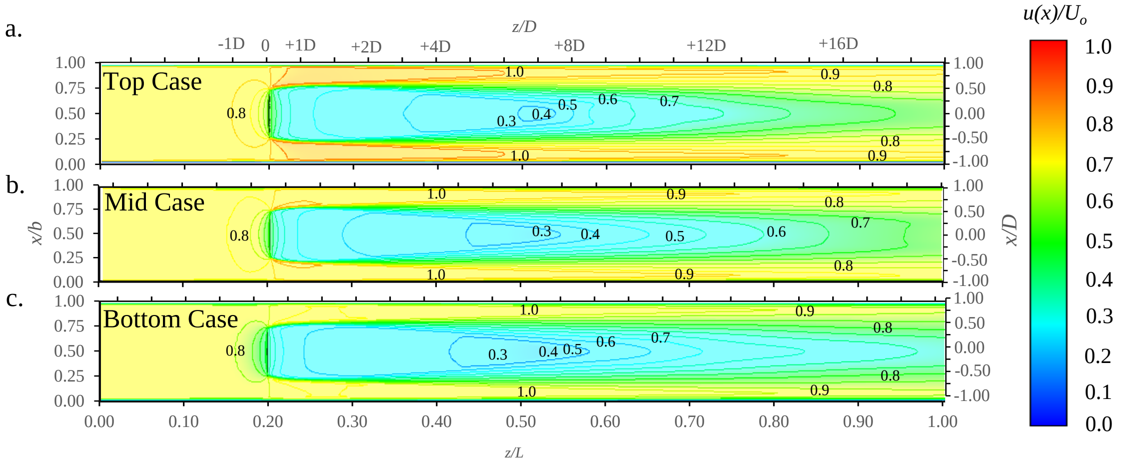

Figure 3-34: Normalised flow field for the turbine in sheared flow (*n*=1/5) and laterally bounded scenario on the horizontal plane.

b) *Different Sheared Flow Profile*

The analyses are continued with different sheared profiles. Two other profiles, *n*=1/7 and *n*=1, are compared with *n*=1/5 for this analysis. The profiles were created using eq. (3.15). Figure 3-35 shows the vertical distribution of velocity at the inlet for each profile. The U_0 for each profile is set, so the maximum velocity has the same magnitude. The simulations are run for the actuator disc installed at the middle of the flume for all sheared flow profiles (mid-case).

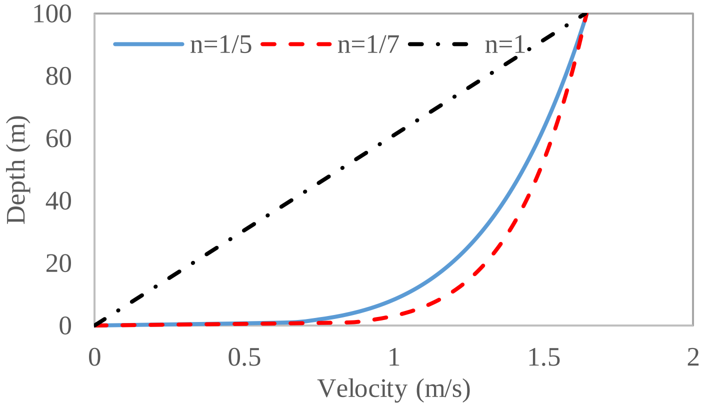

Figure 3-35: The velocity profiles at the inlet

1) Laterally Unbounded

Similar to the previous analysis, the C_T and C_P are calculated based on two different values of U_{in}, $U_{in-disc}$ and U_{in-all}. The C_T and C_P based on U_{in-all} are presented in Figure 3-36 and Table 3-17. The C_T and C_P are higher than the C_T and C_P from the GC07 and the uniform flow. Note that the case of *n*=1/5 is the same previous middle case that has higher optimum C_P than the optimum C_P from the uniform flow and GC07 by ~14%. As shown in the results, the *n*=1/7 profile has a slightly lower optimum C_P than the *n*=1/5 profile, only higher by 11% than the optimum C_P from the uniform flow and GC07.

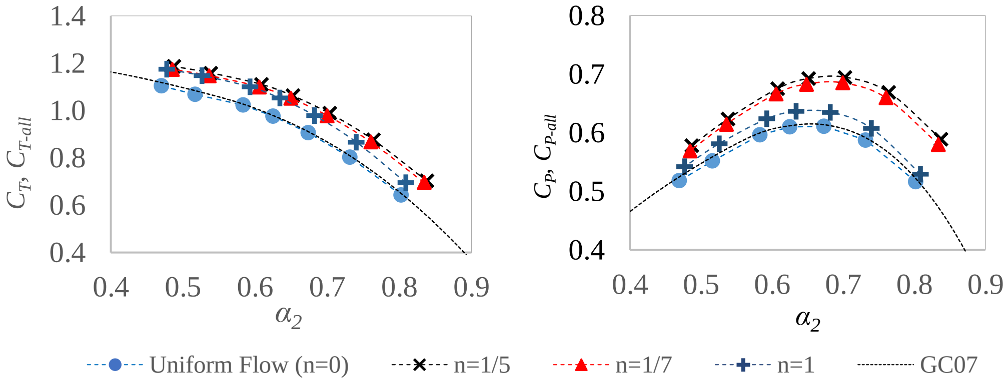

a. Thrust
b. Power

Figure 3-36: Thrust and Power of the different sheared flow profile based on $\boldsymbol{U_{in-all}}$ obtained for different sheared flow profiles for laterally unbounded scenario

Table 3-17: The trust and power coefficient based on $\boldsymbol{U_{in-all}}$ obtained for different sheared flow profiles for the laterally unbounded scenario

K	α_2			$C_{T\text{-}all}$			$C_{P\text{-}all}$		
	n=1/7	n=1/5	n=1	n=1/7	n=1/5	n=1	n=1/7	n=1/5	n=1
1	0.834	0.838	0.809	0.696	0.703	0.655	0.580	0.589	0.530
1.5	0.760	0.764	0.740	0.867	0.876	0.821	0.660	0.670	0.608
2	0.700	0.703	0.682	0.979	0.989	0.931	**0.685**	**0.696**	0.636
2.5	0.649	0.652	0.634	1.053	1.063	1.005	0.683	0.693	**0.637**
3	0.606	0.609	0.593	1.101	1.111	1.053	0.667	0.677	0.624
4	0.536	0.538	0.526	1.148	1.160	1.106	0.615	0.625	0.582
5	0.485	0.487	0.477	1.175	1.187	1.137	0.569	0.579	0.542

These results are consistent with the previous results based on U_{in-all}. The optimum *C*

These results are consistent with the previous results based on U_{in-all}. The optimum C_P is dependent on the fraction of $U_{in-disc}$ and the U_{in-all}. However, an interesting correspondence is seen in the *n*=1 profile. Although the graph shows this profile also has a higher C_T and C_P than the uniform flow and the GC07, for this *n*=1 profile, the magnitude of $U_{in-disc}$ and U_{in-all} (see Table 3-18) are the same because the mid-plane velocity is the same as the average.

Table 3-18: The flux and the $\boldsymbol{U_{in}}$ and $\boldsymbol{U_d}$ from the simulation with and without actuator disc in the different sheared flow profiles for the laterally unbounded scenario.

	Flux (m^3/s)			U_{in} (m/s)		
	n=1/7	n=1/5	n=1	n=1/7	n=1/5	n=1
Simulation without the turbine						
Inlet	35,545.33	33,911.56	20,332.22	1.43	1.37	0.82
Disc	672.47	646.61	370.60	1.49	1.43	0.82
Simulation with the turbine						
K	Flux (m^3/s)			U_d (m/s)		
1	539.33	518.62	300.07	1.192	1.146	0.663
1.5	491.71	472.82	274.46	1.087	1.045	0.607
2	452.43	435.02	253.10	1.000	0.962	0.559
2.5	419.59	403.43	235.10	0.928	0.892	0.520
3	391.64	376.53	219.76	0.866	0.832	0.486
4	346.39	333.11	195.05	0.766	0.736	0.431
5	313.40	301.45	176.90	0.693	0.666	0.391

The result shows that the fluxes of the *n*=1/5 and *n*=1/7 profiles have a higher $U_{in-disc}$ than the U_{in-all}. Meanwhile, for $U_{in-disc}$ the *n*=1 profile has the same magnitude as for U_{in-all}. The C_T and C_P based on $U_{in-disc}$ are presented in Figure 3-37 and Table 3-19. As expected, the *n*=1/5 and *n*=1/7 nearly collapse to the C_T and C_P of the uniform flow and GC07.

These results are consistent with the previous simulations. Meanwhile, the *n*=1 profile has a slightly higher C_T and C_P than the uniform flow and GC07. The discrepancy in the optimum power coefficient is approximately 4.5%, the same distinction with the calculation based on $\boldsymbol{U_{in-all}}$. These results are sensible, since the $\boldsymbol{U_{in-all}}$ and the $\boldsymbol{U_{in-disc}}$ for *n*=1 are the same, therefore, C_T and C_P are also the same. This physics of this is further discussed in section 3.4.

Table 3-19: The trust and power coefficient of the different sheared flow profiles based on $\boldsymbol{U_{in-disc}}$ obtained for different sheared flow profiles for the laterally unbounded scenario

K	α_2			$C_{T\text{-}disc}$			$C_{P\text{-}disc}$		
	n=1/7	n=1/5	n=1	n=1/7	n=1/5	n=1	n=1/7	n=1/5	n=1
1	0.802	0.802	0.810	0.643	0.643	0.656	0.516	0.516	0.531
1.5	0.731	0.731	0.741	0.802	0.802	0.823	0.586	0.586	0.609
2	0.673	0.673	0.683	0.905	0.905	0.933	**0.609**	**0.609**	0.637
2.5	0.624	0.624	0.634	0.973	0.973	1.006	0.607	0.607	**0.638**
3	0.582	0.582	0.593	1.018	1.017	1.055	0.593	0.592	0.626
4	0.515	0.515	0.526	1.061	1.062	1.108	0.547	0.547	0.583
5	0.466	0.466	0.477	1.086	1.087	1.139	0.506	0.507	0.544

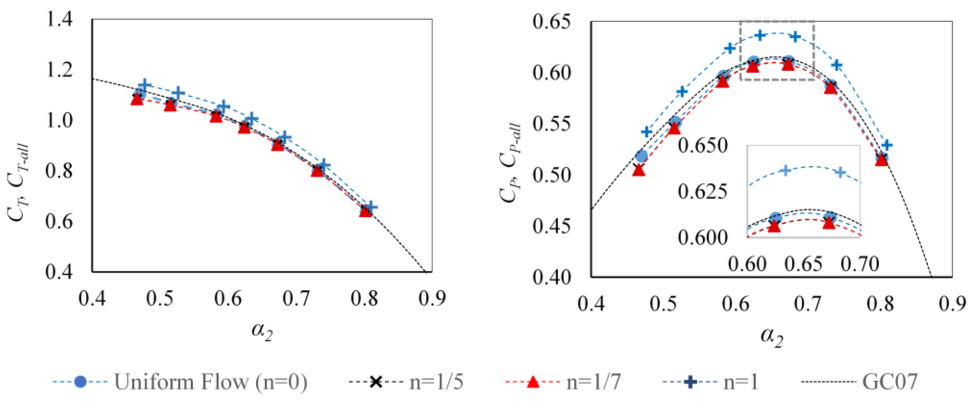

a. Thrust

b. Power

Figure 3-37: Thrust and Power of the different sheared flow profiles based on $\boldsymbol{U_{in-disc}}$ obtained for different sheared profile for the laterally unbounded scenario

2) Laterally Bounded

The simulations are also done for the laterally bounded scenario. The C_T and C_P in Figure 3-38 and Table 3-20 are calculated using $\boldsymbol{U_{in-all}}$. Similar to the previous scenario, the case of the *n*=1/5 profile is the same as the middle case from the analysis in the previous section. As shown in Figure 3-38, C_T and C_P for the *n*=1/5 and *n*=1/7 profiles have higher than for GC07 and the uniform flow case. The optimum C_P of the *n*=1/7 profile is slightly lower than the *n*=1/5 profile, In addition, the optimum C_P of the *n*=1/7 is ~11% higher than the C_P of GC07 and the uniform flow, while the optimum C_P of the *n*=1/5 is ~13% higher than the C_P of GC07 and the uniform flow.

These results of the *n*=1/5 and *n*=1/7 are consistent with the previous results in the laterally unbounded scenario. The comparison of $\boldsymbol{U_{in-disc}}$ and the $\boldsymbol{U_{in-all}}$ in Table 3-21 shows that the $\boldsymbol{U_{in-disc}}$ for the *n*=1/5 and *n*=1/7 is higher than the $\boldsymbol{U_{in-all}}$. $\boldsymbol{U_{in-disc}}$ for *n*=1/7 is 4% higher than $\boldsymbol{U_{in-all}}$ while for the *n*=1/5 is 5% higher. However, the results for the profile of *n*=1 are the opposite from the laterally unbounded scenario. The optimum C_P for this profile almost collapses with the optimum C_P for the uniform flow.

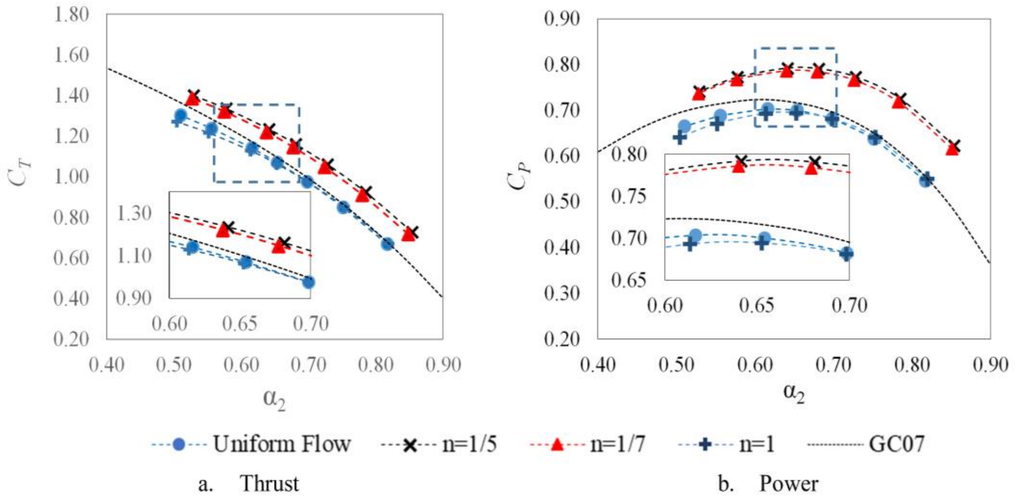

a. Thrust b. Power

Figure 3-38: Thrust and Power of the different sheared flow profile based on $\boldsymbol{U_{in-all}}$ for laterally bounded scenario

Table 3-20: The trust and power coefficient of the different sheared flow profiles based on $\boldsymbol{U_{in-all}}$ for the laterally bounded scenario

K	α_2			$C_{T\text{-}all}$			$C_{P\text{-}all}$		
	n=1/7	n=1/5	n=1	n=1/7	n=1/5	n=1	n=1/7	n=1/5	n=1
1	0.848	0.854	0.820	0.719	0.729	0.672	0.610	0.623	0.551
1.5	0.780	0.785	0.753	0.912	0.924	0.851	0.711	0.726	0.641
2	0.724	0.728	0.698	1.048	1.061	0.975	0.758	0.773	0.681
2.5	0.677	0.681	0.652	1.146	1.160	1.064	0.776	0.791	**0.694**
3	0.638	0.641	0.614	1.220	1.235	1.129	**0.778**	**0.792**	0.693
4	0.575	0.578	0.552	1.322	1.336	1.217	0.760	0.772	0.671
5	0.527	0.529	0.504	1.386	1.400	1.271	0.730	0.741	0.641

Table 3-21: The flux and the $\boldsymbol{U_{in-all}}$ and $\boldsymbol{U_{in-disc}}$ from the simulation with and without actuator disc for the laterally bounded scenario in sheared the different flow profiles.

	Flux (m^3/s)			U_{in} (m/s)		
	n=1/7	n=1/5	n=1	n=1/7	n=1/5	n=1
Simulation without the turbine						
Inlet	6,882.81	6,565.77	3,935.80	1.43	1.37	0.82
Disc	675.17	649.15	372.25	1.49	1.43	0.82
Simulation with the turbine						
K		Flux (m^3/s)			U_d (m/s)	
1	550.14	528.43	304.03	1.216	1.168	0.672
1.5	505.84	485.74	279.41	1.118	1.074	0.618
2	469.52	450.74	259.05	1.038	0.996	0.573
2.5	439.28	421.59	242.02	0.971	0.932	0.535
3	413.73	396.96	227.60	0.915	0.877	0.503
4	372.87	357.62	204.59	0.824	0.791	0.452
5	341.57	327.49	187.04	0.755	0.724	0.413

It is important to note that the optimum C_P of the *n*=1 profile for laterally unbounded flow is higher than the optimum C_P of uniform flow. The correspondence of the $\boldsymbol{U_{in-disc}}$ and the $\boldsymbol{U_{in-all}}$ for that case is irrelevant. Furthermore, as the $\boldsymbol{U_{in-all}}$ is similar to the $\boldsymbol{U_{in-disc}}$ for the *n*=1 profiles, the C_T and C_P normalised to $\boldsymbol{U_{in-all}}$ are the same as the C_T and C_P that normalised to $\boldsymbol{U_{in-disc}}$.

The C_T and C_P that are normalised by $U_{in-disc}$ for the laterally bounded scenario are presented in Figure 3-39 and Table 3-22. It is shown that the C_T and C_P for all sheared profiles almost collapse onto each other. In other words, the C_T and C_P of n=1, 1/5 and 1/7 are below the C_T and C_P from GC07 and the uniform flow. However, it is also important to note that discrepancies between the C_T and C_P of all sheared profiles with the C_T and C_P of the uniform flow and GC07 are approximately 1%.

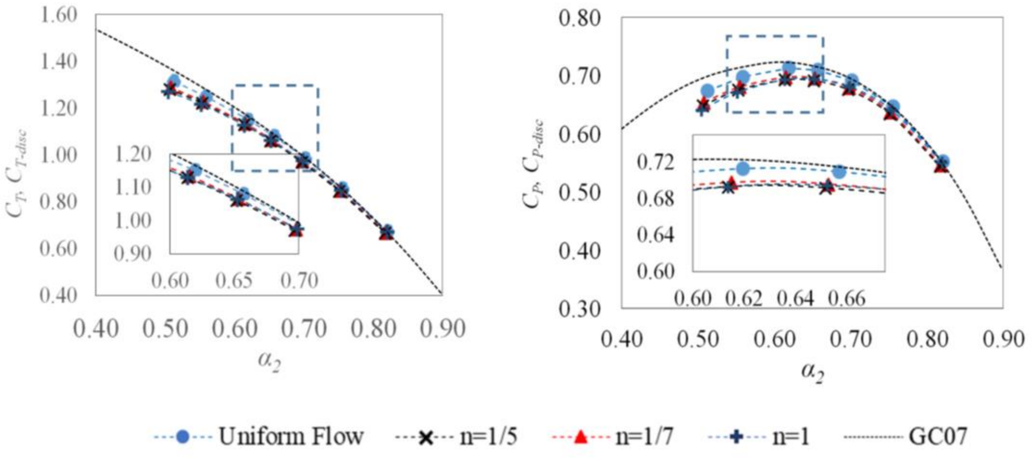

a. Thrust b. Power

Figure 3-39: Thrust and power coefficients based on $U_{in\text{-}disc}$ obtained for different sheared flow profiles for the laterally bounded scenario.

Table 3-22: Thrust and power coefficients based on $U_{in\text{-}disc}$ obtained for different sheared flow profiles for the laterally bounded scenario.

K	α_2			$C_{T\text{-}disc}$			$C_{P\text{-}disc}$		
	n=1/7	n=1/5	n=1	n=1/7	n=1/5	n=1	n=1/7	n=1/5	n=1
1	0.815	0.814	0.817	0.664	0.663	0.667	0.541	0.539	0.545
1.5	0.749	0.748	0.751	0.842	0.840	0.845	0.631	0.628	0.634
2	0.695	0.694	0.696	0.967	0.964	0.969	0.673	0.670	0.674
2.5	0.651	0.649	0.650	1.058	1.054	1.057	0.689	0.685	**0.687**
3	0.613	0.612	0.611	1.126	1.122	1.121	**0.690**	**0.686**	0.686
4	0.552	0.551	0.550	1.220	1.214	1.208	0.674	0.669	0.664
5	0.506	0.504	0.502	1.280	1.273	1.262	0.647	0.642	0.634

3.4 Discussion

As explained at the beginning of this chapter, there are possibilities of extreme sheared profiles does occur at some potential locations due to the existence of ITF. The location in the tropical region means that this area has high precipitation and sunlight intensity. Thus, the influx of freshwater from rainfall and the sunlight penetration to the upper layer of the ocean creates a halocline and thermocline, which maintain flow stratification in the water column. Therefore, a stratified or sheared flow is likely to occur at some of the candidate sites. However, it is important to note that this phenomenon is primarily a deep water one.

The measured current data also shows that there is the possibility that extreme sheared profiles occur at some potential locations. However, there is some uncertainty in the data, especially the moving ADCP data. The tidal velocity is time-varying and so data from the ADCP might not capture reality.

However, the sheared flow might be an important issue for resource assessment in an area like Indonesia. To fully tackle this, a 3D model would be required. However, this would have huge computational cost, and would require significant software development and validation to model extracted power. It would also be very difficult to validate a 3D hydrodynamic model of the region given the available data. The idea of using the 2D depth-averaged model with appropriate choice of the C_T and C_P for the sheared profile is therefore preferred (e.g. Draper *et al*., 2016).

The C_T and C_P could be calculated using two different inlet velocities (U_{in-all} and $U_{in-disc}$), The calculation using U_{in-all} is denoted as $C_{T\text{-}all}$ and $C_{P\text{-}all}$, while using $U_{in-disc}$ is denoted as $C_{T\text{-}disc}$ and $C_{P\text{-}disc}$. It is important to note that the calculation using $U_{in-disc}$ is suggested as the appropriate method to calculate C_T and C_P [Draper *et al*., 2016; Wimhurst, 2018; and Nishino & Wilden, 2012a]. The $C_{T\text{-}disc}$ and $C_{P\text{-}disc}$ calculation shows that the optimum power coefficients are approximately the same for a turbine installed at any elevation in the water column. Therefore, no modification is necessary for the calculation of C_T and C_P for the turbine performance in a sheared profile. The present results exhibit some disagreement with predictions by Draper *et al*.'s 2016 theoretical model.

However, the 2D SWE depth-averaged model only gives the average velocity over all depths. In this case, the model only gives U_{in-all} in its calculation. This chapter has demonstrated that $C_{T\text{-}all}$ and $C_{P\text{-}all}$ depend on the magnitude of $U_{in\text{-}all}$ rather than the magnitude of $U_{in\text{-}disc}$. All simulation cases (different positions and profiles) and scenarios (laterally unbounded and laterally bounded) consistently show that if the turbine is installed where $U_{in\text{-}disc} > U_{in\text{-}all}$, then the resource is underestimated. In contrast, the resource is overestimated if the turbine is installed in an area that has $U_{in-disc}$ weaker than U_{in-all}. Therefore, it is safe to conclude that the 2D depth-averaged model could only give the correct estimates if the velocity represents the velocity at the depth where the turbine is installed.

It is also important to note that some results of the sheared flow cases are perplexing. The simulation shows that C_T and C_P in the n=1 profile are higher than for the GC07 and the uniform flow for the unbounded scenario. While, in the laterally bounded scenario, the C_T and C_P of n=1 are only slightly lower (by ~1%) than the C_T and C_P of the uniform flow and GC07. In contrast, Draper *et al*., 2016 suggest the optimum C_P in the laterally unbounded case should collapse to the GC07 value for any profile, while for the laterally bounded the optimum C_P should be lower by at least 20%.

It might be worthwhile to look at the simulation of the turbine in the Bottom case to understand this phenomenon. The $C_{T\text{-}disc}$ and $C_{P\text{-}disc}$ in the Bottom case also tend to be higher than for GC07 and uniform flow for the laterally unbounded scenario. Like the n=1 case, the Bottom case also tends to have lower $C_{T\text{-}disc}$ and $C_{P\text{-}disc}$ than the GC07 and uniform flow for the laterally bounded scenario.

The n=1 profile and Bottom cases have something in common. The disc is installed at a gradient with relatively mild slope in the sheared flow profile (see Figure 3-40). It is imparted from this fact that the C_T and C_P in the n=1 profile may be higher than in the uniform flow for the laterally unbounded scenario because of this gradient of the velocity profile. The milder the slope of the velocity gradient, the higher the C_T and C_P of the turbine. This effect also appears only to be observable at a very low blockage ratio, as this kind of discrepancy is not observable in the laterally bounded scenario.

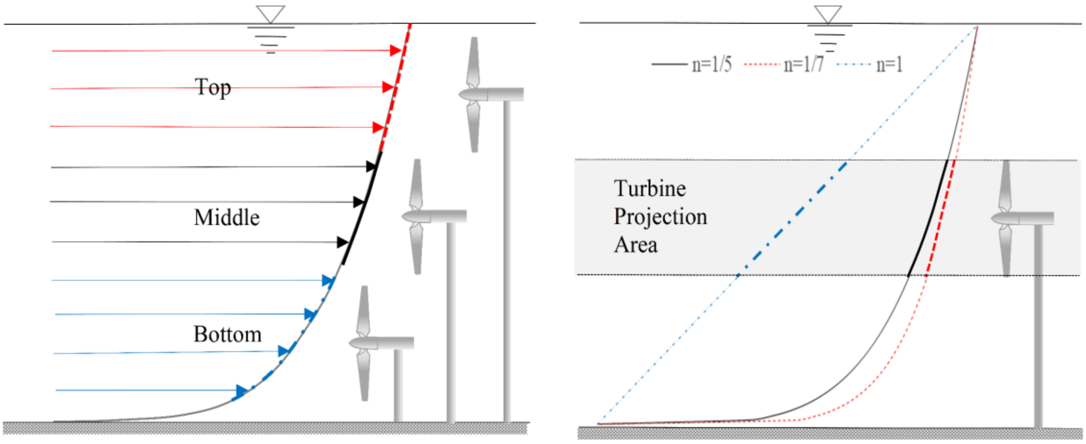

a. The comparison of the turbine in a different position in the sheared flow profile of n=1/5

b. The turbine in the different sheared profile

Figure 3-40: Illustration of the turbine in the bottom case compared to other positions (a) and the turbine in n=1 sheared profile in comparison to the other profiles (b)

However, it is essential to note that the discrepancies between C_T and C_P in the Bottom case and GC07 are minuscule relative to the other errors and uncertainties inherent in tidal stream resource assessment. It is hard to confirm whether this position corresponds to the C_T and C_P of these cases. Therefore, Therefore further research is necessary in order to explain how the Bottom case has higher C_T and C_P than the turbine at the top or how the n=1 profile shows higher C_T and C_P than the other profiles and even higher than the theoretical GC07.

These results show the complexity of the turbine performance in a sheared flow. However, the results also show that the classical theory of GC07 is still reliable and may be used in resource assessment, provided that $U_{in\text{-}disc}$ is used. The discrepancies of C_T and C_P between turbines in different positions and sheared flow profile are relatively small. Furthermore, it might be that the best way to deal with this problem in the resource assessment is just to acknowledge this limitation.

Chapter 4. 2D Modeling of Indonesian Tides

This chapter describes the modelling set-up used for tidal resource assessment analyses in Chapters 5 and 6. A two-dimensional (2D) model is developed due to its simplicity. There are some places in Indonesian waters where the 2D depth-averaged shallow water equation (SWE) numerical solver might not be able to deliver a satisfactory solution due to the complexity of the actual physics. However, a 2D SWE solver can be run in a sensible computing duration for a large domain such as that used in this thesis. Since this thesis is the first major study of resource assessment in Indonesia waters, using a 2D approach might help to understand the complexities of Indonesian waters.

4.1 Review of DG-ADCIRC Solver

Two-dimensional (2D) depth-averaged models are a reasonable option to simulate tidal flow in open ocean domains, since they need less computational time than three-dimensional (3D) models. This numerical model allows prediction of the flow field changes due to tidal arrays (Adcock *et al.*, 2013, Walkington & Burrows, 2009), and enables us to evaluate the environmental impact of these arrays (Ahmadian & Falconer 2012, Xia *et al.* 2010). Since turbines will act as resistance to the flow, adding a turbine or turbines in an array will produce an effect on the flow.

The Discontinuous Galerkin (DG) version of ADvance CIRCulation (ADCIRC), is an open-source solver known as DG-ADCIRC. It solves the shallow water equations to simulate tidal flows (Kubatko *et al.* 2006a, Kubatko *et al.* 2006b) and other nearshore circulations. This solver is used for its versatility in modelling ocean tidal hydrodynamics. Despite the simplifying assumptions, this model can capture the bulk flow through channels and around headlands. Moreover, incorporating the Le Provost global tidal model to generate tidal constituents on its open ocean boundaries makes this model convenient to use (see Le Provost 1995 and Le Provost *et al.* 1995).

This numerical solver uses governing equations that can be expressed as a time-dependent two-dimensional system of non-linear partial differential equations of hyperbolic type, as shown in equations (4.1), (4.2) and (4.3)

$$\frac{\partial \eta}{\partial t} + \frac{\partial}{\partial x}(Hu) + \frac{\partial}{\partial y}(Hv) = 0, \tag{4.1}$$

$$\frac{\partial}{\partial t}(uH) + \frac{\partial}{\partial x}\left(Hu^2 + \frac{1}{2}g(Hu^2 - h^2)\right) + \frac{\partial}{\partial y}(Huv) = g\eta\frac{\partial h}{\partial x} - c_f u\sqrt{u^2 + v^2 +}\, F_c v + Fx, \tag{4.2}$$

$$\frac{\partial}{\partial t}(vH) + \frac{\partial}{\partial x}(Huv) + \frac{\partial}{\partial y}\left(Hv^2 + \frac{1}{2}g(H^2 - h^2)\right) = g\eta\frac{\partial h}{\partial y} - c_f v\sqrt{u^2 + v^2 +}\, F_c u + Fy. \tag{4.3}$$

Eq. (4.1) is the mass conservation equation, where h is the bathymetric depth of the water column below the geoid, H is the total depth of the water column ($H = \eta + h$), η is the free surface elevation, while the variables u and v represent the depth-averaged velocity components in x and y directions. Eqs. (4.2) and (4.3) are the horizontal momentum conservation equations in x and y directions, respectively, where g is the gravitational acceleration, c_f is an empirical bed friction coefficient, F_c is the Coriolis force, and Fx and Fy represent additional forces in the system such as tidal potential, wind or wave radiation stresses.

4.2 Inclusion of the Turbine Model in The Solver

Two methods are in use for prediction of tidal power extractable energy. Either the turbines can be represented as a discontinuity in the flow (e.g. Draper *et al.*, 2010), or the drag applied by the turbines can be smeared over an area by enhancing the bed friction of given mesh nodes (e.g. Sutherland *at al*., 2007; Bryden & Couch, 2007). However, Draper, 2011 argued using an increased bed friction coefficient has drawbacks. This enhanced friction method considers the power extracted from the site which includes both the available power extracted by the turbines, and power loss due to frictional forces and downstream mixing (see Draper, 2011).

4.2.1 Initial Code

The DG-ADCIRC code has been modified by Serhadlıoğlu, 2014 using a momentum sink in a two-dimensional depth-averaged model following Draper, 2011 and Draper *et al.*, 2010. Tidal devices are installed with uniform centre-to-centre spacing. The thrust applied by the tidal turbines is sufficient to dominate other source terms, such as the bed friction and inertia forces. The fence and basin characteristics (e.g., blockage ratio, water depth) change slowly with time, and the wake mixing length is significantly smaller than the element size (see Serhadlıoğlu, 2014 for the detail).

4.2.2 Modifications to the Code

This thesis essentially applies the theory that has been discussed in the previous chapter to explore the tidal energy resources at a real site. As discussed previously in Chapter 2, it could be an advantage to limit the turbine power production. Limiting power and thrust could make the assessment more realistic, since the resources could be calculated with the consideration of turbine capacity. This thesis explores the implementation of Power Capping and Thrust capping, especially for the realistic assessments discussed in Chapter 6. Therefore, further modification to the code is made for this purpose.

A similar implementation of power and thrust capping in the 0-D model, as shown in Chapter 2, is applied here. The power and thrust capping is applied by changing the wake coefficient when the power or thrust reaches the capping limit. Therefore, an algorithm is added in the previous code for this power and thrust capping. A similar modification has been made by Wang, 2017, but his modified model did not run when domain decomposition is used to run the code in parallel. Due to the number of cases and the size of the domain, running the simulations in a parallel computing facility is necessary. Therefore, the modification was required to enable the solver to run on the Arcus-B platform of the Advanced Research Computing (ARC), which is a Haswell (16 core) system (see https://www.arc.ox.ac.uk/arc-systems for detail). Thus, the code is rewritten, incorporating the power and thrust capping for the ARC system.

Modifications are also made for the model to give output for each element. Therefore, the results could be used for the site-site interaction analysis, as later shown in Chapter 5. An idealised model is built for verification of the modifications. The model domain is presented in Figure 4-1. Turbine model from Houlsby *et al.*, 2008 is applied in the middle of the channel.

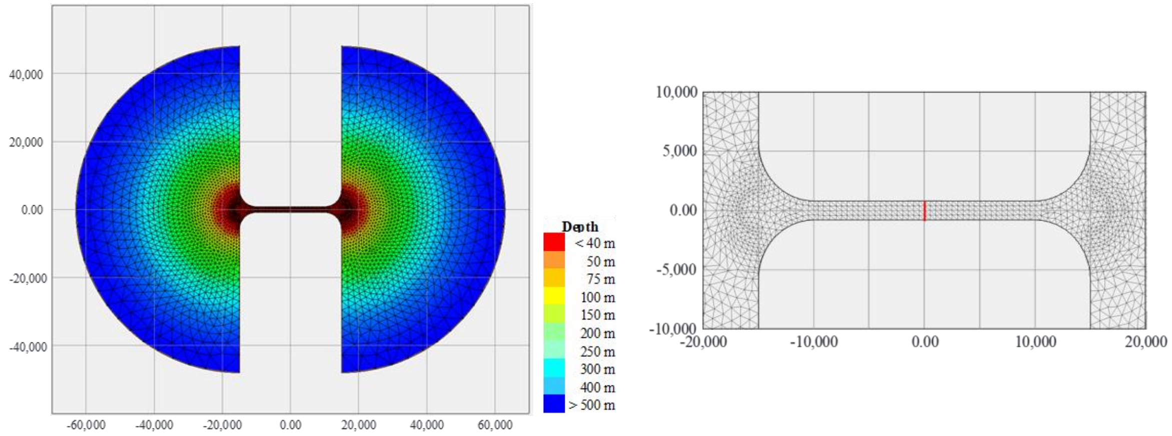

a. Mesh and bathymetric

b. Detailed mesh in the channel

Figure 4-1: Idealised model mesh set-up. The red line in the middle of the channel in a. is the location of the turbine's arrays that represented with Houlsby *et al.*, 2008 model.

The comparison of the results from the models run in the ARC system and personal computer (PC) from Wang 2017 are shown in Figure 4-3 for Power Capping and Figure 4-2 for thrust capping. The results show that the two analyses are the same verifying the new implementation of the code.

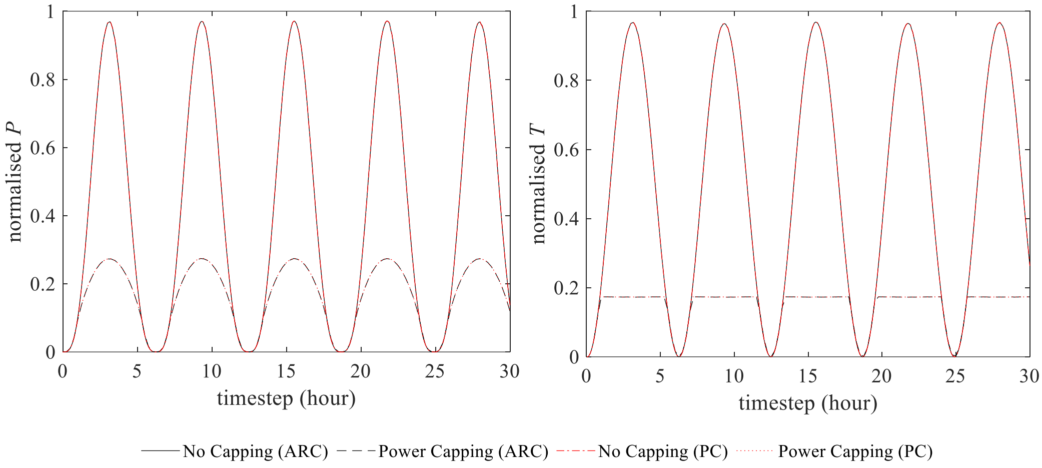

Figure 4-2: The comparison of results between simulation in the ARC system and in a Personal Computer (PC) for thrust capping.

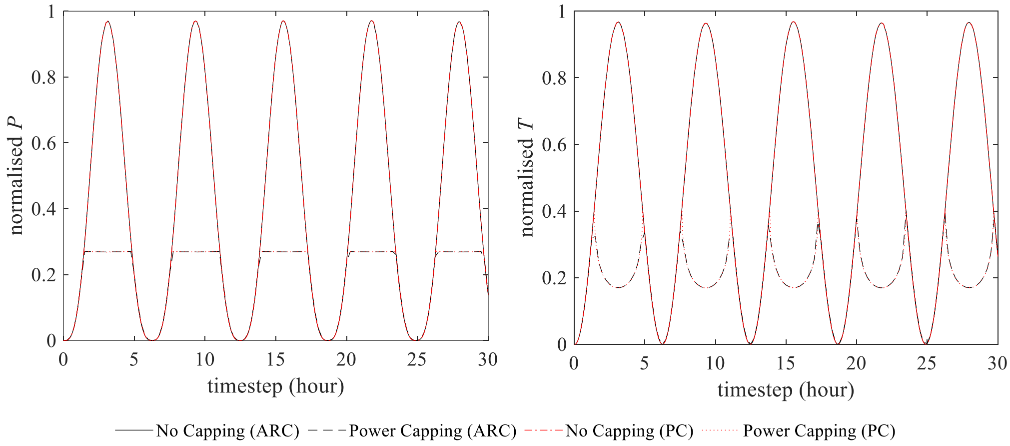

Figure 4-3: The comparison of results between simulation in the ARC system and in a Personal Computer (PC) for power capping

4.3 Tidal Current Modelling in Indonesian Waters

Indonesia is arguably one of the most complex regions in the world for modelling ocean hydrodynamics, due to its geographic complexity with myriads of islands. Rugged bottom bathymetry next to wide shelves of shallow water complicates the currents in the water column. The presence of strong diurnal tidal components along with semidiurnal components leads to complex tidal variations, which demands long computational time for accurate representation. The presence of a net throughflow current complicates the problem further. Relatively few studies of tidal resources have been carried out for this region. Furthermore, reliable data for calibration of the models are sparse in this region. While some data gathered by Indonesian government agencies may exist, little data is available in the open literature.

Many authors have had difficulties when modelling this complex system of Indonesia waters. For instance, there are deficiencies in both Koropitan & Ikeda, 2008, who modelled the Indonesian waters using the three-dimensional Princeton Ocean Model (POM-3D) and Robertson and Ffields 2008 using Regional Ocean Model System (ROMS). Koropitan & Ikeda, 2008's model shows a small discrepancy in amplitude and phase only for M_2 at eleven tide stations on the admiralty tidal chart. However, there are pronounced discrepancies for other principal constituents (S_2, K_1 and O_1). Their paper, Koropitan & Ikeda, 2008, mentions the importance of the bathymetry data source. They argue that the global topography dataset that they used (ETOPO2) is "inaccurate" in central and coastal regions of the Java Sea. They suggest incorporating the bathymetric chart from the DISHIDROS TNI-AL data set in this region.

Robertson and Ffields 2008 claim to have successfully replicated tidal elevation fields as determined from TOPEX /POSEIDON-crossover satellite with 4-6 cm differences of semidiurnal constituents (S_2 -M_2) and 7-10 cm of diurnal constituents (K_1-O_1). However, those figures are the Root Mean Square (RMS) of all points. There are some points with significantly higher discrepancies than the RMS. For example, M_2 in the coordinate of 9°46' S - 133°130 E is higher by +47.7 cm than the data.

Furthermore, some of the tidal resource assessments that have been done in this region are local domain models (see Blunden *et al.*, 2013; Orhan *et al.*, 2015; Orhan *et al.*, 2017; Rachmayani *et al.*, 2006 and Coordinating Team of Research and Technology, 2008). These models assume that the effect of turbines on the nearest boundary is small. This assumption is not strictly true (Garrett & Greenberg, 1977; Adcock *et al.*, 2011; Adcock *et al.*, 2015) since the turbine perturbation may affect the flow-field in an area. A 2D SWE model usually applies either fixed water surface elevation (WSE) or fixed velocity at the boundaries. This process neglects the effect of the turbine that might reach the boundary. Furthermore, as discussed in Chapter 2, Indonesia is passed through by the ITF. This phenomenon means that the perturbation in the flow in this area may have a larger impact on the flow-field at a regional scale, as later demonstrated in Chapter 5.

4.4 Developing the Specific Model and Data Input.

As discussed previously in Chapter 1, five different potential sites are selected for the assessment in this thesis. Three models in DG-ADCIRC are built to solve the SWE in these areas. Following Adcock *et al.*, 2011 and Adcock *et al.*, 2015, the boundaries for all domains are set to be sufficiently far away to ensure the changes due to the presence of turbines are negligible. At the boundary of the model, the water elevation is specified by tidal constituents. Thirteen tidal components are applied at the boundaries, using data from the Le Provost model (Le Provost, 1991, Le Provost *et al.*, 1995). Since this area has a unique feature of a global current, another constituent is added to mimic this circulation.

4.4.1 Specific Modeling

For the resource assessment in the Lingga regency and the Sunda Strait, a DG-ADCIRC model domain is constructed, extending from Malacca Straits, South East China Sea to the Indian Ocean (see Figure 4-4) is built. Hereafter this model domain is called the western domain. Bali-Lombok channel and the Larantuka strait are covered by a domain called the central domain, which spans from the Java Sea to the Arafura Sea and from Makassar Strait to the Indian Ocean, as shown in Figure 4-5. The Sula Archipelago sites are covered by the eastern domain, as shown in Figure 4-6. This domain extends from Australia in the south to the Pacific Ocean and Philippines in the north.

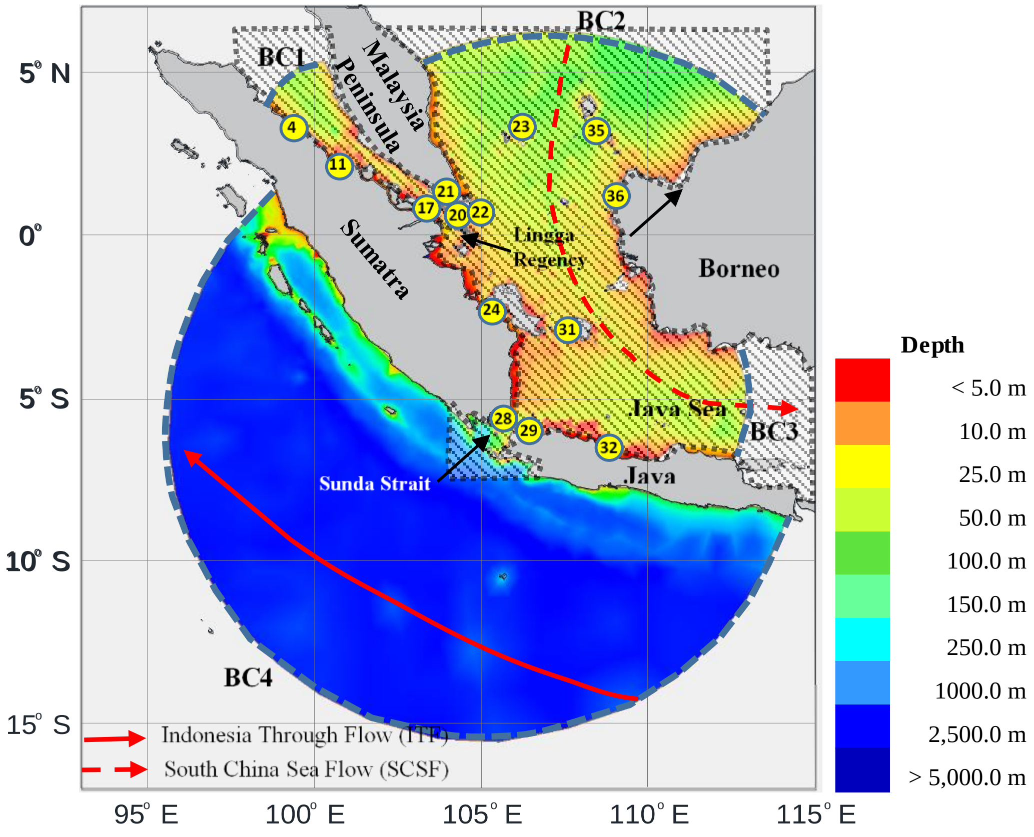

Figure 4-4: The western domain

4.4.2 Bathymetric Data

For the most part, these models adopt the GEBCO bathymetric data. However, as previously discussed, Koropitan & Ikeda, 2008 found that the GEBCO dataset is inaccurate in the central and coastal regions in the Java Sea. A similar inaccuracy is also found to be the case in the models of this thesis. In general, the GEBCO dataset seems inaccurate in the areas of shallow water. Hence, nautical charts bathymetric data, provided by DISHIDROS TNI-AL, a hydro-oceanographic division of the Indonesian Navy, is also incorporated here. Several bathymetric maps from DISHIDROS in the Malacca strait, Riau Archipelago waters, Java Sea, Banda Sea, Makassar Sea and the coast of Papua are combined in all the models.

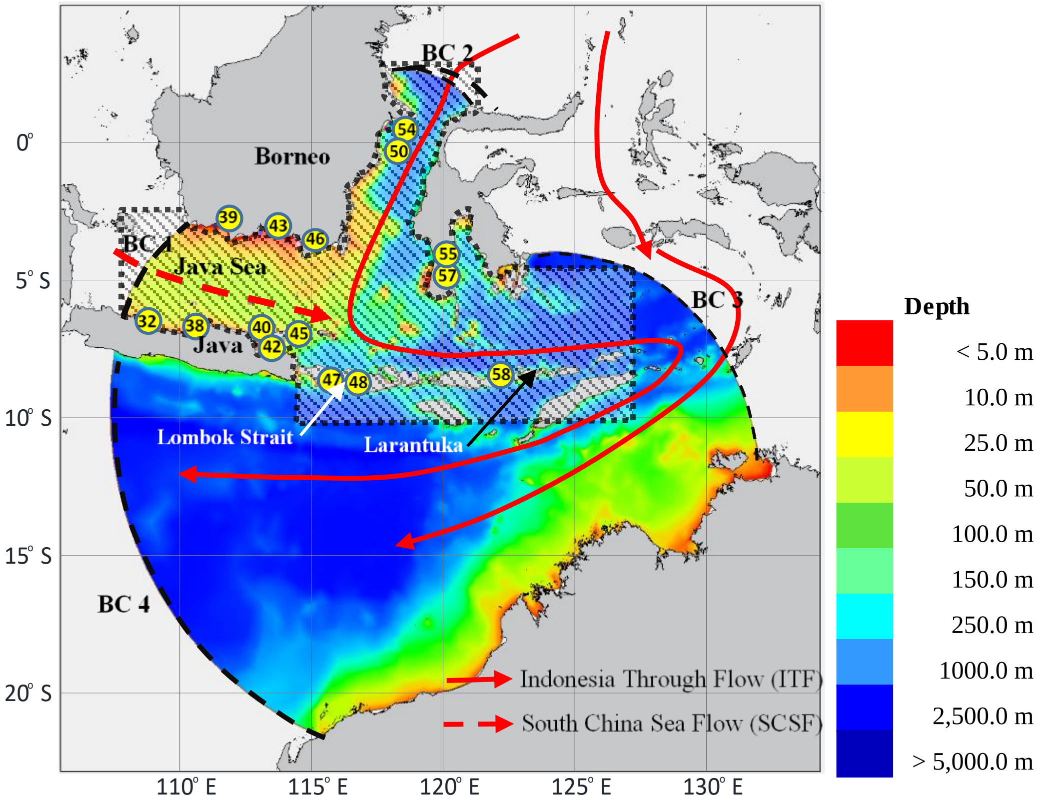

Figure 4-5: The central domain

The nautical chart utility in all domains is shown in the region enclosed by the dotted line (see Figure 4-4 for the western domain, Figure 4-5 for the central domain and Figure 4-6 for the eastern domain). Since these nautical chart data are referred to as Lowest Water Spring (LWS) while GEBCO and Le Provost's model (Le Provost, 1991; Le Provost *et al.*, 1995) is referred to mean sea level (MSL), it is necessary to adjust the datum for the data.

Bathymetric data is also refined at several of the potential sites. The data are obtained from the Marine Geology Research and Development Centre (P3GL), a research agency under the Ministry of Energy and Mineral Resources (MoEMR). The detailed bathymetric survey data in the Lombok straits (Yuningsih, 2008) is shown in the area enclosed by a dotted line (see Figure 4-7).

The bathymetric data from the survey are also embedded in the model for the Larantuka site. The area of bathymetry refinement is shown in Figure 4-8. ADCP measurements and tide observation data in this area were also obtained from P3GL. The ADCP measurement data is at the Larantuka site, while the tide observation was conducted in Boleng Strait. The bathymetry from the survey in Mangole Strait is used in the eastern domain model (see Figure 4-9). ADCP measurements in the Mangole Strait was also obtained from P3GL.

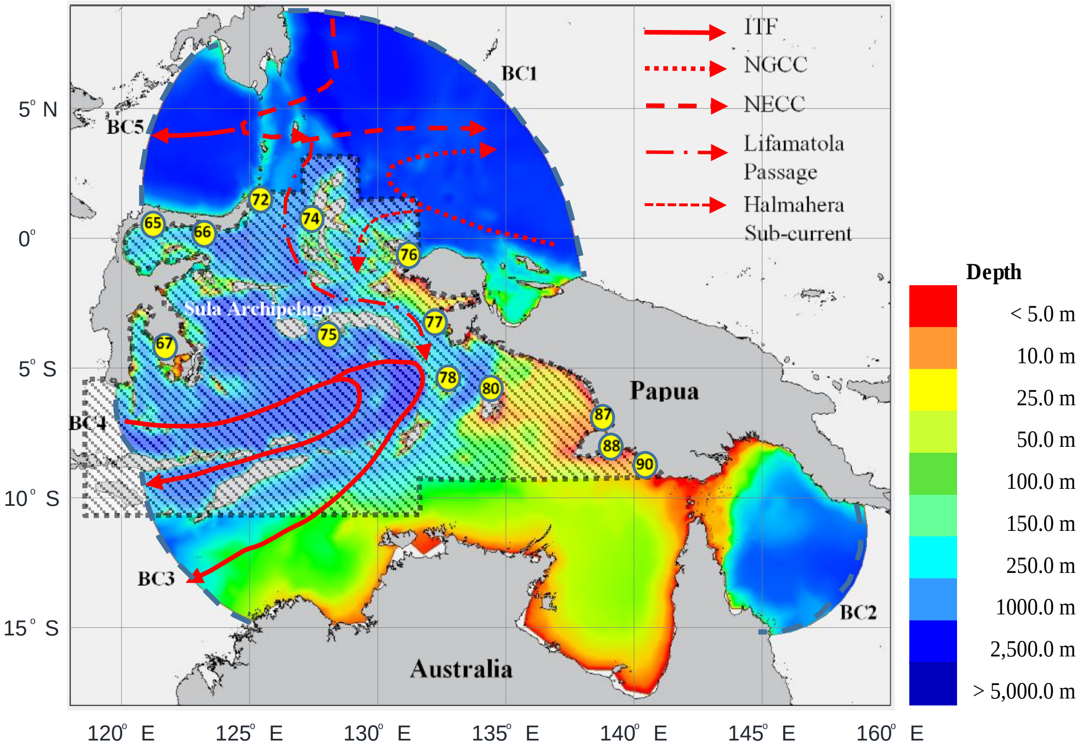

Figure 4-6: The eastern domain

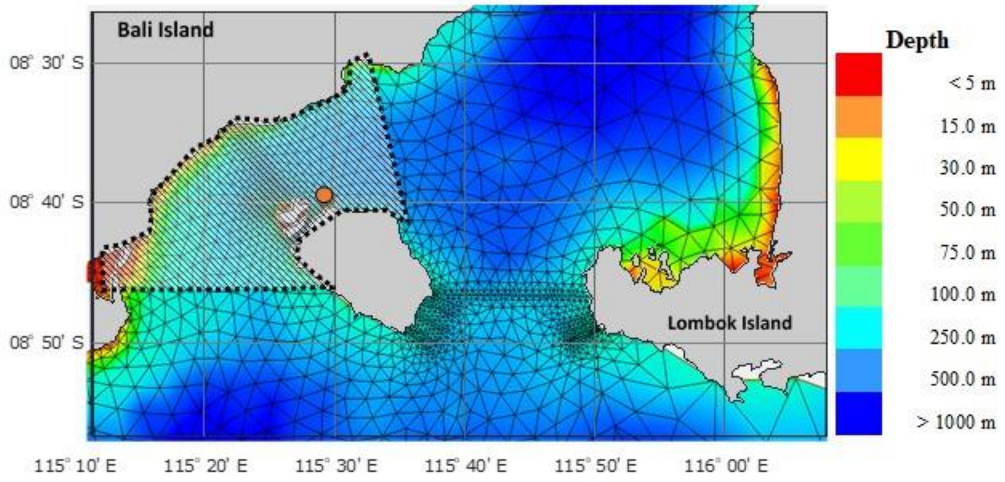

Figure 4-7: The area of the bathymetric survey (within the black dotted line) and mesh for DG-ADCIRC in the Bali and Lombok channel

4.4.3 Inclusion of Residual Current (Indonesian Through Flow)

A small alteration to mean sea level at each boundary is applied to mimic the Indonesian Throughflow (ITF). The mean elevations or mean sea level (MSL) are set with up to 0.01 m or 1 cm differences between the open boundaries. The flow pattern in the western domain is simpler than in other domains. There are two global currents in this region, the South China Sea Flow (SCSF) that flows from the South China Sea to the Java Sea, and the Indonesia Throughflow (ITF) that flows along the south coast of Java to the west coast of Sumatra (see Figure 4-4). The MSL in BC2 is set slightly higher than the MSL in BC3 to mimic this SCSF. The MSL in BC2 is 0.01 m, while in BC3 is 0.005 m. Mimicking the ITF is slightly challenging. The MSL in BC4 is set to change incrementally from 0 m in the north-west element point to 0.01 m in the south-east end.

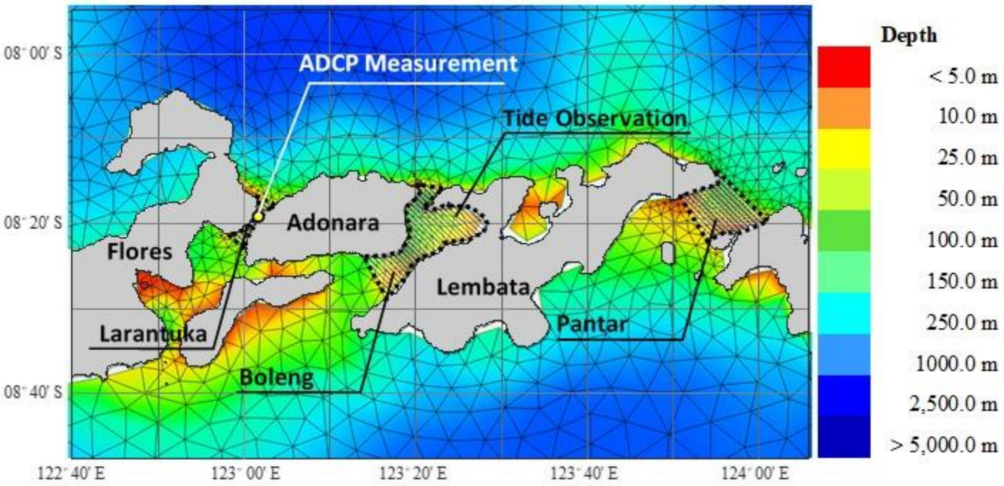

Figure 4-8: Mesh for DG-ADCIRC in Larantuka, Boleng and Pantar Straits. The areas within the black dotted line are the area of the bathymetric survey.

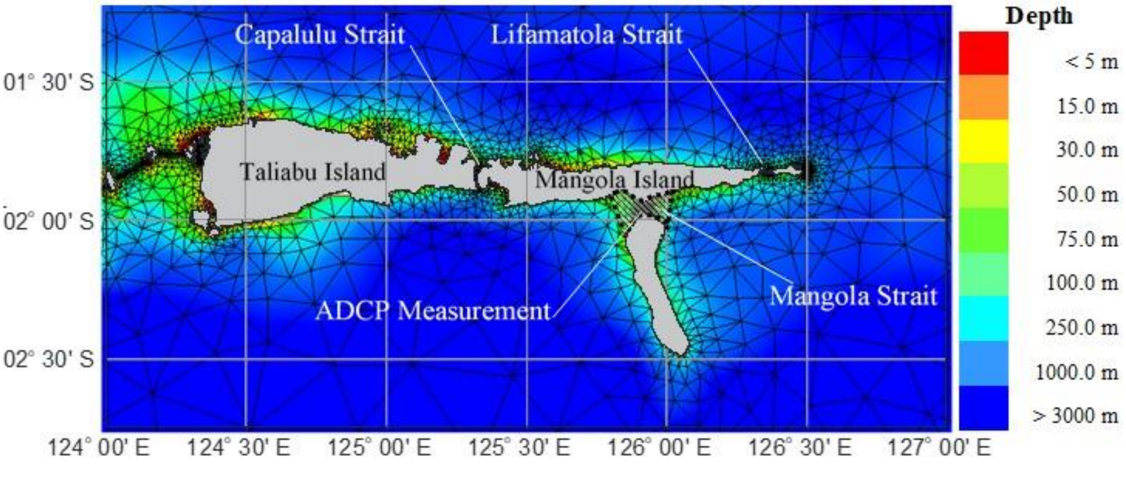

Figure 4-9: Mesh for DG-ADCIRC in Capalulu, Lifamatola and Mangola Straits. The areas within the black dotted line in Mangola Strait is the area of the bathymetric survey.

In the central domain (Figure 4-5), the mean elevation at BC2 is set as 0.01 m, while at BC1 is set as 0.0075m. The mean elevation at BC3 is 0.005, and BC4's mean elevation is set to zero. These head differences between the northern and southern boundaries create a flow in the area of Nusa Penida with a velocity ranging from 0.25-0.35 m/s, which is close to the typically observed values. The residual current in the eastern domain is more complex than in other domains. As shown in Figure 4-6, many sub-currents should be included in the model. However, the model in this eastern domain only focuses on mimicking the sub-current that passes through the Sula Regency. Therefore, the MSL at BC1 is set at 0.01 m and at BC3 it is 0.0 m. The MSL at BC4 is set slightly higher (0.0025 m) than BC3 to mimic the ITF. Meanwhile at BC5 the MSL is set 0.0075 m to create the ITF pattern in the northern part.

As a consequence of the adjustment of mean sea level, the model is required to spin-up for two days before the results from the following 60 days are recorded and harmonically analysed for comparison with the data. Two sets of simulations with different starting points are run, and the water surface elevation (WSE) at certain locations is compared (as shown in Figure 4-10). Figure 4-11 shows examples of spin-up time computations for two simulations, one driven by 13 constituents, the other solely by M_2.

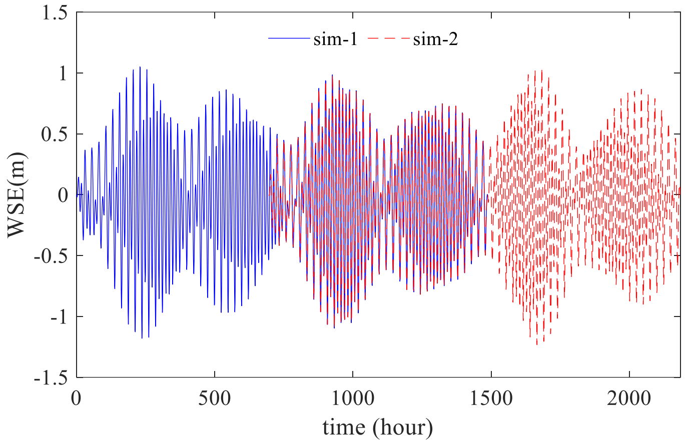

Figure 4-10: Simulation to determine the run-up time for 13 constituents

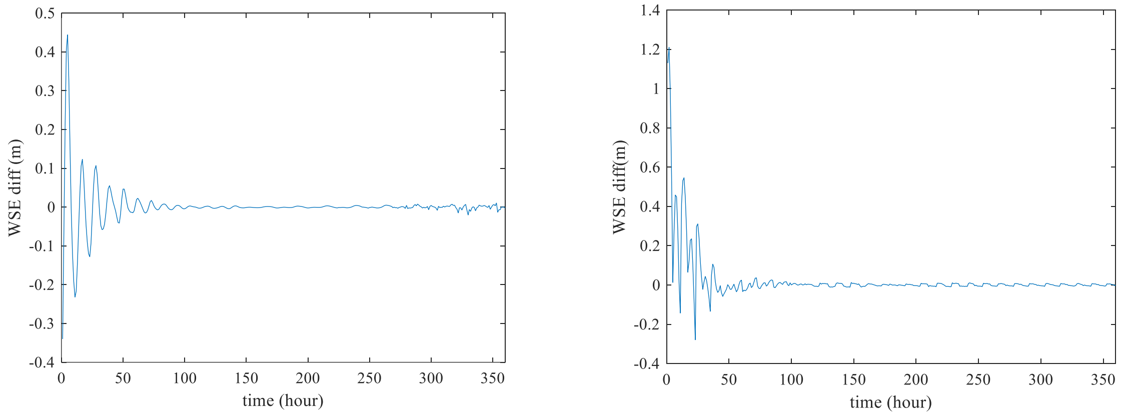

a. the model is run with 13 constituents

b. the model is run with a single constituent (M_2) in the central domain

Figure 4-11: The examples of spin-up time that is needed when in the central domain

4.5 Model Validation

The model is validated using several data sources. As commonly used for model validation, the admiralty chart from regulatory officials is used for the validation here. The models are also validated with a co-tidal chart obtained from satellite data. In several locations, the time series data of tidal observations and ADCP current measurement surveys are also used for validation. The models are also compared for the *Formzahl* number.

4.5.1 Mesh Convergence and Independence

Similar to the mesh independence study in Chapter 3, the analysis of mesh convergence and independence for the shallow water equation (SWE) modelling is also required here. The ADCIRC model is dependent on the mesh quality, as for any other numerical model. In general, the smaller the mesh size, the better the result.

However, as this research requires many simulations, it is important to have a pragmatic simulation duration. The time interval (Δt) is set to 0.5-1 s for all schemes and scenarios in this research. Due to the explicit way in which time derivatives are handled in ADCIRC, this minimum Δt sometimes causes numerical instability. Numerical stability is dictated by the CFL (Courant-Friedrichs-Levy) number. The CFL constraint states that for stability $\frac{\Delta t}{\Delta x}\sqrt{gh} < 1.0$, where Δx is the minimum mesh dimension. Therefore, to avoid instability in the model, either one has to decrease Δt or increase Δx. For the sake of expediency, the minimum grid size is increased to meet this criterion.

Following some previous modelling in Indonesian waters (e.g. Koropitan & Ikeda, 2008 and Robertson & Ffields 2008), validation of tidal constituents used the data from the Admiralty tide table from DISHIDROS TNI AL. The locations of the stations are shown in yellow dots with a number in Figure 4-4, Figure 4-5 and Figure 4-6. The station numbering in this thesis follows the enumeration in the Admiralty table. The validations are conducted separately in the three domains. Although the models are run with 13 constituents, the validations are applied to the principal constituents only (M_2, S_2, K_1, and O_1).

There is no consensus as to what exactly constitutes good or poor agreement in the modelling, since this would depend on the specific conditions and requirements of the model. However, the definition adopted for good agreement for the amplitude (A) in this thesis is that the log ratio of observed to model predictions $\leq$ 20%. Whilst for the phase difference, the good agreement is when $|\phi_{model} - \phi_{data}| \leq 45^o$, where ϕ_{model} is the phase from the model and ϕ_{data} is the phase from tide tables in Tables 4-2 to 4-4. The model results categorised as poor agreement are written in red, while good agreement is written in blue. It is important to note that M_2 is not always the strongest tidal constituent in Indonesian waters. Therefore, this issue is also considered in the validation. The strongest amplitude between M_2, S_2, K_1, and O_1 at each station is written in bold.

Fourteen stations from the admiralty table are selected for each domain. Each model domain uses different tide stations from the Admiralty chart, although some stations are used more than once as the area intersects between the models. The models were run with default bed friction of Cf = 0.0025 for all domains. Three different mesh densities are set for each model domain. The mesh density variation for all domains is shown in Figure 4-12. The parameters of each mesh density are presented in Table 4-1.

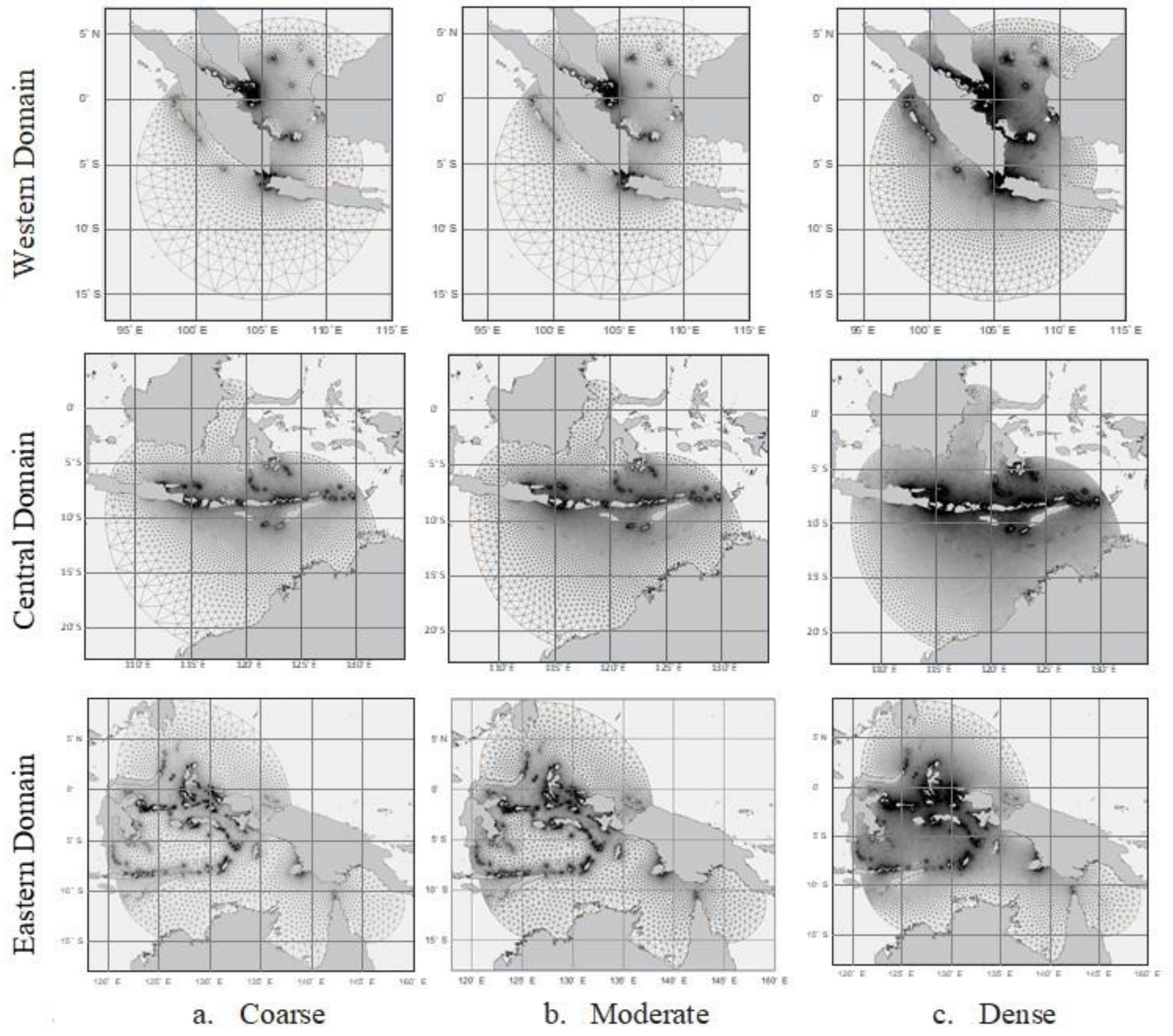

a. Coarse b. Moderate c. Dense

Figure 4-12: Mesh Density for each domain

The number of elements and nodes is varied from the smallest in coarse meshes to the largest in the dense meshes. A mesh with a small element and node number might not be able to mimic the land boundaries in detail. Therefore, there is a limit of mesh coarseness that could be set. Large numbers of elements and nodes are also problematic, as these determine the element front width and node half bandwidth (see Table 4-1). These bandwidths tend to get larger as the number of elements/ nodes mesh is larger. Essentially, these bandwidths are two measures of the demand on computational time. ADCIRC uses the Cuthill-McKee or Inverse Cuthill-McKee scheme for the renumbering process. Minimalizing the bandwidths allows the ADCIRC model to run efficiently (see https://www.xmswiki.com for detail). Therefore, the dense mesh is more expensive in computing resources to run than the coarse mesh. The dense mesh is also computationally demanding as the CFL number is also larger.

Therefore, this analysis is unable to produce a mesh density variation at a similar level to the ANSYS simulation, as shown in Chapter 3, in which meshes with a wide variation from coarse to dense were employed. The stability of the DG-ADCIRC model is very sensitive, and the model stability is dependent on the mesh set-up. A large number of mesh configurations based on trial-and-error were built for this analysis. However, only a few configurations were successful. The model stability becomes a constraint on the mesh set-up. Thus, the variations of the mesh density are not ideal in certain domains. In some cases, the mesh is only refined in the particular area of interest.

Table 4-1: Mesh parameters

Domain	Mesh Parameter	Coarse	Moderate	Dense
Western Domain	Number of Elements	24,822	26,577	106,308
	Number of Nodes	14,124	15,029	56,782
	Max element front width	269	347	549
	Max node half band width	305	393	587
Central Domain	Number of Elements	21,000	34,687	96,352
	Number of Nodes	11,506	18,523	50,242
	Max element front width	211	249	449
	Max node half band width	227	251	466
Eastern Domain	Number of Elements	30,154	66,039	70,520
	Number of Nodes	17,758	17,789	38,326
	Max element front width	358	361	434
	Max node half band width	401	404	472

For instance, the moderate mesh for the western domain has only about 2,500 more elements than the coarse mesh (see Table 4-1). The meshes also appear similar (see Figure 4-12). However, if the area of the Sunda Strait is enlarged, the distinction between the meshes is more observable at the bridge location (see Figure 4-13). The mesh sensitivity analysis for the western domain is presented in Table 4-2, the central domain in Table 4-3, and the eastern domain in Table 4-4. The average root-mean-square (RMS) errors for each constituent are calculated for all the domains and are presented in Table 4-5.

In general, coarse meshes give a better agreement for all domains in term of amplitude. The western domain shows that the moderate mesh gives a relatively better agreement in phase lag, while in other domains, the average errors of phase lag for moderate and coarse meshes are relatively similar. This mesh sensitivity analysis shows the complexity of the models in terms of mesh density. A dense mesh does not guarantee the model will have a better agreement with observed data.

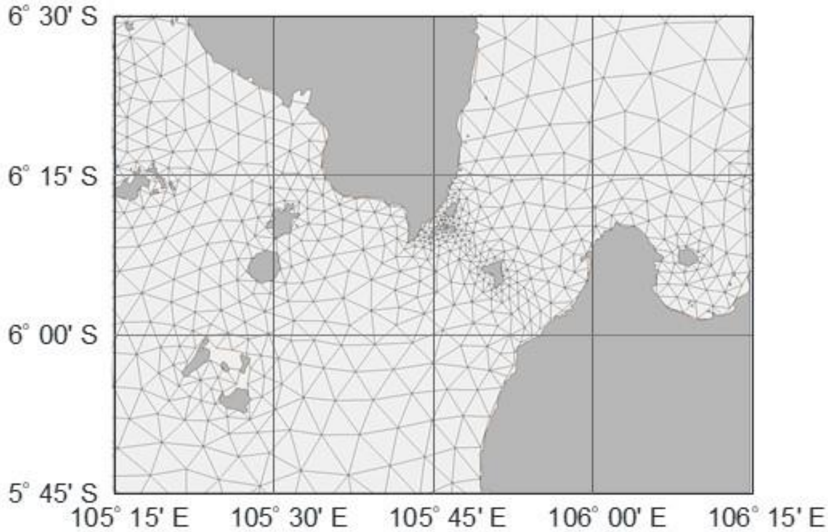

a. Coarse Mesh

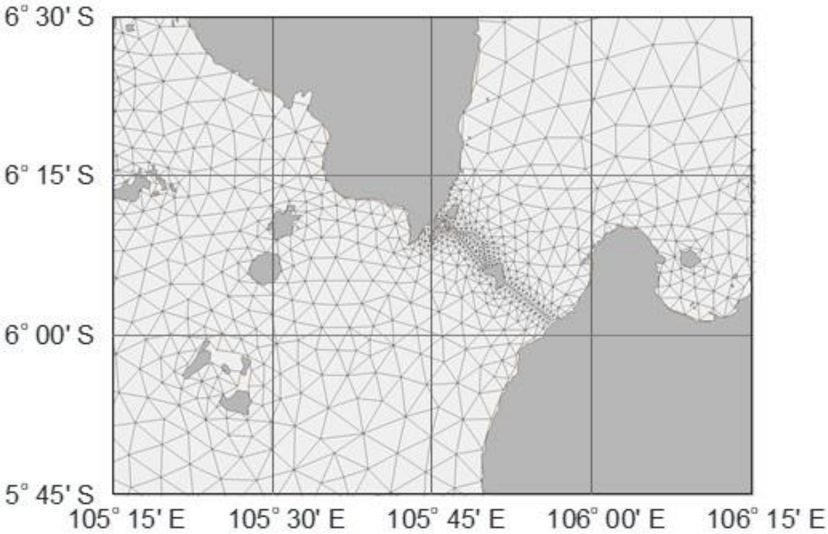

b. Moderate Mesh

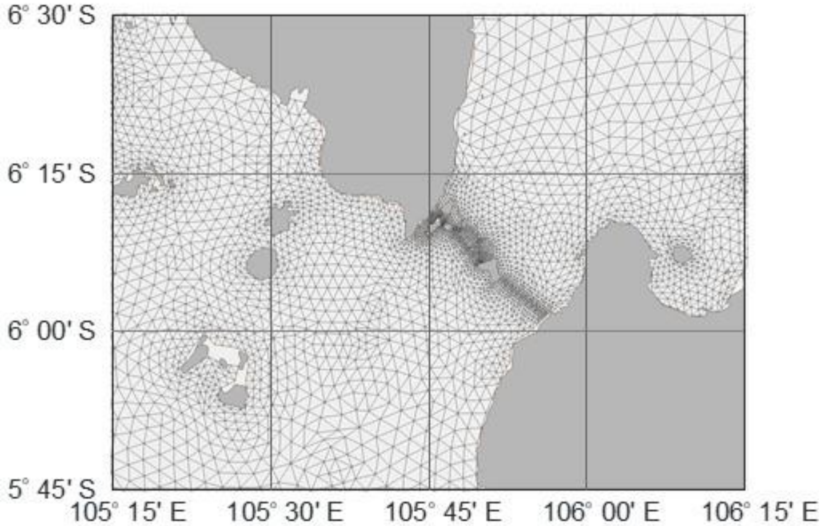

c. Dense Mesh

Figure 4-13: Mesh density at the Sunda Strait for Western Domain, showing the different mesh densities at the bridge location.

Table 4-2: Mesh Sensitivity validation for the Western Domain

Sta.	Location	Lat	Long	Data		Coarse				Moderate				Dense			
						Calculation		Error		Calculation		Error		Calculation		Error	
				A (m)	ϕ (deg)	*A* (m)	ϕ (deg)	*A*	ϕ	*A* (m)	ϕ (deg)	*A*	ϕ	*A* (m)	ϕ (deg)	*A*	ϕ
M_2																	
4	Kuala Tanjung	3.4° N	99.5° E	**0.8**	281.0	1.00	323.8	0.10	42.8	1.01	172.9	0.10	(108.1)	0.99	193.8	0.09	(87.2)
11	Bagan Siapi-Api	2.2° N	100.6° E	**1.7**	226.0	1.85	47.2	0.04	(178.8)	1.87	255.7	0.04	29.7	1.75	280.1	0.01	54.1
17	Pasir Panjang	1.13° N	103.3° E	**0.94**	62.0	0.70	228.2	(0.13)	166.2	0.69	78.9	(0.13)	16.9	0.61	101.8	(0.19)	39.8
20	Batu Ampar	1.17° N	104.0° E	**0.76**	61.0	0.55	225.2	(0.14)	164.2	0.53	79.0	(0.16)	18.0	0.46	99.8	(0.22)	38.8
21	Singapura	1.3° N	103.9° E	**0.8**	62.0	0.55	226.0	(0.16)	164.0	0.54	80.1	(0.17)	18.1	0.47	100.4	(0.23)	38.4
22	Selat Kijang	1.8° N	104.6° E	**0.34**	59.0	0.41	176.1	0.08	117.1	0.37	34.3	0.04	(24.7)	0.36	47.2	0.03	(11.8)
23	Tarempa	3.9° N	106.7° E	0.16	144.0	0.17	157.8	0.04	13.8	0.17	9.7	0.03	(134.3)	0.14	25.0	(0.06)	(119.0)
24	Muntok	2° 5' N	105.16° E	0.3	178.0	0.17	337.7	(0.24)	159.7	0.12	189.1	(0.42)	11.1	0.15	198.1	(0.29)	20.1
28	Bakauhuni	5.9° N	105.8° E	**0.2**	138.0	0.27	90.6	0.14	(47.4)	0.30	297.9	0.18	159.9	0.27	322.0	0.14	4.0
29	Suralaya	5.87° S	106.03° E	**0.12**	161.0	0.26	92.0	0.34	(69.0)	0.28	300.1	0.37	139.1	0.26	324.2	0.33	163.2
31	Tanjung Pandan	2.8° S	107.6° E	0.08	293.0	0.21	209.8	0.43	(83.2)	0.17	57.8	0.34	(55.2)	0.18	87.2	0.34	(25.8)
32	Cirebon	6.7° S	108.6° E	**0.16**	56.0	0.07	50.8	(0.36)	(5.2)	0.05	231.6	(0.53)	175.6	0.04	256.7	(0.61)	20.7
35	Penagi (Ranai)	3.89° S	108.4° E	**0.34**	291.0	0.61	350.3	0.26	59.3	0.56	200.3	0.22	(90.7)	0.55	221.3	0.21	(69.7)
36	Pemangkat	01.2° S	109.0° E	**0.28**	254.0	0.61	350.3	0.34	96.3	0.56	200.3	0.30	(53.7)	0.55	221.3	0.29	(32.7)
S_2																	
4	Kuala Tanjung	3.4° N	99.5° E	0.35	233.0	0.53	241.1	0.18	8.1	0.45	243.7	0.11	10.7	0.44	240.8	0.10	7.8
11	Bagan Siapi-Api	2.2° N	100.6° E	0.9	176.0	0.88	335.2	(0.01)	159.2	0.73	339.4	(0.09)	163.4	0.69	340.3	(0.12)	164.3
17	Pasir Panjang	1.13° N	103.3° E	0.43	9.0	0.28	157.5	(0.18)	148.5	0.22	163.3	(0.30)	154.3	0.19	163.8	(0.36)	154.8
20	Batu Ampar	1.17° N	104.0° E	0.31	4.0	0.19	168.5	(0.21)	164.5	0.14	182.3	(0.33)	178.3	0.13	183.2	(0.37)	179.2
21	Singapura	1.3° N	103.9° E	0.33	9.0	0.19	168.6	(0.23)	159.6	0.15	182.2	(0.35)	173.2	0.13	182.9	(0.40)	173.9
22	Selat Kijang	1.8° N	104.6° E	0.12	4.0	0.08	92.9	(0.18)	88.9	0.05	109.8	(0.36)	105.8	0.05	100.6	(0.38)	96.6
23	Tarempa	3.9° N	106.7° E	0.03	79.0	0.02	104.2	(0.15)	25.2	0.01	101.6	(0.48)	22.6	0.01	151.2	(0.61)	72.2
24	Muntok	2° 5' N	105.16° E	0.16	129.0	0.04	149.6	(0.62)	20.6	0.05	158.3	(0.52)	29.3	0.04	163.7	(0.58)	34.7
28	Bakauhuni	5.9° N	105.8° E	0.11	86.0	0.10	18.6	(0.06)	(67.4)	0.09	17.8	(0.08)	(68.2)	0.08	19.4	(0.13)	(66.6)
29	Suralaya	5.87° S	106.03° E	0.1	78.0	0.09	18.9	(0.05)	(59.1)	0.08	20.8	(0.08)	(57.2)	0.07	21.8	(0.13)	(56.2)
31	Tanjung Pandan	2.8° S	107.6° E	0.07	335.0	0.07	133.6	(0.01)	(21.4)	0.04	142.5	(0.26)	(12.5)	0.04	149.6	(0.24)	(5.4)
32	Cirebon	6.7° S	108.6° E	0.1	183.0	0.04	117.3	(0.40)	(65.7)	0.03	179.0	(0.60)	(4.0)	0.03	152.4	(0.57)	(30.6)
35	Penagi (Ranai)	3.89° S	108.4° E	0.11	250.0	0.16	255.3	0.15	5.3	0.11	256.8	(0.01)	6.8	0.11	256.5	(0.00)	6.5
36	Pemangkat	01.2° S	109.0° E	0.12	218.0	0.16	255.3	0.11	37.3	0.11	256.8	(0.04)	38.8	0.11	256.5	(0.04)	38.5
K_1																	
4	Kuala Tanjung	3.4° N	99.5° E	0.17	359.0	0.18	215.1	0.02	(143.9)	0.21	225.0	0.08	(134.0)	0.20	225.8	0.07	(133.2)
11	Bagan Siapi-Api	2.2° N	100.6° E	0.18	332.0	0.17	249.9	(0.02)	(82.1)	0.21	258.1	0.07	(73.9)	0.20	262.3	0.05	(69.7)
17	Pasir Panjang	1.13° N	103.3° E	0.26	210.0	0.10	49.7	(0.41)	(160.3)	0.13	61.6	(0.30)	(148.4)	0.12	61.0	(0.35)	(149.0)
20	Batu Ampar	1.17° N	104.0° E	0.29	260.0	0.11	349.4	(0.41)	89.4	0.13	6.6	(0.35)	(73.4)	0.12	0.6	(0.38)	(79.4)
21	Singapura	1.3° N	103.9° E	0.29	259.0	0.11	352.2	(0.41)	93.2	0.13	10.7	(0.34)	(68.3)	0.12	3.1	(0.38)	(75.9)
22	Selat Kijang	1.8° N	104.6° E	**0.35**	259.0	0.26	318.3	(0.13)	59.3	0.28	330.2	(0.09)	71.2	0.29	325.4	(0.07)	66.4
23	Tarempa	3.9° N	106.7° E	**0.38**	11.0	0.38	250.0	0.00	59.0	0.42	259.0	0.04	68.0	0.44	259.6	0.06	68.6
24	Muntok	2° 5' N	105.16° E	**0.94**	207.0	0.64	55.7	(0.16)	(151.3)	0.71	65.0	(0.12)	(142.0)	0.64	67.0	(0.16)	(140.0)
28	Bakauhuni	5.9° N	105.8° E	0.08	171.0	0.17	66.7	0.32	(104.3)	0.18	80.6	0.34	(90.4)	0.18	80.7	0.35	(90.3)
29	Suralaya	5.87° S	106.03° E	**0.12**	201.0	0.18	60.3	0.17	(140.7)	0.19	72.7	0.20	(128.3)	0.20	72.8	0.21	(128.2)
31	Tanjung Pandan	2.8° S	107.6° E	**0.72**	221.0	0.49	23.0	(0.16)	(18.0)	0.55	33.4	(0.12)	(7.6)	0.53	32.0	(0.13)	(9.0)
32	Cirebon	6.7° S	108.6° E	**0.14**	312.0	0.21	284.8	0.19	(27.2)	0.23	296.3	0.22	(15.7)	0.25	293.3	0.25	(18.7)
35	Penagi (Ranai)	3.89° S	108.4° E	**0.4**	32.0	0.30	215.1	(0.13)	3.1	0.34	224.1	(0.08)	12.1	0.34	226.1	(0.07)	14.1
36	Pemangkat	01.2° S	109.0° E	0.13	305.0	0.30	215.1	0.36	(89.9)	0.34	224.1	0.41	(80.9)	0.34	226.1	0.42	(78.9)
O_1																	
4	Kuala Tanjung	3.4° N	99.5° E	0.03	153.0	0.05	299.5	0.24	146.5	0.05	136.5	0.21	(16.5)	0.05	166.0	0.21	13.0
11	Bagan Siapi-Api	2.2° N	100.6° E	0.04	162.0	0.05	329.7	0.13	167.7	0.04	165.6	0.02	3.6	0.04	206.7	0.05	44.7
17	Pasir Panjang	1.13° N	103.3° E	0.26	253.0	0.16	165.8	(0.22)	(87.2)	0.17	357.3	(0.19)	104.3	0.14	22.7	(0.27)	(50.3)
20	Batu Ampar	1.17° N	104.0° E	0.29	314.0	0.15	101.8	(0.29)	(32.2)	0.15	295.9	(0.28)	(18.1)	0.13	316.7	(0.34)	2.7
21	Singapura	1.3° N	103.9° E	0.28	310.0	0.15	104.0	(0.27)	(26.0)	0.15	298.8	(0.26)	(11.2)	0.13	318.6	(0.32)	8.6
22	Selat Kijang	1.8° N	104.6° E	0.34	315.0	0.30	58.1	(0.05)	(76.9)	0.30	251.6	(0.05)	(63.4)	0.30	272.6	(0.06)	(42.4)
23	Tarempa	3.9° N	106.7° E	0.3	50.0	0.29	352.8	(0.01)	122.8	0.29	185.5	(0.01)	135.5	0.31	209.6	0.01	159.6
24	Muntok	2° 5' N	105.16° E	0.58	279.0	0.55	131.1	(0.03)	(147.9)	0.54	322.7	(0.03)	43.7	0.49	350.8	(0.08)	71.8
28	Bakauhuni	5.9° N	105.8° E	0.07	159.0	0.04	233.1	(0.21)	74.1	0.05	73.4	(0.19)	(85.6)	0.04	92.7	(0.23)	(66.3)
29	Suralaya	5.87° S	106.03° E	0.06	214.0	0.04	222.6	(0.21)	8.6	0.04	64.4	(0.18)	(149.6)	0.03	81.0	(0.23)	(133.0)
31	Tanjung Pandan	2.8° S	107.6° E	0.42	281.0	0.33	106.0	(0.10)	(175.0)	0.33	298.9	(0.10)	17.9	0.32	323.1	(0.12)	42.1
32	Cirebon	6.7° S	108.6° E	0.05	205.0	0.09	306.6	0.25	101.6	0.09	139.5	0.27	(65.5)	0.09	174.2	0.26	(30.8)
35	Penagi (Ranai)	3.89° S	108.4° E	0.29	133.0	0.23	324.0	(0.09)	11.0	0.24	156.8	(0.08)	23.8	0.25	182.8	(0.06)	49.8
36	Pemangkat	01.2° S	109.0° E	0.18	353.0	0.23	324.0	0.11	(29.0)	0.24	156.8	0.12	(16.2)	0.25	182.8	0.15	(170.2)

Table 4-3: Mesh Sensitivity validation for the Central Domain

Sta.	Location	Lat	Long	Observation		Coarse				Moderate				Dense			
						Calculation		Error		Calculation		Error		Calculation		Error	
				A	ϕ	A	ϕ	A	ϕ	A	ϕ	A	ϕ	A	ϕ	A	ϕ
				(m)	(deg)	(m)	(deg)			(m)	(deg)			(m)	(deg)		
										M_2							
32	Cirebon	8.61° S	108.66° E	**0.16**	56	0.36	16.4	0.35	(39.6)	0.39	296.9	0.39	60.9	0.41	178.7	0.41	122.7
38	Semarang	6.82° S	110.28° E	0.1	102	0.43	8.0	0.64	(94.0)	0.41	284.8	0.62	2.8	0.50	169.8	0.70	67.8
39	Kota Waringin	3.05° S	111.37° E	0.22	182	0.39	6.9	0.25	(175.1)	0.46	287.3	0.32	105.3	0.47	171.9	0.33	(10.1)
40	Surabaya (West)	6.9° S	112.7° E	0.05	344	0.09	183.6	0.26	(160.4)	0.12	108.7	0.39	(55.3)	0.10	354.9	0.30	10.9
43	Teluk Sampit	3.26° S	113.02° E	**0.49**	211	0.46	289.1	(0.03)	78.1	0.49	236.0	(0.00)	25.0	0.50	93.5	0.01	(117.5)
45	Meneng	8.2°S	114.4° E	**0.54**	91	0.50	79.6	(0.03)	(11.4)	0.46	5.9	(0.07)	(85.1)	0.52	246.1	(0.02)	155.1
46	Barito	3.68° S	114.47° E	0.34	209	0.55	236.6	0.21	27.6	0.59	170.9	0.24	(38.1)	0.63	35.0	0.27	(174.0)
47	Benoa (Bali)	8.7° S	115.2° E	**0.71**	73	0.63	63.0	(0.05)	(10.0)	0.63	346.6	(0.05)	93.6	0.66	229.1	(0.03)	156.1
48	Lembar	8.7° S	116° E	0.27	52	0.39	92.8	0.16	40.8	0.41	14.4	0.18	(37.6)	0.42	258.6	0.19	26.6
50	Sungai Kutai	0.5° N	117.87° E	**0.59**	192	0.49	313.5	(0.08)	121.5	0.50	237.4	(0.07)	45.4	0.52	119.8	(0.06)	(72.2)
54	Sangkulirang	0.7° N	118° E	**0.52**	211	0.50	313.6	(0.02)	102.6	0.51	238.2	(0.01)	27.2	0.52	119.6	(0.00)	(91.4)
55	Biringkasi	4.84° S	119.47° E	0.13	252	0.03	215.4	(0.65)	(36.6)	0.04	266.9	(0.50)	14.9	0.04	6.2	(0.57)	(65.8)
57	Makassar	5.2° S	119.4° E	0.08	297	0.13	137.5	0.21	(159.5)	0.07	36.9	(0.06)	(80.1)	0.15	299.9	0.26	2.9
58	Bima	8.4° S	118.7° E	**0.35**	357	0.40	136.9	0.06	(40.1)	0.42	57.8	0.07	(119.2)	0.43	302.1	0.09	(54.9)
										S_2							
32	Cirebon	8.61° S	108.66° E	0.1	183	0.35	251.3	0.54	68.3	0.34	271.5	0.53	88.5	0.31	255.4	0.49	72.4
38	Semarang	6.82° S	110.28° E	0.08	203	0.43	239.0	0.73	36.0	0.36	255.8	0.65	52.8	0.38	243.0	0.68	40.0
39	Kota Waringin	3.05° S	111.37° E	0.06	244	0.39	235.9	0.81	(8.1)	0.41	255.9	0.83	11.9	0.36	243.3	0.78	(0.7)
40	Surabaya (West)	6.9° S	112.7° E	0.08	4	0.12	81.2	0.16	77.2	0.13	96.7	0.20	92.7	0.11	86.8	0.15	82.8
43	Teluk Sampit	3.26° S	113.02° E	0.11	307	0.43	137.1	0.59	(169.9)	0.38	182.6	0.54	(124.4)	0.37	148.5	0.52	(158.5)
45	Meneng	8.2°S	114.4° E	0.29	35	0.20	53.3	(0.17)	18.3	0.19	42.2	(0.17)	7.2	0.22	46.7	(0.13)	11.7
46	Barito	3.68° S	114.47° E	0.05	279	0.54	83.4	1.03	(15.6)	0.52	119.6	1.02	(159.4)	0.47	86.1	0.98	(12.9)
47	Benoa (Bali)	8.7° S	115.2° E	0.33	5	0.27	75.5	(0.08)	70.5	0.22	69.6	(0.18)	64.6	0.26	65.0	(0.10)	60.0
48	Lembar	8.7° S	116° E	0.16	43	0.16	27.6	0.01	(15.4)	0.17	31.5	0.02	(11.5)	0.18	30.5	0.05	(12.5)
50	Sungai Kutai	0.5° N	117.87° E	**0.43**	136	0.41	311.1	(0.02)	175.1	0.34	308.9	(0.10)	172.9	0.38	304.0	(0.05)	168.0
54	Sangkulirang	0.7° N	118° E	**0.34**	154	0.41	311.0	0.08	157.0	0.34	308.0	(0.00)	154.0	0.38	304.1	0.05	150.1
55	Biringkasi	4.84° S	119.47° E	0.17	144	0.35	314.5	0.31	170.5	0.33	321.9	0.28	177.9	0.31	312.4	0.26	168.4
57	Makassar	5.2° S	119.4° E	0.11	165	0.27	311.4	0.38	146.4	0.29	323.1	0.41	158.1	0.23	311.9	0.32	146.9
58	Bima	8.4° S	118.7° E	0.1	305	0.11	275.3	0.02	(29.7)	0.07	297.1	(0.14)	(7.9)	0.06	278.8	(0.20)	(26.2)
										K_1							
32	Cirebon	8.61° S	108.66° E	**0.14**	312	0.14	300.4	0.00	(11.6)	0.16	312.2	0.07	0.2	0.13	302.9	(0.03)	(9.1)
38	Semarang	6.82° S	110.28° E	**0.22**	7	0.23	252.6	0.01	65.6	0.26	269.6	0.07	82.6	0.22	255.3	0.00	68.3
39	Kota Waringin	3.05° S	111.37° E	**0.36**	34	0.34	231.6	(0.02)	17.6	0.42	246.1	0.07	32.1	0.34	235.4	(0.02)	21.4
40	Surabaya (West)	6.9° S	112.7° E	**0.54**	43	0.53	215.2	(0.01)	172.2	0.58	228.8	0.03	5.8	0.51	220.2	(0.03)	177.2
43	Teluk Sampit	3.26° S	113.02° E	**0.6**	24	0.68	230.7	0.05	26.7	0.75	254.1	0.10	50.1	0.66	237.0	0.04	33.0
45	Meneng	8.2°S	114.4° E	0.32	87	0.30	163.8	(0.02)	76.8	0.35	181.7	0.03	94.7	0.28	171.6	(0.05)	84.6
46	Barito	3.68° S	114.47° E	**0.64**	20	0.65	222.7	0.00	22.7	0.74	241.5	0.06	41.5	0.61	226.9	(0.02)	26.9
47	Benoa (Bali)	8.7° S	115.2° E	0.25	59	0.27	151.7	0.03	92.7	0.30	164.3	0.08	105.3	0.25	157.5	0.00	98.5
48	Lembar	8.7° S	116° E	0.36	76	0.32	170.7	(0.05)	94.7	0.35	183.2	(0.01)	107.2	0.30	177.8	(0.09)	101.8
50	Sungai Kutai	0.5° N	117.87° E	0.24	73	0.23	138.9	(0.02)	65.9	0.26	150.0	0.03	77.0	0.21	145.0	(0.06)	72.0
54	Sangkulirang	0.7° N	118° E	0.19	69	0.23	138.3	0.08	69.3	0.26	148.1	0.14	79.1	0.21	145.0	0.04	76.0
55	Biringkasi	4.84° S	119.47° E	**0.32**	65	0.33	165.8	0.01	100.8	0.36	174.7	0.05	109.7	0.31	172.5	(0.02)	107.5
57	Makassar	5.2° S	119.4° E	**0.28**	59	0.33	167.6	0.07	108.6	0.37	177.6	0.12	118.6	0.31	173.7	0.04	114.7
58	Bima	8.4° S	118.7° E	**0.3**	56	0.35	174.9	0.07	118.9	0.39	187.2	0.11	131.2	0.32	181.0	0.03	125.0
										O_1							
32	Cirebon	8.61° S	108.66° E	0.05	205	0.11	163.7	0.34	(41.3)	0.11	73.2	0.34	(131.8)	0.11	163.6	0.33	(41.4)
38	Semarang	6.82° S	110.28° E	0.08	128	0.17	195.0	0.33	67.0	0.16	104.8	0.30	(23.2)	0.17	196.1	0.33	68.1
39	Kota Waringin	3.05° S	111.37° E	0.16	131	0.27	207.0	0.22	76.0	0.29	116.9	0.26	(14.1)	0.26	208.0	0.22	77.0
40	Surabaya (West)	6.9° S	112.7° E	0.26	101	0.32	217.8	0.10	116.8	0.32	124.7	0.09	23.7	0.32	219.1	0.10	118.1
43	Teluk Sampit	3.26° S	113.02° E	0.31	96	0.40	228.9	0.11	132.9	0.38	143.2	0.09	47.2	0.39	231.9	0.10	135.9
45	Meneng	8.2°S	114.4° E	0.13	117	0.17	208.6	0.11	91.6	0.18	115.0	0.14	(2.0)	0.17	209.8	0.12	92.8
46	Barito	3.68° S	114.47° E	0.33	79	0.38	231.5	0.07	152.5	0.39	141.0	0.07	62.0	0.38	232.9	0.06	153.9
47	Benoa (Bali)	8.7° S	115.2° E	0.12	84	0.14	206.9	0.08	122.9	0.14	111.6	0.07	27.6	0.14	207.2	0.08	123.2
48	Lembar	8.7° S	116° E	0.24	96	0.17	211.8	(0.15)	115.8	0.17	117.2	(0.16)	21.2	0.17	212.7	(0.15)	116.7
50	Sungai Kutai	0.5° N	117.87° E	0.15	111	0.15	179.0	0.00	68.0	0.15	82.7	(0.01)	(28.3)	0.15	179.2	(0.00)	68.2
54	Sangkulirang	0.7° N	118° E	0.19	103	0.15	178.6	(0.10)	75.6	0.15	81.4	(0.11)	(21.6)	0.15	179.4	(0.11)	76.4
55	Biringkasi	4.84° S	119.47° E	0.2	95	0.17	204.2	(0.07)	109.2	0.16	105.4	(0.09)	10.4	0.17	204.8	(0.07)	109.8
57	Makassar	5.2° S	119.4° E	0.17	90	0.16	207.0	(0.01)	117.0	0.17	109.1	(0.01)	19.1	0.16	208.1	(0.02)	118.1
58	Bima	8.4° S	118.7° E	0.1	104	0.16	216.9	0.19	112.9	0.15	122.6	0.18	18.6	0.16	217.6	0.19	113.6

Although the coarse mesh in the western domain gives a better average RMS error of amplitude than other meshes, the phase lags are better in the moderate mesh in general than the coarse mesh. For instance, stations in the Malacca strait (Stations 4 and 11), and Riau Archipelago (Stations 17, 20, 21 and 22) have a relatively similar agreement in term of amplitude in both coarse and moderate mesh (see Table 4-2).

Table 4-4: Mesh Sensitivity validation for the Eastern Domain

Sta.	Location	Lat	Long	Observation		Coarse				Moderate				Dense			
						Calculation		Error		Calculation		Error		Calculation		Error	
				A	*ϕ*	*A*	*ϕ*	*A*	*ϕ*	*A*	*ϕ*	*A*	*ϕ*	*A*	*ϕ*	*A*	*ϕ*
				(m)	(deg)	(m)	(deg)			(m)	(deg)			(m)	(deg)		
									M_2								
65	Muotong	00.4^o N	121.23^o E	**0.25**	249.0	0.27	247.7	0.03	(1.3)	0.20	152.9	(0.09)	(96.1)	0.44	169.1	0.25	(79.9)
66	Gorontalo	00.5^o N	123.05^o E	**0.22**	251.0	0.22	247.6	(0.01)	(3.4)	0.17	152.7	(0.12)	(98.3)	0.36	169.2	0.21	(81.8)
67	Kolaka	04.0^o S	121.58^o E	**0.55**	355.0	0.69	149.1	0.10	(25.9)	0.72	70.3	0.11	(104.7)	0.56	312.1	0.01	(42.9)
72	Bitung	1.5° N	125.2° E	**0.36**	214.0	0.32	297.9	(0.04)	83.9	0.28	222.8	(0.11)	8.8	0.48	153.1	0.13	(60.9)
74	Ternate	00.8° N	127.4° E	**0.27**	185.0	0.29	291.7	0.03	106.7	0.24	216.6	(0.04)	31.6	0.40	133.6	0.17	(51.4)
75	Ambon	03.7° S	128.2° E	**0.47**	318.0	0.74	162.1	0.20	(155.9)	0.80	80.4	0.23	(57.6)	0.40	313.5	(0.07)	(4.5)
76	Sorong	00.8° S	131.2° E	**0.41**	165.0	0.51	317.4	0.10	152.4	0.50	242.0	0.09	77.0	0.55	141.2	0.13	(23.8)
77	Fak-Fak	02.9° S	132.3° E	**0.4**	327.0	0.86	170.8	0.33	(156.2)	0.93	88.3	0.37	(58.7)	0.42	322.1	0.02	(4.9)
78	Tual	05.6° S	132.7° E	**0.44**	324.0	0.89	169.7	0.31	(154.3)	0.97	87.2	0.34	(56.8)	0.47	317.2	0.03	(6.8)
80	Dobo	05.8° S	134.2° E	**0.61**	319.0	0.94	173.1	0.19	(145.9)	1.02	90.9	0.22	(48.1)	0.47	320.6	(0.11)	1.6
83	Aiduna	04.5° S	135.3° E	**0.45**	155.0	0.83	192.4	0.27	37.4	0.86	110.6	0.28	(44.4)	0.37	335.7	(0.09)	0.7
87	Sungai Digul	07.1° S	138.7° E	1.22	66.0	1.26	116.5	0.01	50.5	1.35	32.2	0.04	(33.8)	0.32	172.3	(0.58)	106.3
88	Selat Muli	08.1° S	138.9° E	**1.84**	22.0	1.05	165.0	(0.24)	143.0	1.00	76.4	(0.26)	54.4	0.06	52.5	(1.46)	30.5
90	Merauke	08.5° S	140.4° E	**1.13**	340.0	1.43	168.5	0.10	(171.5)	1.43	84.3	0.10	(75.7)	0.48	207.6	(0.37)	(132.4)
									S_2								
65	Muotong	00.4^o N	121.23^o E	0.17	192.0	0.29	290.9	0.23	98.9	0.38	280.4	0.35	88.4	0.33	306.0	0.29	114.0
66	Gorontalo	00.5^o N	123.05^o E	0.22	188.0	0.23	290.7	0.02	102.7	0.30	279.8	0.14	91.8	0.26	306.1	0.08	118.1
67	Kolaka	04.0^o S	121.58^o E	0.14	292.0	0.12	210.5	(0.07)	(81.5)	0.17	183.4	0.09	(108.6)	0.14	144.0	0.01	(148.0)
72	Bitung	1.5° N	125.2° E	0.26	169.0	0.23	297.8	(0.06)	128.8	0.30	288.9	0.07	119.9	0.31	303.1	0.07	134.1
74	Ternate	00.8° N	127.4° E	0.22	148.0	0.22	296.6	(0.00)	148.6	0.29	287.3	0.12	139.3	0.29	292.4	0.11	144.4
75	Ambon	03.7° S	128.2° E	0.17	250.0	0.09	225.2	(0.26)	(24.8)	0.16	201.3	(0.02)	(48.7)	0.09	149.6	(0.26)	(100.4)
76	Sorong	00.8° S	131.2° E	0.18	150.0	0.18	307.5	(0.01)	157.5	0.24	299.6	0.13	149.6	0.25	302.3	0.15	152.3
77	Fak-Fak	02.9° S	132.3° E	0.22	230.0	0.12	236.6	(0.28)	6.6	0.19	213.9	(0.06)	(16.1)	0.10	164.7	(0.32)	(65.3)
78	Tual	05.6° S	132.7° E	0.22	249.0	0.11	226.2	(0.30)	(22.8)	0.19	204.7	(0.06)	(44.3)	0.12	149.3	(0.26)	(99.7)
80	Dobo	05.8° S	134.2° E	0.19	240.0	0.12	229.2	(0.21)	(10.8)	0.21	208.3	0.03	(31.7)	0.12	152.9	(0.19)	(87.1)
83	Aiduna	04.5° S	135.3° E	0.11	122.0	0.10	254.7	(0.04)	132.7	0.19	228.3	0.23	106.3	0.10	169.4	(0.05)	47.4
87	Sungai Digul	07.1° S	138.7° E	0.31	338.0	0.30	202.1	(0.01)	(135.9)	0.39	156.2	0.10	(1.8)	0.12	352.2	(0.40)	14.2
88	Selat Muli	08.1° S	138.9° E	0.8	298.0	0.18	268.5	(0.65)	(29.5)	0.23	216.7	(0.54)	(81.3)	0.02	212.2	(1.70)	(85.8)
90	Merauke	08.5° S	140.4° E	0.46	237.0	0.18	241.9	(0.42)	4.9	0.33	207.7	(0.14)	(29.3)	0.07	309.6	(0.80)	72.6
									K_1								
65	Muotong	00.4^o N	121.23^o E	**0.22**	75.0	0.25	153.7	0.05	78.7	0.14	119.6	(0.19)	44.6	0.12	80.1	(0.28)	5.1
66	Gorontalo	00.5^o N	123.05^o E	**0.19**	77.0	0.24	153.7	0.10	76.7	0.14	119.4	(0.15)	42.4	0.11	80.0	(0.24)	3.0
67	Kolaka	04.0^o S	121.58^o E	**0.34**	59.0	0.40	187.8	0.07	128.8	0.24	152.6	(0.16)	93.6	0.18	106.3	(0.28)	47.3
72	Bitung	1.5° N	125.2° E	**0.28**	102.0	0.20	137.2	(0.14)	35.2	0.11	102.6	(0.39)	0.6	0.10	65.8	(0.46)	(36.2)
74	Ternate	00.8° N	127.4° E	0.14	91.0	0.19	138.1	0.14	47.1	0.11	104.9	(0.11)	13.9	0.06	96.2	(0.38)	5.2
75	Ambon	03.7° S	128.2° E	0.29	36.0	0.39	183.7	0.13	147.7	0.23	150.3	(0.11)	114.3	0.16	119.2	(0.27)	83.2
76	Sorong	00.8° S	131.2° E	0.23	134.0	0.21	78.0	(0.04)	(56.0)	0.12	43.2	(0.29)	(90.8)	0.05	281.4	(0.71)	147.4
77	Fak-Fak	02.9° S	132.3° E	0.19	9.0	0.41	186.5	0.33	177.5	0.24	152.8	0.09	143.8	0.16	122.5	(0.07)	113.5
78	Tual	05.6° S	132.7° E	0.18	32.0	0.42	188.9	0.37	156.9	0.25	155.7	0.13	123.7	0.18	119.4	(0.01)	87.4
80	Dobo	05.8° S	134.2° E	0.28	35.0	0.44	191.9	0.20	156.9	0.25	159.3	(0.04)	124.3	0.17	124.2	(0.22)	89.2
83	Aiduna	04.5° S	135.3° E	**0.37**	336.0	0.50	224.3	0.13	(111.7)	0.31	189.1	(0.08)	(146.9)	0.08	142.5	(0.67)	(13.5)
87	Sungai Digul	07.1° S	138.7° E	**1.3**	291.0	1.24	331.8	(0.02)	40.8	0.80	294.0	(0.21)	3.0	0.18	178.2	(0.86)	(112.8)
88	Selat Muli	08.1° S	138.9° E	1.12	265.0	0.72	1.7	(0.19)	(83.3)	0.45	329.1	(0.39)	64.1	0.02	41.7	(1.68)	(43.3)
90	Merauke	08.5° S	140.4° E	0.8	215.0	0.64	0.3	(0.10)	(34.7)	0.42	325.0	(0.28)	110.0	0.12	273.1	(0.84)	58.1
									O_1								
65	Muotong	00.4^o N	121.23^o E	0.14	114.0	0.13	154.6	(0.02)	40.6	0.10	338.7	(0.13)	44.7	0.10	58.6	(0.14)	(55.4)
66	Gorontalo	00.5^o N	123.05^o E	0.14	106.0	0.13	154.5	(0.04)	48.5	0.10	338.5	(0.15)	52.5	0.10	58.3	(0.15)	(47.7)
67	Kolaka	04.0^o S	121.58^o E	0.22	83.0	0.16	192.8	(0.14)	109.8	0.13	16.6	(0.24)	(66.4)	0.11	91.1	(0.30)	8.1
72	Bitung	1.5° N	125.2° E	0.14	134.0	0.12	141.7	(0.07)	7.7	0.09	325.9	(0.17)	11.9	0.10	48.1	(0.16)	(85.9)
74	Ternate	00.8° N	127.4° E	0.1	112.0	0.12	142.1	0.06	30.1	0.09	326.8	(0.05)	34.8	0.06	57.9	(0.22)	(54.1)
75	Ambon	03.7° S	128.2° E	0.21	47.0	0.17	187.4	(0.09)	140.4	0.13	12.3	(0.20)	(34.7)	0.10	96.9	(0.32)	49.9
76	Sorong	00.8° S	131.2° E	0.13	187.0	0.12	98.3	(0.03)	(88.7)	0.10	282.9	(0.13)	95.9	0.02	334.4	(0.73)	147.4
77	Fak-Fak	02.9° S	132.3° E	0.15	76.0	0.18	189.3	0.08	113.3	0.14	13.8	(0.02)	(62.2)	0.10	98.4	(0.17)	22.4
78	Tual	05.6° S	132.7° E	0.12	37.0	0.18	192.3	0.19	155.3	0.15	17.5	0.09	(19.5)	0.11	96.4	(0.04)	59.4
80	Dobo	05.8° S	134.2° E	0.17	54.0	0.19	194.4	0.06	140.4	0.15	20.6	(0.05)	(33.4)	0.10	101.1	(0.21)	47.1
83	Aiduna	04.5° S	135.3° E	0.21	19.0	0.22	220.4	0.03	21.4	0.20	45.7	(0.03)	26.7	0.06	102.9	(0.58)	83.9
87	Sungai Digul	07.1° S	138.7° E	1.14	338.0	0.51	331.4	(0.35)	(6.6)	0.53	142.6	(0.33)	(15.4)	0.04	155.3	(1.42)	(2.7)
88	Selat Muli	08.1° S	138.9° E	1.14	306.0	0.30	355.7	(0.59)	49.7	0.28	170.3	(0.61)	(135.7)	0.02	335.8	(1.78)	29.8
90	Merauke	08.5° S	140.4° E	0.5	283.0	0.25	346.9	(0.30)	63.9	0.25	164.8	(0.30)	(118.2)	0.10	191.8	(0.72)	(91.2)

However, the phase lags in those stations fall into the poor category in the coarse mesh. Since the difference between the coarse mesh and moderate mesh in the western domain is relatively small, the moderate mesh is selected for the resource assessment analysis in the western domain. The moderate mesh is preferable for the central domain (see Table 4-3). In general, the moderate mesh has a relatively better agreement for amplitudes and phase legs in this domain. The moderate mesh has approximate 30,000 elements and 11,000 nodes. With these numbers, the simulation could be run with reasonable computation time.

Table 4-5: Summary of root mean square errors for all domains

	Coarse		Moderate		Dense	
	A	ϕ	A	ϕ	A	ϕ
Western Domain						
M_2	0.20	97.64	0.22	48.87	0.22	51.80
S_2	0.18	73.62	0.29	84.47	0.29	77.66
K_1	0.21	87.27	0.21	53.96	0.21	80.11
O_1	0.16	86.17	0.17	53.96	0.17	63.23
Central Domain						
M_2	0.21	79.40	0.21	50.36	0.23	79.67
S_2	0.34	57.11	0.35	81.60	0.33	70.40
K_1	0.03	94.35	0.07	81.37	0.03	85.60
O_1	0.12	83.83	0.07	81.37	0.12	102.91
Eastern Domain						
M_2	0.14	99.16	0.17	60.41	0.26	44.89
S_2	0.18	77.57	0.15	75.51	0.34	98.81
K_1	0.14	95.15	0.19	79.71	0.50	60.37
O_1	0.14	72.60	0.18	53.71	0.50	56.07

The coarse mesh, in general, shows better performance in amplitude than other meshes in the eastern domain (see Table 4-4). However, the moderate mesh shows slightly better agreement in phase lags than the coarse mesh. Since the assessment requires a significant number of simulations, this consideration is taken into account before selecting the mesh density. As the coarse mesh has significantly fewer elements and nodes than the moderate mesh, the coarse mesh is preferred for this domain.

4.5.2 Bed Friction Tuning

After the meshes are selected, the next step is to tune the bed friction. As shown in Chapter 2, the SWE model is sensitive to bed friction. The models are tuned here to achieve a better agreement with the data. For clarity, the selected meshes used in the analyses are enlarged here. The selected meshes for the western domain, the central domain, and the eastern domain are shown in Figure 4-14, Figure 4-15, Figure 4-16, respectively.

This bed friction tuning uses similar categorisation for the good and poor agreement as the mesh sensitivity study, discussed in section 4.5.1. Similar stations for each domain are also used in this analysis. Different values of bed friction (*Cf*) are examined, the aim being to improve agreement with the observed data. For simplicity, this thesis only shows the results of three different bed frictions for each domain.

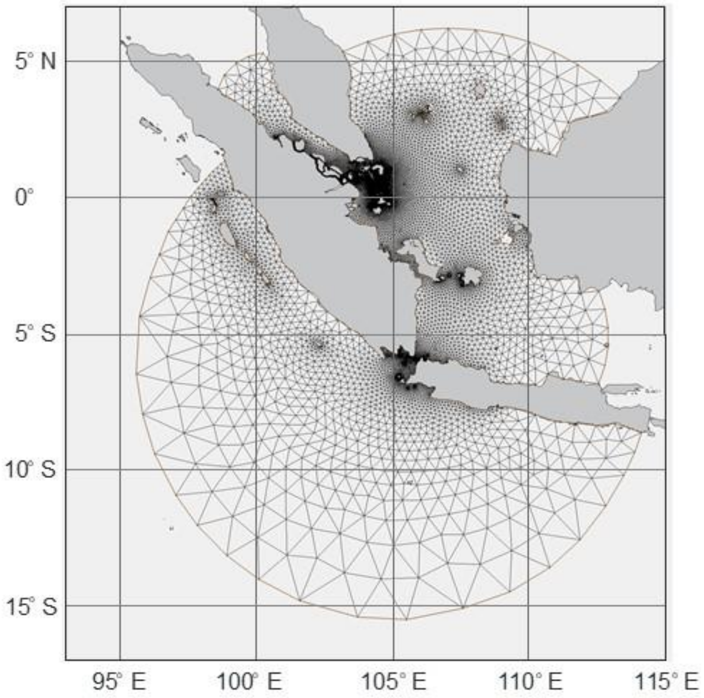

Figure 4-14: The selected mesh (moderate mesh) for the Western Domain.

The validation results for the western domain, as shown in Table 4-6, compared the bed friction *Cf* = 0.0015, *Cf* = 0.0025 and *Cf* = 0.0030. Tuning bed friction to get a satisfactory agreement in this domain is challenging suggesting that inaccuracies in friction are not the key factor in model inaccuracy. In some locations and components, the low bed friction might give a better agreement than high bed friction. However, in other cases, the high friction gives better agreement. The poor agreements for M_2 in this domain are mainly located in the Java Sea (stations 32, 35 and 36), near the model boundary (BC2). However, station 35, Penagi, shows better agreement at high bed friction. Between these stations, only station 36 shows poor agreement against K_1. The validation data shows that the model has a better agreement for M_2 in the case of high friction (*Cf* = 0.0030) for the stations in the Malacca straits (Stations 4 and11), while in Riau Archipelago (Stations 17, 20, 21 and 22) better agreement is obtained at low bed friction (*Cf* = 0.0015).

The stations in Riau Archipelago are close to the Lingga Regency site. The validation also shows a good agreement at station 28, one of the closest locations for the potential site in the Sunda Strait. While station 29, also close to the Sunda strait, has a poor agreement for the M_2 constituent. However, this station has a better agreement with the data for K_1. This station has the M_2 and K_1 components at the same amplitude. Therefore, *Cf* = 0.0015 is used for this domain.

The simulations in the central domain show the tendency towards good agreement at higher friction. Therefore, the bed friction values *Cf* = 0.0020, *Cf* = 0.0025 and *Cf* = 0.0035 are compared here. The validation in the central domain shows a better agreement for diurnal components (K_1 and O_1) than the semidiurnal components (M_2 and S_2), as shown in Table 4-7. The validation for K_1 meets the category of good agreement for all stations in this domain. The diurnal components also show a better agreement at high bed friction (*Cf* = 0.0035) than at low friction (*Cf* = 0.0020). Poor agreement for M_2 is shown in the area of Java Sea (stations 32, 38, 39 and 40). These stations are located in relatively shallow water. Although, these stations show better agreement with the data in K_1, the poor agreement at some stations for M_2 can be explained in term of the station locations. The Admiralty data might not show an accurate coordinate position, since the data are usually specified to one minute of arc. It is essential to look in detail at the station's location for this validation.

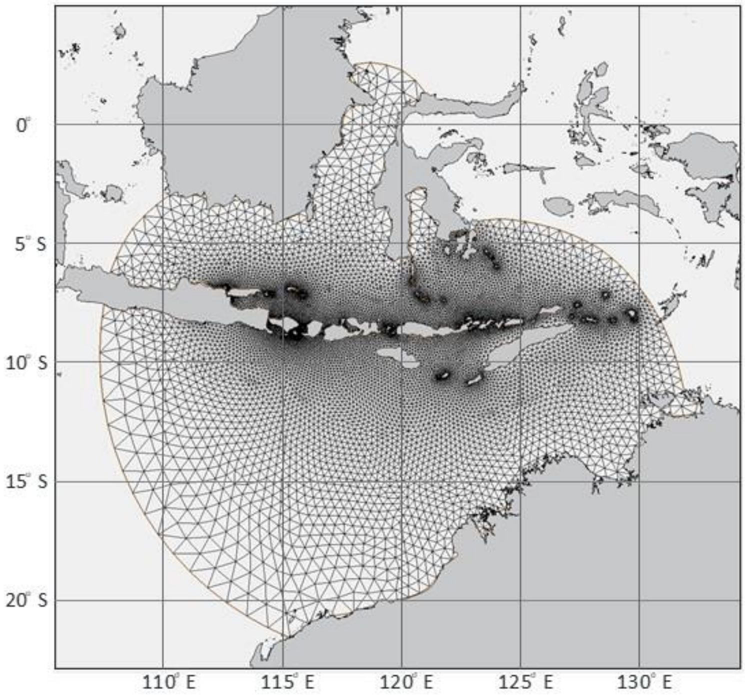

Figure 4-15: The selected (moderate mesh) mesh for the Central Domain

Since this admiralty data is for navigational purpose, the stations are mainly located in the area of ports or navigation channels. Some of the stations at ports are located in river channels (e.g. stations 35, 40, 43 and 50) where the tidal characteristics may differ significantly from those in the adjacent open sea, which is modelled in the analysis. The precise location for station 45 is unknown since the eastern navigation channel of Surabaya is 70 miles long. Station 40 is close to an *amphidromic* point. Therefore, unsatisfactory validation for the station in this area can be expected.

The eastern domain shows that the validation in amplitude is improved significantly at high bed friction (see Table 4-8). This improvement here shown by the increasing number of stations that have a good agreement category in the high bed friction. The poor agreement is mostly in the stations located on the Papua coast (station 77, 78, and 88). Station 77, Fak-fak, is located in an enclosed estuary that is not detailed in this model. Station 78, Aiduna, is in a river estuary that is also not detailed in the model. Station 88 (Selat Muli) is located in a narrow strait between Muli island and the main island of Papua. The model uses regional bathymetry data that might be inaccurate for these narrow straits.

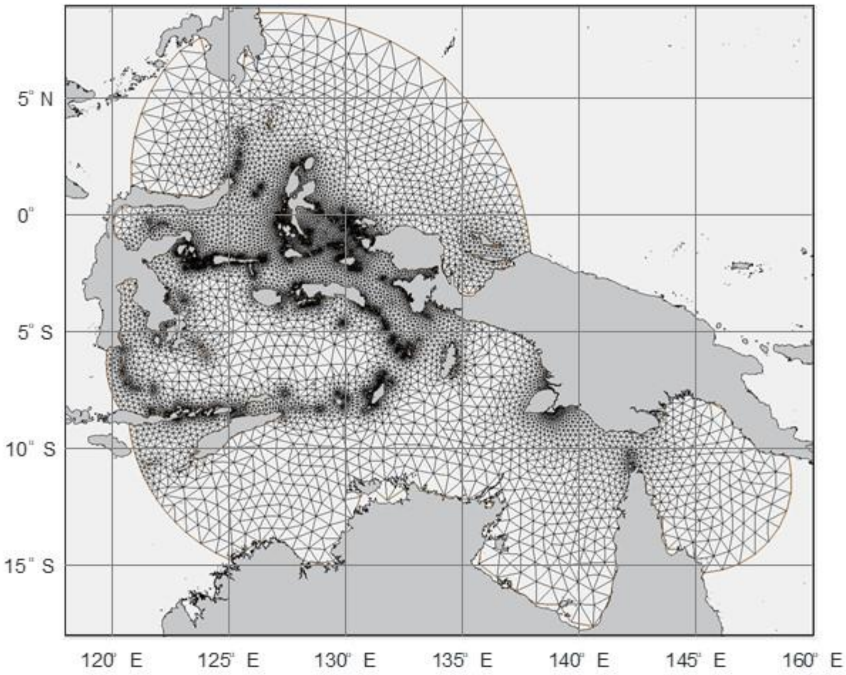

Figure 4-16: The selected (coarse) Mesh for the Eastern Domain

It can be concluded the models have relatively good agreement in term of amplitude. However, the phase lag does not have as good agreement as amplitude does. Bed friction adjustment creates a dilemma in the tuning process. A high friction makes the phase in some stations fall into the category of poor agreement, which also occurs in other domains as well.

An explanation of this poor agreement could be related to the time reference. The DISHIDROS 2004 data uses a local time reference, while the Le Provost model uses Greenwich Mean Time (GMT) as reference. The local time reference is problematic for the model with a large domain as used here. Indonesia has three different local time zones, WIB in Sumatra and Java with GMT +7, WITA in Borneo, Sulawesi, Bali and Nusa Tenggara with GMT +8 and WIT for Maluku and Papua with GMT +9. There is a possible discrepancy related to time reference which it has not been possible to resolve. Further validation is carried out to assess this inaccuracy.

Table 4-6: Bed friction tuning for the Western Domain

Sta.	Location	Lat	Long	Data		*Cf* =0.0015				*Cf* =0.0025				*Cf* =0.0030			
						Calculation		Error		Calculation		Error		Calculation		Error	
				A (m)	*ϕ* (deg)	*A* (m)	*ϕ* (deg)	*A*	*ϕ*	*A* (m)	*ϕ* (deg)	*A*	*ϕ*	*A* (m)	*ϕ* (deg)	*A*	*ϕ*
M_2																	
4	Kuala Tanjung	3.4° N	99.5° E	**0.8**	281.0	1.02	177.1	0.11	(103.9)	1.01	172.9	0.10	(108.1)	1.00	171.7	0.10	(109.3)
11	Bagan Siapi-Api	2.2° N	100.6° E	**1.7**	226.0	2.20	252.3	0.11	26.3	1.87	255.7	0.04	29.7	1.75	257.3	0.01	31.3
17	Pasir Panjang	1.13° N	103.3° E	**0.94**	62.0	0.95	78.5	0.00	16.5	0.69	78.9	(0.13)	16.9	0.61	79.2	(0.19)	17.2
20	Batu Ampar	1.17° N	104.0° E	**0.76**	61.0	0.73	77.6	(0.02)	16.6	0.53	79.0	(0.16)	18.0	0.47	79.8	(0.21)	18.8
21	Singapura	1.3° N	103.9° E	**0.8**	62.0	0.74	78.7	(0.04)	16.7	0.54	80.1	(0.17)	18.1	0.47	80.9	(0.23)	18.9
22	Selat Kijang	1.8° N	104.6° E	**0.34**	59.0	0.49	37.5	0.16	(21.5)	0.37	34.3	0.04	(24.7)	0.33	33.2	(0.01)	(25.8)
23	Tarempa	3.9° N	106.7° E	0.16	144.0	0.24	13.3	0.18	(130.7)	0.17	9.7	0.03	(134.3)	0.15	8.7	(0.03)	(135.3)
24	Muntok	2° 5' N	105.16° E	0.3	178.0	0.13	213.3	(0.35)	35.3	0.12	189.1	(0.42)	11.1	0.11	182.4	(0.44)	4.4
28	Bakauhuni	5.9° N	105.8° E	**0.2**	138.0	0.31	292.6	0.19	154.6	0.30	297.9	0.18	159.9	0.30	299.5	0.17	161.5
29	Suralaya	5.87° S	106.03° E	**0.12**	161.0	0.29	294.1	0.39	133.1	0.28	300.1	0.37	139.1	0.28	302.0	0.36	141.0
31	Tanjung Pandan	2.8° S	107.6° E	0.08	293.0	0.21	52.6	0.43	(60.4)	0.17	57.8	0.34	(55.2)	0.16	59.9	0.30	(53.1)
32	Cirebon	6.7° S	108.6° E	**0.16**	56.0	0.06	261.5	(0.44)	25.5	0.05	231.6	(0.53)	175.6	0.05	222.8	(0.55)	166.8
35	Penagi (Ranai)	3.89° S	108.4° E	**0.34**	291.0	0.68	203.5	0.30	(87.5)	0.56	200.3	0.22	(90.7)	0.53	199.1	0.19	(91.9)
36	Pemangkat	01.2° S	109.0° E	**0.28**	254.0	0.68	203.5	0.38	(50.5)	0.56	200.3	0.30	(53.7)	0.53	199.1	0.28	(54.9)
S_2																	
4	Kuala Tanjung	3.4° N	99.5° E	0.35	233.0	0.45	246.7	0.11	13.7	0.45	243.7	0.11	10.7	0.44	242.9	0.10	9.9
11	Bagan Siapi-Api	2.2° N	100.6° E	0.9	176.0	0.88	334.5	(0.01)	158.5	0.73	339.4	(0.09)	163.4	0.68	341.5	(0.12)	165.5
17	Pasir Panjang	1.13° N	103.3° E	0.43	9.0	0.31	161.4	(0.14)	152.4	0.22	163.3	(0.30)	154.3	0.19	164.4	(0.36)	155.4
20	Batu Ampar	1.17° N	104.0° E	0.31	4.0	0.20	176.7	(0.19)	172.7	0.14	182.3	(0.33)	178.3	0.13	185.3	(0.39)	1.3
21	Singapura	1.3° N	103.9° E	0.33	9.0	0.21	176.6	(0.20)	167.6	0.15	182.2	(0.35)	173.2	0.13	185.1	(0.40)	176.1
22	Selat Kijang	1.8° N	104.6° E	0.12	4.0	0.07	113.7	(0.21)	109.7	0.05	109.8	(0.36)	105.8	0.04	108.6	(0.43)	104.6
23	Tarempa	3.9° N	106.7° E	0.03	79.0	0.02	88.1	(0.17)	9.1	0.01	101.6	(0.48)	22.6	0.01	118.7	(0.64)	39.7
24	Muntok	2° 5' N	105.16° E	0.16	129.0	0.05	149.8	(0.46)	20.8	0.05	158.3	(0.52)	29.3	0.04	159.5	(0.57)	30.5
28	Bakauhuni	5.9° N	105.8° E	0.11	86.0	0.10	13.3	(0.05)	(72.7)	0.09	17.8	(0.08)	(68.2)	0.09	20.0	(0.11)	(66.0)
29	Suralaya	5.87° S	106.03° E	0.1	78.0	0.09	14.5	(0.02)	(63.5)	0.08	20.8	(0.08)	(57.2)	0.08	23.4	(0.10)	(54.6)
31	Tanjung Pandan	2.8° S	107.6° E	0.07	335.0	0.05	134.0	(0.14)	(21.0)	0.04	142.5	(0.26)	(12.5)	0.03	146.7	(0.31)	(8.3)
32	Cirebon	6.7° S	108.6° E	0.1	183.0	0.03	158.4	(0.58)	(24.6)	0.03	179.0	(0.60)	(4.0)	0.02	182.8	(0.62)	(0.2)
35	Penagi (Ranai)	3.89° S	108.4° E	0.11	250.0	0.12	262.7	0.05	12.7	0.11	256.8	(0.01)	6.8	0.10	254.8	(0.03)	4.8
36	Pemangkat	01.2° S	109.0° E	0.12	218.0	0.12	262.7	0.01	44.7	0.11	256.8	(0.04)	38.8	0.10	254.8	(0.07)	36.8
K_1																	
4	Kuala Tanjung	3.4° N	99.5° E	0.17	359.0	0.21	221.7	0.09	(137.3)	0.21	225.0	0.08	(134.0)	0.20	226.3	0.08	(132.7)
11	Bagan Siapi-Api	2.2° N	100.6° E	0.18	332.0	0.22	249.0	0.10	(83.0)	0.21	258.1	0.07	(73.9)	0.20	261.6	0.06	(70.4)
17	Pasir Panjang	1.13° N	103.3° E	0.26	210.0	0.13	59.0	(0.30)	(151.0)	0.13	61.6	(0.30)	(148.4)	0.13	62.5	(0.30)	(147.5)
20	Batu Ampar	1.17° N	104.0° E	0.29	260.0	0.13	12.1	(0.33)	(67.9)	0.13	6.6	(0.35)	(73.4)	0.13	4.1	(0.35)	(75.9)
21	Singapura	1.3° N	103.9° E	0.29	259.0	0.14	16.0	(0.32)	(63.0)	0.13	10.7	(0.34)	(68.3)	0.13	8.2	(0.35)	(70.8)
22	Selat Kijang	1.8° N	104.6° E	**0.35**	259.0	0.27	335.4	(0.12)	76.4	0.28	330.2	(0.09)	71.2	0.29	328.6	(0.08)	69.6
23	Tarempa	3.9° N	106.7° E	**0.38**	11.0	0.40	255.6	0.02	64.6	0.42	259.0	0.04	68.0	0.43	260.3	0.05	69.3
24	Muntok	2° 5' N	105.16° E	**0.94**	207.0	0.82	60.4	(0.06)	(146.6)	0.71	65.0	(0.12)	(142.0)	0.67	66.6	(0.15)	(140.4)
28	Bakauhuni	5.9° N	105.8° E	0.08	171.0	0.19	80.3	0.38	(90.7)	0.18	80.6	0.34	(90.4)	0.17	81.2	0.33	(89.8)
29	Suralaya	5.87° S	106.03° E	**0.12**	201.0	0.20	73.8	0.22	(127.2)	0.19	72.7	0.20	(128.3)	0.18	72.9	0.19	(128.1)
31	Tanjung Pandan	2.8° S	107.6° E	**0.72**	221.0	0.57	32.8	(0.10)	(8.2)	0.55	33.4	(0.12)	(7.6)	0.54	33.8	(0.13)	(7.2)
32	Cirebon	6.7° S	108.6° E	**0.14**	312.0	0.19	292.1	0.13	(19.9)	0.23	296.3	0.22	(15.7)	0.25	297.3	0.25	(14.7)
35	Penagi (Ranai)	3.89° S	108.4° E	**0.4**	32.0	0.33	219.7	(0.08)	7.7	0.34	224.1	(0.08)	12.1	0.34	225.8	(0.07)	13.8
36	Pemangkat	01.2° S	109.0° E	0.13	305.0	0.33	219.7	0.41	(85.3)	0.34	224.1	0.41	(80.9)	0.34	225.8	0.41	(79.2)
O_1																	
4	Kuala Tanjung	3.4° N	99.5° E	0.03	153.0	0.05	124.6	0.22	(28.4)	0.05	136.5	0.21	(16.5)	0.05	140.3	0.21	(12.7)
11	Bagan Siapi-Api	2.2° N	100.6° E	0.04	162.0	0.04	128.9	0.03	(33.1)	0.04	165.6	0.02	3.6	0.04	175.8	0.02	13.8
17	Pasir Panjang	1.13° N	103.3° E	0.26	253.0	0.21	1.9	(0.08)	(71.1)	0.17	357.3	(0.19)	104.3	0.16	356.0	(0.22)	103.0
20	Batu Ampar	1.17° N	104.0° E	0.29	314.0	0.18	303.6	(0.21)	(10.4)	0.15	295.9	(0.28)	(18.1)	0.14	292.6	(0.30)	(21.4)
21	Singapura	1.3° N	103.9° E	0.28	310.0	0.18	306.2	(0.18)	(3.8)	0.15	298.8	(0.26)	(11.2)	0.15	295.7	(0.28)	(14.3)
22	Selat Kijang	1.8° N	104.6° E	0.34	315.0	0.33	257.3	(0.02)	(57.7)	0.30	251.6	(0.05)	(63.4)	0.30	249.4	(0.06)	(65.6)
23	Tarempa	3.9° N	106.7° E	0.3	50.0	0.28	186.4	(0.04)	136.4	0.29	185.5	(0.01)	135.5	0.30	185.4	(0.00)	135.4
24	Muntok	2° 5' N	105.16° E	0.58	279.0	0.65	318.1	0.05	39.1	0.54	322.7	(0.03)	43.7	0.50	324.4	(0.06)	45.4
28	Bakauhuni	5.9° N	105.8° E	0.07	159.0	0.06	70.6	(0.04)	(88.4)	0.05	73.4	(0.19)	(85.6)	0.04	75.9	(0.23)	(83.1)
29	Suralaya	5.87° S	106.03° E	0.06	214.0	0.06	66.7	0.00	(147.3)	0.04	64.4	(0.18)	(149.6)	0.03	65.8	(0.25)	(148.2)
31	Tanjung Pandan	2.8° S	107.6° E	0.42	281.0	0.34	298.9	(0.09)	17.9	0.33	298.9	(0.10)	17.9	0.32	299.0	(0.11)	18.0
32	Cirebon	6.7° S	108.6° E	0.05	205.0	0.11	111.8	0.35	(93.2)	0.09	139.5	0.27	(65.5)	0.09	150.1	0.27	(54.9)
35	Penagi (Ranai)	3.89° S	108.4° E	0.29	133.0	0.23	155.8	(0.11)	22.8	0.24	156.8	(0.08)	23.8	0.24	157.2	(0.07)	24.2
36	Pemangkat	01.2° S	109.0° E	0.18	353.0	0.23	155.8	0.10	(17.2)	0.24	156.8	0.12	(16.2)	0.24	157.2	0.13	(15.8)

Table 4-7: Bed friction tuning for the Central Domain

Sta.	Location	Lat	Long	Observation		*Cf* =0.0020				*Cf* =0.0025				*Cf* =0.0035			
						Calculation		Error		Calculation		Error		Calculation		Error	
				A (m)	ϕ (deg)	*A* (m)	ϕ (deg)	*A*	ϕ	*A* (m)	ϕ (deg)	*A*	ϕ	*A* (m)	ϕ (deg)	*A*	ϕ
											M_2						
32	Cirebon	8.61° S	108.66° E	**0.16**	56	0.43	298.5	0.43	62.5	0.39	296.9	0.39	60.9	0.33	294.5	0.32	58.5
38	Semarang	6.82° S	110.28° E	0.1	102	0.46	286.8	0.66	4.8	0.41	284.8	0.62	2.8	0.35	281.9	0.54	179.9
39	Kota Waringin	3.05° S	111.37° E	0.22	182	0.51	288.7	0.37	106.7	0.46	287.3	0.32	105.3	0.40	285.4	0.26	103.4
40	Surabaya (West)	6.9° S	112.7° E	0.05	344	0.12	106.5	0.37	(57.5)	0.12	108.7	0.39	(55.3)	0.12	111.4	0.39	(52.6)
43	Teluk Sampit	3.26° S	113.02° E	**0.49**	211	0.56	230.3	0.06	19.3	0.49	236.0	(0.00)	25.0	0.39	244.6	(0.10)	33.6
45	Meneng	8.2°S	114.4° E	**0.54**	91	0.47	3.5	(0.06)	(87.5)	0.46	5.9	(0.07)	(85.1)	0.45	2.8	(0.08)	(88.2)
46	Barito	3.68° S	114.47° E	0.34	209	0.67	168.6	0.29	(40.4)	0.59	170.9	0.24	(38.1)	0.48	175.2	0.15	(33.8)
47	Benoa (Bali)	8.7° S	115.2° E	**0.71**	73	0.64	346.6	(0.05)	93.6	0.63	346.6	(0.05)	93.6	0.62	346.6	(0.06)	93.6
48	Lembar	8.7° S	116° E	0.27	52	0.42	15.1	0.19	(36.9)	0.41	14.4	0.18	(37.6)	0.40	13.5	0.17	(38.5)
50	Sungai Kutai	0.5° N	117.87° E	**0.59**	192	0.50	237.1	(0.07)	45.1	0.50	237.4	(0.07)	45.4	0.51	237.7	(0.06)	45.7
54	Sangkulirang	0.7° N	118° E	**0.52**	211	0.51	238.1	(0.01)	27.1	0.51	238.2	(0.01)	27.2	0.52	238.5	(0.00)	27.5
55	Biringkasi	4.84° S	119.47° E	0.13	252	0.03	268.4	(0.64)	16.4	0.04	266.9	(0.50)	14.9	0.06	265.4	(0.33)	13.4
57	Makassar	5.2° S	119.4° E	0.08	297	0.08	43.2	(0.01)	(73.8)	0.07	36.9	(0.06)	(80.1)	0.06	23.1	(0.15)	(93.9)
58	Bima	8.4° S	118.7° E	**0.35**	357	0.42	57.6	0.08	(119.4)	0.42	57.8	0.07	(119.2)	0.41	58.3	0.06	(118.7)
											S_2						
32	Cirebon	8.61° S	108.66° E	0.1	183	0.37	272.2	0.57	89.2	0.34	271.5	0.53	88.5	0.30	270.9	0.48	87.9
38	Semarang	6.82° S	110.28° E	0.08	203	0.39	257.1	0.69	54.1	0.36	255.8	0.65	52.8	0.31	254.2	0.59	51.2
39	Kota Waringin	3.05° S	111.37° E	0.06	244	0.42	256.8	0.85	12.8	0.41	255.9	0.83	11.9	0.37	254.9	0.79	10.9
40	Surabaya (West)	6.9° S	112.7° E	0.08	4	0.12	95.9	0.18	91.9	0.13	96.7	0.20	92.7	0.13	98.3	0.22	94.3
43	Teluk Sampit	3.26° S	113.02° E	0.11	307	0.41	177.5	0.57	(129.5)	0.38	182.6	0.54	(124.4)	0.33	191.1	0.47	(115.9)
45	Meneng	8.2°S	114.4° E	0.29	35	0.20	45.6	(0.16)	10.6	0.19	42.2	(0.17)	7.2	0.20	43.1	(0.17)	8.1
46	Barito	3.68° S	114.47° E	0.05	279	0.56	118.5	1.05	(160.5)	0.52	119.6	1.02	(159.4)	0.45	121.8	0.96	(157.2)
47	Benoa (Bali)	8.7° S	115.2° E	0.33	5	0.22	69.7	(0.18)	64.7	0.22	69.6	(0.18)	64.6	0.21	69.8	(0.19)	64.8
48	Lembar	8.7° S	116° E	0.16	43	0.17	32.8	0.03	(10.2)	0.17	31.5	0.02	(11.5)	0.17	29.4	0.02	(13.6)
50	Sungai Kutai	0.5° N	117.87° E	**0.43**	136	0.34	308.8	(0.11)	172.8	0.34	308.9	(0.10)	172.9	0.34	308.9	(0.10)	172.9
54	Sangkulirang	0.7° N	118° E	**0.34**	154	0.34	307.9	(0.00)	153.9	0.34	308.0	(0.00)	154.0	0.34	308.1	0.00	154.1
55	Biringkasi	4.84° S	119.47° E	0.17	144	0.32	321.6	0.27	177.6	0.33	321.9	0.28	177.9	0.33	322.2	0.29	178.2
57	Makassar	5.2° S	119.4° E	0.11	165	0.28	322.6	0.41	157.6	0.29	323.1	0.41	158.1	0.29	323.7	0.42	158.7
58	Bima	8.4° S	118.7° E	0.1	305	0.07	297.2	(0.16)	(7.8)	0.07	297.1	(0.14)	(7.9)	0.08	296.3	(0.11)	(8.7)
											K_1						
32	Cirebon	8.61° S	108.66° E	**0.14**	312	0.18	302.4	0.10	(9.6)	0.16	312.2	0.07	0.2	0.15	326.7	0.04	14.7
38	Semarang	6.82° S	110.28° E	**0.22**	7	0.30	263.6	0.13	76.6	0.26	269.6	0.07	82.6	0.21	279.7	(0.02)	92.7
39	Kota Waringin	3.05° S	111.37° E	**0.36**	34	0.49	242.3	0.14	28.3	0.42	246.1	0.07	32.1	0.34	252.1	(0.03)	38.1
40	Surabaya (West)	6.9° S	112.7° E	**0.54**	43	0.64	227.5	0.07	4.5	0.58	228.8	0.03	5.8	0.49	230.5	(0.04)	7.5
43	Teluk Sampit	3.26° S	113.02° E	**0.6**	24	0.85	250.8	0.15	46.8	0.75	254.1	0.10	50.1	0.62	259.0	0.02	55.0
45	Meneng	8.2°S	114.4° E	0.32	87	0.34	181.4	0.03	94.4	0.35	181.7	0.03	94.7	0.33	181.3	0.02	94.3
46	Barito	3.68° S	114.47° E	**0.64**	20	0.82	239.7	0.11	39.7	0.74	241.5	0.06	41.5	0.63	244.1	(0.01)	44.1
47	Benoa (Bali)	8.7° S	115.2° E	0.25	59	0.30	164.4	0.08	105.4	0.30	164.3	0.08	105.3	0.30	164.3	0.08	105.3
48	Lembar	8.7° S	116° E	0.36	76	0.36	183.5	(0.00)	107.5	0.35	183.2	(0.01)	107.2	0.35	183.1	(0.02)	107.1
50	Sungai Kutai	0.5° N	117.87° E	0.24	73	0.26	150.3	0.03	77.3	0.26	150.0	0.03	77.0	0.26	149.7	0.03	76.7
54	Sangkulirang	0.7° N	118° E	0.19	69	0.26	148.3	0.14	79.3	0.26	148.1	0.14	79.1	0.26	147.8	0.14	78.8
55	Biringkasi	4.84° S	119.47° E	**0.32**	65	0.36	175.1	0.05	110.1	0.36	174.7	0.05	109.7	0.35	174.3	0.04	109.3
57	Makassar	5.2° S	119.4° E	**0.28**	59	0.38	177.9	0.13	118.9	0.37	177.6	0.12	118.6	0.37	177.4	0.12	118.4
58	Bima	8.4° S	118.7° E	**0.3**	56	0.39	187.3	0.12	131.3	0.39	187.2	0.11	131.2	0.39	187.2	0.11	131.2
											O_1						
32	Cirebon	8.61° S	108.66° E	0.05	205	0.12	338.7	0.38	133.7	0.11	312.2	0.34	107.2	0.10	311.9	0.29	106.9
38	Semarang	6.82° S	110.28° E	0.08	128	0.18	338.5	0.35	30.5	0.16	312.2	0.30	4.2	0.13	311.8	0.22	3.8
39	Kota Waringin	3.05° S	111.37° E	0.16	131	0.32	16.6	0.29	(114.4)	0.29	350.3	0.26	39.3	0.25	350.1	0.19	39.1
40	Surabaya (West)	6.9° S	112.7° E	0.26	101	0.34	325.9	0.12	44.9	0.32	299.6	0.09	18.6	0.28	299.5	0.04	18.5
43	Teluk Sampit	3.26° S	113.02° E	0.31	96	0.41	12.3	0.12	(83.7)	0.38	344.9	0.09	68.9	0.33	344.4	0.03	68.4
45	Meneng	8.2°S	114.4° E	0.13	117	0.18	13.8	0.13	(103.2)	0.18	347.0	0.14	50.0	0.17	346.1	0.11	49.1
46	Barito	3.68° S	114.47° E	0.33	79	0.42	17.5	0.11	(61.5)	0.39	350.2	0.07	91.2	0.34	349.2	0.02	90.2
47	Benoa (Bali)	8.7° S	115.2° E	0.12	84	0.14	20.6	0.07	(63.4)	0.14	352.5	0.07	88.5	0.14	351.2	0.07	87.2
48	Lembar	8.7° S	116° E	0.24	96	0.17	45.7	(0.15)	(50.3)	0.17	19.8	(0.16)	(76.2)	0.16	17.0	(0.16)	(79.0)
50	Sungai Kutai	0.5° N	117.87° E	0.15	111	0.15	142.6	(0.01)	31.6	0.15	126.4	(0.01)	15.4	0.15	130.9	(0.01)	19.9
54	Sangkulirang	0.7° N	118° E	0.19	103	0.15	170.3	(0.11)	67.3	0.15	152.3	(0.11)	49.3	0.15	156.4	(0.11)	53.4
55	Biringkasi	4.84° S	119.47° E	0.2	95	0.17	164.8	(0.08)	69.8	0.16	142.4	(0.09)	47.4	0.16	143.8	(0.09)	48.8
57	Makassar	5.2° S	119.4° E	0.17	90	0.17	0.0	(0.01)	(90.0)	0.17	0.0	(0.01)	(90.0)	0.16	0.0	(0.02)	(90.0)
58	Bima	8.4° S	118.7° E	0.1	104	0.15	0.0	0.18	(104.0)	0.15	0.0	0.18	(104.0)	0.15	0.0	0.18	(104.0)

Table 4-8: Bed friction tuning for the Eastern Domain

Sta.	Location	Lat	Long	Observation		*Cf* =0.0025				*Cf* =0.0035				*Cf* =0.0050			
						Calculation		Error		Calculation		Error		Calculation		Error	
				A (m)	ϕ (deg)	*A* (m)	ϕ (deg)	*A*	ϕ	*A* (m)	ϕ (deg)	*A*	ϕ	*A* (m)	ϕ (deg)	*A*	ϕ
M_2																	
65	Muotong	00.4° N	121.23° E	**0.25**	249.0	0.24	44.6	(0.01)	(24.4)	0.25	9.2	0.00	(59.8)	0.27	14.3	0.03	(54.7)
66	Gorontalo	00.5° N	123.05° E	**0.22**	251.0	0.20	44.1	(0.05)	(26.9)	0.20	9.0	(0.03)	(62.0)	0.22	14.1	(0.01)	(56.9)
67	Kolaka	04.0° S	121.58° E	**0.55**	355.0	0.70	286.6	0.10	(68.4)	0.68	265.1	0.09	(89.9)	0.67	265.7	0.08	(89.3)
72	Bitung	1.5° N	125.2° E	**0.36**	214.0	0.32	85.5	(0.05)	(128.5)	0.33	57.2	(0.03)	(156.8)	0.34	57.5	(0.02)	(156.5)
74	Ternate	00.8° N	127.4° E	**0.27**	185.0	0.29	81.3	0.02	(103.7)	0.30	51.7	0.04	(133.3)	0.31	52.4	0.06	(132.6)
75	Ambon	03.7° S	128.2° E	**0.47**	318.0	0.77	296.3	0.21	(21.7)	0.74	278.2	0.20	(39.8)	0.71	279.8	0.18	(38.2)
76	Sorong	00.8° S	131.2° E	**0.41**	165.0	0.53	100.1	0.11	(64.9)	0.53	75.3	0.11	(89.7)	0.53	75.4	0.11	(89.6)
77	Fak-Fak	02.9° S	132.3° E	**0.4**	327.0	0.89	304.2	0.35	(22.8)	0.85	287.0	0.33	(40.0)	0.83	288.9	0.32	(38.1)
78	Tual	05.6° S	132.7° E	**0.44**	324.0	0.93	303.2	0.32	(20.8)	0.89	286.0	0.30	(38.0)	0.86	287.7	0.29	(36.3)
80	Dobo	05.8° S	134.2° E	**0.61**	319.0	0.98	306.9	0.21	(12.1)	0.94	289.6	0.19	(29.4)	0.91	291.5	0.17	(27.5)
83	Aiduna	04.5° S	135.3° E	**0.45**	155.0	0.87	323.8	0.28	168.8	0.81	309.6	0.25	154.6	0.76	312.5	0.23	157.5
87	Sungai Digul	07.1° S	138.7° E	1.22	66.0	1.40	243.2	0.06	177.2	1.17	236.9	(0.02)	170.9	0.95	243.8	(0.11)	177.8
88	Selat Muli	08.1° S	138.9° E	**1.84**	22.0	1.13	288.6	(0.21)	86.6	0.88	285.8	(0.32)	83.8	0.67	291.7	(0.44)	89.7
90	Merauke	08.5° S	140.4° E	**1.13**	340.0	1.48	296.9	0.12	(43.1)	1.21	286.8	0.03	(53.2)	0.97	292.0	(0.07)	(48.0)
S_2																	
65	Muotong	00.4° N	121.23° E	0.17	192.0	0.40	280.4	0.37	88.4	0.40	278.8	0.37	86.8	0.40	278.7	0.37	86.7
66	Gorontalo	00.5° N	123.05° E	0.22	188.0	0.31	279.8	0.15	91.8	0.32	278.5	0.16	90.5	0.32	278.5	0.16	90.5
67	Kolaka	04.0° S	121.58° E	0.14	292.0	0.18	183.4	0.11	(108.6)	0.18	186.3	0.11	(105.7)	0.18	187.1	0.11	(104.9)
72	Bitung	1.5° N	125.2° E	0.26	169.0	0.31	288.9	0.07	119.9	0.31	288.8	0.08	119.8	0.31	288.7	0.08	119.7
74	Ternate	00.8° N	127.4° E	0.22	148.0	0.30	287.3	0.13	139.3	0.30	286.7	0.13	138.7	0.30	286.6	0.14	138.6
75	Ambon	03.7° S	128.2° E	0.17	250.0	0.17	201.3	0.00	(48.7)	0.17	206.4	0.01	(43.6)	0.18	207.5	0.01	(42.5)
76	Sorong	00.8° S	131.2° E	0.18	150.0	0.24	299.6	0.13	149.6	0.24	299.6	0.13	149.6	0.24	299.6	0.13	149.6
77	Fak-Fak	02.9° S	132.3° E	0.22	230.0	0.21	213.9	(0.02)	(16.1)	0.21	218.1	(0.01)	(11.9)	0.22	219.1	(0.01)	(10.9)
78	Tual	05.6° S	132.7° E	0.22	249.0	0.21	204.7	(0.03)	(44.3)	0.21	210.9	(0.02)	(38.1)	0.21	212.1	(0.02)	(36.9)
80	Dobo	05.8° S	134.2° E	0.19	240.0	0.22	208.3	0.06	(31.7)	0.22	213.8	0.07	(26.2)	0.23	215.0	0.07	(25.0)
83	Aiduna	04.5° S	135.3° E	0.11	122.0	0.19	228.3	0.24	106.3	0.19	237.1	0.23	115.1	0.19	239.3	0.24	117.3
87	Sungai Digul	07.1° S	138.7° E	0.31	338.0	0.37	156.2	0.08	(1.8)	0.31	175.7	0.01	(162.3)	0.29	182.5	(0.03)	(155.5)
88	Selat Muli	08.1° S	138.9° E	0.8	298.0	0.24	216.7	(0.53)	(81.3)	0.18	239.8	(0.65)	(58.2)	0.16	244.3	(0.70)	(53.7)
90	Merauke	08.5° S	140.4° E	0.46	237.0	0.32	207.7	(0.16)	(29.3)	0.26	223.7	(0.25)	(13.3)	0.24	228.5	(0.29)	(8.5)
K_1																	
65	Muotong	00.4° N	121.23° E	**0.22**	75.0	0.15	119.6	(0.18)	44.6	0.15	120.2	(0.17)	45.2	0.15	119.9	(0.17)	44.9
66	Gorontalo	00.5° N	123.05° E	**0.19**	77.0	0.14	119.4	(0.14)	42.4	0.14	120.1	(0.13)	43.1	0.14	119.9	(0.13)	42.9
67	Kolaka	04.0° S	121.58° E	**0.34**	59.0	0.24	152.6	(0.15)	93.6	0.24	153.2	(0.15)	94.2	0.24	153.1	(0.15)	94.1
72	Bitung	1.5° N	125.2° E	**0.28**	102.0	0.12	102.6	(0.38)	0.6	0.12	103.4	(0.38)	1.4	0.12	103.4	(0.37)	1.4
74	Ternate	00.8° N	127.4° E	0.14	91.0	0.11	104.9	(0.09)	13.9	0.11	104.9	(0.09)	13.9	0.12	104.9	(0.09)	13.9
75	Ambon	03.7° S	128.2° E	0.29	36.0	0.23	150.3	(0.10)	114.3	0.24	149.7	(0.09)	113.7	0.24	149.5	(0.09)	113.5
76	Sorong	00.8° S	131.2° E	0.23	134.0	0.12	43.2	(0.28)	(90.8)	0.12	43.7	(0.28)	(90.3)	0.12	43.6	(0.28)	(90.4)
77	Fak-Fak	02.9° S	132.3° E	0.19	9.0	0.24	152.8	0.10	143.8	0.25	152.5	0.11	143.5	0.25	151.9	0.12	142.9
78	Tual	05.6° S	132.7° E	0.18	32.0	0.25	155.7	0.14	123.7	0.26	155.0	0.15	123.0	0.26	154.2	0.16	122.2
80	Dobo	05.8° S	134.2° E	0.28	35.0	0.26	159.3	(0.03)	124.3	0.27	157.5	(0.02)	122.5	0.27	156.4	(0.01)	121.4
83	Aiduna	04.5° S	135.3° E	**0.37**	336.0	0.30	189.1	(0.09)	(146.9)	0.29	186.3	(0.10)	(149.7)	0.28	182.2	(0.12)	(153.8)
87	Sungai Digul	07.1° S	138.7° E	**1.3**	291.0	0.76	294.0	(0.23)	3.0	0.63	304.6	(0.31)	13.6	0.51	309.6	(0.41)	18.6
88	Selat Muli	08.1° S	138.9° E	1.12	265.0	0.47	329.1	(0.38)	64.1	0.39	335.7	(0.46)	70.7	0.31	339.5	(0.56)	74.5
90	Merauke	08.5° S	140.4° E	0.8	215.0	0.40	325.0	(0.30)	110.0	0.34	326.2	(0.37)	111.2	0.28	326.3	(0.46)	111.3
O_1																	
65	Muotong	00.4° N	121.23° E	0.14	114.0	0.11	338.7	(0.12)	44.7	0.11	312.0	(0.12)	18.0	0.11	311.6	(0.11)	17.6
66	Gorontalo	00.5° N	123.05° E	0.14	106.0	0.10	338.5	(0.14)	52.5	0.10	312.0	(0.14)	26.0	0.10	311.6	(0.13)	25.6
67	Kolaka	04.0° S	121.58° E	0.22	83.0	0.13	16.6	(0.23)	(66.4)	0.13	350.2	(0.23)	87.2	0.13	349.9	(0.23)	86.9
72	Bitung	1.5° N	125.2° E	0.14	134.0	0.10	325.9	(0.16)	11.9	0.10	299.5	(0.16)	165.5	0.10	299.4	(0.16)	165.4
74	Ternate	00.8° N	127.4° E	0.1	112.0	0.09	326.8	(0.03)	34.8	0.09	299.9	(0.03)	7.9	0.09	299.7	(0.03)	7.7
75	Ambon	03.7° S	128.2° E	0.21	47.0	0.14	12.3	(0.19)	(34.7)	0.14	344.6	(0.19)	117.6	0.14	344.0	(0.19)	117.0
76	Sorong	00.8° S	131.2° E	0.13	187.0	0.10	282.9	(0.12)	95.9	0.10	256.6	(0.12)	69.6	0.10	256.5	(0.12)	69.5
77	Fak-Fak	02.9° S	132.3° E	0.15	76.0	0.14	13.8	(0.02)	(62.2)	0.14	346.5	(0.02)	90.5	0.14	345.6	(0.02)	89.6
78	Tual	05.6° S	132.7° E	0.12	37.0	0.15	17.5	0.09	(19.5)	0.15	349.6	0.09	132.6	0.15	348.5	0.09	131.5
80	Dobo	05.8° S	134.2° E	0.17	54.0	0.16	20.6	(0.04)	(33.4)	0.16	351.8	(0.04)	117.8	0.15	350.4	(0.04)	116.4
83	Aiduna	04.5° S	135.3° E	0.21	19.0	0.19	45.7	(0.04)	26.7	0.18	18.3	(0.07)	(0.7)	0.17	15.1	(0.09)	(3.9)
87	Sungai Digul	07.1° S	138.7° E	1.14	338.0	0.50	142.6	(0.35)	(15.4)	0.41	128.8	(0.44)	(29.2)	0.33	134.9	(0.54)	(23.1)
88	Selat Muli	08.1° S	138.9° E	1.14	306.0	0.29	170.3	(0.59)	(135.7)	0.24	154.5	(0.68)	(151.5)	0.19	159.9	(0.79)	(146.1)
90	Merauke	08.5° S	140.4° E	0.5	283.0	0.24	164.8	(0.32)	(118.2)	0.20	143.1	(0.40)	(139.9)	0.16	145.2	(0.49)	(137.8)

4.5.3 Validation to Co-Tidal Chart from Satellite Data

The results are compared with the co-tidal chart from satellite altimetry data (Ray *et al.*, 2005), which is only available for M_2 and K_1 only. Figure 4-17 shows the co-tidal chart for amplitude and phase for M_2, while Figure 4-18 shows the charts for K_1. The colour code from the model follows the colour code presented in Ray *et al.*, 2005's co-tidal charts.

In general, the models exhibit relatively good agreement with satellite data. The amplitude and the phase of M_2 in the Java Sea have minor mismatches with the satellite data (see the Western and Central domain in Figure 4-17). As mentioned previously, this area is of shallow water. The validation of the tidal constituents, as discussed in the previous section, shows that this area tends to have a better agreement for higher bed friction (stations 32, 38, 39, 43, and 46 in Table 4-7). Therefore, this area might require even higher bed friction. However, increasing the bed friction in a particular area, differing from in another area, might create further undesirable complexity.

The co-tidal charts of K_1 from the model are similar to the satellite co-tidal chart for the area. Therefore, the strategy in this thesis is to accept this limitation. The DG-ADCIRC solver seems unable to capture the complexity of tidal hydrodynamics in this area. However, this area is not in the proximity of any potential site.

It is also important to note that the co-tidal charts from altimetry data from Ray *et al.*, 2005 do not cover all of Indonesian waters. Only the central domain is covered entirely by the satellite data. Therefore, in some model domains, this data only validates a partial area of the model.

4.5.4 Field Survey Data Validation

The models are also validated against field measurement data (ADCP measurement and tide observation) for several potential sites. The tide observation data and ADCP measurements that are used here are obtained from P3GL. The data are not ideal, due to the relatively short period of observation. However, they may show qualitatively how well the model fits the tidal pattern. Validation against ADCP data for a longer duration (say 15 days) would be desirable, but such data are not available.

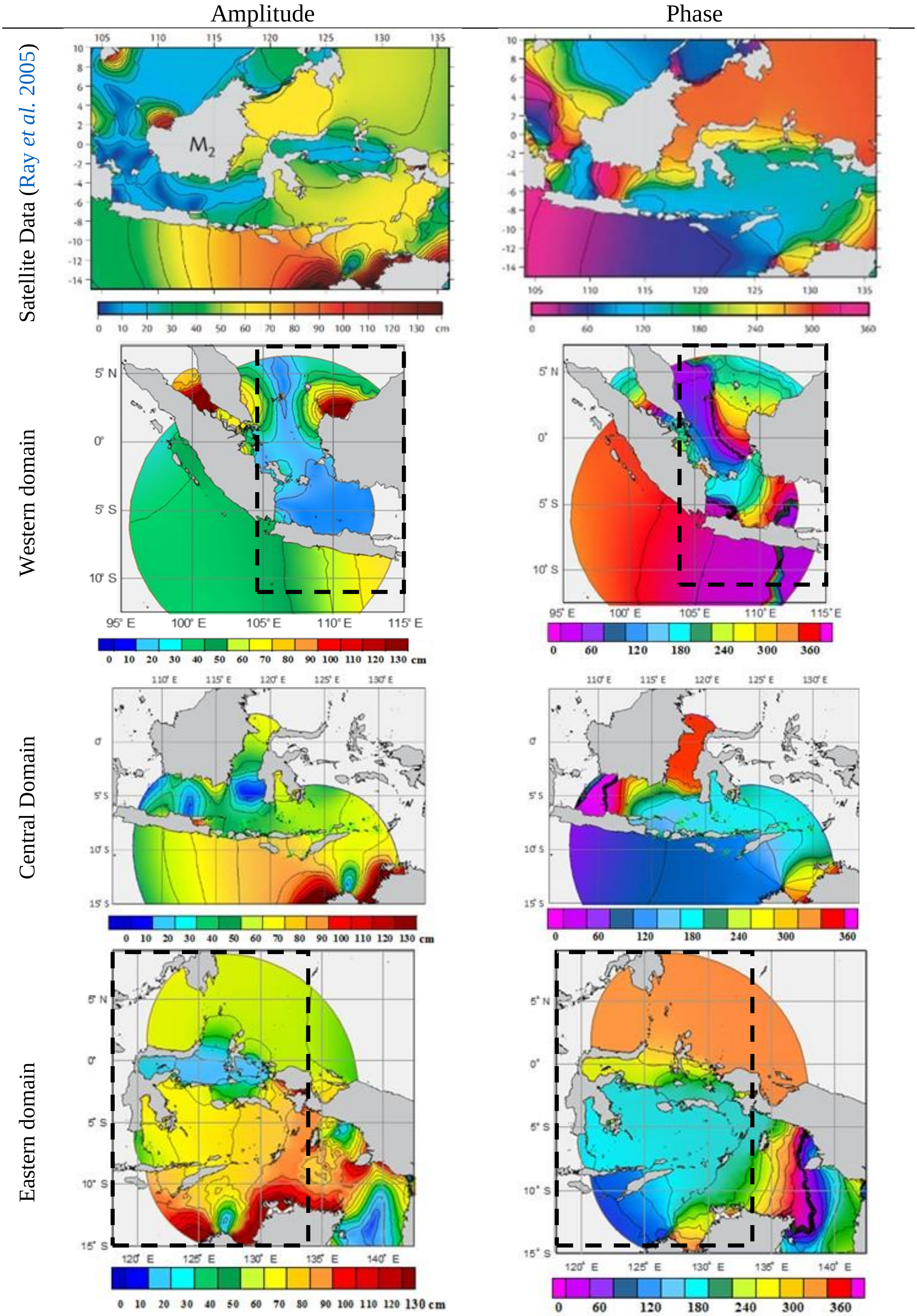

Figure 4-17: Comparison of M₂ co-tidal charts from satellite altimetry based on Ray *et al.*, 2005 and the co-tidal chart from the models. The dashed lines show the coverage of Ray *et al.*, 2005

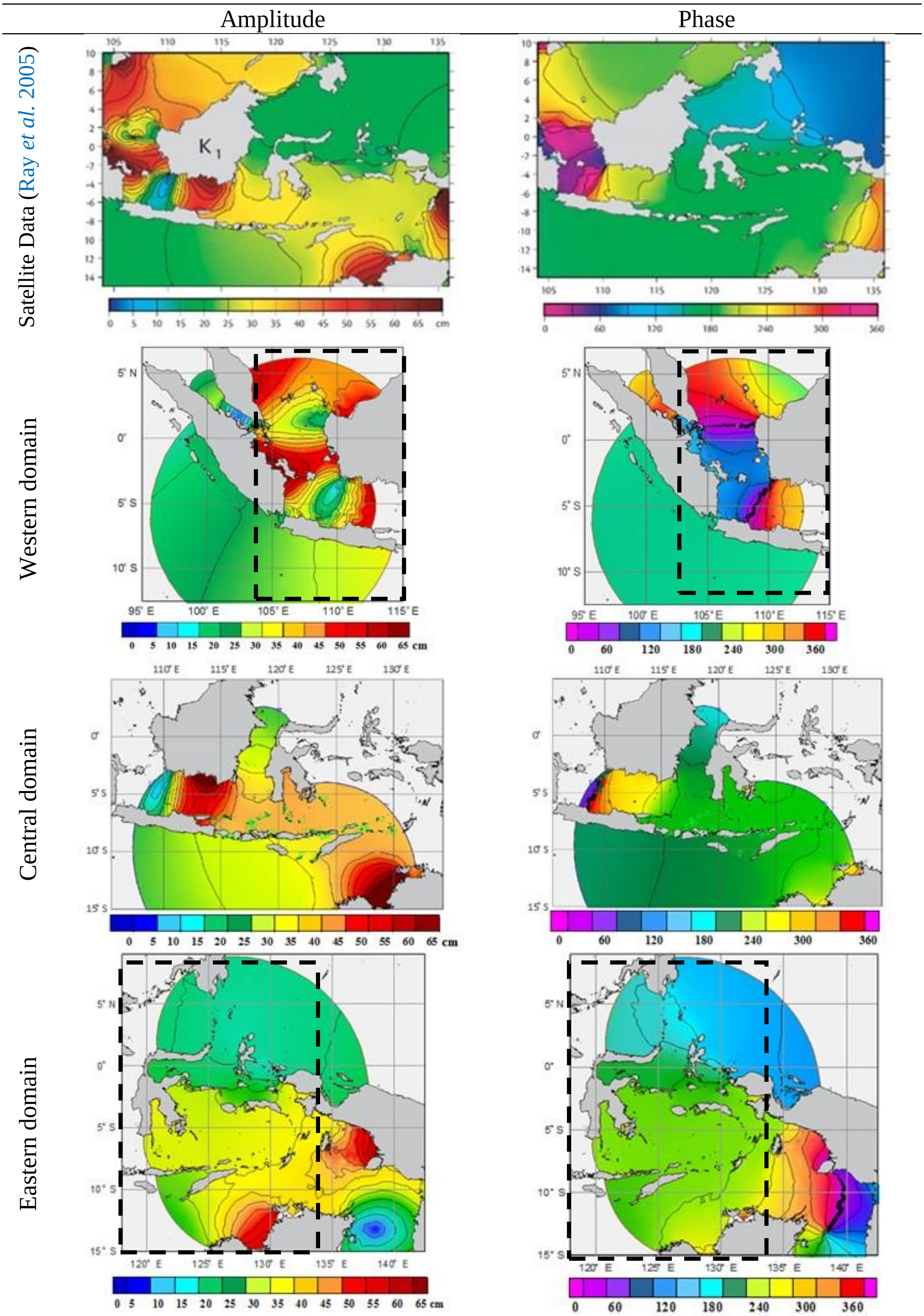

Figure 4-18: Comparison of K1 co-tidal charts from satellite altimetry based on Ray *et al.*, 2005 and the co-tidal chart from the models. The dashed lines show the coverage of Ray *et al.*. 2005

Since the surveys were conducted at various different times, the models are run for the specific date to match the survey date. The tidal observation and ADCP measurements in Toyopakeh Strait, that is located on the North East side of Nusa Lembongan Island, as indicated by the orange circle in Figure 4-7, was carried out from 4 - 14 April 2008. The tidal elevation predictions are in good agreement with survey data, as presented in Figure 4-19 a. However, the comparison of ADCP current measurements and the model results is not as good as for the elevation (see Figure 4-19 b). However, despite the fact that the model gives smaller velocity magnitudes, this comparison shows that the model matches the velocity pattern quite well.

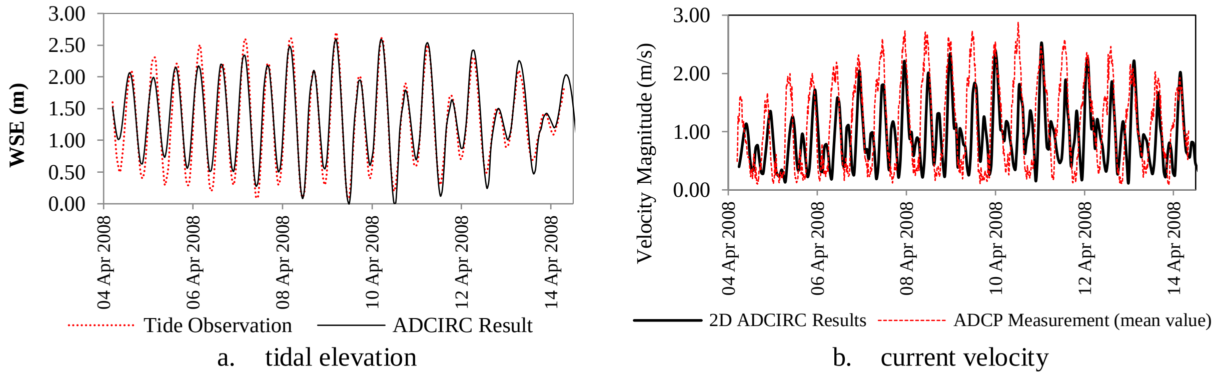

a. tidal elevation

b. current velocity

Figure 4-19: Comparison of model and observations in Toyopakeh straits based on Yuningsih, 2008.

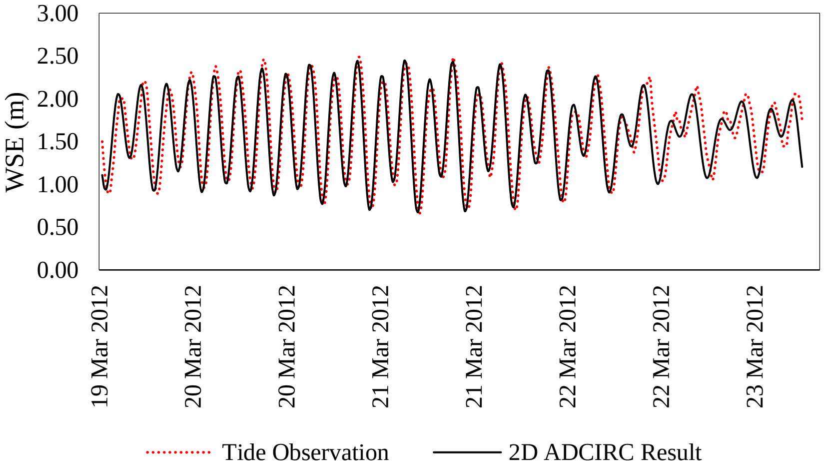

Figure 4-20: Comparison of model and tidal elevation observations in Boleng Straits.

The tide observation and ADCP measurement data in Larantuka are at a different location on a different date. The tide observation data is from Boleng strait, while the ADCP measurement data is from Larantuka strait (see Figure 4-8). The tide observation data in Boleng strait is dated from 19 - 23 March 2012 (see Figure 4-20), while the ADCP measurement in Larantuka is from 28 November 2007 to 4 December 2007 (see Figure 4-21). Similar to the validation in Lombok strait, the tide elevation data shows better agreement than the ADCP data. The validation of flow velocity magnitude shows better agreement in this location than at Lombok strait. However, the data ADCP in Larantuka strait appears problematic in the first two days of measurement, as shown in Figure 4-21.

The eastern domain for the Sula regency sites is only validated against ADCP data due to there being no observation data for the tide elevation in this site. The ADCP measurement was conducted in Mangole strait, as shown in Figure 4-9. The ADCP data is dated from 17 to 21 November 2007. The velocity from DG-ADCIRC model agrees well with the ADCP data in this location (see Figure 4-22).

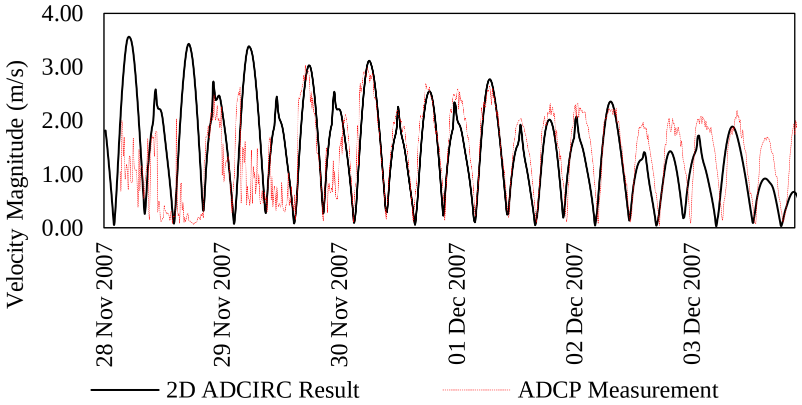

Figure 4-21: Comparison of current velocity from model and measurement using ADCP in Larantuka Strait

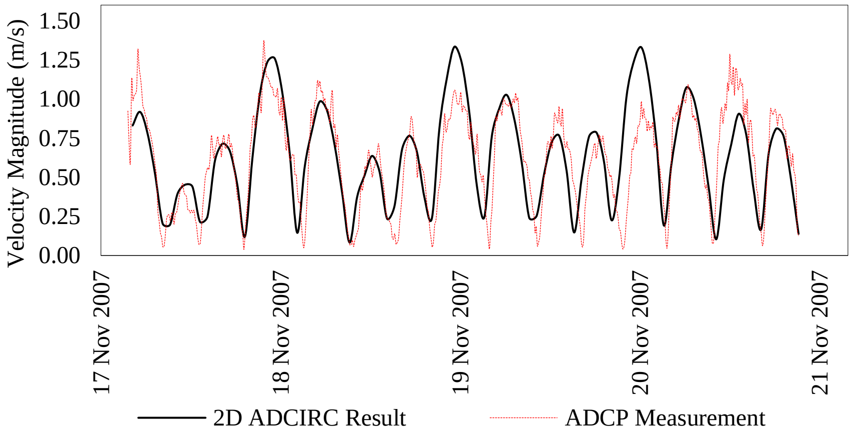

Figure 4-22: Comparison of current velocity from model and measurement using ADCP in Mangole Strait (Eastern Domain)

The validation in the western domain is also for ADCP data only. The measurement in this location was conducted at Carita Beach (see Figure 4-23) from 9 to 14 October 2010. The validation against ADCP measurement data for this site is problematic, as the velocity magnitude in the measurement location is low (see Figure 4-24). Although the model gives a lower magnitude in velocity than the measurement, the DG-ADCIRC model captures the pattern of velocity at this location.

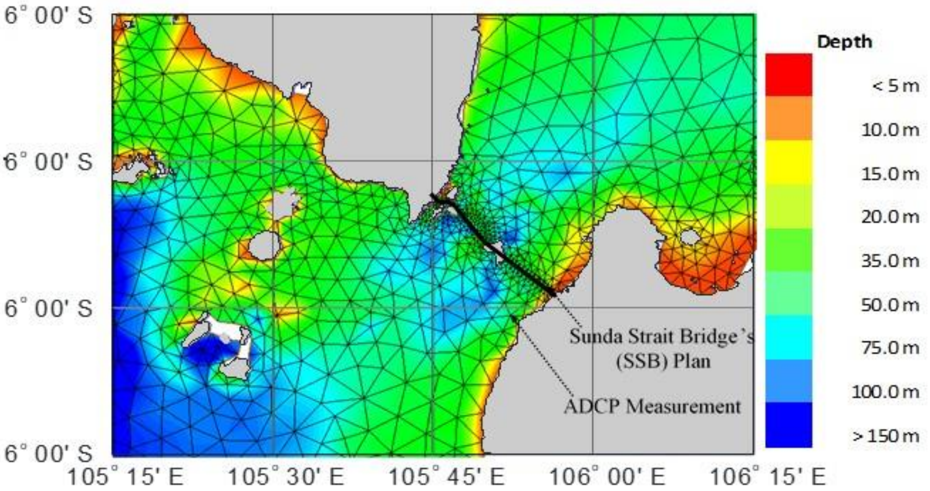

Figure 4-23: The ADCP measurement in Sunda Strait

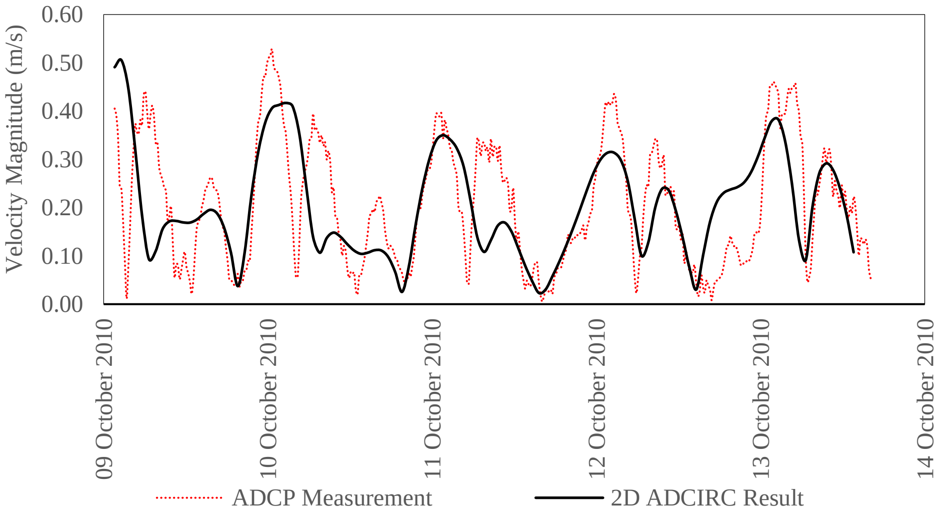

Figure 4-24: Comparison of current velocity from model and measurement using ADCP in Sunda Strait (Western Domain)

4.5.5 Validation of *Formzahl* Number

As mentioned in Chapter 1, the main objective of this thesis is to understand the nature of tidal energy resources with multiple tidal components. Moreover, the site selection for analysis in this thesis is based on tidal type. Therefore it also useful to compare the *Formzahl* number in the models with the *Formzahl* number in the data.

The *Formzahl* data are obtained from each station used in the validation in section 4.5.1. The *Formzahl* numbers for the western, central and eastern domains are presented in Figure 4-25, Figure 4-26 and Figure 4-27, respectively. The *Formzahl* numbers of the models are obtained from the co-tidal charts from the simulations. The colour coded shading corresponds to tidal type. Meanwhile the numbered circles indicate the *Formzahl* number from the admiralty tide table. The colour code of each station follows the tidal type. The station locations are the same as presented in the previous figures (see Figure 4-4,Figure 4-5, and Figure 4-6 for the stations' reference).

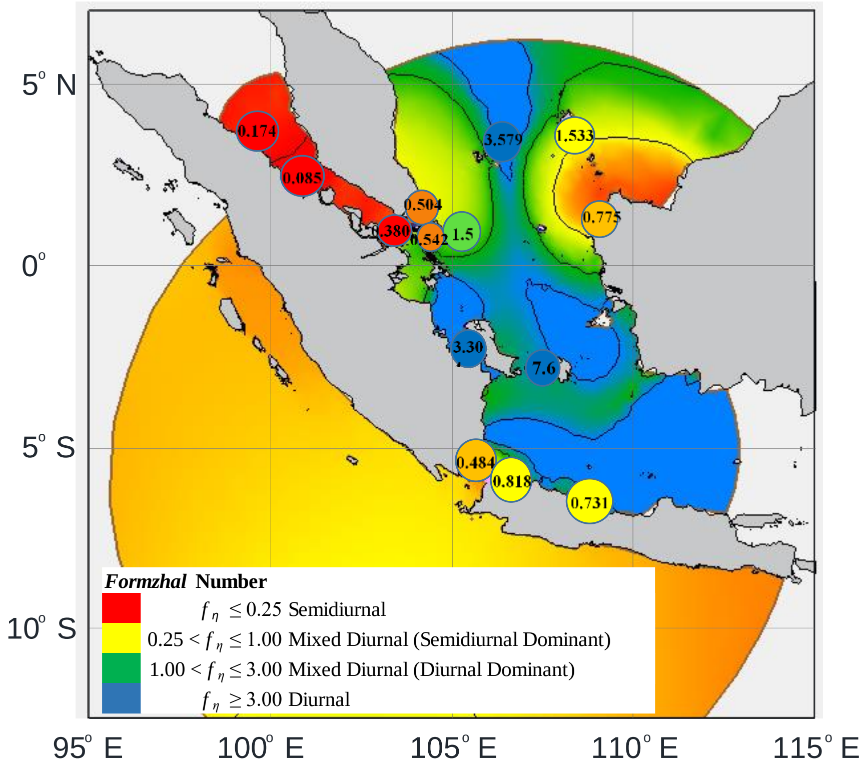

Figure 4-25: *Formzahl* number in the western domain

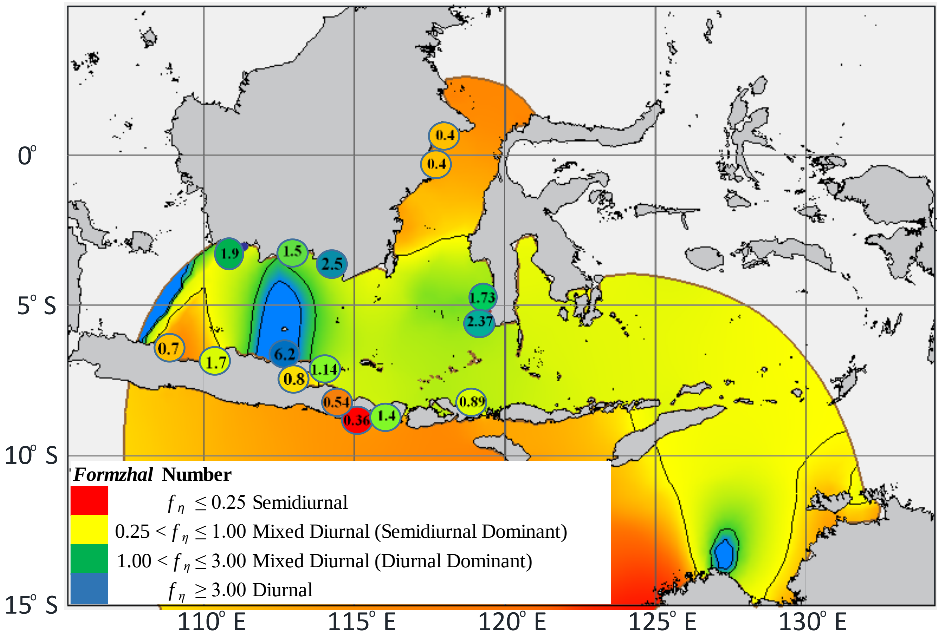

Figure 4-26: *Formzahl* number in the central domain

The simulated *Formzahl* number distribution matches that observed at the majority of stations. However, some differences are exhibited at stations in the Java Sea. A station in the western domain shows this mismatch. The *Formzahl* number from the model is diurnal, while the data is in the category of mixed-diurnal with semidiurnal dominant. However, this issue does not appear in the central domain.

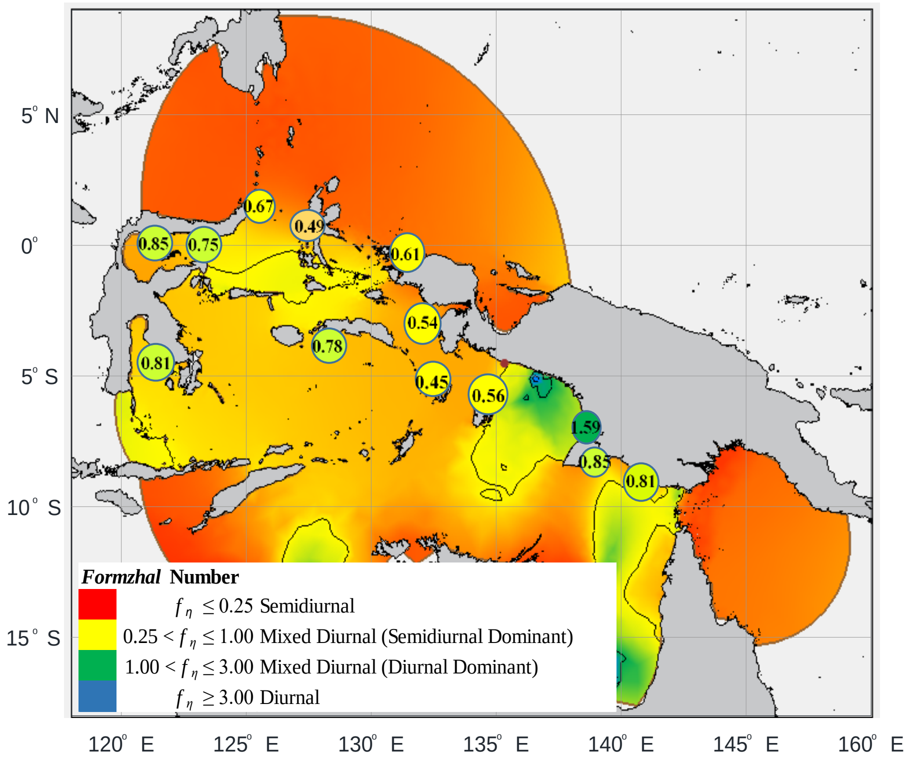

Figure 4-27: *Formzahl* number in the eastern domain

4.6 Discussion

Modifications of the DG-ADCIRC code have been made for the purpose of the assessment in this thesis. The revised model is more sophisticated and allows deeper analysis in the assessment, such as site-site interactions that will be examined in Chapter 5, or the realistic turbine deployment with considering the number of turbines in each element, that will be addressed in Chapter 6.

Modelling tidal hydrodynamics in Indonesia is indeed challenging, as shown in this chapter. Achieving a model at the level of fidelity that has been done in the other regions is difficult for this region. Other authors, as mentioned at the beginning of this chapter, have also encountered these difficulties, confirming the challenges of modelling tidal hydrodynamics in this area.

However, having a model that is reliable is also essential for a resource assessment. Therefore, this thesis uses several approaches to validate the Indonesian models. Based on the validation, these models appear to represent the tidal hydrodynamic in Indonesian waters, with an acceptable accuracy to make a robust resource assessment.

Chapter 5. Resource Assessment and Analysis of Sites

This chapter describes resource assessment for sites in Indonesian waters, assuming uniform blockage ratio. Before conducting an assessment, the potential sites are identified using the metric of kinetic power. The average kinetic power per unit vertical area for each point in a depth-averaged flow at each individual sites is calculated using Eq. (5-1).

$$E_k = \frac{1}{2}\rho v^3, \tag{5-1}$$

where E_k is kinetic power flux (W/m^2), ρ is seawater density ($1025\ \mathrm{kg/m^3}$) and v is the velocity (m/s).

The site-site interactions, the appropriate model domain, the appropriate number of constituents used in the simulation and the long-term variability of tidal resources are also discussed in this chapter. As mentioned in Chapter 1, five different locations are considered. The analysis have a location-dependent focus. In general, this chapter's assessments are focused on determining the upper bound limit of the resources, evaluating the most potential locations for the tidal turbine along the strait and conducting site-site interactions analyses. Later, this chapter also demonstrates that each location represents a different flow pattern regime represented by the *Formzahl* number, the long-term variability and annual variation of the power production, as discussed in Chapter 2.

5.1 Larantuka: Tidal Resource from the Palmerah Tidal Bridge

As described in Chapter 1, an 810 m long bridge, named the Pancasila Palmerah, is planned to connect the islands, linking the eastern tip of Flores Island and the smaller island Adonara. A series of turbines will be installed beneath the bridge to generate electricity from the tidal current, with the aim of providing electricity for over 100,000 people in the region. As part of the NTT Provincial Government vision to develop the region further, a technical feasibility report (Tidal Bridge DV, 2017) has been delivered describing the project. Furthermore, the Palmerah Tidal Bridge project has National Strategic Project status, emphasizing the national interest.

Tidal Bridge BV, a joint venture between a Dutch engineering firm, Strukton International and the venture capital fund Dutch Expansion, has been awarded the Palmerah Tidal Bridge project. With an estimated investment of US$225 million, this tidal power plant promises to deliver power capacity of 18 to 23 MW (Hicks, 2017). This project may be followed by an extension to a capacity of 90 to 115 MW.

5.1.1 Evaluating the Project Deliverables

The proposed location of the tidal bridge, based on Tidal Bridge DV, 2017, is shown in Figure 5-1a. As mentioned in the technical feasibility report, the bridge alignment is determined based on the current conditions and technical aspects of bridge construction (see Tidal Bridge DV, 2017). Unfortunately, the report does not discuss the resource assessment in detail.

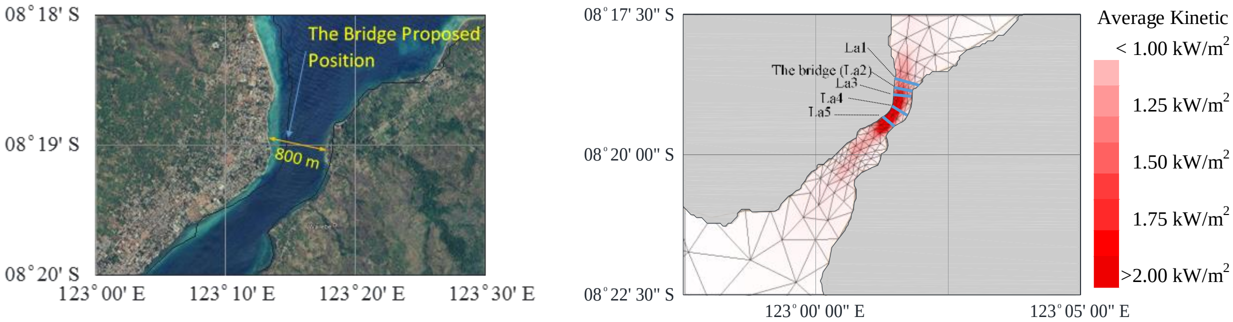

a. Map from Google Earth and the proposed bridge position based on Jan-Vos *et al.* 2017

b. Average kinetic power in Larantuka Strait, showing alternative array locations, including the bridge location at La2.

Figure 5-1: Proposed bridge location and average kinetic power in Larantuka Strait

The mesh in the area of the turbines follows the alignment of the tidal bridge as shown in Figure 5-1b. The idealised turbine model is run for three values of wake coefficient (α_4), the simulations covering four neap spring cycles lasting 62 days and two blockage ratios (B= 0.1 for low blockage and B= 0.4 for high blockage).

As shown in Figure 5-2a, the maximum powers differ from one two-week neap spring cycle to the next. Since the area is located in a region of mixed diurnal/semidiurnal tides, the available power shows a significant neap-spring cycle fluctuation. The peak of power production is also different in each daily cycle (Figure 5-2b). After interpolating the optimum α_4, as shown in Figure 5-3, the available mean power for the idealised case and low blockage is 4.67MW. This number is far below the 18 to 23MW as promised by the promoters of the scheme. The maximum power available is 24.82MW for the same optimum value of α_4 =0.38 as for the average power (Figure 5-3). The maximum available power might reach 25MW, and this figure is close to the capacity quoted for the first stage of the project (18 to 23MW). However, this power is only achievable once or twice a month (see Figure 5-2). Presumably, the quoted figures should be interpreted as the maximum power that can be exploited from the given site.

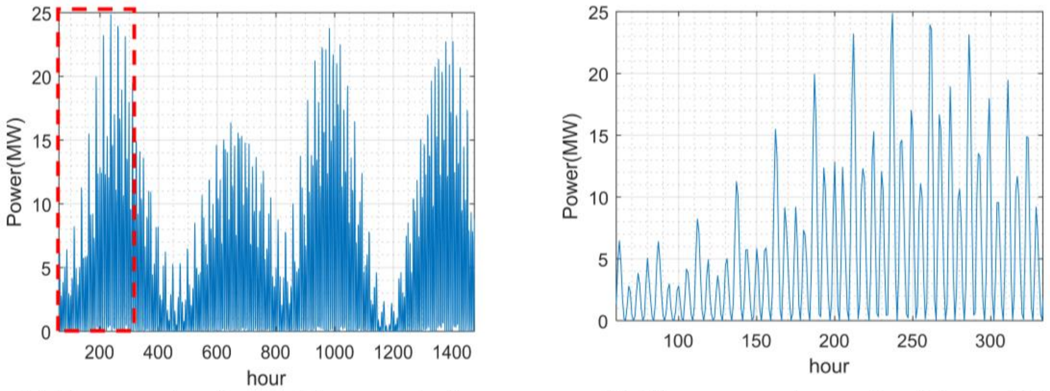

(a) Two months of available power in time series

(b) First neap spring cycle of the available power (dashed line box in Fig. 4(a))

Figure 5-2: Time series of available power at Pancasila Palmerah bridge for low blockage ratio (*B*= 0.1) and $\alpha_4 =$ 0.40

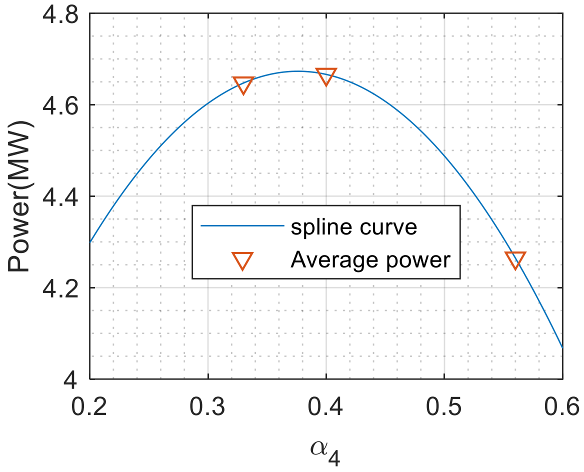

Figure 5-3: Variation in average power removed by turbines at Pancasila Palmerah bridge with wake coefficient for high blockage ratio (*B*= 0.4)

There is a planned extension to the project to deliver 90 to 115MW. The analysis is therefore extended to investigate this figure. As discussed in Chapter 1, the hypothetically highest achievable blockage ratio is about *B*= 0.4. Therefore, the simulations are also run with this assumption. As in the previous simulations, those at high blockage ratio (*B*= 0.4) are also run with three different α_4 values. Following the same method as for low blockage ratio, the optimum average gives 19.06MW available power, and the maximum available power is 87.09MW, both at α_4 =0.53. Although this is still below the target of 90 to115MW, the target of 90MW is almost reached (see Figure 5-4).

The assessment using actuator disc is an upper bound of the resources (Adcock *et al.*, 2013), and in reality, the maximum achievable power is expected to be lower than ~87MW (Chen *et al.*, 2019). This means that the target of 115MW is unlikely to be achieved. Furthermore, the maximum power is not obviously the best metric for describing the resource, since this value is only available fortnightly or monthly. To assess whether the project target can be met, the assessment is further expanded to consider other possible locations.

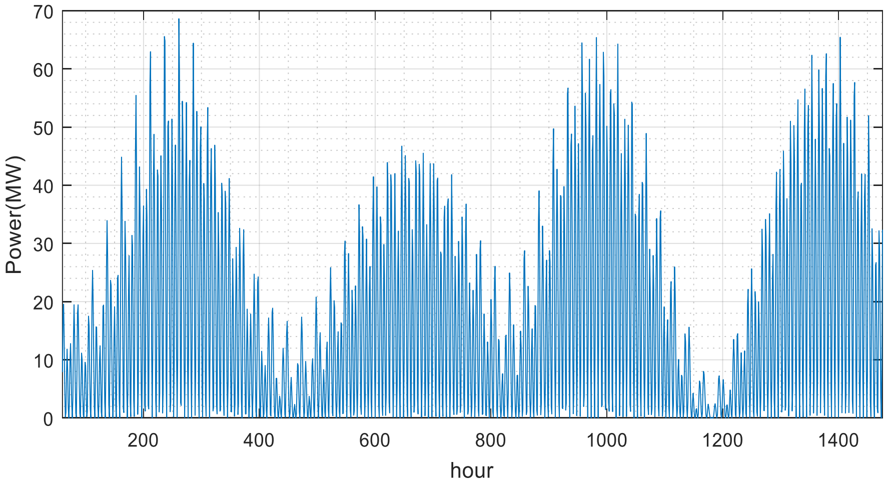

Figure 5-4: Time series of power removed by turbines at the tidal bridge for high blockage ratio (*B*= 0.4) and $\alpha_{4=}$ 0.56

5.1.2 Alternative Locations for Tidal Turbine Arrays

As mentioned in the beginning of this Chapter, the kinetic power can be used to determine the potential locations for tidal energy extraction. Figure 5-1b shows potential locations near the proposed bridge alignment that can be considered. The possible alignments of turbine fences follow the mesh arrangement as shown in Figure 5-1b, where the mesh in the model is aligned perpendicular to the principal flow direction. Five different locations are assessed, including the proposed bridge position. Following similar methods to those used above, the other sites are assessed in the same manner (runs for three different α_4 values and use of a cubic spline to obtain the optimum average available power).

5.1.3 Multi-array Schemes

Here we also consider multi-fence schemes. The proposed location of the bridge is used as one of the fence positions. The results of simulations for low blockage ratio are shown in Table 5-1. The first column of the Table shows the scheme simulated, while the subsequent columns show the average power at the given site. The final column shows the α_4 value at which the power is achieved. For the La1La2La3La4La5 scheme, for example, the results shown in columns La1 to La5 list the available power and α_4 value at each individual site, while the total power presented in the penultimate column is the total available power achieved by the scheme.

Table 5-1 shows, for instance, that the La4 fence gives ~5.4MW of available power. This is higher than the current proposed position of the fence at the bridge (La2), although the fence length for

La4 is shorter than any other fence. As expected, the multi-fence schemes give lower available power at each individual fence for a higher number of fences. For this low blockage scenario, however, the reductions for the multi-fence configurations are relatively small. Occupying all five arrays, for example, only reduces the average available power by around 25% from the sum of the individual fences operated alone.

Table 5-1: Average available power in Larantuka Strait (in MW)

Array Lines	La1	La2	La3	La4	La5
Fence Length (m)	702.61	665.61	665.16	507.80	663.79
Cross Section (m^2)	16,480.42	13,900.56	13,708.63	12,337.51	16,116.73

Scheme	Average Power (in MW)													
	Low Blockage (B = 0.1)							High Blockage (B = 0.4)						
	La1	La2	La3	La4	La5	Total	α_4	La1	La2	La3	La4	La5	Total	α_4
La1	3.56	-	-	-	-	3.56	0.36	16.90	-	-	-	-	16.90	0.49
La2	-	4.67	-	-	-	4.67	0.38	-	19.06	-	-	-	19.06	0.53
La3	-	-	4.96	-	-	4.96	0.38	-	-	19.32	-	-	19.32	0.56
La4	-	-	-	5.40	-	5.40	0.38	-	-	-	22.52	-	22.52	0.60
La5	-	-	-	-	3.87	3.87	0.38	-	-	-	-	16.12	16.12	0.50
La1-La2	3.04	4.42	-	-	-	7.46	0.40	10.39	14.71	-	-	-	25.10	0.60
La2-La3	-	4.13	4.52	-	-	8.64	0.41	-	12.13	14.17	-	-	26.30	0.60
La2-La4	-	4.20	-	5.04	-	9.25	0.40	-	13.11	-	17.96	-	31.07	0.60
La2-La5	-	4.43	-	-	3.63	8.06	0.40	-	14.07	-	-	11.26	25.33	0.60
La1-La2-La3-La4	2.52	3.63	3.97	4.43	-	14.55	0.44	5.28	7.43	8.58	10.20	-	31.49	0.60
La1-La2-La3-La4-La5	2.41	3.48	3.82	4.27	2.85	16.84	0.45	4.50	6.32	7.29	8.65	5.40	32.16	0.60

As for low blockage scenario, the La4 fence gives the highest average power output for high blockage (B= 0.4). This site also performs better in the multi-fence schemes. At high blockage, the interference between fences placed upstream-downstream of each other is greater. The reduction in power for five fences is about 66% of the sum of the powers from the individual sites each operated alone.

The maximum available power is also analysed here. As presented in Table 5-2, these show similar interactions for multi-fence configurations. Regarding the projected delivery of ~115MW capacity, none of low blockage schemes, including the multi-fence schemes, achieves the ~115MW. Therefore, the final stage of this project could only be achievable with high blockage.

Table 5-2: Maximum available power in Larantuka (in MW)

Scheme	Low Blockage (B = 0.1)							High Blockage (B = 0.4)						
	La1	La2	La3	La4	La5	Total	α_4	La1	La2	La3	La4	La5	Total	α_4
La1	15.98	-	-	-	-	15.98	0.36	74.80	-	-	-	-	74.80	0.39
La2	-	24.85	-	-	-	24.85	0.37	-	87.71	-	-	-	87.71	0.40
La3	-	-	28.02	-	-	28.02	0.37	-	-	90.53	-	-	90.53	0.40
La4	-	-	-	29.51	-	29.51	0.37	-	-	-	103.92	-	103.92	0.37
La5	-	-	-	-	22.21	22.21	0.37	-	-	-	-	79.10	79.10	0.39
La1-La2	13.47	22.21	-	-	-	35.68	0.37	43.25	66.38	-	-	-	109.63	0.40
La2-La3	-	20.50	24.15	-	-	44.64	0.37	-	48.65	63.31	-	-	111.96	0.40
La2-La4	-	21.55	-	25.71	-	47.25	0.37	-	52.13	-	76.62	-	128.76	0.37
La2-La5	-	23.13	-	-	19.96	43.10	0.37	-	61.80	-	-	50.25	112.05	0.40
La1-La2-La3-La4	11.02	16.73	20.66	21.78	-	70.20	0.38	21.23	29.59	35.25	40.88	-	126.94	0.41
La1-La2-La3-La4-La5	10.60	16.11	19.73	20.75	15.03	82.23	0.38	18.19	25.35	29.23	33.91	25.34	132.02	0.41

At high blockage, schemes with two or more arrays can give a maximum power output of about 115 MW. Of the two fence schemes, the La2La4 scheme is the most promising, and the ~115 MW target might be achieved with a high blockage, two fence scheme. If four or more fences were installed, the fences would only operate at 25-30% of individual capacities.

5.1.4 The Effect of Tidal Arrays on the Global Current at Larantuka

The flow field changes in the area are calculated by comparing the average flow at each node before and after the turbines are installed in the model. Figure 5-5 shows the flow change for a turbine fence installed at the bridge position (scheme La2). The low blockage case is presented in Figure 5-5a and high blockage Figure 5-5b. Red indicates increased flow, and blue indicates decreased flow due to the deployment of turbines.

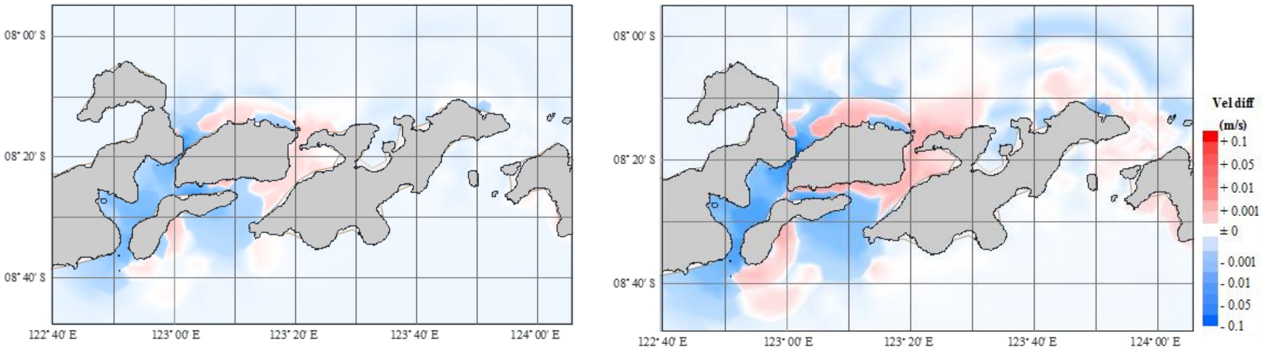

a. Low blockage ratio (*B*= 0.1) **b.** High blockage ratio (*B*= 0.4)

Figure 5-5: Flow field change for a turbine array deployed at the bridge location

The figures show that high blockage causes the flow to divert to nearby channels or the Boleng and Alor Straits. These results also imply that a high blockage ratio such as 0.4 is not just hard to achieve in reality, but has negative consequences, since the flow diversion might have a significant impact on the regional flows. For high blockage, therefore, the effect on global current should be considered.

At high blockage, the flow fields changes significantly in the region. As discussed in (Firdaus *et al.*, 2020), the model considers the Indonesian Throughflow (ITF). The flow pattern of the ITF in the Bali-NTT islands chain follows the pattern described by Gordon, 2005 as presented in Figure 5-6. Figure 5-7 presents flow changes in the relatively distant straits of Lombok, Alas, Sape, Linta and Molo (area of observation in Figure 5-7), which show the flow at these sites slightly increases.

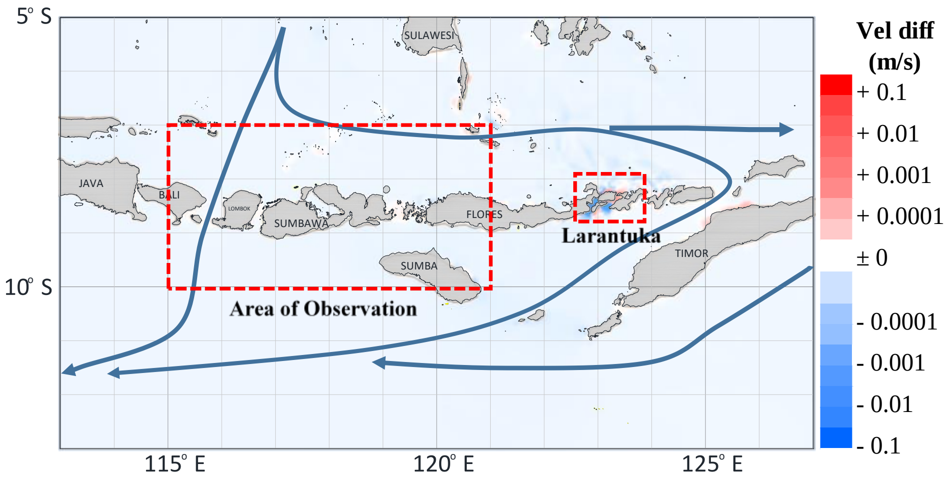

Figure 5-6: The flow changes in the region and the effect on ITF at high blockage ratio (*B*= 0.4)

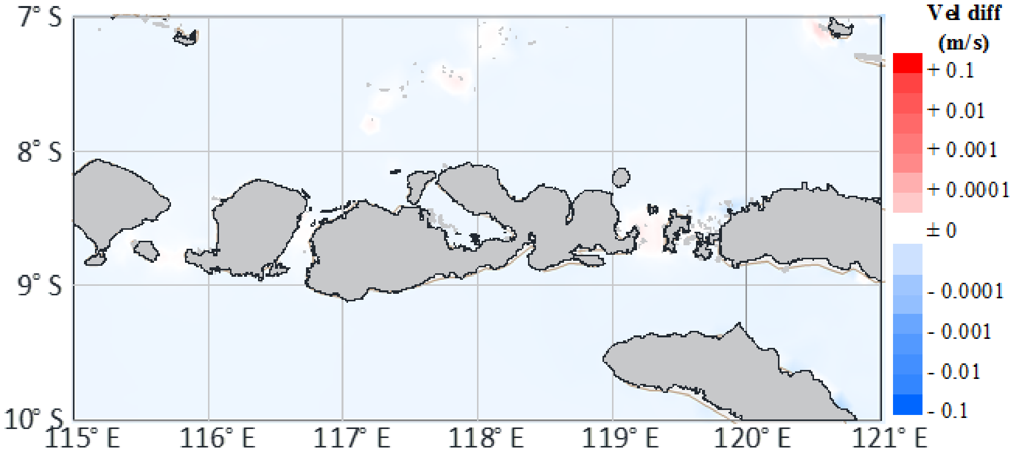

Figure 5-7: Change in flow field distant from the tidal bridge site for the case of the turbines at high blockage ratio (*B*= 0.4).

5.2 Electricity from Tidal Streams in the Bali-Lombok Channels

The strait between Bali and Lombok Islands has been earmarked by turbine developers for tidal energy extraction. Two UK based companies, SBS INTL LTD (SBS) and Simec-Atlantis Resources Limited (Atlantis), have been awarded an exclusive site development agreement with PLN, a state company to provide electricity in Indonesia, in 2021, to develop commercial-scale tidal arrays in the Lombok Strait (SimecAtlantis, 2020). The project will progressively deliver 150MW, and the first phase of the project is deploying 12MW arrays for phase 1, expanding to 70MW in the next phase. Ultimately, they aim to reach the target of 150MW by 2023. Unfortunately, there is no report in the public domain about the details of this project. It is also unclear where the exact site location(s) are, since the Lombok Strait, between Bali Island and Lombok, is divided into three straits, Badung, Toyopakeh and Lombok Strait (see Figure 5-8). All three straits exhibit strong currents.

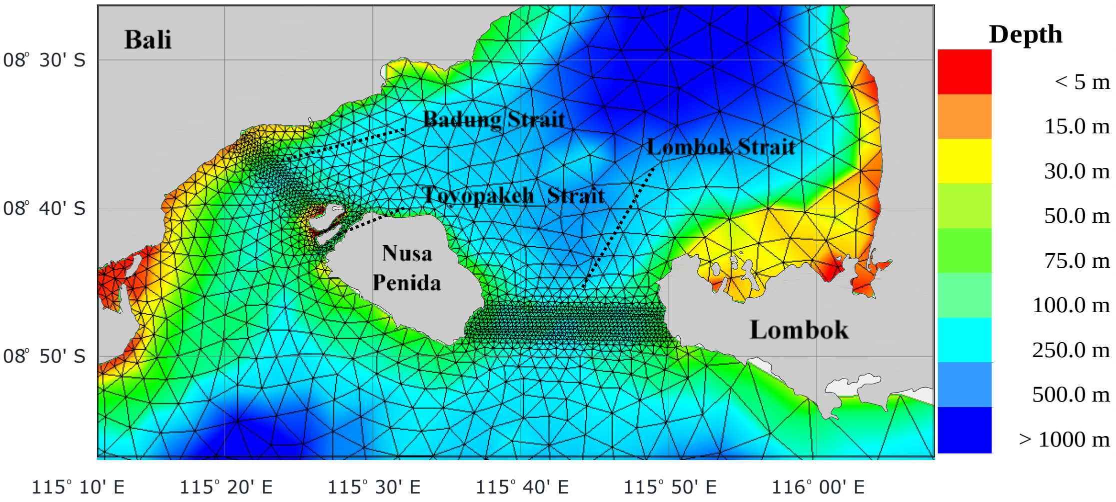

Figure 5-8: The bathymetry in the vicinity of potential sites at Lombok Strait

5.2.1 Potential Sites in the Bali-Lombok Channel

The first assessment for these sites is based on the presumption that the entire channel could be occupied by turbine fences. Following Firdaus *et al*. 2019, the turbine fences are installed as a ~13.8km long turbine array at Nusa Penida (A), ~980m long array at Toyopakeh (B) Strait and 25km long array at Lombok (C) Strait. In the first step of the analysis, a fence of turbines occupies the whole channel width in each strait. As shown in Figure 5-8, the model meshes follow the fence alignments. The average current velocity field, as shown in Figure 5-9, confirms that these locations have potential for tidal energy extraction.

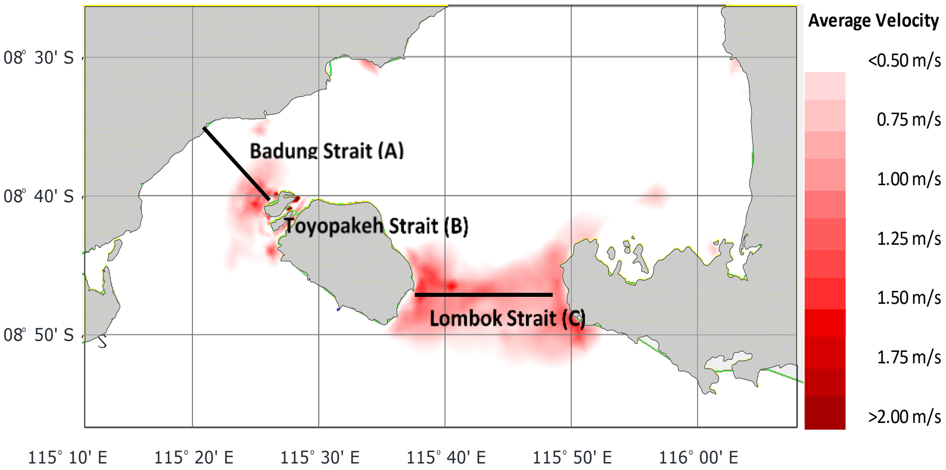

Figure 5-9: The average flow speed in the vicinity of the Bali-Lombok channel, predicted using DG-ADCIRC simulation (Firdaus *et al.*, 2019).

In a similar way to the Larantuka site, three different wake coefficients (α_4) are applied to each array. An example of available power time series is presented in Figure 5-10. Average available power is calculated for each case and plotted against α_4, similar to the previous location. The optimum α_4 at which maximum available power is achieved is obtained by fitting a cubic spline through the data points. The entire assessment is carried out for two blockage ratios: *B*= 0.1 (low blockage) and *B*= 0.4 (high blockage).

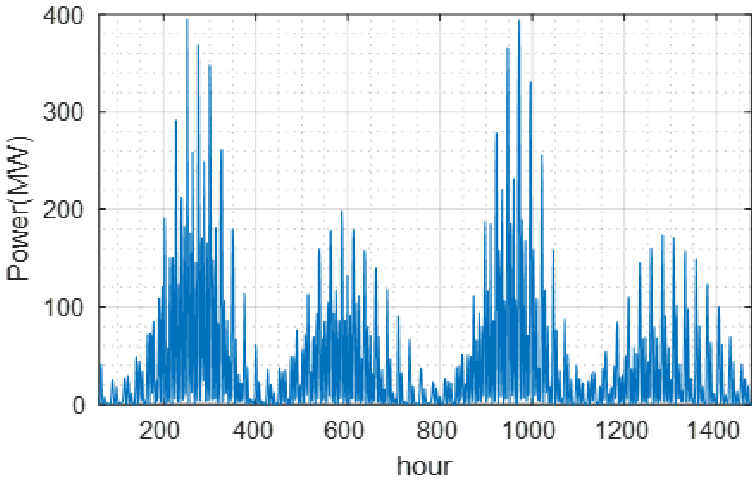

Figure 5-10: Available power time series for individual fences at the Badung Strait (A)

The average resource at Nusa Penida is approximately ~39MW, at Toyopakeh is ~4.4MW and at Lombok is ~273MW at low blockage ratio. SBS and Atlantis promised to deliver 150MW electricity from this site. It seems this can be achieved at low blockage from Lombok Strait. At high blockage, the resources increase significantly, and is about five to six times higher than for low blockage case. In detail the resource at Nusa Penida is ~232MW or almost six times higher, Toyopakeh is ~22MW or about five times higher and Lombok is ~1.8GW, more than six times higher than the resources at *B*= 0.1. These results show that the given sites are promising for tidal turbine implementation.

This study indicates that the total theoretical power potential of the Bali waters is approximately ~2.05GW (from three sites exploited simultaneously at high blockage). The estimates have been obtained using a 2D depth-averaged numerical model. This should represent be an improvement on previous assessments based on the undisturbed kinetic flux (Coordinating team of Research and Technology, 2008, Rachmayani *et al.* 2006 and Orhan *et al.*, 2017).

5.2.2 Site-site Interactions

Since there are three straits parallel to each other, the schemes modelled in this study are ABC, AB, AC and BC. The letters represent each channel used for tidal energy generation. For example, the ABC scheme means all channels are harnessed simultaneously and AB means that turbines are deployed at the Badung Strait (A) and the Toyopakeh Strait (B).

a) *Multiple Constituents*

Table 5-3 shows the average power obtained for optimum wake coefficient for different schemes and the two blockage ratios. The Table also shows the resources from each array in any given scheme. The final column shows the optimum wake coefficient for the model. At low blockage, the power at C (the Lombok Strait) decreases from ~293MW to ~267MW for scheme ABC, while A remains at ~39MW and B remains at ~4.4MW. The small decrease at C is also present in other schemes such as BC and AC: the output from the fence at C decreases while A and B remain at the same value as when they are exploited individually. Fences A and B have no diminishing effect on each other when the resources are harnessed simultaneously.

Table 5-3: Average available power for each scheme in Bali-Lombok

		Badung Strait (A)		Toyopakeh Strait (B)				Lombok Strait (C)		
Cross section (m^2)		1,446,938.45		114,352.18				4,316,438.29		
Fence length (m)		13,893.73		994.48				25,008.72		
	Average Power (MW)									
Schemes	Low Blockage (B = 0.1)					High Blockage (B = 0.4)				
	A	B	C	Total	α_4	A	B	C	Total	α_4
Badung Strait (A)	39.2	-	-	39.2	0.34	231.6	-	-	231.6	0.44
Toyopakeh Strait (B)	-	4.4	-	4.4	0.35	-	21.8	-	21.8	0.48
Lombok Strait (C)	-	-	292.8	292.8	0.34	-	-	1,834.7	1,834.7	0.41
AB	39.3	4.4	-	43.7	0.34	252.3	25.0	-	277.3	0.43
BC	-	4.4	266.6	270.9	0.34	-	22.7	1,757.7	1,780.4	0.41
AC	39.1	-	266.9	306.0	0.34	245.5	-	1,771.9	2,017.4	0.41
ABC	39.3	4.4	267.1	310.8	0.34	252.0	24.6	1,777.1	2,053.7	0.41

At high blockage, the trend at C is again observed. The average at C decreases from ~1.83GW when the channel is harnessed individually to ~1.78GW when the channel is exploited simultaneously with the other two channels (scheme ABC). The same trend is exhibited in other schemes, the resources at C tend to decrease when it is exploited in parallel with other channels. However, these effects are small.

In contrast, the other two channels show a slight increase in power at high blockage when they are exploited simultaneously, the available power at Badung Strait increases from about ~231MW to ~252MW while Toyopakeh's resource rises from ~22MW to ~25MW when all channels are exploited simultaneously. This trend is consistent for other scenarios. The available power at Badung Strait increases from 231MW to 245MW while at Toyopakeh shows a small increase from 21.8MW to 22.7MW when they are exploited simultaneously with the Lombok Strait. Meanwhile, when Badung and Toyopakeh are exploited simultaneously, Badung Strait increases approximately from 231 to 252MW while Toyopakeh increases from ~21MW to ~25MW.

The percentage resource changes due to site-site interactions are shown in Table 5-4, which shows the output of each array in different schemes in comparison to its output as an individual array. The colour schemes express whether the array extracts more or less power than the individual capacity. Blue means more available power while red means less available power compared to the individual capacity. The Lombok Strait consistently exhibits a decrease due to site-site interactions, with about 9% loss at low blockage and 4% loss at high blockage. The increase at other sites is only apparent at high blockage.

Table 5-4: Ratio of resource in combined array compare to that in each individual array in Bali-Lombok.

Schemes	Low Blockage (B = 0.1)				High Blockage (B = 0.4)			
	A/A*	B/B*	C/C*	All/All*	A/A*	B/B*	C/C*	All/All*
Badung Strait (A)	100.00%				100.00%			
Toyopakeh Strait (B)		100.00%				100.00%		
Lombok Strait (C)			100.00%				100.00%	
AB	100.32%	101.26%		100.41%	108.95%	114.94%		109.47%
BC		100.06%	91.03%	91.16%		104.18%	95.80%	95.90%
AC	99.89%		91.15%	92.18%	106.02%		96.57%	97.63%
ABC	100.23%	101.42%	91.20%	92.39%	108.81%	112.87%	96.86%	98.35%

* The available power from single array schemes

Since the resources calculated here are based on the optimum wake coefficient, it is useful also to compare the results at each α_4. Figure 5-11 shows the average resources plotted against wake coefficient for the different schemes at each of the three sites. Based on the figures, the resources at the Badung Strait (Figure 5-11A) tend to be higher for parallel array schemes than for the individual array scheme. Consider scheme AC, where the turbines are installed at Badung Strait (A) and the Lombok Strait (C), the average available powers at all three different α_4 values and from the cubic spline maximum are higher than the scheme of the individual array (scheme C). At higher α_4 the average available power from scheme AC tends to a rapid decline. The same pattern is also observed at Toyopakeh (Figure 5-11, B). However, the average extractions are still higher for combined arrays than for the individual array.

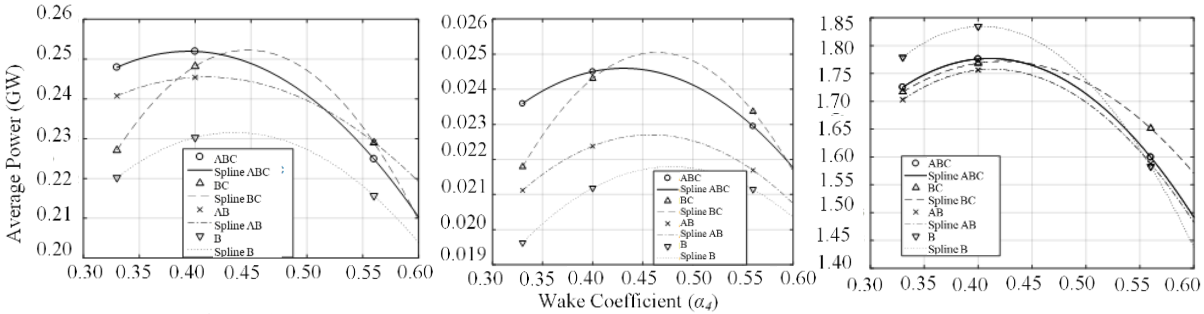

Badung (A)

Toyopakeh (B)

Lombok (C)

Figure 5-11: Average available power for high blockage (B= 0.4) of turbine arrays in Bali-Lombok

At Lombok Strait (Figure 5-11, C, the average power at low α_4 for the individual array scheme (scheme C) is higher than for the multi-array schemes. It is worth observing though that at higher α_4 the average available power is lower than for the multi-array schemes. Thus, this lower average available power for multi-array schemes is only applicable at low α_4.

b) Single Constituents

Following the method that is used by Draper *et al.* 2014 and Coles *et al.* 2017, this study also uses M_2 as single constituent to drive the numerical simulation to investigate this further. The case of Bali-Lombok channels is used for this analysis. The tidal fences layout for this scenario follows Figure 5-9. It is important to note, these assessments are based on the simulation of tidal fences blocking the entire channel. The average available power for Bali sites is presented in Table 5-5. The estimates of average available power are typically 50% of the simulations run with 13 constituents. For example, the simulations run with 13 constituents in the Lombok Strait produce ~250 MW while the simulations driven by just M_2 produce ~127 MW.

Table 5-5: Average available power resource for each scheme in Bali-Lombok from simulations that are driven by M_2 only.

Schemes	Low Blockage (B = 0.1)					High Blockage (B = 0.4)				
	A	B	C	Total	α_4	A	B	C	Total	α_4
Badung Strait (A)	19.9	-	-	19.9	0.35	127.2	-	-	127.2	0.41
Toyopakeh Strait (B)	-	2.7	-	2.7	0.35	-	14.5	-	14.5	0.47
Lombok Strait (C)	-	-	122.9	122.9	0.33	-	-	912.0	912.0	0.38
AB	19.9	2.8	-	22.7	0.35	131.2	15.6	-	146.8	0.41
BC	-	2.7	122.9	125.6	0.33	-	14.2	915.5	929.7	0.38
AC	19.7	-	123.0	142.7	0.34	124.5	-	913.4	1,037.9	0.39
ABC	19.8	2.7	123.1	145.6	0.34	128.4	15.2	917.0	1,060.6	0.39

The results also imply that the interaction between the sites from the simulation driven by M_2 only is different from the interactions obtained from the simulation that is driven by 13 constituents. The simulation that is driven by 13 constituents shows that the Lombok Strait (C) produces less for multi-array scenarios than the single array scenario (see Table 5-3). However, the simulations driven by M_2 only show the opposite trend.

Table 5-6 shows that the Badung (A) and Toyopakeh (B) Straits produce less than their individual capacities when operated simultaneously with the tidal fence installed in Lombok Strait (C). Therefore, this analysis further confirms that the simulations run with single constituent are unable to capture the whole picture of tidal resources in an area, including the interaction between channels in parallel.

Table 5-6: The fraction of available power in Bali-Lombok from simulations that are driven by M_2 only

Schemes	Low Blockage (B = 0.1)				High Blockage (B = 0.4)			
	A/A*	B/B*	C/C*	All/All*	A/A*	B/B*	C/C*	All/All*
Badung Strait (A)	100.00%				100.00%			
Toyopakeh Strait (B)		100.00%				100.00%		
Lombok Strait (C)			100.00%				100.00%	
AB	100.29%	100.91%		100.36%	103.16%	107.72%		103.63%
BC		99.38%	100.05%	100.03%		98.12%	100.39%	100.35%
AC	99.32%		100.13%	100.01%	97.86%		100.16%	99.88%
ABC	99.60%	100.13%	100.18%	100.10%	100.94%	104.97%	100.55%	100.66%

5.2.3 More Realistic Tidal Arrays

The arrays blocking the channels might not be feasible in reality. Since this area is a part of the international shipping route, the assumption that a high level of blockage can be achieved is unrealistic. Therefore, it is sensible to investigate more realistic arrays. The deployment of arrays partially spanning the channel will reduce the net power available from the values given in the previous analysis.

This analysis uses simulations with three different wake coefficients (α_4) and two different blockage ratios. The tidal hydrodynamic models are driven by 13 tidal constituents. The average velocity was used to determine the fence lines across the potential channel in the previous analyses (see Figure 5-9). For this analysis, the average kinetic power is used to determine the potential locations. Figure 5-12 shows the average kinetic power in the Bali-Lombok area.

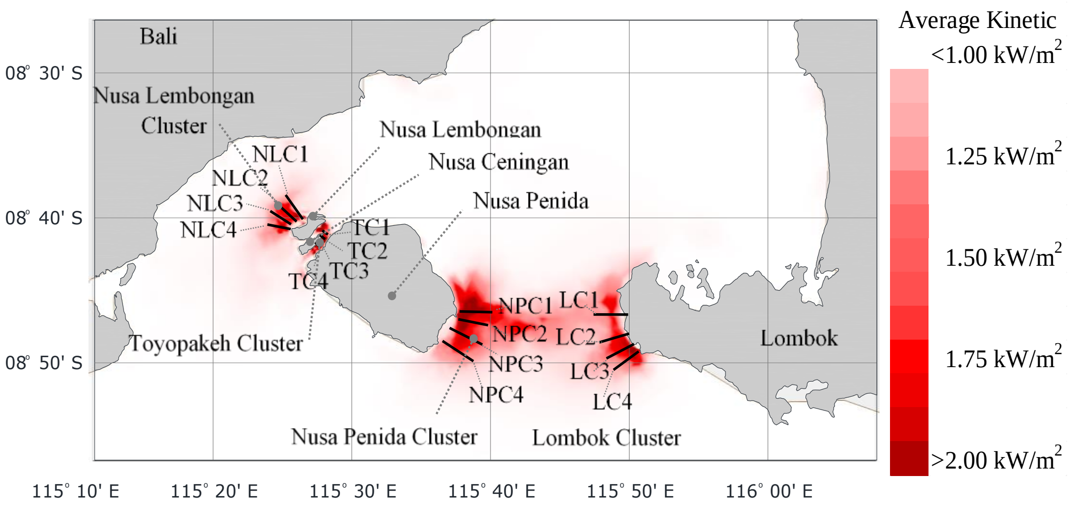

Figure 5-12: Average kinetic power in the vicinity of potential tidal turbine array locations in the Lombok Straits.

Four potential locations in the Lombok straits are identified for the realistic tidal arrays (see Figure 5-12). The potential locations in Badung Strait are in the coastal area of Nusa Lembongan Island. Anywhere along the Toyopakeh's channel has potential for energy exploitation. Hence, several lines could be drawn for turbine fences. Two clusters of potential locations in Lombok Strait are identified from the average kinetic power, one adjacent to Nusa Penida Island and another next to Lombok Island. These potential locations are named; Nusa Lembongan Cluster (NLC), Toyopakeh Cluster (TC), Nusa Penida Cluster (NPC) and Lombok Cluster (LC).

These locations also have a depth suitable for a turbine deployment. The operating tidal stream turbines that are currently available in the market are suitable for locations with the depth < 50 m. However, there is the possibility of extracting energy from deeper water using floating tidal turbines. Based on the experiences of the offshore wind turbine industries, 100 m depth might be still acceptable for floating tidal turbines. Figure 5-13 shows the bathymetry around the turbine arrays at the potential locations. The potential lines of turbine fence are not solely based on the average kinetic power, but also consider the water depth.

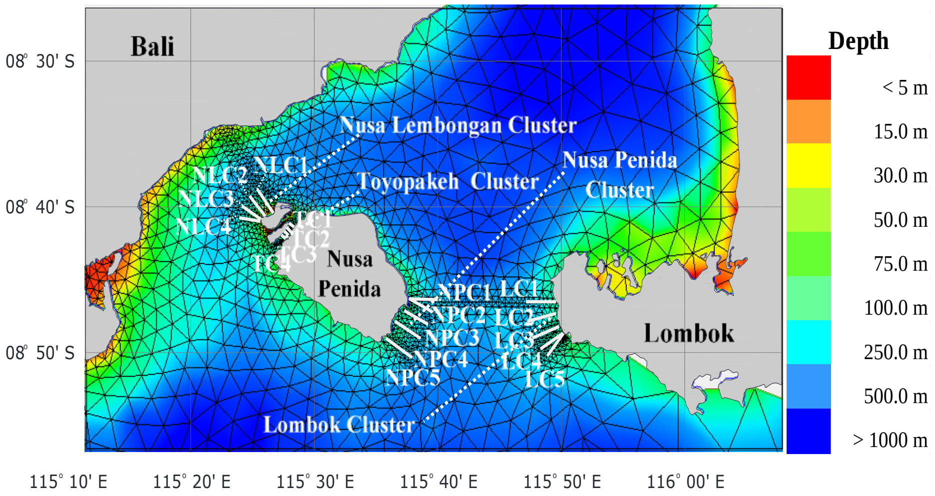

Figure 5-13: The bathymetry around the array lines of the turbines in Lombok straits

The analyses in this section also include site-site interactions. Since there are some fence lines for each location, the site-site interactions in an upstream-downstream manner, are also reported here. These analyses are discussed for each location along with the resource assessments. It should be borne in mind, that these further investigations still use a uniform blockage ratio. Despite calling these more realistic arrays, they are not completely realistic. Since turbine developers would prefer to deploy the same size turbines along the turbine fences, the uniform blockage ratios are unlikely to be implemented in reality.

a) The Nusa Lembongan Cluster (NLC)

Although only occupying a quarter of the channel cross-section, some of the lines in the NLC extract half of the power from the whole channel cross-section at low blockage ratio (Badung

Strait's A-line from section 5.2.2). For example, the NLC1 and NLC 2 lines produce ~21MW and ~19 MW at low blockage ratio (see Table 5-7). Meanwhile, the A-line in Badung Strait, which is ~13.9 km long, approximately produces ~39 MW at low blockage ratio (see Table 5-3). Given that, the NLC1 and NLC2 lines occupy only ~2.9 km of the channel's cross-section, or less than a quarter of Badung Strait's width. Although the NLC3 and NLC4 array lines are not as good as NLC1 and NLC2 at low blockage, both these arrays in the NCL still have better available power per cross-section area than the array across the entire channel (the A-Line).

All array lines together (NLC1-NLC2- NLC3- NLC4) produce more potential power than the A-line. Nevertheless, the total lengths of the NLC fence lines are almost the same as the length of the A-line. The combination of three array lines from the NLC (NLC1- NLC2- NLC3 or NLC1-NLC2-NLC4) have larger power than the A-line. In brief, the array-lines in the NLC have better potential than a single line of turbines spanning across the channel at low blockage ratio.

The A-line performs better than the NLC lines at high blockage ratio. The available power per cross-section for the A-line is higher than the NLC (see Table 5-3 and Table 5-7). Essentially, four times the extraction at low blockage scenario is harnessed at high blockage in the NLC arrays. However, the line spanning across the channel in the Badung Strait at high blockage could extract six-time more than its capacity at low blockage. The A-line extraction at high blockage extracts almost one-and-a-half times that extracted from the combination of the entire NLC arrays (NLC1-NLC2- NLC3- NLC4). The A-line alone produces ~231 MW while NLC1- NLC2- NLC3-NLC4 only produces ~164MW. This shows that arrays arranged in series might no longer be attractive at high blockage.

Table 5-7: The average available power in the NLC (in MW)

	NLC1	NLC2	NLC3	NLC4
Cross Section (m^2)	271,377	293,937	298,004	307,154
Fence Length (m)	2,949	2,931	3,323	3,484

Schemes	Low Blockage (B = 0.1)						High Blockage (B = 0.4)					
	NLC1	NLC2	NLC3	NLC4	Total	α_4	NLC1	NLC2	NLC3	NLC4	Total	α_4
NLC1	21.41	-	-	-	21.41	0.36	89.97	-	-	-	89.97	0.55
NLC2	-	19.22	-	-	19.22	0.34	-	91.12	-	-	91.12	0.52
NLC3	-	-	17.01	-	17.01	0.35	-	-	83.35	-	83.35	0.50
NLC4	-	-	-	14.08	14.08	0.35	-	-	-	75.41	75.41	0.49
NLC1-NLC2-NLC3-NLC4	18.81	15.84	13.42	11.94	60.00	0.40	57.59	34.74	28.44	43.99	164.75	0.60
NLC1-NLC2-NLC3	19.47	16.40	14.15	-	50.02	0.40	60.86	40.92	42.83	-	144.61	0.60
NLC1-NLC2-NLC4	19.59	16.59	-	12.60	48.78	0.39	62.99	42.77	-	49.51	155.28	0.60
NLC1-NLC4	20.83	-	-	13.32	34.15	0.37	77.85	-	-	55.20	133.05	0.57
NLC1-NLC3	20.52	-	15.26	-	35.78	0.38	74.66	-	52.07	-	126.73	0.60

Table 5-8 presents the fraction of the available power over the capacity of each individual array in a single array scenario. At low blockage, the NLC1- NLC2- NLC3- NLC4 scheme still produces

84% of its individual capacities, while at high blockage the NLC combined arrays only produce 50% of their total individual capacities. Some of the arrays in the combination, NLC2 and NLC3 even operate at less than half of their individual capacity. This further confirms that the fence lines arranged in series might be unattractive at high blockage.

As an individual array at the NLC, the NLC2 fence line operates slightly better than NLC1 at high blockage, despite the fact that the NLC1 line has better power output than the NLC2 line at low blockage. The NLC2 fence performs poorly in three- or four-line scenarios. As presented in Table 5-8, NLC2 operates at only 38% to 47% in the multi-array schemes at high blockage. The lines in the middle produce much less power when exploited simultaneously in proportion to their individual schemes than the arrays at the ends of series. This is because the fence lines in the middle experience loss of power for flows in both directions in a bi-directional cycle when exploited simultaneously, while the lines at the ends experience loss of power from the half of the tidal cycle only.

The numbering of array lines is in consecutive order, so the NLC1 fence line is closer to the NLC2-line than to the NLC3-line. Therefore, the NLC1-line to the NLC4-line in the NLC1- NLC4 scenario is farther than the NLC1 line to NLC3 line in the NLC1- NLC3 scheme. Table 5-8 shows that the NLC1- NLC4 scenario has a higher fraction than the NLC1- NLC3 at both blockage ratios, although the NLC1- NLC3 has slightly higher magnitude than the NLC1- NLC4 at low blockage, due to the NLC3 line having higher available power than NLC4. Based on these fractions, one could conclude that the perpendicular distance between the array lines is essential for the reducing the losses from the series interactions.

Table 5-8: The fraction of available power in combined array to the individual array in the NLC

Schemes	Low Blockage (*B* = 0.1)					High Blockage (*B* = 0.4)				
	NLC1	NLC2	NLC3	NLC4	All	NLC1	NLC2	NLC3	NLC4	All
	NLC1*	NLC2*	NLC3*	NLC4*	All*	NLC1*	NLC2*	NLC3*	NLC4*	All*
NLC1	100%					100%				
NLC2		100%					100%			
NLC3			100%					100%		
NLC4				100%					100%	
NLC1-NLC2-NLC3-NLC4	88%	82%	79%	85%	84%	64%	38%	34%	58%	48%
NLC1-NLC2-NLC3	91%	85%	83%		87%	68%	45%	51%		55%
NLC1-NLC2-NLC4	92%	86%		90%	89%	70%	47%		66%	61%
NLC1-NLC4	97%			95%	96%	87%			73%	80%
NLC1-NLC3	96%		90%		93%	83%		62%		73%

b) *The Toyopakeh Cluster (TC)*

Following the previous codification of the fence lines, the lines in the TC are coded as TC1, TC2, TC3 and TC4 (see Figure 5-12). The assessment of this cluster expands the assessment in the Toyopakeh Strait. The analysis is focused on the individual lines along the channel of the Toyopakeh Strait. The parallel interactions in the next section require analysis. For practicality, the analysis is limited to interactions when the entire array lines are operated simultaneously (TC1-TC2- TC3- TC4 scheme).

At low blockage ratio, the cross-sectional area of the channel determines the magnitude of the available power. As shown in Table 5-9, the resources from TC1 to TC4 are proportion to the cross-sectional area of the array lines. This is not the case at high blockage. The TC2 line has more power, yet has a smaller cross-sectional area than TC1.

Table 5-9: The average available power in the TC (in MW)

Schemes	TC1	TC2	TC3	TC4
Cross Section (m^2)	72,926	68,651	60,521	43,051
Fence Length (m)	952	896	775	449

	Low Blockage (B = 0.1)						High Blockage (B = 0.4)					
	TC1	TC2	TC3	TC4	Total	α_4	TC1	TC2	TC3	TC4	Total	α_4
TC1	10.88	-	-	-	10.88	0.36	26.51	-	-	-	26.51	0.60
TC2	-	8.40	-	-	8.40	0.37	-	31.96	-	-	31.96	0.60
TC3	-	-	7.24	-	7.24	0.37	-	-	26.76	-	26.76	0.57
TC4	-	-	-	5.50	5.50	0.37	-	-	-	22.99	22.99	0.60
TC1-TC2-TC3-TC4	7.98	6.21	5.29	3.87	23.35	0.45	16.03	12.19	9.40	6.98	44.59	0.60
TC1-TC2	9.51	7.46	-	-	16.98	0.41	25.92	19.91	-	-	45.83	0.60

The fraction of available power in the multi-array scheme shows that the arrays in the TC will produce even less power as a fraction of the individual sites than at the previous cluster (NLC). At low blockage, the fractions of the average power from the TC arrays show the fence lines on the multi-array schemes only operates in around 70%-74%. These numbers are lower than the fraction from NLS which operated at 79%-88% of the individual capacity.

This severe performance reduction apparently is typical of the interactions in a channel site like Toyopakeh Strait. This is similar to the Larantuka Strait whether at low blockage or at high blockage. At low blockage, the Larantuka tidal bridge also operated at 71%-82% of the individual capacity. At high blockage, the fractions of individual sites are around 30-48 %, which is similar to the fraction of Larantuka Strait for the four array lines scheme. However, TC1 shows an anomaly in high blockage scenario, as this line still produces 60% of its individual capacity.

c) *The Nusa Penida Cluster (NPC)*

As mentioned previously, the NPC is in the eastern side of the Lombok Strait, adjacent to the Nusa Penida Island. As shown in Figure 5-13, this thesis considers five arrays from the potential locations in the NPC. The lines of NPC1 are almost at a similar location to NPC2, both lines basically only have a different orientation. It is thought that NPC2 will give higher power than NPC1 due to the flow orientation at the maximum velocity. As shown in Figure 5-14, the flow vectors are more perpendicular to the C2's fence-line than to NPC1. Average available power in the NPC1 line is ~51 MW at low blockage and ~273 MW at high blockage while the NPC2 line only produces ~42 MW at low blockage and ~245 MW at high blockage (see Table 5-10). This is due to the fact that the LMADT model in the ADCIRC code does not take the flow orientation into account.

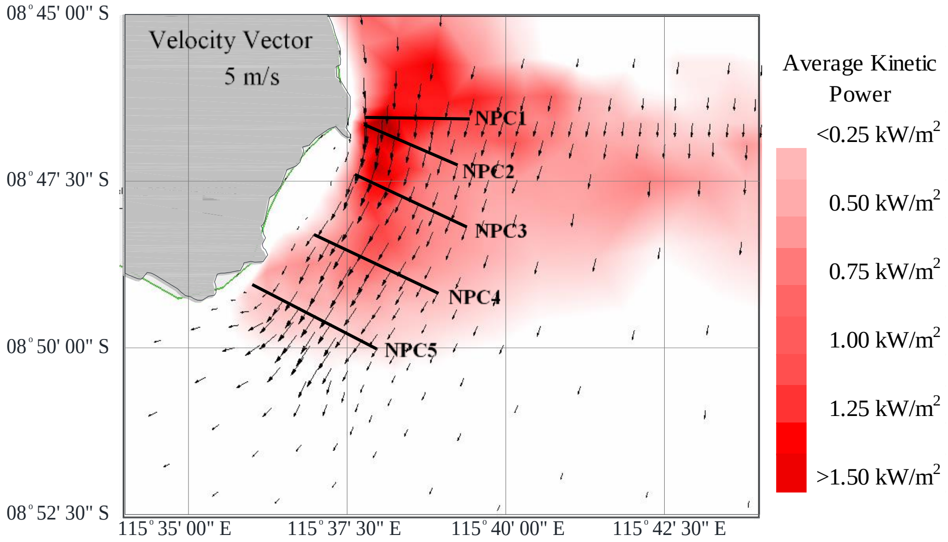

Figure 5-14: The flow orientation and the average kinetic power in the NPC

Table 5-10: The average available power in the NPC

			NPC1			NPC2		NPC3			NPC4			NPC5
Cross Section (m^2)			423,995			451,086		585,001			570,221			505,527
Fence Length (m)			2,991			2,886		3,552			3,911			4,045
Schemes	Low Blockage (B = 0.1)							High Blockage (B = 0.4)						
	NPC1	NPC2	NPC3	NPC4	NPC5	Total	α_4	NPC1	NPC2	NPC3	NPC4	NPC5	Total	α_4
NPC1	51.14	-	-	-	-	51.14	0.34	273.56	-	-	-	-	273.56	0.51
NPC2	-	42.56	-	-	-	42.56	0.34	-	245.78	-	-	-	245.78	0.48
NPC3	-	-	50.23	-	-	50.23	0.34	-	-	287.15	-	-	287.15	0.47
NPC4	-	-	-	45.08	-	45.08	0.34	-	-	-	240.92	-	240.92	0.50
NPC5	-	-	-	-	23.12	23.12	0.35	-	-	-	-	125.54	125.54	0.47
NPC2-NPC3-NPC4-I	-	38.62	45.62	39.74	20.29	144.26	0.38	-	127.74	137.90	112.67	79.61	457.92	0.60
NPC1-NPC3	49.35	-	47.51	-	-	96.86	0.36	204.64	-	197.69	-	-	402.33	0.55
NPC1-NPC5	50.42	-	-	-	21.89	72.31	0.36	238.06	-	-	-	97.67	335.73	0.53
NPC2-NPC3	-	40.82	48.19	-	-	89.01	0.36	-	171.87	214.10	-	-	385.97	0.56
NPC2-NPC5	-	41.73	-	-	22.13	63.86	0.36	-	199.84	-	-	104.94	304.78	0.53

Lombok Strait is known to possess the largest tidal energy resource in Indonesian waters. Based on this assumption, a single line of turbines could occupy the entire channel cross-section (see section 5.2.2). The Lombok Strait can produce 1.8 GW just from a single line of turbines. The combined fences that span only part of the channel could not produce the same magnitude of the single line spanning across the entire channel. However, most of the NPC fence lines essentially perform better than the line occupying the entire channel (the C-line in the Lombok Strait).

Although the C-line produces ~292 MW at low blockage and ~1.834 GW at high blockage, in terms of power per swept area, it essentially only produces ~61 W/m^2 at low blockage and ~ 425 W/m^2 at high blockage in the Lombok Strait. Meanwhile, the average power per cross-section area of the NPC1, NPC2, NPC3, NPC4 and NPC5 fence lines is ~120 W/m^2, ~94 W/m^2, ~ 85 W/m^2 , ~79 W/m^2, ~45 W/m^2 at low blockage, and ~645 W/m^2, ~544 W/m^2, ~490 W/m^2, ~422 W/m^2, ~248W/m^2 at high blockage, respectively. Based on these numbers, it is safe to conclude that most of the NPC lines perform better than the C array. The available power per cross-section areas in NPC4 is slightly higher than that for the C-line at low blockage but the power per area is equivalent to the NPC-line at high blockage. Only NPC5 does not perform better than the C-line. These results are reasonable, since the NPC5 line has lower average kinetic power density than the C-line (see Figure 5-14).

As for the NLC, the turbine fences that partially span across the channel make the NPC site become a headland type site. The fractions of the array-lines are still at 88%-99% at low blockage and 47%-87% at high blockage compared to the individual capacity in the multi-array schemes (see Table 5-11). These fractions are slightly higher than the available power from the Larantuka and Toyopakeh sites in the series case.

According to the previous sites, the array lines in series have a better performance when the perpendicular distance between the fence-lines' alignment is greater. Meanwhile, the NPC1 fence-line alignment is not perfectly parallel to the other fence-lines. This configuration is good for examining the nature of interactions in series. Therefore, this section investigates the difference of interaction of the NPC1 to the other lines compared to the NPC2 to the same lines.

NPC1 performs slightly better than the NPC2, especially at high blockage (see Table 5-11). However, NPC3 and NPC4 extract less power when they are exploited simultaneously with NPC1 than NPC2. This might be due to the distance between the fence-lines. The distance of NPC2 and NPC3 to NPC1 is farther than the distance from NPC2. Therefore, it is uncertain whether the alignment orientation or the distance determines the magnitude of interaction.

Table 5-11: The fraction of available power in the NPC

Schemes	Low Blockage (B = 0.1)						High Blockage (B = 0.4)					
	NPC1/NPC1*	NPC2/NPC2*	NPC3/NPC3*	NPC4/NPC4*	NPC5/NPC5*	All/All*	NPC1/NPC1*	NPC2/NPC2*	NPC3/NPC3*	NPC4/NPC4*	NPC5/NPC5*	All/All*
NPC1	100%					100%	100%					100%
NPC2		100%				100%		100%				100%
NPC3			100%			100%			100%			100%
NPC4				100%		100%				100%		100%
NPC5					100%	100%					100%	100%
NPC2-NPC3-NPC4-NPC5		91%	91%	88%	88%	90%		52%	48%	47%	63%	51%
NPC1-NPC3	96%		95%			96%	75%		69%			72%
NPC1-NPC5	99%				95%	97%	87%				78%	84%
NPC2-NPC3		96%	96%			96%		70%	75%			72%
NPC2-NPC5		98%			96%	97%		81%			84%	82%

* The available power from single array schemes

d) *The Lombok Cluster (LC)*

Five lines have been drawn in the area of strongest kinetic power in the LC for an assessment (see Figure 5-15). Unlike the NLC, the strongest magnitude in the Lombok Cluster (LC) is not located in the C-line. LC1 in this cluster is a small portion of C-line from section 5.2.2. As seen in Figure 5-15, the strongest average kinetic power density is in the LC3, LC4 and LC5 fence-lines.

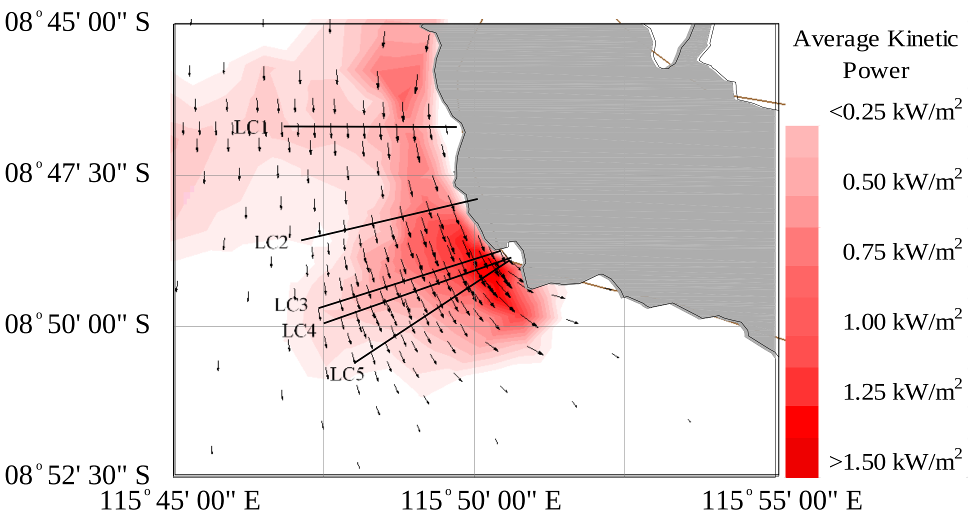

Figure 5-15: The flow orientation and the average kinetic power in the LC

Table 5-12 shows that LC1 has the highest average available power amongst the fence lines. LC1 extracts ~39 MW at low blockage while the other lines extract less than 30 MW. The extraction at high blockage follows the same pattern with LC1, which extracts in an average of ~252 MW and the others only extract less than 200 MW on average. However, this extraction is based on uniform blockage ratio. The high average extraction in the LC1 is due to the fact that it has the largest cross-section area (see Table 5-12).

In a similar way to the previous cluster, NLC, the average available power could be presented as the average available power per cross-section area. Based on this metric, the LC3 fence-line has the highest average power per area with ~82 W/m^2 at the low blockage and ~477 W/m^2 at high blockage while LC1 only extracts ~60 W/m^2 and ~380 W/m^2 at low and high blockages respectively.

Table 5-12: The average available power in the LC

	LC1	LC2	LC3	LC4	LC5
Cross Section (m^2)	659,421	440,169	358,363	473,761	354,793
Fence Length (m)	4,484	3,933	3,866	5,391	3,874

Schemes	Low Blockage (B = 0.1)							High Blockage (B = 0.4)						
	LC1	LC2	LC3	LC4	LC5	Total		LC1	LC2	LC3	LC4	LC5		
LC1	39.84	-	-	-	-	39.84	0.34	252.07	-	-	-	-	252.07	0.51
LC2	-	28.95	-	-	-	28.95	0.34	-	170.08	-	-	-	170.08	0.48
LC3	-	-	29.65	-	-	29.65	0.34	-	-	171.11	-	-	171.11	0.47
LC4	-	-	-	24.10	-	24.10	0.34	-	-	-	143.60	-	143.60	0.50
LC5	-	-	-	-	23.21	23.21	0.35	-	-	-	-	135.59	135.59	0.47
LC1-LC2-LC3	38.80	26.50	28.09	-	-	93.40	0.38	197.86	86.75	118.86	-	-	403.47	0.60
LC1-LC2-LC4	38.82	26.99	-	22.87	-	88.68	0.36	201.25	93.32	-	101.25	-	395.82	0.56
LC1-LC2-LC5	38.90	26.92	-	-	22.13	87.94	0.36	202.86	91.60	-	-	100.54	395.00	0.55
LC1-LC3-LC5	38.85	-	27.75	-	21.73	88.33	0.36	203.16	-	104.53	-	90.43	398.11	0.54
LC1-LC2	39.34	28.24	-	-	-	67.58	0.36	219.89	132.13	-	-	-	352.02	0.53
LC1-LC4	39.28	-	-	23.57	-	62.84	0.355	220.65	-	-	119.61	-	340.27	0.53

The fractions of available power in multi-array schemes compared to their individual capacity further confirm that the headland sites have better performance in series interactions than the channel type sites. Table 5-13 shows that the arrays in series are able to extract 92%-99% of their individual capacities at low blockage and 51% - 88% at high blockage.

Table 5-13: The fraction of available power in the LC

Schemes	Low Blockage (B = 0.1)						High Blockage (B = 0.4)					
	$\frac{LC1}{LC1^*}$	$\frac{LC2}{LC2^*}$	$\frac{LC3}{LC3^*}$	$\frac{LC4}{LC4^*}$	$\frac{LC5}{LC5^*}$	$\frac{All}{All^*}$	$\frac{LC1}{LC1^*}$	$\frac{LC2}{LC2^*}$	$\frac{LC3}{LC3^*}$	$\frac{LC4}{LC4^*}$	$\frac{LC5}{LC5^*}$	$\frac{All}{All^*}$
LC1	100%					100%	100%					100%
LC2		100%				100%		100%				100%
LC3			100%			100%			100%			100%
LC4				100%		100%				100%		100%
LC5					100%	100%					100%	100%
LC1-LC2-LC3	97%	92%	95%			95%	78%	51%	69%			68%
LC1-LC2-LC4	97%	93%		95%		95%	80%	55%		71%		70%
LC1-LC2-LC5	98%	93%			95%	96%	80%	54%			74%	71%
LC1-LC3-LC5	98%		94%		94%	95%	81%		61%		67%	71%
LC1-LC2	99%	98%				98%	87%	78%				83%
LC1-LC4	99%			98%		98%	88%			83%		86%

* The available power from single array schemes

The two fence line scenarios also confirm that the distance between array lines determines the fraction of extraction. Although the LC1 LC4 scheme has equal fractions with LC1- LC2 at low blockage compared to the individual turbine-fences, it performs slightly better than D1D2 at high blockage. The arrays are coded in a consecutive order. LC1 accordingly is further from LC4 than LC2.

Based on the magnitude of average power, LC1- LC2- LC3 extracts the highest magnitude of the available power from three fence lines operated simultaneously. The LC1- LC2- LC5 option gives the highest fraction of available power from three lines of turbines in series. Therefore, both combinations are included in the analysis of site-site interactions in parallel manner's analyses.

5.2.4 The Interaction between More-Realistic-Turbine Arrays

The interaction for these more-realistic-arrays is carried out for two different interactions. Firstly, the interaction between single arrays in each site or cluster, and secondly, the interaction between the clusters itself. As it is adjacent to the NPC, the LC might interact with the NPC. These interactions are worth investigating.

a) Single Array Interactions

The fence-line codes for this analyses follow the numbering in the series interactions (the lines at NLC using NLC1 to NLC4, TC using TC1 to TC4, and etc.). The NLC1, TC3, NPC1, LC1 and LC4 lines are selected for these analyses. Except for TC3 and LC4, the three other lines represent the highest average available power from the single lines. TC3 is selected because this line is the closest to the B-line from section 5.2.2 while the LC4 is selected to represent a line that is not in the same alignment as NPC1. For practicality, this section only analyses the interactions of three line-arrays exploited simultaneously (NLC1-TC3-NPC1 scheme).

This section, therefore, analyses the interactions between the array-lines in the NPC and the LC, with a single line selected from each cluster. Except for the array lines in the LC, LC1 and LC4 are selected to analyse the interaction between two lines that are inline to each other and at different alignments. NPC1 and LC1 are in the same alignment from the Lombok Strait's C-line, while NPC1 and LC4 are in a different alignment (see Figure 5-12).

Table 5-14: The average power single fence lines of more realistic arrays in the parallel manner interaction

	NLC1	TC3	NPC1	LC1	LC4
Cross Sectional (m^2)	271,377	60,521	423,995	659,421	473,761
Fence Length (m)	2,949	775	2,991	4,484	5,391

Schemes	Low Blockage (B = 0.1)							High Blockage (B = 0.4)						
	NLC1	TC3	NPC1	LC1	LC4	Total	α_4	NLC1	TC3	NPC1	LC1	LC4	Total	α_4
NLC1	21.41	-	-	-	-	21.41	0.36	89.97	-	-	-	-	89.97	0.55
TC3	-	7.24	-	-	-	7.24	0.37	-	26.76	-	-	-	26.76	0.60
NPC1	-	-	51.14	-	-	51.14	0.34	-	-	273.56	-	-	273.56	0.51
LC1	-	-	-	39.84	-	39.84	0.34	-	-	-	252.07	-	252.07	0.44
LC4	-	-	-	-	24.10	24.10	0.34	-	-	-	-	143.60	143.60	0.45
NLC1-TC3-NPC1	21.46	7.26	51.26	-	-	79.98	0.35	94.00	26.29	276.02	-	-	396.31	0.52
NLC1-LC1	-	-	51.10	39.81	-	90.92	0.34	-	-	270.43	246.25	-	516.69	0.48
NLC1-LC4	-	-	51.18	-	24.09	75.27	0.34	-	-	272.85	-	142.68	415.53	0.49

The power production at multiple arrays operated simultaneously shows almost no interaction at low blockage (see Table 5-14). While at high blockage, NLC1 and NPC1 extract higher average power in the multi-array scheme (NLC1-TC3-NPC1 scheme) than the single array schemes. NLC1 extracts ~90MW on average when operated as a single array while in NLC1-TC3-NPC1 it produces ~94MW. C1 shows a similar tendency, that the average available power at NLC1-TC3-NPC1 schemes is ~2MW higher than in the single array scenario.

b) *Turbine Cluster Interaction*

This chapter takes the analysis further to investigate parallel interaction between the clusters discussed in 5.2.3. Following the clusters' name from the previous section, each cluster is coded as the Nusa Lembongan Cluster (NLC), Toyopakeh Cluster (TC), Nusa Penida Cluster (NPC), and Lombok Cluster (LC). The multi-array configuration for each cluster is selected from the scheme which has the most array lines. For instance, scheme NLC1- NLC2- NLC3- NLC4 for NLC and NPC2-NPC3-NPC4-NPC5 for NPC (see the second column in the Table 5-15).

Table 5-15: The average power of clustered array arrays in the parallel interaction

	NLC	TC	NPC	LC(A)	LC(B)
Total Fence Length (m)	12,686	3,072	14,394	12,284	12,225
Total Cross Sectional (m^2)	1,170,472	245,148	2,111,835	1,457,953	1,372,577

Schemes	Low Blockage (B = 0.1)							High Blockage (B = 0.4)						
	NLC	TC	NPC	LC(A)	LC(B)	Total	α_4	NLC	TC	NPC	LC(A)	LC(B)	Total	α_4
NLC	60.00	-	-	-	-	60.00	0.40	164.75	-	-	-	-	164.75	0.60
TC	-	23.35	-	-	-	23.35	0.45	-	44.59	-	-	-	44.59	0.60
NPC	-	-	144.26	-	-	144.26	0.38	-	-	443.88	-	-	443.88	0.56
LC(A)	-	-	-	93.40	-	93.40	0.36	-	-	-	403.47	-	403.47	0.55
LC(B)	-	-	-	-	66.59	66.59	0.36	-	-	-	-	301.56	301.56	0.54
NLC-TC-NPC-LC(A)	61.06	23.49	144.64	94.53	-	323.71	0.38	173.18	45.36	456.64	408.90	-	1,084.08	0.60
NLC-TC-NPC-LC(B)	61.00	23.17	144.76	-	67.13	296.06	0.38	171.98	45.52	458.76	-	294.90	971.17	0.60
NLC-TC-NPC	61.14	23.30	144.93	-	-	229.37	0.39	164.53	43.61	443.38	-	-	651.52	0.60
NLC-TC	62.17	23.28	-	-	-	85.45	0.41	177.53	45.48	-	-	-	223.01	0.60
NLC-NPC	58.93	-	144.45	-	-	203.38	0.38	161.74	-	463.22	-	-	624.96	0.60
NPC-LC(A)	-	-	143.85	93.93	-	237.77	0.39	-	-	447.56	401.16	-	848.72	0.60
NPC-LC(B)	-	-	143.82	-	67.16	210.98		-	-	447.11	-	303.05	750.16	0.60
NLC-LC1	59.87	-	-	93.76	-	153.64	0.37	163.21	-	-	414.60		577.80	0.60

Two schemes are selected in the LC, the LC1-LC2-LC3 for LC(A) and the LC1-LC3-LC5 for LC(B), that represent two different conditions for the interaction. The LC1-LC2-LC3 scheme represents array lines with a close perpendicular distance, and the LC1-LC3-LC5 represents a larger perpendicular distance between the fence-lines. Since LC1 shows more sensitivity than LC4 in interaction with NPC1 (especially at high blockage from the single lines interactions), it is worth examining the difference of interaction within the dense multi-arrays configuration the NPC1-NPC2-NPC3 scheme and the spread arrays of NPC1-NPC3-NPC5.

The interactions between the clusters compare the available power from each cluster in the multi-cluster scenario to the single cluster. The average available powers of each cluster are calculated with the sum of all single array lines within the clusters. As a result, this section only investigates the interaction between the clusters. There are also interactions within the individual lines in the clusters due to the existence of the other clusters, but these occurrences are neglected in this analysis.

Examination of the average power harnessed by each cluster reveals that most clusters exhibit a positive trend in parallel interactions (see Table 5-15). Considering NPC for instance, this cluster tends to harness higher average power in the multi-array schemes at both blockage ratios. Bearing in mind that the C-line array of the Lombok Strait channel suffers losses in multi-array schemes. The NLC cluster harnesses slightly lower power in multi-cluster scheme than in the single cluster scenario when it is exploited alongside the NPC concurrently. The difference of the average available power between multi-cluster schemes and single cluster schemes is only approximately ~1 MW. In section 5.3.2, however, the same tendency is exhibited in the interaction of the array spanning across the channel.

Table 5-16: The ratio between average power of the combined cluster to that of the single cluster scheme.

Schemes	Low Blockage (B = 0.1)					High Blockage (B = 0.4)				
	NLC NLC*	TC TC*	NPC NPC*	LC(A) LC(A)*	LC(B) LC(B)*	NLC NLC*	TC TC*	NPC NPC*	LC(A) LC(A)*	LC(B) LC(B)*
NLC	100%					100%				
TC		100%					100%			
NPC			100%					100%		
LC(A)				100%					100%	
LC(B)					100%					100%
NLC-TC-NPC-LC(A)	102%	101%	100%	101%		105%	102%	103%	101%	
NLC-TC-NPC-LC(B)	102%	99%	100%		101%	104%	102%	103%		98%
NLC-TC-NPC	102%	100%	100%			100%	98%	100%		
NLC-TC	104%	100%				108%	102%			
NLC-NPC	98%		100%			98%		104%		
NPC-LC(A)			100%	101%				101%	99%	
NPC-LC(B)			100%		101%			101%		100%
NLC-LC1	100%			100%		99%			103%	

* The available power from single array schemes

The average power from the multi-cluster schemes in proportion to average power of the single cluster schemes gives a clear picture of the interaction. Table 5-16 lists values of the ratio between the average power of each cluster in the combined cluster scheme to that of the single cluster schemes. The NLC tends to extracts 2%-8% more power in the multi-cluster schemes than the single cluster schemes at both blockages, except when this cluster operates concurrently with the NPC cluster.

The LC2 shows more sensitivity in the parallel interactions than the LC1 at high blockage. As presented in Table 5-16, LC2 tends to extract less power when operated in NLC-TC-NPC-LC2 scheme than in the single cluster scheme. Conversely, LC1 produces less available power when exploited with NPC than its individual capacity.

5.2.5 Flow Field Changes

a) The Flow Field Changes for Turbine Arrays Occupying the Entire Channel

It is important to examine the flow field change to further understand the site-site interactions in this region. As an example, Figure 5-16a shows the flow changes for the AB scheme and Figure 5-16b for the ABC scheme. As seen in the figures, the overall flow in the region decreases for the ABC scheme, while (apart from locally near the turbines) they tend to increase for the AB scheme.

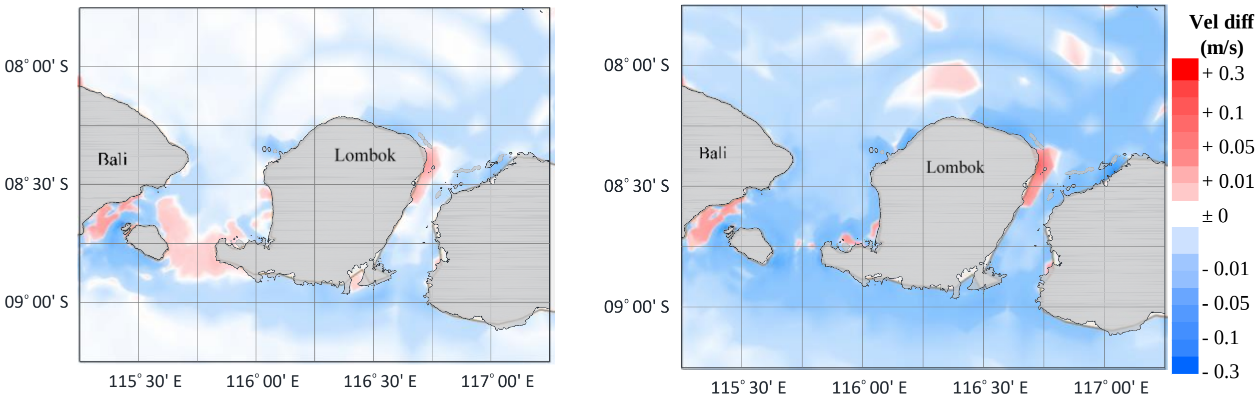

a. Turbines installed only in sites A and B

b. Turbines installed in all straits, Nusa Penida (A), Toyopakeh (B) and Lombok (C).

Figure 5-16: Flow field changes for Bali-Lombok sites

The significant deceleration in the ABC scheme implies that the flow is partially diverted to another channel. Figure 5-16b also shows that the flow accelerates slightly at the northern and eastern parts of the Lombok Island. Therefore, it is safe to conclude that the complexity of interactions in this scenario is related to flow diversion.

b) The Flow Field Changes for the Scenario of Realistic Turbine Array

The interaction for the realistic turbine array scenarios is different from the previous interactions discussed, where the turbine fences block the entire cross-section of the channel. In a realistic scenario, the interactions between channels in the realistic array are small, including the interaction between array clusters. Figure 5-17 shows the flow field changes for realistic arrays. The flow field changes are exhibited in the area around the turbine arrays only. Therefore, this result demonstrates that the realistic scenarios only affect a small area in the channels.

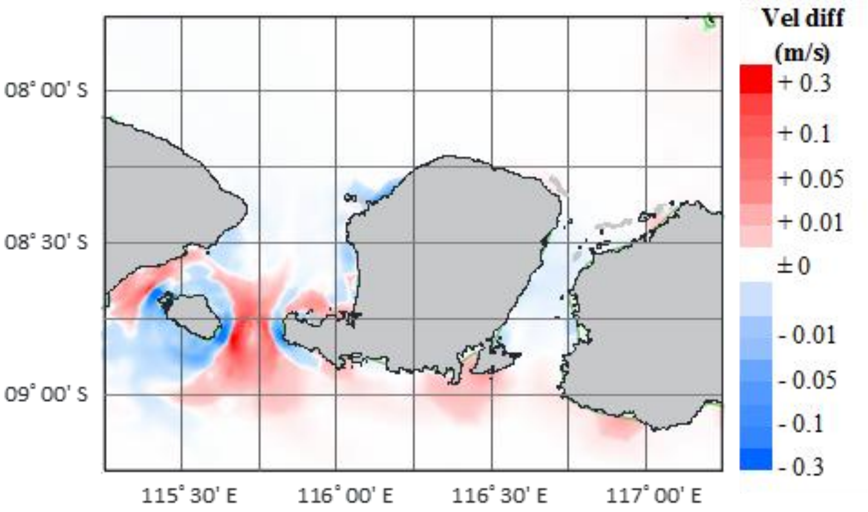

Figure 5-17: Flow field changes for turbines installed in all straits, Nusa Penida Cluster (NLC), Toyopakeh Cluster (TC) and Lombok Cluster 1 (LC1).

c) Flow Field Changes and Their Effect on the Global Current

The ~2.053 GW resource in Bali waters might be obtained by deploying turbines in all channels at high blockage. However, it is necessary to consider the effect on global currents. Since ITF is a part of the so called “Global Ocean Conveyor Belt”, these small changes might have an impact to the global ocean system.

The comparison of flow field changes between ABC scenario and AB scenario implies that the flow is diverted to C when only A and B are occupied by turbines, while scheme ABC generally decreases the flow field in the entire region. The flow field change is not just in the area of the turbine arrays. As shown in Figure 5-18, the flow field decreases in a significant the area of the Indonesian Through Flow (ITF).

5.2.6 Energy Provision and Delivery Targets

The delivery target of 150 MW, as mentioned in the beginning of this section, is highly achievable for Bali-Lombok sites. The target is still achievable for the arrays that only consider a part of the channel’s cross-section with a certain depth. The clusters around three islands of Nusa Lembongan, Nusa Ceningan and Nusa Penida (The NLC, TC and NPC) have the potential to supply the Bali demand. The resources from two clusters only, the NLC and NPC, are up to ~620 MW. As discussed in Chapter 1, Bali gets its electricity mainly from coal (426 MW) and from diesel power (408 MW). Hence, these options provide opportunities to shift Bali’s energy sources to a greener energy source.

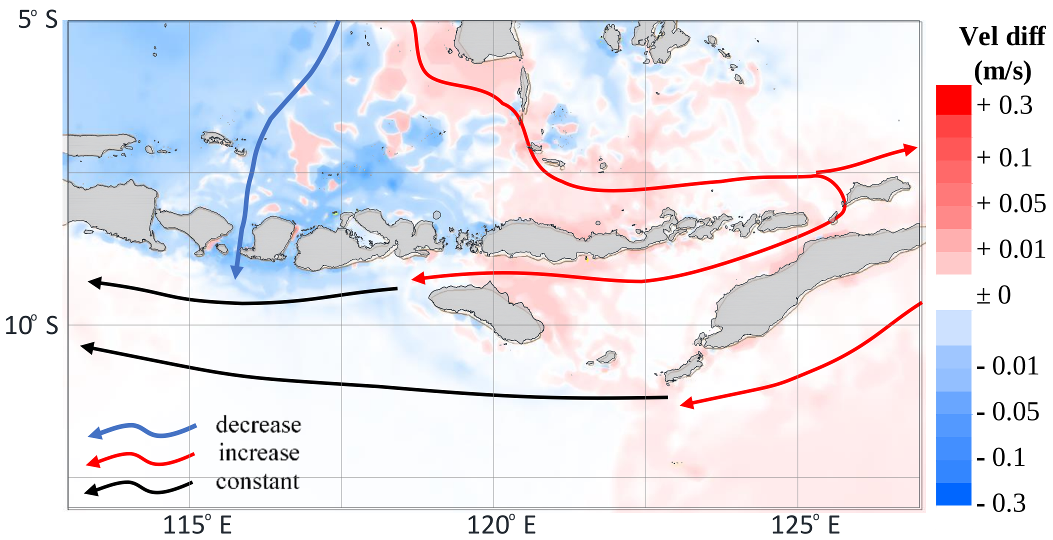

Figure 5-18: The effect of turbine arrays on the global current (the turbines are installed in all straits (ABC) and using a simulation with 13 tidal constituents)

Located in the other side of the Lombok Strait, the Lombok Cluster (LC) is more suitable to meet demand by Lombok Island. The RUPTL 2018 mentioned that the Lombok system has a plan to build 100 MW and 150 MW in 2019 and 2025. While the potential resources from the LC exceed this plan, these resources might be used to displace the existing power production as well.

5.3 Tidal Resources from the Sunda Strait Bridge

The Sunda Strait Bridge (SSB) project is a planned road and railway megaproject to connect two of the most populated islands in the country, Sumatra and Java. A series of bridges, carrying a six-lane highway and double-track railway, are traversing three islands of Panjurit, Sangiang, and Ular. There are five possible sections across the 27 km length strait that consist of bridge segments and road segments. Unfortunately, this project has been shelved for financial reasons, as the revenue from the bridge operation cannot attract private sector to investment.

Several authors have considered the tidal energy potential regarding this bridge plan (Sandro *et al.* 2014; Novico *et al.* 2016). Unfortunately, there is no thorough study on the resource assessment that has been carried out. This section discusses the tidal resources in the alignment of the bridge based on SSB projects. SSB proximity to the most populated Island in Indonesia means it has no problem with the demand for electricity. This section has allowed for the possibility of extracting more power by slightly changing the bridge alignment.

5.3.1 The Bridge Alternatives

The original plan of the bridge is divided into five sections (see Figure 5-19). The first and second segments are from Java to Ular Islands, and from Ular to Sangiang Islands. Since Ular Island is small, its inclusion in the model affects the CFL number and the timestep of the models. Therefore, Ular Island is ignored in the model, and the bridge segments (segment 1 and segment 2) are joined for simplicity. Additionally, segment 5 in the original plan, from Panjurit to Sumatra Islands, is also changed. Segment 5, in this thesis, is relocated to the narrow straits between Panjurit - Bakauheni Islands and the strait between Bakauheni - Sumatra Islands (the dots line in Figure 5-19). By detouring this segment, this thesis investigates the opportunity to increase the available power.

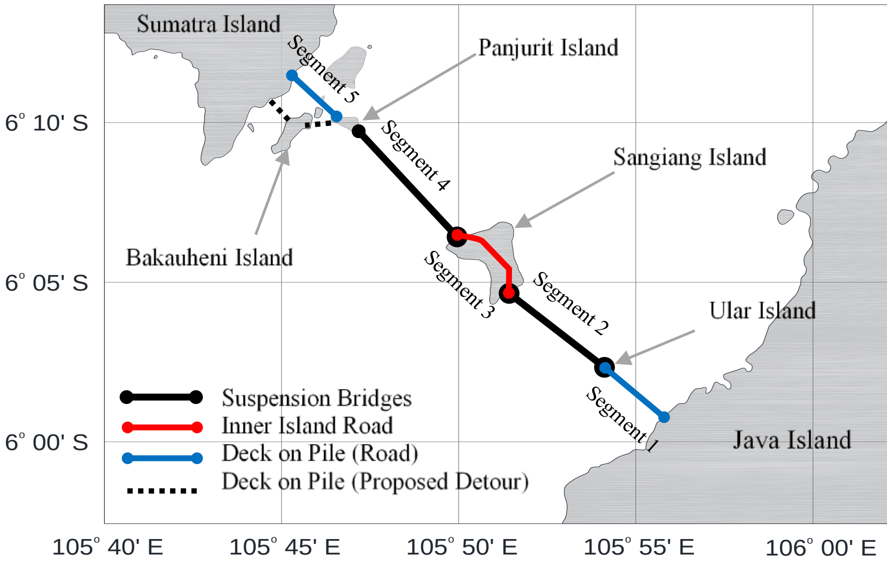

Figure 5-19: The Sunda Strait Bridge (SSB) plan's segment

This thesis divided the bridge into four segments, excluding the road segment at Sangiang Island (the bridge only segments). In order to distinguish with the original segments, the first to fourth segments are coded as SS1, SS2, SS3 and SS4 (see Figure 5-20). The first segment (SS1) is from Java Island to Sangiang Island, the second segment (SS2) is from Sangiang Island to Panjurit Island and the third segment (SS3) is from Panjurit Island to Bakauheni Island and the last segment (SS4) is from Bakauheni to Sumatra Island.

There are two alternatives for Sunda Strait Bridge's alignment. The first alternative follows the shortest distances between the Islands (SS2-1). However, this alignment has to pass across the strait where it is 70 m deep. This alternative consequently requires a bridge of 3,300 m span, one of the largest in the world, making the construction cost very high. The second alternative follows the shallow part of the strait. There is an option with the depth only 25-35 m, but the alignment creates a significant detour. Figure 5-20 shows the bridge alignment at SS2-2 is detoured to follow the shallow part of the strait.

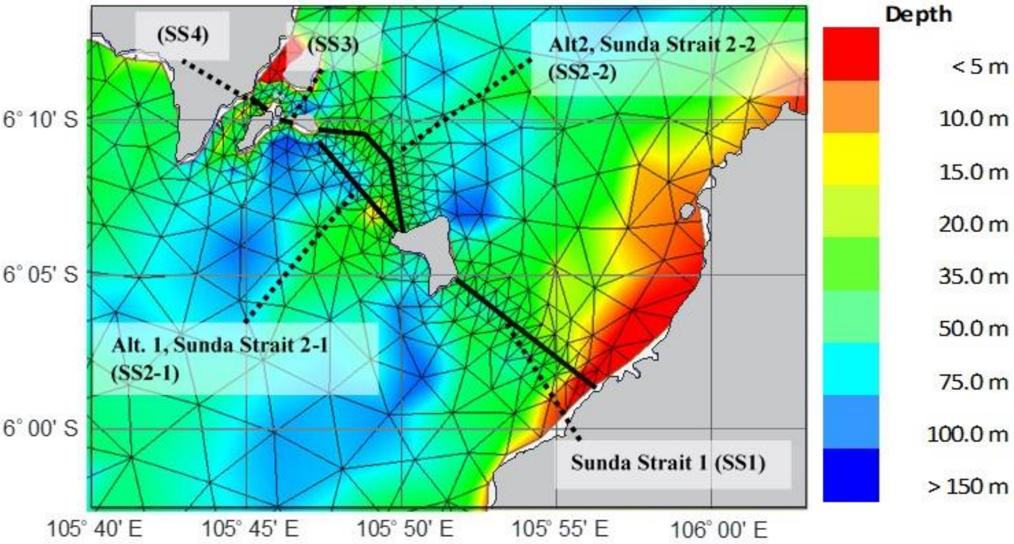

Figure 5-20: The bridge alignment's alternatives

5.3.2 Available Power

As with the previous sites, the assessment is carried out for three different wake velocity coefficients (0.33, 0.40 and 0.56) and two different blockage ratios (*B*=0.1 for low blockage and *B*=0.4 for high blockage). The models are also run to represent four neap spring cycles (62 days) and optimum average power obtained using the cubic spline function. The available power at the bridge is presented in Figure 5-21, showing only 15 days of simulation for clarity.

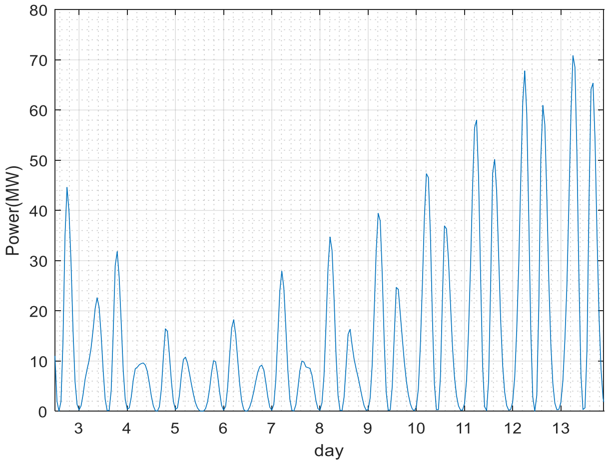

Figure 5-21: Typical available power over 15 days at bridge section 1 (SS1) for *B*=0.1 and α_4= 0.33

As shown in Table 5-17, at low blockage, the entire ALT1 (SS1, SS2-1, SS3 and SS4) extracts ~83MW, whereas the entire ALT2 (SS1, SS2-1, SS3 and SS4) produces ~128 MW. This trend is continued at high blockage (*B*=0.4), ALT1 produces ~569 MW and ALT2 produces ~770 MW. For both alternatives, the most power comes from SSB2 segments (SSB2-1 and SSB2-2).

Table 5-17: Available power in the Sunda Strait Bridge (SSB) alternative

Bridge Section	SS1	SS2-1	SS2-2	SS3	SS4
Fence Length (m)	10,486	7,973	9,570	602	1,215
Cross Section (m2)	314,848	445,035	319,649	10,529	31,565

Schemes	Low Blockage (B = 0.1)							High Blockage (B = 0.4)						
	SS1	SS2-1	SS2-2	SS3	SS4	Total	α_4	SS1	SS2-1	SS2-2	SS3	SS4	Total	α_4
SS1	32.02	-	-	-		32.02	0.34	202.33	-	-	-		202.33	0.43
SS2-1	-	47.48	-	-	-	47.48	0.34	-	283.89	-	-	-	283.89	0.43
SS2-2	-	-	91.01	-	-	91.01	0.36	-	-	458.59	-	-	458.59	0.49
SS3	-		-	3.40	-	3.40	0.37	-		-	13.92	-	13.92	0.55
SS4		-	-	-	3.66	3.66	0.35		-	-	-	18.39	18.39	0.48
SS1 and SS2-1(ALT 1)	32.30	44.60	-	-	-	76.90	0.34	218.32	299.41	-	-	-	517.73	0.40
SS1 and SS2-2 (ALT2)	32.27	-	88.47	-	-	120.74	0.35	223.56	-	482.78	-	-	706.34	0.43
SS1,SS2-1, SS3, SS4 (ALT 1)	32.53	44.58	-	3.66	2.78	83.56	0.34	221.78	307.25	-	17.75	22.68	569.45	0.40
SS1,SS2-2, SS3, SS4 (ALT 2)	32.46	-	89.75	3.24	2.74	128.18	0.35	227.56	-	497.97	19.23	25.32	770.08	0.42
SS2-1,SS3, SS4 (ALT 1)	-	47.46	-	3.65	2.78	53.89	0.34	-	290.86	-	16.74	20.77	328.37	0.42
SS2-2,SS3, SS4 (ALT 2)	-	-	92.32	3.21	2.74	98.28	0.35	-	-	472.57	17.83	22.92	513.32	0.47
SS3 and SS4	-	-	-	3.32	2.75	6.07	0.36	-	-	-	14.28	17.61	31.89	0.33

This result is interesting and counter intuitive. As shown in Table 5-17, despite SS2-2 having a longer span than SS2-1, the cross-section of SS2-1 is larger than SS2-2. The SS2-1 is ~7.9 km long and SS2-2 only 9.5 km long, and the cross-sectional area of SS2-2 is only 319,649 m^2 while SS2-1 is 445,035 m^2. The available power is equivalent to the cross-sectional area of the channel and SS2-1 has larger area than SS2-2. As the blockage ratio is uniform, SS2-1 should produce more power than SS2-2 based on the cross-sectional area.

The average undisturbed kinetic power explains this result. As shown in Figure 5-22, the average kinetic power at SS2-2 section is higher than the kinetic power at SS2-1. Although the kinetic power does not provide a rigorous resource assessment, this metric demonstrates that it is convenient to determine the potential location of tidal energy devices. Further investigations are discussed in section 5.4.4 through understanding the flow field change.

5.3.3 Array Interactions

This thesis proposes changes in bridge alignment, from Panjurit Island to Sumatra Island, with an additional detour from Panjurit Island to Bakauheni Island then to the Sumatra Island. This detour would improve the viability of the bridge by increasing the tidal stream power availability.

Furthermore, the interaction analyses are performed to investigate how useful these additional segments are. Based on the average kinetic energy, SS3 and SS4 exhibit the potential for tidal energy (see Figure 5-22 for the detail). Although both SS3 and SS4 are relatively narrow, these channels could make a significant contribution to the total available power. At the same time, the additional construction cost would be minimal. At low blockage ratio, SS3 and SS4 produce ~3.4

MW and ~3.6 MW, while at high blockage ratio, these narrow channels could extract ~13.9 and 18.4 MW for the single array scenario (see Table 5-17 in detail).

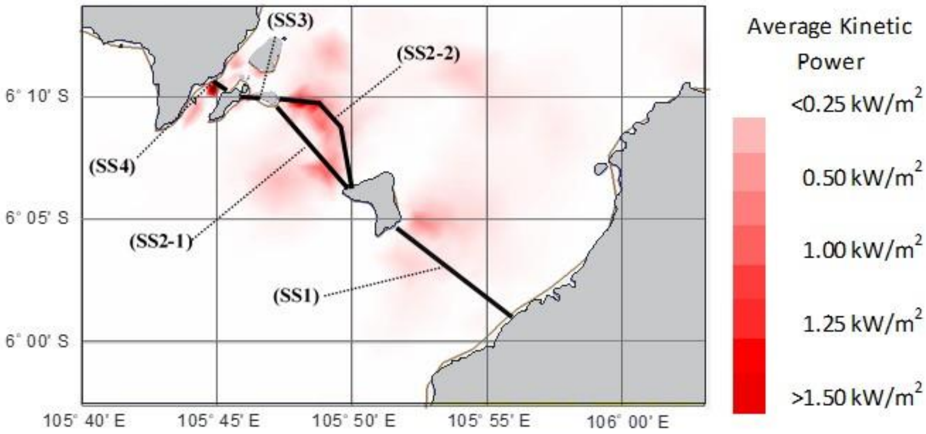

Figure 5-22: The average kinetic power at Sunda Strait's bridge sections

Table 5-18 provides the fraction of available power from each scheme with respect to the single array scheme. At low blockage (*B*=0.1), the available powers at SS3 is slightly higher in ALT1 multiple array schemes (using SS2-1 segment) than in single array (SS3 only). In ALT2 or using SS2-2 segment, the available power in multi-array scenarios is slightly higher than in single array scenario for SS3. Power production for SS3 in the multi-array scenarios is ~7–8% higher or 5% lower than in the single array scenario. However, the differences are relatively small, approximately ~200-300 kW.

Table 5-18: The fraction of power production at Sunda Strait Bridge (SSB)

Schemes	Low Blockage (*B* = 0.1)						High Blockage (*B* = 0.4)					
	SS1	SS2-1	SS2-2	SS3	SS4	All	SS1	SS2-1	SS2-2	SS3	SS4	All
	SS1*	SS2-1*	SS2-2*	SS3*	SS4*	All*	SS1*	SS2-1*	SS2-2*	SS3*	SS4*	All*
SS1	100%	-	-	-	-	-	100%	-	-	-	-	-
SS2-1	-	100%	-	-	-	-	-	100%	-	-	-	-
SS2-2	-	-	100%	-	-	-	-	-	100%	-	-	-
SS3	-	-	-	100%	-	-	-	-	-	100%	-	-
SS4	-	-	-	-	100%	-	-	-	-	-	100%	-
SS1 and SS2-1(ALT 1)	101%	94%	-	-	-	97%	108%	105%	-	-	-	106%
SS1 and SS2-2 (ALT2)	101%	-	97%	-	-	98%	110%	-	105%	-	-	107%
SS1,SS2-1, SS3, SS4 (ALT 1)	102%	94%	-	108%	76%	97%	110%	108%	-	127%	123%	110%
SS1,SS2-2, SS3, SS4 (ALT 2)	101%	-	99%	95%	75%	99%	112%	-	109%	138%	138%	113%
SS2-1,SS3, SS4 (ALT 1)	-	100%	-	107%	76%	99%	-	102%	-	120%	113%	104%
SS2-2,SS3, SS4 (ALT 2)	-	-	101%	95%	75%	100%	-	-	103%	128%	125%	105%
SS3 and SS4	-	-	-	98%	75%	86%	-	-	-	103%	96%	99%

*the available power from single array schemes

The available power at SS4 is significantly lower than that obtained with multi-array scenarios for both ALT1 and ALT2 at low blockage. The model predicts that SS4 segment will extract approximately 24%~25% less for any multi-array scenario than a single array for both alternatives (ALT1 and ALT2). SS4 is even "losing" 25% of its potential when operated together with SS3.

At high blockage, both SS3 and SS4 tend to extract more power in multiple array scenarios. Therefore, the option of detouring the bridge lane for additional power to SS3 and SS4 might be lucrative for high blockage only. This conclusion, however, is based on the amount of available power. It would be necessary to carry out economic or financial analysis to see whether the detouring options are economically beneficial for the bridge project.

Regarding the option of selecting ALT1 or ALT2, this model suggests that ALT2 (SS2-2) is more advantageous than ALT1 (SS2-1). For instance, SS2-1 produces less power than SS2-2 for multi-array schemes at low blockage. At high blockage, SS2-2 extracts a higher fraction of available power than SS2-2. SS1 produces slightly more energy when exploited simultaneously with SS2-2 than with SS2-1, although the difference in average available power at SS1 from ALT1 and ALT2 is only 1%. Moreover, SS3 and SS4 generate more electricity in ALT2 than ALT1 at high blockage. These facts show that ALT2 has more advantages than ALT1.

5.3.4 Understanding the Flow Field Change and the Interaction with the South China Sea Current

As ALT2 (SS2-2) gives higher average available power than ALT1 (SS2-1), the flow field changes around both alternatives are used to verify these results. Figure 5-23 compares flow fields between SS2-1 and SS2-2. The figures show that flow diversions at the channel between the Java and the Sangiang Islands are observed more for the SS2-2 scenario (Figure 5-23b) than for SS2-1 (Figure 5-23a). Consequently, the flow is decelerated more in SS2-2 than SS2-1, as shown by the blue intensity at the bridge locations (see Figure 5-23b). These figures demonstrate that the flow field changes are in accordance with the finding that the available power from SS2-2 is larger than from SS2-1.

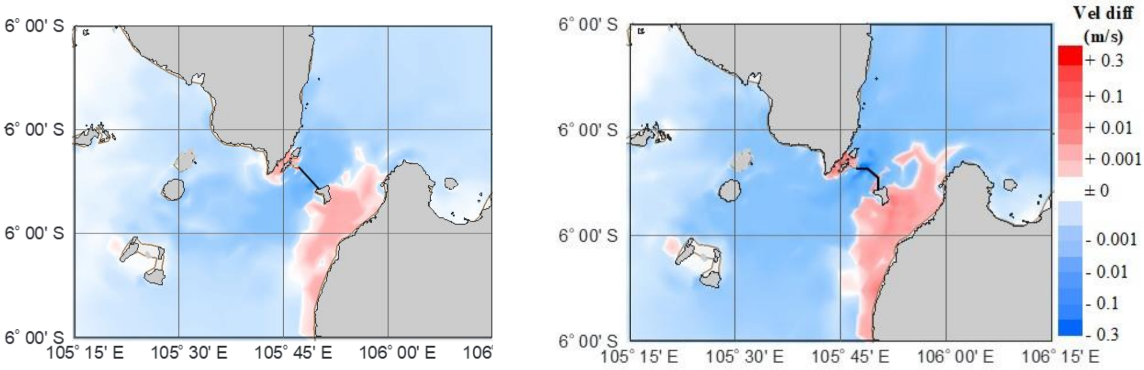

a. The flow field at SS2-1 (ALT1) b. The flow field at SS2-2 (ALT2)

Figure 5-23: The comparison of the flow field for SS2-1 and SS2-2 for B=0.4

Previous studies (Draper *et al.* 2014 and Coles *et al.* 2017) have suggested that parallel interactions give an advantage to turbine developers. Here, the opposite is observed, and hence this discrepancy requires further attention. In Lombok straits, the peculiarities of the interaction are explained by examining the flow diversion to the adjacent straits. However, the nature of interaction in Sunda Strait is different from the interactions in the Lombok Strait. Sunda Strait is between Sumatra and Java Islands, each far larger than Bali and Lombok. It is very unlikely that diversion occurs to the other end of Sumatra or Java Islands.

Furthermore, the South China Sea (SCS) throughflow moves south-eastward from the SCS to the Java Sea (Gordon *et al.* 2012). Unlike the global current (ITF) which passes through Lombok straits, the SCS throughflow does not go through to the Sunda Strait (see Chapter 2 and 4 for detail). The effect of turbine arrays on the global current (SCS) in Sunda Strait is presented in Figure 5-24.

SS2-1 and SS2-2 tend to have less available power than their individual capacity when exploited simultaneously with SS1 (see Table 5-17 and Table 5-18). Both schemes (SS2-1 and SS2-2) extract power that is ~3MW lower than their individual average capacity in multi-array scenarios with SS1 segment. However, the flow diversion is unable to explain the peculiarity of these results since Figure 5-24a shows almost no changes over a large area of the domain.

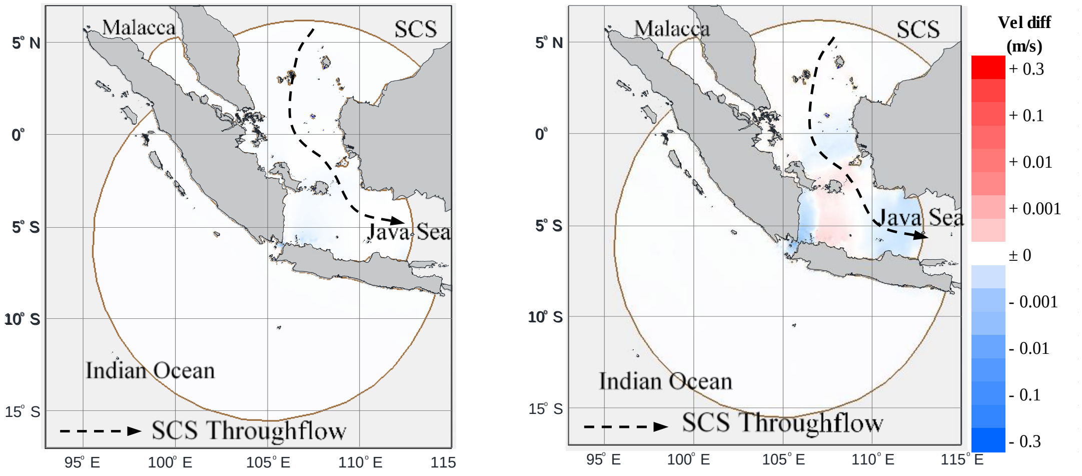

a. Low blockage (B=0.1) and α_4 =0.33 **b.** High blockage (B=0.4) and α_4 =0.56

Figure 5-24: Flow field change on ALT2 (SS1, SS2-2, SS3 and SS4).

The available power from SS1 and SS2 (SS2-1 or SS2-2) tends to be higher for multi-array scenarios than for their individual capacities. Conversely, the flow is accelerated in some part of the Java Sea at high blockage (Figure 5-24b). These results are, seemingly, counter-intuitive as regards to the flow diversion to another channel. The flow field, therefore, would be expected to be the opposite way around, with no increase in flow in the direction of the SCS caused by flow at high blockage.

The flow field changes around the turbine arrays further confirm the peculiar increases and decreases in velocity for high blockage ratio scenario. As shown in Figure 5-25, the deceleration areas are larger at high blockage than for low blockage. The flows around the turbine arrays decelerate around the fence lines for both blockage scenarios (B= 0.1 and B= 0.4). However, the increase in velocity occurs in the near field area at low blockage (B= 0.1), while at high blockage (B= 0.4) decrease in velocity is observed over a very large area. These results demonstrate the unexpected complexity of the site-site interactions.

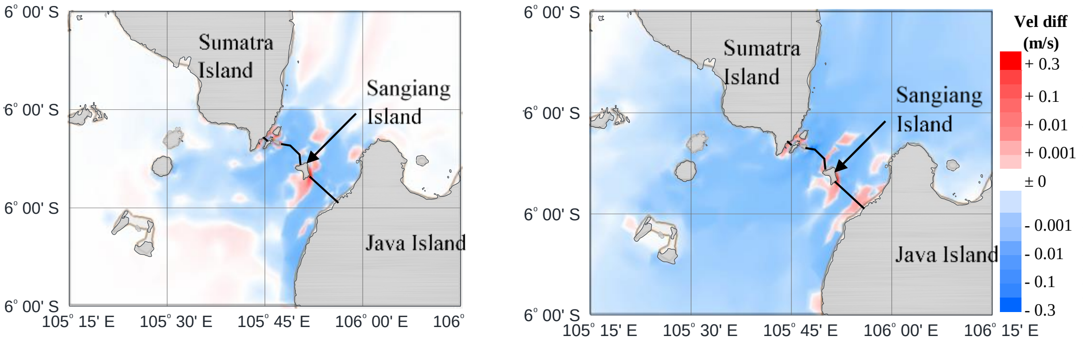

a. Low blockage (B=0.1) and α_4 =0.33 **b.** High blockage (B=0.4) and α_4 =0.56

Figure 5-25: Flow field changes at turbine arrays for ALT2

5.4 Providing Electricity for the Marginal Sites in the Lingga Regency

Besides representing the resource assessment in the diurnally tidal regime, the Lingga Regency also represents a marginal site. This area needs electricity, however, the demand is relatively small. As mentioned in Chapter 1, the Lingga Regency is the area with the highest System Average Interruption Duration Index (SAIDI) in Indonesia. The SAIDI in the Lingga Regency is 12 hours, which means the electricity is only available for a few hours a day.

As shown in Figure 5-26, there are two potential locations in the Lingga Regency, Temiang Strait and Dasi Strait. Both sites are in the diurnal tidal regime and are also close to the Senayang district, which has the highest SAIDI in the Lingga Regency (see Figure 5-27). The most populated towns in the regency are Dabo and Daik (the regency's capital). Although categorised as marginal sites, these sites may have potential for exploitation in the longer term.

5.4.1 The Selected Sites for Assessment

Six different locations that have been identified as potential locations for tidal turbines. Most of these locations have depth of 20-25 m, which is ideal for tidal turbines (see Figure 5-28). As with previous locations, the assessments are done using three different α_4 values and two uniform blockage ratios at each location (B=0.1 for low blockage and B=0.4 for high blockage).

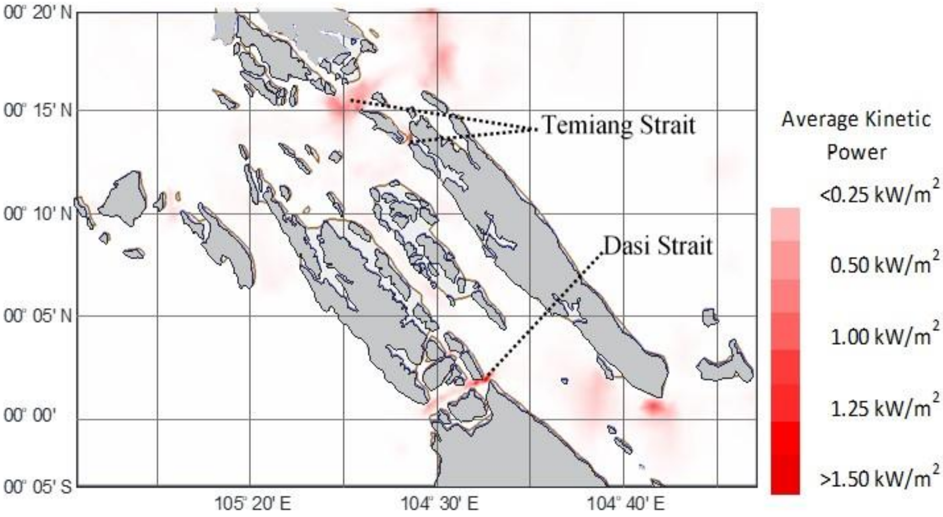

Figure 5-26: The average kinetic power in Temiang and Dasi Straits

At Temiang Strait, an average of ~1 MW, ~940 kW and ~590 kW at the low blockage, and ~5.7 MW, ~5.6 MW and ~3 MW at high blockage are produced in Temiang 1, Temiang 2 and Temiang 3 respectively. These power productions increase in proportion to the fence length and the area of the cross-section of the strait. As shown in Table 5-19, Temiang 1 has the longest fence and the largest cross-sectional area compared to Temiang 2 and Temiang 3. Therefore, it is reasonable that Temiang 1 produces the highest average power in the Temiang Strait.

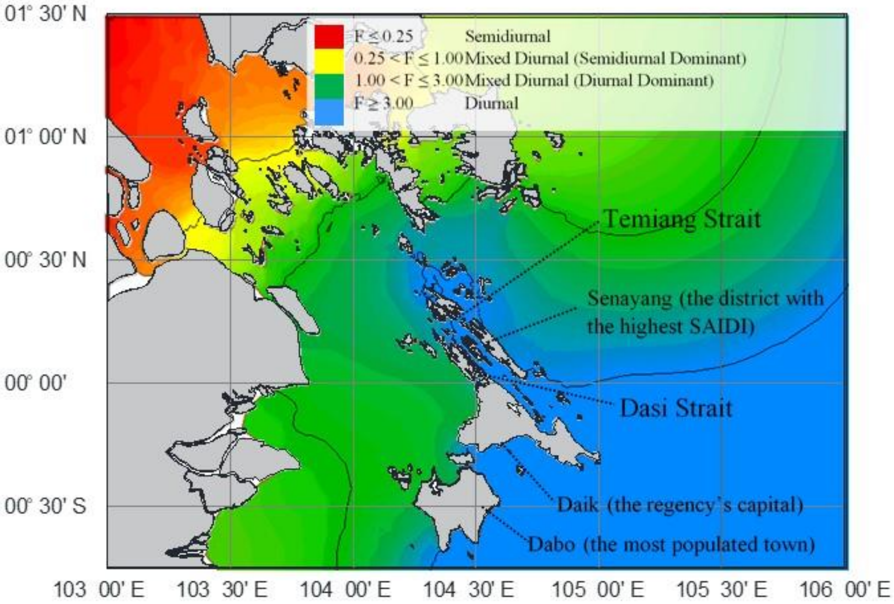

Figure 5-27: The *formzahl* number/form factor in the Lingga Regency

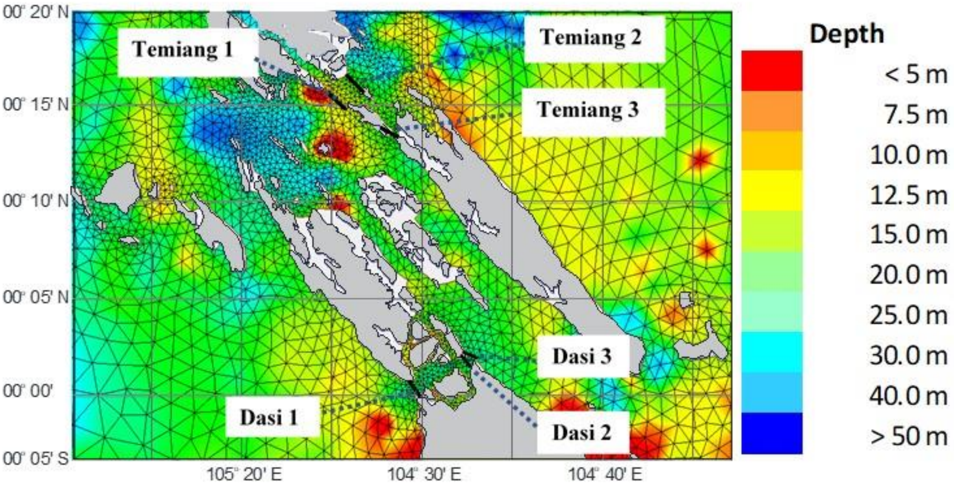

Figure 5-28: The alternative location of tidal turbines in the Lingga Regency

Interesting results are obtained for Dasi Strait. The average power from the shortest fence length and the smallest cross-sectional area, Dasi 3, is slightly higher than Dasi 2, even though Dasi 2 has a larger cross-sectional area than Dasi 3. Meanwhile, the highest average available power is from Dasi 1, despite the average kinetic power, as shown in Figure 5-26, being smaller than at the other locations.

The power pattern follows a diurnal tidal pattern for most of the daily cycle. Figure 5-29 shows an example of available power in Temiang 1. The available power time series exhibits two peaks in most daily cycles, except in the neap tide time (day 5 to 7). This condition could be explained as resulting from the influence of semidiurnal constituents. Although this site is located in a diurnal area (as shown in Figure 5-27), the form factor or *Formzahl* number is, however, about 2.9~3.1. The *Formzahl* number is slightly above the limit of diurnal and mixed diurnal limit.

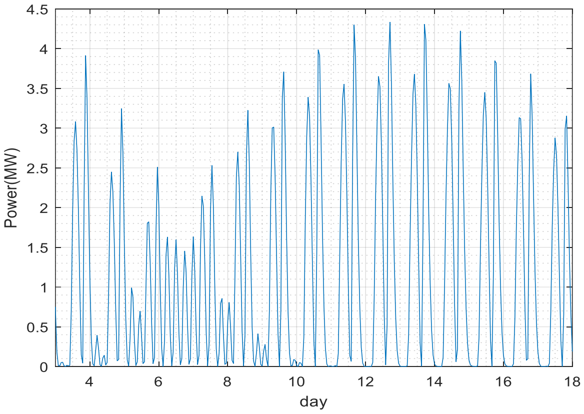

Figure 5-29: The typical of power output at Temiang1 from a model run with 13 tidal constituents (α_4=0.33 and B=0.1)

5.4.2 On Different Constituent Driven Models

As seen in the assessment of the semidiurnal sites, running the simulations with solely M_2, will give at least 80% accuracy [Blanchfield *et al.*, 2008; Coles *et al.*, 2017; Draper *et al.*, 2014; Sutherland *et al.*, 2007]. One could assume that the simulations run with K_1 give the highest accuracy for the simulations with a single constituent in the diurnal tidal regime. However, Table 5-19 shows that the simulation results do not show this. The simulations predict very low values of average and maximum power if run with K_1 solely. Bearing this in mind, the results are obtained from the optimum available average power of three different α_4s. The α_4 of each simulation is almost the same (α_4=0.34~0.35 for low blockage ratio (B=0.1) and α_4= 0.42~0.50 for high blockage ratio or B=0.4). Therefore, although the available power presented in the table is a by-product of cubic spline fitting, it is very unlikely that the results will display a different pattern.

Table 5-19: The available power from simulations run with different tidal constituents

Blockage	Location		13 Constituents		$M_2K_1S_2O_1$		M_2K_1		M_2		K_1		S_2		O_1	
			Ave Power (MW)	α_4	Ave Power (MW)	α_4	Ave Power (MW)	α_4	Ave Power (MW)	α_4	Ave Power (MW)	α_4	Ave Power (MW)	α_4	Ave Power (MW)	α_4
B = 0.1	Temiang 1	Ave	1.19	0.34	1.09	0.34	0.97	0.34	2.03	0.35	0.34	0.34	0.26	0.34	0.38	0.34
		Max	5.37		4.77		3.81		4.55		0.78		0.62		0.87	
	Temiang 2	Ave	0.94	0.34	0.85	0.34	0.75	0.34	1.65	0.35	0.25	0.34	0.19	0.34	0.30	0.34
		Max	4.88		3.82		3.37		4.30		0.62		0.52		0.68	
	Temiang 3	Ave	0.59	0.35	0.54	0.35	0.48	0.35	0.91	0.35	0.16	0.35	0.11	0.35	0.17	0.35
		Max	3.03		2.81		2.22		2.28		0.45		0.30		0.50	
	Dasi 1	Ave	0.77	0.34	0.72	0.34	0.72	0.34	1.56	0.34	0.17	0.34	0.23	0.34	0.19	0.34
		Max	4.37		4.17		3.14		3.64		0.43		0.56		0.49	
	Dasi 2	Ave	0.78	0.35	0.74	0.35	0.72	0.35	1.52	0.35	0.19	0.35	0.25	0.35	0.22	0.35
		Max	4.21		3.93		2.95		3.38		0.52		0.65		0.56	
	Dasi 3	Ave	0.78	0.35	0.74	0.35	0.74	0.35	1.45	0.35	0.20	0.35	0.27	0.35	0.22	0.35
		Max	4.68		4.31		3.37		3.63		0.53		0.67		0.61	
B = 0.4	Temiang 1	Ave	5.70	0.46	5.26	0.46	4.61	0.45	9.09	0.46	1.57	0.45	1.30	0.44	1.79	0.45
		Max	27.33		21.50		17.06		18.52		3.42		2.87		3.51	
	Temiang 2	Ave	5.57	0.44	5.08	0.44	4.50	0.44	9.41	0.46	1.48	0.44	1.20	0.43	1.74	0.44
		Max	27.98		21.82		18.71		22.86		3.55		2.96		3.63	
	Temiang 3	Ave	3.00	0.49	2.76	0.49	2.41	0.49	4.47	0.50	0.80	0.49	0.57	0.47	0.84	0.49
		Max	14.87		13.81		10.70		10.77		2.10		1.24		1.77	
	Dasi 1	Ave	4.89	0.42	4.60	0.42	4.57	0.42	9.49	0.43	1.08	0.41	1.52	0.41	1.17	0.42
		Max	29.11		27.45		20.62		23.13		2.80		3.67		3.13	
	Dasi 2	Ave	4.04	0.48	3.80	0.48	3.73	0.47	7.57	0.48	0.96	0.47	1.33	0.47	1.09	0.48
		Max	19.43		18.08		15.02		16.50		2.63		2.85		2.33	
	Dasi 3	Ave	4.30	0.46	4.07	0.46	4.05	0.46	7.77	0.47	1.08	0.46	1.51	0.45	1.18	0.46
		Max	23.80		21.97		17.08		17.95		2.75		3.20		2.72	

Table 5-20 shows only ~22%-~28% of the average and ~10% to 15% of the maximum power from simulations run with 13 constituents is given by the assessment driven by K_1 only. These values are slightly lower than the results from simulations run with O_1 only. These results show that, although in the diurnal tidal regime where K_1 plays an important role in the harmonic tidal process, the assessments are giving low accuracy if run solely with K_1.

If the simulations were run with M_2, it would underestimate the maximum power by ~70%-~80% from the simulation driven by 13 constituents. Meanwhile, M_2, simulation will overestimate the average available power by 171% to 200% or twice the average power from the simulations with 13 constituents. These results mean that assessments from a simulation that is driven solely by M_2 might be unreliable in some areas, not just those with a diurnal tidal regime. Detailed analysis of the perplexing overestimate of power is discussed in section 5.4.5.

Table 5-20: The Comparison of results from simulations run with the principal constituent to 13 Constituents

Blockage	Location	$\frac{M_2K_1S_2O_1}{13\,Const}$		$\frac{M_2K_1}{13\,Const}$		$\frac{M_2}{13\,Const}$		$\frac{K_1}{13\,Const}$		$\frac{S_2}{13\,Const}$		$\frac{O_1}{13\,Const}$	
		Ave	Max	Ave	Max	Ave	Max	Ave	Max	Ave	Max	Ave	Max
B = 0.1	Temiang 1	92%	89%	81%	71%	171%	85%	28%	15%	22%	12%	32%	16%
	Temiang 2	91%	78%	80%	69%	176%	88%	26%	13%	20%	11%	32%	14%
	Temiang 3	92%	93%	81%	73%	154%	75%	27%	15%	18%	10%	29%	16%
	Dasi 1	94%	95%	93%	72%	203%	83%	22%	10%	30%	13%	24%	11%
	Dasi 2	94%	93%	92%	70%	194%	80%	24%	12%	32%	15%	28%	13%
	Dasi 3	95%	92%	94%	72%	186%	78%	25%	11%	34%	14%	28%	13%
B = 0.4	Temiang 1	92%	79%	81%	62%	160%	68%	28%	12%	23%	10%	31%	13%
	Temiang 2	91%	78%	81%	67%	169%	82%	27%	13%	22%	11%	31%	13%
	Temiang 3	92%	93%	80%	72%	149%	72%	27%	14%	19%	8%	28%	12%
	Dasi 1	94%	94%	93%	71%	194%	79%	22%	10%	31%	13%	24%	11%
	Dasi 2	94%	93%	92%	77%	188%	85%	24%	14%	33%	15%	27%	12%
	Dasi 3	95%	92%	94%	72%	181%	75%	25%	12%	35%	13%	28%	11%

The comparison of available power from simulations driven by single constituents can be seen in Figure 5-30. The time series of available power from the simulation that is driven solely by M_2 peaked at 4.5 MW (Figure 5-30a) while none of the other simulations driven by single constituents, K_1, O_1 and S_2 can reach 1 MW (see Figure 5-30b, c and d). This implies that, although this area is in a diurnal tidal regime based on WSE (where diurnal components should be stronger than the semidiurnal), the power extraction shows that M_2 is a stronger constituent driving the current flow than any other constituent.

As discussed previously, the available power run with 13 constituents still exhibits the pattern of the diurnal cycle, or two peaks in most of the daily cycle (Figure 5-29). Figure 5-31a shows the velocity has a different pattern to WSE. Thus, the time series of the available power will have a different pattern to the WSE as well. Therefore, it is safe to assume that the harmonic composition of WSE in the Temiang, described by the *Formzahl* number, does not reflect the harmonic composition of velocity and power series. Since the velocity is driven by head difference, it is worth examining the comparison between the velocity and head difference. The head difference is obtained from the difference in WSE at point 1 and point 2 as shown in Figure 5-26. The comparison, as presented in Figure 5-31b, shows the similarity between head difference and velocity.

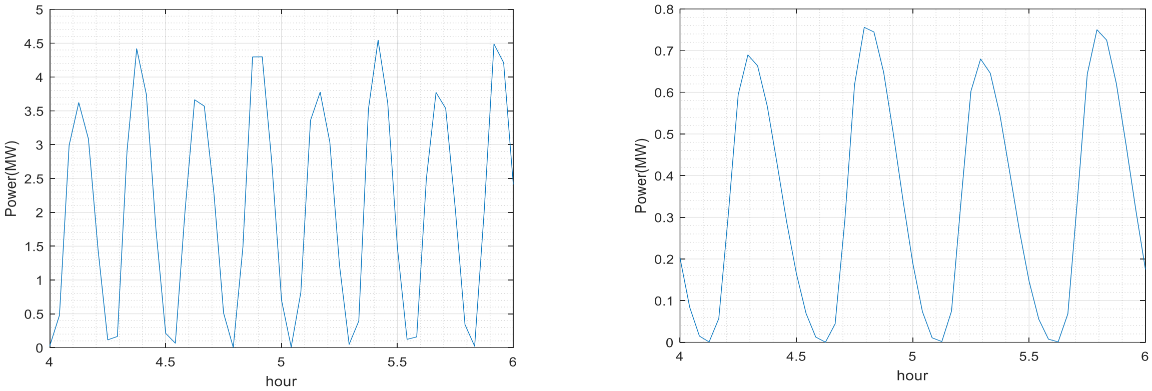

a. M_2 only b. K_1 only

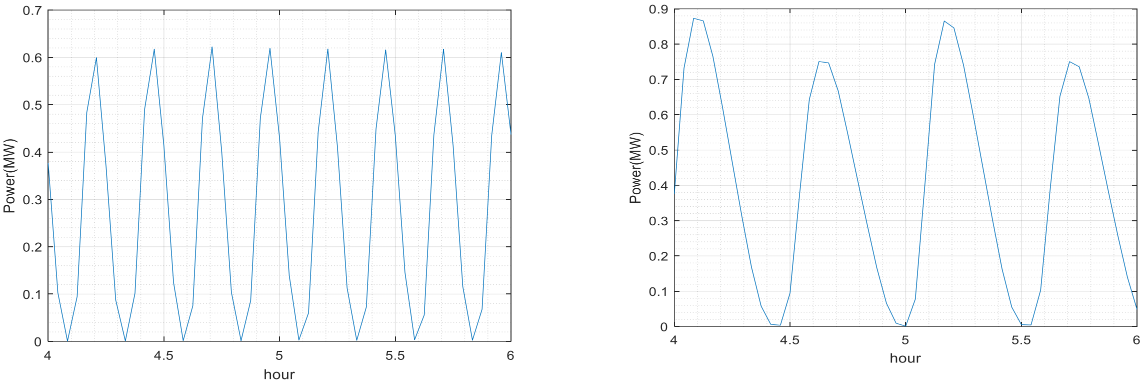

c. S_2 only d. O_1 only

Figure 5-30: The power production at Temiang Strait from single constituents driven model

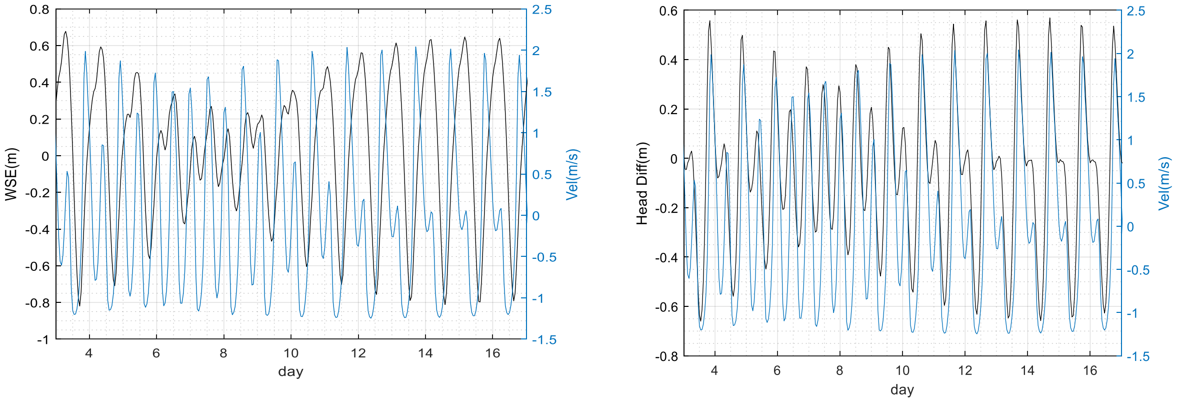

a. The comparison with WSE b. The comparison with the head difference

Figure 5-31: Velocity comparison with WSE and head difference in Temiang Strait

This explains how the available power has a diurnal cycle (see Figure 5-32a) and the semidiurnal amplitude. Since available power is the cube of velocity, it is obvious that the cubic operation reduces the small fluctuation of the diurnal component in the velocity (see Figure 5-32b). As seen in the results, the power is predominantly determined by the semidiurnal constituent and has a diurnal cycle for most of the time. The results also imply that the *Formzahl* number of WSE is not an accurate metric to characterize the tidal energy in the diurnal or in semidiurnal tidal regime.

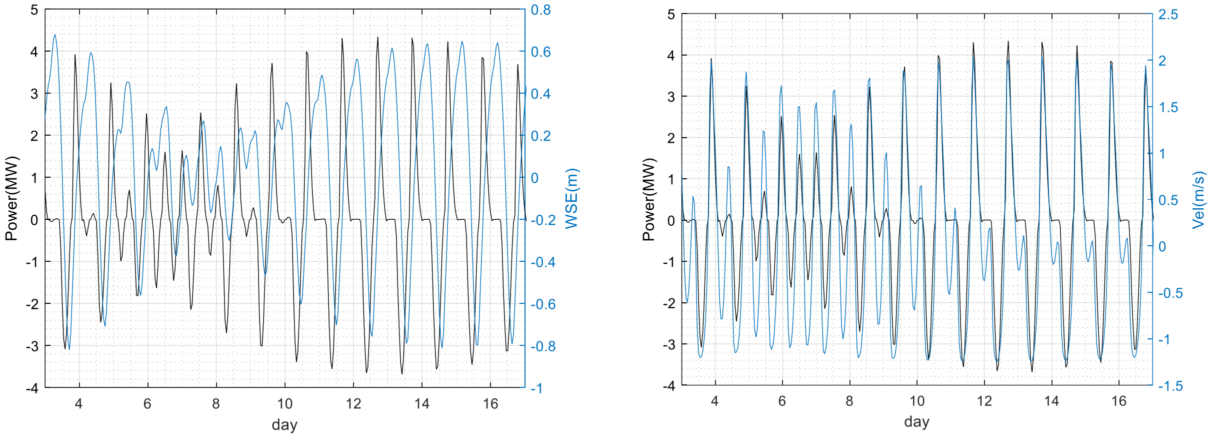

a. The comparison with WSE b. The comparison with the velocity

Figure 5-32: Comparison between available power and velocity time series for Temiang Strait

It is interesting to investigate why the simulation run solely with M_2 overestimates the results and how the M_2 gives higher results than K_1 for the assessment in the diurnal tidal regime. This is examined below.

5.4.3 Analysis in The Frequency Domain

Previous analysis shows that the WSE cycles do not reflect the power cycle as well as the velocity cycles. Further analysis can be done by examining the WSE and velocity in the frequency domain. Similar to the analyses in Chapter 2, FFT analysis is employed to provide further comparison between WSE and velocity. Figure 5-33 shows that the highest spectrum energy density of WSE and flow speed in Temiang Strait is inverted. WSE exhibits higher energy density for the low-frequency constituents while the velocity on the other way around, showing higher energy density for the high-frequency constituents. The tidal constituents can be recognised based on the frequencies. The diurnal component, O_1, is the dominant component in WSE and the semidiurnal component, M_2, is the dominant in velocity. Since $\omega = \frac{2\pi}{T}$, therefore the spectrum can be conveniently represented based on a period (in Figure 5-33b).

This result verifies that the *Formzahl* number of WSE is the best characterisation for tidal resource assessment. It also verifies that there is no short-cut to running a long simulation for an assessment in the area where the WSE is diurnal. Complex tidal constituents and longer computational time are inevitable for areas with stronger diurnal constituents.

Chapter 4 has shown that the Temiang Strait is closer to being an inertia-dominated channel (the terminology of GC05) in terms of M_2 with phase lag ~90°. Whereas in terms of K_1 and O_1 (the strongest component in WSE), this channel can be characterised as somewhere between inertia- and drag-dominated with phase leg ~25° to ~ 40°. Since the simulation is run with multiple constituents, there is no straightforward method to characterise the channel.

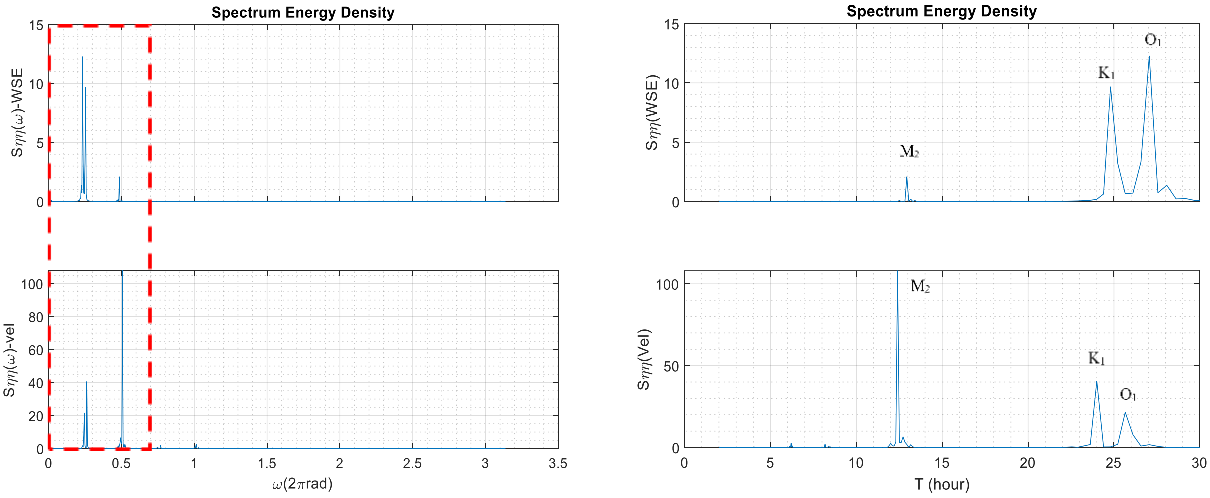

a. frequency domain

b. zoom in of red dash box at Figure 5-33a

Figure 5-33: Spectrum energy density of the WSE and the velocity in the Temiang Strait

However, since M_2 is the dominant constituent in the velocity field, one could assume that the channel is closer to being inertia-dominated channel. Therefore, based on GC05 terminology (Garrett and Cummins, 2005), the kinetic flux is inappropriate for resource assessment in this channel.

5.4.4 The *Formzahl* Number

Harmonic analysis of WSE and velocity are conducted for this location. However, since the DG-ADCIRC results (fort.64 file) provide the flow speed in a Cartesian coordinate (*u* and *v*), the total magnitude of velocity should be calculated by $a_{Vel} = \sqrt{{a_u}^2 + {a_v}^2}$. Then, the *Formzahl* number for velocity (f_v) is calculated from the total magnitude, taking into account their bi-directional nature (see Chapter 1 for the detail).

As discussed at the beginning of Chapter 1, this thesis distinguishes the WSE *Formzahl* (f_η) and the velocity *Formzahl* (f_v). Figure 5-34 shows the comparison between f_η and f_v. Based on WSE, the Lingga Regency potential sites are in the diurnal regime (Figure 5-34a) for which the f_η number is > 3.0. Nevertheless, the f_v shows more variation in the area, most of areas are in the mixed diurnal with the yellowish colour scheme. This f_v number explains the inversion in the WSE and the velocity spectrum energy density.

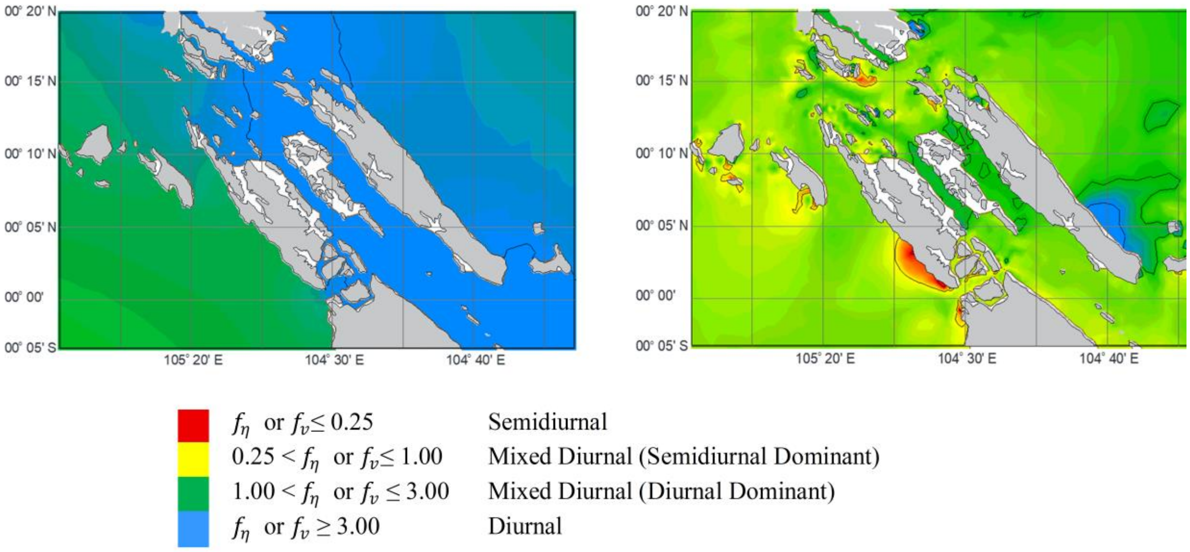

a. WSE *formzahl* (f_η)

b. Velocity *formzahl* (f_v).

Figure 5-34: The comparison of WSE *formzahl* (f_η) and the velocity *formzahl* (f_v).

5.4.5 The Peculiarity of Available Power from the M₂ Driven Simulation

The peculiar overestimation of available power from simulations driven by just M_2 requires further analysis (see Table 5-20). The velocity co-tidal chart of M_2 might provide an explanation. Figure 5-35 shows the comparison of M_2 co-tidal chart in velocity. The colour schemes show that the M_2 from the simulation solely driven by M_2 are larger than the M_2 from the simulation driven by 13 constituents.

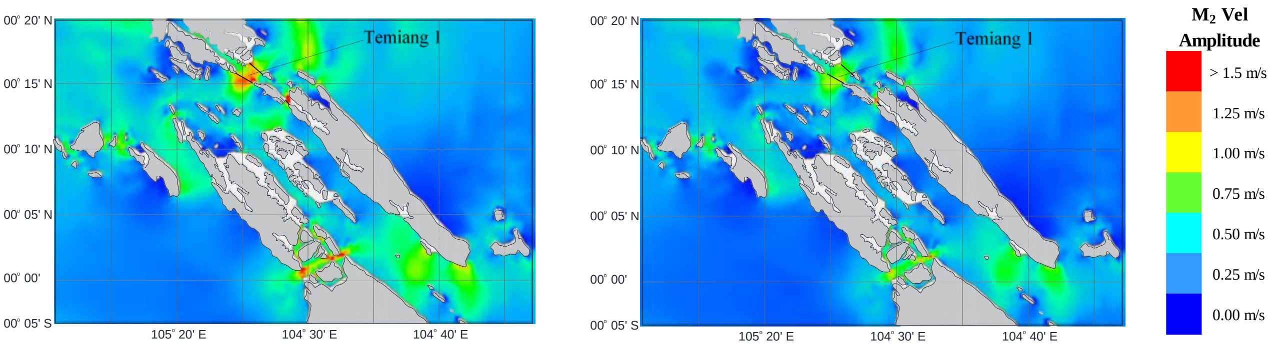

a. the M_2 flow speed from the simulation driven by M_2 only

b. the M_2 flow speed from the simulation driven by 13 constituents

Figure 5-35: The comparison velocity co-tidal chart of M_2 by the constituents driven

The maximum flow speed obtained by the simulation with the M_2 tide is 1.5 m/s, larger than the estimate of 1.0 m/s obtained with 13 tide constituents. Hence, the fraction of 150%-200% shown in Table 5-20 seems sensible. These arbitrary results demonstrate the uncertainty from an assessment that is driven by a single constituent only.

5.4.6 Electricity Provision from the Tidal Stream and the Appropriate Approach for Resource Assessment

Although this area has a potential for tidally driven energy, the magnitude is relatively small. As shown in Table 5-19, amongst six straits, only Temiang Strait (T1) could extract ~1MW electricity at low blockage ratio (*B*=0.1). Based on the population of Lingga, the region needs about 10 ~ 11 MW electricity supply. At high blockage, the channels could produce 4~5 MW approximately. Tidal energy, therefore, could be used to meet electricity demand in this area, provided high blockage tidal fences are installed and multiple channels are exploited.

However, this area cannot rely on tidal energy only. Figure 5-36 shows that the available power in this area has ~5 hours slack time during neap tide. As discussed in Chapter 1, this area has twelve hours SAIDI at the moment. Although SAIDI could be improved from 12 hours to 5~6 hours, it is likely that the deployment of tidal turbines in the area would not be sufficient to achieve zero SAIDI on its own.

Table 5-20 shows that the simulation driven by M_2 and K_1 could provide 80-90% of the average and ~69% to 73% of the maximum power, while simulations run with four principal diurnal and semidiurnal constituents (M_2, S_2, O_1 and K_1) could give 80%-94% of the average and ~69% to 73% of the maximum power obtained from simulations run with 13 constituents. These results imply that assessment using just M_2 and K_1 could give satisfactory results.

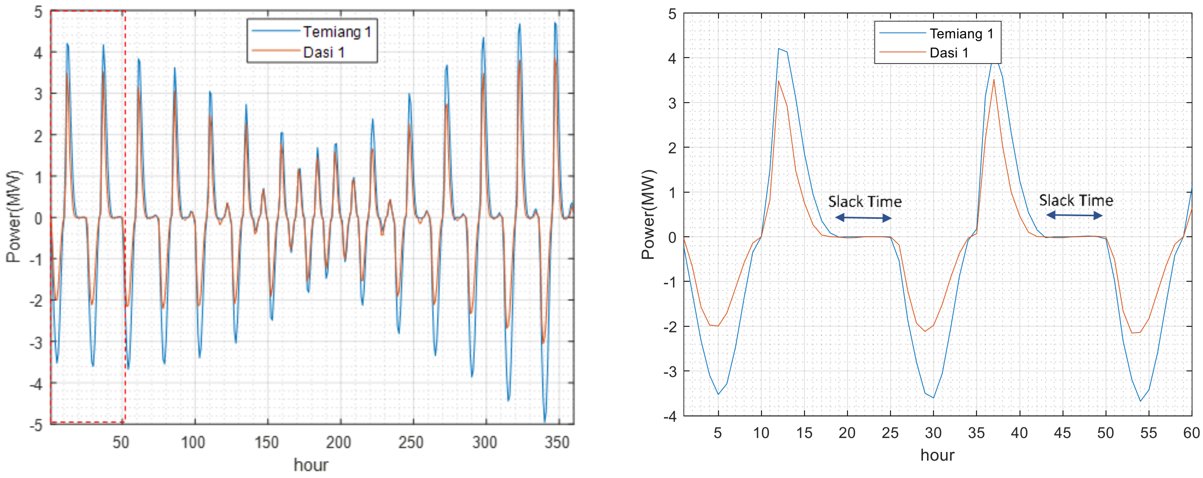

a. The fifteen days of available power

b. The sixty hours of extraction at spring tide (the red dash box at figure a)

Figure 5-36: Time series of available power at Temiang and Dasi Straits for *B*=0.1 and α_4 from the simulations that are driven by 13 constituents

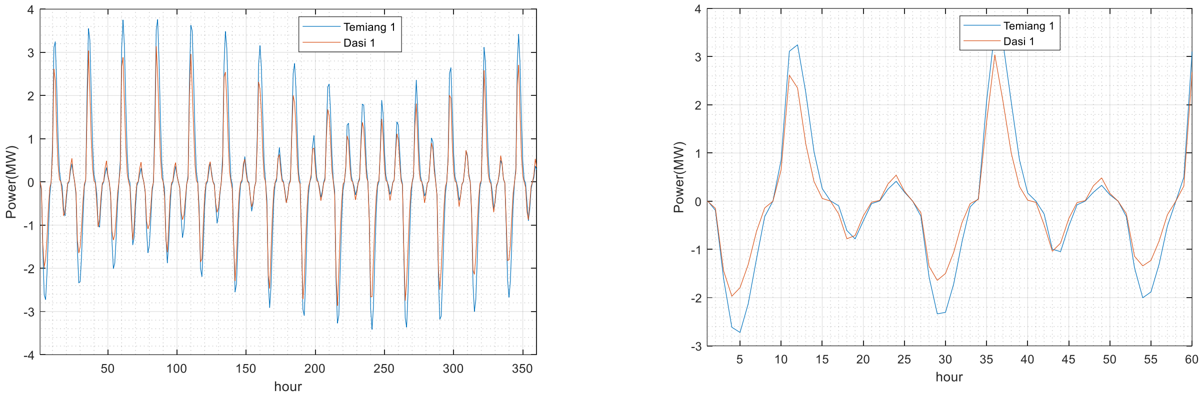

a. The fifteen days of available power from simulations that are driven by M_2K_1

b. The first sixty hours of available power frc simulation driven by M_2K_1

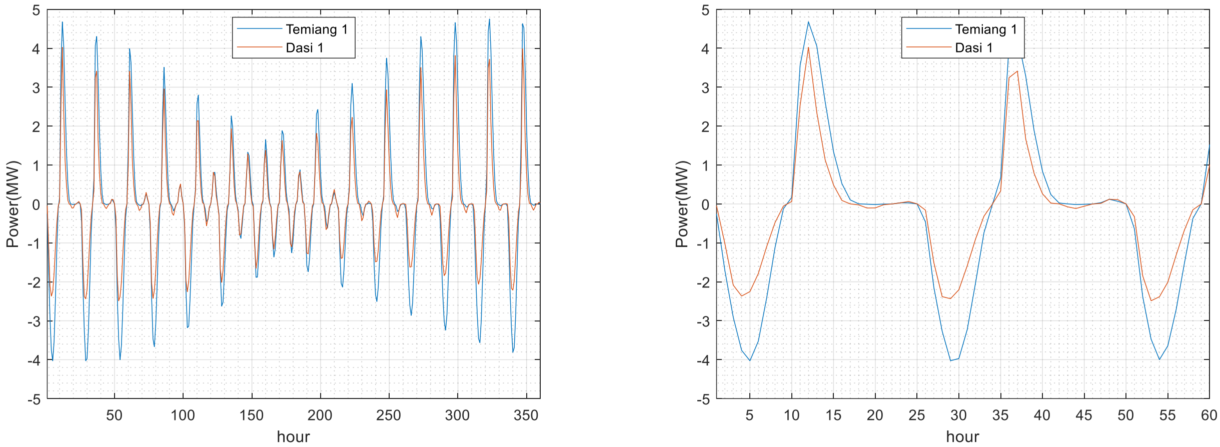

c. The fifteen days of available power from simulations that are driven by $M_2S_2K_1O_1$

d. The first sixty hours of available power frc simulation that are driven by $M_2S_2K_1O_1$

Figure 5-37: Time series of available power at Temiang and Dasi Straits for B=0.1 and α_4 from the simulations that are driven by principal constituents only

However, simulations that are driven by four principal diurnal and semidiurnal constituents not only give more accurate available power estimates but also could provide better information on the flow pattern. Figure 5-37 shows the comparison of available power in the time domain between the simulations driven by M_2 and K_1 (Figure 5-37a and Figure 5-37b) and the simulations driven by four principal diurnal and semidiurnal constituents (Figure 5-37c and Figure 5-37d). The simulations that are driven by M_2 and K_1 are unable to capture the pattern of the available power as well as the slack time as shown by the simulations that are driven by M_2, S_2, O_1 and K_1 (Figure 5-37d). Hence, it is safe to conclude that is an appropriate assessment should be conducted by using at least the four principal constituents (M_2, S_2, O_1 and K_1).

5.5 The Site-Site Interaction in the Unusual Channel Configuration of the Sula Regency

Surrounded by deep bathymetry, Sula regency's waters are a unique system. These islands are in the middle of the semi-enclosed basin of the Maluku Sea and the interior Banda Sea. Narrow straits which are connecting the deep-sea basins of the Maluku and the Banda Sea, exhibit strong currents. At the edge of the islands, a strong current passes the headland. The flow of the global thermohaline circulation through the riverbed trough, called the Lifamatola passage, makes the current in this location highly stratified or strongly sheared (see Figure 5-38).

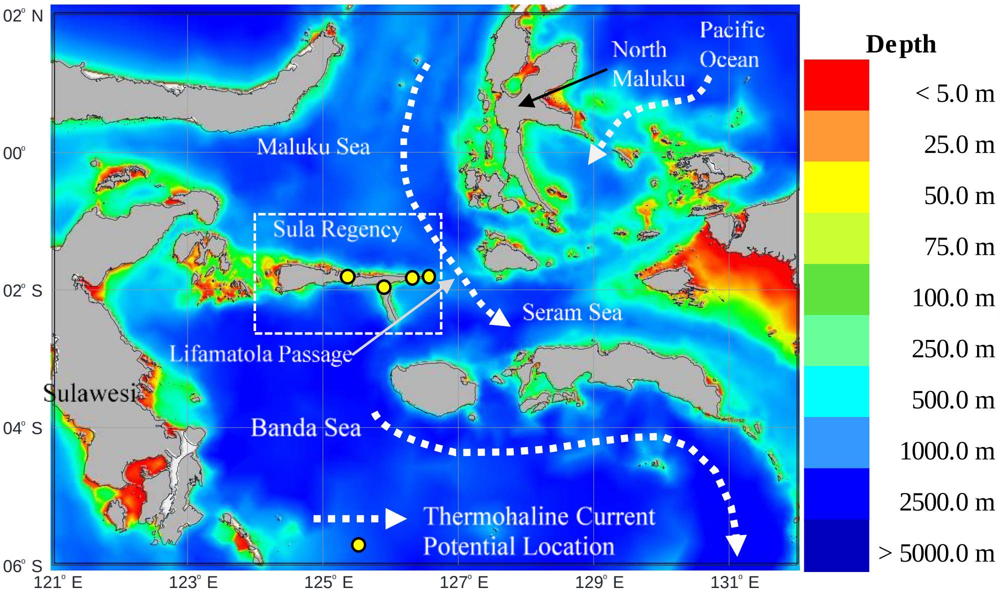

Figure 5-38: Bathymetry of Sula Regency's water, the dashed lines are the thermohaline current in the region (see Gordon *et al.*, 2012)

5.5.1 The Potential Sites

The previous sections have demonstrated the beneficial use of average kinetic power to identify potential locations for tidal energy. Figure 5-39 shows the average kinetic power in the Sula Regency and the potential location in the Sula Regency. At least four different locations have been recognised as potential locations. Three straits and a headland, the Capalulu (Cp), Lifamatola (Lf), Mangola (Mg), and Lifamatola headland (LH), show potential for tidal energy.

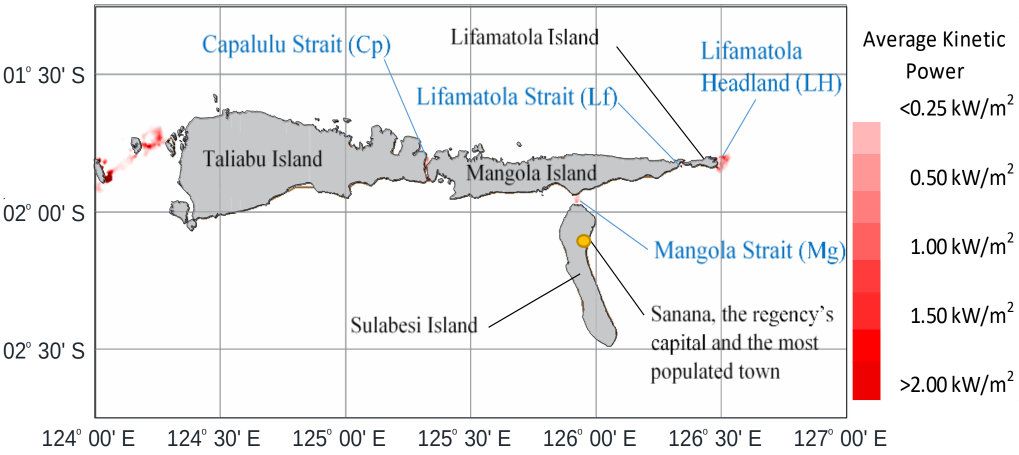

Figure 5-39: Average kinetic power at potential sites in the Sula Regency.

As discussed in Chapter 1, the most populated region is on the east coast of Sulabesi Island. Sanana, the capital and most populated town, is located in the east coast Sulabesi (see Figure 5-39). Based on this fact, Mangola has the most potential to deploy tidal turbines since this site is near a town in the regency. Therefore, there is no problem with demand. However, the Capalulu Strait is interesting as it has the potential for both islands (Taliabu and Mangola Islands).

5.5.2 The Resources at Capalulu Strait

Capalulu Strait has been recognised as a potential site in the Sula Regency (Prabowo, 2012). The narrow strait between Taliabu and Mangola Islands has flow magnitude up to 5 m/s. Figure 5-40 indicates the locations of the Capalulu site and possible tidal fences. The average kinetic power shows that there are two potential locations in Capalulu accordingly (Figure 5-40a). These locations have a bathymetric range of 25-35 m as shown in Figure 5-40b. The depth range is ideal for the current stage of the available technologies in the market.

Both locations are also close to the surrounding settlements. However, most of the settlements are closer to the Capalulu 1 (Cp1) rather than the Capalulu 2 (Cp2) (see Figure 5-40b). Cp1, therefore, has a better position than Cp2 in terms of demand. This section analyses the resources of both potential locations, including the interaction between the locations.

The average available power shows that Cp2 gives power almost double from Cp1 (see Figure 5-41). At low blockage, the available power at Cp1 is about 5 MW whereas that at Cp2 is ~10 MW. Meanwhile, at high blockage, Cp2 could extract ~42 MW and Cp1 only ~ 26.6 MW (see Table 5-21). These results are due to Cp1 having a larger cross-sectional area than Cp2. Bearing this in mind, the simulations are carried out for uniform blockage. Available power at Cp1 and Cp2 is therefore investigated further.

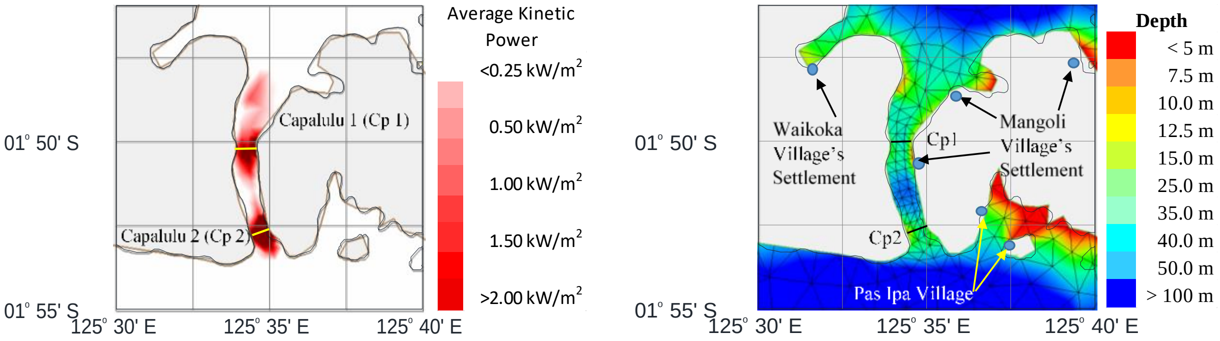

a. The average kinetic Power **b.** The bathymetry

Figure 5-40: The potential locations at Capalulu Strait

Table 5-21: The average available power from Capalulu Strait (in MW)

			Cp1				Cp2	
Fence Length (m)			1,167				1,126	
Cross Section (m^2)			33,395				23,445	
Schemes	Low Blockage (*B* = 0.4)				High Blockage (*B* = 0.4)			
	Cp1	Cp2	Total	α_4	Cp1	Cp2	Total	α_4
Cp1	5.15	-	5.15	0.35	26.60	-	26.60	0.47
Cp2	-	10.08	10.08	0.36	-	42.72	42.72	0.52
Cp1-Cp2	4.65	9.78	14.43	0.38	16.85	34.56	51.40	0.60

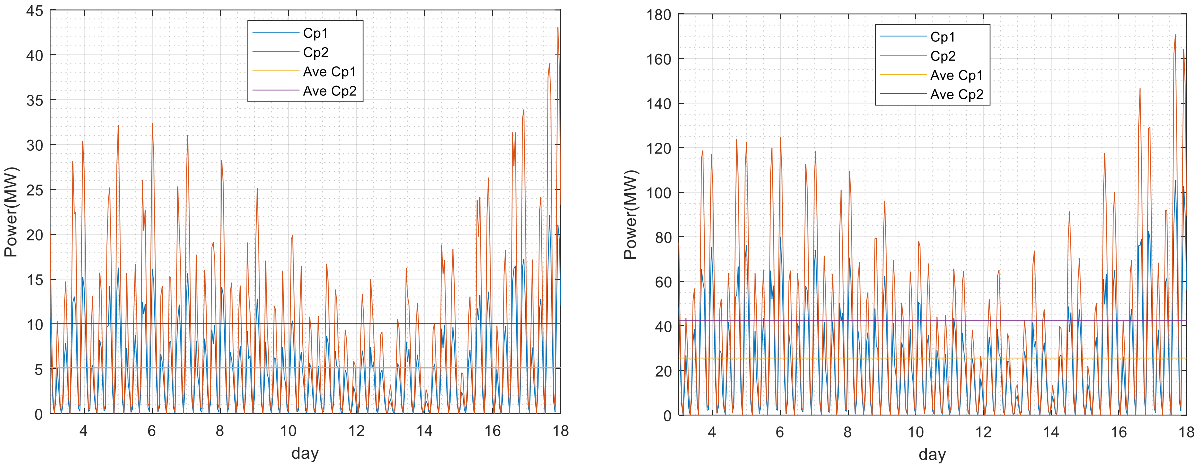

a. Low Blockage Ratio (*B*=0.1)

b. High Blockage Ratio (*B*=0.4)

Figure 5-41: Time series of available power at Capalulu Strait

Figure 5-42 compares the flow field changes obtained at Capalulu 1 (Cp1) and Capalulu 2 (Cp2). The flow field changes are the difference in average flow speed, from simulations with turbines installed and the simulations at the existing condition. Cp2 shows higher flow reduction than Cp2. Therefore, this Cp1 and Cp2 will have unique interaction when exploited simultaneously.

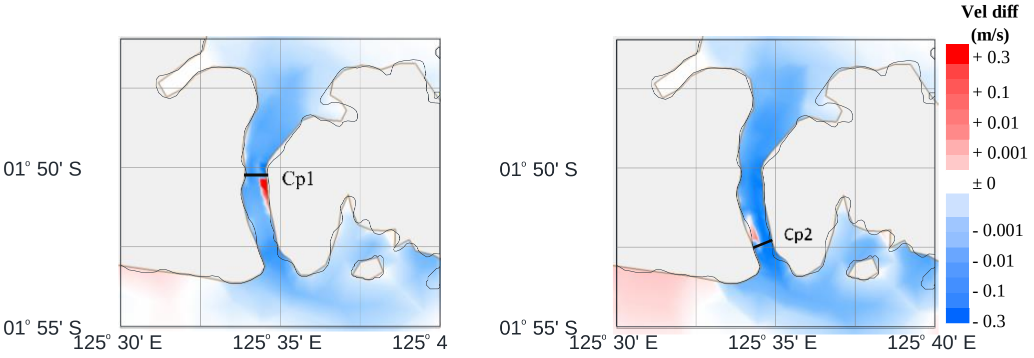

a. Capalulu 2 (Cp1)

b. Capalulu 1 (Cp2)

Figure 5-42: The flow field change at Capalulu for high blockage *B*=0.4 and α_4=0.56

Table 5-22 shows that Cp2 has more advantages than Cp1, in terms of average power reduction when both sites are exploited simultaneously. Cp2 experiences lower losses for multi-array scenarios than Cp1 for both blockage ratios. At low blockage and multi-array scenario, Cp1 produces 90% of the single array's average power while Cp2 produces only 3% less than the single array. This trend continues at high blockage; Cp2 has has higher fraction at multi-array scenarios compared to the single array than Cp1. Therefore, if the demand (determined by the distance to the settlement area) is taken out of the equation, Cp2 is apparently more desirable for turbine developers.

Table 5-22: The fraction of the Capalulu Strait's average available power

	B = 0.1			B = 0.4		
Schemes	Cp1 / Cp1*	Cp2 / Cp2*	All / All*	Cp1 / Cp1*	Cp2 / Cp2*	All / All*
Cp1	100%			100%		
Cp2		100%			100%	
Cp1-Cp2	90%	97%	95%	63%	81%	74%

* The available power from single array schemes

5.5.3 Lifamatola Headland (LH)

An area with vast potential is located at the end of Lifamatola Island. Located next to the deep water of the Maluku Sea's famous trough, Lifamatola passage, this site represents a unique case of headland type of tidal energy potential site. A tiny gap between Lifamatola Island and Mangola Island, Lifamatola Strait, also has a strong current (see Figure 5-43). The flow field in both locations is known to interact with global thermohaline circulation. Unfortunately, these locations are not near the settlements. However, it is worth investigating these locations due to their unusual features.

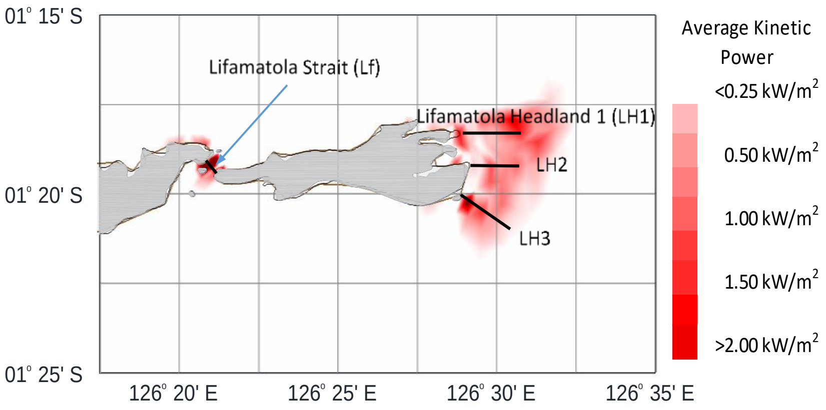

Figure 5-43: Average kinetic power at Lifamatola Strait and the Headland

Lifamatola headland is interesting regarding its interaction with the global thermohaline. If Lombok and Larantuka Straits are representing the interaction of the relatively shallow water strait, the Lifamatola represents the interaction of turbine fence with global thermohaline in deep water off a headland. Based on its geometry and the average kinetic power, this thesis analyses three potential locations at Lifamatola headland. As shown in Figure 5-43, the three locations are placed at the high average kinetic energy. Following the offshore wind turbine experience, presumably, the acceptable depth for tidal turbine deployment is less than 100 m deep. As shown in Figure 5-44, the fence lines in Lifamatola headland are in the acceptable depth for deployment.

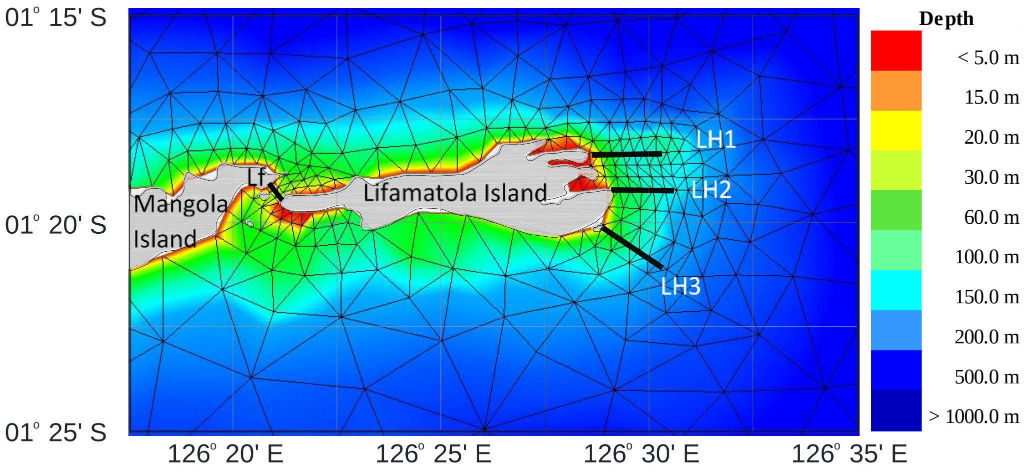

Figure 5-44: The bathymetry at Lifamatola Strait and the headland

Based on the colour intensity as presented in Figure 5-43, LH2 has the lowest average kinetic power flux. This fence line is also the shortest and the smallest cross-sectional area amongst the fence lines. However, the average power from this LH2 is higher than the average power from LH3 (see Table 5-23). Although the kinetic power flux and cross-sectional area of both fence lines indicate the LH3 should be higher than LH2. Meanwhile, the comparison of available power at LH1 and LH2 is somewhat perplexing. The average available power at LH2 is slightly higher than LH1 at low blockage, while LH1 extracts higher average power than LH2 at high blockage.

Table 5-23: The average available power at Lifamatola Headland (in MW)

	LH1	LH2	LH3
Fence Length (m)	4,031	3,599	4,036
Cross Section (m^2)	382,983	378,771	572,283

Schemes	Low Blockage (B = 0.1)					High Blockage (B = 0.4)				
	LH1	LH2	LH3	Total	α_4	LH1	LH2	LH3	Total	α_4
LH1	29.26	-	-	29.26	0.36	135.57	-	-	135.57	0.52
LH2	-	30.39	-	30.39	0.36	-	123.88	-	123.88	0.52
LH3	-	-	26.72	26.72	0.36	-	-	120.47	120.47	0.51
LH1-LH2-LH3	25.77	24.84	24.02	74.63	0.39	83.41	61.45	81.46	226.32	0.60
LH1-LH3	26.97	-	25.56	52.53	0.37	105.47	-	93.98	199.45	0.58
LH1-LH2	27.66	27.50	-	55.16	0.38	95.46	86.87	-	182.33	0.60
LH2-LH3	-	27.30	25.00	52.30	0.38	-	97.66	92.20	189.86	0.59

Although LH2 seems promising when exploited alone, this array line is vulnerable when other arrays are exploited. As shown in Table 5-23, the average available power from the LH2 fence is 30 MW for the low blockage scenario. Power extraction reduces to 24~27 MW from its individual capacity when exploited with other arrays simultaneously. At high blockage ratio, this tendency is more obvious. The average available power for a single array at LH2 is half that of other fence configurations. The fraction of the average available power on the Lifamatola headland is presented in Table 5-24.

Table 5-24: The fraction of average available power at Lifamatola Headland

Schemes	*B* = 0.1				*B* = 0.4			
	LH1	LH2	LH3	All	LH1	LH2	LH3	All
	LH1*	LH2*	LH3*	All*	LH1*	LH2*	LH3*	All*
LH1	100%				100%			
LH2		100%				100%		
LH3			100%				100%	
LH1-LH2-LH3	88%	82%	90%	86%	62%	50%	68%	60%
LH1-LH3	92%		96%	94%	78%		78%	78%
LH1-LH2	95%	90%		92%	70%	70%		70%
LH2-LH3		90%	94%	92%		79%	77%	78%

*the available power from single array schemes

Table 5-24 implies that the fractions of average power production for multi-array scenarios are significantly lower than for other fences at LH2. For example, the fraction at LH1 falls to 88-95% and LH3 to 90-96% from the production of a single array. Meanwhile, LH2 produces only 82-90% of the average power for a single array scenario when exploited with other fences simultaneously at the same blockage ratio.

5.5.4 The Unique Interaction between Lifamatola and Mangola Straits

Manola Strait has the most potential for tidal power development given its proximity to Sanana, the most populated town in Sula Regency, given the correlation between electricity demand and energy investment. As shown in Table 5-25, Mangola Strait could extract ~4.8 MW at low blockage ratio (*B*=0.1) and ~20 MW at high blockage ratio (*B*=0.4). These numbers are even relatively small compared to Capalulu 2 (Cp2). The cross-section of Cp2 is approximately one-quarter that of the Mangola Strait. Therefore, Cp2 might have more potential than Mangola (Mg), despite Cp2 being slightly further away.

Mangola Strait creates a unique set of site-site interactions. Unlike the previous sites, the configurations in this region are not strictly in parallel. Mangola Strait cross-section line is in a perpendicular orientation to the cross-section lines of Capalulu, Lifamatola Strait and the headland of Lifamatola. The site-site interactions in this section are carried out for the interaction of single-line arrays. The Cp2 and LH2 are selected to represent the single line array of the Capalulu Strait and Lifamatola Headland respectively.

Table 5-25 shows, at low blockage, the available power from multi-array scenarios is about the same magnitude compared to the single array scenarios. However, the multi-array scenarios are different to single array scenario at high blockage ratio. The Lifamatola Headland 2 (LH2) extracts ~5MW higher on average when harnessed simultaneously to the other sites.

Table 5-25: The average available power at Sula Regency (in MW)

	Cp2	Mg	Lf	LH2
Fence Length (m)	1,126	4,242	941	3,599
Cross Section (m^2)	23,445	112,361	19,921	378,771

Schemes	Low Blockage (B = 0.1)						High Blockage (B = 0.4)					
	Cp2	Mg	Lf	LH2	Total	α_4	Cp2	Mg	Lf	LH2	Total	α_4
Capalulu Strait 2 (Cp2)	10.08	-	-	-	10.08	0.36	42.72	-	-	-	42.72	0.52
Mangola Strait (Mg)	-	4.84	-	-	4.84	0.35	-	20.62	-	-	20.62	0.36
Lifamatola Strait (Lf)	-	-	2.55	-	2.55	0.36	-	-	11.18	-	11.18	0.54
Lifamatola Headland2 (LH2)	-	-	-	30.39	30.39	0.36	-	-	-	123.88	123.88	0.52
Mg-Lf	-	4.84	2.55	-	7.39	0.36	-	20.91	9.19	-	30.10	0.37
Cp2-Mg-Lf-LH2	10.09	4.83	2.55	30.39	47.86	0.37	42.49	22.91	10.97	128.72	205.09	0.60
Cp2-Lf-LH2	10.09	-	2.55	30.39	43.03	0.51	42.58	-	11.08	128.19	181.85	0.55
Cp2-Mg-Lf	10.08	4.84	2.55	-	17.47	0.55	33.50	20.51	8.98	-	62.99	0.36
Cp2-Lf	10.08	-	2.55	-	12.63	0.49	42.55	-	11.18	-	53.73	0.55
Cp2-Mg	10.07	4.83	-	-	14.90	0.55	42.47	22.95	-	-	65.42	0.60
Lf-LH2	-	-	2.55	30.39	32.94	0.60	-	-	11.07	128.16	139.23	0.55

Even though the LH is exploited with a small channel like Lf, it shows that the average available power in the multi-array schemes are higher than the production in the single array when both sites are exploited concurrently. Meanwhile, the available power of Lf remains at the same magnitude as its single array extraction. The small magnitude difference in the single array scenario and the multi-array scenario of Lf-LH2 is negligible since it is still in the range of simulation error.

Similar to the previous locations, Table 5-26 shows the fraction of available power and its single array extractions. This table shows that Mangola Strait tends to extract higher average available power from multi-array schemes. Therefore, this site has some attractive features, although it might be less interesting as regards power production. There is a possibility that the site will produce more power when there is another investment for the region.

Table 5-26: The fraction of the average available power at the Sula Regency

Schemes	Low Blockage (B = 0.1)					High Blockage (B = 0.4)				
	Cp2	Mg	Lf	LH2	Total	TC1	TC2	TC3	TC4	Total
	Cp2*	Mg*	Lf*	LH2*	Total*	TC1*	TC2*	TC3*	TC4*	Total*
Capalulu Strait 2 (Cp2)	100%					100%				
Mangola Strait (Mg)		100%					100%			
Lifamatola Strait (Lf)			100%					100%		
Lifamatola Headland2 (LH2)				100%					100%	
Mg-Lf		100%	100%		100%		101%	82%		95%
Cp2-Mg-Lf-LH2	100%	100%	100%	100%	100%	99%	111%	98%	104%	103%
Cp2-Lf-LH2	100%		100%	100%	100%	100%		99%	103%	102%
Cp2-Mg-Lf	100%	100%	100%		100%	78%	99%	80%		85%
Cp2-Lf	100%		100%		100%	100%		100%		100%
Cp2-Mg	100%	100%			100%	99%	111%			103%
Lf-LH2			100%	100%	100%			99%	103%	103%

*the available power from single array schemes

Moreover, the fraction also shows that the Mangola Strait acts as a parasite to the neighbouring sites, Capalulu2 (Cp2) and Lifamatola Strait (Lf), at high blockage. Table 5-26 shows, once Mangola Strait is exploited simultaneously with Cp2 and Lf, both straits tend to extract less power than its individual capacity. The Lf only extracts 82% of the individual capacity when operated alongside the Mg.

Moreover, the channels in the Sula Regency have more available power when Lifamatola headland (LH) is introduced to multi-array schemes. In a similar way to the Mangola Strait, although LH might not attract the turbine developer due to its distance to the settlements, the site might be lucrative in the future. Furthermore, this headland makes the other sites extract more power in multi-array scenarios.

5.5.5 The Interactions with the Array Cluster at Sula Regency Waters

Since Lifamatola headland and Capalulu Strait have the potential for a clustered array like the Lombok site, this option is also considered for future development. In a similar way to Bali-Lombok sites, the interaction is just analysed within the cluster. The available powers and their interaction between clusters in the Sula Regency are presented in Table 5-27.

Table 5-27: The average power and its interaction between clusters in the Sula Regency (in MW)

	Cp Cluster	Mg	Lf	LH Cluster
Fence Length (m)	2,293	4,242	941	4,031
Cross Section (m2)	56,841	112,361	19,921	382,983

Schemes	Low Blockage (B = 0.1)						High Blockage (B = 0.4)					
	Cp Cluster	Mg	Lf	LH Cluster	Total	α_4	Cp Cluster	Mg	Lf	LH Cluster	Total	α_4
Cp1-Cp2 (Cp Cluster)	14.43	-	-	-	14.43	0.38	51.40	-	-	-	51.40	0.60
Mangola Strait (Mg)	-	4.84	-	-	4.84	0.35	-	20.62	-	-	20.62	0.36
Lifamatola Strait (Lf)	-	-	2.55	-	2.55	0.36	-	-	11.18	-	11.18	0.54
LH1-LH2-LH3 (LH cluster)	-	-	-	74.63	74.63	0.39	-	-	-	226.32	226.32	0.60
Cp Cluster-Mg-Lf-LH Cluster	14.43	4.81	2.54	74.62	96.41	0.55	51.81	22.87	10.97	226.36	312.02	0.60
Cp Cluster-Mg	14.43	4.83	-	-	19.26	0.60	36.80	20.29	-	-	57.10	0.35
Lf-LH Cluster	-	-	2.54	74.62	77.16	0.35	-	-	11.09	230.20	241.29	0.60
Mg-Lf-LH cluster	-	4.81	2.54	74.61	81.97	0.60	-	22.86	10.97	226.28	260.11	0.60

In a similar way to single-line array interactions, the interaction in the Sula Regency shows that there is almost no interaction at low blockage. At high blockage, similar trends are exhibited from this configuration. The Mangola Strait still has a parasitic impact for other sites. The interaction of the Mangola Strait with Cp Cluster-Mg for example, once this cluster is exploited alongside Mangola Strait, the average available power is down to ~36 MW. In the single array scheme, this cluster could extract power an average of ~51 MW.

Unlike the Mangola Strait, the Lifamatoa Headland Cluster (LH Cluster) exhibits a positive impact on the combined sites. The fractions of the available power from multi-array schemes to its individual capacity are presented in Table 5-28.

Table 5-28: The fraction of average power for the array clusters at Sula Regency

Schemes	Low Blockage (*B* = 0.1) Cp Cluster / Cp Cluster*	Mg / Mg*	Lf / Lf*	LH Cluster / LH Cluster*	Total / Total*	High Blockage (*B* = 0.4) Cp Cluster / Cp Cluster*	Mg / Mg*	Lf / Lf*	LH Cluster / LH Cluster*	Total / Total*
Cp1-Cp2 (Cp Cluster)	100%					100%				
Mangola Strait (Mg)		100%					100%			
Lifamatola Strait (Lf)			100%					100%		
LH1-LH2-LH3 (LH cluster)				100%					100%	
Cp Cluster-Mg-Lf-LH Cluster	100%	100%	100%	100%	100%	101%	111%	98%	100%	101%
Cp Cluster-Mg	100%	100%			100%	72%	98%			79%
Lf-LH Cluster			100%	100%	100%			99%	102%	102%
Mg-Lf-LH cluster		99%	100%	100%	100%		111%	98%	100%	101%

*the available power from single cluster/array schemes

5.5.6 Flow-Fields Changes at Maluku and Banda Seas

Since these sites are in the path of the thermohaline circulation, it is important to understand the effect of turbine fences deployment to the current. According to the previous results, the channels extract less power for the multi-array scenarios, except for Mangola. Therefore, it would be sensible to start the investigation here. Figure 5-45 shows that the deployment of turbines in this channel has no significant impact on the global thermohaline circulation.

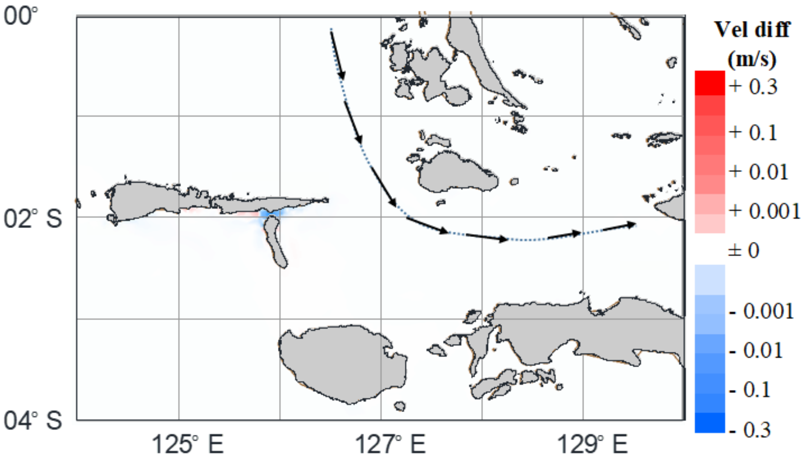

Figure 5-45: Flow field changes due to a line of turbines array installed at Mangola (Mg) Strait (simulation run at high blockage ratio B=0.4 and α_4=0.56)

The simulation of turbine fences installed simultaneously at Capalulu, Mangola and Lifamatola shows small changes in the flow-field for the global-current pathway (see Figure 5-46). It indicates that the turbine fences in those straits have very little impact on the thermohaline circulation, even at high blockage ratio. Meanwhile, when the Lifamatola Headland is introduced to a multi-array scheme, the flow field at a global scale starts to change (see Figure 5-47). Therefore, it is safe to conclude the Lifamatola headland can affect the global current that passes through the Maluku and Banda Seas.

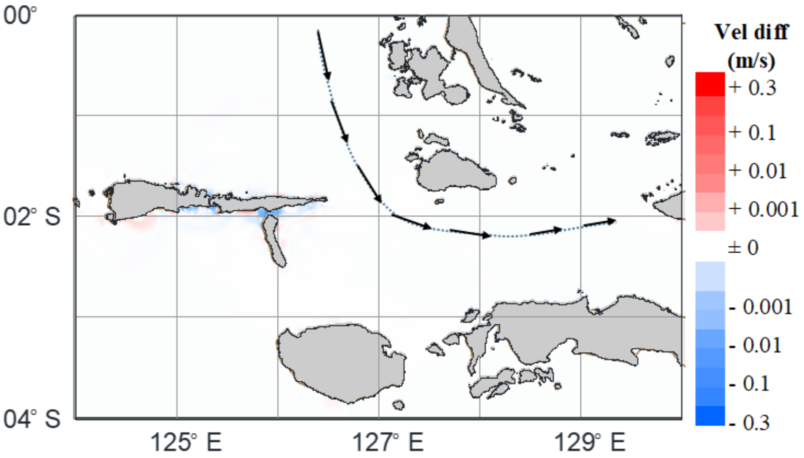

Figure 5-46: Flow field changes for turbine arrays installed at Capalulu (Cp), Mangola (Mg) and Lifamatola (Lf) (simulation run at high blockage ratio B=0.4 and α_4=0.56)

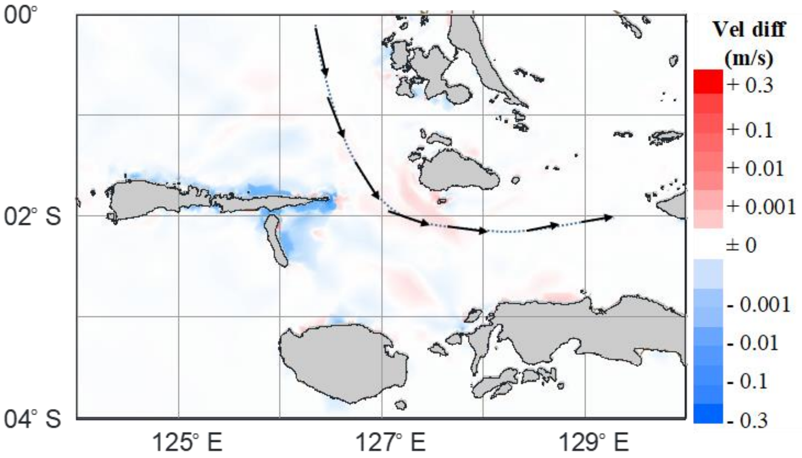

Figure 5-47: Flow field changes for turbine arrays installed at Capalulu (Cp), Mangola (Mg), Lifamatola (Lf) and Lifamatola Headland (LH) (simulation run at high blockage ratio B=0.4 and α_4=0.56)

This chapter, therefore, further investigates the effect of turbine fence deployments at Lifamatola headland. The flow-field changes from turbine fences deployment at Lifamatola Headland are shown in Figure 5-48. These figures are from the simulation of high blockage ratio, B= 0.4 and α_4= 0.56. The LH2 (Figure 5-48b) creates different flow-field changes compared to LH1 (Figure 5-48a) and LH3 (Figure 5-48c).

Unlike at other locations, the flow-field changes from the deployment at LH2 tend to slow the flow down. Figure 5-48b (the zoomed out figure) at the global scale shows the bluish colour scheme at Lifamatola passage, the path of the global current. Meanwhile, a large area of flow acceleration caused by the bypass flow of LH2 can be seen in the near field (see the zoom in Figure 5-48b).

This accelerated zone is more pronounced than that of the multi-arrays (Figure 5-48d).These results are sensible since turbine array deployment at Lifamatola Headland will obstruct the global current directly. The flow-field changes at Lifamatola passage make the flow field across the region change as well.

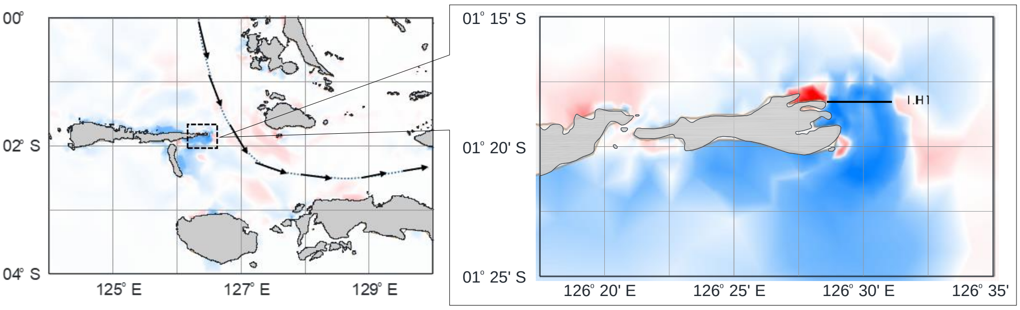

a. Flow field from LH1

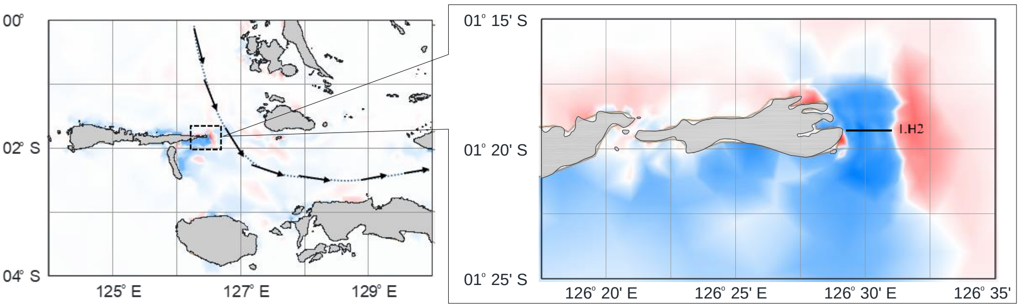

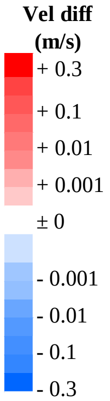

b. Flow field from LH2

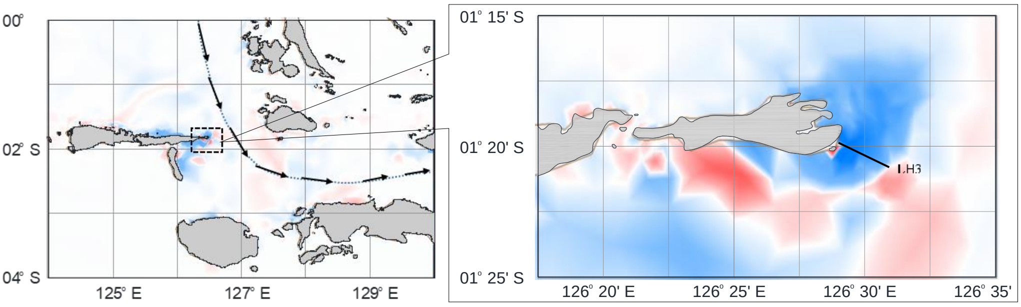

c. Flow field from LH3

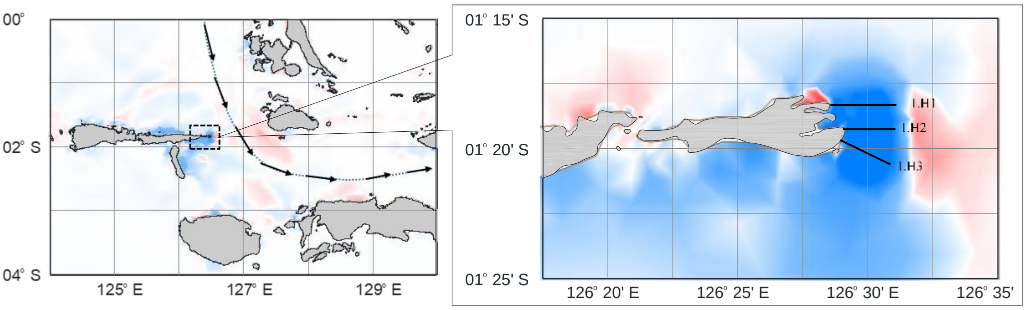

d. Flow field from LH1-LH2-LH3

Figure 5-48: Flow field changes for the scenarios at Lifamatola Headland, the arrow lines at zoom-out figures are the global thermohaline circulation

5.6 *Formzahl* Numbers

As discussed in Chapter 2, the velocity variation may differ from the water surface elevation (WSE). The power variations are inherent with the velocity variation. These variations could be reflected by the *Formzahl* number. The assessment in the Lingga Regency demonstrates that the WSE *Formzahl* number (f_η) is not the same as the velocity *Formzahl* number (f_v).

5.6.1 Western Domain

Since the *Formzahl* number for the Lingga Regency has been analysed in section 5.4.4, the analysis for the western domain here is focused on the Sunda Strait. If Lingga regency waters exhibit diurnal tidal cycles in WSE, Sunda Strait is closer to semidiurnal or mixed diurnal, with semidiurnal dominant. The colour scheme in Figure 5-49a shows that the f_η of Sunda Strait around the bridge is closer to semidiurnal, while the velocity f_v is closer to diurnal cycles.

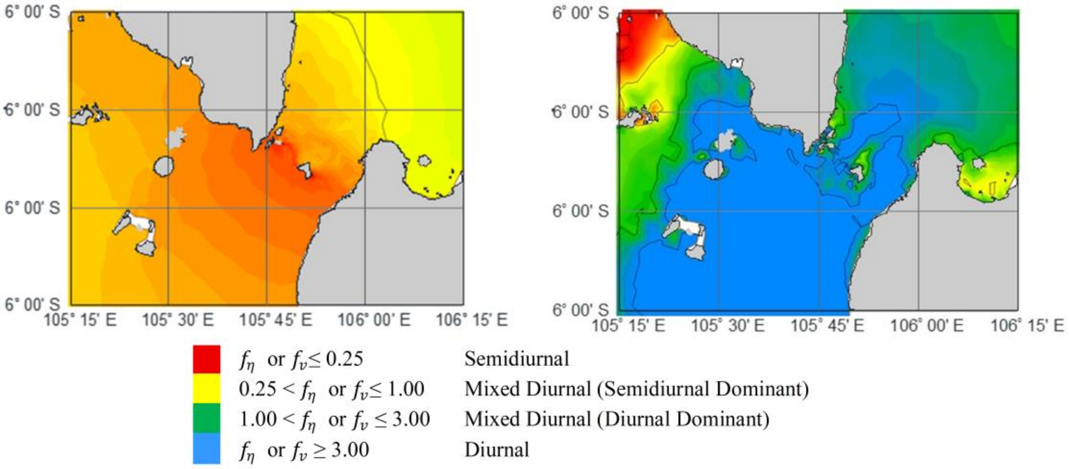

a. WSE *formzahl* (f_η)

b. velocity *formzahl* (f_v).

Figure 5-49: The *Formzahl* number for WSE and flow speed in Sunda Strait

Transforming the WSE and the velocity from the time domain to the frequency domain for this location further confirms these results. Figure 5-50 shows energy spectra of WSE and velocity for Sunda Strait. In contrast to Temiang Strait, the energy spectra for Sunda Strait show that the WSE of this area tends to semidiurnal while the velocity tends to diurnal.

The available power in the time series is differentiated by the flow direction when the power is generated. Similar to the Temiang Strait, negative power means the power is generated when the velocities go southward, while positive power means the velocities go northward. Figure 5-51 shows that the WSE is a semidiurnal cycle, while available power is closer to a diurnal cycle.

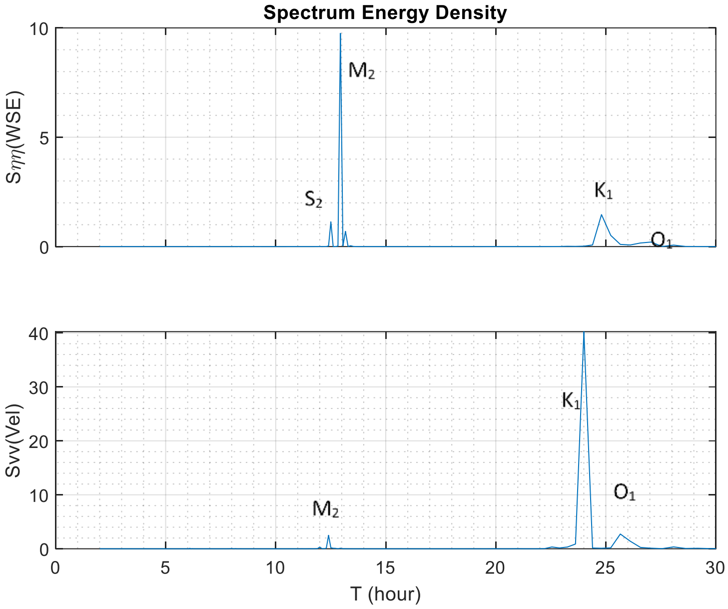

Figure 5-50: Energy density spectra for Water Surface Elevation (WSE) and Flow Speed at Sunda Strait Bridge (SSB) at the bottom.

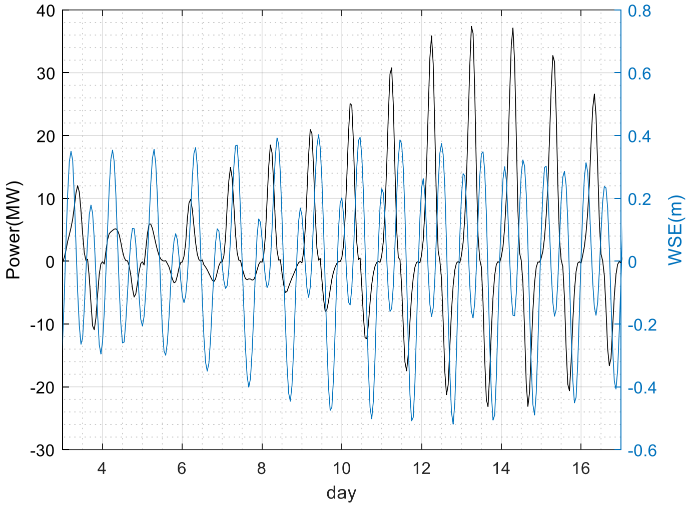

Figure 5-51: The comparison of WSE and available power in the Sunda Strait Bridge (SSB)

5.6.2 Central Domain

In a similar way to Sunda Strait, the f_η in the island chain of Bali-Nusatenggara WSE (Figure 5-52) is different from the f_v (Figure 5-53). There are two locations are selected for assessment in the Bali-Nusa Tenggara region. Figure 5-54 shows that there is no pattern of the relationship of f_η and f_v. For the Bali-Lombok channel, the f_v (Figure 5-54b) are relatively more complicated than the f_η (Figure 5-54a). The f_v numbers have more variation in area of potential interest. In consequence, the fence-lines across the channel have different available power patterns.

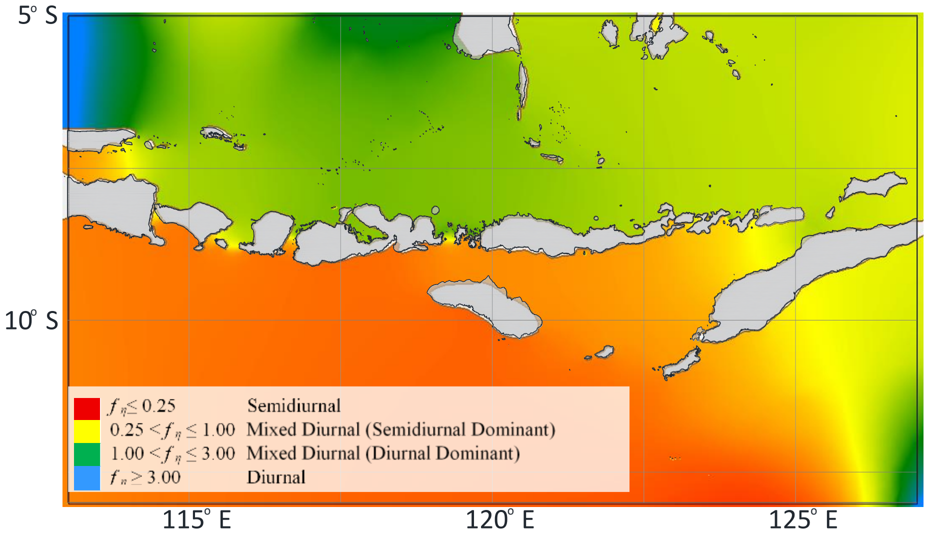

Figure 5-52: WSE *Formzahl* (f_η) in the island chain of Bali-Nusa Tenggara

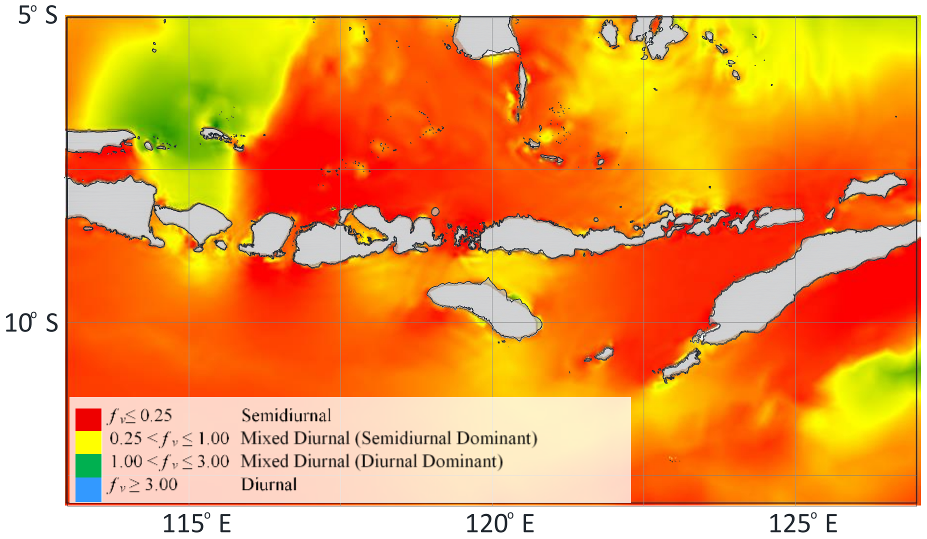

Figure 5-53: Velocity magnitude *Formzahl* (f_v) in the island chain of Bali-Nusa Tenggara

However, the Larantuka sites show more consistency of velocity *Formzahl* (f_v) in the channel lengthwise, although the WSE *Formzahl* (f_η) shows a gradation from mixed semidiurnal to mixed diurnal (see Figure 5-54 d). It can be concluded the Larantuka channel is closer in tidal behaviour to most sites in the Northern hemisphere (the UK, US and Canada).

Table 5-29 shows that an assessment from simulations driven solely by M_2 and S_2 gives 80%-82%, and S_2 27%-30% average powers respectively compared to corresponding results from simulations that are driven by 13 constituents. Whilst simulations driven by diurnal constituents (K_1 or O_1) show that the average power from both constituents is relatively insignificant compared to the average available power from the simulation driven by 13 constituents. These results are similar to the Pentland Firth (in detail, see Adcock *et al.* 2014). However, simulations driven solely by M_2

give just 40%-42% of the maximum available power from the simulation run with 13 constituents. Therefore, the approach of using just a single constituent might be incapable of capturing the whole picture of available power.

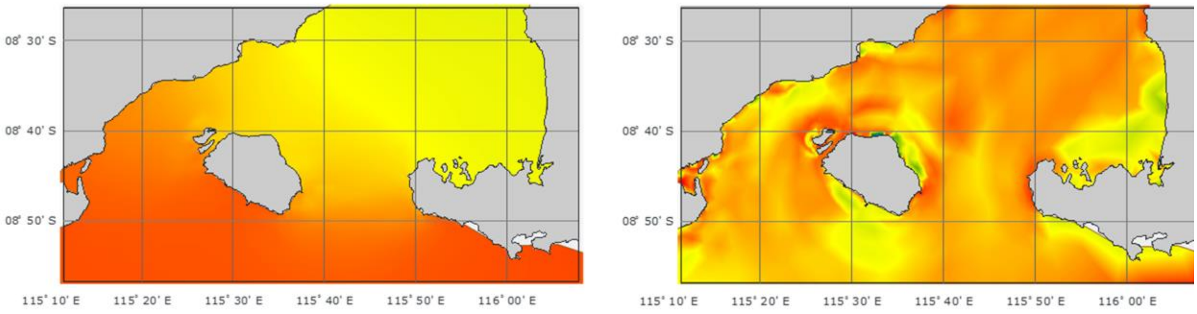

a. WSE *formzahl* (f_η) in the Bali-Lombok Channel

b. The velocity *formzahl* (f_v) in the Bali-Lombok Channel

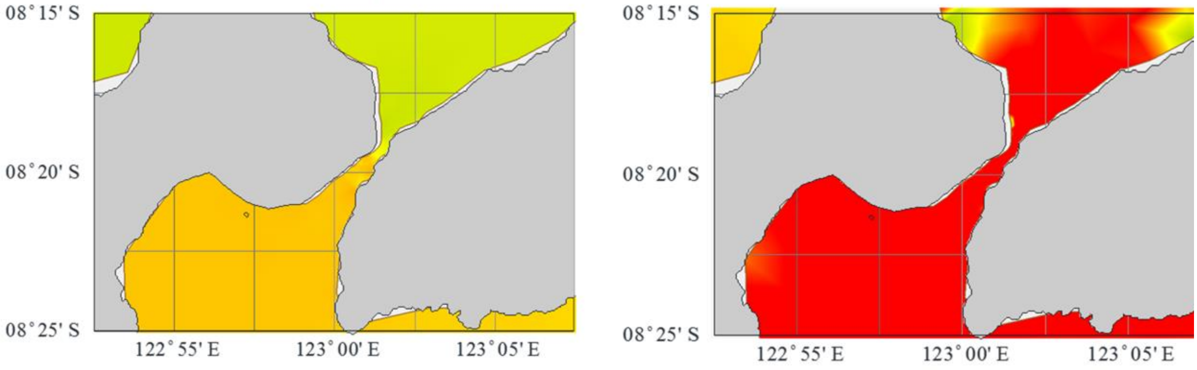

c. WSE *formzahl* (f_η) in the Larantuka

d. The velocity *formzahl* (f_v) in the Larantuka

🟥	f_η or $f_v \leq 0.25$	Semidiurnal
🟨	$0.25 < f_\eta$ or $f_v \leq 1.00$	Mixed Diurnal (Semidiurnal Dominant)
🟩	$1.00 < f_\eta$ or $f_v \leq 3.00$	Mixed Diurnal (Diurnal Dominant)
🟦	f_η or $f_v \geq 3.00$	Diurnal

Figure 5-54: The *formzahl* number for Bali-Lombok channel and Larantuka

Table 5-29: The available power based on various constituent(s) driven model in Larantuka

Scheme	Power				Ave	Max
	Ave (MW)	α_4	Max (MW)	α_4	Ave of 13 Const	Max of 13 Const
B = 0.1						
13 Const	4.67	0.38	24.85	0.37	100.00%	100.00%
M_2	3.77	0.37	10.12	0.37	80.57%	40.73%
S_2	1.30	0.36	3.63	0.36	27.73%	14.61%
K_1	0.11	0.36	0.34	0.36	2.45%	1.36%
O_1	0.0038	0.34	0.02	0.34	0.08%	0.06%
B = 0.4						
13 Const	19.06	0.53	87.71	0.40	100.00%	100.00%
M_2	15.70	0.52	37.38	0.52	82.38%	42.62%
S_2	5.83	0.50	14.49	0.50	30.57%	16.52%
K_1	0.55	0.48	1.49	0.48	2.87%	1.70%
O_1	0.022	0.43	0.08	0.43	0.12%	0.09%

Hence, this analysis further confirms that a resource assessment in Indonesia using an individual dominant constituent might be inappropriate. For example, the resource assessments of using just

M_2 in the Larantuka will lead to underestimation of the resource. This despite the area being in the semidiurnal regime.

5.6.3 Eastern Domain

A similar analysis could be conducted for the eastern domain as well. Figure 5-55a shows the f_η in the Sula Regency waters are in the range of mixed diurnal. The northern side is mixed diurnal with diurnal dominant, while the southern side is the mixed diurnal with semidiurnal dominant. The f_v in this area shows most of the potential sites are closer to semidiurnal with f_v = 0.3 approximately (see Figure 5-55.b). Therefore, the velocity pattern in this location is similar to the Bali sites.

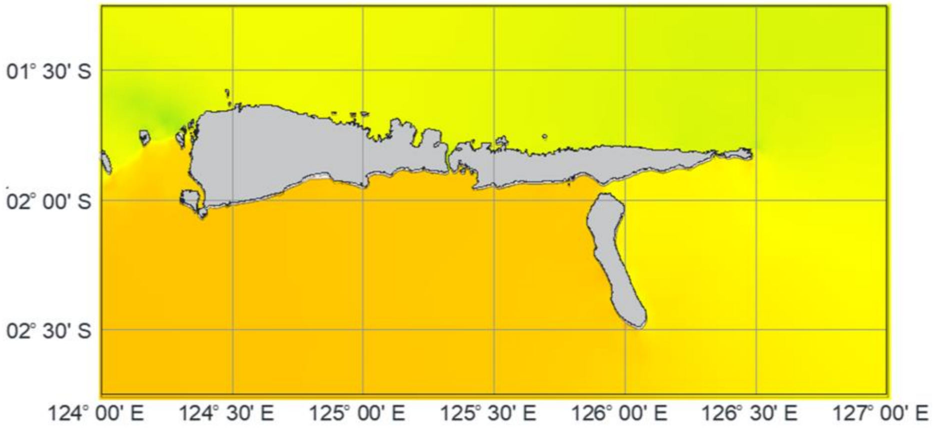

a. WSE *formzahl* (f_η)

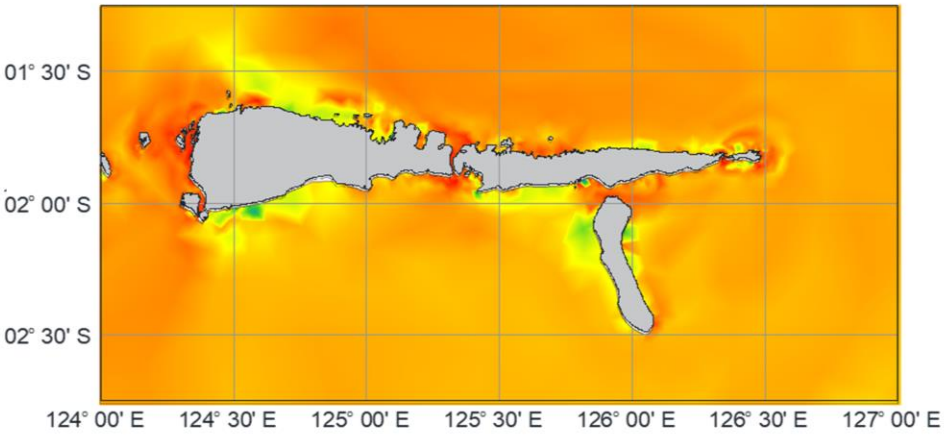

b. velocity *formzahl* (f_v)

🟥	f_η or $f_v \leq 0.25$	Semidiurnal
🟨	$0.25 < f_\eta$ or $f_v \leq 1.00$	Mixed Diurnal (Semidiurnal Dominant)
🟩	$1.00 < f_\eta$ or $f_v \leq 3.00$	Mixed Diurnal (Diurnal Dominant)
🟦	f_η or $f_v \geq 3.00$	Diurnal

Figure 5-55: The *formzahl* number for the Sula Regency in the Eastern Domain

5.7 Power Variation

The long-term variability and annual power variation are analysed further here. The exercise in Chapter 2 shows that the interaction of the semidiurnal components (M_2 and S_2) with the diurnal components (K_1 and O_1) creates an annual cycle. The long-term variability is also addressed here.

However, it is computationally expensive to conduct such analysis. Therefore, the long term variability analysis is only limited to one location only while the annual power variation is conducted for two selected locations, Larantuka and the Sunda Strait Bridge.

5.7.1 Long-Term Variability

As mentioned in Chapter 2, Adcock *et al.*, 2014 have shown forcing the model with additional constituents (K_1, K_2, MU_2, N_2, NU_2 and O_1), in addition to M_2 and S_2 on the Pentland Firth yields a small increase in the theoretical available power averaged over a long period of time. Given that it has a similar tidal velocity regime to the Pentland Firth, Larantuka is selected for this investigation. Another motivation for selecting Larantuka is because there is an imminent project of tidal energy that has been proposed. Therefore, performing this analysis is beneficial for further analyses in the next chapter.

Following the same approach as Adcock *et al.*, 2014, this thesis investigates the long-term variation in Indonesian sites. This long-term variability analysis is the extension of analysis from the Larantuka site. The simulation run for ten years covers more than half of a *Metonic* cycle (18.6 years) and is divided annually for each simulation. Since this analysis is computationally demanding, the simulation is only run for the proposed bridge location. The simulations are run with a single wake coefficient (α_4= 0.33) for two different blockage ratios (B= 0.1 and B= 0.4) for simplicity. The average of annual power in the bridge location is presented in Figure 5-56.

a. Low blockage ratio (B= 0.1)

b. High blockage ratio (B= 0.4)

Figure 5-56: Average available power time series at Larantuka tidal bridge (La2 array)

For both blockage ratios, small variations in average power are exhibited within ten years. For the lower blockage ratio, the lowest available power is about 4.9 MW (2010 and 2020) while the highest is ~5.12 MW (2014). The discrepancy between the highest and the lowest only yields small variation, ~0.2 MW approximately. At high blockage, the difference between the highest and the lowest available power is ~1 MW. Hence, the variation of this long-term simulation is 5% for both blockage ratios.

The long term variation is dictated by nodal factor. Since ADCIRC uses Le Provost tidal model to generate the boundary conditions, and Le Provost Model uses nodal-factors for long term variation, this long-term variability could be analysed from the nodal factor. Figure 5-58 shows the nodal factor for M_2 and K_1. M_2 is the strongest component in Larantuka. Therefore, the long-term variability is dictated by M_2 nodal factor. The shape of long-term variation follows the shape of M_2 nodal factor more (Figure 5-58a) than of K_1 nodal factor (Figure 5-58b).

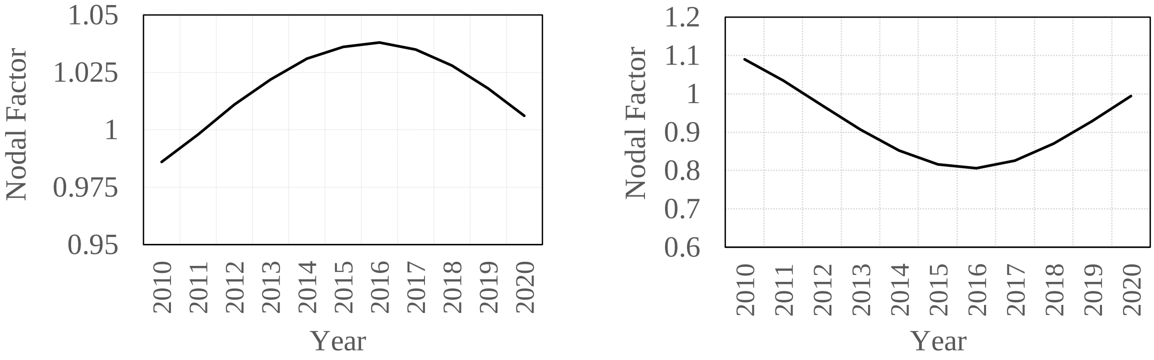

a. M_2 b. K_1

Figure 5-57: Time series of Le Provost nodal factor at Larantuka

As discussed in Chapter 2, the nodal factor of M_2 is determined by the equation $n = 1.00 - 0.037\cos(N)$, where N=0 in June 2006. Therefore, the nodal factor for a complete cycle could be generated. The nodal factor for a complete cycle of M_2 is shown in Figure 5-58. If the fluctuation of available power in Larantuka based on the 10 years simulation is approximately 5%, the longer period (a *Metonic* cycle) the fluctuation could be 8%-10%.

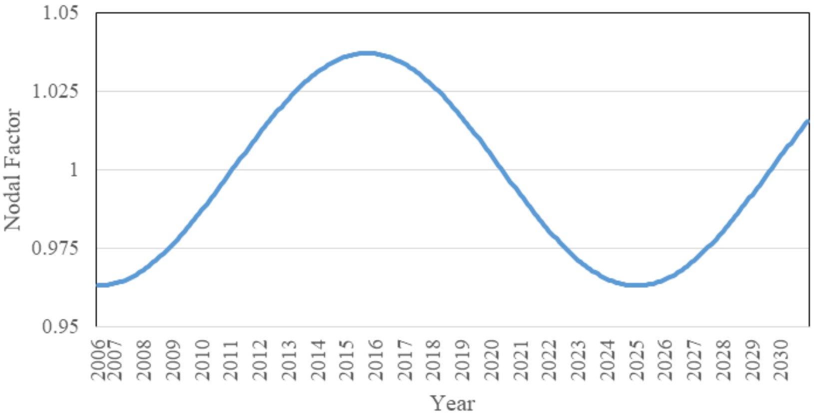

Figure 5-58: Theoretical nodal factor for M_2

The predictability of the average available power fluctuation could be beneficial for turbines developers. If the available power follows the M_2 nodal factor as shown in Figure 5-58, the developers could prepare for a decline in available power from 2020 to 2030. This information could be used in financial modelling as well, and the project feasibility could take this fluctuation into account.

5.7.2 Annual Variation

As discussed in Chapter 2, the interaction of diurnal and semidiurnal components create an annual cycle. However, the peaks of this annual variation occur at the different time in term of solstices and equinoxes. Two locations are selected for the annual variation analysis in this Thesis. Larantuka and Sunda Strait Bridge (SSB) are selected because both locations present extreme cases.

Larantuka is located where the tidal flow speed follows a mainly semidiurnal pattern. However, this location still has diurnal components. The SSB is the location where the diurnal components are pronounced, and the semidiurnal components are still significant. Figure 5-59 shows typical power time series over a year at Larantuka and SSB. The peak of the neap-spring cycle of the power variation at Larantuka fluctuates from 20 MW to 35 MW for the low blockage ratio (B = 0.1), while for the high blockage (B = 0.4) varied from 50 MW to 35 MW.

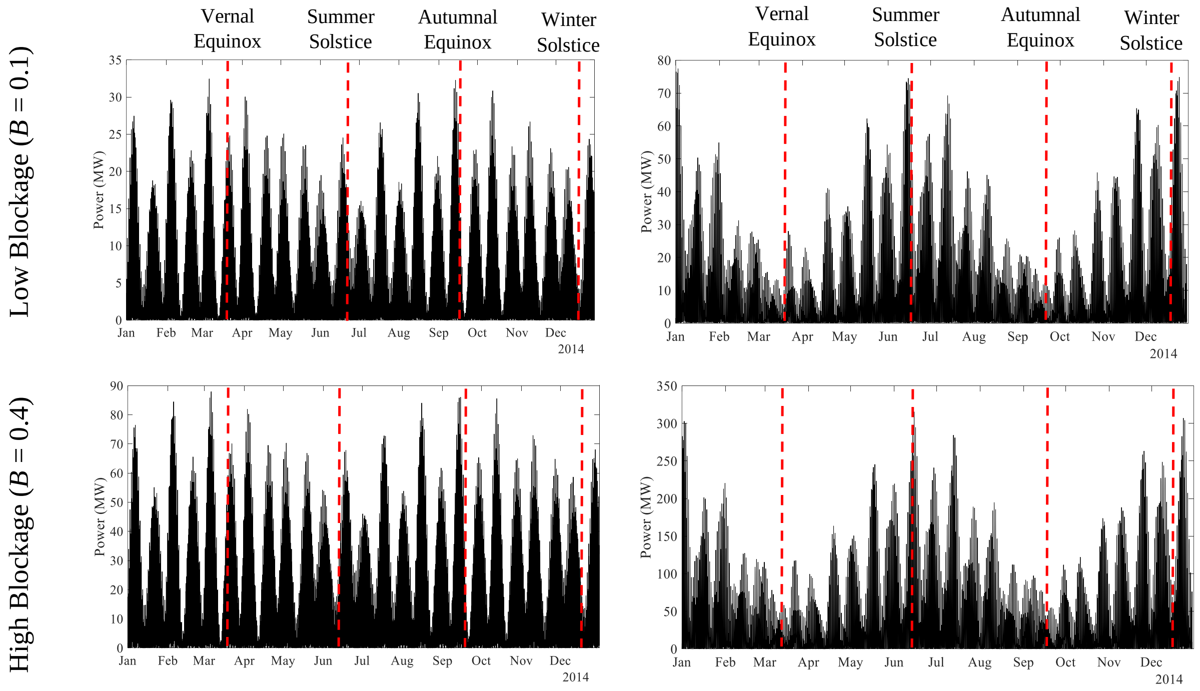

a. Larantuka b. Sunda Strait Bridge (SSB)

Figure 5-59: Power time series in 2014 for Larantuka Strait and Sunda Straits

Meanwhile, the neap-spring cycle's peaks of power removed by the turbines in the SSB varied from 20 MW to 80 MW for $B = 0.1$ and from 100 MW to 300 MW for $B = 0.4$. Figure 5-59 shows that the Larantuka and SSB peaked at a different time in the annual solstices-equinoxes. Power extracted at Larantuka peaked during equinoxes whereas that at SSB peaked at solstices. If the daily cycles are removed, the fluctuation pattern will be shown clearly.

Figure 5-60 shows the annual and semi-annual variations in power at both locations after low-pass filtering to remove the daily cycle. This graph shows the annual variations from three different years that have been selected to be representative of the variation. The power variations show that the peak and valley at the equinox and solstice, respectively, are consistent between different years.

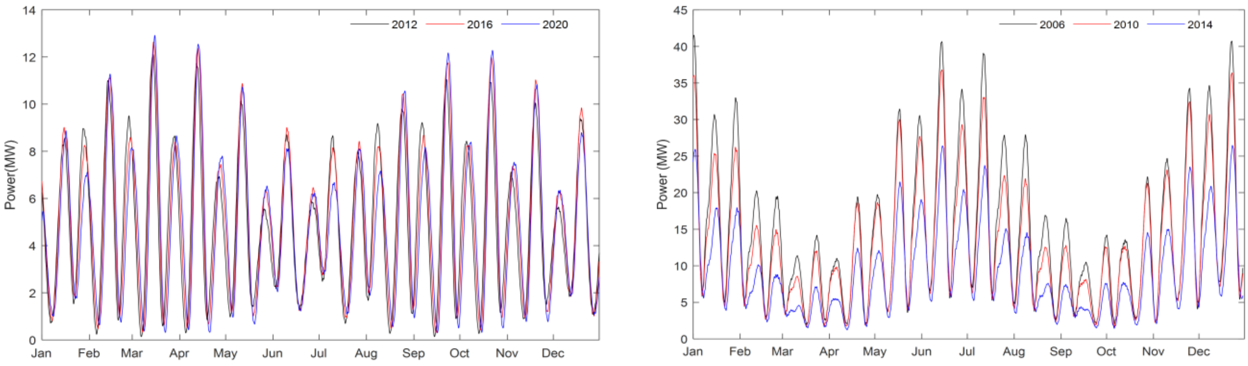

a. Larantuka

b. Sunda Strait Bridge (SSB)

Figure 5-60: Annual power variation after low-pass filtering to remove the daily cycle for B = 0.1 at Larantuka and Sunda Strait Bridge.

The annual time series after low-pass filtering for both locations show the variation of monthly peak within the year. These results imply that the power average also varies within the months. The variations between years are represented as error bars in Figure 5-61. It shows that the discrepancies between years are only in the range of 5%. These results are consistent with the long-term variability analysis, as shown in the previous section. This analysis also shows that the monthly average power will vary significantly. The variations in Larantuka are from 85% to 115%. Meanwhile, the monthly average power varies from 40% to 150% with respect to the average annual power production at SSB.

5.8 Discussion

Most of this chapter discussed site-site interactions. Two types of site-site interactions are discussed here, series type interaction and parallel type interaction. This chapter consistently shows that if tidal fences are arranged in series (upstream and downstream arrangement), they will produce less power in multi-array scenarios rather than as single fences. The site-site interactions in series that are analysed in Larantuka, Lombok and the Sula Regency represent the channel type and the headland type. Although there are small differences in term of “reduction” in the average power of upstream-downstream interaction for the channel type and headland type, this thesis argues this typical interaction does not need further investigation.

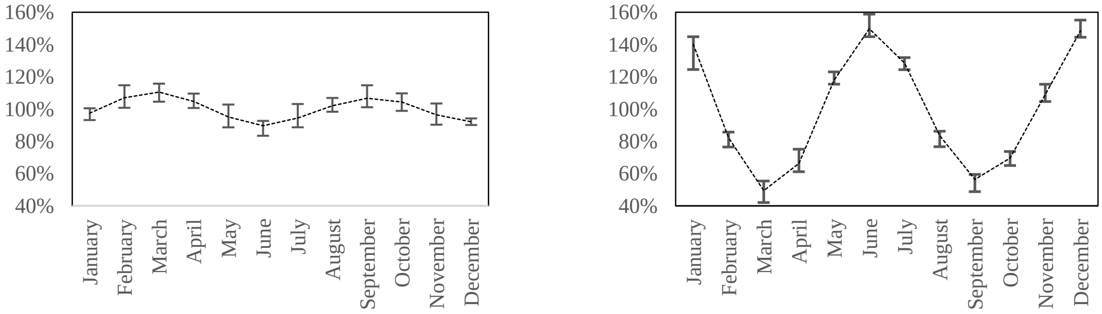

a. Larantuka
b. Sunda Strait Bridge

Figure 5-61: The monthly average power in reference to the annual average power from the multi-years simulation with error bar

However, the site-site interactions in the parallel are somewhat perplexing. Draper *et al.*, 2014 and Coles *et al.* 2017 consistently show that turbine arrays installed in parallel will have higher available power than the sum of the individual turbine power capacities. It implies that the parallel interactions give an advantage for power production. However, this chapter has demonstrated that parallel interactions can be complicated. Three different cases in this chapter demonstrate three different interactions. The number of important constituents appears to play an important role in the inconsistency of parallel interactions.

The FFT analysis of the five locations shows the different characteristics of WSE and flow speed *Formzahl* number (f_η and f_v) in each location. Therefore, it is safe to conclude that each location not just represents different population-based demand, as discussed in Chapter 1. Each location also represents a different power variation characteristic as discussed in section 5.6. By and large, the Larantuka represents the semidiurnal tidal stream type, and the SSB represent the diurnal type, whereas other locations are mixed-diurnal.

This chapter also conducted the long-term variability analysis for the Larantuka site and found the long-term variation in this site follows the M_2 nodal factor. This result conforms with the analysis from Adcock *et al.*, 2014 concerning the Pentland Firth. The variation of average power varied within 5% for the Larantuka site.

The annual variation confirmed the annual variation produced from a tidal regime with strong interaction between semidiurnal and diurnal components. These variations lead to two important findings. Firstly, the selection of a particular month for an assessment is critical. For instance, an assessment that is conducted in March or September will give an overestimate of the resource, whereas an assessment form the simulation that represents June and December will give an underestimate of the average available power. Based on these conditions, it is safe to conclude that the simulations which represent the period between April-May, July-August, October-November, and January-February, are the best solution for the limited simulation time. Secondly, the turbine developer could anticipate the low productivity of available power in June and December. Hence, electricity provision could be maintained during this low production period.

However, the most important information of this chapter concerns the resources at each location based on the uniform blockage ratio. This chapter also shows the utility of kinetic power in determining potential locations. Each potential location in this thesis was initially determined … kinetic power flux in the domain of interest. Table 5-30 summarises the estimated tidal resource at each location. If the magnitude of a resource is the only consideration on the viability of tidal energy extraction, some locations will be suitable for large scale turbine deployment. The total resources from five different locations are ~0.5 GW at a low blockage ratio and ~3.1 GW at a higher blockage ratio. However, in order fully to assess viability it is necessary to consider local demand.

Table 5-30: Summary of tidal resources in Indonesian waters

Location	Detail	Total fence lengths	Average depth	Average power removed by turbines	
				B = 0.1 (MW)	B = 0.4 (MW)
Larantuka	the bridge location	~ 0.7 km	20m- 35m	3.56	16.90
	Mutli-arrays scenario	~ 2.4 km	20m- 35m	16.84	32.16
Bali-Lombok Site	Occupying the entire channel				
	All channel	~39.8 km	35m-300m	310.77	2,053.68
	Badung Strait	~13.8 km	35m-250m	39.18	231.56
	Toyopakeh	~0.9 km	75m-100m	4.37	21.79
	Lombok Strait	~25.0 km	35m-300m	292.83	1,834.72
	Partially occupying the channe and multi-arrays				
	Nusa Lembongan	~ 12.7 km	35m- 40m	21.41	89.97
	Toyopakeh	~ 3.1 km	75m-100m	7.24	26.76
	Nusa Penida	~ 14.4 km	40m- 60m	51.14	273.56
	Lombok Island	~ 12.3 km	35m- 40m	39.84	252.07
Sunda Strait	SS1	~10.4 km	35m- 50m	32.30	227.56
	SS2	~7.9 km	35m- 50m	89.75	458.59
Lingga Regency	Dasi Strait	~1.3 km	20m- 35m	0.77	4.30
	Temiang Strait	~3.3 km	20m- 35m	0.5-1.0	
Sula Regency	Capalulu	~2.3 km	30m- 40m	14.43	51.40
	Mangola Strait	~4.2 km	25m- 35m	4.84	20.62
	Lifamatola Strait	~0.9 km	20m- 30m	2.55	11.18
	Lifamatola Headland	~4.0 km	30m-100m	74.63	226.32

Chapter 6. Realistic Turbine Deployment

In reality, turbines array will not take up the entire cross-section of a channel. There are always areas that do not meet the bathymetric constraints for the turbines. This is one reason why a uniform blockage ratio is unrealistic. Furthermore, turbine developers would prefer to have each turbine of a similar size. Therefore, an adjustment to the blockage ratio would be beneficial to assess the opportunity of tidal stream energy resources in such an area.

This chapter addresses resource assessments with a realistic turbine deployment. Limitations, such as bathymetric and environmental constraints, are implemented here. The turbines are also modelled with a more realistic approach. A blockage ratio based on turbine dimensions and the space between the turbines is used for the assessment here. This chapter also addresses the financial and economic viability of each potential site. The assessments here are focused on the selected particular lines of farms in each potential site, as shown in Chapter 5.

6.1 Implementing Realistic Arrays in the Model

The assessments in this section use available commercial turbines as a reference. Following the wind turbine industry, the development of tidal turbines has also focused on horizontal axis, axial flow designs. The turbine developer list from the European Marine Energy Centre (EMEC) shows that tidal turbines are dominated by horizontal axis axial flow turbines (see EMEC 2020). Furthermore, the turbines in serious consideration for deployment in Indonesian waters are also mostly horizontal axis types—for example, the Atlantis turbine (Simecatlantis 2020) and Sabella (Offshore-energy 2015).

Having turbines with the same size in a farm would be advantageous, since this option could reduce the capital cost. Therefore, the bathymetric depth in a potential location should accommodate the turbine diameter. Tidal power exploitation in a strait also requires considering the freeboard above the turbine for water elevation fluctuation due to tidal floods and ebbs. The turbine developers also need to consider the distance below the turbine for sedimentation and other processes.

For example, a 10 m diameter turbine may require at least 10 m + 2 m +5 m depth, where the 2 m is the clearance of the turbines to the seabed, and the 5 m is the clearance for freeboard above the turbine to account for tidal elevation change. Therefore, it is required to have a bathymetric depth that meets with the installation needs. Thus, not the entire channel could be used for tidal resource exploitation.

The blockage ratio calculation here is based on the assumption of a horizontal axis turbine, with geometry defined by the turbine diameter and the space between the turbines. The main constraint regarding the turbine size in the deployment is the water depth. A potential site should have adequate water depth for the turbine to be able to operate efficiently.

6.1.1 Calculating the Blockage Ratio Based On the Number of Installed Turbines

The turbines could be mounted on the sea bed or installed on the floating devices. Figure 6-1 shows an illustration of a turbine array across a channel. The turbine model used in DG-ADCIRC is the Houlsby-Whelan model, in which the power output is calculated based on the blockage ratio and Froude number. The blockage ratio is calculated for each element of the DG-ADCIRC model as the total area of turbines over the area of element cross-section (the area shading in the figures).

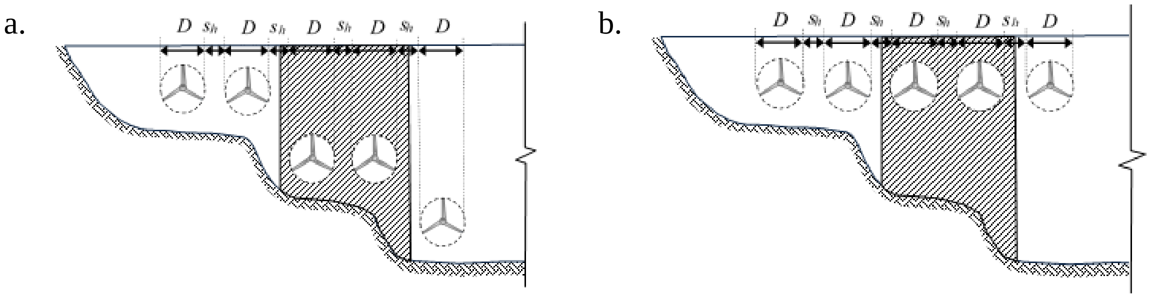

Figure 6-1: Parameters defining blockage ratio. Figure a. is for a turbine mounted on the seabed, while b is for a floating turbine.

This definition can be used to adjust the blockage ratio based on the number of turbines installed in an element. In this realistic scenario, the blockage for each element edge is calculated based on the following equation,

$$B_E = \frac{n_t A_t}{A_E}, \tag{6.1}$$

where B_E is the blockage ratio for the element, A_t is the area of the turbine ($A_t = \frac{\pi D^2}{4}$), n_t is the number of turbines that are installed in the area, and A_E is the cross-sectional area of the element. The number of turbines is calculated by considering the turbine size and the bathymetry.

6.1.2 Introducing Turbine Stacking

In some cases, several turbines could be installed in a water column. Therefore, turbine developers could maximise power production on a farm. Figure 6-2 illustrates a stacking arrangement for turbines. In deeper water more than one turbine could be installed at different levels in the water column.

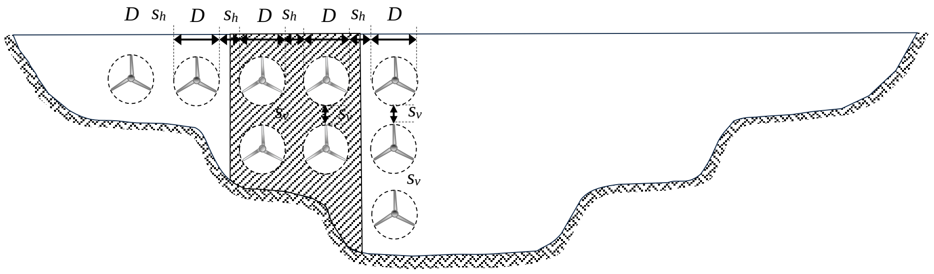

Figure 6-2: Turbine arrangement in stacking

The number in each stack (n_s) is considered for calculating the blockage ratio. Stacking could give higher blockage for a channel, since turbines with smaller diameter could occupy almost the entire cross-section area. The n_s is determined by the turbine diameter and the vertical space between the turbines, as shown in eq. (6.2). It is important to note that the n_s here is the maximum number of turbines in a stack.

$$n_s = \frac{d_E}{D + s_v}, \tag{6.2}$$

where d_E is the depth of the element. A pre-processing algorithm seeks the shallowest depth from two adjacent nodes. Meanwhile, D is turbine diameter, and s_v is the tip-to-tip vertical spacing between turbines.

The number of turbines in a cross-sectional line of an element (t_E) is given by

$$t_E = \frac{l_E}{D + s_h}, \tag{6.3}$$

where l_E is the length of the element with adequate depth for the turbines, and s_h is the tip-to-tip horizontal spacing between turbines (see and Figure 6-2). For simplicity, it is assumed that the space between turbines in a stack is similar to the space between turbines in a cross-sectional line. Therefore, the horizontal tip-to-tip spacing is equal to the vertical tip-to-tip spacing ($s_h = s_v = s$). Then the number of turbines (n_t) is determined by the number of stacks and number of turbines in each stack ($n_t = t_E \times n_s$).

As the DG-ADCIRC model implements the blockage at the nodes, the blockage at each node (B_N) is determined from the average blockage ratio for the adjacent elements $\left(B_N = \frac{B_{E(i)}+B_{E(i+1)}}{2}\right)$. For the nodes at the edge of the mesh, the blockage is that of the adjacent element ($B_N = B_E$).

6.2 Assessment Based On Realistic Turbine Deployment

The realistic assessments in this section are conducted for the selected arrays based on the assessment in Chapter 5. The implementation of turbine size and spacing between turbines is employed with the limitation of bathymetric depth across the arrays. Power capping and thrust capping are also applied in the assessments. Following the discussion in Chapter 2, the power capping for the different tidal types varies following the tidal velocity type.

The five locations selected for analysis represent different socio-economic drivers for the energy demand; they also represent the different tidal types. As discussed in Chapter 5, Larantuka has a semidiurnal pattern of velocity, while Sunda strait is diurnal type. The other three locations, Lingga, Sula and Bali-Lombok, are in the mixed diurnal areas. Since the simulation in DG-ADCIRC is computationally demanding, the power or thrust capping is applied only to the selected arrays in each location based on the average power in Chapter 5.

The aim is to demonstrate the application of a realistic array in an assessment, including the implementation of capping strategies in the three different tidal velocity patterns (diurnal, semidiurnal and mixed-diurnal). As the Larantuka and Sunda straits are the only locations that represent semidiurnal and diurnal, in these locations, both power capping and thrust capping are applied. Only power capping is applied in the Bali-Lombok sites and Lingga regency sites. Thrust capping is applied at the Sula regency's site.

The utility of a capping metric, as discussed in Chapter 2, is demonstrated here. The metrics of power factor (F_P), thrust factor (F_T) and maximum thrust factor ($F_{T,max}$) are implemented in the analysis of capping strategies. The fraction of power capping limit with average power $\left(\frac{\hat{P}}{P_1}\right)$for power capping and the fraction of thrust capping limit with the average thrust $\left(\frac{\hat{T}}{T_1}\right)$ for thrust capping are also used here. The maximum power factor $\left(F_{P,max}\right)$, the fraction of maximum power of the turbine after the capping over maximum power before the capping, is also considered. The $F_{P,max}$ is applied to check how the maximum power is reduced.

6.2.1 Larantuka Tidal Bridge

As mentioned in Chapters 1 and 5, this location is a candidate site for tidal energy in Indonesia. The realistic assessment here is focused on turbine selection, which is based on the turbine diameter (D), space between the turbine (s) and the number of turbines in a stack (n_s). Some of the results here also presented by Firdaus *et al.* 2020. The realistic turbine deployment in that paper is limited to one turbine selection (D = 10 m, s = 10 m, and n_s = 1). Alternatives are considered later in Section 6.2.1.

a) Realistic Array Interaction in Larantuka Site

Although the assessment at this site follows the previous array schemes (see Chapter 5), the array alignments in the realistic cases are slightly different from the previous simulations (see Figure 6-3). As seen in the figure, the fence does not occupy the channel's entire cross-section for all arrays. The turbine model is employed only in regions with adequate depth for turbines with D = 10 m, s = 10 m, n_s = 1.

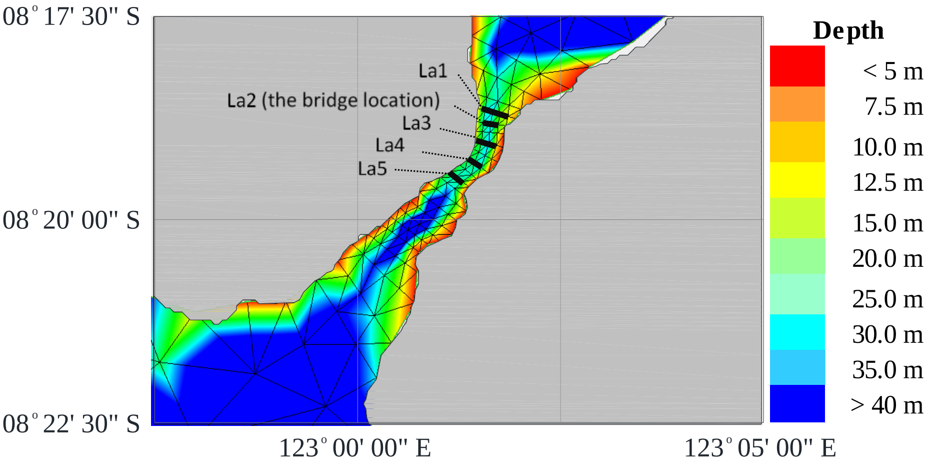

Figure 6-3: Mesh for DG-ADCIRC model of realistic arrays for turbine D = 10 m, s = 10 m, n_s = 1

As for the uniform blockage simulations, the realistic case is also run with three different α_4 values and the optimum α_4 obtained that maximises average power production. The results are shown in Table 6-1. Similar to the simulation with the uniform flow, the simulations for realistic deployment also show that the current position of the tidal bridge is not the most advantageous for power production. As an individual array, the bridge could deliver more power if it was installed at the southward location La3 nearby. This higher power is because the number of turbines that can be realistically installed in this array is higher than at the proposed bridge position.

Based on these results, the realistic case gives a slightly higher average power output than the uniform blockage ratio (low blockage scenario). For instance, the average power at La1 at B=0.1 is 3.56 MW (see Table 5-1 in Chapter 5), while using turbines with D=10, s=10 m gives an average power of 5.1 MW. The average power in the area of the tidal bridge (La2) in the uniform blockage B = 0.1 is only 4.67 MW, whereas in the realistic scenario the average power is 5.0 MW (higher by approximately 7%). Almost all arrays show higher power compared to the uniform blockage scenario at low blockage ratio ($B = 0.1$). Only La5 has an average power that is 25% lower than the uniform blockage of $B = 0.1$. These results can be explained by investigating the local blockage and global blockage in this site.

Table 6-1: Average Energy Extraction for Realistic Arrays with $D = 10$ m and $s = 10$ m

	La1	La2	La3	La4	La5		
Fence Length (m)	702	665	665	508	664		
Cross Section (m^2)	16,480	13,900	13,708	12,337	16,117		
Realistic Fence Length (m)	523	336	491	349	411		
Realistic Cross Section (m^2)	12,915	9,115	12,114	9,640	11,670		
Num. of Turbines (units)	25	16	23	17	19		
Total Turbine Area (m^2)	1,963	1,256	1,806	1,335	1,492		
Local Blockage (B_L)	0.15	0.14	0.15	0.14	0.13		
Global Blockage (B_G)	0.12	0.09	0.13	0.11	0.09		
Power	La1 (MW)	La2 (MW)	La3 (MW)	La4 (MW)	La5 (MW)	Total (MW)	α_4
La1-La2-La3-La4-La5	3.53	3.18	5.67	4.47	1.91	18.77	0.48
La1-La2-La3-La4	3.72	3.35	5.98	4.73	-	17.77	0.48
La1-La2	4.57	4.40	-	-	-	8.97	0.41
La2-La3	-	4.05	6.95	-	-	11.00	0.42
La2-La4	-	4.34	-	5.65	-	9.98	0.40
La2-La5	-	4.78	-	-	2.73	7.51	0.39
La1	5.10	-	-	-	-	5.10	0.39
La2	-	5.00	-	-	-	5.00	0.37
La3	-	-	7.11	-	-	7.11	0.40
La4	-	-	-	5.74	-	5.74	0.38
La5	-	-	-	-	2.84	2.84	0.36

b) Local Blockage Effects

The increased average power for the realistic case compared to uniform $B = 0.1$ can be explained using two approaches. The first is by comparing local blockage and global blockage. As shown in Table 6-1, at the proposed bridge location (La2), the global blockage is 0.09, less than the blockage at uniform blockage scenario ($B = 0.1$). However, the local blockage of 0.14 is slightly higher than the uniform blockage ratio.

The global-blockage (B_G) is the ratio of the total swept area of the turbines to the entire area of channel cross-section, while "local blockage" (B_L) is the fraction of the cross-sectional area of just the elements that are occupied by turbines. These correspond to the definitions also used by Nishino & Willden, 2013. For any given array, the local blockage is slightly higher than the global blockage as the array does not extend to the full width of the channel.

Nishino & Willden, 2013 showed that within the range of blockages considered here, for constant B_G ratio, the limit of power extraction increased as B_L ratio increases. Although the study employed actuator discs, the flow modelling used steady-state 3D Reynolds-Averaged Navier-Stokes (RANS) equations. Therefore, there are differences between Nishino & Willden's model and the present Larantuka model because Nishino & Willden's model does not account for the inertia of the flow.

However, their conclusion is also applicable for resource assessment with a 2D actuator disc model. Thus, the increase in power output can be explained. Note though that not all results show this increasing trend. The La5 array produces an average power output that is significantly lower than the B=0.1 case.

This result also shows that although B_L is important, B_G also plays an essential role in power production. Consider La3 for example: although this fence has slightly higher local blockage than La2 and La4, the average power in the realistic scenario in La3 is 43% higher than uniform blockage (B=0.1). Meanwhile, for La2 and La4 in the realistic scenario, the average power is only 7% and 6% higher than that for the uniform flow blockage scenario with B=0.1.

Bonar *et al.*, 2019 argue that relaxing the ideal and steady state flow assumptions reveals a more complicated problem involving continuous mixing between the core and bypass flows, and demonstrates the need for a new theoretical framework to provide a more accurate description of tidal turbine performance. However, they also point out that in the problem of partial-width arrays in channels, it is not immediately clear whether, or how, the effects of array-scale flow diversion could be incorporated within the DG-ADCIRC framework.

Secondly, the 2D DG-ADCIRC and Houlsby-Whelan model will not model in detail the flow passing the edge of the turbine fence. As the turbine arrays, in this case, are partial arrays, the flow field involves an important bypass flow. Figure 6-4 shows the flow field change in the region due to turbine installation at the proposed bridge position. Similar to the previous analysis in Chapter 5, the diverted flows in the neighbouring straits (Boleng and Alor) change, but the flow in the area of the turbine array also changes significantly.

The flow field changes at the proposed bridge site can be seen in Figure 6-5. The flow field in the elements without turbines increases while in the elements with turbines, the flow decreases. The flow in the bypass area is slightly increased when the turbine array is introduced.

c) *Expansion of Turbine Selection*

This expansion further explores the global blockage (B_G) and local blockage (B_L) effect in the Larantuka strait. Two different turbine dimensions are added in the simulation here. Turbines with the diameter (D) = 14 m (D14) and 4 m (D4) are investigated in this section. The tip-to-tip spacing (s) of turbines is also varied. Two options of tip-to-tip spacing, of one diameter and a half diameter, are used in this section. Since the D4 turbine could be stacked, this turbine is installed with a maximum stacking of $n_s = 3$. The nomenclature for the turbine schemes here is arranged by the D, s and n_s. For example, the D14s7$\mathrm{n_s}$1 is the scheme with D =14 m, s = 7 m and n_s = 1, while D4s2$\mathrm{n_s}$3 is for D = 4 m, s = 2 m and n_s = 3.

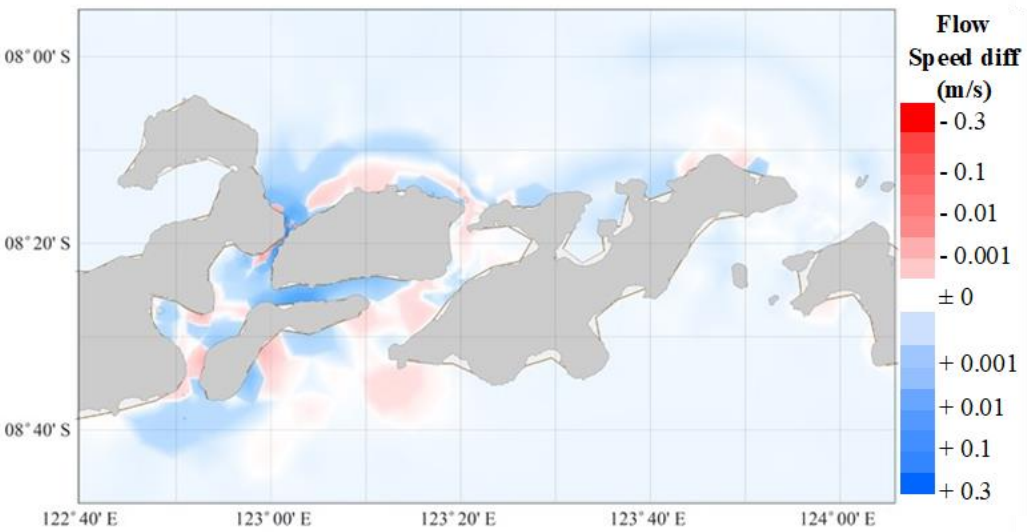

Figure 6-4: Flow field around the channel for realistic arrays of turbines with D = 10m and s = 10m. The array is installed at La2 (the proposed position for the tidal bridge)

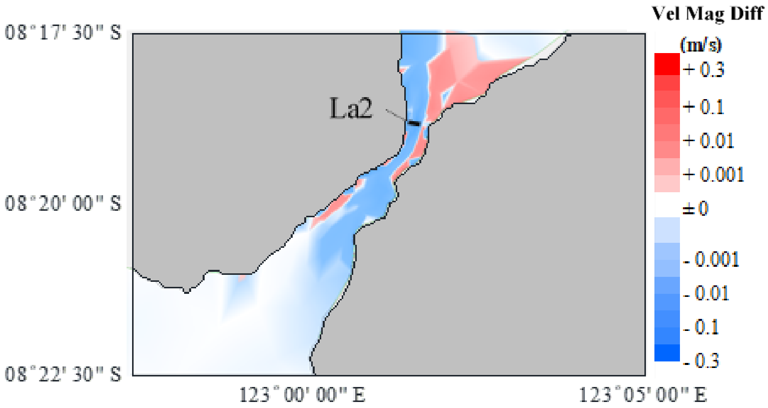

Figure 6-5: Flow field around the bridge location in Larantuka Strait for the realistic array with turbine D = 10 m and s = 10 m

The simulation results with these additional turbines are presented in Table 6-2. The results shown in this table are only for the individual array. The turbine selection of D14 and D4 (with the maximum stacking) gives a unique characteristic in term of B_G and B_L. The turbine with D4 consistently provides the $B_G = B_L$ while the D = 14 m has B_L significantly higher than B_G. The D4 turbine schemes could occupy the entire channel, while the D14 scheme only occupies a partial cross-section of the channel (see Figure 6-6). The fence length (F_L) and the cross-sectional area of the channel (*Ac*) that is occupied by the turbine schemes are equal to the F_L and *Ac* of the channel (presented in the grey shading in Table 6-2).

Table 6-2: Power and thrust from the realistic deployment in the Larantuka Strait

Turbine Scheme	F_L (m)	Ac (m^2)	n_t (units)	A_t (m^2)	B_L	B_G	$\overline{P_1}$ (MW)	$P_{1,max}$ (MW)	$\frac{\overline{P_1}}{nt}$ (MW)	$\frac{P_{1,max}}{nt}$ (MW)	$\overline{T_1}$ (MN)	$T_{1,max}$ (MN)	$\frac{\overline{T_1}}{nt}$ (MN)	$\frac{T_{1,max}}{nt}$ (MN)	CF	α_4
A1	703	16,480														
D14s14ns1	339	9,429	12	1,847	0.20	0.11	5.71	26.24	0.48	2.19	2.44	9.91	0.20	0.83	0.22	0.39
D14s7ns1			16	2,463	0.26	0.15	8.11	36.87	0.51	2.30	3.80	15.37	0.24	0.96	0.22	0.42
D4s4ns3	703	16,480	150	1,885	0.11	0.11	4.19	19.69	0.03	0.13	1.65	6.87	0.01	0.05	0.21	0.37
D4s2ns3			286	3,594	0.22	0.22	8.68	39.68	0.03	0.14	4.03	16.44	0.01	0.06	0.22	0.41
A2	666	13,901														
D14s14n_s1	164	4,874	5	770	0.16	0.06	2.81	15.16	0.56	3.03	1.02	4.65	0.20	0.93	0.19	0.36
D14s7n_s1			7	1,078	0.22	0.08	4.28	22.65	0.61	3.24	1.69	7.67	0.24	1.10	0.19	0.38
D4s4n_s3	666	13,901	142	1,784	0.13	0.13	6.39	33.21	0.04	0.23	2.28	9.57	0.02	0.07	0.19	0.40
D4s2n_s3			245	3,079	0.22	0.22	10.80	52.97	0.04	0.22	4.46	18.44	0.02	0.08	0.20	0.44
A3	665	13,709														
D14s14n_s1	174	5,093	6	924	0.18	0.07	4.76	25.12	0.79	4.19	1.63	7.29	0.27	1.22	0.19	0.36
D14s7n_s1			8	1,232	0.24	0.09	6.77	34.80	0.85	4.35	2.50	11.08	0.31	1.39	0.19	0.42
D4s4n_s3	665	13,709	162	2,036	0.15	0.15	3.12	39.48	0.02	0.24	2.54	10.90	0.02	0.07	0.08	0.40
D4s2n_s3			268	3,368	0.25	0.25	5.26	62.62	0.02	0.23	5.03	20.06	0.02	0.07	0.08	0.46
A4	508	12,338														
D14s14n_s1	349	9,641	11	1,693	0.18	0.14	7.55	42.08	0.69	3.83	2.62	11.85	0.24	1.08	0.18	0.40
D14s7n_s1			15	2,309	0.24	0.19	10.32	56.24	0.69	3.75	3.90	17.19	0.26	1.15	0.18	0.44
D4s4n_s3	508	12,338	128	1,608	0.13	0.13	6.67	36.38	0.05	0.28	2.18	9.66	0.02	0.08	0.18	0.39
D4s2n_s3			223	2,802	0.23	0.23	11.80	57.76	0.05	0.26	4.73	18.00	0.02	0.08	0.20	0.45
A5	664	16,117														
D14s14n_s1	411	11,671	13	2,001	0.17	0.12	4.05	24.33	0.31	1.87	1.72	8.20	0.13	0.63	0.17	0.38
D14s7n_s1			19	2,925	0.25	0.18	6.21	36.35	0.33	1.91	2.93	13.68	0.15	0.72	0.17	0.41
D4s4n_s3	664	16,117	158	1,985	0.12	0.12	2.91	25.15	0.02	0.16	1.65	7.65	0.01	0.05	0.12	0.37
D4s2n_s3			285	3,581	0.22	0.22	5.73	44.51	0.02	0.16	4.18	16.85	0.01	0.06	0.13	0.45

As shown in the results, the turbine schemes with the smaller tip-to-tip spacing, in general, give better average power removed by the turbines ($\overline{P_1}$) than for larger spacing. For instance, the turbine with *D* = 14 m gives $\overline{P_1}$ of 8.11MW if they are installed with s = 7 m at La1 array, while installed with s = 8 m, they only produce 5.72 MW at the same array. The small spacing schemes also give better performance than the larger ones in terms of average power per turbine $\left(\frac{\overline{P_1}}{nt}\right)$. Sixteen turbines installed in NLC1 with 7 m tip-to-tip spacing produce an average of 0.51 MW per turbine while twelve turbines in 14 m spacing schemes only produce an average of 0.48 MW per turbine. This analysis also shows different turbine schemes perform better in different arrays. The D14s7n$_s$1 scheme gives the best total average power in La1, La4 and La5. Meanwhile, D10s10n$_s$1 gives the best average power in La2 and La3.

These results show the correlation between B_L and the power removed by turbines is more complex than originally expected. Although B_L has a significant impact on some cases, the B_G value still affects $\overline{P_1}$. For instance, the $\overline{P_1}$ from the *D* = 10 m (D10) scheme in La2 (see Table 6-1) is slightly higher than both of the D14 schemes (D14s7n$_s$1 and D14s14n$_s$1), even though the D14 schemes have higher B_L than the D10. The D10 scheme gives an average power of 5.00 MW or 3.98 kW per unit turbine area for La2, set against the D14 schemes (D14s14n$_s$1 and D14s7n$_s$1) which only have an average power of 2.81 MW (3.65 kW/m^2) and 4.28 MW (3.97 kW/m^2) respectively at the same location.

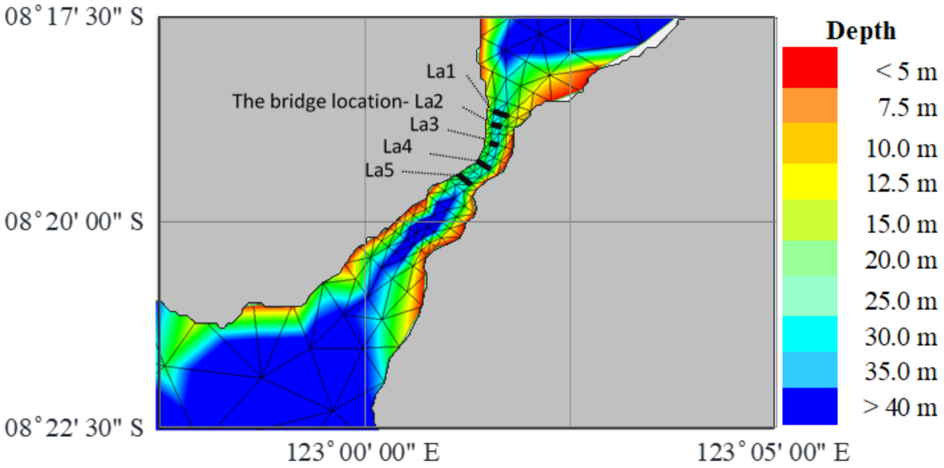

Figure 6-6: The D14 fences in DG-ADCIRC mesh

In terms of local blockage, the D14s14n$_s$1 and D14s7n$_s$1 schemes have B_L = 0.16 and 0.22 respectively, while the D10 scheme has lower local blockage B_L = 0.15. These figures suggest that the D10 scheme still has higher average power per square meter of turbine area, although this scheme has lower B_L than both D14 schemes. This can be explained by considering global blockage. As shown in Table 6-2, the B_G of D10 is slightly higher than both the D14 schemes. The D10 scheme has B_G = 0.09, while the D14s14n$_s$1 and D14s7n$_s$1 schemes only have B_G = 0.06 and 0.08 respectively.

However, these global blockage and local blockage effects are not the major factor in explaining the results in the D = 4 m (D4) schemes. These D4 schemes have relatively high B_L and B_G in certain arrays. Nevertheless, both of D4 schemes (D4s4n$_s$3 and D4s2n$_s$3), in general, give lower average power than both of the D14 and the D10 schemes. For instance, compare the D14s7n$_s$1 and D4s2n$_s$3 schemes in the La2 array. The D14s7n$_s$1 has higher average power than D4s2n$_s$3, even though the D4s2n$_s$3 scheme has slightly higher B_G than the D14s7n$_s$1 and both schemes have the same B_L. Nonetheless, the D14s7n$_s$1 has an average of 3.97 kW/m^2 turbine area, while D4s2n$_s$3 only produces 1.27 kW/m^2 turbine area.

This result suggests that occupying the entire channel might not be advantageous. The turbine schemes with D = 4 m (D4 schemes) that occupy the whole cross-section of the channel cannot deliver the highest average power, although these schemes have high B_L and B_G. The flow field change in the area shows that D4s2ns3 exhibits higher negative differences (decreasing velocity) in general than D14s7ns1 (see Figure 6-7).

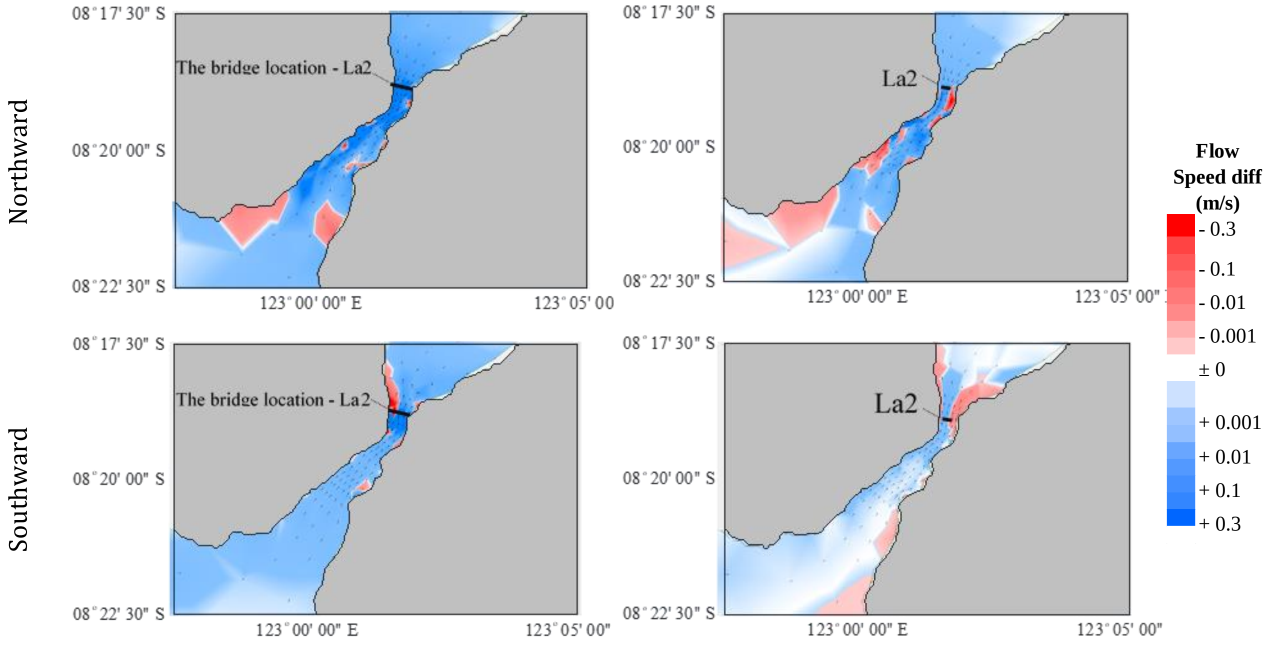

D4s2ns3 scheme D14s7ns1 scheme

Figure 6-7: The flow-field change at maximum power production for turbine scheme with D = 14 m and D = 4 m in southward and northward directions

Given that D14s7ns1 only occupies the middle part of the channel, the flow field changes in either side of the fence display positive changes in maximum power production for the southward and northward flow directions. The average flow-field changes in the area also show a similar trend for both schemes (see Figure 6-8).

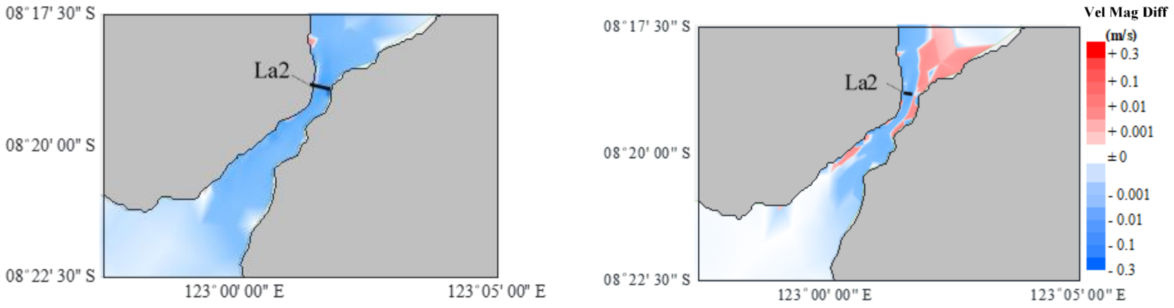

a. D4s2n$_s$3 scheme b. D14s7n$_s$1 scheme

Figure 6-8: The comparison of average flow-field change for turbine scheme with D = 14 m and D = 4 m.

The results in Table 6-2 also show the maximum power removed by the turbine ($P_{1,max}$). This $P_{1,max}$ corresponds to the required turbine capacity. In order to obtain the $\overline{P}_1$with the same magnitude as discussed previously, the generator for each turbine should be installed with a capacity that could capture the $P_{1,max}$. However, as discussed in Chapter 2, turbine developers aim for a capacity factor (*CF*) in the range of 0.25-0.45 if the turbines are to be cost-effective. The *CF* in this analysis is obtained from a fraction of P_1 and $P_{1,max}$. Based on *CF*, this result also suggests that larger turbines give a better relative *CF*.

d) Implementation of Power Capping Strategy

As this location represents the semidiurnal tidal type, both thrust and power capping strategies are implemented here. The capping strategy simulations are only conducted for the three different arrays (La1, La2 and La4) to save the computational time in the ARC system. Four turbine schemes, D14s14n$_s$1, D14s7n$_s$1, D4s4n$_s$3 and D4s2n$_s$3, are applied in each array. An example power and thrust variation of a power capping strategy at La2 (the bridge location) is presented in Figure 6-9. The thrust variation is also reduced while power variation is truncated in the capping limit due to the α_4 tuning. Similar simulations are also done for other turbine schemes and arrays. The details of power and thrust variation are presented in Figure 6-10. Hereinafter, the power and thrust variation for other capping strategies are presented only for the last neap-spring cycle.

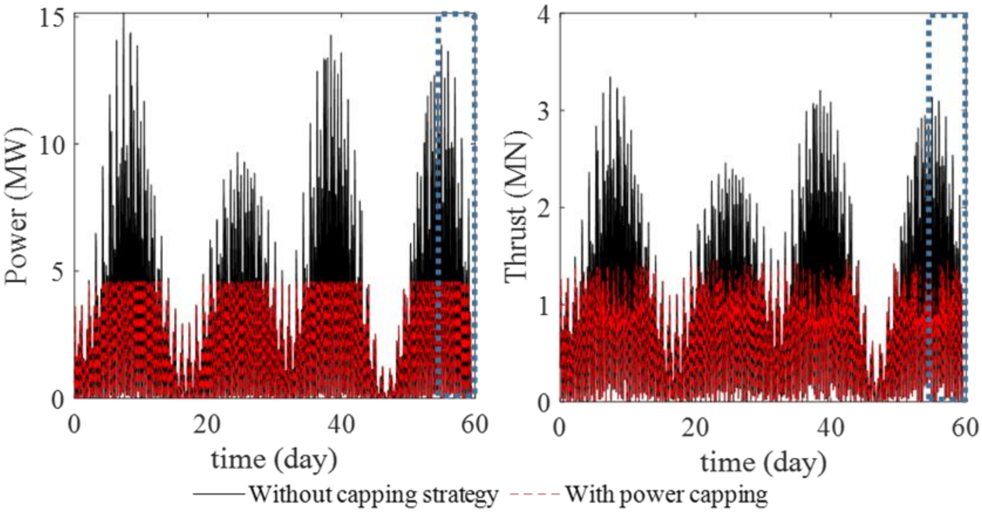

Figure 6-9: The comparison of power and thrust variation with and without power capping for the simulation of D14s7n$_s$1 in La2 with α_4 =0.4

A summary of simulations for power capping strategies of all arrays and turbine schemes is presented in Table 6-3. The power capping limits that are set in $\frac{\hat{P}}{\overline{P}_1}$ vary from 1.25~4. These capping limits increase Capacity Factors that were previously in a range of 0.18 to 0.22 in the selected arrays to 0.24 to 0.50. For instance, the D14s7n$_s$1 turbine scheme at bridge location (La2) only has a *CF* of 0.19 without the capping strategy. The *CF* increases to 0.5 with the power capping strategy. However, this strategy has consequences for the total average power removed by the turbine ($\overline{P_1}$) which has decreased to 2.70 MW, while without the capping strategy the $\overline{P_1}$ is 4.28 MW. This means the power factor (F_P) here is relatively low (only 0.63, which means the average power decreased by 37%).

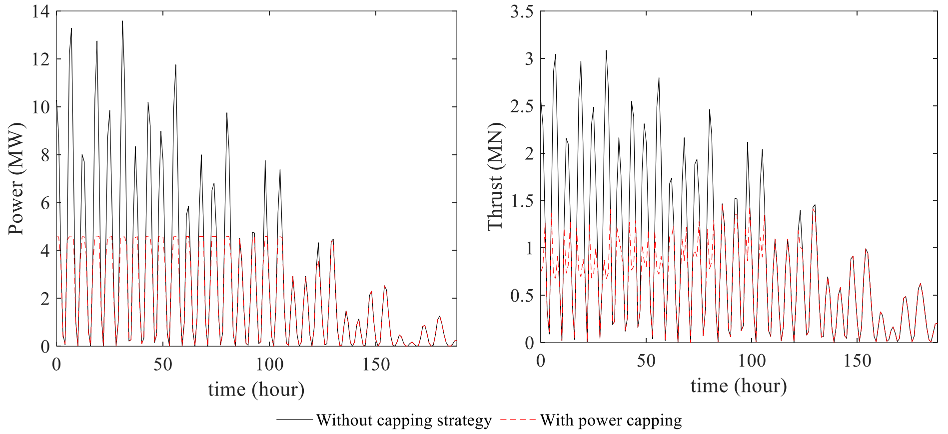

Figure 6-10: The comparison of power and thrust variation with and without power capping from the last neap-spring cycles (the blue dotted line boxes from Figure 6-9) for the simulation of D14s7n$_s$1 in La2 with α_4 =0.4

Table 6-3: Summary of simulations with the power capping strategy at Larantuka

Turbine Scheme	$\overline{P_1}$ (MW)	$P_{1,max}$ (MW)	$\frac{\overline{P_1}}{nt}$ (MW)	$\frac{P_{1,max}}{nt}$ (MW)	$\overline{T_1}$ (MN)	$T_{1,max}$ (MN)	$\frac{\overline{T_1}}{nt}$ (MN)	$\frac{T_{1,max}}{nt}$ (MN)	$\frac{\widehat{P_1}}{\overline{\overline{P_1}}}$	F_p	$F_{p,max}$	F_T	$F_{T,max}$	$\frac{\overline{P_1}}{A_t}$ (kW/m^2)	*CF*	α_4 (opt)
La1																
D14s14n$_s$1	4.79	11.51	0.40	0.96	1.86	3.64	0.15	0.30	2.02	0.84	0.44	0.76	0.37	0.22	0.42	0.38
D14s7n$_s$1	6.05	12.79	0.38	0.80	2.45	4.50	0.15	0.28	1.58	0.75	0.35	0.65	0.29	0.15	0.47	0.41
D4s4n$_s$3	4.35	17.34	0.03	0.12	1.23	3.99	0.01	0.03	4.14	1.04	0.88	0.74	0.58	0.02	0.25	0.37
D4s2n$_s$3	8.51	33.08	0.03	0.12	3.92	9.15	0.01	0.03	3.81	0.98	0.83	0.97	0.56	0.01	0.26	0.41
La2																
D14s14n$_s$1	2.07	4.58	0.41	0.92	0.69	1.57	0.14	0.31	1.63	0.74	0.30	0.67	0.34	0.54	0.45	0.36
D14s7n$_s$1	2.70	5.35	0.39	0.76	0.94	2.08	0.13	0.30	1.25	0.63	0.24	0.55	0.27	0.36	0.50	0.38
D4s4n$_s$3	6.31	25.87	0.04	0.18	2.21	5.75	0.02	0.04	4.05	0.99	0.78	0.97	0.60	0.02	0.24	0.39
D4s2n$_s$3	10.19	17.84	0.04	0.07	2.90	8.09	0.01	0.03	1.65	0.94	0.34	0.65	0.60	0.01	0.57	0.56
La4																
D14s14n$_s$1	4.98	9.93	0.45	0.90	1.56	2.98	0.14	0.27	1.32	0.66	0.24	0.60	0.25	0.27	0.50	0.39
D14s7n$_s$1	6.09	11.15	0.41	0.74	2.02	3.71	0.13	0.25	1.08	0.59	0.20	0.52	0.22	0.18	0.55	0.41
D4s4n$_s$3	6.37	22.51	0.05	0.18	2.04	4.80	0.02	0.04	3.38	0.96	0.62	0.94	0.50	0.03	0.28	0.38
D4s2n$_s$3	11.63	39.29	0.05	0.18	4.55	11.68	0.02	0.05	3.33	0.99	0.68	0.96	0.65	0.02	0.30	0.37

The power capping strategy that is applied in La2 for the D14s7n$_s$1 turbine scheme decreases the maximum thrust from 7.67 MN to 2.08 MN or the $F_{T,max}$=0.27 and the average thrust also decreases from 1.69 MN to 0.94 MN, or F_T=0.55. The power capping strategy also means a reduction of generator capacity. The generator capacity is determined by maximum power per turbine ($\frac{P_{1,max}}{nt}$). For example, the capping limit for the D14s7n$_s$1 turbine scheme in La2 array gives a generator capacity of 0.76 MW per turbine, while without power capping the turbine developer has to provide turbines with generator capacity of 3.24 MW.

It is interesting to observe the power capping implementation of the D4s4ns3 scheme for the La1 array. The power capping strategy for this scheme gives F_P = 1.04, which means the $\overline{P_1}$ for the power capping is slightly higher than the $\overline{P_1}$ without any capping. This strategy gives $F_{P,max}$=0.88, which means the power variation is reduced by 12% from the maximum. Meanwhile, the capping strategy for this turbine scheme gives F_T = 0.74 and $F_{T,max}$ = 0.58. This means the capping strategy reduces the average thrust by 26% and the maximum thrust by 42%.

The power and thrust variation of the D4s4ns3 scheme in the La1 array is presented in Figure 6-11. We can see the peak of power variation in the capping strategy is only slightly lower than the peak with no capping (see Figure 6-11a). Meanwhile, the peak of thrust variation with power capping is significantly lower than the thrust without power capping (see Figure 6-11a). However, the power variation pattern in the power capping scenario is seemingly not as expected, with the truncation at a particular level. The power and thrust variations in the power capping strategy show different peaks in each daily variation.

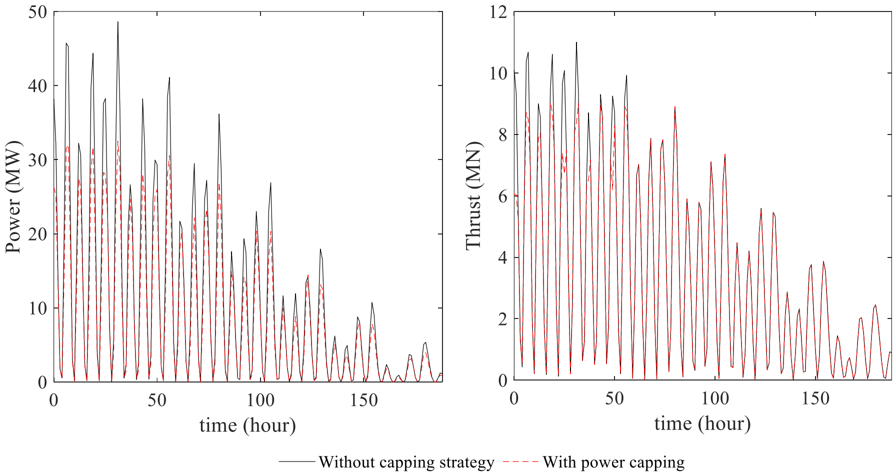

Figure 6-11: The comparison of power and thrust variation with and without power capping from two last neap-spring cycles for the simulation of D4s4ns1 in La1 with α_4 =0.4.

To clarify this issue, we need to look in detail at power and thrust variations within the elements in the model. There are four elements for the D4s4ns3 scheme in the La1 array, as shown in Figure 6-12. The average kinetic power is similar to the average kinetic power presented in Chapter 5 (Figure 5-2). This figure shows the flow across the channel is varied. The flow at the side of the channel is less energetic than the flow in the middle. Therefore, power production along the array is also varied. The detailed power and thrust variations are compared between el.1 (the area with the less energetic flow) and el.2 (the segment with a more energetic flow) in Figure 6-13.

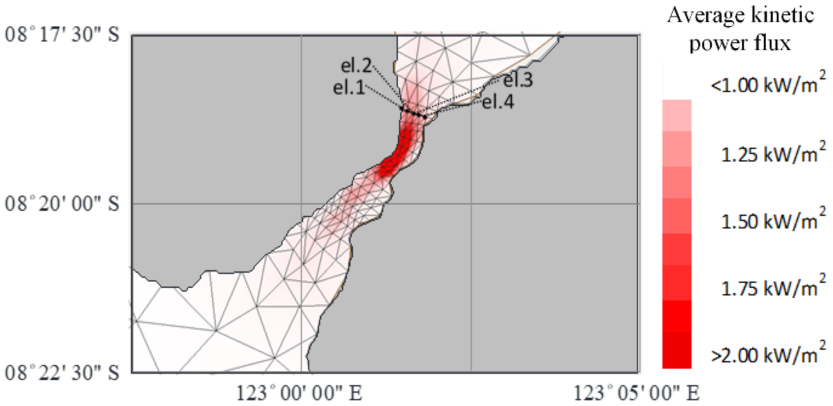

Figure 6-12: Elements at La1 array and local distribution of average kinetic power flux

It is shown that the power capping only occurs in the energetic part of the channel. In this case, we see the power variation is only truncated in the el.2 (see Figure 6-13a), while in el.1 the power variation with power capping is similar to the power variation from the simulation without capping (see Figure 6-13c). The variation in thrust is similar to the variation in power. The simulation's thrust variation with power capping implemented in el.1 is the same as the thrust variation with no power capping (see Figure 6-13b). While for el.2, the thrust variation in the capping scheme follows the thrust variation trend that is expected for a power capping strategy (see Figure 6-13d).

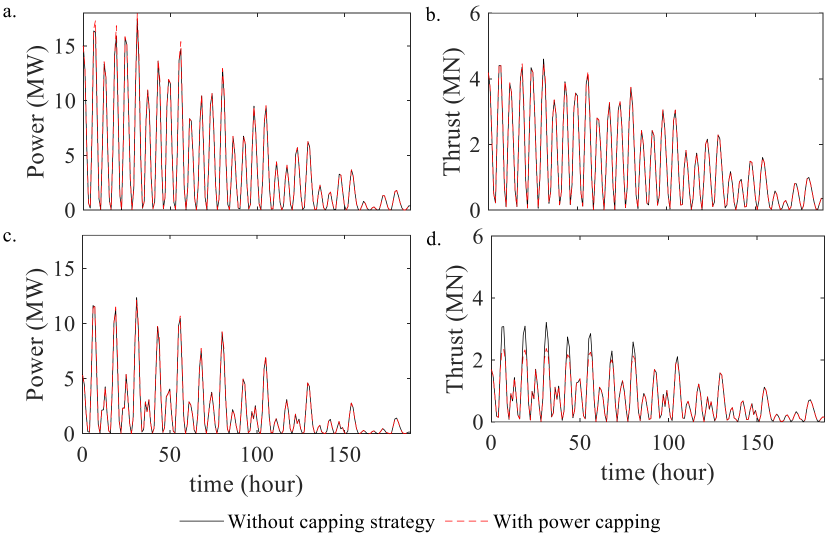

Figure 6-13: The detailed comparison of power and thrust variation in el.1 (a. for power variation and b. for thrust variation) and el.2 (c. for power variation and d. for thrust variation) from Figure 6-11.

e) *Thrust Capping Strategy*

The implementation of thrust capping in this location represents analysis for a semidiurnal tidal location. However, thrust capping could be a sensible option, because the turbines are intended to be installed in the bridge structure. The thrust reduction means that the load applied to the bridge structure is also decreased. Therefore, the bridge's CAPEX could be lowered with this strategy.

A similar example from the D14s14n_s1 scheme for thrust capping is presented in Figure 6-14. The pattern exhibited in this example shows that the thrust is truncated at 1 MN, or approximately 25% ($F_{T,max}$ = 0.25) of the maximum thrust without thrust capping. As a result, the maximum power is reduced to 55% ($F_{P,max}$ = 0.55) of the maximum power without capping.

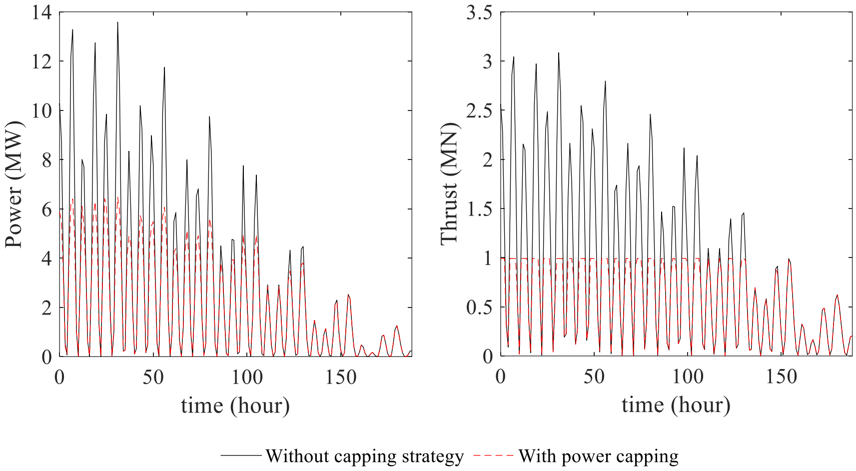

Figure 6-14: The comparison of power and thrust variation with and without thrust capping from two last neap-spring cycles for the simulation of D14s14ns1 in La1 with α_4 =0.4.

However, thrust capping on the D14s14n_s1 scheme only reduces the average power by approximately 19% (F_P = 0.81). Another advantage of this strategy is that the average thrust ($\overline{T}_1$) decreases by 36% (F_T = 0.64). The Capacity Factor also slightly increases to 0.31 from 0.19 in the simulation without capping (see Table 6-2).

The summary of simulations from the thrust capping strategy is shown in Table 6-4, which indicates that setting the thrust limit at $\frac{\hat{T}}{\overline{T}_1}$ ~1 gives F_P in the range of 0.77~0.8. However, the capacity factor is only approximately 0.3, which is relatively lower than the *CF* from the power capping strategy. Meanwhile, limiting the thrust at $\frac{\hat{T}}{\overline{T}_1}$ ~2 could give a relatively higher F_P. As shown in the table, the F_P for the D4s4n_s3 and D4s2ns3 schemes with thrust capping limits at $\frac{\hat{T}}{\overline{T}_1}$ ~1.5 is in the range 0.9~1.0. However, the *CF* for these schemes is relatively low.

For instance, the D4s2ns3 scheme in the La2 array shows F_P and $F_{P,max}$ are both 1.01, which means that this thrust capping strategy gives slightly higher power when the capping strategy is implemented. The power and thrust variations at the optimum wake coefficient (α_4-*opt*) of 0.4 confirm that the power variation with thrust capping is slightly higher than the power variation without capping (see Figure 6-15a). However, the thrust variation in the thrust capping case is relatively lower than the thrust from the simulation without capping (see Figure 6-15b).

Table 6-4: Summary of simulations with the thrust capping strategy at Larantuka

Turbine Scheme	$\overline{P_1}$ (MW)	$P_{1,max}$ (MW)	$\frac{\overline{P_1}}{nt}$ (MW)	$\frac{P_{1,max}}{nt}$ (MW)	$\overline{T_1}$ (MN)	$T_{1,max}$ (MN)	$\frac{\overline{T_1}}{nt}$ (MN)	$\frac{T_{1,max}}{nt}$ (MN)	$\frac{\hat{T}_1}{\overline{T_1}}$	F_p	$F_{p,max}$	F_T	$F_{T,max}$	$\frac{\overline{P_1}}{A_t}$ (kW/m^2)	CF	α_4
La1																
D14s14ns1	4.63	14.32	0.39	1.19	1.60	2.49	0.13	0.21	1.02	0.81	0.55	0.66	0.25	0.21	0.32	0.37
D14s7ns1	6.80	21.50	0.42	1.34	2.48	3.84	0.15	0.24	1.01	0.84	0.58	0.65	0.25	0.17	0.32	0.39
D4s4ns3	3.97	16.05	0.03	0.11	1.47	3.34	0.01	0.02	2.02	0.95	0.82	0.89	0.49	0.01	0.25	0.36
D4s2ns3	8.06	29.56	0.03	0.10	3.25	6.20	0.01	0.02	1.54	0.93	0.74	0.81	0.38	0.01	0.27	0.39
La2																
D14s14n_s1	2.11	6.75	0.42	1.35	0.64	0.99	0.13	0.20	0.97	0.75	0.45	0.62	0.21	0.55	0.31	0.36
D14s7n_s1	3.30	10.74	0.47	1.53	1.04	1.60	0.15	0.23	0.95	0.77	0.47	0.61	0.21	0.44	0.31	0.37
D4s4n_s3	6.36	29.95	0.04	0.21	1.99	5.29	0.01	0.04	2.32	0.99	0.90	0.87	0.55	0.03	0.21	0.40
D4s2n_s3	10.87	53.64	0.04	0.22	3.92	11.33	0.02	0.05	2.54	1.01	1.01	0.88	0.84	0.01	0.20	0.40
La4																
D14s14n_s1	5.34	16.60	0.49	1.51	1.48	2.15	0.13	0.20	0.82	0.71	0.39	0.56	0.18	0.29	0.32	0.38
D14s7n_s1	7.82	25.19	0.52	1.68	2.28	3.34	0.15	0.22	0.86	0.76	0.45	0.59	0.19	0.23	0.31	0.40
D4s4n_s3	6.14	23.04	0.05	0.18	1.77	3.23	0.01	0.03	1.48	0.92	0.63	0.81	0.33	0.03	0.27	0.37
D4s2n_s3	11.34	30.08	0.05	0.13	3.17	10.11	0.01	0.05	2.14	0.96	0.52	0.67	0.56	0.02	0.38	0.56

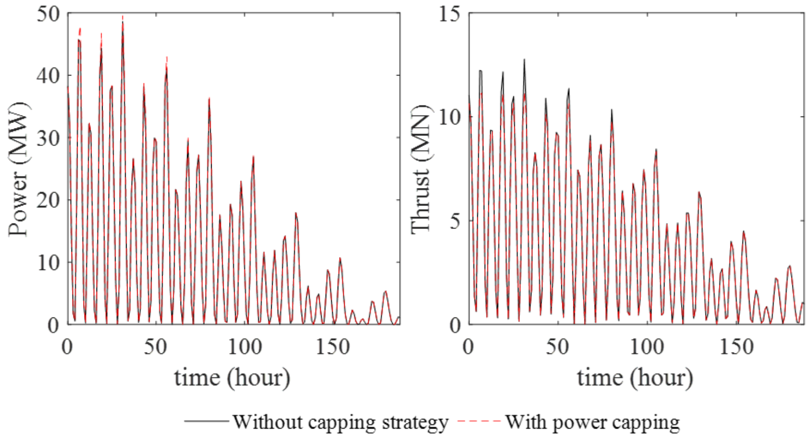

Figure 6-15: The comparison of power and thrust variation with and without thrust capping from two last neap-spring cycles of the D4s2n_s3 scheme in La2 with α_4 =0.4.

These results are similar to the pattern that has been shown in the 0-D analysis in Chapter 2. These examples of power and thrust capping strategy demonstrate how these metrics could determine which approach is most advantageous. The decreases in thrust and generator capacity imply a reduction of capital expenditure for turbine deployment. Simultaneously, the average power production is also reduced.

6.2.2 The Nautilus Project in Bali-Lombok

As mentioned in Chapter 1, this area has been awarded to SBS International and Simec Atlantis for 30 years Power Purchase Agreement (PPA). The Nautilus Project involves deployment of 24m rotor diameter AR2000 turbines across all phases of the project (SimecAtlantis 2020). Therefore, the assessment here is based on this turbine diameter (*D*). A variation of tip-to-tip spacing between turbines is employed in this analysis.

SBS International has stated that the Nautilus project would ensure that the tidal turbine exactly matches local tidal resource characteristics in the Lombok Strait. The export power cable route plan from SBS International is presented in Figure 6-16. Based on this information, a realistic assessment in Bali-Lombok is applied for the Nusa Lembongan (NLC), Nusa Penida (NPC) and Lombok (LC) Clusters only.

Based on the proximity to the transmission cable route and the substations (as shown in Figure 6-9), six different arrays from NLC, NPC and LC are selected for the assessment here. The NLC1 and NLC2 arrays are selected from the Nusa Lembongan cluster, NPC1 and NPC2 for the Nusa Penida cluster and LC3 and LC4 for the Lombok cluster. These arrays are also the potential locations with the highest average power production from each cluster (see Chapter 5).

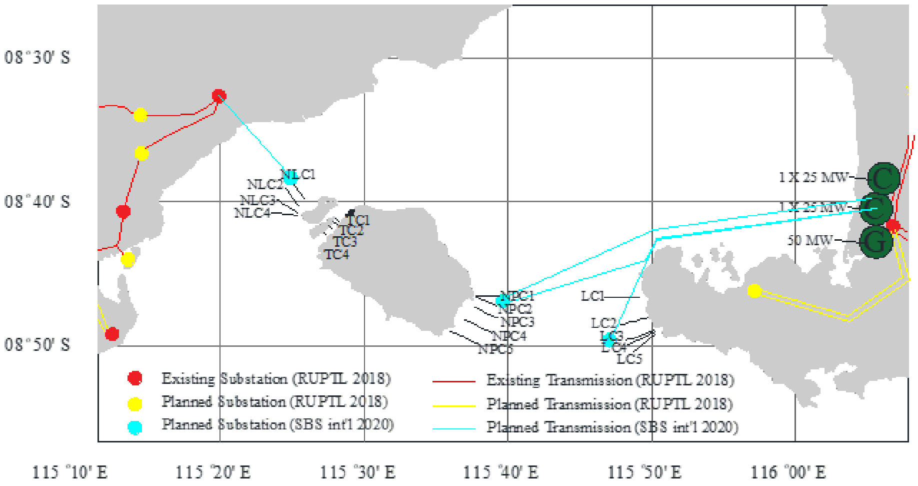

Figure 6-16: Tidal turbine transmission plan. Cyan lines and circles represent the planned transmission cables and export substations for the tidal turbines in Lombok strait (SBS-International, 2020)

However, as later discussed in this chapter, some of the arrays might be problematic because they are located inside a Marine Protection Area (MPA). SBS International and Atlantis mention that their contract includes the preparation of EIA/AMDAL, an environmental and social-economic impact assessment (SBS-International, 2020). This EIA study may allow installing the tidal turbine inside the MPA, if they can convince the authority that their turbines have low impact to the environment. Unfortunately, at the time of writing, such a document is still inaccessible.

a) *Power Production from D24 Turbine*

A similar terminology for the turbine schemes as for the previous section is used here. The stacking scenario is also applied to the turbine schemes. However, since the maximum depth of each array is varied here, the maximum stacking for each array is varied as well. Therefore, the n_s values of the schemes coded here as "max" for simplicity. For instance, D24s24n$_s$max means the scheme has D = 24 m, s = 24 m, and n_s is more than a single turbine in a stack, if applicable.

The arrays in LC (LC3 and LC4) have the longest fences amongst other arrays (see Table 6-5). Therefore, these arrays could have a larger number of the turbines than other arrays if the turbines are installed conventionally or a single turbine per stack (n_s = 1). As a result, these arrays give the largest total average power removed by the turbines ($\overline{P_1}$).

However, the arrays in NPC (NPC1 and NPC2) have deeper bathymetry on average along the fences. The cross-sectional area of the fences in these arrays are larger than other fences, and the number of turbines that could be installed in these fences are larger than other fences when the maximum stacking is applied. Hence, the arrays in NPC (NPC1 and NPC2) give greater $\overline{P_1}$ than other arrays. The bathymetric depth for the LC3 array is inadequate for more than one stacking option if the turbines are installed with a tip-to-tip spacing of 24 m. Therefore, the D24s24n$_s$max scheme for LC3 shows similar results to D24s24n$_s$1. Since a pre-processing algorithm sets the turbine arrangements in the model, this arrangement is included in the results.

This assessment also shows that deployment of turbines in the arrays in Bali-Lombok sites produces an average power $\left(\frac{\overline{P_1}}{n_t}\right)$ of 0.39 - 0.49 MW per turbine for the schemes with n_s =1. Similar to the previous assessment at Larantuka, it is also found that fences with a closer gap between turbines will remove more power than schemes with larger tip-to-tip spacing (see Table 6-5). In the majority of cases, schemes with s = 12 m have slightly higher $\frac{\overline{P_1}}{n_t}$ than the schemes with s = 24 m. For instance, 24s24n$_s$1 produces an average of 0.41 MW per turbine in NLC1, while 24s12n$_s$1 has 0.42 MW per turbine in the same array. This higher $\frac{\overline{P_1}}{n_t}$ corresponds to the increased blockage ratio of the array. In this analysis, the global blockage (B_G) is the arrays' average blockage ratio instead of the channel blockage ratio since the arrays do not occupy the entire channel cross-section.

However, if the maximum stacking scenario is applied, the arrays in the NLCs (NLC1 and NLC2) have lower $\frac{\overline{P_1}}{n_t}$ than the schemes with n_s =1 even though the blockages are higher. For instance, the D24s24n$_s$1 schemes in NLC1 and NLC2 have $\frac{\overline{P_1}}{n_t}$ = 0.41 and 0.34 MW per turbine respectively. Meanwhile, the NLC1 and NLC2 arrays in D24s24n$_s$max have only an average of 0.37 and 0.31 MW per turbine, respectively. If we look at the B_G, both D24s24n$_s$max schemes have B_G=0.12 while both D24s24n$_s$1 schemes only have B_G=0.09. Further investigations are made regarding this in a more detailed assessment later in this section.

The simulations at these sites also provide the maximum power ($P_{1,max}$ and $\frac{P_{1,max}}{n_t}$). Based on the $\frac{P_{1,max}}{n_t}$, all turbines exceed the capacity of that planned by SBS and Atlantis. The AR2000 turbines that are planned to be installed in this site have a specification of 2 MW power capacity (see SimecAtlantis, 2020 for detail). Therefore, a power capping strategy is applicable in this site. This strategy might also give an advantage as the turbines in this simulation have low Capacity Factors (*CF*). Without any capping strategy, the turbines in this site only have *CF* in the range of 0.07 - 0.13.

Table 6-5: Assessment result with realistic turbine parameter in Bali-Lombok sites

Scheme	Array	F_L (m)	Ac (m^2)	n_t (unit)	B_G	$\overline{P_1}$ (MW)	$P_{1,max}$ (MW)	$\frac{\overline{P_1}}{n_t}$ (MW)	$\frac{P_{1,max}}{n_t}$ (MW)	$\overline{T_1}$ (MN)	$\frac{\overline{T_1}}{n_t}$ (kN)	$T_{1,max}$ (MN)	$\frac{T_{1,max}}{n_t}$ (kN)	α_4	*CF*
D24s24n$_s$1	NLC1	2,457	256,475	50	0.09	20.48	300.82	0.41	6.02	9.55	190.96	73.67	1,473.46	0.38	0.0
	NLC2	2,931	293,937	60	0.09	20.33	254.00	0.34	4.23	10.67	177.78	72.85	1,214.21	0.37	0.0
	NPC1	2,991	423,995	60	0.06	29.68	286.20	0.49	4.77	12.52	208.60	70.63	1,177.23	0.34	0.1
	NPC2	2,886	451,086	58	0.06	23.22	193.67	0.40	3.34	10.49	180.91	53.64	924.76	0.33	0.1
	LC3	3,866	358,363	80	0.10	32.98	268.94	0.41	3.36	16.35	204.41	82.12	1,026.46	0.35	0.1
	LC4	3,935	364,713	80	0.10	31.45	252.07	0.39	3.15	15.92	198.97	78.94	986.79	0.35	0.1
D24s12n$_s$1	NLC1	2,457	256,475	65	0.11	27.12	389.36	0.42	5.99	13.13	201.97	99.99	1,538.28	0.38	0.0
	NLC2	2,931	293,937	78	0.12	27.16	332.56	0.35	4.26	14.37	184.22	97.51	1,250.11	0.40	0.0
	NPC1	2,991	423,995	80	0.09	41.06	409.43	0.51	5.12	17.69	221.07	102.06	1,275.75	0.34	0.1
	NPC2	2,886	451,086	76	0.08	31.31	268.13	0.41	3.53	14.33	188.57	74.54	980.82	0.34	0.1
	LC3	3,866	358,363	104	0.13	45.13	365.08	0.43	3.51	22.94	220.55	114.51	1,101.04	0.35	0.1
	LC4	3,935	364,713	104	0.13	43.06	342.84	0.41	3.30	22.30	214.46	110.02	1,057.84	0.36	0.1
D24s24n$_s$max	NLC1	2,457	256,475	70	0.12	25.98	363.89	0.37	5.20	12.76	182.34	94.90	1,355.73	0.37	0.0
	NLC2	2,931	293,937	80	0.12	25.12	314.19	0.31	3.93	13.38	167.27	91.27	1,140.86	0.37	0.0
	NPC1	2,991	423,995	120	0.13	69.84	690.97	0.58	5.76	31.42	261.84	180.07	1,500.57	0.36	0.1
	NPC2	2,886	451,086	128	0.13	57.07	511.77	0.45	4.00	28.18	220.16	151.57	1,184.13	0.35	0.1
	*LC3**	*3,866*	*358,363*	*80*	*0.10*	*32.99*	*268.95*	*0.41*	*3.36*	*16.31*	*203.89*	*81.88*	*1,023.44*	*0.35*	*0.1*
	LC4	3,935	364,713	90	0.11	32.89	264.96	0.37	2.94	16.77	186.29	83.58	928.70	0.35	0.1
D24s12n$_s$max	NLC1	2,457	256,475	143	0.25	54.07	712.89	0.38	4.99	27.52	192.43	196.42	1,373.53	0.44	0.0
	NLC2	2,931	293,937	156	0.24	51.82	591.36	0.33	3.79	29.15	186.85	186.35	1,194.53	0.41	0.0
	NPC1	2,991	423,995	156	0.17	172.75	1,670.65	1.11	10.71	82.90	531.39	464.46	2,977.31	0.41	0.1
	NPC2	2,886	451,086	156	0.16	145.90	1,266.21	0.94	8.12	77.60	497.43	405.69	2,600.59	0.39	0.1
	LC3	3,866	358,363	117	0.15	72.72	589.26	0.62	5.04	38.96	333.01	195.66	1,672.34	0.38	0.1
	LC4	3,935	364,713	117	0.15	70.43	566.85	0.60	4.84	39.11	334.28	195.85	1,673.91	0.38	0.1

** Maximum number of turbines per stack in this array is just a single turbine (ns = 1)*

The simulations also show the thrusts that are applied to the turbines. The average total thrust ($\overline{T}_1$), the maximum thrust ($T_{1,max}$) for all fences, the average thrust per turbine $\left(\frac{\overline{T_1}}{n_t}\right)$ and the maximum thrust per turbine $\frac{T_{1,max}}{n_t}$ are calculated from these simulations. The simulations suggest that the turbines will have a higher thrust (both $\frac{\overline{T_1}}{n_t}$ and $\frac{T_{1,max}}{n_t}$) when they are installed with closer tip-to-tip spacing.

For instance, the turbines of the NPC1 array have $\frac{\overline{T_1}}{n_t}$ of ~208 kN in the 24s24n_s1 scheme while in 24s12n_s1 the $\frac{\overline{T_1}}{n_t}$ is ~221 kN per turbine. A similar trend is also exhibited in the $\frac{T_{1,max}}{n_t}$, the 24s24n_s1 scheme shows the maximum thrust per turbine is ~1,275 kN, while the 24s24n_s1 scheme only has of 1,177 kN per turbine. It is implied from this simulation that the thrust per turbine seems to increase when the gap between turbines is smaller. Therefore, despite having an advantage of a slight increase in average power per turbine, the turbine also needs to deal with the increasing thrust.

b) *Detailed Assessment*

In this analysis, the details of power and thrust on each array are investigated. The results shown in Table 6-5 are broken down for each element. Figure 6-17 shows the mesh detail for all arrays used in the analysis. This numbering system is different from the element numbering in DG-ADCIRC model. Since the mesh in the DG-ADCIRC model for the array location is arranged with the same size of each element, each element in the array has the same number of turbines. Except for element 1 in C2, ten turbines are installed in each element for the D24s24n_s1 scheme. Meanwhile, the D24s12n_s1 has thirteen turbines installed in each element for all arrays (see Table 6-6).

This detail also shows the turbines number per stack that is applied in each element. For instance, D24s24$n_s$max scheme in NPC1 has two stacking levels in el.3 and el.4 with 20 turbines, three stacking level in el.5 and el.6 with 30 turbines in each element, while other elements only have one level only with ten turbines in each element. The number of turbines also shows that the D24s24$n_s$max scheme at LC3 has no additional stacking in the elements.

The turbine arrangement in the elements leads to the different local blockage (B_L) for both one-stacking schemes (D24s24n_s1 and D24s12n_s1). Table 6-6 shows that the B_L is larger in the elements near to the land than the elements further away. This trend in B_L is expected. As the turbine size is uniform, the B_L follows the depth trend along the fence. The local blockages in the maximum stacking schemes are increased. For instance, element 4 of the NLC1 array in the D24s24n_s1 scheme has B_L = 0.07, while in the D24s24$n_s$max scheme the same element has B_L = 0.15.

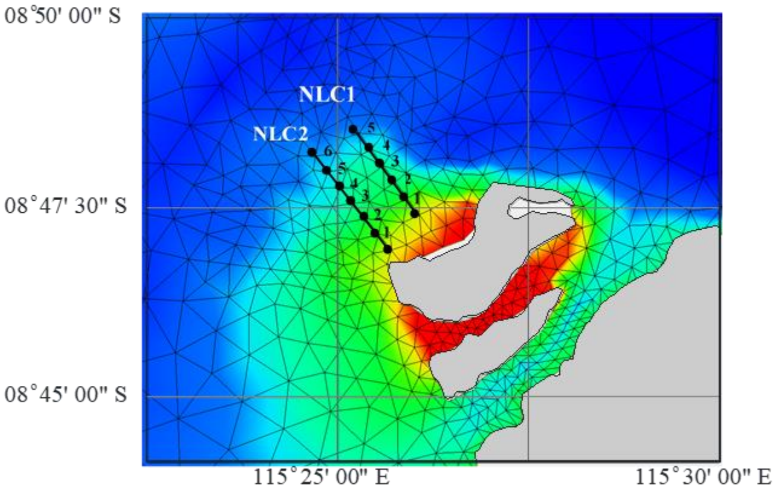

a. Nusa Lembongan Cluster

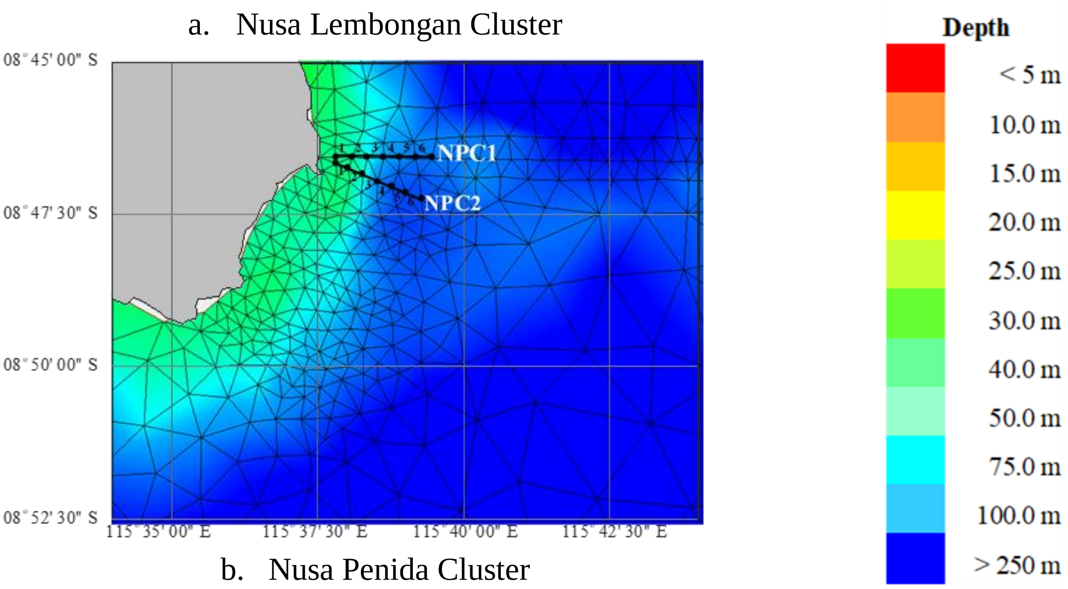

b. Nusa Penida Cluster

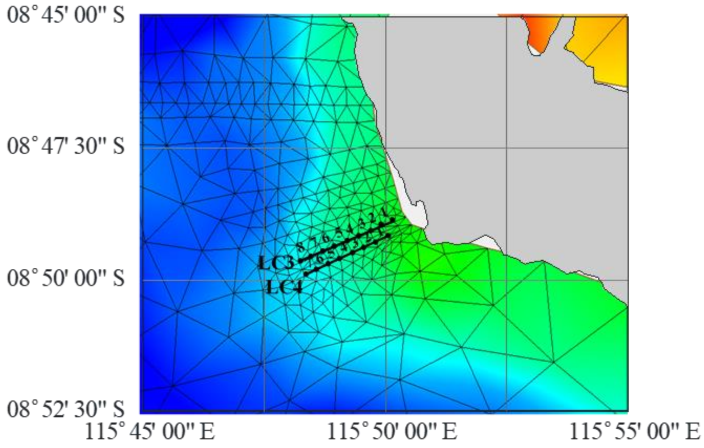

c. Lombok Cluster

Figure 6-17: Details of mesh elements and bathymetry for each cluster in the Bali-Lombok

The average power production in each element is related to B_L. The further from the land have deeper bathymetry than the close to the coastline. As the turbines in all elements have the same size, the elements further from land have smaller B_L (see Table 6-7). The power production is also higher in the elements where the maximum stacking schemes are applied, as more turbines are installed in these elements.

Table 6-6: The number of turbines (n_t), the B_G and B_L in each element

Scheme	Array	n_t									B_G	B_L							
		Total	el.1	el.2	el.3	el.4	el.5	el.6	el.7	el.8		el.1	el.2	el.3	el.4	el.5	el.6	el.7	el.8
D24s24n$_s$1	A1	50	10	10	10	10	10				0.09	0.16	0.11	0.09	0.07	0.06			
	A2	60	10	10	10	10	10	10			0.09	0.22	0.14	0.09	0.08	0.07	0.06		
	C1	60	10	10	10	10	10	10			0.06	0.10	0.08	0.07	0.06	0.05	0.05		
	C2	58	8	10	10	10	10	10			0.06	0.10	0.09	0.07	0.05	0.04	0.04		
	D3	80	10	10	10	10	10	10	10	10	0.10	0.14	0.13	0.11	0.11	0.10	0.09	0.08	0.08
	D4	80	10	10	10	10	10	10	10	10	0.10	0.15	0.13	0.11	0.10	0.09	0.09	0.08	0.07
D24s12n$_s$1	A1	65	13	13	13	13	13				0.12	0.21	0.14	0.12	0.10	0.08			
	A2	78	13	13	13	13	13	13			0.12	0.28	0.18	0.12	0.10	0.09	0.08		
	C1	78	13	13	13	13	13	13			0.13	0.13	0.11	0.09	0.07	0.07	0.07		
	C2	78	13	13	13	13	13	13			0.13	0.13	0.12	0.09	0.06	0.06	0.06		
	D3	104	13	13	13	13	13	13	13	13	0.10	0.19	0.16	0.15	0.14	0.13	0.12	0.11	0.10
	D4	104	13	13	13	13	13	13	13	13	0.11	0.20	0.17	0.15	0.14	0.12	0.11	0.10	0.10
D24s24n$_s$max	A1	70	10	10	10	**20**	**20**				0.11	0.16	0.11	0.09	**0.15**	**0.12**			
	A2	80	10	10	10	10	**20**	**20**			0.12	0.22	0.14	0.09	0.08	**0.14**	**0.13**		
	C1	120	10	10	**20**	**20**	**30**	**30**			0.09	0.10	0.08	**0.13**	**0.11**	**0.16**	**0.15**		
	C2	128	8	10	**20**	**30**	**30**	**30**			0.08	0.10	0.09	**0.13**	**0.15**	**0.13**	**0.13**		
	*D3**	*80*	*10*	*10*	*10*	*10*	*10*	*10*	*10*	*10*	*0.13*	*0.14*	*0.13*	*0.11*	*0.11*	*0.10*	*0.09*	*0.08*	*0.08*
	D4	90	10	10	10	10	10	10	10	**20**	0.13	0.15	0.13	0.11	0.10	0.09	0.09	0.08	**0.15**
D24s12n$_s$max	A1	143	13	**26**	**26**	**39**	**39**				0.25	0.24	**0.29**	**0.23**	**0.28**	**0.21**			
	A2	156	13	13	**26**	**26**	**39**	**39**			0.24	0.25	0.27	**0.20**	**0.25**	**0.28**	**0.18**		
	C1	156	13	13	**26**	**26**	**39**	**39**			0.17	0.26	0.22	**0.28**	**0.30**	**0.28**	**0.28**		
	C2	156	13	13	**26**	**26**	**39**	**39**			0.16	0.26	0.24	**0.26**	**0.26**	**0.29**	**0.29**		
	D3	169	13	13	13	**26**	**26**	**26**	**26**	**26**	0.15	0.19	0.16	0.15	**0.27**	**0.25**	**0.23**	**0.22**	**0.21**
	D4	182	13	13	13	**26**	**26**	**26**	**26**	**39**	0.15	0.20	0.17	0.15	**0.27**	**0.25**	**0.23**	**0.21**	**0.29**

* *Maximum number of turbines per stack in this array is just a single turbine (ns = 1)*

Two turbines per stack, **three turbines per stack**

Table 6-7: The average power ($\overline{P_1}$) and the Capacity Factor (*CF*) in each element

Scheme	Array	MW									*CF*								
		Total	el.1	el.2	el.3	el.4	el.5	el.6	el.7	el.8	Overall	el.1	el.2	el.3	el.4	el.5	el.6	el.7	el.8
D24s24n$_s$1	A1	20.48	4.86	5.03	4.18	3.67	2.74				0.07	0.06	0.07	0.07	0.08	0.06			
	A2	20.33	3.39	4.50	3.61	3.17	3.05	2.61			0.08	0.07	0.07	0.08	0.08	0.08	0.08		
	C1	29.68	5.19	5.15	5.12	5.24	4.59	4.39			0.10	0.10	0.11	0.11	0.10	0.10	0.10		
	C2	23.22	4.61	4.91	4.06	3.33	3.18	3.14			0.12	0.12	0.14	0.12	0.11	0.10	0.11		
	D3	32.98	5.98	5.25	4.46	4.08	3.69	3.33	3.15	3.04	0.12	0.11	0.13	0.13	0.13	0.12	0.11	0.11	0.11
	D4	31.45	6.19	5.35	4.39	3.90	3.43	2.98	2.71	2.50	0.12	0.12	0.13	0.13	0.13	0.12	0.11	0.11	0.11
D24s12n$_s$1	A1	27.12	6.51	6.64	5.47	4.84	3.66				0.07	0.06	0.07	0.07	0.08	0.07			
	A2	27.16	4.58	5.98	4.81	4.22	4.06	3.51			0.08	0.11	0.10	0.06	0.07	0.08	0.08		
	C1	41.06	7.11	7.18	7.00	6.98	6.39	6.39			0.10	0.11	0.11	0.10	0.10	0.10	0.09		
	C2	31.31	6.45	6.55	5.41	4.44	4.25	4.21			0.12	0.12	0.13	0.12	0.10	0.10	0.11		
	D3	45.13	8.25	7.16	6.09	5.59	5.06	4.55	4.29	4.14	0.12	0.11	0.13	0.13	0.13	0.13	0.12	0.11	0.11
	D4	43.06	8.52	7.30	6.02	5.34	4.71	4.08	3.68	3.40	0.12	0.12	0.13	0.14	0.13	0.13	0.12	0.11	0.11
D24s24n$_s$max	A1	25.98	4.83	5.03	4.16	**5.86**	**6.09**				0.07	0.06	0.07	0.07	**0.06**	**0.08**			
	A2	25.12	3.39	4.49	3.60	3.16	**4.75**	**5.74**			0.08	0.06	0.10	0.08	0.08	**0.08**	**0.08**		
	C1	69.84	5.19	8.15	**11.09**	**14.58**	**15.60**	**15.23**			0.10	0.10	0.11	**0.10**	**0.10**	**0.10**	**0.10**		
	C2	57.07	4.65	7.53	**11.66**	**11.46**	**10.87**	**10.89**			0.11	0.13	0.12	**0.12**	**0.11**	**0.10**	**0.10**		
	*D3**	*32.98*	*5.98*	*5.25*	*4.46*	*4.08*	*3.69*	*3.33*	*3.15*	*3.04*	*0.12*	*0.11*	*0.13*	*0.13*	*0.13*	*0.13*	*0.11*	*0.12*	*0.11*
	D4	32.89	6.18	5.35	4.39	3.90	3.43	3.00	2.69	**3.95**	0.12	0.12	0.13	0.13	0.13	0.13	0.11	0.11	**0.11**
D24s12n$_s$max	A1	54.07	5.91	**9.78**	**11.66**	**13.51**	**13.21**				0.07	0.07	**0.06**	**0.07**	**0.09**	**0.08**			
	A2	51.82	4.64	5.91	**7.51**	**9.36**	**11.48**	**12.93**			0.09	0.03	0.10	**0.10**	**0.10**	**0.11**	**0.10**		
	C1	172.75	16.03	21.05	**31.44**	**35.66**	**32.76**	**35.81**			0.10	0.05	0.07	**0.09**	**0.12**	**0.17**	**0.23**		
	C2	145.90	15.37	18.74	**24.26**	**27.57**	**29.47**	**30.49**			0.12	0.05	0.07	**0.10**	**0.14**	**0.19**	**0.26**		
	D3	72.72	8.14	7.10	6.07	**9.12**	**11.89**	**9.99**	**10.64**	**9.77**	0.12	0.11	0.12	0.13	**0.10**	**0.13**	**0.12**	**0.13**	**0.14**
	D4	70.43	8.42	7.27	5.99	**8.71**	**11.13**	**9.65**	**8.49**	**10.77**	0.12	0.12	0.10	0.09	**0.11**	**0.12**	**0.17**	**0.19**	**0.12**

* *Maximum number of turbines per stack in this array is just a single turbine (ns = 1)*

Two turbines per stack, **three turbines per stack**

Table 6-7 shows that the *CF* values are vary slightly across the elements for all schemes. For instance, the NPC2 array in the D24s24n$_s$1 scheme has *CF* = 0.13 at el.2 while at el.4 the *CF* is

0.10. The overall *CF* for this array is 0.12. This *CF* indicates the maximum power removed by the turbines varies, as does the average power.

Table 6-8 shows the $\frac{\overline{P_1}}{n_t}$ and $\frac{P_{1,max}}{n_t}$ for each of the elements. An interesting feature is observed in the stacking schemes for NPC1 and NPC2 arrays. The elements with the maximum stacking scheme have higher $\frac{\overline{P_1}}{n_t}$ and $\frac{P_{1,max}}{n_t}$ than in stacking schemes with a single turbine per stack (for the same elements). For instance, el.3 of NPC1 and NPC2 arrays in the D24s24nsmax scheme have a 0.55 and 0.58 MW/per turbine, respectively, while in the D24s24ns1 scheme, this element only gives 0.51 and 0.41 MW per turbine. The maximum values of $\frac{P_{1,max}}{n_t}$ also show a similar trend in the elements with more than one stacking.

Table 6-8: The average power per turbine and the maximum power per turbine in each element

Scenario	Array	$\frac{\overline{P_1}}{n_t}$ (MW)									$\frac{P_{1,max}}{n_t}$ (MW)								
		All	el.1	el.2	el.3	el.4	el.5	el.6	el.7	el.8	All	el.1	el.2	el.3	el.4	el.5	el.6	el.7	el.8
D24s24n$_s$1	A1	0.41	0.50	0.49	0.42	0.37	0.27				6.21	8.13	7.45	6.26	4.82	4.41			
	A2	0.34	0.45	0.34	0.36	0.32	0.30	0.26			4.33	6.00	4.65	4.29	3.89	3.76	3.38		
	C1	0.49	0.52	0.51	0.51	0.52	0.46	0.44			4.79	5.23	4.88	4.62	5.11	4.41	4.49		
	C2	0.40	0.58	0.49	0.41	0.33	0.32	0.31			3.41	4.72	3.63	3.30	3.14	3.02	2.92		
	D3	0.41	0.60	0.52	0.45	0.41	0.37	0.33	0.32	0.30	3.41	5.33	4.14	3.34	3.07	2.96	2.90	2.83	2.73
	D4	0.39	0.62	0.54	0.44	0.39	0.34	0.30	0.27	0.25	3.20	5.16	4.14	3.26	3.00	2.75	2.61	2.44	2.28
D24s12n$_s$1	A1	0.42	0.50	0.51	0.42	0.37	0.28				6.13	8.09	7.55	6.17	4.84	3.98			
	A2	0.35	0.35	0.46	0.37	0.32	0.31	0.27			4.31	3.15	4.56	6.23	4.69	3.72	3.50		
	C1	0.53	0.54	0.55	0.55	0.54	0.49	0.49			5.25	4.99	4.99	5.46	5.42	5.10	5.53		
	C2	0.40	0.50	0.50	0.42	0.34	0.33	0.32			3.48	3.98	3.90	3.39	3.32	3.22	3.07		
	D3	0.43	0.63	0.55	0.47	0.43	0.39	0.35	0.33	0.32	3.57	5.66	4.34	3.50	3.25	3.07	3.01	2.93	2.82
	D4	0.41	0.66	0.56	0.46	0.41	0.36	0.31	0.28	0.26	3.36	5.49	4.33	3.43	3.16	2.86	2.71	2.53	2.36
D24s24n$_s$max	A1	0.37	0.48	0.50	0.42	**0.29	**0.30				5.63	7.99	7.30	6.11	**5.02	**3.98			
	A2	0.31	0.34	0.45	0.36	0.32	**0.24	**0.29			4.00	5.83	4.63	4.26	3.86	**3.00	**3.70		
	C1	0.58	0.52	0.82	**0.55	**0.73	***0.52	***0.51			5.76	5.40	7.47	**5.40	**7.26	***5.20	***5.10		
	C2	0.45	0.58	0.75	**0.58	***0.38	***0.36	***0.36			4.01	4.55	6.16	**4.84	***3.45	***3.53	***3.61		
	*D3**	*0.41*	*0.60*	*0.52*	*0.45*	*0.41*	*0.37*	*0.32*	*0.33*	*0.30*	*3.41*	*5.33*	*4.14*	*3.34*	*3.06*	*2.96*	*2.90*	*2.73*	*2.83*
	D4	0.37	0.62	0.54	0.44	0.39	0.34	0.30	0.27	**0.20	2.99	5.17	4.14	3.26	3.00	2.75	2.61	2.43	**1.80
D24s12n$_s$max	A1	0.38	0.45	**0.38	**0.45	***0.35	***0.34				5.08	6.86	**5.81	**6.63	***3.91	***4.15			
	A2	0.33	0.36	0.45	**0.29	**0.36	***0.29	***0.33			3.86	11.03	4.63	**3.00	**3.54	***2.67	***3.20		
	C1	1.11	1.23	1.62	**1.21	**1.37	***0.84	***0.92			10.71	27.00	24.82	**13.41	**11.58	***4.83	***4.08		
	C2	0.94	1.18	1.44	**0.93	**1.06	***0.76	***0.78			8.12	21.62	21.04	**9.32	**7.69	***3.91	***3.00		
	D3	0.43	0.63	0.55	0.47	**0.35	**0.46	**0.38	**0.41	**0.38	3.55	5.72	4.40	3.55	**3.55	**3.42	**3.33	**3.24	**2.70
	D4	0.39	0.65	0.56	0.46	**0.34	**0.43	**0.37	**0.33	***0.28	3.18	5.54	5.71	5.22	**3.13	**3.62	**2.20	**1.73	***2.23

* Maximum number of turbines per stack in this array is just a single turbine (ns = 1)

Two turbines per stack, **three turbines per stack**

Meanwhile, the arrays in the other clusters (NLC and LC) have a lower $\frac{\overline{P_1}}{n_t}$ and $\frac{P_{1,max}}{n_t}$ when the maximum stacking is introduced. For instance, the $\frac{\overline{P_1}}{n_t}$ in NLC1 for D24s24n$_s$1 is 0.41 MW, while for D24s24n$_s$, $\frac{\overline{P_1}}{n_t}$ is only 0.37 MW at the same array. A similar trend is also shown for other arrays (NLC2, LC3 and LC4) and other turbine schemes (D24s12n$_s$1 and D24s12n$_s$max).

The elements near to the element where the turbines are installed with more than one turbine per stack also show the trend of increasing $\frac{\overline{P_1}}{n_t}$ and $\frac{P_{1,max}}{n_t}$ when the stacking schemes are applied in

NPC1 and NPC2. For instance, the el.2 of NPC1 array in D24s24n$_s$max gives an average of 0.82 MW per turbine, while in the D24s24ns1 scheme, this element only has a 0.51 MW per turbine. To note, the el.2 only has one stacking level, or the same number of turbines in both schemes (D24s24n$_s$1 and D24s24n$_s$max).

In consequence, the turbines are also experiencing increasing thrust when the stacking schemes are applied. Following the trend of $\frac{\overline{P_1}}{n_t}$ and $\frac{P_{1,max}}{n_t}$, the $\frac{\overline{T_1}}{n_t}$ and $\frac{T_{1,max}}{n_t}$ values in NPC1 and NPC2 are higher in the elements where schemes of maximum stacking are applied (see Table 6-8 and Table 6-9). The el.5 of the NPC1 array in the D24s24n$_s$max scheme is also higher than el.5 of NPC1 in the D24s24n$_s$max scheme, although this element has similar B_L in both schemes.

Table 6-9: The average thrust per turbine and the maximum thrust per turbine in each element

Scenario	Array	$\frac{\overline{T_1}}{n_t}$ (MN)									$\frac{T_{1,max}}{n_t}$ (MN)								
		All	el.1	el.2	el.3	el.4	el.5	el.6	el.7	el.8	All	el.1	el.2	el.3	el.4	el.5	el.6	el.7	el.8
D24s24n$_s$1	A1	0.19	0.22	0.23	0.17	0.14	0.19				1.51	1.80	1.92	1.48	1.22	1.12			
	A2	0.18	0.13	0.19	0.24	0.19	0.16	0.15			1.24	1.37	1.70	1.30	1.08	1.02	0.94		
	C1	0.21	0.22	0.22	0.21	0.22	0.19	0.19			1.18	1.31	1.14	1.18	1.22	1.11	1.11		
	C2	0.18	0.25	0.21	0.18	0.16	0.15	0.15			0.94	1.22	1.01	0.88	0.83	0.86	0.88		
	D3	0.20	0.28	0.26	0.19	0.20	0.22	0.16	0.16	0.17	1.04	1.46	1.24	1.04	0.93	0.97	0.85	0.88	0.91
	D4	0.20	0.29	0.15	0.16	0.18	0.20	0.22	0.27	0.14	1.00	1.46	1.26	1.04	0.95	0.80	0.84	0.89	0.75
D24s12n$_s$1	A1	0.20	0.24	0.24	0.18	0.14	0.20				1.56	1.95	2.01	1.26	1.06	1.53			
	A2	0.18	0.14	0.21	0.25	0.19	0.16	0.15			1.26	1.51	1.80	1.33	1.05	0.97	0.89		
	C1	0.23	0.24	0.24	0.23	0.22	0.21	0.22			1.31	1.41	1.29	1.33	1.31	1.24	1.27		
	C2	0.18	0.22	0.22	0.18	0.16	0.16	0.16			0.96	1.08	1.07	0.92	0.87	0.91	0.93		
	D3	0.22	0.31	0.28	0.20	0.22	0.24	0.17	0.17	0.18	1.11	1.61	1.35	0.99	1.05	1.13	0.90	0.93	0.96
	D4	0.21	0.32	0.15	0.17	0.19	0.21	0.24	0.29	0.14	1.07	1.61	1.37	1.12	1.02	0.94	0.89	0.84	0.79
D24s24n$_s$max	A1	0.18	0.23	0.23	0.19	⁑ **0.15**	⁑ **0.17**				1.36	1.80	1.92	1.48	⁑ **1.36**	⁑ **1.06**			
	A2	0.17	0.16	0.19	0.23	0.19	⁑ **0.16**	⁑ **0.12**			1.14	1.36	1.70	1.30	1.07	⁑ **1.09**	⁑ **0.82**		
	C1	0.26	0.22	0.35	⁑ **0.24**	⁑ **0.32**	⁂ **0.24**	⁂ **0.24**			1.50	1.30	1.86	⁑ **1.36**	⁑ **1.86**	⁂ **1.41**	⁂ **1.40**		
	C2	0.22	0.25	0.33	⁑ **0.28**	⁂ **0.19**	⁂ **0.20**	⁂ **0.19**			1.18	1.21	1.65	⁑ **1.40**	⁂ **1.06**	⁂ **1.09**	⁂ **1.10**		
	*D3**	*0.20*	*0.28*	*0.26*	*0.19*	*0.20*	*0.22*	*0.16*	*0.16*	*0.17*	*1.02*	*1.46*	*1.24*	*1.04*	*0.93*	*0.96*	*0.85*	*0.88*	*0.90*
	D4	0.19	0.29	0.14	0.16	0.18	0.20	0.22	0.27	⁑ **0.11**	0.93	1.45	1.26	1.04	0.95	0.79	0.84	0.88	⁑ **0.62**
D24s12n$_s$max	A1	0.19	0.20	⁑ **0.18**	⁑ **0.27**	⁂ **0.19**	⁂ **0.15**				1.37	1.64	⁑ **1.46**	⁑ **1.89**	⁂ **1.21**	⁂ **1.11**			
	A2	0.19	0.59	0.20	⁑ **0.12**	⁑ **0.16**	⁂ **0.13**	⁂ **0.17**			1.19	1.47	1.71	⁑ **1.06**	⁑ **1.25**	⁂ **1.02**	⁂ **1.22**		
	C1	0.53	0.56	0.75	⁑ **0.59**	⁑ **0.66**	⁂ **0.41**	⁂ **0.44**			2.98	3.23	3.95	⁑ **3.23**	⁑ **3.72**	⁂ **2.34**	⁂ **2.54**		
	C2	0.50	0.56	0.70	⁑ **0.47**	⁑ **0.58**	⁂ **0.43**	⁂ **0.44**			2.60	2.63	3.43	⁑ **2.35**	⁑ **3.06**	⁂ **2.37**	⁂ **2.41**		
	D3	0.23	0.29	0.27	0.52	⁑ **0.18**	⁑ **0.11**	⁑ **0.21**	⁑ **0.22**	⁑ **0.23**	1.16	1.55	1.30	1.09	⁑ **0.90**	⁑ **1.11**	⁑ **1.15**	⁑ **1.21**	⁑ **1.28**
	D4	0.21	0.30	0.39	0.44	⁑ **0.25**	⁑ **0.18**	⁑ **0.12**	⁑ **0.14**	⁂ **0.17**	1.08	1.56	1.33	1.09	⁑ **1.23**	⁑ **1.13**	⁑ **1.03**	⁑ **0.88**	⁂ **0.91**

** this scheme is similar to the D24s24n$_s$max, the turbines stacking in this array is only gives one stacking (ns=1)*

⁑ **Two stacks,** ⁂ **Three stacks**

Meanwhile other arrays show the opposite trend. The elements without the additional stacking experience lower $\frac{\overline{P_1}}{n_t}$ and $\frac{P_{1,max}}{n_t}$ in the D24s24n$_s$max schemes. For instance, el.1 of the NLC2 array gives $\frac{\overline{P_1}}{n_t}$ = 0.34 MW and $\frac{P_{1,max}}{n_t}$ = 5.83 MW in the D24s24n$_s$1 scheme. While in the D24s24n$_s$max scheme, the same element gives $\frac{\overline{P_1}}{n_t}$ = 0.45 MW and $\frac{P_{1,max}}{n_t}$ = 6.00 MW. Although this element still has similar B_L in both schemes.

The comparison of flow field changes between two schemes could perhaps explain this increase or decrease in power and thrust. A snapshot of flow field changes, at the time step of maximum power and thrust, shows that the flows in D24s12$n_s$max show a positive difference (increased flow) in both tidal directions (see Figure 6-18b). Meanwhile, the results for D24s12n_s1 exhibit opposite behaviour for the northward and southward tidal directions. Figure 6-18a shows the northward tidal direction has a negative difference, while the southward direction has a positive difference.

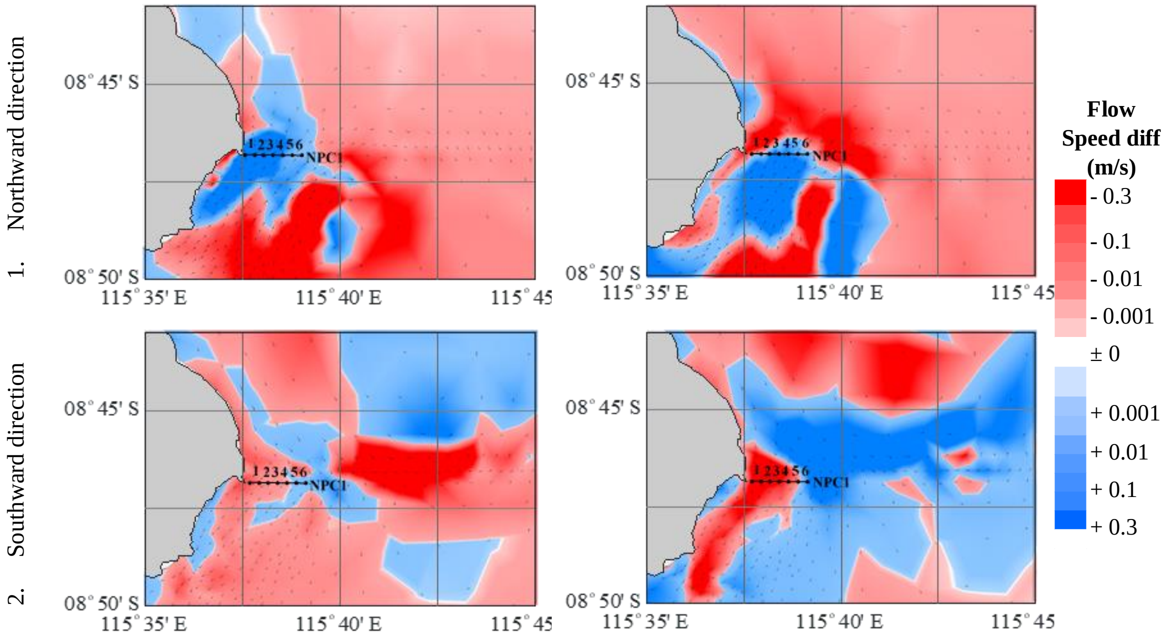

a. D24s12ns1 b. D24s12nsmax

Figure 6-18: Snapshot of flow field changes at maximum power production for the NPC1 turbine array in both tidal cycle directions.

Meanwhile, the NLC1 array shows a different flow field change in the northward direction. The flow field change at el. 5 in NLC1 of the D24s12n_s1 scheme has a positive change (see Figure 6-19.1.a). While in D24s12$n_s$max, the flow field change at the same element is negative. This means that the implementation of maximum stacking reduces the advantage gained by having an acceleration boost in the flow field. In the southward direction, the maximum stacking of the D24s12$n_s$max scheme pushes the “flow acceleration” in the bypass flow farther to the middle of the channel.

A similar pattern is also observed in the LC3 array. As shown in Figure 6-20, the flow field in the D24s12n_s1 scheme has a positive change in the half of the array line for the southward direction. This positive change is diminished in the D24s12$n_s$max scheme. We see a greater flow field change in the area of the bypass flow.

c) The Development Phases.

The Nautilus Project plans to install turbines over a number of phases. The initial demonstration phase consists of installing a total capacity of 12 MW from six turbines in the first site (see SimecAtlantis 2020). It is unclear whether SBS International and Simec Atlantis have decided at which site will deploy their first turbines; either on the Lombok side or the Bali side.

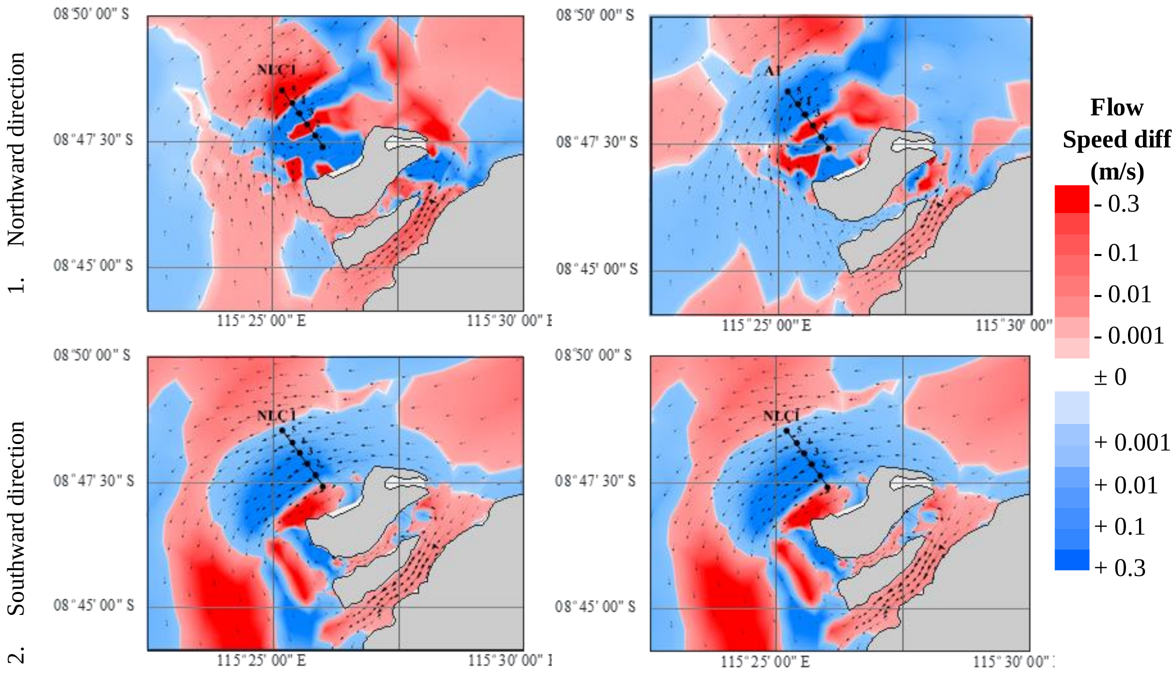

a. D24s12n_s1 b. D24s12$n_s$max

Figure 6-19: Snapshot of flow field changes at maximum power production for the NLC1 turbine array in both tidal cycle directions

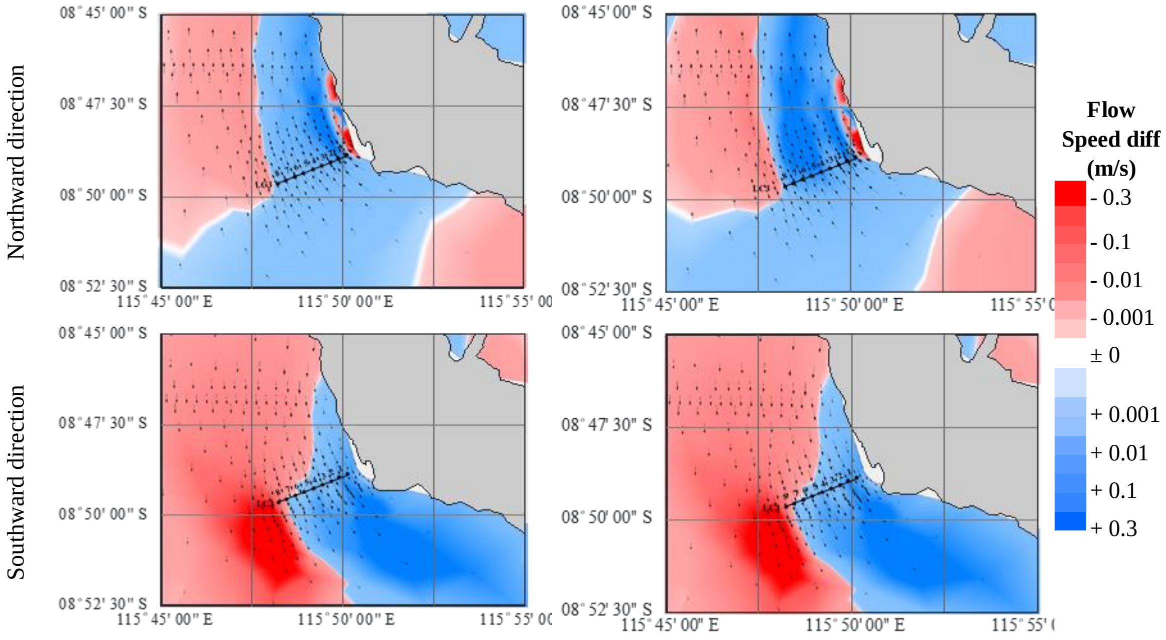

a. D24s12n_s1 b. D24s12$n_s$max

Figure 6-20: Snapshot of flow field changes at maximum power production for the LC3 turbine array in both tidal cycle directions

The analysis aims to explore the possibility of the turbines extracting different amounts of power when deployed in stages. One array for each cluster is selected for this analysis. The NLC1 array is selected for the Nusa Lembongan cluster, NPC1 for the Nusa Penida cluster, and LC3 for the Lombok cluster. Presumably, the most sensible option for the initial stage is deploying the turbines near the coastline. Therefore, three elements for the NPC1 and LC3 arrays and two elements for the NLC1 array near the coastline are analysed for the phased development scenario (see Table 6-10).

The simulations in this analysis are run based on one, two and three elements. The schemes for all elements in Table 6-10 are similar to the schemes in the previous section (Table 6-7). This shows that the analysis based on a single element or several elements gives slightly different results from the simulation with all elements. Each cluster has different characteristics as regards the staging. The NLC1 array in NC1 extracts slightly higher power for the smaller array in e1-1. In all element scenarios, this element removes power at an average of 6.51 MW. When the simulation is run for an individual element (A1, el-1), this element's power production is 6.93 MW, higher than the all elements by ~0.4 MW.

Table 6-10: The average power and Capacity Factor (*CF*) in different phase sequence. The simulations are run with turbine scheme of D24s12n$_s$1

Schemes	Average Power $-\overline{P_1}(MW)$			α_4	Capacity Factor - *CF*		
	el-1	el-2	el-3		el-1	el2	el3
Nusa Lembongan Cluster (NLC)							
NLC1 (all element)	6.51	6.64	5.47	0.38	0.06	0.07	0.07
NLC1, el-1-2	6.66	6.86	-	0.41	0.07	0.06	-
NLC1, el-1	6.93	-	-	0.39	0.06	-	-
NLC1, el-2	-	5.84	-	0.36	-	0.06	-
Nusa Penida Cluster (NPC)							
NPC1 (all element)	7.00	7.18	7.11	0.34	0.11	0.11	0.10
NPC1, el-1-2-3	8.15	7.18	7.06	0.35	0.10	0.11	0.10
NPC1, el-1	7.69	-		0.35	0.10	-	-
NPC1, el-2	-	8.32	-	0.34	-	0.11	-
NPC1, el-3	-	-	8.24	0.34	-	-	0.11
Lombok Cluster (LC)							
LC3 (all element)	8.25	7.16	6.09	0.35	0.11	0.13	0.13
LC3, el-1-2-3	8.31	7.15	6.15	0.36	0.11	0.13	0.13
LC3, el-1	8.36	-	-	0.36	0.11	-	-
LC3, el-2	-	6.81	-	0.36	-	0.13	-
LC3, el-3	-	-	5.74	0.35	-	-	0.13

Meanwhile, the individual element scheme gives lower average power than the all element and el-1-2 schemes for the elements farther from the coastline. A similar trend is also observed in LC3 for the LC. The individual arrays tend to have lower average power when run in an individual element scheme. The capacity factors for all development schemes are relatively similar. This means that changes in maximum power mimic changes in average power.

The NPC1 array in NPC consistently shows that the simulations with the individual element remove higher power than the simulation of all elements. For elements farther from the coastline, the discrepancies are larger. Perhaps this is because this array is very sensitive to flow diversion. The comparison of the average flow-field changes between the simulations shows that the element near the coast (el.1-Figure 6-21 a.) creates a more significant diversion than the simulation of el.3 (Figure 6-21 c.).

d) *Capping Strategy for Turbine Design*

A power capping strategy could be used to assess the tidal resources with the planned generator capacity for the turbine. The AR2000 is a turbine has a capacity of 2 MW, therefore the simulation is expanded with this turbine specification. The maximum power per turbine ($\frac{P_{1,max}}{nt}$) implies the turbine capacity. Thus, the power capping scenario implemented aims to match the $\frac{P_{1,max}}{nt}$ with the AR2000 turbine capacity.

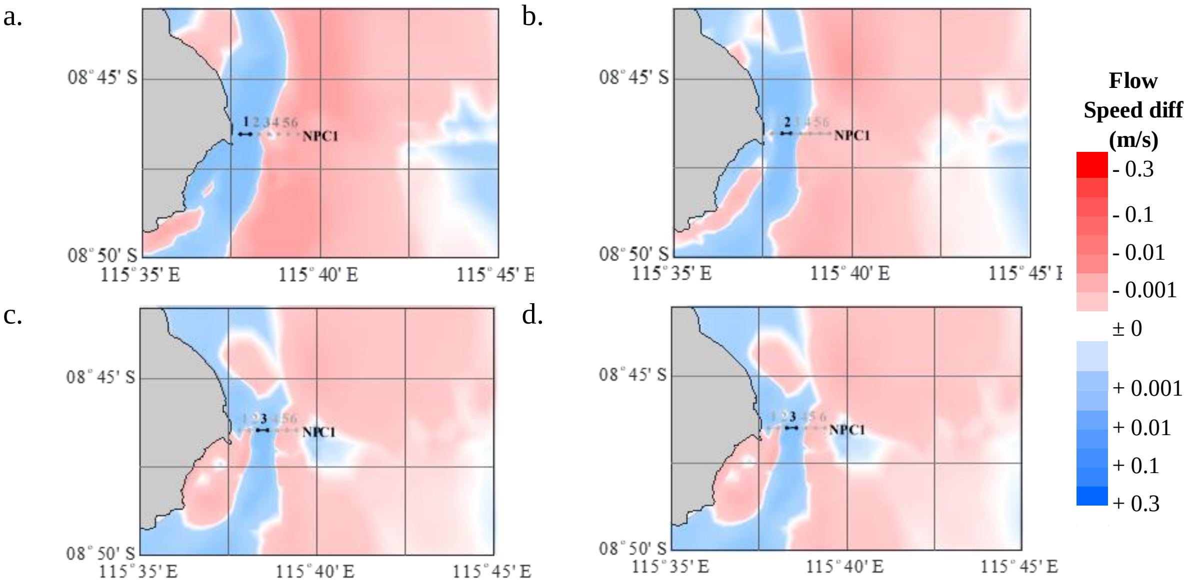

Figure 6-21: The average flow field change of simulations for the staging sequences in the NPC1 array. a. is the simulation only run with el.1 only, b is el.2 only, c. is el. 3 and d. is for the simulation of el.1,2, and 3.

Since the simulation is computationally demanding, the capping strategy is only applied for the D24s24n$_s$1 and D24s12n$_s$1 schemes. The capping metrics for the capping strategy are again used here for later analysis. The power capping implementation, listed in Table 6-11, does not attain

$\frac{P_{1,max}}{nt}$ exactly at 2MW, since several iterations are required to obtain these results, whereas the simulations are computationally costly.

The summary of these results shows that the average power ($\overline{P_1}$) only reduces by 5-11% from the simulation without a capping strategy. As shown in the table, the power factor (F_P) ranges from 0.89 to 0.94. This strategy gives the advantage of a relatively significant reduction in maximum thrust. As shown in the table, the maximum thrust is decreased by about 37-64%.

This small reduction in the average power is also followed by a reduction in average thrust. The F_T shows that the average thrusts when implementing a capping strategy in AR2000 are similar to the case without the capping. These results are confirmed by the example of the power and thrust variations with and without capping for the D24s12n$_s$1 scheme from the NLC1 array, as shown in Figure 6-22. Detail of the last neap-spring cycle is presented in Figure 6-23.

Table 6-11: Assessment result for 2MW turbines installed in Bali-Lombok sites

Schemes	Array	$\overline{P_1}$	$P_{1,max}$	$\frac{\overline{P_1}}{nt}$	$\frac{P_{1,max}}{nt}$	$\overline{T_1}$	$T_{1,max}$	$\frac{\overline{T_1}}{nt}$	$\frac{T_{1,max}}{nt}$	$\frac{\hat{P}}{\overline{P_1}}$	F_P	$F_{P,max}$	F_T	$F_{T,max}$	CF	α_4
		MW	*MW*	*MW*	*MW*	*MN*	*MN*	*kN*	*kN*							
D24s24n$_s$1	NLC1	19.27	95.26	0.39	1.91	6.94	27.02	138.71	540.30	4.65	0.94	0.32	0.73	0.37	0.20	0.4
	NLC2	19.32	123.90	0.32	2.06	10.64	39.57	177.35	659.55	6.09	0.95	0.49	1.00	0.54	0.16	0.3
	NPC1	27.46	122.52	0.46	2.04	11.62	37.41	193.63	623.46	4.13	0.93	0.43	0.93	0.53	0.22	0.3
	NPC2	22.14	114.36	0.38	1.97	9.98	33.44	172.04	576.51	4.93	0.95	0.59	0.95	0.62	0.19	0.3
	LC3	30.84	153.79	0.39	1.92	15.48	52.20	193.51	652.48	4.66	0.93	0.57	0.95	0.64	0.20	0.3
	LC4	29.58	153.46	0.37	1.92	15.18	49.98	189.80	624.78	4.88	0.94	0.61	0.95	0.63	0.19	0.3
D24s12n$_s$1	NLC1	24.10	136.35	0.37	2.10	12.61	42.52	193.95	654.15	5.03	0.89	0.35	0.96	0.43	0.18	0.3
	NLC2	25.52	151.01	0.33	1.94	14.72	49.74	188.71	637.66	5.56	0.94	0.45	1.02	0.51	0.17	0.3
	NPC1	37.33	156.71	0.47	1.96	16.17	50.70	202.11	633.72	3.82	0.91	0.38	0.91	0.50	0.24	0.3
	NPC2	29.88	154.20	0.39	2.03	13.73	45.68	180.71	601.04	4.93	0.95	0.58	0.96	0.61	0.19	0.3
	LC3	42.38	216.39	0.41	2.08	22.09	73.09	212.43	702.81	4.79	0.94	0.59	0.96	0.64	0.20	0.3
	LC4	40.68	216.74	0.39	2.08	21.73	70.79	208.95	680.72	5.03	0.94	0.63	0.97	0.64	0.19	0.3

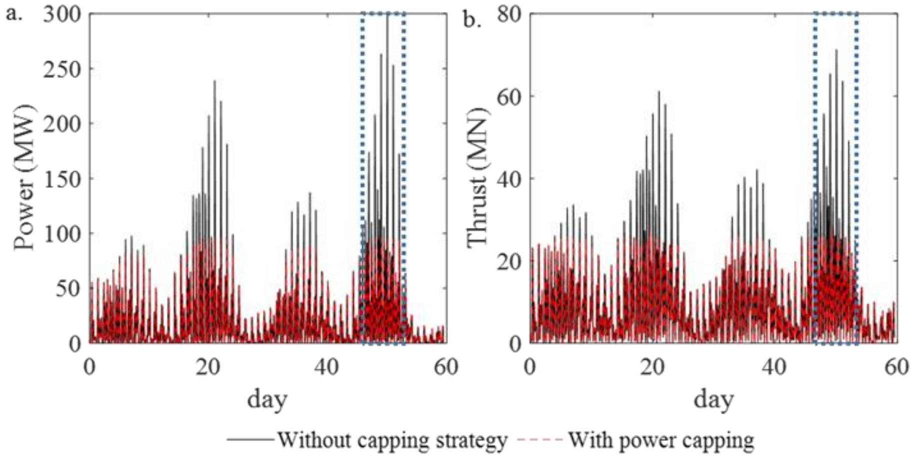

Figure 6-22: The power and thrust variation from the simulation with and without power capping strategy for D24s12ns1 scheme with α_4 = 0.4 in NLC1. (a. power, and b. thrust)

Furthermore, the application of power capping for AR2000 also increases the *CF* for this location. Previously, the *CF* in Bali-Lombok sites is only in the range of 0.07 - 0.13. The capacity factors increase to 0.17 – 0.23 when implementing power capping.

6.2.3 Sunda Strait Bridge

The realistic assessment for this site aims to explore the opportunity of tidal energy extraction with the bridge construction. Therefore, the thrust that is produced by the turbines is also important for the assessment here. The bridge structure is considered as the support structure for the turbines.

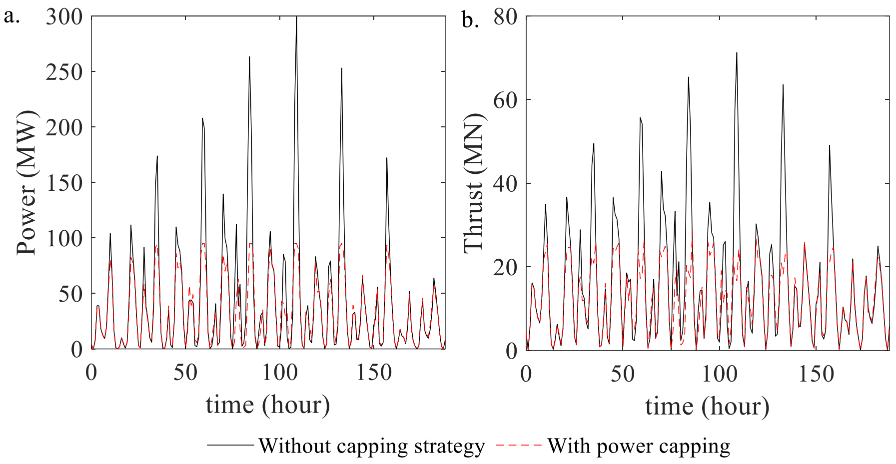

Figure 6-23: The last neap spring cycle of power and thrust variation from the simulation with and without power capping strategy for D24s12ns1 scheme with α_4 = 0.4 in NLC1. (Detail from dotted line boxes in Figure 6-22)

a) The Assessment without Capping Strategy

Two turbine sizes are used in this assessment, *D* = 24 m (D24) and *D* = 4 m (D4). The D24 turbine schemes are run with two options of tip-to-tip spacing 0.5 × *D* or 12 m and 1×*D* = 24 m. The D24 schemes have only one stacking layer (D24s24n_s1 and D24s12n_s1), while the D4 schemes are run with one tip-to-tip spacing only (*s* = 2 m). Two types of maximum stacking distinguish the D4 schemes, maximum of three turbines per stack (D4s2n_s3) and stacking set to the maximum at every element (D4s2$n_s$max).

The results summary shows that the segments of the bridge have different optimal turbine layouts. This preference is based on the total average power removed by the turbines per total area of turbines ($\frac{\overline{P_1}}{A_t}$). For instance, the D24 schemes (D24s24n_s1 and D24s12n_s1) give a higher $\frac{\overline{P_1}}{A_t}$ than the D4 schemes (D4s2n_s3 and D4s2$n_s$max) in the SS1 segment (see Table 6-12). The D24s24n_s1 scheme gives 248.52 W/m^2 while D4s2n_s3 only gives $\frac{\overline{P_1}}{A_t}$ of 183.42 W/m^2 and D4s2$n_s$max only gives 233.77 W/m^2. Meanwhile, the D4 schemes provide a better performance in terms of $\frac{\overline{P_1}}{A_t}$ than D24 for both alternatives of the SS2 bridge segment (SS2-1 and SS2-2).

However, in terms of total average power removed by the turbine ($\overline{P_1}$), the D4s2n$_s$max scheme gives a significantly higher P_1 than other schemes. However, this scheme requires installation of almost 20,000 4m diameter turbines. This scheme also shows a significantly higher $\overline{P_1}$ for the SS2-2's segment. This implies that rerouting the bridge alignment to the shallower area could almost double the power production.

Table 6-12: The summary of power and thrust from D24 and D4 turbines in the SSB

Schemes	**Seg.**	F_L	Ac	nt	B_G	$\overline{P_1}$	$P_{1,max}$	$\frac{\overline{P_1}}{nt}$	$\frac{P_{1,max}}{nt}$	$\frac{\overline{P_1}}{A_t}$	$\bar{T_1}$	$T_{1,max}$	$\frac{\bar{T_1}}{nt}$	$\frac{T_{1,max}}{nt}$	α_4	CF
		m	m^2	$unit$		(MW)	(MW)	(kW)	(kW)	(W/m^2)	(MN)	(MN)	(kN)	(kN)		
D24s24n$_s$1	SS1	4,993.40	215,508.50	100	0.21	11.70	81.80	116.95	818.03	258.52	10.67	56.96	106.66	569.55	0.40	0.14
	SS2-1	4,484.83	348,115.12	90	0.12	7.12	52.12	79.15	579.09	174.96	6.55	35.89	72.73	398.74	0.35	0.14
	SS2-2	6,046.10	221,653.73	119	0.24	19.47	123.61	163.62	1,038.76	361.68	15.56	79.47	130.74	667.83	0.39	0.16
D24s12n$_s$1	SS1	4,993.40	215,508.50	130	0.27	16.08	111.24	123.68	855.69	273.40	16.05	85.21	123.46	655.43	0.42	0.14
	SS2-1	4,484.83	348,115.12	117	0.15	9.88	71.90	84.43	614.55	186.62	9.52	52.97	81.38	452.75	0.36	0.14
	SS2-2	6,046.10	221,653.73	161	0.33	28.83	177.41	179.04	1,101.90	395.77	25.88	131.75	160.73	818.32	0.42	0.16
D4s2n$_s$3	SS1	9,570.27	319,648.51	4,671	0.18	10.77	71.25	2.30	15.25	183.42	10.31	52.89	2.21	11.32	0.37	0.15
	SS2-1	8,988.01	306,632.23	4,399	0.18	11.18	77.12	2.54	17.53	202.16	9.67	50.99	2.20	11.59	0.39	0.14
	SS2-2	7,972.99	445,035.18	3,818	0.11	37.35	215.57	9.78	56.46	778.57	23.42	110.52	6.14	28.95	0.42	0.17
D4s2n$_s$max	SS1	9,570.27	319,648.51	7,506	0.30	22.05	145.04	2.94	19.32	233.77	23.29	122.90	3.10	16.37	0.40	0.15
	SS2-1	8,988.01	306,632.23	7,138	0.29	34.10	228.80	4.78	32.05	380.12	38.22	204.00	5.36	28.58	0.40	0.15
	SS2-2	7,972.99	445,035.18	11,288	0.32	59.47	332.52	5.27	29.46	419.23	44.45	205.91	3.94	18.24	0.45	0.18

b) Detailed Assessment of the Bridge Segment

However, selection of the preceding options may not be wise if the decision is merely determined by power production. As the plan is to install the turbines on the bridge structure, the turbines' maximum thrust is also essential since this thrust will affect the bridge's construction cost.

Therefore, it would be beneficial to investigate the detailed thrust in each element from the simulation. The D24 turbines only occupy half of the channel, while the D4 occupies almost the entire segment. Figure 6-24 presents details of the elements, with 24 m diameter turbines installed at e1.1 – e1.10 in SS1 and D4 turbines are installed in most of the elements. A similar arrangement is also shown in the SS2-1 and SS2-2 segments. The D24 turbines only occupy the deeper part of the channel.

The average and maximum thrust are investigated here to understand the complexity of the decision-making process for installing the turbines to the bridge structure. The comparison of the average power and the maximum thrust in each segment for SS1 is presented in Figure 6-25. The bar chart shows that the turbine size decision may not be as simple as a selection based on the average power or capacity factor.

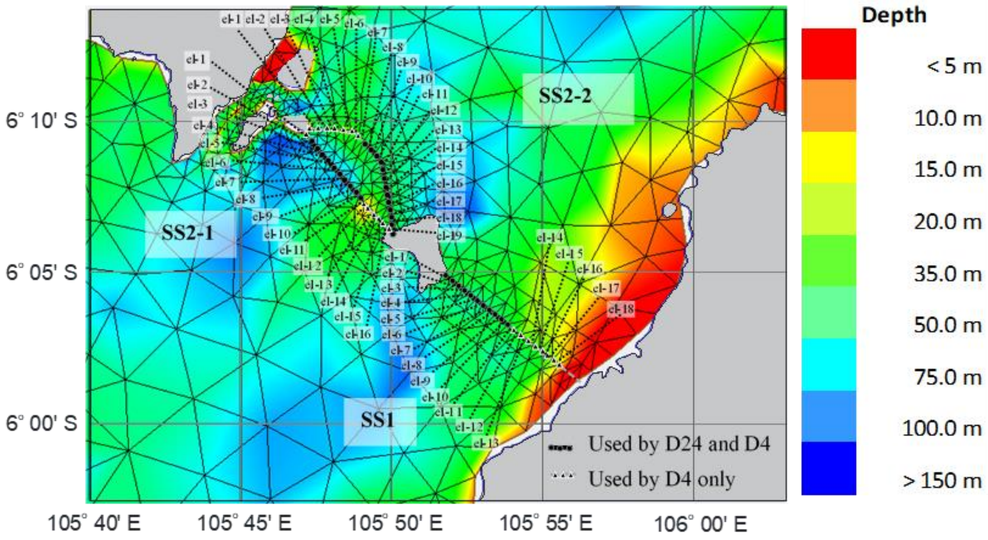

Figure 6-24: Detail of mesh elements and bathymetry in the vicinity of Sunda Strait

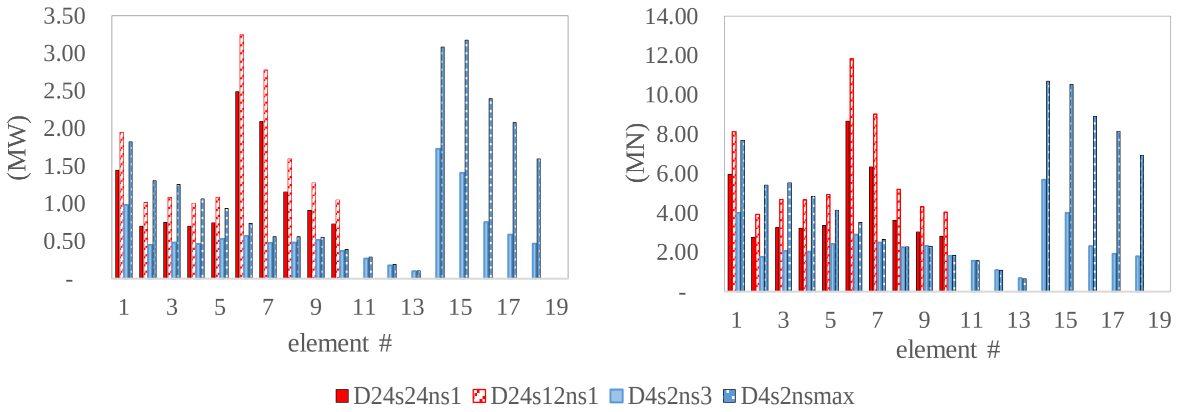

a. Average Power

b. Maximum Thrust

Figure 6-25: Average power and maximum thrust for each element of turbines deployment in SS1 section of SSB

For instance, installing approximately 7,500 turbines in D4s2$n_s$max gives a total of 22.05 MW $\overline{P}_1$, while the D24s12n_s1 scheme produces a total average power of 16 MW from just 130 turbines. However, the total average power varies along the SS1 bridge span. As shown in Figure 6-25, the average power for D24s12n_s1 peaks in the middle of the SS1 bridge span, while D4s2nsmax peaks in the channel's shallow area. The turbines do not occupy this area for D24s12n_s1.

In consequence, these $\overline{P}_1$ variations give similar maximum thrusts for both schemes. The D24s12n_s1 scheme gives maximum thrust at el.6 and el.7 following the variation of $\overline{P}_1$. Meanwhile, the peak of maximum thrust for D4s2$n_s$max occurs at at el.15-17. This maximum thrust variation shows the D24s12n_s1 and D4s2$n_s$max schemes exert a similar load on the bridge span. However, the peak values of $T_{1,max}$ occur in shallow water for D4s2n$_s$max, but in deeper water for D24s2n$_s$1. In this case, D4s2n$_s$max has an advantage over D24s12n$_s$1, because having a stronger bridge pile in the shallow water is relatively less costly than in the deeper water.

A similar investigation is applied at SS2-1 and SS2-2 in terms of the D24s12n$_s$1 and D4s2n$_s$max schemes. For instance, D4s2n$_s$max gives better power production than D24s12n$_s$1 in SS2-1. Based on the total $\overline{P}_1$, as shown in Table 6-12, the 117 turbines in the D24s12n$_s$1 scheme give $\overline{P}_1$ of 9.88 MW while D4s2n$_s$max produces three times the $\overline{P}_1$ from D24s12n$_s$1. However, the D4s2n$_s$max scheme requires 7,138 turbines to provide 34.10 MW of total average power ($\overline{P}_1$). The $\overline{P}_1$ variation for the D4s2n$_s$max peaks at one location along the bridge segment, while D24s12n$_s$1 has two peaks (see Figure 6-26.a). The $\overline{P}_1$ on el.3 is almost twice the $\overline{P}_1$ at other elements. Therefore, selecting the D4s2n$_s$max scheme will give a broader variation in power production than D24s12n$_s$1.

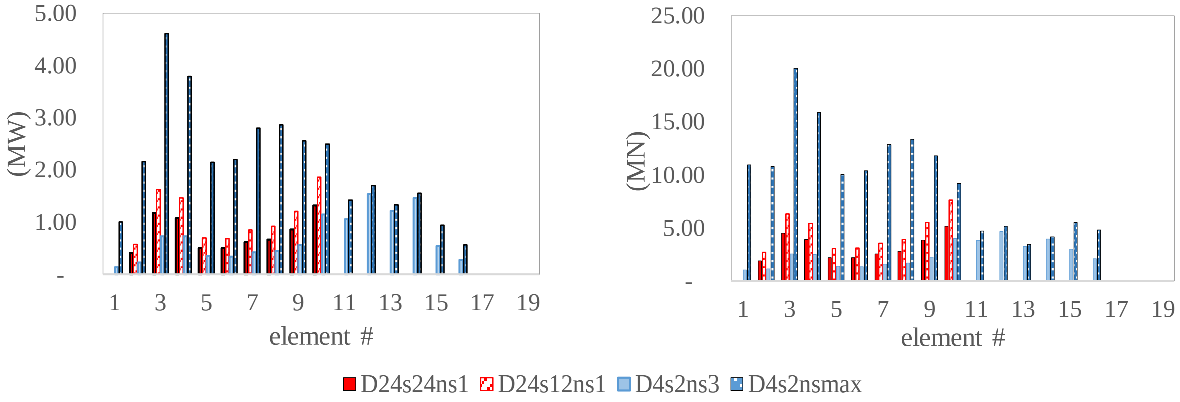

a. Average Power

b. Maximum Thrust

Figure 6-26: Histograms of average power and maximum thrust with each element of turbines deployed in the SS2-1 section of SSB.

Another consequence is the D4s2n$_s$max scheme has three times the maximum thrust on the bridge span. The peak of $T_{1,max}$ variation for D4s2n$_s$max at el.3 reaches 20 MN, while D24s12n$_s$1 only has approximately 7.6 MN at el.10 (see Figure 6-26b). This $T_{1,max}$ could make the cost of the bridge structure increase significantly if the D4s2n$_s$max scheme is applied on the SS1 bridge segment.

Meanwhile, D4s2n$_s$max has more advantages than D24s12n$_s$1 in SS2-2. Due to the bathymetry, D24s12n$_s$1 cannot occupy the entire SS2-2 bridge segment, while D4s2n$_s$max could install turbines at most of the bridge's segments. At the elements where the D24s12n$_s$1 scheme does not exist, D4s2n$_s$max produces more power than D24s12n$_s$1 (see Figure 6-27a). The D4s2n$_s$max scheme scheme produces twice the total $\overline{P}_1$ than the D24s12n$_s$1 scheme. Meanwhile, the highest $T_{1,max}$

variation across the bridge segments of the D4s2$n_s$max scheme is slightly lower than for D24s12n_s1 (see Figure 6-27b).

These figures and comparisons of D24s12n_s1 and D4s2$n_s$max show that the D4s2$n_s$max scheme could maximise the power production from the area that supposedly has less power potential, since it is an area of less energetic flow. To understand how D4s2$n_s$max could produce more power in such an area, again, we could find an explanation from the flow field change. The comparisons of the average flow field change from D24s12n_s1 and D4s2$n_s$max on each bridge segment are presented in Figure 6-28.

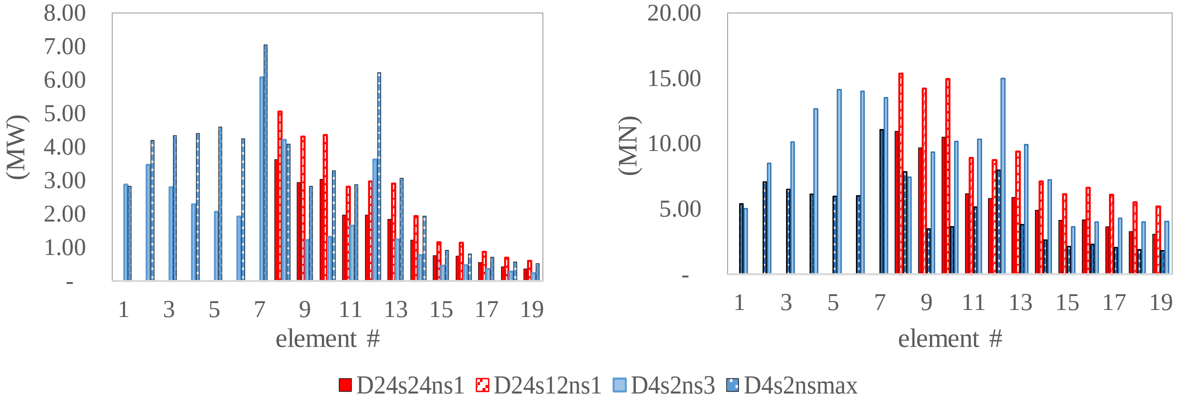

a. Average Power b. Maximum Thrust

Figure 6-27: Histograms of average power and maximum thrust with each element of turbines deployed in the SS2-2 section of SSB.

The average flow-field changes of both schemes (D24s12n_s1 and D4s2$n_s$max) in the SS1 segment are positive in the shallow area near the Java coastline. This means that the flow in that area is accelerated when the turbines are introduced to the flow. The high power of the D4s2$n_s$max scheme in the elements near to Java's coastline, as shown in Figure 6-24, occurs when this acceleration is present (see Figure 6-28.1).

A similar pattern is also observed at SS2-1 and SS2-2. The increased velocity in the flow-field gives high power production for the D4s2$n_s$max scheme. Occupying the segments near Sangiang Island, as shown in SS2-1, pushes the flow to increase in the middle part of the channel (see Figure 6-28.2.b). Therefore, the power peaks at that element.

The flow field change in SS2-2 for the D24s12n_s1 scheme shows that the flow tends to decelerate in the area with the turbines (see Figure 6-28.3.a). As this scheme does not have turbines over the entire bridge segment, a positive flow field change is observed in the bypass flow area. Meanwhile, the D4s2$n_s$max scheme occupies most of the bridge segment and presents an area near the Sangiang island with a positive average flow field change. That section has the peak power production along the bridge segment.

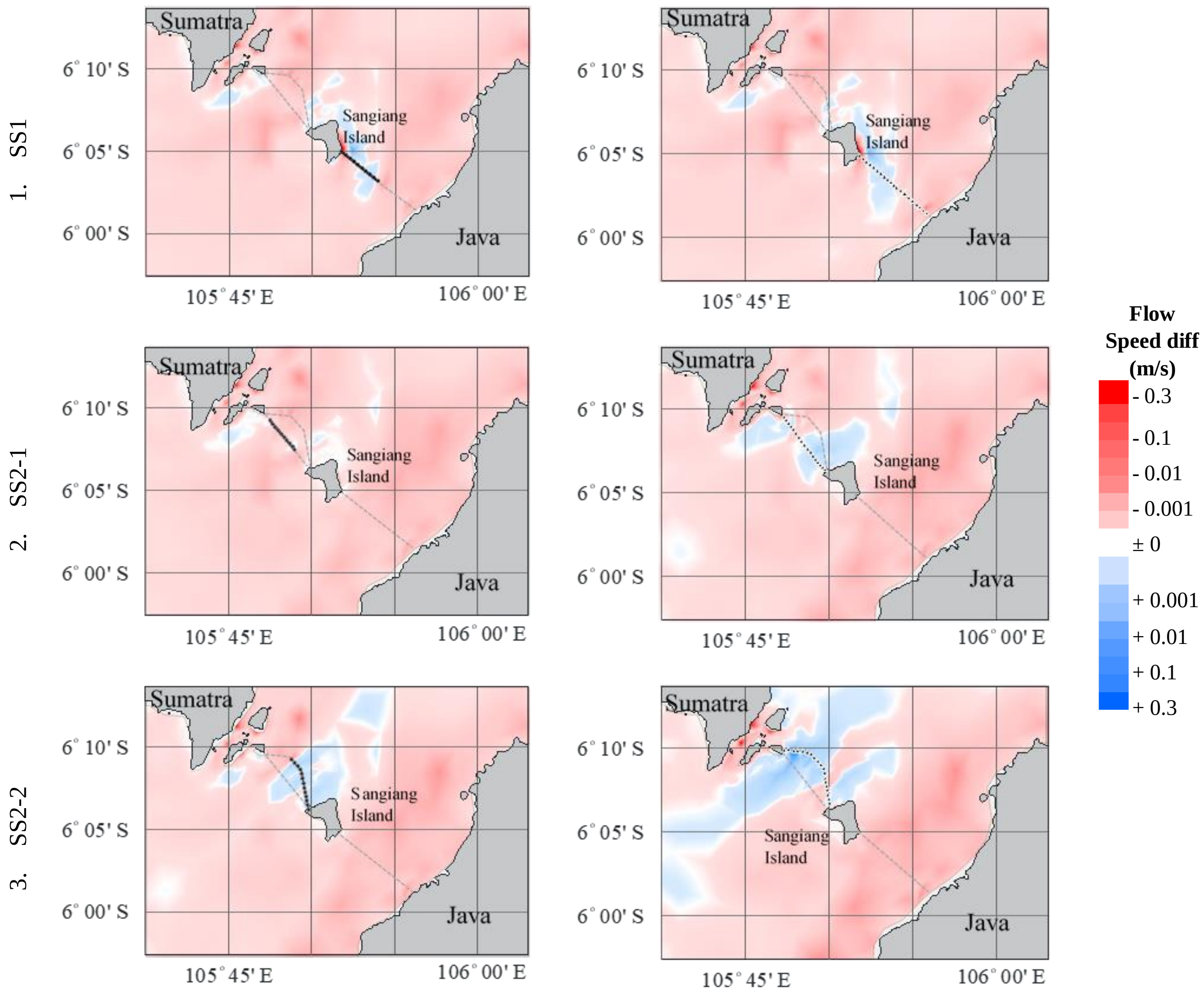

a. D24s12n_s1 b. D4s4$n_s$max

Figure 6-28: The average flow-field changes for each turbine scheme in the bridge segments for D24s12ns1 and D4s4nsmax schemes showing the impact of the turbines on the regional flow.

The selection of an alternative alignment on the second bridge segment (SS2-1 or SS2-2) can also be conducted by looking at the of $\overline{P}_1$ and $T_{1,max}$ along the span. As shown in Figure 6-27b, the highest $T_{1,max}$ of 15 MN is produced from D4s2$n_s$max for alternative 2 of the second bridge segment (SS2-2), while at SS2-1 the highest $T_{1,max}$ from the same scheme is 20 MN. Therefore, this shows that having a longer bridge route in SS2-2 does not just give a significantly higher $\overline{P}_1$, it also gives a lower $T_{1,max}$.

c) Capping Strategies

As it represents an area with a diurnal flow pattern, both power capping and thrust capping strategy are applied in this location. The examples of power and thrust variations for the D4s2$n_s$max scheme in el.1 of the SS2-1 bridge segment are shown in Figure 6-29 (with the last two cycles is presented in Figure 6-30) for power capping, and Figure 6-31 for thrust capping (detail for the last two cycles are presented in Figure 6-32). The summary of the power capping strategy in the SSB segment is presented in Table 6-13, and the summary of thrust capping is shown in Table 6-14.

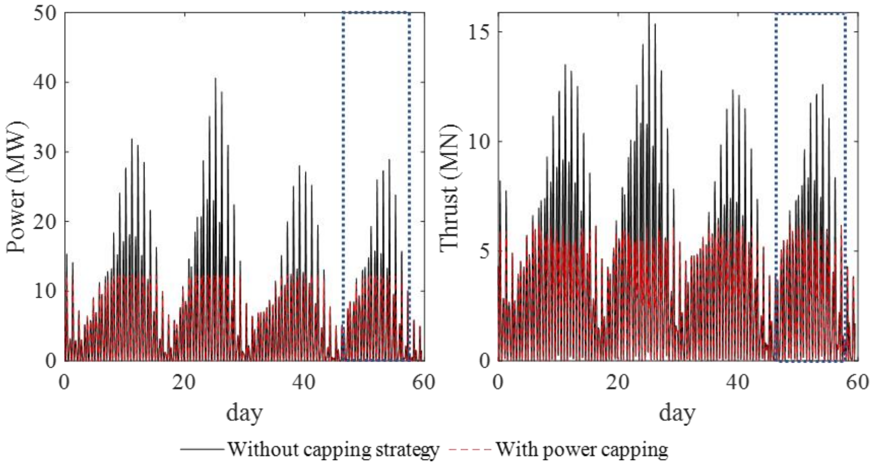

Figure 6-29: The power and thrust variation of the simulation with and without thrust capping strategy of D24s12n$_s$1 scheme with α_4 = 0.4 in SS2-2, el 1.

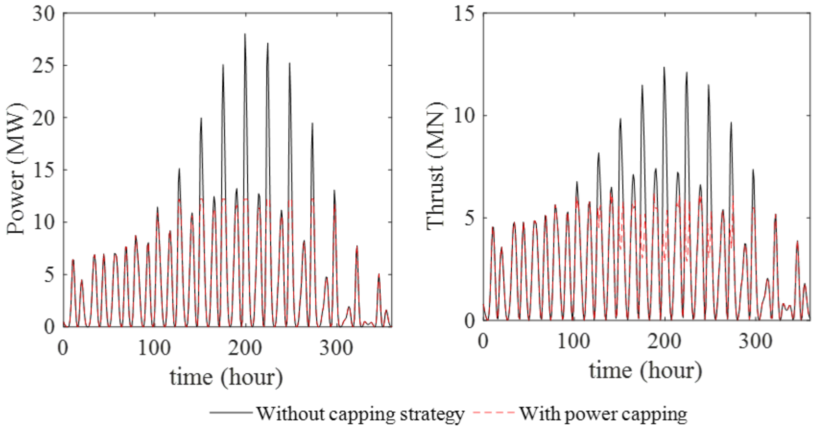

Figure 6-30: The power and thrust variation of last neap spring cycle corresponding to blue dotted lines in Figure 6-29.

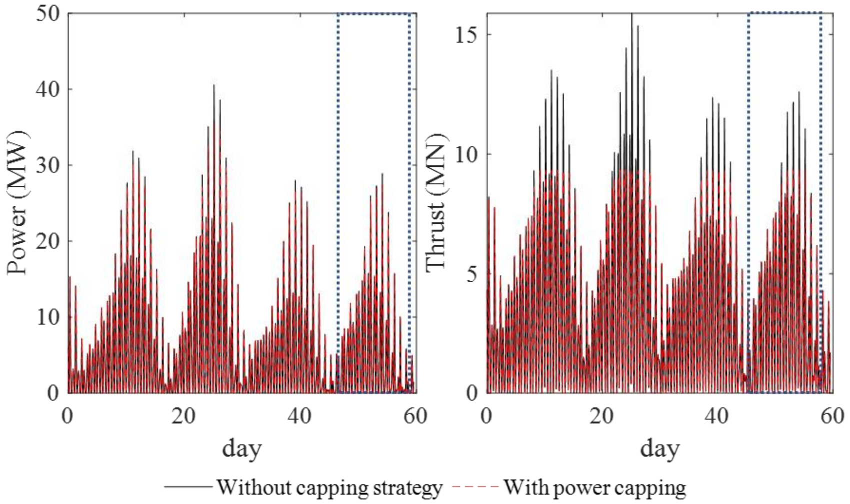

Figure 6-31: The power and thrust variation of the simulation with and without thrust capping strategy of D4s2n$_s$max scheme with α_4 = 0.4 in SS2-2, el 1.

These summaries show that the power capping strategy increases the capacity factors slightly more than the thrust capping strategy. For instance, the power capping strategy for the D4s2n$_s$max scheme increases the *CF* from 0.15-0.18 to 0.18-0.24 (see Table 6-13), while the thrust capping strategy only increases it to 0.16-0.21(see Table 6-14).

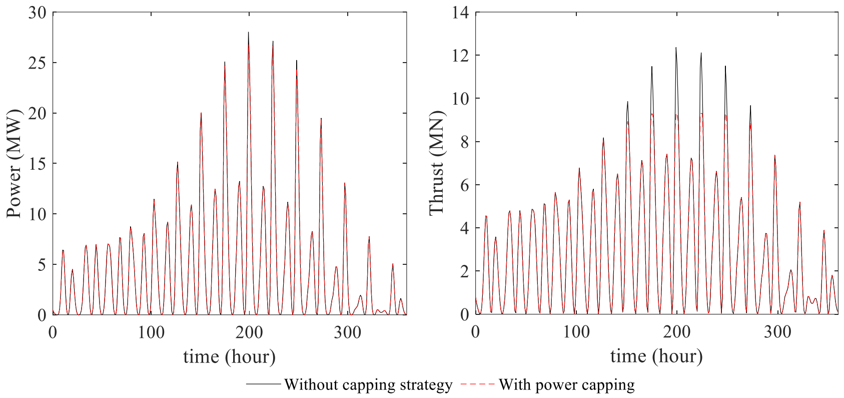

Figure 6-32: The power and thrust variation of last neap spring cycle slightly more than the thrust capping strategy in Figure 6-31.

Table 6-13: Summary of simulations with the power capping strategy in SSB

Schemes	**Seg.**	$\overline{P_1}$ (MW)	$P_{1,max}$ (MW)	$\frac{\overline{P_1}}{nt}$ (kW)	$\frac{P_{1,max}}{nt}$ (kW)	$\frac{\overline{P_1}}{A_t}$ (W/m^2)	$\overline{T_1}$ (MN)	$T_{1,max}$ (MN)	$\frac{\overline{T_1}}{nt}$ (kN)	$\frac{T_{1,max}}{nt}$ (kN)	$\frac{\widehat{P_1}}{\overline{\overline{P_1}}}$	F_p	F_T	$F_{T,max}$	α_4	*CF*
D24s24n$_s$1	SS1	10.45	47.09	104.50	470.94	231.00	9.50	24.53	94.96	245.26	4.03	0.89	0.89	0.43	0.38	0.2
	SS2-1	6.85	38.91	76.11	432.38	168.24	6.25	19.63	69.45	218.14	5.46	0.96	0.95	0.55	0.34	0.1
	SS2-2	15.05	57.99	126.46	487.33	279.53	12.02	30.94	101.01	260.01	2.98	0.77	0.77	0.39	0.38	0.2
D24s12n$_s$1	SS1	15.71	82.90	120.81	637.71	267.05	15.55	60.70	119.64	466.90	5.16	0.98	0.97	0.71	0.42	0.1
	SS2-1	9.86	67.11	84.28	573.62	186.30	9.49	41.15	81.08	351.71	6.79	1.00	1.00	0.78	0.36	0.1
	SS2-2	26.57	133.66	165.01	830.20	364.75	23.80	108.16	147.80	671.80	4.64	0.92	0.92	0.82	0.41	0.2
D4s2n$_s$3	SS1	10.16	53.03	2.18	11.35	173.13	9.82	31.97	2.10	6.84	4.93	0.94	0.95	0.60	0.36	0.1
	SS2-1	10.37	50.76	2.36	11.54	187.66	8.75	21.76	1.99	4.95	4.54	0.93	0.91	0.43	0.38	0.2
	SS2-2	24.73	74.74	6.48	19.57	515.54	15.11	27.82	3.96	7.29	2.00	0.66	0.65	0.25	0.38	0.3
D4s2n$_s$max	SS1	21.91	125.04	2.92	16.66	232.27	23.05	80.47	3.07	10.72	5.67	0.99	0.99	0.91	0.40	0.1
	SS2-1	34.04	224.82	4.77	31.50	379.46	38.12	149.01	5.34	20.87	6.59	1.00	1.00	0.97	0.40	0.1
	SS2-2	54.18	221.29	4.80	19.60	381.97	39.58	111.60	3.51	9.89	3.72	0.91	0.89	0.67	0.43	0.2

Table 6-14: Summary of simulations with the thrust capping strategy in SSB

Schemes	**Seg.**	$\overline{P_1}$ (MW)	$P_{1,max}$ (MW)	$\frac{\overline{P_1}}{nt}$ (kW)	$\frac{P_{1,max}}{nt}$ (kW)	$\frac{\overline{P_1}}{A_t}$ (W/m^2)	$\overline{T_1}$ (MN)	$T_{1,max}$ (MN)	$\frac{\overline{T_1}}{nt}$ (kN)	$\frac{T_{1,max}}{nt}$ (kN)	$\frac{\widehat{T_1}}{\overline{\overline{T_1}}}$	F_p	F_T	$F_{T,max}$	α_4	*CF*
D24s24n$_s$1	SS1	11.66	76.02	116.60	760.18	10.50	10.50	34.47	104.95	344.66	3.23	1.00	0.98	0.80	0.39	0.15
	SS2-1	7.10	49.42	78.87	549.15	6.46	6.46	25.43	71.79	282.55	3.88	1.00	0.99	0.87	0.35	0.14
	SS2-2	19.30	106.98	162.20	898.98	15.21	15.21	55.52	127.80	466.52	3.57	0.99	0.98	0.77	0.39	0.18
D24s12n$_s$1	SS1	16.07	107.76	123.62	828.96	15.84	15.84	50.78	121.85	390.60	3.16	1.00	0.99	0.84	0.41	0.15
	SS2-1	9.85	68.73	84.18	587.43	9.38	9.38	36.29	80.13	310.17	3.81	1.00	0.98	0.88	0.35	0.14
	SS2-2	28.69	162.43	178.22	1,008.90	25.47	25.47	87.88	158.21	545.86	3.40	1.00	0.98	0.81	0.41	0.18
D4s2n$_s$3	SS1	10.18	51.79	2.18	11.09	173.38	9.48	28.30	2.03	6.06	2.75	0.95	0.92	0.66	0.36	0.20
	SS2-1	10.22	55.56	2.32	12.63	184.93	8.07	22.31	1.83	5.07	2.31	0.91	0.83	0.56	0.36	0.18
	SS2-2	27.03	102.59	7.08	26.87	563.38	14.40	29.10	3.77	7.62	1.24	0.72	0.61	0.31	0.37	0.26
D4s2n$_s$max	SS1	21.92	131.11	2.92	17.47	232.35	22.68	74.51	3.02	9.93	3.20	0.99	0.97	0.84	0.39	0.17
	SS2-1	33.95	217.24	4.76	30.43	378.44	37.04	127.88	5.19	17.92	3.35	1.00	0.97	0.83	0.39	0.16
	SS2-2	55.63	259.54	4.93	22.99	392.20	37.29	90.44	3.30	8.01	2.03	0.94	0.84	0.54	0.41	0.21

Both power capping and thrust capping strategies are able to keep the average power removed by turbines at the same level as without a capping strategy. The D4s2n$_s$max scheme shows the F_P, for both capping strategies, is in the range of 0.94-1.0. Therefore, based on *CF*, the power capping strategy gives a greater advantage. However, if we consider the maximum thrust, the thrust capping strategy gives lower $F_{T,max}$ than power capping. Based on these facts, the thrust capping is more advantageous for the D4s2n$_s$max turbine scheme compared to the SSB structure.

Figure 6-33 presents the detailed distribution of $\overline{P_1}$ and $T_{1,max}$ along the span, for the power and thrust capping strategies for the D4s2n$_s$max scheme. These details show that thrust capping could reduce the maximum thrusts at every element significantly. Based on this comparison, the thrust capping strategy is more advantageous than the power capping strategy. For example, the maximum thrusts on SS2-2 are lower for almost every element.

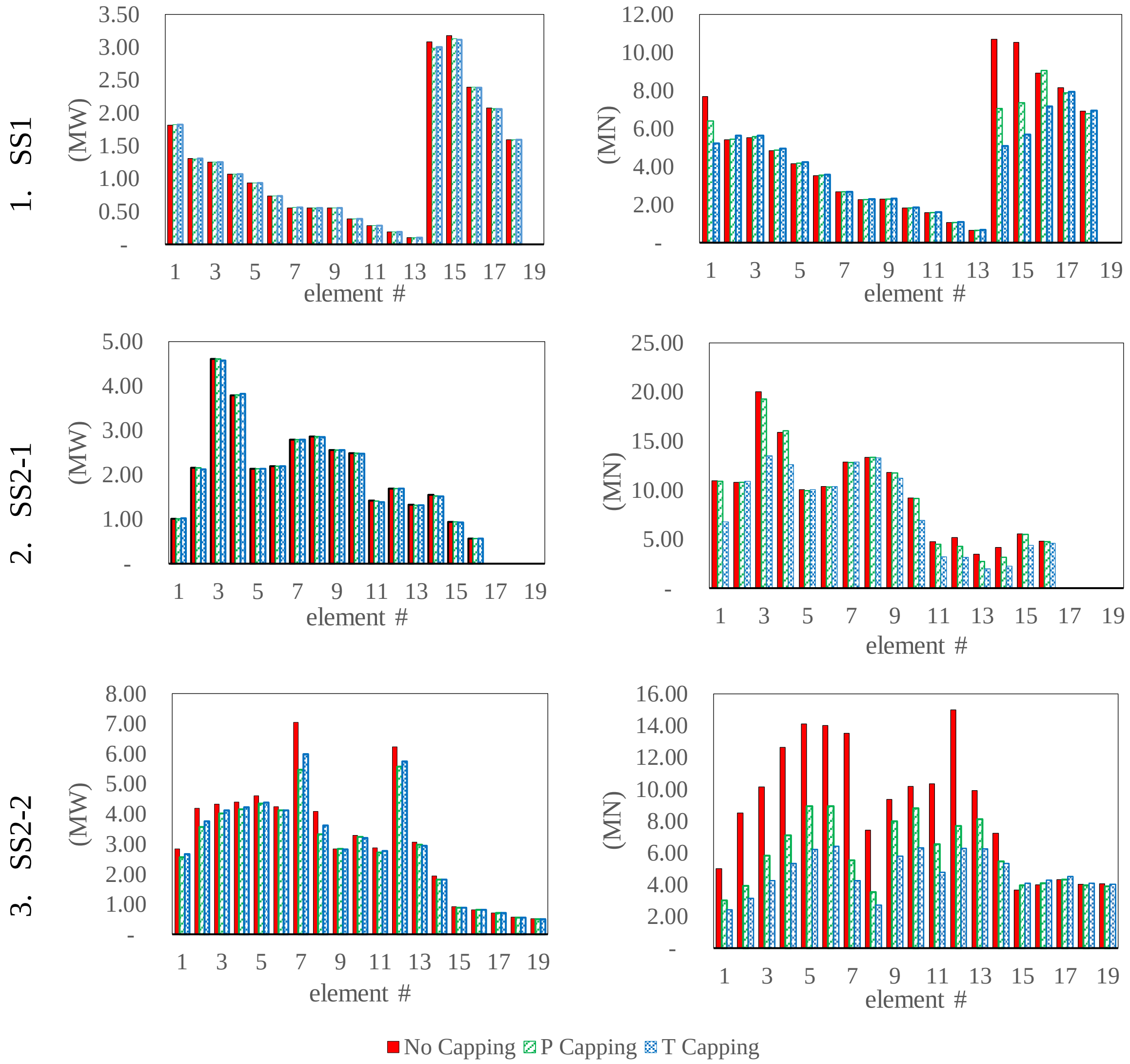

a. Average power b. Maximum thrust

Figure 6-33: Histograms of average power and maximum thrust with each element for capping strategies in D4s2n$_s$max scheme in the SSB

6.2.4 Lingga Regency

The assessments for this location are undertaken to investigate the possibility of using other resources to support an existing unreliable power plant. Based on the SAIDI and SAIFI, as discussed in Chapter 1, the population of Lingga has access to electricity for an average of only 12 hours per day. Therefore, a hybrid system between fossil fuel-based power plant and tidal turbines might help remedy this problem. Based on the population, the demand in this area is approximately 8 MW.

a) *Realistic Turbine Deployment Based Assessment in Lingga Regency*

Two of the potential sites from each strait in Chapter 5 (Temiang1 and Dasi1) are selected for the assessment here. The assessment in the Lingga Regency site aims to explore the opportunity for deployment of small size turbines. Therefore, two turbine sizes, *D* = 4 m (D4) and *D* = 7 m (D7), are selected for this assessment. Four turbine schemes (D4s4n$_S$1, D7s7n$_S$1, D4s2n$_S$3, and D7s3n$_S$1) are analysed. The summary of results of the assessment using these schemes is presented in Table 6-15, showing that there is a possibility to generate approximately 8 MW average power from the tidal stream. The D7s3n$_S$2 scheme gives a total average power for both Temiang1and Dasi1 of 8.8 MW.

b) *Capping Strategy Implementation*

The power capping strategy implementation in this location shows that F_P could be maintained at 0.9 with a significant reduction of maximum thrust. For instance, D7s7n$_S$1 and D4s4n$_S$1 at Dasi 1 have F_P values of 0.96 and 0.95, respectively, with $F_{T,max}$ of 0.69 and 0.62 (see Table 6-16). However, this strategy only gives capacity factors of 0.25 and for the D7s7n$_S$1 and 0.26 for the D4s4n$_S$1.

Table 6-15: Summary of realistic cases in Lingga Regency

Schemes	**Seg.**	F_L (m)	Ac (m^2)	n_t (units)	B_G	B_L	$\overline{P_1}$ (MW)	$P_{1,max}$ (MW)	$\frac{\overline{P_1}}{nt}$ (kW)	$\frac{P_{1,max}}{n_t}$ (kW)	$\bar{T_1}$ (MN)	$T_{1,max}$ (MN)	$\frac{\overline{T_1}}{nt}$ (kN)	$\frac{T_{1,max}}{n_t}$ (kN)	$\frac{\overline{P_1}}{A_t}$ (kW/m^2)	α_4	CF
D7s7n$_s$1	Temiang 1	2,592.16	27,231.30	181	0.22	0.26	3.52	15.87	19.44	87.66	2.73	8.04	15.09	44.45	0.51	0.39	0.22
	Dasi 1	1,345.28	31,045.26	95	0.12	0.12	0.89	5.00	9.34	52.68	0.66	2.47	6.90	26.05	0.24	0.34	0.18
D4s4n$_s$1	Temiang 1	2,592.16	32,235.78	395	0.15	0.15	1.83	8.16	4.64	20.65	1.28	4.10	3.24	10.38	0.37	0.35	0.22
	Dasi 1	1,345.28	31,045.26	165	0.07	0.07	0.47	2.62	2.83	15.91	0.32	1.23	1.96	7.48	0.23	0.34	0.18
D7s3n$_s$2	Temiang 1	2,592.16	27,231.30	255	0.30	0.36	5.62	25.30	22.03	99.20	4.98	13.59	19.52	53.30	0.57	0.43	0.22
	Dasi 1	1,345.28	31,045.26	233	0.29	0.29	3.20	18.98	13.74	81.45	3.02	10.90	12.95	46.76	0.36	0.39	0.17
D4s2n$_s$3	Temiang 1	3,175.55	32,235.78	528	0.21	0.21	2.63	11.68	4.98	22.12	1.96	6.14	3.71	11.62	0.40	0.37	0.23
	Dasi 1	1,345.28	31,045.26	608	0.25	0.25	2.42	14.16	3.99	23.29	2.13	7.84	3.50	12.89	0.32	0.37	0.17

A slightly higher *CF* is obtained in Tamiang 1. Both the D7s7n$_s$1 and D4s4n$_s$1 schemes show that *CF* values of 0.35 and 0.32 are obtained by setting F_P to 0.83 and 0.85. These capping limits give $F_{T,max}$ of 0.57 and 0.60. This means the maximum thrust reductions in Tamiang 1 are only slightly lower than in Dasi 1.

Therefore, the capping limits for the D7s3n$_s$2 and D4s2n$_s$3 schemes are set so that F_P is as close as possible to 0.9. By setting the capping limit of $\frac{\hat{P}}{\overline{P_1}}$ slightly higher than in previous schemes, the power capping strategy of the D7s7n$_s$1 and D4s4n$_s$1schemes shows that the corresponding values of power factor are close to 0.9. This power capping limit leads to reductions in average thrust by 5-14% and in maximum thrust by 24-49% compare to previous simulations without capping.

Table 6-16: Summary of assessment with power capping strategy in Lingga Regency

Schemes	**Seg.**	$\overline{P_1}$ (MW)	$P_{1,max}$ (MN)	$\frac{\overline{P_1}}{nt}$ (kW)	$\frac{P_{1,max}}{n_t}$ (kN)	$\overline{T_1}$ (MN)	$T_{1,max}$ (MN)	$\frac{\overline{T_1}}{nt}$ (kN)	$\frac{T_{1,max}}{n_t}$ (kN)	$\frac{\hat{P}}{\overline{P_1}}$	F_P	$F_{P,max}$	F_T	$F_{T,max}$	α_4	CF
D7s7n$_s$1	Temiang 1	2.92	8.45	16.12	46.66	2.12	4.61	11.70	25.44	2.40	0.83	0.53	0.78	0.57	0.38	0.35
	Dasi 1	0.85	3.33	8.93	35.06	0.62	1.70	6.51	17.93	3.76	0.96	0.67	0.94	0.69	0.34	0.25
D4s4n$_s$1	Temiang 1	1.56	4.92	3.95	12.45	1.05	2.47	2.67	6.24	2.68	0.85	0.60	0.82	0.60	0.35	0.32
	Dasi 1	0.44	1.74	2.70	10.55	0.29	0.76	1.75	4.62	3.73	0.95	0.66	0.89	0.62	0.43	0.26
D7s3n$_s$2	Temiang 1	5.16	17.22	20.23	67.54	4.34	9.27	17.00	36.36	3.07	0.92	0.68	0.87	0.68	0.42	0.30
	Dasi 1	3.07	13.06	13.17	56.05	2.87	8.30	12.31	35.64	4.08	0.96	0.69	0.95	0.76	0.33	0.23
D4s2n$_s$3	Temiang 1	2.34	7.76	4.42	14.69	1.68	3.99	3.18	7.55	2.95	0.89	0.66	0.86	0.65	0.36	0.30
	Dasi 1	2.27	8.56	3.74	14.08	1.19	4.01	1.96	6.59	3.53	0.94	0.60	0.56	0.51	0.40	0.27

More importantly, this power capping strategy for the D7s3n$_s$2 scheme could maintain both arrays (Temiang 1 and Dasi 1) with a total average power of 8 MW as required by the Lingga Regency to increase SAIDI and SAIFI.

6.2.5 Sula Regency

The assessments based on realistic turbine deployment in Sula Regency are implemented in three locations, Capalulu strait, The Mangole strait and Lifamatola headland. Similar to the Lingga Regency, Sula Regency also represents a location with marginal demand.

a) Turbine Deployment in Sula Regency

Three different turbine sizes, *D* = 24 m, *D* = 10 m and *D* = 4 m, are used in the assessment here. The assessment is conducted with the tip-to-tip spacing between the turbines equal to the diameter (*s* = *D*). The summary of the assessments presented in Table 6-17 shows that the D10s10n$_s$1 scheme performs better than other schemes (based on the average power removed by turbines per total area of the turbines—$\frac{\overline{P_1}}{A_t}$) in the Capalulu (Cp1) and Mangole Strait (Mg). Conversely, the D4s4nsmax scheme is the best option for Lifamatola Headland (LH2), also based on $\frac{\overline{P_1}}{A_t}$.

However, the D10s10n$_s$1 scheme removes significantly less total power compared to other schemes in all arrays. For instance, the 21 turbines of the D10s10n$_s$1 scheme only remove an average of 3.98 MW in Cp1, while the eight turbines of the D24s24ns1 scheme could remove an average of 6.51 MW. This number corresponds to the global blockage ratio (B_G) and local blockage (B_L). Both of B_G and B_L on the D10s10n$_s$1 scheme are smaller than in other schemes.

Table 6-17: Summary of the assessment based on realistic turbine deployment in Sula Regency

Turbines Schemes	**Loc**	F_L (m)	Ac (m^2)	nt (unit)	B_G	B_L	$\overline{P_1}$ (MW)	$P_{1,max}$ (MW)	$\frac{\overline{P_1}}{nt}$ (kW)	$\frac{P_{1,max}}{nt}$ (MW)	$\frac{\overline{P_1}}{A_t}$ kW/m^2	$\overline{T_1}$ (MN)	$T_{1,max}$ (MN)	$\frac{\overline{T_1}}{nt}$ (kN)	$\frac{T_{1,max}}{nt}$ (MN)	α_4	CF
D24s24n$_s$1	Cp1	420.79	14,446.06	8	0.11	0.25	6.51	32.07	814.69	4.01	1.80	3.58	10.68	447.35	1.86	0.39	0.20
	Mg	1,590.61	61,766.71	33	0.13	0.24	7.72	52.24	234.40	1.58	0.52	5.91	22.39	178.96	0.94	0.41	0.15
	LH2	3,534.10	368,410.89	71	0.08	0.09	20.35	198.61	287.22	2.80	0.63	9.20	50.27	129.60	0.94	0.43	0.10
D10s10n$_s$1	Cp1	420.79	14,446.06	21	0.05	0.11	3.98	19.61	189.69	0.93	2.41	1.86	6.10	54.34	0.22	0.35	0.20
	Mg	1,590.61	61,766.71	78	0.05	0.10	4.40	28.18	56.52	0.36	0.72	2.85	11.39	22.46	0.12	0.35	0.16
	LH2	3,534.10	368,410.89	171	0.04	0.04	9.30	91.75	54.47	0.54	0.69	4.26	24.50	22.89	0.15	0.34	0.10
D4s4nsmax	Cp1	1,167.23	33,395.18	340	0.13	0.13	6.97	34.45	20.51	0.10	1.63	3.28	10.44	9.65	0.03	0.36	0.20
	Mg	3,711.41	100,777.38	1254	0.14	0.16	7.43	47.02	5.92	0.04	0.47	5.15	19.82	4.11	0.02	0.37	0.16
	LH2	3,599.36	378,770.70	5376	0.18	0.18	57.59	535.34	10.71	0.10	0.85	32.87	160.64	6.11	0.03	0.40	0.11

This summary again demonstrates the complexity of relating B_L and B_G to power removed by the turbines. The D4s4n$_s$max scheme removed a slightly higher power than D24s24n$_s$1 in Cp1, although the D24s24n$_s$1 scheme has a significantly higher B$_L$ than D4s4n$_s$max at this location. Nevertheless, the D4s4n$_s$max only has a slightly higher B_G than D24s24n$_s$1 at this location. In this case, B_G is relatively more important than B_L.

In contrast, D24s24n$_s$1 has a slightly higher $\overline{P}_1$ than D4s4n$_s$max in the Mangole strait (Mg). Notwithstanding, the B_G of D4s4n$_s$max at this location is slightly higher than in D24s24n$_s$1. At the same time, we could see that D24s24n$_s$1 has a higher B_L than D4s4n$_s$max in this location. The D24s24n$_s$1 scheme does not occupy the entire cross-section of the channel in Cp1. However, comparing the average flow field between D24s24n$_s$1 and D4s4nsmax shows a positive change in the area of bypass flow for both turbine schemes (see Figure 6-34). Therefore, an explanation based on the advantage of having a positive velocity difference in the flow field change might not be applicable for this case.

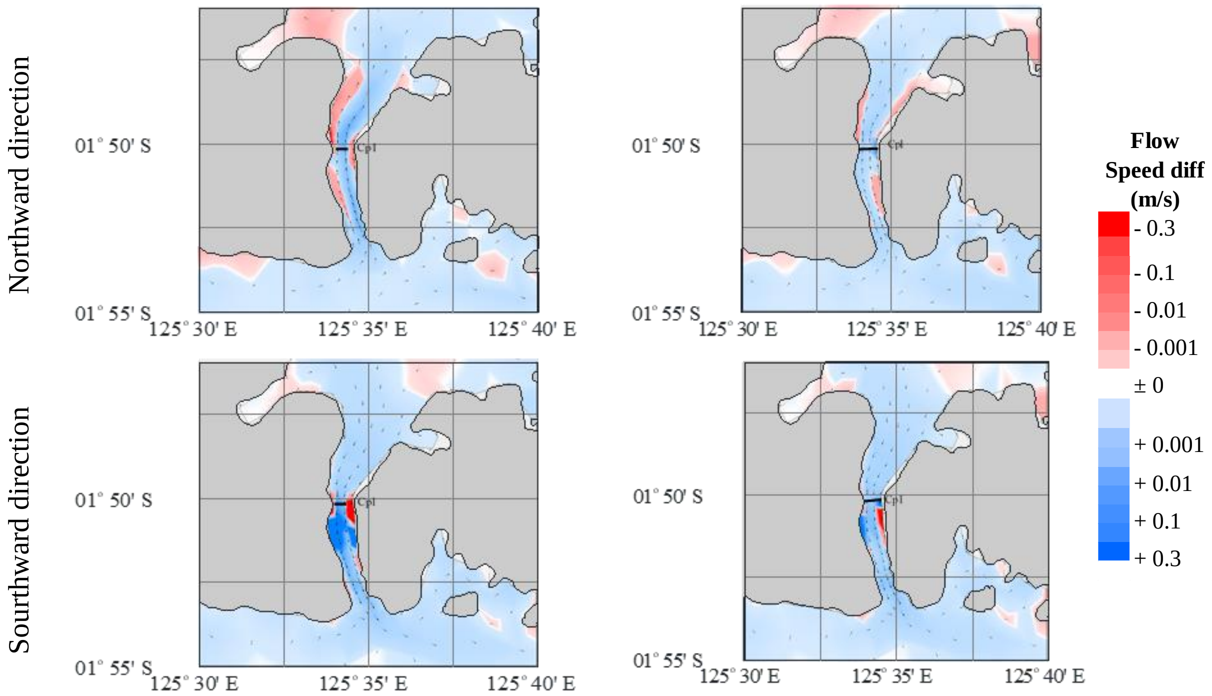

a. D24s24n$_s$1 b. D4s4n$_s$max

Figure 6-34: Comparison of flow field change snapshots for D24s24n$_s$1 and D4s4n$_s$max at configurations at maximum power variation in Capalulu Strait (Cp1)

Similarly, the comparison of the flow-field change in Mangole Strait cannot explain the correlation between high B_L or B_G with power removed by the turbines. Nonetheless, the flow field change does not imply there is an advantage to be gained by not occupying the entire cross-section of the channel to allow part of the channel to carry increased flow speed with average power production. The D24s24n$_s$1 scheme in Mg solely occupies the energetic part of the channel, whereas D4s4n$_s$max occupies almost the entire cross-section of the channel (see Figure 6-35). Both schemes get the benefit of acceleration in part of the array. Therefore, the only explanation of why the D24s24n$_s$1 has higher $\overline{P}_1$ than D4s4n$_s$max is due to the value of B_L in the D24s24n$_s$1 being higher than in D4s4n$_s$max.

b) Implementation of Thrust Capping Strategy

Sula Regency, as well as the Bali-Lombok sites and Lingga Regency, represents a mixed-diurnal tidal type. The other two previous locations implement a power capping strategy. Therefore, a thrust capping strategy is applied in Sula Regency. The example of the power and thrust variation with and without the thrust capping strategy in the Capalulu Strait, Sula Regency is presented in Figure 6-36.

The summary of the simulation with thrust capping strategy is shown in Table 6-18. Similar to the previous locations, the implementation of thrust capping in a mixed-diurnal tidal type could be targeted to have the F_P as close as possible 1.00. This means the average power in the capping strategy is at the same level as without capping. For instance, the F_P from the thrust capping in the D24s24n$_s$1 scheme ranges from 0.93-0.98 in three different locations. However, the maximum power ($P_{1,max}$) values reduce by 14% to 27%.

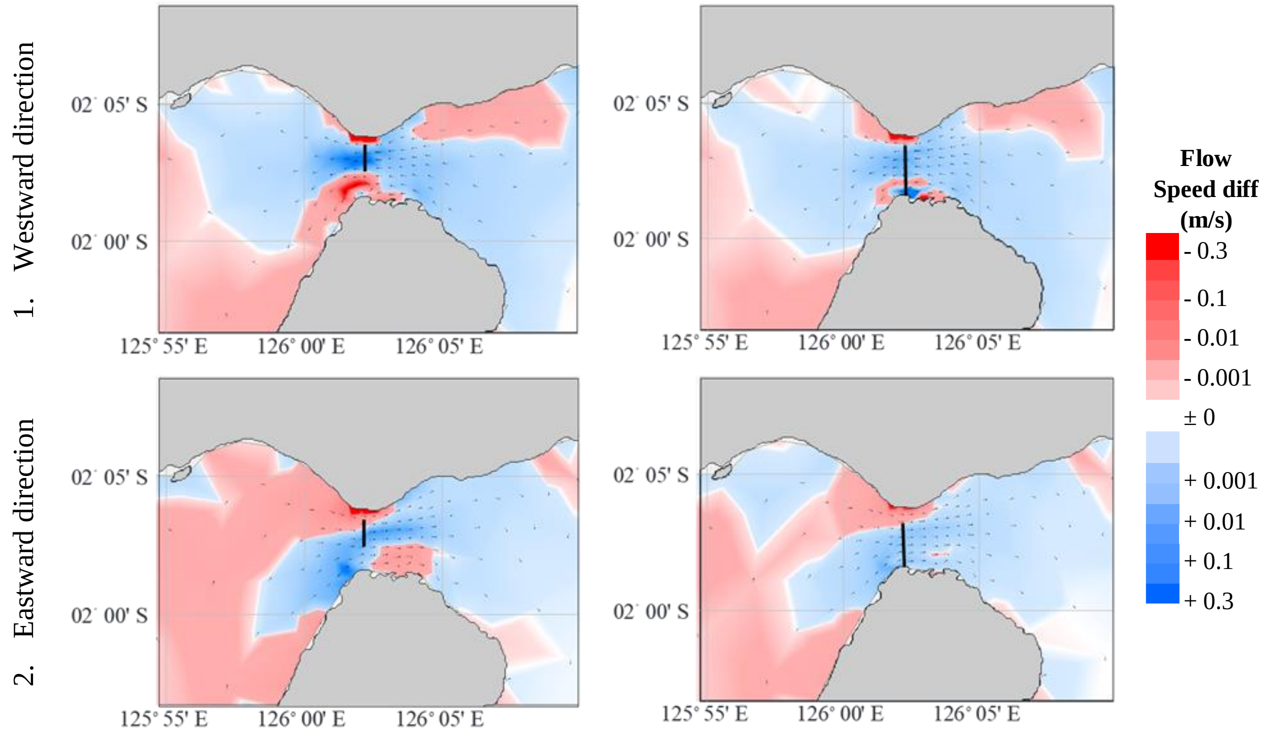

a. D24s24n$_s$1 b. D4s4n$_s$max

Figure 6-35: Comparison of flow field change snapshots for D24s24n$_s$1 and D4s4n$_s$max configurations at maximum power variation in Mangole Strait (Mg)

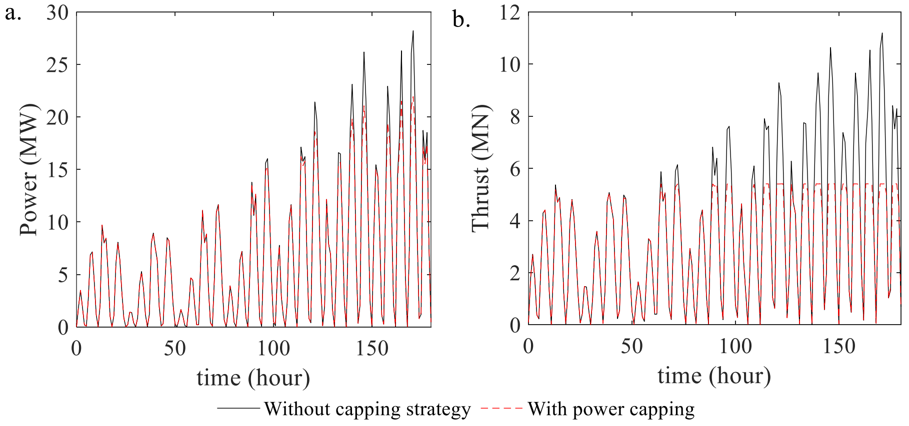

Figure 6-36: Power and thrust variation during the last two neap spring cycles for simulations with and without thrust capping for the D24s24n$_s$1 scheme with α_4 = 0.4 in the Capalulu Strait, Sula Regency.

Similar to the implementation of thrust capping strategy in other tidal regimes, thrust capping in Sula Regency shows the advantage of reducing both $\overline{T}_1$ and $T_{1,max}$ simultaneously. Application of thrust capping in the D24s24ns1 scheme could give $F_T = 0.5$, which means the maximum thrust in the capping strategy is reduced to half of the maximum thrust from the simulation without the capping.

Table 6-18: Summary of the assessment with thrust capping strategy in Sula Regency

Turbines Schemes	Loc	$\overline{P_1}$ (MW)	$P_{1,max}$ (MW)	$\frac{\overline{P_1}}{nt}$ (kW)	$\frac{P_{1,max}}{nt}$ (MW)	$\overline{T_1}$ (MN)	$T_{1,max}$ (MN)	$\frac{\overline{T_1}}{nt}$ (kN)	$\frac{T_{1,max}}{nt}$ (MN)	$\frac{\overline{\hat{T}}}{\overline{T_1}}$	F_p	$F_{p,max}$	F_T	$F_{t,max}$	α_4	CF
D24s24n$_s$1	Cp1	6.20	23.86	0.77	2.98	2.89	5.41	361.73	0.68	1.51	0.95	0.74	0.81	0.51	0.38	0.26
	Mg	7.55	44.96	0.23	1.36	5.57	14.77	168.92	0.45	2.50	0.98	0.86	0.94	0.66	0.33	0.17
	LH2	18.96	125.94	0.27	1.77	8.86	25.15	124.85	0.35	2.73	0.93	0.63	0.96	0.50	0.33	0.15
D10s10n$_s$1	Cp1	3.63	12.65	0.17	0.60	1.52	2.71	72.37	0.13	1.46	0.91	0.64	0.82	0.45	0.35	0.29
	Mg	3.93	16.72	0.05	0.21	2.31	4.78	29.56	0.06	1.68	0.89	0.59	0.81	0.42	0.35	0.24
	LH2	6.85	32.86	0.04	0.19	2.96	6.17	17.28	0.04	1.45	0.74	0.36	0.69	0.25	0.35	0.21
D4s4nsmax	Cp1	4.91	13.80	0.01	0.04	1.88	2.70	5.52	0.01	0.82	0.70	0.40	0.57	0.26	0.35	0.20
	Mg	6.09	23.85	0.00	0.02	3.62	6.67	2.89	0.01	1.29	0.82	0.51	0.70	0.34	0.36	0.16
	LH2	40.62	179.20	0.01	0.03	19.03	33.94	3.54	0.01	1.03	0.71	0.33	0.58	0.21	0.38	0.11

6.3 Environmental Constraints

Besides the bathymetric constraints considered in the previous section, the tidal resource assessment should also examine environmental constraints. Tidal turbine technology may impact the environment.

6.3.1 Marine Spatial Planning and Zoning Regulation

Based on law number 34/2014, marine spatial planning governs utilisation of ocean territory in Indonesia. Therefore, Indonesia's tidal energy exploitation should comply with the existing zoning based on marine spatial planning in the area. Some of the potential locations may be located in a marine conservancy zone.

For instance, the water around Nusa Penida islands was declared as a Marine Protected Area (MPA) based on the Ministry of Marine Affairs and Fisheries Decree No. 2/ 2009 and No. 30/2010. As shown in Figure 6-37, the site with the highest potential resources is located in the core area of the MPA. As briefly mentioned in section 6.2.2, SBS International and SimecAtlantis are preparing an EIA document as part of their PPA contract.

It is possible that the EIA document could change the MPA restrictions. Therefore, the developers should consider preparing options such as considering turbine arrays outside the MPA. The MPA area mostly covers the most energetic part of the tidal stream, as shown in Figure 6-37. Half of the line arrays in Nusa Lembongan Cluster (NLC) are outside the MPA, while in Nusa Penida Cluster (NPC) some of the arrays are entirely inside the MPA. The NPC1 and NPC2 arrays in the NPC are also in the most energetic part based on the average kinetic power. However, those two arrays are in the core zone of the MPA, which means these arrays are inside the conservancy area. Therefore, these two arrays would probably not get approval if they were proposed.

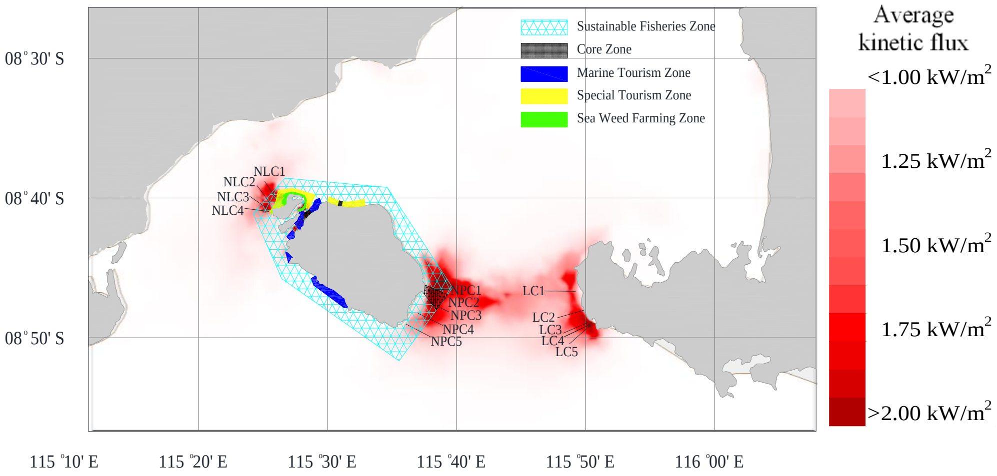

Figure 6-37: Nusa Penida Marine Protected Area (MPA) and tidal array clusters

As discussed in section 6.2.2, the NLC1 and NLC2 in NLC and NPC1 and NPC2 in NPC have the most potential for the Nautilus Project. However, there is still an opportunity to exploit tidal energy with half of the arrays in NLC and extend some of the NPC arrays to comply with the MPA (see Figure 6-38). These extensions are still in a depth of < 100m. Therefore, the construction cost perhaps could be maintained. The NLC3 in NLC and NPC3 in NPC, outside the previously selected arrays in section 6.2.2, are also included in the simulations.

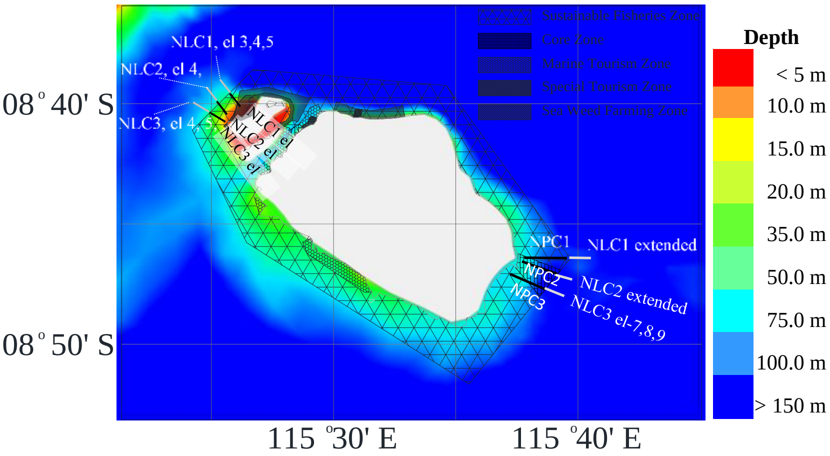

Figure 6-38: Tidal array clusters in respect to the MPA

Simulations for each array in compliance with the MPA are run here. Similar to the previous analyses, three wake coefficients (α_4 = 0.33, 0.4 and 0.56), are used in this simulation. Using the spline feature in Matlab, the optimum α_4 is obtained for each array. The summary of the results of the simulations is presented in Table 6-19.

Table 6-19: Summary of power and thrust for arrays complying with MPA at Bali-Lombok sites.

Scheme	Array	F_L	Ac	nt	B_G	$\overline{P_1}$	$P_{1,max}$	$\frac{\overline{P_1}}{nt}$	$\frac{P_{1,max}}{nt}$	$\bar{T}_1$	$T_{1,max}$	$\frac{\bar{T}_1}{nt}$	$\frac{T_{1,max}}{nt}$	α_4	CF
		m	m^2	unit		MW	MW	MW	MW	MN	MN	kN	kN		
D24s24n$_s$1	NLC1, el 3-4-5	1,469	184,354	30	0.07	13.06	173.01	0.44	5.77	6.63	44.52	221.04	1,484.13	0.37	0.08
	NLC2, el 4-5-6	1,463	169,428	30	0.08	7.93	81.12	0.26	2.70	4.50	25.91	150.01	863.59	0.34	0.10
	NLC3, el 4-5-6	1,493	192,424	30	0.07	5.32	55.44	0.18	1.85	3.33	19.11	110.94	637.16	0.36	0.10
	NPC1.2 (extended)	1,487	263,812	30	0.05	11.89	100.12	0.40	3.34	3.97	24.37	132.38	812.41	0.46	0.12
	NPC2.2 (extended)	986	201,724	20	0.04	5.48	58.76	0.27	2.94	2.76	16.93	138.18	846.33	0.34	0.09
	NPC3, el 7-8-9	1,522	313,159	30	0.04	8.72	100.13	0.29	3.34	4.30	27.57	143.40	919.05	0.33	0.09
D24s12n$_s$1	NLC1, el 3-4-5	1,469	184,354	39	0.10	17.33	224.93	0.44	5.77	9.12	61.06	233.86	1,565.68	0.36	0.08
	NLC2, el 4-5-6	1,463	169,428	39	0.10	10.67	113.27	0.27	2.90	6.25	36.10	160.25	925.54	0.35	0.09
	NLC3, el 4-5-6	1,493	192,424	39	0.09	7.14	74.32	0.18	1.91	4.60	26.82	117.91	687.59	0.35	0.10
	NPC1.2 (extended)	1,487	263,812	39	0.07	14.94	136.40	0.38	3.50	6.95	38.34	178.22	983.00	0.34	0.11
	NPC2.2 (extended)	986	201,724	26	0.06	7.27	77.82	0.28	2.99	3.73	22.76	143.33	875.24	0.34	0.09
	NPC3, el 7-8-9	1,522	313,159	39	0.06	12.53	142.71	0.32	3.66	6.31	40.06	161.85	1,027.23	0.34	0.09

The results indicate that the Nautilus Project still has the potential to exploit tidal energy outside the MPA. For instance, 30 turbines of the extended NPC1.2 turbine arrays in the D24s24ns1 scheme could remove 13.06 MW, while 39 turbines with 12 m tip-to-tip spacing (D24s12n$_s$1 scheme) could remove an average of 14.94 MW in the same array. These results show that the average power per turbine $\left(\frac{\overline{P_1}}{nt}\right)$ from almost all arrays (NLC2, NPC1 and NPC2) is lower than the $\frac{\overline{P_1}}{nt}$ of the same arrays in the previous simulation in section 6.2.2 (see Table 6-5). Only the NLC1 scheme that has a slightly higher $\frac{\overline{P_1}}{nt}$ is compliant with the MPA requirements, compared to previous simulations in section 6.2.2. The simulation that complies with the MPA restrictions gives 0.44 MW/per turbine, while the previous simulation for NLC1, as shown in Table 6-5, gives 0.41 MW/per turbine

Although the turbine fence could be built outside the core area, the turbine's impact in the area should be considered. The flow field changes in the MPA area show that the turbine arrays affect the average flow-field around the array. For instance, the NLC1 and NLC2 arrays change the average flow-field in the seaweed farm area (see Figure 6-39). In general, the average difference in flow speed in this area is lower with turbines than without turbines. Although it is unclear whether this change could negatively affect the productivity of the seaweed farm, careful consideration of this issue is required.

Similarly, a flow field change in the core area of the MPA also occurs. Figure 6-40 shows that the extended NPC1 (NPC1.2) and the extended NPC2 (NPC2.2) still affect the core area of the MPA. The core area of the MPA is probably the natural breeding ground, the spawning ground for pelagic fishes. Therefore these changes could harm the spawning process in this area. Similar to the NLC1 and NLC2 arrays, plans to exploit the resources of this area should carefully take note of this impact.

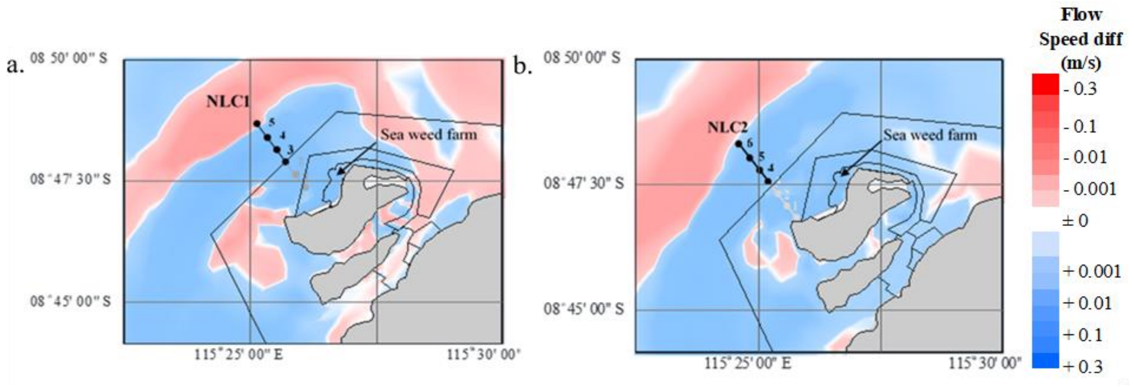

Figure 6-39: The average flow field changes for NLC1, el 3-4-5 (a.) and NLC2, el 4-5-6

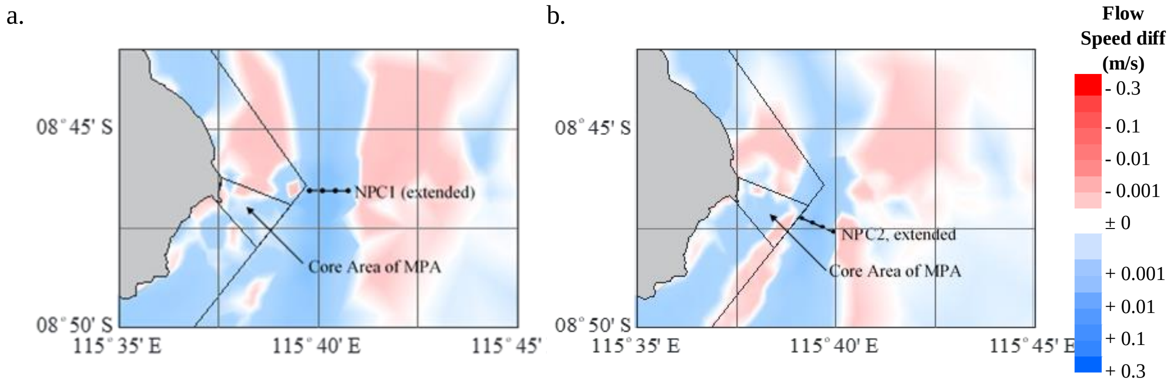

Figure 6-40: The average flow field changes for (a.) NPC1 extended and (b.) NPC2 extended

6.3.2 Constraint on Marine Life

Tidal turbines may also have an impact on marine life in the area. Dadswel *et al.*, 2018 show that the axial flow tidal turbine in Annapolis River, the Bay of Fundy, Canada, caused a high rate of anadromous fish mortality in the area. This condition leads to a decline in fish caught by the local fishermen. A similar impact could occur in the potential sites of Indonesia.

Indonesia is home to exotic animals. For instance, the Nusa Penida island is home for ocean sunfish (*Mola mola*) and manta rays (*Manta birostris*) that come to this area seasonally, especially in Toyopakeh strait. This makes the deployment of tidal turbine in Toyopakeh strait complex. Careful planning to avoid a detrimental effect on the endangered fishes is necessary.

Indonesian water also provides an important migratory corridor for endangered sea mammals such as pygmy blue whales (*Balaenoptera musculus brevicauda*). This gentle giant migrates from the Australian coast to the Mollucas seas in Indonesian waters (Double *et al.* 2014, Möller *et al.*, 2020).

Unfortunately, there is a chance that the migratory pathway conflicts with the location for tidal energy exploitation. Both the Larantuka Strait and Lifamatola Headland are locations that may conflict with the migratory route of blue whales (see Figure 6-41).

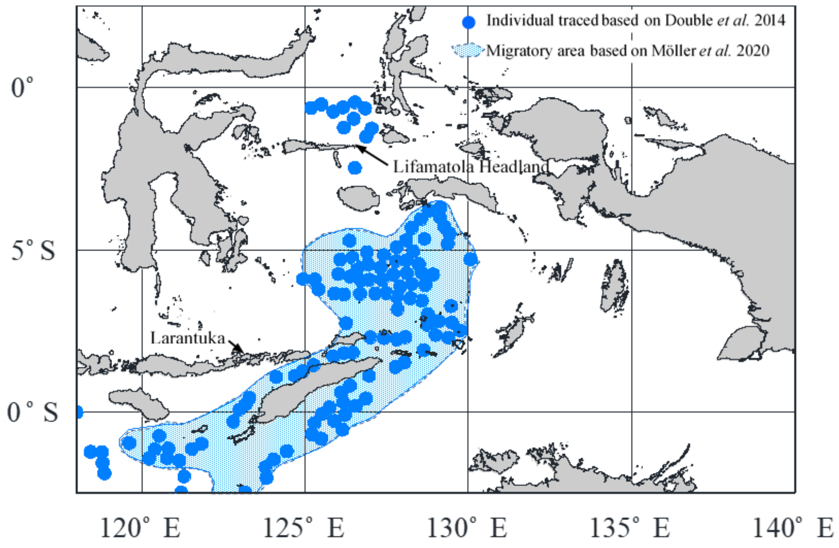

Figure 6-41: The migratory area of pigmy blue whale based on Double *et al.*, 2014 and Möller *et al.* 2020 in conjunction with two potential areas of tidal energy exploitation.

6.4 Economic Viability

Financial feasibility is a major concern for tidal turbine development, and is only dealt with in a preliminary fashion in this thesis. The private investment risk for tidal energy projects remains high for the turbine. In the European market, tidal stream power technology is still unable to compete with more established wind and solar power technologies.

6.4.1 *CAPEX* and *OPEX* Estimation

The Capital Expenditure (*CAPEX*) is the total capital required, including the pre-development costs, electrical systems infrastructure and construction cost. There is some *CAPEX* estimation for the ongoing projects from two potential locations that are assessed in this thesis. The estimated budget for the tidal turbine deployment in Larantuka, including surrounding works, is USD 225 million (Tidal-Bridge 2020), or GBP 166.5 million, or GBP 5.5 million per MW (with an exchange rate of 0.74 GBP/USD). The total installed capacity plan for this site is 30 MW. Meanwhile, the total cost estimate of tidal energy harnessing in the Bali-Lombok straits is USD 750 million or GBP 555 million for the total capacity of 150MW, or GBP 3.6 million per MW (Simec Atlantis 2020), based on 75×2 MW AR2000 turbines to installed in the Bali-Lombok strait.

The estimates for Bali-Lombok are significantly higher than the proposed budget in the Alderney Race. The proposal of a tidal farm composed of 42 tidal energy converters (*TEC*) each with a capacity of 1.2 MW would only cost EUR 111.191 million, or GBP 98.96 million, or GBP 2.8 million per MW, for device manufacture and installation, including pre-development costs such as concept and design costs (Segura *et al.*, 2017). This budget means the TEC's price in the Alderney Race is only approximately GBP 2.35 million per turbine. Meanwhile the AR2000 in Bali-Lombok cost GBP 7.4 million per turbine. For the comparison, the TEC blade diameter in the Alderney Race is 20 m, while the AR2000 is 24 m, and both TECs are stand-alone type, yet the AR2000 cost more than three times the TEC cost in Alderney Race.

The budget estimates in Bali-Lombok, as well as Larantuka, are even higher than the rule of thumb for the budget estimates for the early-stage development of TEC. The general estimated capital cost for tidal turbines is between GBP 1400/kW, and GBP 3000/kW [Ramos & Iglesias, 2013; Astariz *et al.*, 2015; Allan *et al.*, 2011]. Therefore, a tidal turbine project should be in the range of that general estimate. Note that the budget estimates for the project in the Alderney Race was GBP 1,963.5/kW. Based on that estimate, the project cost of 150 MW turbine in the Bali-Lombok should be in the range of GBP 210 million to GBP 450 million. Meanwhile, the 30 MW installed capacity in Larantuka should cost GBP 42 – 90 million. However, perhaps the total budget for the Larantuka project includes the cost of the bridge structure as well, while the budget estimate in the Bali-Lombok site may not be just for the 150 MW total capacity.

The Operational Expenditure (*OPEX*) consists of all labour costs, production loss costs, maintenance costs, and insurance costs. The *OPEX* cost can be estimated as 2.5% of the *CAPEX* cost (Zupone *et al.*, 2015). However, the Alderney Race turbine farm's breakdown cost estimated the *OPEX* cost, with the inclusion of insurance cost, is 4.41% of the total manufacturing and installation costs (Segura *et al.*, 2017).

Therefore, *CAPEX* and *OPEX* are calculated in correspondence with the total installed capacity in each location here. The lowest *CAPEX* are calculated based on the assumption of GBP 1400/kW, and GBP 3000/kW for the highest. Meanwhile, the lowest value of *OPEX* is calculated based on 2.5% of the lowest *CAPEX*, while the highest value is 4.41% of the highest *CAPEX*.

6.4.2 Annual Energy Production (*AEP*)

The estimated annual energy yield or Annual Energy Production (*AEP*) here is calculated from the $\overline{P}_1$. This approach may be slightly different to *AEP* from a "direct" calculation based on the area of the power variation curve. This "direct" calculation is based on the summation of daily power production. The comparison of energy production based on power variation is shown in Table 6-20.

Since the simulation only runs for 62 days, the comparison of energy production is calculated for a month only. Therefore, instead of *AEP*, the term Monthly Energy Production (*MEP*) is used here. As the simulations in each array are only run for three different α_4 values (0.33, 0.4 and 0.56), the calculation of *MEP1* is taken from α_4 of 0.4. These comparisons show that both methods only differ a tiny fraction. Therefore the *AEP* is calculated from $\overline{P}_1$ for simplicity.

Table 6-20: Summary of energy production calculation results. MEP1 is the calculation based on the average power removed by the turbines ($\overline{P}_1$) while MEP2 is calculated directly from the power variation.

Schemes	Array	n_t (units)	$\overline{P}_1$ (α_4=0.4) (MW)	*MEP1* (GWh)	*MEP2* (GWh)	diff
Larantuka Sites						
D14s14ns1	La1	12	5.71	4.110	4.107	100.063%
	La2	5	2.81	2.016	2.015	100.064%
D14s7ns1	La1	16	8.10	5.829	5.826	100.063%
	La2	7	4.28	3.075	3.073	100.064%
D4s4ns3	La1	150	4.19	3.011	3.009	100.063%
	La2	142	6.39	4.601	4.599	100.062%
D4s2ns3	La1	286	8.67	6.246	6.242	100.062%
	La2	245	10.80	7.732	7.727	100.061%
Bali-Lombok Sites						
D24s24ns1	NLC1	50	20.45	14.726	14.710	100.113%
	NLC2	60	20.28	14.602	14.595	100.044%
	NPC1	60	29.43	21.193	21.196	99.986%
	NPC2	58	23.00	16.562	16.569	99.961%
	LC3	80	44.86	32.301	32.280	100.068%
	LC4	80	42.83	30.839	30.819	100.068%
D24s12ns1	NPC1	80	40.73	29.328	29.309	100.064%
	NPC2	76	31.05	22.358	22.343	100.066%

The *AEP* for each location is calculated only for the selected scheme and array (see Table 6-21). For the Larantuka tidal bridge, for instance, the *AEP* is calculated for two turbine schemes in two different arrays. The La2 scheme is the proposed bridge location, and La4 is the array that gave a better result. Tidal Bridge DV predicted the annual energy production in Larantuka tidal bridge would be 80GWh/year (Tidal-Bridge, 2020), with a total installation capacity of 30 MW. This *AEP* calculation shows that the *AEP* 80 GWh could be reached by installing 245 turbines each with *D* = 4 m at the proposed bridge location.

However, some adjustments are applied here, especially for the ongoing projects. The Nautilus Project, for instance, plans to install 75 turbines in the Bali-Lombok strait. Meanwhile, the arrays in Lombok Site (LC3 and LC4), as discussed in section 6.2.2, have 80-104 turbines (see Table 6-21). Therefore, the *AEP* that is used in later analyses is calculated based on the average power removed by a single turbine ($\frac{\overline{P_1}}{nt}$).

Table 6-21: The *AEP* calculations on selected schemes and arrays based on the simulation results in the previous section.

Scheme	Array	n_t (units)	No Capping			Power Capping				Thrust Capping			
			$\overline{P_1}$ (MW)	$\frac{P_{1,max}}{nt}$	*AEP* (GWh)	$\overline{P_1}$ (MW)	$\frac{P_{1,max}}{nt}$	F_P	*AEP* (GWh)	$\overline{P_1}$ (MW)	$\frac{P_{1,max}}{nt}$	F_P	*AEP* (GWh)
The Larantuka tidal bridge													
D14s7n$_s$1	La2	7	4.28	3.24 MW	37.45	2.70	0.76 MW	0.63	23.61	3.30	1.53 MW	0.77	28.88
	La4	15	10.32	3.75 MW	90.41	6.09	0.74 MW	0.59	53.34	7.82	1.68 MW	0.76	68.47
D4s2n$_s$3	La2	245	10.80	0.22 MW	94.58	10.19	0.07 MW	0.94	89.27	10.87	0.22 MW	1.01	95.18
	La4	223	11.80	0.26 MW	103.38	11.63	0.18 MW	0.99	101.92	11.34	0.13 MW	0.96	99.37
The Nautilus Project in Bali-Lombok													
D24s24n$_s$1	LC3	80	32.98	3.36 MW	288.91	30.84	1.92 MW	0.93	270.13				
	LC4	80	31.45	3.15 MW	275.49	29.58	1.92 MW	0.94	259.11				
D24s12n$_s$1	LC3	104	45.13	3.51 MW	395.37	42.38	2.08 MW	0.94	371.29				
	LC4	104	43.06	3.30 MW	377.19	40.68	2.08 MW	0.94	356.35				
Sunda Strait Bridge													
D4s2n$_s$max	SS1	7,506	22.05	19.32 kW	193.16	21.91	16.66 kW	0.99	191.92	21.92	17.47 kW	0.99	191.99
	SS2-1	7,138	34.10	32.05 kW	298.68	34.04	31.50 kW	1.00	298.17	33.95	30.43 kW	1.00	297.36
	SS2-2	11,288	59.47	29.46 kW	520.94	54.18	19.60 kW	0.91	474.64	55.63	22.99 kW	0.94	487.35
D24s12n$_s$1	SS1	130	16.08	0.86 MW	140.85	15.71	0.64 MW	0.98	137.58	16.07	0.83 MW	1.00	140.78
	SS2-1	117	9.88	0.61 MW	86.53	9.86	0.57 MW	1.00	86.38	9.85	0.59 MW	1.00	86.28
	SS2-2	161	28.83	1.10 MW	252.51	26.57	0.83 MW	0.92	232.72	28.69	1.01 MW	1.00	251.35
Lingga Regency													
D7s7n$_s$1	Temiang 1	181	3.52	87.66 kW	30.82	2.92	46.66 kW	0.83	25.56				
	Dasi 1	95	0.89	52.68 kW	7.77	0.85	35.06 kW	0.96	7.43				
D7s3n$_s$2	Temiang 1	255	5.62	99.20 kW	49.20	5.16	67.54 kW	0.92	45.19				
	Dasi 1	233	3.20	81.45 kW	28.03	3.07	56.05 kW	0.96	26.87				
Sula Regency													
D24s24n$_s$1	Cp1	8	6.52	4.01 MW	57.09					6.20	2.98 MW	0.95	54.31
	Mg	33	7.74	1.58 MW	67.76					7.55	1.36 MW	0.98	66.18
	LH2	71	20.39	2.80 MW	178.64					18.96	1.77 MW	0.93	166.05
D4s4n$_s$max	Cp1	340	6.97	101.34 kW	61.08					4.91	40.59 kW	0.70	43.01
	Mg	1254	7.43	37.49 kW	65.07					6.09	19.02 kW	0.82	53.39
	LH2	5376	57.59	99.58 kW	504.53					40.62	33.33 kW	0.71	355.83

The *AEP* for other locations is also adjusted by setting the power factor (F_P). For instance, both capping strategies that were applied on the D14s7n$_S$1 schemes at Larantuka may not be ideal, since the F_P is lower than 0.8, while the turbine capacities, defined by $\frac{P_{1,max}}{nt}$, for the power capping strategies are 0.76 MW and 0.74 MW for La2 and La4, respectively. These turbine capacities could be increased to 1 MW for both arrays. Therefore, the *AEP* calculation used in the later analyses is based on the no-capping scenario. The adjustment is made with an assumption that F_P is in the range of 0.80-0.95.

6.4.3 Levelised Cost of Energy (*LCOE*)

The *LCOE* is the most common method for estimating the cost of lifetime generated energy. The *LCOE* is defined as the total cost over the total energy output ratio, expressed in terms of the present value equivalent. Therefore, this *LCOE* is comparable to the electricity generation cost or BPP, as discussed in Chapter 1. In general, the *LCOE* is calculated as;

$$LCOE = \frac{CAPEX + \sum_{t_p=0}^{n}(OPEX).(1+i_r)^{-t_p}}{\sum_{t_p=1}^{n}(AEP).(1+i_r)^{-t_p}}, \tag{6.4}$$

where, i_r is the interest rate used for discounting costs each year back to a reference time period during the lifetime of the project (t_p). The i_r that used in the LCOE calculation here is 12.5%, which is higher than the i_r commonly used in publications for European countries, with i_r in the order of 10% (Vazquez & Iglesias, 2016b). The t_p, in this case, is assumed similar to the PPA contract duration. It should be noted that the *OPEX* calculations start from t_p= 0 to include the project cost at the beginning of the first year, while the *AEP* starts at t_p= 1.

The *LCOE* calculations for each location are presented in Table 6-22. Based on this calculation, the *LCOE* in the Larantuka Tidal Bridge (La2) should be lucrative with range GBP 51.3 – 125.1/MWh for the D14s7ns1 scheme, while for D4s2n$_s$3 it is GBP 63.3-154.2/MWh. This LCOE suggests that turbines of dimeter 14 m are more suitable at Larantuka.

The *LCOE* for the La4 is also better than the *LCOE* at the proposed bridge location. The *LCOEs* at La4 lie in the range GBP 45.6-166.6/MWh. These *LCOE*s are significantly lower than the *LCOE* based on the proposed budget estimate with the *AEP* from Tidal Bridge DV. The *LCOE* based on the proposal is GBP 502.1/MWh. The *LCOE*s in Larantuka are also lower than the *LCOE* in Alderney Race. Segura *et al.*, 2017 suggested the LCOE in the Alderney Race is in the range of EURO 0.10-0.20/kWh or GBP 89 – 178/MWh.

The *LCOE*s in the Bali-Lombok sites are at the range of GBP 128-330/MWh. This range means this project is economically viable if the developer could obtain a certain *CAPEX* and *OPEX* level. Vasquez & Iglesias, 2016b suggested *LCOE* should be lower than GBP 0.25/kWh or GBP

250/MWh to reach economic viability. Like the Larantuka, the proposed budget estimate in this site also gives the *LCOE* of approximately GBP 505/MWh.

This *LCOE* result shows that the tidal turbine deployment in the SSB is economically viable for the D24s12n_s1 scheme, while D4s2$n_s$max gives *LCOE* > GBP 1,000/MWh. This result means occupying the entire bridge span may not profitable, even though D4s2nsmax gives a higher average $\bar{P}_1$ than the D24s12n_s1 scheme.

Table 6-22: *LCOE* calculation for selected locations

Scheme				Capacity				Cost Estimation		
	Array	n_t (units)	F_P	Turbine (MW)	Total (MW)	$\frac{AEP}{n_t}$ (GWh)	*AEP* (GWh)	*CAPEX* (million GBP)	*OPEX* (million GBP)	*LCOE* GBP/MWh
The Larantuka tidal bridge										
D14s7n_s1	La2	7	0.80	1.00	7.0	4.28	29.96	9.8 - 21.0	0.25 - 0.93	51.3 - 125.1
	La4	15	0.80	1.00	15.0	4.82	72.33	21.0 - 45.0	0.53 - 1.98	45.6 - 111.1
D4s2n_s3	La2	245	0.90	0.10	24.5	0.35	85.12	34.3 - 73.5	0.86 - 3.24	63.3 - 154.2
	La4	223	0.90	0.13	29.0	0.42	93.04	40.58 - 87.0	1.01 - 3.84	68.5 - 166.9
Proposed					*30.0*		*80.00*	225	*9.92*	*502.1*
The Nautilus Project in Bali-Lombok										
D24s24n_s1	LC3	75	0.95	2.00	150.0	3.43	257.31	210 - 450	5.25 - 19.85	128.1 - 312.2
	LC4	75	0.95	2.00	150.0	3.27	245.36	211 - 450	5.25 - 19.86	134.4 - 327.4
D24s12n_s1	LC3	75	0.93	2.00	150.0	3.54	265.16	212 - 450	5.25 - 19.87	124.3 - 303.0
	LC4	75	0.93	2.00	150.0	3.37	252.97	213 - 450	5.25 - 19.88	130.3 - 317.6
Proposed					*150.0*		*265.16*	*750*		*505.0*
Sunda Strait Bridge (SSB)										
D4s2$n_s$max	SS1	7,506	0.90	0.18	1,313.6	0.02	173.84	1,838.97 - 3,940.7	45.97 - 173.78	1,466.0 - 3,630.2
	SS2-1	7,138	0.90	0.30	2,141.4	0.04	268.82	2,997.96 - 6,424.2	74.95 - 283.31	1,750.7 - 4,266.7
	SS2-2	11,288	0.90	0.20	2,257.6	0.04	468.84	3,160.64 - 6,772.8	79.02 - 298.68	1,058.3 - 2,579.1
D24s12n_s1	SS1	130	0.95	0.60	78.0	1.03	133.81	109.20 - 234.0	2.73 - 10.32	128.1 - 312.2
	SS2-1	117	0.95	0.60	70.2	0.70	82.20	98.28 - 210.6	2.46 - 9.29	187.7 - 457.4
	SS2-2	161	0.95	0.85	136.9	1.49	239.89	191.59 - 410.6	4.79 - 18.11	125.4 - 305.6
Lingga Regency										
D7s3n_s2	Tem. 1	255	0.90	0.65	165.8	0.17	44.28	232.05 - 497.25	5.80 - 21.93	822.6 - 2,004.8
	Dasi 1	233	0.90	0.55	128.2	0.11	25.23	179.41 - 384.45	4.49 - 16.95	1,116.2 - 2,720.4
Sula Regency										
D24s24n_s1	Cp1	8	0.85	2.50	20.0	6.07	48.53	28.0 - 60.0	0.70 - 2.65	90.6 - 220.7
	Mg	33	0.95	1.20	39.6	1.95	64.37	55.44 - 118.80	1.39 - 5.24	135.2 - 329.7
	LH2	71	0.95	1.80	127.8	2.39	169.70	178.92 - 383.40	4.47 - 16.91	165.5 - 403.4
D4s4$n_s$max	Cp1	340	0.85	0.04	13.6	0.15	51.92	19.04 - 40.80	0.48 - 1.80	57.6 - 140.3
	Mg	1,254	0.95	0.02	25.1	0.05	61.82	35.11 - 75.24	0.88 - 3.32	89.2 - 217.3
	LH2	5,376	0.95	0.03	161.3	0.09	479.30	225.79 - 483.84	5.64 - 21.34	74.0 - 180.2

Based on the *LCOE* for the selected schemes and arrays of the marginal locations, only the Sula Regency sites show economic viability, while the Lingga Regency sites give *LCOE* > GBP 250/MWh. This result also tells us that in the Sula Regency, the small turbines, represented by D4s4$n_s$max, are more preferable in terms of meeting economic viability than the large-sized turbines with 24 m diameter. In some Sula Regency sites, the D24s24nsmax is only economically viable if the *CAPEX* and *OPEX* could be ensured in the low range.

6.4.4 Financial Model

The *LCOE* may not directly reflect the minimum electricity tariff that should be applied from the TEC. The authorities and turbine developer may also need financial modelling for the decision-making process. Therefore, financial modelling is performed to explore the economic viability further in this chapter. Modelling financial simulations is complex, since it depends on the contract clauses or types. In Indonesia, there are few schemes of public-private partnership. Comprehensive research in economics would be required to compare the cases of the five locations shown in this thesis. Therefore, only two locations, the Nautilus Project in Bali-Lombok and the Larantuka tidal bridge are analysed with a financial model in this section. Both locations are ongoing projects that consider similar types of PPP schemes (30 years of PPA).

The decision-making process usually requires certain economic indicators such as Net Present Value (*NPV*), the estimated Internal Rate of Return (*IRR*), the Discounted Payback Period (*DPBP*), and the Benefit-Cost Ratio (*BCR*). The NPV is represented by the difference between the present values of cash inflows, here denoted as the benefit of the project (B_{tp}), with the present value of cash outflow, here denoted as the cost of the project (C_{tp}). The *NPV* is usually used to analyse the profitability of a project or a projected investment (i_r). Therefore, the *NPV* is calculated by the following equation.

$$NPV = \sum_{t_p=i}^{n} \frac{B_{tp} - C_{tp}}{(1+i_r)^{t_p}}, \tag{6.5}$$

The *IRR* is defined as the annual discount rate that makes the *NPV* in equation (6.5) equal to zero. This *IRR* metric, from a financial perspective, provides the gross annual profitability per monetary unit involved in the project.

The discounted payback period (*DPBP*) is the number of periods taken for a project to get the breakeven point (*BEP*) after the initial expenditure. This metric is regarded as a suitable method to evaluate the risk in the investment. The *DPBP* could be analysed from the discounted cash flow positive difference of benefit and cost (time taken to get the *NPV*+).

The financial simulations for the Larantuka tidal bridge and the Nautilus Project in Bali-Lombok are run for the highest value of *CAPEX* and *OPEX* ranges. The D4s2n$_s$3 scheme is used for

Larantuka while the financial analysis of the Nautilus project uses the D24s12n$_s$1 scheme. Both cases set i_r at 12.5%. It is important to note that these financial calculations are preliminary and for illustration only.

The *DPBP* analysis from the Benefit-Cost difference could be used to compare the various tariffs. Five different tariffs are set for each location. The simulation at Larantuka uses tariffs at £ 0.150/kWh, £ 0.175/kWh, £ 0.200/kWh, £ 0.225/kWh, and £ 0.250/kWh, while tariffs of £ 0.325/kWh, £ 0.350/kWh, £ 0.375/kWh, £ 0.400/kWh, and £ 0.425/kWh are set for the Nautilus Project in Bali-Lombok. Based on these tariffs, the Larantuka tidal bridge only achieves payback within the PPA contract period (30 years) for tariffs above £ 0.200/kWh, while the Nautilus Project should set their tariff at £ 0.375/kWh (see Figure 6-42).

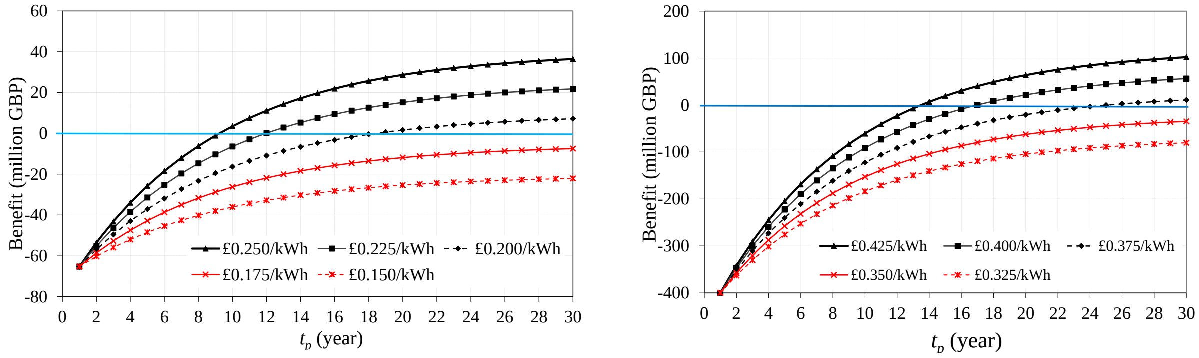

a. The Larantuka Tidal Bridge

b. The Nautilus Project (the Bali-Lombok)

Figure 6-42: The *DPBP* for the various tariffs, with the interest rates (i_r) is set at 12.5% for both Locations

However, those tariffs only gave the DPBP > 15 years. This means it takes more than half of the PPA contract period for the investors and the developers to benefit from the project. Another concern that may emerge is on the sensitivity to the different *IRR*. The investors might need to see whether the project is high risk if the *IRR* is higher than 12.5%, or the authorities might need to explore the lowest tariff with an appropriate *IRR*.

The sensitivity analysis of the different *IRR* can be conveniently analysed using the Benefit-Cost Ratio (*BCR*) indicator. The *BCR* essentially is the ratio between the total discounted B_{tp} over the discounted B_{tp} and can be expressed as:

$$BCR = \frac{Discounted\ value\ of\ incremental\ benefits}{Discounted\ value\ of\ incremental\ costs} \tag{6.6}$$

An economically viable project could be defined with *BCR*>1 for the expected *DPBP*.

Therefore, the analyses are performed for each previous tariff in both projects. The DPBP here is set at 15 years while the *IRR*s are varied from 8.5% to 35% for both project cases. The simulations show that the Larantuka project could have a tariff of ₤ 0.200/kWh with the *DPBP* ≤15 years if the *IRR* is at least 11%, while the Nautilus Project should set the IRR < 9 % to get the *DPBP* less than 15 years. Based on these results, it is safe to conclude that it would be convenient if the electricity tariffs from tidal turbine generator are set as ≥ ₤ 0.250/kWh in the Larantuka tidal Bridge, while at the Bali-Lombok site the economic viability is only met if the tariff is ≥ ₤ 0.400/kWh (see Figure 6-43).

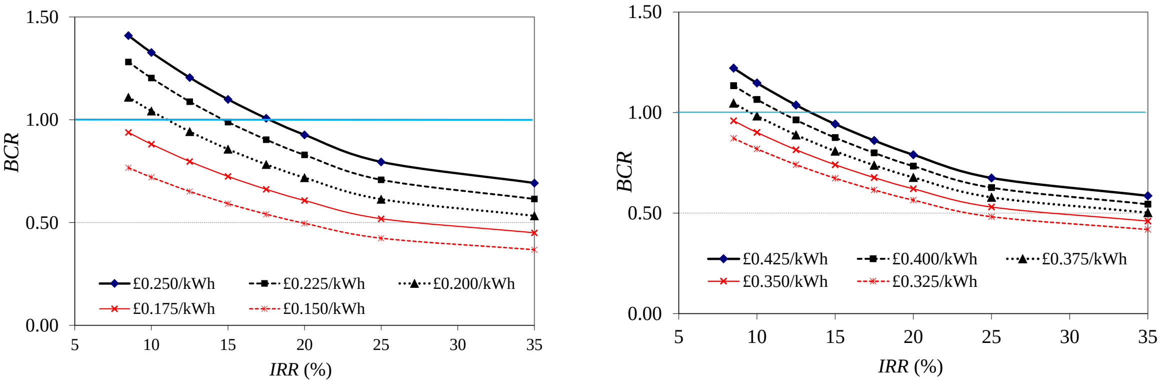

a. The Larantuka Tidal Bridge

b. The Nautilus Project (the Bali-Lombok)

Figure 6-43: The sensitivity analyses of the different tariffs to the *BCR* vs I_r in the Larantuka Tidal Bridge

6.5 Summary and Discussion

This chapter has presented resource assessments at selected locations based on realistic turbine deployment. The turbine dimensions determined by diameter (*D*), tip-to-tip spacing (*s*) and the number of turbines per stack (n_s) are interpreted as the blockage ratio. Besides using the realistic specifications, it is possible to apply the power or thrust capping strategy in the 2D DG-ADCIRC solver. This chapter also demonstrates the utility of various capping metrics, as discussed in the theoretical approach in Chapter 2, in the 2D SWE numerical model. This chapter further confirms that both power and thrust capping strategies could maintain the average power removed by the turbine as close as possible to the $\overline{P}_1$ without capping strategy (F_P=1). At the same time, the maximum thrust is truncated as low as possible. Therefore, it is safe to conclude that the power factor and maximum thrust factor are more important than the Capacity Factor (*CF*) as indicators in the decision-making regarding tidal energy exploitation.

There are some important notes on the assessment results at particular locations. Similar to the previous analysis with uniform blockage at Larantuka, the simulations with realistic blockage show that the tidal bridge's current proposed position is less advantageous than at another location (La3) simulated in this study. Although the results show a higher output compared to the uniform blockage results, and explanations have been postulated, the exact reasons remain uncertain.

There are two possible explanations. Firstly, the increase could be because the local blockage ratio is higher than the uniform blockage ratio modelled. However, at the site with the lowest average flow velocity, the average resources in a realistic case are lower than the result of the simulation with the uniform blockage, even though the local blockage is higher. Secondly, the methodology for including turbines in the shallow water model cannot capture all the physics of a partial array, and in particular, the modelling of the bypass flow may be inadequate.

The *LCOE* analysis shows that almost all locations that are assessed in this chapter are economically viable (based on the category of viability if *LCOE* < GBP 250/MWh, following Vasquez & Iglesias, 2016b). Only the schemes in the Lingga Regency show a high LCOE for all selected arrays. The Larantuka sites and the Sula Regency sites even show a *LCOE* below GBP 100/MWh. This *LCOE* is even lower than the common *LCOE* in the fixed bottom offshore wind turbines that commonly have *LCOE* in range of USD 150-175/MWh or GBP 110-130/MWh (Wiser *et al.*, 2016; Lamy & Azevedo, 2018).

The viability based on the *LCOE* may still be required to be examined with a financial model. For instance, the Larantuka tidal bridge only becomes economically viable if the tariff in that area could be set at least at ₤ 0.250/kWh. This tariff might be higher than the *BPP* in this area that is only $ 0.200/kWh or ₤ 0.150/kWh. Therefore a feed-in-tariff policy to cover the deficit is required to make this project viable.

The Nautilus Project at Bali-Lombok faces more complicated circumstances. The assessment for this location shows that the project could be economically viable at a certain *CAPEX* and *OPEX* level in the range of <GBP 250/MWh. However, the financial simulation shows the electricity tariff at this location might be significantly higher than the BPP in the Bali and West Nusa Tenggara Provinces. Bali's BPP is USD 68.1/MWh or ₤0.5/kWh, while the BPP in West Nusa Tenggara is USD 191.8/MWh or ₤0.141/kWh. The financial model shows that the project could be economically viable if the tariff is equal to ₤ 0.400/kWh. This means it will take a substantial amount of government subsidy to make this project viable.

This location is also complex due to the potential conflict with an environmental constraints. Some of the potential locations in Bali-Lombok sites are in a marine conservancy area. Therefore, exploiting that area might face a public challenge. A similar potential conflict has also been found in other locations such as the Laratuka and Lifamatola Headland. This location might conflict with the migratory corridor of the endangered pygmy blue whales.

Chapter 7. Conclusions and Future Research

This thesis explores the opportunity for tidal turbine developments in Indonesian waters. In the quest to understand the resources in this area, exploration of the background theory regarding tidal dynamics, energy generation from a tidal stream, and the economic viability of projects are also addressed in this thesis. Some of the research questions raised in this thesis are addressed through the assessments at real sites.

7.1 Conclusions

The most important conclusion from this thesis is about the nature of the resource and the opportunity of harnessing tidal energy in Indonesia. Although the main objectives of this thesis are exploring the opportunities for tidal power in Indonesia, some general findings are applicable for assessments at any other similar sites.

7.1.1 The Opportunities and Limitations of Tidal Resources in Indonesia

This thesis begins with exploring Indonesian policy regarding energy provision in the past five years. As discussed in Chapter 1, although the Indonesian government seems hesitant to utilise green and renewable energy, the opportunity remains. This thesis identifies a great opportunity for tidal energy resources exploitation in Indonesia. Five different locations are selected as representative sites to assess tidal resource assessment in Indonesia: the Larantuka Strait, Lombok Strait, Sunda Strait, Lingga Regency and Sula Regency. The total theoretical resources are approximately 5 GW from these five different locations (as shown in Chapter 5).

The assessments based on realistic turbine deployment in (Chapter 6) also found that some sites are economically viable for commercial turbine developers. By and large, tidal energy is arguably one of the promising future energy sources for Indonesia. A summary of the resource assessments is presented in Table 7-1. It is important to note that the assessment in this thesis is limited to five locations. Obviously, there are many other potential locations in Indonesian waters. Although employing a realistic turbine deployment strategy, the resources assessed in this thesis might come with some limitations. One important limitation is the use of actuator discs to represent turbines. This simplification will lead to an overestimate of the power.

This great opportunity also comes with a challenge. Although there is potential, the Tidal Energy Conversion (TEC) power plant might struggle to make the tariffs meet the standard price (BPP) in

Indonesia (see Table 7-1). Government intervention in regulatory aspects, such as the tariff regime, might be essential for the materialisation of tidal energy investment in Indonesia.

Table 7-1: The summary of tidal resources assessment in Indonesian water

Location	Potential Arrays Length	Theoretical Resources	Realistic Resources		Environmental Constraints		Economic Viability	
			$\frac{\overline{P_1}}{n_t.A_t}$	*AEP*	Conflict	Remarks	*LCOE*	*Estimated Tariffs*
		(MW)	(kW/m^2)	(GWh)			(GBP/MWh)	
The Larantuka Strait								
The proposed Bridge	~0.8 km	3.50 - 17.0	3.5 - 3.3	30-85	Yes	Migratory Pathway	51 - 167	250.0
The most potential location	~0.9 km		4.2 - 4.5	72-93	Yes	Migratory Pathway	45 - 125	250.0
The Lombok Strait								
Nusa Lembongan	4 × ~3.0 km	21.8 - 231.6	0.8 - 0.9	257.31	Yes	MPA (Seaweed farm)	N/A	N/A
Toyopakeh	5 × ~0.8 km	7.2 - 27.8	N/A	245.36	Yes	MPA (Core, Hatchery)	N/A	N/A
Nusa Penida	5 × ~3.0 km	51 - 273	0.9 - 1.1	265.16	Yes	MPA (Core, Hatchery)	N/A	N/A
Lombok	5 × ~3.0 km	40 - 252	0.9 - 1.0	252.97	No	N/A	128 - 327	250.0
Sunda Strait Bridge (SSB)								
SS1	~10.4 km	32 - 227	0.2 - 0.3	173.84	No	N/A	128 - 312	N/A
SS2	~7.9 km	90 - 460	0.3 - 0.8	268.82	No	N/A	125 - 305	N/A
Lingga Regency								
Temiang Strait	~1.3 km	0.8 - 4.3	0.4 - 0.6	44.28	No	N/A	820 - 2,000	N/A
Dasi Strait	~3.3 km	0.5 - 1.0	0.2 - 0.4	25.23	No	N/A	1,100 - 2,700	N/A
Sula Regency								
Capalulu Strait	~2.3 km	14.50 - 51.40	1.6 - 2.4	48.53	No	N/A	57 - 140	N/A
Mangola Strait	~4.2 km	4.48 - 20.62	0.6 - 0.7	64.37	No	N/A	90 - 217	N/A
Lifamatola Strait	~0.9 km	2.55 - 11.18	N/A	N/A	No	N/A	N/A	N/A
Lifamatola Headland	~4.0 km	74.60 - 226.3	0.6 - 0.8	169.70	Yes	Migratory Pathway	74 - 180	N/A

7.1.2 General Findings

There are some general findings that are perhaps noteworthy for a tidal resource assessment or for the marine renewable energy field in general; these are summarised here. One of the important issues is the characteristics of the tidal power variation in a tidal regime with multiple constituents. Some new metrics are introduced, and the utility of the metrics is demonstrated here.

a) The Appropriate Number of Constituents in An Assessment

This thesis assesses tidal energy resource in a region with pronounced diurnal constituents (K_1 and O_1). As discussed in Chapter 1, the UK and Canadian waters are areas with dominant semidiurnal components, so the tidal resource assessments in the UK and Canada could be conducted using only one or two semidiurnal constituents (M_2 only or both M_2 and S_2). This method apparently could give satisfactory results with a simulation that is less computationally demanding. Meanwhile, in Indonesia, most of the area exhibits strong mixed diurnal components.

We might think an assessment in a diurnal tidal regime could be conducted by using a K_1 and O_1 driven model. However, this thesis found that such a simplification could lead to underestimates or overestimates of the resource. Therefore, the assessment with the constituent reduction method is full of uncertainty. Furthermore, the assessments driven by a single constituent might unable to capture the site-site interactions correctly. For example, the site-site interactions might be different if run with limited constituents (see Chapter 5).

b) *Semidiurnal-Diurnal Pattern and Formzhal Number*

The dominant constituents in water surface elevation (WSE) do not necessarily correspond to the dominant constituents of the tidal current. The semidiurnal-diurnal category in the WSE (commonly using a *Formzahl* number or a form factor) might be misleading if used directly in tidal resource assessment. For example, the sites in Lingga Regency have a diurnal tidal regime based on WSE. However, the flow in that area does not conform with that pattern, but the tidal flows in that area follow a mixed diurnal pattern. Meanwhile, the WSE in the Sunda Straits is semidiurnal, but, the flow is diurnal.

Therefore, this thesis introduces the velocity *Formzahl* number (f_v) as an indicator of tidal velocity pattern. The f_v is distinguished from the commonly used WSE *Formzahl* (f_η). This thesis also demonstrates there is no simple correlation between f_v and f_η.

c) *Power and Thrust Variations*

Having an area with strong diurnal components also means the power and thrust also vary. The power and thrust do not just vary on a daily basis. This thesis found that an area with relatively equal semidiurnal-diurnal components will also have an annual variation, which follows the solstice-equinox cycle pattern. This means that an assessment conducted at the equinox time (the vernal equinox on March 21st and the autumnal equinox on September 21st) or solstice time (the summer solstice on June 21st and the winter solstice in December 21st) might give an underestimate or overestimate of power.

Therefore an assessment in Indonesian waters should avoid running simulations with the initial time around the solstice or equinox periods if it is only run for a short period of say one, two or even four neap-spring cycles. This thesis also argues that any current measurements or tidal elevation observations for a tidal resource assessment study should avoid being conducted at the solstice or equinox times.

d) *Tidal Asymmetry*

The interaction of semidiurnal and diurnal components creates an asymmetric pattern. This tidal asymmetry makes the flow move unevenly in a bi-directional flow. It is worth considering this asymmetric phenomenon in turbine design for deployment in mixed-diurnal areas. The asymmetry also makes the capacity factor (*CF*) naturally low. Applying power or thrust capping might not increase *CF* without losing significant potential average power. Therefore, a decision-making process in any mixed-diurnal area, and perhaps in semidiurnal and diurnal areas as well, should not just rely on the *CF*.

e) *Power Capping and Thrust Capping Strategies*

This thesis introduces various capping metrics and demonstrates the utility of the metrics in the assessments. The power factor (F_P), thrust factor (F_T) and maximum thrust factor ($F_{T,max}$) are convenient parameters for an assessment of the capping strategies. Both capping strategies could maintain the average power removed by the turbine as close as possible to the $\overline{P}_1$ without a capping strategy ($F_P = 1$). At the same time, the maximum thrust is truncated as low as possible. Therefore, this thesis argues that the F_P and $F_{T,max}$ are more important than the *CF* as indicators in decision-making regarding tidal energy exploitation.

f) *Turbine Performance in a Sheared Flow*

Since the thermohaline circulation passes through Indonesia, a strong flow stratification occurs in this area. The terms flow-stratification and sheared-flow are not interchangeable. There are fundamental differences in the terms used. Flow stratification is usually used in the oceanographic field to describe the vertically varied flow, due to the interaction of thermohaline currents and another current. The flow stratification is maintained by the density difference due to temperature and salinity differences in a water column. Therefore flow stratification usually refers to flow speed differences in deep waters. Meanwhile, sheared flow usually refers to flow speed differences in a water column due to friction from the seabed. Therefore, sheared flow is used by the tidal turbine community to explain such phenomenon which usually occur in relatively shallow water.

However, these phenomena are similar in regard to tidal turbine performance. Initially, the existence of strongly sheared flow was thought to affect turbine performance. Chapter 3 is essentially dedicated to investigating this issue. However, the difference in turbine performance in a sheared flow is small for the blockage ratios considered. Therefore, the available theoretical approaches that were developed based on the uniform flow are still valid in such areas. It is also important to emphasize here that the investigation in Chapter 3 addresses the sheared flow problem rather than the flow stratification.

g) The utility of Kinetic Energy

This thesis also demonstrates that kinetic energy flux is useful for an assessment (see Chapter 5). The potential locations could be determined by looking at the highest average kinetic power density in an area. However, the kinetic power might be insufficient for a proper resource assessment. An assessment is not just about determining the potential location but also determines the magnitude of available power.

h) Local Blockage (B_L), Global Blockage (B_G) and Flow-Field Changes

This thesis also encountered the complex problem of local and global blockage interactions while exploring the opportunities of using a realistic turbine deployment. In this thesis, some cases show that an array with a larger B_L will remove a larger power from the stream than an array with smaller B_L, although that array has smaller B_G. However, in other cases, it is shown that the B_G is still important regarding the extraction of power by the turbine array. For instance, the Larantuka case shows that B_L plays an important role in having a higher $\overline{P}_1$. However, the Sula Regency assessment shows that B_G is more important.

An array with a higher $\overline{P}_1$ has an increasing flow-field change in the bypass flow area, although its B_L or B_G is low. Therefore, this thesis argues that occupying the channel's entire cross-section might be a disadvantage. However, the reason for this is as yet unknown, and therefore, no strong conclusion can be drawn.

The flow field changes are also found useful to understand further the results and consequences of introducing the turbines into a stream. For example, in the Bali-Lombok channel, flow diversion might explain some peculiar results in the assessment and the site-site interactions. Flow field changes are also used to analyse the effect of turbine arrays on the global current.

7.2 Future Research

This thesis has presented a preliminary assessment of the potential for tidal energy in Indonesia. It concluded that there are multiple opportunities for development, but much detailed work remains to be done. For instance, uncertainty in the tidal energy extraction, deeper economic analyses, and application to the other potential locations in the assessment are all gaps in understanding and could be recommended for a holistic assessment in the future.

The future research recommended in this thesis is also to understand the impact of tidal turbine deployment on the environment. Humans are good at inventing to solve problems, but we often fail to anticipate our invention's consequences. Tidal energy is not just to answer the scarcity of fossil fuel, but also to provide another source of power that is more environmentally friendly. However, we often forget that every perturbation to the natural flow could disturb nature's equilibrium. Therefore, understanding the impact on nature would be a wise step.

7.2.1 Uncertainty of tidal energy extraction

There are uncertainties in the tidal energy extraction, from the understanding of the nature of tidal variation and its coupling with other phenomena such as wind and wave to the nature of power generation from the tidal stream as well. Kreitmair, 2018 and Kreitmair *et al.*, 2019 discuss the uncertainty issue due to bed friction. However, this thesis implies there are other uncertainties due to tidal variation and the current ocean phenomenon in general. For instance, complexity of effects of stratified flow on the turbine might also add uncertainty as this thesis only investigates the turbine performance in sheared flow. This uncertainty might be worth investigating in the future.

7.2.2 Further Economic studies

This thesis has conducted a financial analysis. However, the analyses are still in the preliminary stage to demonstrate what can be done for the actual projects in Indonesia. Therefore, it requires deeper analyses before such investment is undertaken. A deeper study is also required in terms of power purchasing contract between the government and the private sector. A thorough study in economic and financial fields might be required for such problems.

7.2.3 Environmental Impact Issues

This thesis found that some of the promising locations might conflict with the environment. For instance, the most promising location in the Lombok Strait is in the core zone of a marine protected area. This location is a natural breeding area for the pelagic fish. Deploying tidal turbines in this site might harm this important ecosystem.

As briefly discussed in Chapter 6, tidal energy exploitation in such an area might have detrimental environmental effects. A disturbance in the natural breeding area could harm the spawning process of the fish. This area is also an important migratory corridor for endangered species such as blue whale. Furthermore, this thesis also shows a significant change in the flow-field when the turbines are introduced to the water. Therefore, although ostensibly environmentally friendly, turbine deployment in the ocean water might affect marine life in the area. Understanding the impact perhaps could prevent some unwanted outcomes from the tidal energy extraction. Therefore, a comprehensive environmental impact study is necessary before installing turbines in Indonesian waters.

7.2.4 Tidal Energy Exploitation Effect on the Global Current

As discussed in this thesis, the Indonesian Through Flow (ITF) is the manifestation of the global-current in Indonesian waters. Most of the potential locations are in the pathway of this ITF. Therefore, there is a possibility that the turbine fences will obstruct this current. Such issues should be addressed, as the ITF is related to the so-called "Great Ocean Conveyor Belt" and this phenomenon is related to the global climate. Causing a global-current change might affect the global ocean system.

This thesis does not try to answer the questions on what happens to the climate when the turbine fences obstruct the current. However, such an analysis might give an early understanding of how the turbine arrays might affect the global-current. The questions remain open for further researches in the oceanographic-climate related field. Therefore, this well-intentioned endeavour, shifting from fossil fuel energy sources to a more eco-friendly source such as tidal energy, should not lead us to another catastrophic problem.

7.2.5 Application to Other Potential Sites in Indonesia

As mentioned in Chapter 1, there are many potential sites for tidal energy generation in Indonesia. Besides the five locations selected in this thesis, there are ten locations that are already recognised as potential locations. The potential sites might not just be limited to the ten potential locations. For instance, this thesis shows that the narrow straits in the Bali-Nusa Tenggara islands chain exhibit strong currents. These locations might be worth investigating in the future.

7.2.6 Further Complexity and Turbine Optimisation Studies

This thesis revealed complexities in the tidal flow variation. However, the investigation is limited to the astronomical and long-term tidal constituents. Meanwhile, there are other constituents such as the shallow-water constituents such as M_4 and M_6 that might create further complexity. Furthermore, the interaction with other natural forces such as wind and wave is another source of complexity. Moreover, the stochastic nature of wind and wave make the interaction even more complex than the deterministic factors such as shallow-water constituents.

Furthermore, the analyses of the capping strategy in this thesis demonstrated the opportunities for turbine operation optimisation. Therefore, turbine performance optimisation with appropriate optimisation tools might be worth investigating in the future.

References

Adcock, T. A. A., Borthwick, A. G. L., & Houlsby, G. T. (2011). *The open boundary problem in modelling tidal energy extraction*. 9th EWTEC, Southampton, U.K.

Adcock, T. A. A., & Draper, S. (2014). Power extraction from tidal channels – Multiple tidal constituents, compound tides and overtides. *Renewable Energy*, *63*, 797–806.

Adcock, T. A. A., Draper, S., Houlsby, G. T., Borthwick, A. G. L., & Serhadlıoğlu, S. (2013). The available power from tidal stream turbines in the Pentland Firth. *Proceedings of the Royal Society A: Mathematical, Physical and Engineering Sciences*, *469*(2157), 20130072.

Adcock, T. A. A., Draper, S., & Nishino, T. (2015). Tidal power generation – A review of hydrodynamic modelling. *Proceedings of the Institution of Mechanical Engineers, Part A: Journal of Power and Energy*, *229*(7), 755–771.

Adcock, T. A. A., Draper, S., Willden, R. H. J., & Vogel, C. R. (2021). The Fluid Mechanics of Tidal Stream Energy Conversion. *Annual Review of Fluid Mechanics*, *53*(1), 287–310.

Ahmadian, R. and Falconer, R.A. (2012). Assessment of array shape of tidal stream turbines on hydro-environmental impacts and power output, *Renewable Energy*, 44: 318-327.

Alisjahbana, A. S., & Busch, J. M. (2017). Forestry, Forest Fires, and Climate Change in Indonesia. *Bulletin of Indonesian Economic Studies*, *53*(2), 111–136.

Allan, G., Gilmartin, M., McGregor, P., & Swales, K. (2011). Levelised costs of Wave and Tidal energy in the UK: Cost competitiveness and the importance of “banded” Renewables Obligation Certificates. *Energy Policy*, *39*(1), 23–39.

ANDRITZ HYDRO Hammerfest. (2012). *Renewable energy from tidal currents* (AH Hammerfest.01.en 04.12). ANDRITZ HYDRO Hammerfest P.O. BOX 403 N-9615 Hammerfest, Norway.

ANSYS, Inc. (2018). *ANSYS ICEM CFD Tutorial Manual*.

Arief, D., & Murray, S. P. (1996). Low-frequency fluctuations in the Indonesian throughflow through Lombok Strait. *Journal of Geophysical Research: Oceans*, *101*(C5), 12455–12464.

Astariz, S., Vazquez, A., & Iglesias, G. (2015). Evaluation and comparison of the levelized cost of tidal, wave, and offshore wind energy. *Journal of Renewable and Sustainable Energy*, *7*(5), 053112.

BPS Bali (2020). *Badan Pusat Statistik Provinsi Bali* [Dataset]. https://bali.bps.go.id

Betz, A. (1920). Das Maximum der Theoretisch Moglichen Ausnutzung des Windes durch Wind-motoren. *Zeitschrift Für Das Gesamte Turbinenwesen*, *26*, 307–309.

Black and Veatch (2005). Phase II UK tidal stream energy resource assessment. *Technical Report, London:* Black & Veatch Corporation.

Blanchfield, J., Garrett, C., Rowe, A., & Wild, P. (2008). Tidal stream power resource assessment for Masset Sound, Haida Gwaii. *Proceedings of the Institution of Mechanical Engineers, Part A: Journal of Power and Energy*, *222*(5), 485–492.

Blanton, J. O., Lin, G., & Elston, S. A. (2002). Tidal current asymmetry in shallow estuaries and tidal creeks. *Continental Shelf Research*, *22*(11–13), 1731–1743.

Blunden, L. S., Bahaj, A. S., & Aziz, N. S. (2013). Tidal current power for Indonesia? An initial resource estimation for the Alas Strait. *Renewable Energy*, *49*, 137–142.

Bonar, P. A. J., Chen, L., Schnabl, A. M., Venugopal, V., Borthwick, A. G. L., & Adcock, T. A. A. (2019). On the arrangement of tidal turbines in rough and oscillatory channel flow. *Journal of Fluid Mechanics*, *865*, 790–810.

Boud, R. (2003), Status and Research Development Priorities for Marine Current and Wave Energy. *AEAT report number AEAT/ENV/1054*, International Energy Agency.

BPPT. (2016). *Outlook Energi Indonesia (Indonesia Energy Outlook) 2016* (ISBN 978-602-74702-0-0). Pusat Teknologi Sumber Daya Energi Dan Industri Kimia (Center For Technology Of Energy Resources And Chemical), Badan Pengkajian Dan Penerapan Teknologi (Agency for The Assessment And Application Of Technology). https://www.bppt.go.id

BPS. (2018, July 3). *Statistik Indonesia (Statistical Yearbook of Indonesia)* [Dataset]. Badan Pusat Statistik/BPS-Statistics Indonesia.

https://www.bps.go.id/publication/2018/07/03/5a963c1ea9b0fed6497d0845/statistik-indonesia-2018.html

BPS. (2019, July 4). *Statistik Indonesia (Statistical Yearbook of Indonesia) 2019* [Dataset]. Badan Pusat Statistik. https://www.bps.go.id/publication/2019/07/04/daac1ba18cae1e90706ee58a/statistik-indonesia-2019.html

Bray, N. A., Wijffels, S. E., Chong, J. C., Fieux, M., Hautala, S., Meyers, G., & Morawitz, W. M. L. (1997). Characteristics of the Indo-Pacific Throughflow in the eastern Indian Ocean. *Geophysical Research Letters*, *24*(21), 2569–2572.

Bryden, I. G., & Couch, S. J. (2007). How much energy can be extracted from moving water with a free surface: A question of importance in the field of tidal current energy? *Renewable Energy*, *32*(11), 1961–1966.

Cahya, G. H. (2020, February 26). Climate change cause of Greater Jakarta floods, BMKG says. *The Jakarta Post*. https://www.thejakartapost.com/news/2020/02/26/climate-change-behind-2020-floods-that-displaced-thousands-in-jakarta-agency-says.html

Chen, L., Bonar, P. A. J., Vogel, C. R., & Adcock, T. A. A. (2019). A note on the tuning of tidal turbines in channels. *Journal of Ocean Engineering and Marine Energy*, *5*(1), 85–98.

Chen, X., & Nordhaus, W. D. (2011). Using luminosity data as a proxy for economic statistics. *Proceedings of the National Academy of Sciences*, *108*(21), 8589–8594.

Chernetsky, A. S., Schuttelaars, H. M., & Talke, S. A. (2010). The effect of tidal asymmetry and temporal settling lag on sediment trapping in tidal estuaries. *Ocean Dynamics*, *60*(5), 1219–1241.

Coles, D. S., Blunden, L. S., & Bahaj, A. S. (2017). Assessment of the energy extraction potential at tidal sites around the Channel Islands. *Energy*, *124*, 171–186.

Coles, D. S., Blunden, L. S., & Bahaj, A. S. (2020). The energy yield potential of a large tidal stream turbine array in the Alderney Race. *Philosophical Transactions of the Royal Society A: Mathematical, Physical and Engineering Sciences*, *378*(2178), 20190502.

Coordinating Team of Research and Technology. (2008). *Final report on Current Measurement on two location with mechanical Team of Pda Archimede, Italy in West Lombok (report in Bahasa Indonesia)*. Centre of Marine Geology Research and Development, Ministry of Energy and Mineral Resources, Republic of Indonesia.

Dadswell, M. J., Spares, A. D., Mclean, M. F., Harris, P. J., & Rulifson, R. A. (2018). Long-term effect of a tidal, hydroelectric propeller turbine on the populations of three anadromous fish species. *Journal of Fish Biology*, *93*(2), 192–206.

Diela, T., & Widianto, S. (2020, January 5). After Indonesia’s deadly floods, few hear climate ‘wake up call’. *Reuters*. https://www.reuters.com/article/us-indonesia-floods-climate-change-idUSKBN1Z305X

DISHIDROS. (2004). *Daftar Pasang Surut Kepulauan Indonesia (Tide Tables Indonesian Archipelago)*. Dinas Hidrooseanografi TNI AL, Republik Indonesia.

Doodson, A. T., & Warburg, H. D. (1941). *Admiralty Manual of Tides*. H.M. Stationery Office.

Double, M. C., Andrews-Goff, V., Jenner, K. C. S., Jenner, M.-N., Laverick, S. M., Branch, T. A., & Gales, N. J. (2014). Migratory Movements of Pygmy Blue Whales (Balaenoptera musculus brevicauda) between Australia and Indonesia as Revealed by Satellite Telemetry. *PLoS ONE*, *9*(4), e93578.

Draper, S. (2011). *Tidal Stream Energy Extraction in Coastal Basins* (PhD Thesis). University of Oxford

Draper, S., Adcock, T. A. A., Borthwick, A. G. L., & Houlsby, G. T. (2014). Estimate of the tidal stream power resource of the Pentland Firth. *Renewable Energy*, *63*, 650–657.

Draper, S., Houlsby, G. T., Oldfield, M. L. G., & Borthwick, A. G. L. (2010). Modelling tidal energy extraction in a depth-averaged coastal domain. *IET Renewable Power Generation*, *4*(6), 545.

Draper, S., Nishino, T., Adcock, T. A. A., & Taylor, P. H. (2016). Performance of an ideal turbine in an inviscid shear flow. *Journal of Fluid Mechanics*, *796*, 86–112.

Dronkers, J. (1986). Tidal asymmetry and estuarine morphology. *Netherlands Journal of Sea Research*, *20*(2–3), 117–131.

EMEC. (2020, February 19). *Tidal developers: EMEC: European Marine Energy Centre*. Http://Www.Emec.Org.Uk/. http://www.emec.org.uk/marine-energy/tidal-developers/

Encyclopaedia Britannica. (2020). *Thermohaline circulation | oceanography*. Retrieved January 2 2020, from https://www.britannica.com/science/thermohaline-circulation

Feng, M., Zhang, N., Liu, Q., & Wijffels, S. (2018). The Indonesian throughflow, its variability and centennial change. *Geoscience Letters*, *5*(1), 6342–6355.

Fieux, M., Andrié, C., Charriaud, E., Ilahude, A. G., Metzl, N., Molcard, R., & Swallow, J. C. (1996). Hydrological and chlorofluoromethane measurements of the Indonesian throughflow entering the Indian Ocean. *Journal of Geophysical Research: Oceans*, *101*(C5), 12433–12454.

Firdaus, A. M., Houlsby, G. T., & Adcock, T. A. A. (2019). Resource estimates in Lombok Straits, Indonesia. *Proceeding of 13th European Wave and Tidal Energy Conference, 2019. ISSN 2309-1983*. 13th European Wave and Tidal Energy Conference, 2019, Naples, Italy.

Firdaus, A. M., Houlsby, G. T., & Adcock, T. A. A. (2020). Tidal energy resource in Larantuka Strait, Indonesia. *Proceedings of the Institution of Civil Engineers - Energy*, *173*(2), 81–92.

Firdaus, A. M., Houlsby, G. T., & Adcock, T. A. A. (2017). Opportunities for Tidal Stream Energy in Indonesian Waters. *Proceedings of the 12th European Wave and Tidal Energy Conference 2017. (ISSN 2309-1983)*, 887-1-887–7.

Fleming, C. F. (2014). *Tidal turbine performance in the offshore environment* (PhD Thesis). University of Oxford.

Foreman, M. G. G., & Henry, R. F. (1989). The harmonic analysis of tidal model time series. *Advances in Water Resources*, *12*(3), 109–120.

Fraenkel, P.L., (2007). Marine current turbines: pioneering the development of marine kinetic energy converters, *P. Mech. Eng. A: J. Pow*., 221: 159-169.

Froude, R. E. (1889). On the part played in propulsion by differences of fluid pressure. *Transaction of the Institute of Naval Architects*, *30*, 390–405.

Garrett, C., & Greenberg, D. (1977). Predicting Changes in Tidal Regime: The Open Boundary Problem. *Journal of Physical Oceanography*, *7*(2), 171–181.

Garrett, C. & Cummins, P. (2004). Generating tidal power from currents. *J Waterway, Port, Coastal and Ocean Eng*, 130:114–118.

Garrett, C., & Cummins, P. (2005). The power potential of tidal currents in channels. *Proceedings of the Royal Society A: Mathematical, Physical and Engineering Sciences*, *461*(2060), 2563–2572.

Garrett, C., & Cummins, P. (2007). The efficiency of a turbine in a tidal channel. *Journal of Fluid Mechanics*, *588*, 243–251.

Gaurier, B., Druault, P., Ikhennicheu, M., & Germain, G. (2020). Experimental analysis of the shear flow effect on tidal turbine blade root force from three-dimensional mean flow reconstruction. *Philos T R Soc A*, *378*(2178), 20200001.

Godfrey, J. S. (1996). The effect of the Indonesian throughflow on ocean circulation and heat exchange with the atmosphere: A review. *Journal of Geophysical Research: Oceans*, *101*(C5), 12217–12237.

Godin, G. (1972). *Analysis of Tides*. University of Toronto Press.

Gordon, A. (2005). Oceanography of the Indonesian Seas and Their Throughflow. *Oceanography*, *18*(4), 14–27.

Gordon, A. L., Huber, B. A., Metzger, E. J., Susanto, R. D., Hurlburt, H. E., & Adi, T. R. (2012). South China Sea throughflow impact on the Indonesian throughflow. *Geophysical Research Letters*, *39*(11).

Gordon, A. L., Ma, S., Olson, D. B., Hacker, P., Ffield, A., Talley, L. D., Wilson, D., & Baringer, M. (1997). Advection and diffusion of Indonesian Throughflow Water within the Indian Ocean South Equatorial Current. *Geophysical Research Letters*, *24*(21), 2573–2576.

Gordon, A. L., Sprintall, J., Van Aken, H. M., Susanto, D., Wijffels, S., Molcard, R., Ffield, A., Pranowo, W., & Wirasantosa, S. (2010). The Indonesian throughflow during 2004–2006 as observed by the INSTANT program. *Dynamics of Atmospheres and Oceans*, *50*(2), 115–128.

Goward Brown, A. J., Neill, S. P., & Lewis, M. J. (2017). Tidal energy extraction in three-dimensional ocean models. *Renewable Energy*, *114*, 244–257.

Hautala, S. L., Sprintall, J., Potemra, J. T., Chong, J. C., Pandoe, W., Bray, N., & Ilahude, A. G. (2001). Velocity structure and transport of the Indonesian Throughflow in the major straits restricting flow into the Indian Ocean. *Journal of Geophysical Research: Oceans*, *106*(C9), 19527–19546.

Herawati, H., & Santoso, H. (2011). Tropical forest susceptibility to and risk of fire under changing climate: A review of fire nature, policy and institutions in Indonesia. *Forest Policy and Economics*, *13*(4), 227–233.

Hicks, R. (2017, May 9). Indonesia to build 'world's largest' tidal power plant. *Eco-Business*. https://www.eco-business.com/news/indonesia-to-build-worlds-largest-tidal-power-plant/

Hicks, S. D. (2006). *Understanding tides*. NOAA National Ocean Service.

Hoitink, A. J. F., Hoekstra, P., & van Maren, D. S. (2003). Flow asymmetry associated with astronomical tides: Implications for the residual transport of sediment. *Journal of Geophysical Research*, *108*(C10), 1–13.

Houlsby, G. T., Draper, S., & Oldfield, M. L. G. (2008). *Application of linear momentum actuator disc theory to open channel flow* (OUEL Report 2297/08). Dept. of Engineering Science, University of Oxford.

Houlsby, G. T., & Vogel, C. R. (2017). The power available to tidal turbines in an open channel flow. *Proceedings of the Institution of Civil Engineers - Energy*, *170*(1), 12–21.

Karsten, R. H., McMillan, J. M., Lickley, M. J., & Haynes, R. D. (2008). Assessment of tidal current energy in the Minas Passage, Bay of Fundy. *Proceedings of the Institution of Mechanical Engineers, Part A: Journal of Power and Energy*, *222*(5), 493–507.

Kashino, Y., Watanabe, H., Herunadi, B., Aoyama, M., & Hartoyo, D. (1999). Current variability at the Pacific entrance of the Indonesian Throughflow. *Journal of Geophysical Research: Oceans*, *104*(C5), 11021–11035.

Ke, S., Wen-Quan, W., & Yan, Y. (2020). The hydrodynamic performance of a tidal-stream turbine in shear flow. *Ocean Engineering*, *199*, 107035.

Koropitan, A. F., & Ikeda, M. (2008). Three-dimensional modeling of tidal circulation and mixing over the Java Sea. *Journal of Oceanography*, *64*(1), 61–80.

Kreitmair, M. J. (2018). *Uncertainty Quantification in Tidal Energy Resource Assessment* (PhD Thesis). University of Edinburgh. http://hdl.handle.net/1842/36084

Kreitmair, M. J., Draper, S., Borthwick, A. G. L., & van den Bremer, T. S. (2019). The effect of uncertain bottom friction on estimates of tidal current power. *Royal Society Open Science*, *6*(1), 180941. https://doi.org/10.1098/rsos.180941

Kubatko, E. J., Westerink, J.J., and Dawson, C. (2006a). hp Discontinuous Galerkin methods for advection dominated problems in shallow water flow, *Comput. Methods Appl. Mech.Engrg*., 196: 437-451.

Kubatko, E. J., Westerink, J.J., and Dawson, C. (2006b). An unstructured grid morphodynamic model with a discontinuous Galerkin method for bed evolution. *Ocean Modelling*, 15: 71-89

Kunaifi, & Reinders, A. (2018). Perceived and Reported Reliability of the Electricity Supply at Three Urban Locations in Indonesia. *Energies*, 11(1), 140.

Lamy, J. V., & Azevedo, I. L. (2018). Do tidal stream energy projects offer more value than offshore wind farms? A case study in the United Kingdom. *Energy Policy*, *113*, 28–40.

Lanchester, F. W. (1915). A contribution to the theory of propulsion and the screw propeller. *Journal of the American Society for Naval Engineers*, *27*(2), 509–510.

Launder, B. E., & Spalding, D. B. (1974). The numerical computation of turbulent flows. *Computer Methods in Applied Mechanics and Engineering*, *3*(2), 269–289.

Le Provost, C. (1991). Generation of overtides and compound tides (review). *Tidal Hydrodynamics. John Wiley and Sons., In Parker, Bruce B. (ed.)*, 269–295.

Le Provost, C., Genco, M. L., Lyard, F., Vincent, P., & Canceil, P. (1994). Spectroscopy of the world ocean tides from a finite element hydrodynamic model. *Journal of Geophysical Research*, *99*(C12), 24777.

Le Provost, C., Genco, M.-L., & Lyard, F. (1995). Modeling and predicting tides over the World Ocean. *Quantitative Skill Assessment for Coastal Ocean Models*, 175–201.

Lukas, R., Yamagata, T., & McCreary, J. P. (1996). Pacific low-latitude western boundary currents and the Indonesian throughflow. *Journal of Geophysical Research: Oceans*, *101*(C5), 12209–12216.

Lin, J., Borthwick, A., Lin, B., & Draper, S. (2020). Power extraction by a water turbine in inviscid free surface flow with vertical shear. *European Journal of Mechanics - B/Fluids*, *79*, 401–418. https://doi.org/10.1016/j.euromechflu.2019.10.002

Law (Indonesia) number 34/2014 on ocean utilities (UU Nomor 32 Tahun 2014 tentang Kelautan). Available at http://jdih.kkp.go.id/peraturan/1-uu-32-2014.pdf (Accessed: January 2020).

MacKay, D (2007). *Under-estimation of the UK tidal resource*. Technical Report, Cavendish Laboratory, University of Cambridge.

Mayer, B., Damm, P. E., Pohlmann, T., & Rizal, S. (2010). What is driving the ITF? An illumination of the Indonesian throughflow with a numerical nested model system. *Dynamics of Atmospheres and Oceans*, *50*(2), 301–312.

Mazda, Y., Kanazawa, N., & Wolanski, E. (1995). Tidal asymmetry in mangrove creeks. *Hydrobiologia*, *295*(1–3), 51–58.

McNaughton, J. (2013). *Turbulence modelling in the near-field of an axial flow tidal turbine using Code_Saturne* (PhD Thesis). School of Mechanical, Aerospace & Civil Engineering, University of Manchester.

Measey, M. (2010). Indonesia: A Vulnerable Country in the Face of Climate Change. *Global Majority E-Journal*, *1*(1), 31–45.

Menter, F. R. (1992). Influence of freestream values on k-omega turbulence model predictions. *AIAA Journal*, *30*(6), 1657–1659.

Menter, F. R. (1994). Two-equation eddy-viscosity turbulence models for engineering applications. *AIAA Journal*, *32*(8), 1598–1605.

Meyers, G., Bailey, R. J., & Worby, A. P. (1995). Geostrophic transport of Indonesian throughflow. *Deep Sea Research Part I: Oceanographic Research Papers*, *42*(7), 1163–1174.

Morey, S. L., Shriver, J. F., & O'Brien, J. J. (1999). The effects of Halmahera on the Indonesian throughflow. *Journal of Geophysical Research: Oceans*, *104*(C10), 23281–23296.

MoEMR. (2018). *Electrification Ratio 2017* [Dataset]. Kementrian Energi dan Sumber Daya Mineral/KESDM (Ministry of Energy and Mineral Resources/MoEMR).

Mukhtasor, Susilohadi, Erwandi, Pandoe, W., Iswadi, Firdaus, A. M., Prabowo, H., Sudjono, E., Prasetyo, E., & Ilahude, D. (2014). *Indonesian Ocean Energy Potency; Technical Notes on Indonesia Potential Ocean Energy (report in Bahasa Indonesia)*. Centre for Marine Geology Research and Development (P3GL), Ministry of Energy and Mineral Resources-Republic Indonesia and Indonesian Ocean Energy Association (INOCEAN).

Murray, S. P., & Arief, D. (1988). Throughflow into the Indian Ocean through the Lombok Strait, January 1985–January 1986. *Nature*, *333*(6172), 444–447.

Möller, L. M., Attard, C. R. M., Bilgmann, K., Andrews-Goff, V., Jonsen, I., Paton, D., & Double, M. C. (2020). Movements and behaviour of blue whales satellite tagged in an Australian upwelling system. *Scientific Reports*, *10*(1), 1–19.

Minister (Indonesia) of Energy and Mineral Resources (MoEMR) decree No 1772 K/20/MEM/2018 on electricity generation cost (Keputusan Mentri ESDM No 1772 K/20/MEM/2018 tentang Biaya Pokok Pembangkitan Listrik-BPP) available at https://jdih.esdm.go.id/storage/document/Kepmen-esdm-77-Thn%202019.pdf (Accessed: January 2020)

Minister (Indonesia) of Marine Affairs and Fisheries (MMAF) Decree No. 2/ 2009 regarding Marine Protected Area (MPA) Establishment Procedures (Peraturan Mentri Kelautan dan Perikanan PER.02/MEN/2009 Tentang Tata Cara Penetapan Kawasan Konservasi Perairan). Available at https://kkp.go.id/djprl/artikel/756-peraturan-menteri-kelautan-dan-perikanan-no-02-tahun-2009 (Accessed: January 2020)

Minister (Indonesia) of Marine Affairs and Fisheries (MMAF) Decree No. 30/2010 regarding MPA Management Plan and Zoning System (Peraturan Menteri Kelautan dan Perikanan Republik Indonesia Nomor Per.30/Men/2010 Tentang Rencana Pengelolaan Dan Zonasi Kawasan Konservasi Perairan). Available at http://jdih.kkp.go.id/peraturan/per-30-men-2010.pdf (Accessed: January 2020)

Minister (Indonesia) of Energy and Mineral Resources (MoEMR) No 50/2017 on utilisation of renewable energy sources of electricity provision (Peraturan Mentri ESDM No 50/2017 tentang pemanfaatan sumber energi terbarukan untuk penyediaan tenaga listrik). Available at https://jdih.esdm.go.id/peraturan/PerMen%20ESDM%20NO.%2050%20TAHUN%202017.pdf (Accessed: January 2020)

Neill, S. P., Hashemi, M. R., & Lewis, M. J. (2014). The role of tidal asymmetry in characterizing the tidal energy resource of Orkney. *Renewable Energy*, *68*, 337–350.

Nidzieko, N. J. (2010). Tidal asymmetry in estuaries with mixed semidiurnal/diurnal tides. *Journal of Geophysical Research*, *115*(C8), 1–13.

Nishino, T., & Willden, R. H. J. (2012a). Effects of 3-D channel blockage and turbulent wake mixing on the limit of power extraction by tidal turbines. *International Journal of Heat and Fluid Flow*, *37*, 123–135.

Nishino, T., & Willden, R. H. J. (2012b). The efficiency of an array of tidal turbines partially blocking a wide channel. *Journal of Fluid Mechanics*, *708*, 596–606.

Nishino, T., & Willden, R. H. J. (2013). Two-scale dynamics of flow past a partial cross-stream array of tidal turbines. *Journal of Fluid Mechanics*, *730*, 220–244.

NOAA. (2020). *Types and Causes of Tidal Cycles - Tides and Water Levels*. NOAA’s National Ocean Service Education. Retrieved January 2 2020, from https://oceanservice.noaa.gov/education/tutorial_tides/tides07_cycles.html#1

NOAA/NGDC. (2015). *VIIRS Daily Mosaic* [Dataset]. NOAA/NGDC - Earth Observation Group - Defense Meteorological Satellite Progam, Boulder. https://ngdc.noaa.gov/eog/

Novico, F., Astawa, I. N., Sinaga, A., & Ali, A. (2016). Seafloor Morphology Influences on Current Condition in a Sunda Strait Bridge Project Using Numerical Model. *Bulletin of the Marine Geology*, *30*(2), 55.

offshore-energy.biz. (2015, February 12). Sabella’s tidal turbines to power Indonesia. *Offshore Energy*. https://www.offshore-energy.biz/sabellas-tidal-turbines-to-power-indonesia/

O’Hara Murray, R., & Gallego, A. (2017). A modelling study of the tidal stream resource of the Pentland Firth, Scotland. *Renewable Energy*, *102*, 326–340.

Orhan, K., Mayerle, R., Narayanan, R., & Pandoe, W. (2017). Investigation of the energy potential from tidal stream currents in Indonesia. *Coastal Engineering Proceedings*, *35*, 10.

Orhan, K., Mayerle, R., & Pandoe, W. W. (2015). Assesment of Energy Production Potential from Tidal Stream Currents in Indonesia. *Energy Procedia*, *76*, 7–16.

Parker, B. B. (2007). *Tidal analysis and prediction* (NOAA Special Publication NOS CO-OPS 3). NOAA, NOS Center for Operational Oceanographic Products and Services Silver Spring, MD.

PLN. (2019). *Statistik PLN (PLN’s Statistic) 2018* (ISSN : 0852 - 8179) [Dataset]. Perusahaan Listrik Negara (State Electric Company-Indonesia). https://web.pln.co.id/statics/uploads/2019/07/Buku-Statistik-2018-vs-Indo-Final.pdf

Potemra, J. T., Hautala, S. L., & Sprintall, J. (2003). Vertical structure of Indonesian throughflow in a large-scale model. *Deep Sea Research Part II: Topical Studies in Oceanography*, *50*(12–13), 2143–2161.

Prabowo, H. (2012). *Main Report on Tidal Resources Ocean Energy (report in Bahasa Indonesia) Atlas Potensi Energi Laut*. M&E, Vol. 10, No. 4, December 2012.

Presidential (Indonesia) Regulation 2014 (PP No. 79/2014). Available at https://jdih.esdm.go.id/peraturan/PP%20No.%2079%20Thn%202014.pdf (Accessed: 20 January 2020)

Pugh, D. T. (1987). *Tides, Surges and Mean Sea-Level* (1st ed.) [E-book]. John Wiley & Sons, Ltd. http://eprints.soton.ac.uk/id/eprint/19157

PWC. (2018). *Power in Indonesia: Investment and Taxation Guide* (November 2017-5th edition). PwC Indonesia. https://www.pwc.com/id/en/energy-utilities-mining/assets/power/power-guide-2017.pdf

Rachmat, B. (2013). *An Academic Note on Tidal Resource Mapping for National Energy Security; case study in Bali-East Nusatenggara Waters (report in Bahasa Indonesia)*. Centre of Marine Geology Research and Development, Ministry of Energy and Mineral Resources, Republic of Indonesia.

Rachmayani, R., Nagara, G. A., Suprijo, T., & Ningsih, N. S. (2006, September). *Investigation of the Energy Potential from Tidal Stream Currents in Indonesia*. Environmental Technology and Management Conference 2006 September 7-8, 2006, Bandung, West Java, Indonesia.

Rahmstorf, S. (2002). Ocean circulation and climate during the past 120,000 years. *Nature*, *419*(6903), 207–214. https://doi.org/10.1038/nature01090

Rahmstorf, S., Box, J. E., Feulner, G., Mann, M. E., Robinson, A., Rutherford, S., & Schaffernicht, E. J. (2015). Exceptional twentieth-century slowdown in Atlantic Ocean overturning circulation. Nature Climate Change, 5(5), 475–480. https://doi.org/10.1038/nclimate2554

Ramos, V., & Iglesias, G. (2013). Performance assessment of Tidal Stream Turbines: A parametric approach. *Energy Conversion and Management*, *69*, 49–57.

Rankine, W. J. M. (1865). On the mechanical properties of propellers. *Transaction of the Institute of Naval Architects*, *6*, 13–39.

Ray, R., Egbert, G., & Erofeeva, S. (2005). A Brief Overview of Tides in the Indonesian Seas. *Oceanography*, *18*(4), 74–79. https://doi.org/10.5670/oceanog.2005.07

Robertson, R., & Ffield, A. (2008). Baroclinic tides in the Indonesian seas: Tidal fields and comparisons to observations. *Journal of Geophysical Research*, *113*(C7), 1–22.

RUPTL 2018-2027. Minister of Energy and Mineral Resources Decree No 1567 K/21/MEM 2018 on the Electricity Supply Business Plan (Rencana Umum Penyediaan Tenaga Listrik-RUPTL) 2018-2027. Available at https://web.pln.co.id/statics/uploads/2018/04/RUPTL-PLN-2018-2027.pdf. (Accessed: January 2020)

Sandro, R., Arnudin, Tussadiah, A., Utamy, R. M., Pridina, N., & Afifah, L. N. (2014). Study of Wind, Tidal Wave and Current Potential in Sunda Strait as an Alternative Energy. *Energy Procedia*, *47*, 242–249. https://doi.org/10.1016/j.egypro.2014.01.220

SBS International. (n.d.). *SBS Intl Ltd - Renewable Energy for everyone now - for a clean, green future*. SBS Intl Ltd. Retrieved 12 January 2020, from http://www.sbsintl.com/nautilus-150mw-project.html

Schureman, P. (1958). *Manual of Harmonic Analysis and Prediction of Tides* ([Revised 1940 edition reprinted 1958 with corrections, reprinted 2001]). United States Government Printing Office Washington, DC, 317pp. (US Coast and Geodetic Survey, Special Publication 98).

Scully, M. E., & Friedrichs, C. T. (2007). Sediment pumping by tidal asymmetry in a partially mixed estuary. *Journal of Geophysical Research*, *112*(C7), 1–12.

Segura, E., Morales, R., & Somolinos, J. (2017). Cost Assessment Methodology and Economic Viability of Tidal Energy Projects. *Energies*, *10*(11), 1806.

Serhadlıoğlu, S. (2014) *Tidal Stream Resource Assessment of the Anglesey Skerries and the Bristol Channel* (PhD Thesis). University of Oxford.

Serhadlıoğlu, S., Adcock, T. A. A., Houlsby, G. T., Draper, S., & Borthwick, A. G. L. (2013). Tidal stream energy resource assessment of the Anglesey Skerries. *International Journal of Marine Energy*, *3–4*, e98–e111.

SimecAtlantis Energy (2020). *Lombok, Indonesian Archipelago | Tidal Projects*. Simecatlantis. https://simecatlantis.com/projects/indonesia/

Sprintall, J., Gordon, A. L., Koch-Larrouy, A., Lee, T., Potemra, J. T., Pujiana, K., & Wijffels, S. E. (2014). The Indonesian seas and their role in the coupled ocean–climate system. *Nature Geoscience*, *7*(7), 487–492.

Sprintall, J., Wijffels, S. E., Molcard, R., & Jaya, I. (2009). Direct estimates of the Indonesian Throughflow entering the Indian Ocean: 2004–2006. *Journal of Geophysical Research*, *114*(C7), 1–19.

Susanto, R. D., & Song, Y. T. (2015). Indonesian throughflow proxy from satellite altimeters and gravimeters. *Journal of Geophysical Research: Oceans*, *120*(4), 2844–2855.

Sutherland, G., Foreman, M., & Garrett, C. (2007). Tidal current energy assessment for Johnstone Strait, Vancouver Island. *Proceedings of the Institution of Mechanical Engineers, Part A: Journal of Power and Energy*, *221*(2), 147–157.

Tharakan, P. (2015). *Summary of Indonesia's Energy Sector Assessment* (No. 09, December 2015). ADB Papers on Indonesia (Asian Development Bank). https://www.adb.org/sites/default/files/publication/178039/ino-paper-09-2015.pdf

The World Bank. (2020). *GDP growth (annual %) | Data* [Dataset]. World Bank national accounts data, and OECD National Accounts data files. https://data.worldbank.org/indicator/ny.gdp.mktp.kd.zg

Tidal Bridge DV. (2017). *Palmerah Tidal Bridge – Technical Feasibility* (SI_2017002_PS04_REP_00070).

Tidal Bridge DV. (2020, January 10). *The Indonesian electricity company PLN and signed a Memorandum of Understanding (MoU) for the development of tidal power plant in Flores.* https://www.tidalbridge.com/news/pln-and-tidal-bridge-signed-a-mou-partnership-in-development-of-tidal-power-plant-in-flores/

Tillinger, D., & Gordon, A. L. (2009). Fifty Years of the Indonesian Throughflow. *Journal of Climate*, *22*(23), 6342–6355.

Tyler, S., & Beiter, P. (2020). *2018 Cost of Wind Energy Review* (NREL/TP-5000-74598). Golden, CO: National Renewable Energy Laboratory.

van Aken, H. M., Brodjonegoro, I. S., & Jaya, I. (2009). The deep-water motion through the Lifamatola Passage and its contribution to the Indonesian throughflow. *Deep Sea Research Part I: Oceanographic Research Papers*, *56*(8), 1203–1216.

van Kuik, G. A. M. (2007). The Lanchester–Betz–Joukowsky limit. *Wind Energy*, *10*(3), 289–291.

Vazquez, A., & Iglesias, G. (2016a). A holistic method for selecting tidal stream energy hotspots under technical, economic and functional constraints. *Energy Conversion and Management*, *117*, 420–430.

Vazquez, A., & Iglesias, G. (2016b). Capital costs in tidal stream energy projects – A spatial approach. *Energy*, *107*, 215–226.

Vellinga, M., & Wood, R. A. (2007). Impacts of thermohaline circulation shutdown in the twenty-first century. *Climatic Change*, *91*(1–2), 43–63.

Vennell, R. (2011). Tuning tidal turbines in-concert to maximise farm efficiency. *Journal of Fluid Mechanics*, *671*, 587–604.

Vennell, R. (2012). The energetics of large tidal turbine arrays. *Renewable Energy*, *48*, 210–219.

Vermeer, L. J., Sørensen, J. N., & Crespo, A. (2003). Wind turbine wake aerodynamics. *Progress in Aerospace Sciences*, *39*(6–7), 467–510.

Vogel, C. R. (2014). *Theoretical Limits to Tidal Stream Energy Extraction* (PhD Thesis). University of Oxford.

Vogel, C. R., Willden, R. H. J., & Houlsby, G. T. (2019). Tidal stream turbine power capping in a head-driven tidal channel. *Renewable Energy*, *136*, 491–499.

Vranes, K., Gordon, A. L., & Ffield, A. (2002). The heat transport of the Indonesian Throughflow and implications for the Indian Ocean heat budget. *Deep Sea Research Part II: Topical Studies in Oceanography*, *49*(7–8), 1391–1410. https://doi.org/10.1016/s0967-0645(01)00150-3

Wang, T. (2017). *Application of combined power and thrust capping to tidal turbine farms* (Master's Thesis). University of Oxford.

Wang, T., & Adcock, T. A. A. (2019). Combined power and thrust capping in the design of tidal turbine farms. *Renewable Energy*, *133*, 1247–1256.

Whelan, J. I., Graham, J. M. R., & Peiró, J. (2009). A free-surface and blockage correction for tidal turbines. *Journal of Fluid Mechanics*, *624*, 281–291.

Wijffels, S., Sprintall, J., Fieux, M., & Bray, N. (2002). The JADE and WOCE I10/IR6 Throughflow sections in the southeast Indian Ocean. Part 1: water mass distribution and variability. *Deep Sea Research Part II: Topical Studies in Oceanography*, *49*(7–8), 1341–1362.

Wimshurst. (2018). *Tip Flow Corrections for Horizontal Axis Wind and Tidal Turbine Rotors* (PhD Thesis). University of Oxford.

Wiser, R., Jenni, K., Seel, J., Baker, E., Hand, M., Lantz, E., & Smith, A. (2016). Expert elicitation survey on future wind energy costs. *Nature Energy*, *1*(10), 1–8.

Wunsch, C. (2002). OCEANOGRAPHY: What Is the Thermohaline Circulation? *Science*, *298*(5596), 1179–1181.

www.bps.go.id. (2020). *Population Data Per Province* [Dataset]. BPS (Indonesian Statistical Beureau). https://www.bps.go.id/subject/12/kependudukan.html#subjekViewTab3 www.kepsulkab.bps.go.id/. (2016, July 22). *Population and Population Density of Sula Regency* [Dataset]. Badan Pusat Statistik Kabupaten Kepulauan Sula. https://kepsulkab.bps.go.id/statictable/2016/07/22/8/jumlah-penduduk-dan-laju-pertumbuhan-penduduk-kabupaten-kepulauan-sula-2010-2014-dan-2015.html

www.ntb.bps.go.id. (2020). *Badan Pusat Statistik Provinsi Nusa Tenggara Barat* [Dataset]. Badan Pusat Statistik Provinsi Nusa Tenggara Barat. https://ntb.bps.go.id/subject/12/kependudukan.html#subjekViewTab3

www.ntt.bps.go.id. (2020). *Projection of population 2010-2020 in Regencies and Cities (Proyeksi Penduduk 2010-2020 Menurut Kabupaten/Kota (Jiwa)), 2020* [Dataset]. BPS of Nusa Tenggara Timur Province. https://ntt.bps.go.id/indicator/12/28/1/proyeksi-penduduk-2010-2020-menurut-kabupaten-kota.html

Walkington, I. and Burrows, R. (2009) Modelling tidal stream power potential. *Applied Ocean Research*, 31(4): 239-245.

Wyrtki, K. (1961). *Physical Oceanography of the Southeast Asian waters 1961* (Scientific Results of Marine Investigations of the South China Sea and the Gulf of Thailand 1959-1961. NAGA REPORT Volume 2). The University of California Scripps Institution of Oceanography La Jolla, California.

Xia, J., Falconer, R.A. and Lin, B. (2010) Numerical model assessment of tidal stream energy resources in the Severn Estuary, UK, *Proceedings of the Institution of Mechanical Engineers Part A: Journal of Power and Energy*, 224(7): 969-983.

Yosi, M. (2013). *Research on Tidal Resources as New and Renewable Energy in Raja Ampat Water, West Papua (report in Bahasa Indonesia)*. Centre for Marine Geology Research and Development, Ministry of Energy and Mineral Resources, Republic of Indonesia.

Yuningsih, A. (2008). *Research Report on Tidal Resources as New and Renewable Energy in Toyopakeh (Bali) (report in Bahasa Indonesia)* (No.03/LAP/P2K/P3GL/X/2008). Research Report on Tidal Resources as New and Renewable Energy in Toyopakeh (Bali) (report in Bahasa Indonesia).

Zupone, G. L., Amelio, M., Barbarelli, S., Florio, G., Scornaienchi, N. M., & Cutrupi, A. (2015). Levelized Cost of Energy: A First Evaluation for a Self Balancing Kinetic Turbine. *Energy Procedia*, *75*, 283–293.